The Dissertation Committee for Clinton Miller Wood Certifies that this is the approved version of the following dissertation:

Field Investigation of Topographic Effects using Mine Seismicity

Committee:

Brady R. Cox, Supervisor

Loukas F. Kallivokas

Ellen M. Rathje

Kenneth H. Stokoe II

Clark R. Wilson

Field Investigation of Topographic Effects using Mine Seismicity

by

Clinton Miller Wood, B.S.C.E.; M.S.C.E.

Dissertation

Presented to the Faculty of the Graduate School of

The University of Texas at Austin

in Partial Fulfillment

of the Requirements

for the Degree of

Doctor of Philosophy

The University of Texas at Austin

August 2013

Acknowledgements

I would like to express my great appreciation to my advisor, Dr. Brady R. Cox. His support, guidance, and enthusiasm have been invaluable during my graduate career. He has involved me in so many challenging and interesting projects that have allowed me to travel all over the world, meet people throughout the profession, and gain firsthand knowledge in so many aspects of earthquake engineering. I will be forever grateful for all my graduate experiences. It has truly been a rewarding experience to work with him and to call him a dear friend.

I am grateful for the advice and help from my dissertation committee members, Dr. Loukas Kallivokas, Dr. Ellen Rathje, Dr. Kenneth Stokoe II, and Dr. Clark Wilson. I am also grateful for the advice and suggestions from the topographic effects research team, Dr. Adrian Rodriguez-Marek, Dr. Brady Cox, Dr. Dominic Assimaki, Dr. Miguel Pando, and Dr. Joseph Wartman.

I would like to extend my thanks to the faculty members at the University of Arkansas that expanded my knowledge in geotechnical engineering, Dr. Brady Cox, Dr. Norman Dennis, Dr. John McCartney, and Dr. Richard Coffman.

I am particularly grateful for the assistance of all the organizations and individuals that helped in setting up and conducting my experiments. In particular, I thank NEES@UTexas personnel, Dr. Farn-Yuh Menq and Robert Kent for their help in deploying the instrumentation and preparing the NEES equipment for the experiment, IRIS/PASSCAL personnel, particularly Steve Azevedo, and Jennifer Tarnowski, for their help deploying the instrumentation, Deer Creek Coal Mine personnel, particularity Clayton Cox and Ken Fleck, for information on the position, schedule, and operations of

the coal mine, and Curtis and Catherine Steel for letting us use their trucks, ATVs, and tools during the experiment. I would like to thank Dr. Kristine Pankow, Dr. James Pechmann, and Meagan Boltz, from the University of Utah, for their help in locating hypocenters. I would also like to thank Reinaldo Silvestry, Cristobal Afanador, and Richard Deschenes Jr. for their help in identifying the seismic events and picking P-wave arrivals.

I would like to acknowledge the support of this project from the National Science Foundation through NSF grant CMMI-0927178 and Seed Grant support from the National Center for Airborne Laser Mapping (NCALM) for airborne LiDAR data flown over the study area. I would also like to acknowledge NEES@UTexas and IRIS/PASSCAL for the seismic equipment used in this study.

I am grateful to my parents Jim and Karen Wood for giving me guidance throughout my life, and providing me with the opportunity and support to pursue my education. I am grateful to my brothers, Matt and Brad Wood, for providing assistance along the way, and keeping me humble throughout my life. Finally, I am grateful to my fiancée, Megan Riley, for always being there for me, and for putting up with me while writing my dissertation.

Field Investigation of Topographic Effects using Mine Seismicity

Clinton Miller Wood, Ph.D.

The University of Texas at Austin, 2013

Supervisor: Brady R. Cox

This dissertation details work aimed at better understanding topographic effects in earthquake ground motions. The experiment, conducted in Central-Eastern Utah, used frequent and predictable seismicity produced by underground longwall coal mining as a source of low-intensity ground motions. Locally-dense arrays of seismometers deployed over various topographic features were used to passively monitor seismic energy produced by mining-induced implosions and/or stress redistribution in the subsurface.

The research consisted of two separate studies: an initial feasibility experiment (Phase I) followed by a larger-scale main study (Phase II). Over 50 distinct, small-magnitude ($M_L < 1.6$) seismic events were identified in each phase. These events were analyzed for topographic effects in the time domain using the Peak Ground Velocity (PGV), and in the frequency domain using the Standard Spectral Ratio (SSR) method, the Median Reference Method (MRM), and the Horizontal-to-Vertical Spectral Ratio (HVSR) method. The polarities of the horizontal ground motions were also visualized using directional analyses. The various analysis methods were compared to assess their ability to estimate amplification factors and determine the topographic frequencies of interest for each feature instrumented. The MRM was found to provide the most consistent, and presumably accurate, estimates of the amplification factor and frequency range for topographic effects.

Results from this study clearly indicated that topographic amplification of ground motions does in fact occur. These amplifications were very frequency dependent, and the frequency range was correctly estimated in many, but not all, cases using simplified, analytical methods based on the geotechnical and geometrical properties of the topography. Amplifications in this study were found to generally range from 2 to 3 times a reference/baseline site condition, with some complex 3D features experiencing amplifications as high as 10. Maximum amplifications occurred near the crest of topographic features with slope angles greater than approximately 15 degrees, and the amplifications were generally oriented in the direction of steepest topographic relief, with some dependency on wave propagation direction.

Table of Contents

List of Tables

List of Figures

Chapter 1: Introduction

1.1 Topographic Effects

Topographic effects refer to the amplification, de-amplification, or frequency modification of seismic waves in the vicinity of topographic features. Certain topographic features are believed to resonate, diffract and/or focus incident seismic waves generating large amplifications or reductions of ground shaking over relatively small spatial distances. Qualitative observations and quantitative ground motion recordings on or near topographic features in past earthquakes have shown that structural and geotechnical damage tends to increase near the crest, or sharp edges, of topographic features, making topography an important parameter for ground motion prediction. Some examples of observed damage attributed to topographic effects include: the 1971 M_w 6.6 San Fernando (Boore 1972), 1983 M_w 6.5 Coalinga (Celebi 1991), 1985 M_w 7.8 Chile (Celebi 1987), 1987 M_w 5.9 Whittier Narrows (Kawase and Aki 1990), 1994 M_w 6.7 Northridge (Ashford and Sitar 1997), and 2010 M_w 7.0 Haiti (Rathje et al. 2011) earthquakes. These examples, and many other earthquakes, demonstrate the possible influence of topography on the intensity of ground shaking. As a result of the damage caused by earthquakes, a considerable amount of work has been done to understand and quantify the effects of topography on earthquake ground motions.

Researchers and practitioners have approached the problem from four main avenues: (1) field observations of earthquake damage patterns and strong motion recordings, (2) experimental studies using arrays of sensors placed strategically on topography to record aftershocks or other weak motion data, (3) theoretical and analytical estimates for simple 2D cross sections, and (4) numerical modeling of 2D and 3D simplified topography. Despite much work in the area of topographic effects, the phenomenon is still not well understood. As such, the effects of topography are currently

not accounted for in the United States building codes or ground motion prediction equations, even though significant evidence has shown topography can play a significant role in the response of sites during an earthquake.

1.2 RESEARCH SIGNIFICANCE

The amplification of seismic ground motion in the vicinity of topographic features such as hillsides, ridges, and canyons is a well-documented phenomenon that has yet to be addressed in design codes. A prominent example of this so-called "topographic effect" is the extraordinary damage patterns on topographic ridges following the 2010, M_w 7.0 Port-au-Prince, Haiti earthquake, where damage was concentrated on ridge and other topographic features (Hough et al. 2011). As tectonics and topography are closely related, most seismically active regions of the world are also areas of significant topographic relief. In recent decades, urban sprawl and population growth have changed the land use patterns of underdeveloped land near or on topographic features. As such, an increasing portion of the world's inhabitants and infrastructure are in areas susceptible to topographic effects.

While it is recognized that topographic amplification can elevate seismic risk, there is currently no consensus on how to reliably quantify its effects. Researchers and practitioners have approached the problem from four main avenues (which are discussed in Chapter 2): (1) field observations of earthquake damage patterns and strong motion recordings, (2) experimental studies using arrays of sensors placed strategically on topography to record aftershocks or other weak motion data, (3) theoretical and analytical estimates for simple 2D cross sections, and (4) numerical modeling of 2D and 3D simplified topography. Despite all the work in the area of topographic effects, the phenomenon is still not well understood. The inability to quantify these effects has

delayed the development and inclusion of topographic effects in design codes and ground motion prediction equations. This lack of guidelines leaves an important seismic risk factor unaccounted for in routine design.

Although studies looking into topographic effects have been conducted in recent years on real topography (Buech et al. 2010, Massa et al. 2010, Marzorati et al. 2011), these studies have been limited in the amount of data collected, the quality of data recorded, the density of sensors deployed along the topography, the various geometric features instrumented, and the Vs characterization of the topography. Often these studies record amplification on topographic features, but with little understanding of the velocity structure associated with the feature. As a result, they cannot accurately determine if the measured amplification is the result of topographic effects or site effects, which can lead to a misunderstanding of topographic effects. Moreover, poor geometrical and subsurface characterization of topographic features reduces the accuracy of theoretical equations and numerical simulations, leading to poor comparisons between numerical results and experimental results. Ultimately, a dataset of well-recorded ground motions over well-characterized topographic features is needed to fully understand topographic effects, and to be used to calibrate numerical models to fully understand the linear and non-linear response of topographic features.

1.3 SCOPE OF RESEARCH

This dissertation details work by researchers at the University of Arkansas at Fayetteville (UA) and the University of Texas at Austin (UT) aimed at recording ground motions on full-scale topographic features. This project is one part of the larger Network for Earthquake Engineering Simulation (NEES) project "NEES-CR: Topographic Effects in Strong Ground Motion – From Physical and Numerical Modeling to Design". The

project has four main avenues of investigation: (1) Empirical Data Analysis: a review of the strong ground motion (GM) database to investigate potential bias from stations on irregular topography (conducted by Virginia Tech), (2) Experimental Data Collection: acquisition and processing of GM recorded on irregular topography with dense instrumentation arrays (this study), (3) Physical Modeling: centrifuge modeling of 2D slopes and ridges with various configurations and levels of input (conducted by University of Washington), (4) Numerical Modeling: finite element/finite difference parametric studies using models calibrated with centrifuge and field ground motions (conducted by Georgia Tech).

This experiment used the frequent and predictable seismicity produced by underground longwall coal mining in the Wasatch Plateau – Book Cliffs coal mining region of Central-Eastern Utah. The area was home to significant topographic relief due to a series of North-South trending Grabens formed by relatively young uplift and East-West extension. To record ground motions on this topography, locally dense arrays of seismometers were deployed over various topographic features. The arrays were then used to passively monitor seismic energy produced by mining-induced implosions and/or stress redistribution in the subsurface caused by coal extraction deep below the surface.

The research consisted of two separate studies. The first phase (Phase I) of the study was intended as a pilot study with limited extent to insure that topographic effects could be accurately recorded on full-scale features using the weak motion seismicity produced by coal mining. To accomplish this, a 3D surface array of 3-component, 1-Hz geophones was deployed over a steep mountain peak in the Manti-La Sal National Forest in Central-Eastern Utah. The surface array of 12 stations extended in an East-West orientation 750 m horizontally and 110 m vertically, while extending horizontally 550 m in a North-South direction. The sensors were attached via cables to a single data

acquisition system and set to record continuously. Passive seismic activity was recorded for 7 consecutive days, wherein 52distinct, small-magnitude ($M_L < 1.6$) seismic events were detected. In addition, surface wave testing was conducted near the topographic array to determine small-strain shear stiffness profiles of the mountain.

The second phase (Phase II) of the study was the main study, in which the number and quality of the sensors were increased along with the overall size of the topographic array. In Phase II, a total of 27 broadband and short period seismometers were deployed in a 3D "H" pattern and circular array over a 25 km^2 area. Each sensor was attached to an individual datalogger and synchronized via GPS timing. Ground motions were recorded for approximately 10 days, wherein a significant number of distinct, small-magnitude ($M_L < 1.6$) seismic events were detected. Of which, 52 of the largest events were selected for further analysis.

The data from each study was analyzed for topographic effects using the standard spectral ratio (SSR) method, the Median Reference Method (MRM), and the Horizontal-to-Vertical Spectral Ratio (HVSR) method. The polarity of the horizontal components was also visualized using a directional analysis. The results were used to evaluate the resonant frequencies and amplification factors for the topography instrumented in each study. These methods were compared to assess their ability to accurately estimate the amplification factors for the topographic features and to accurately determine the topographic frequencies of interest. These values, determined from the field study, were compared to theoretically estimated topographic frequencies, to assess the ability of each theoretical method to properly estimate the resonant frequency for real world topography, based on the mechanical and geometrical properties of the topography. In addition, and beyond the scope of this dissertation, but within the bounds of the NEES-CR research

project, the data set will be used as a validation/calibration data set for 3D numerical models of real topography.

1.4 ORGANIZATION OF DISSERTATION

This research consists of two main experimental field studies: (1) the pilot study in the summer of 2010 (referred to as Phase I herein) and (2) the main study in the summer of 2011 (referred to as Phase II herein). This dissertation contains nine chapters that detail the field work, data processing and results of both studies.

In Chapter 1, the phenomenon of topographic effects is briefly introduced, along with the need to further understand these effects so they can eventually be accounted for in U.S. building codes and ground motion prediction relationships. A brief overview of the current research is provided, along with a chapter-by-chapter detail of the dissertation.

In Chapter 2, background information on topographic effects is provided, including significant observations, recorded field evidence, theoretical equations for topographic frequency estimation, and numerical modeling performed to further understand topographic effects. In addition, a summary of key findings and knowledge based on the literature is provided.

In Chapter 3, information on the study area, including geology, digital elevation models and underground mining activity is provided. The equipment used during Phase I is detailed, along with how the stations were deployed along the topography. The recording and processing of the Phase I seismic records are also explained.

In Chapter 4, information on equipment used in Phase II is provided, along with how the stations were deployed and their location on the topography. The location of mining activity relative to the recording stations is explained, along with how the event hypocenters were located from the recorded data. The processing of the records is also

explained, along with the methods used to estimate topographic effects from the Phase II data.

In Chapter 5, the surface wave testing conducted during Phase I is detailed. The equipment, data collection setup, and processing are explained. The shear wave velocity profile obtained near the topographic profile is presented to establish the small-strain shear stiffness of the feature.

In Chapter 6, the frequency ranges of expected topographic amplification are estimated for each instrumented feature using the analytical methods proposed by Ashford and Sitar (1997) and Paolucci (2002),coupled with the geometry and stiffness of the features. These analytical estimates provide a range of approximate frequencies where topographic effects may be present in the Phase I and Phase II recorded data.

In Chapter 7, the results of Phase I are presented, including the SSR, MRM, and HVSR analyses. The frequency responses of each sensor, using all three methods, are compared for a single event (17801) and the median response of 52 individual events. Finally, the median responses of all the stations are compared relative to the SSR, MRM and HVSR processing methods.

In Chapter 8, the results of Phase II are presented, including the SSR, MRM, and HVSR analyses. The frequency responses of each sensor, in the three geometric arrays are compared for a single event (200.19.5) and the median response of 52 individual events. Finally, the median responses of all the stations are compared relative to the SSR, MRM, and HVSR processing methods.

In Chapter 9, the dissertation is summarized, conclusions from Phase I and II are presented, and the final results are established for the research. Future research and refinements for this research are also suggested.

Chapter 2: Topographic Effects on Ground Motions - Background

2.1 INTRODUCTION

Topographic effects are often defined as the amplification or modification of Earthquake ground motions by hillsides, ridges, buttes, or canyons. Though topographic effects are a well-documented phenomenon with observation going back over a century and recorded evidence published for over 40 years, they are currently unaccounted for in most building codes. In addition, current ground motion attenuation models such as the "Next Generation of Ground-Motion Attenuation Models" (NGA), do not account for topographic effects. This lack of accounting is a result of the difficult problem of properly measuring and explaining the topographic amplification phenomenon. This chapter reviews and summarizes techniques used by various authors to study the topographic amplification phenomenon; including strong motion observations, field measurements, theoretical evaluations, and numerical modeling.

2.2 FIELD OBSERVATIONS

Charles Darwin was one of the first to describe topographic effects after observing fractured and displaced soil on narrow ridges following the February 20, 1835 Chilean earthquake (Barlow 1933). However, it was not until later that scientists started directly linking fractures and churned ground on topographic features to "Topographic Effects". Plafker (1967), Boore (1972), and Ponti and Wells (1991) each made observation of churned ground, ground fissures, and overturned boulders on topographic features following strong motion events. These types of damage are indicative of very strong ground motion and likely amplification above that of surrounding flat topography. An example of ground fissures following strong motion is shown in Figure 2.1. In

Figure 2.1: Example of ground fissures on topographic features (Haeussler et al. 2004).

addition, observations of earthquake induced landslides and rock slope failures on topographic features were observed by Sepulveda et al. (2005) and Khazai and Sitar (2003). Also, indicating strong ground motion and likely amplification.

For more populated areas, observations of higher structural damage or collapse of buildings on topographic features, especially at the peak of ridges, is indicative of topographic effects (Bouckovalas and Kouretzis 2001; Carver and Hartzell 1996; Gao et al. 1996; Hough et al. 2010 and 2011). One of the more complete examples of the use of structural damage patterns to investigate topographic effects was presented following the 2010 Mw7.0 Port-au-Prince earthquake by Rathje et al. (2010). The authors used damage maps overlain on a LiDAR generated DEM slope map of Port-au-Prince (shown in Figure 2.2). The authors indicate significantly higher damage in areas of the city with

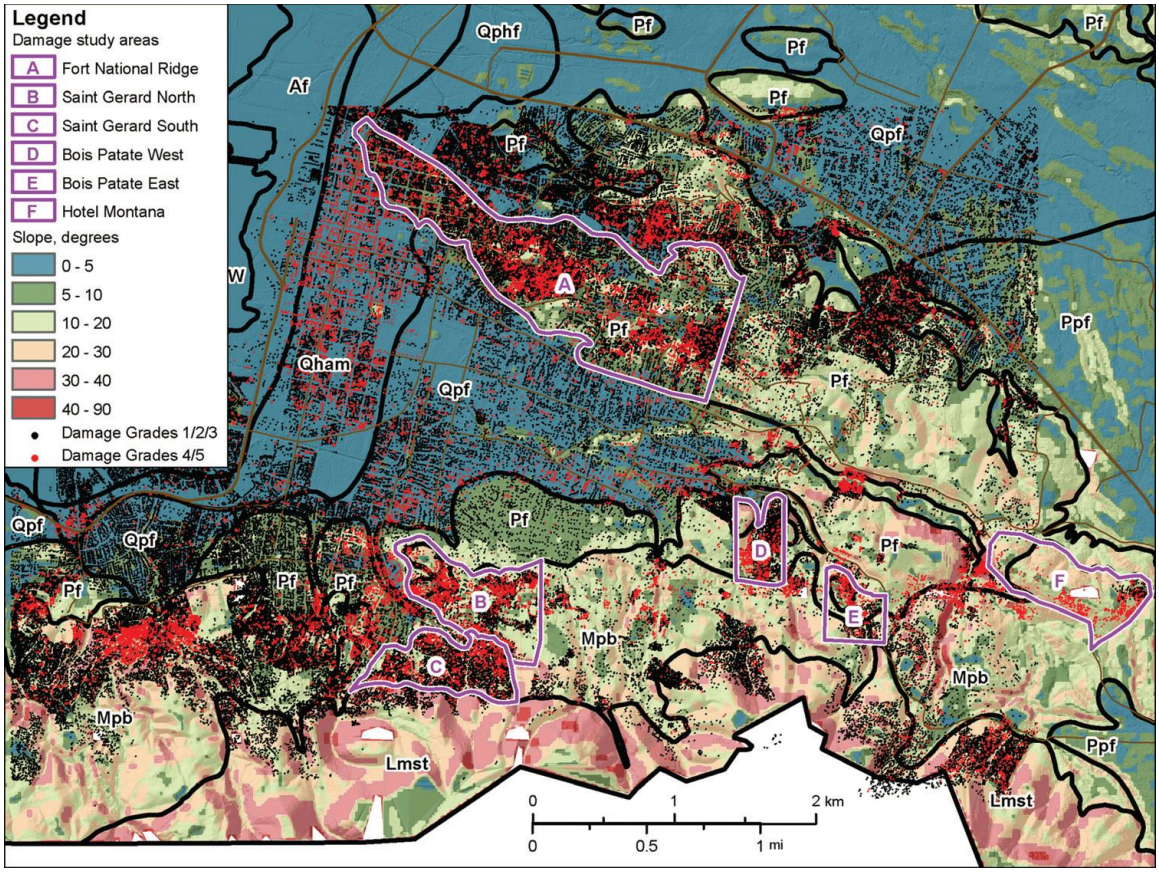

Figure 2.2: UNOSAT damage map overlain on a slopes angles map of Port-au-Prince (Rathje et al. 2010).

high slope angles (indicated by purple outlines). The author's attribute the damage to possible topographic effects, but also indicate that the high concentration of damage could result from a combination of soil amplification and/or slope failures together with topographic amplification, since is it often difficult to separate the different seismic phenomenon.

A list of recent studies in which observed damage patterns were tied to the crest or slopes of topographic features is presented in Table 2.1. The studies document damage patterns from earthquakes ranging from moment magnitude 5.6 to 7.8. Many of these studies are discussed in further details in this chapter.

Table 2.1: Recent studies where observations of damages patterns were correlated to the crests and slopes topographic features (Formatted after Massa et al. 2010).

Date (dd/mm/yy)	M_W	Location	Reference
6 May 1976	6.4	Friuli	Bramati et al., 1980
23 November 1980	6.9	Irpinia	Faccioli, 1986
3 March 1985	7.8	Chile	Celebi, 1987
1 October 1987	5.9	Whittier Narrows	Kawase and Aki, 1990
18 October 1989	6.9	Loma Prieta	Ponti and Wells, 1991; Hartzell et al., 1994
17 January 1994	6.9	Northridge	Bouchon and Barker, 1996; Spudich et al., 1996
15 June 1995	6.2	Egion	Athanasopoulos et al., 1999
26 September 1997	6.0	Umbria-Marche	Marra et al., 2000; Donati et al., 2001
25 January 1999	6.2	Eje Kafetero	Rastrepo and Cowan, 2000
7 September 1999	5.8	Athene	Kallou et al., 2001
13 January 2001	7.7	El Salvador	Bommer et al., 2002
31 October 2002	5.6	Molise	Massa et al., 2004; Isella et al., 2004
6 April 2009	6.3	L' Aquila	Marzorati et al., 2009
12 January 2010	7.0	Haiti	Hough et al. 2011

2.3 NUMERICAL MODELING

Numerical simulation of two dimensional, and more recently three dimensional, slopes, ridges, cliffs, and mountain peaks have been conducted by many different authors (Geli 1988; Assimaki et al. 2005). Models have grown in complexity as techniques, computers, and modeling software have evolved. Some examples of the techniques used in numerical modeling include the finite difference method (Boore 1972; Zahradnik and Urban 1984), the finite element method (Smith 1975; Athanasopolous and Zervas 1993; Assimaki et al. 2005), the integral equation method (Sills 1978), boundary methods (Sanchez-Sesma et al. 1982), discrete wavenumber methods (Bouchon 1973; Bard 1982), spectral methods (Kosloft et al. 1990; Paolucci 1999), and the Aki-Larner method (Geli 1988; Wong and Jennings 1975).

Although the techniques used by authors vary significantly, the parameters used in each analysis remain nearly the same. For modeling topographic effects, there are three main parameters that are believed to control the seismic response of mountains and

ridges. The first parameter is the overall shape of the feature. The most important characteristics of the shape are the length, height, slope angle, and whether the feature is relatively more 2D (similar to a ridge) or 3D (such as a mountain peak). These characteristics influence both the resonant frequency and amplification level of the feature. The second parameter is the stiffness profile of the mountain. The shear (Vs) and compression (Vp) wave velocities of the feature define the stiffness, which combined with the thickness of each layer influence the resonant frequency, but also the possible soil site effects of the feature. The final parameter is the incident wavefield. The wave type (P, in-plane shear (SV), or anti-plane shear (SH)), the horizontal azimuth, the vertical zenith angle, the frequency content, and the amplitude all influence the location and magnitude of the seismic response of topographic features. Researchers often select singular parameters for individual studies and simplify more complicated parameters to reduce the computational intensity of the problem. However, this simplification can bias the amplification factors and resonant frequencies determined from the models. Regardless, numerical models provide the best way to perform parametric studies on the influence of each of the different parameters listed above. Below is a review of the most influential publications related to numerical modeling of topographic features.

In 1972, Boore published a study looking at the effect of SH waves (anti-plane) on simple topography. He was one of the first to identify that amplification for topographic features only occurred for wavelengths comparable to the width or size of a feature and simply states that structures built on rock that were once considered immune to large amplification are now considered vulnerable to the high acceleration caused by topographic effects. His paper opened the door to later studies looking directly at the problem of topographic effects. In 1973, Bouchon performed the first parametric study on topographic effects using the Aki and Larner Method (Aki and Larner 1970). Bouchon

propagated SH, SV, and P waves across ridge and valley topographic features with varying zenith angles to assess how the amplification varied across each feature. The results indicated that amplification always occurs at the ridge top and attenuation (de-amplification) always occurs near the flank of the feature, with maximum amplifications of 20-45% observed. For waves with zenith angles less than 40 degrees from horizontal, the zone of amplification shifted from the peak of the feature to the far side or "sun" side of the feature opposite the incoming waves. Moreover, attenuation of the ground motion was observed on the near or "shadow" side of the feature nearest the incoming waves. This phenomenon was later confirmed by Kawase and Aki 1990 and Ashford and Sitar 1997. In addition, SV waves (in-plane) with incident angles of 35 degrees produced the greatest amplifications of approximately 100% compared to flat ground, while vertical incident SV and P waves only produced amplifications of 50%. This indicates that waves propagating at zenith angles less than vertical may be more damaging in terms of topographic effects than standard vertical propagating waves. For valleys, attenuation occurred in the central valley while amplification occurred near the rim, indicating that valleys appear to respond in an opposing fashion to ridges. One of the most fundamental questions answered by Bouchon relates to the response of features with different slope angles (i.e., height/(length/2)). The numerical modeling results indicate that as the steepness/sharpest (i.e., the slope) of the feature increases the maximum amplification at the crest also increases. Finally, Bouchon confirmed that only wavelengths comparable to the dimensions of the feature affect the topographic response, as first determined by Boore (1972).

The next major contributor to the understanding of topographic effects from numerical studies came from Geli (1988). The author published a comprehensive summary of the literature on topographic effects and performed a parametric study

comparing the response of topographic features to various wave types. Geli determined that attenuation at the base of the hill, first recognized by Boore (1972), is related to the intersection of primary waves with outward going diffracted waves, thereby adding de-constructively. In addition, it was determined that incident in-plane SV waves produce the highest amplification followed by anti-plane SH waves and finally P waves, which produced significantly less amplification. When Geli (1988) investigated the influence of groups of ridges on topographic response, it was determined that isolated ridges have a slightly lower amplification than groups of neighboring ridges. In addition, the center ridge has a slightly greater amplification than the outer ridges. When a more complex analysis was performed- where topography, layering, and periodicity were investigated individually and simultaneously- it was determined that a simple summation of each individual parameter does not reproduce the complex response of the whole system. This complicates the problem of modeling topographic features with simple 2D models and requires more complex models than previously assumed.

Athanasopoulos and Zervas (1993) looked at the effects of size ratio (k) and shape ratio (s) on topographic response using vertically propagating SV waves. The size ratio (k) is the total base width divided by the principal wavelength, while the shape ratio (s) is the height divided by the half-width of the feature. The results showed that the shape ratio (i.e., the steepness of the feature) is inversely proportional to the measured amplification factor of a feature (i.e., the steeper a slope the lower the amplification factor). This contradicts earlier findings by Geli (1998). The authors also observed that the shape ratio can influence the resonant frequency of the feature. The authors explain that for typical shape ratios of 0.45 to 0.16, the size ratio varies between 2 and 0.85, with 1.5 being the most common value (i.e., for steeper features the critical wavelength is larger than the width of the feature and for shallow slopes the critical wavelength is shorter than the

width of the slope). This finding indicates that the resonate frequency of a feature is controlled by the height, width, and velocity structure of the feature.

In 1997, Ashford and Sitar (1997) and Ashford et al. (1997) conducted a parametric study to assess the influence of wave inclination on the topographic amplification of steep costal bluffs (i.e., cliffs) using SH and SV waves on slopes with face angles of 45-90 degrees (30-90 degrees for SV waves) from vertical. The results indicate that ground motions are amplified for waves traveling into the slope and attenuated for waves traveling away from the slope. The total site amplification also shifted spatially to the side of the slope opposing wave propagation but overall amplification factors for the cliff remained the same. Any amplification of topographic effects was met by an equal attenuation of soil site effects. Moreover, evidence shows that for soil profiles with high impedance contrasts, amplification from soil site effects exceeds that of topographic effects. Therefore, vertically propagating waves (both SV and SH) were determined to be the critical wave of interest for amplification experiments.

Paolucci (2002) used both a closed form solution and several numerical models to test the amplification patterns of various ridge geometries. Paolucci concluded that 2D ridges, where L>>W, produced a more broadband amplification pattern, while for isolated ridges the resonate frequency tended to dominate. Paolucci next compared his results to those estimated by the frequency independent amplification factors presented in Euro Code 8 (i.e., 1.2 and 1.4). He found that Euro Code 8 can underestimate the recorded amplification factors by up to 40% at the resonant frequency of the ridge and overestimate the amplification of other frequencies. This is an excellent argument against the use of a frequency independent amplification factor for topographic effects in design codes.

The next major parametric study was conducted by Assimaki et al. (2005) to evaluate the effects of local soil conditions on the diffraction mechanisms near the vertex of cliff-type topography. The simulations were carried out for homogenous soil over bedrock, a two layer soil profile, and a random medium. Results show that the horizontal layering and heterogeneity of the soil can influence the topographic amplification factor, both increasing and/or decreasing the recorded ground motions. Ultimately, the soil conditions were shown to affect the spatial distribution, aggravation level, and frequency content of ground motions. In addition, the total measured amplification could not be explained using the geometry of the feature alone, therefore the soil profile played a key role in the measured ground motions. Later in 2005 and in 2007, Assimaki et al. (2005b) and Assimaki and Kausel (2007) investigated the contribution of kinematic soil-structure interaction on topographic amplification. Their results indicate that stiff structures near the crest of ridges tend to filter high frequencies. However, the vertical motions tended to induce a rocking motion into the structure. Overall, it was determined that soil-structure interaction beneficially altered the topography amplification factors in the vicinity of the crest.

Lee et al. (2009a) developed a 3D spectral element mesh to model real topography. The simulations show that the topography can change the PGV by + or – 50% relative to the free-field. In addition, the topography was shown to affect the propagation of body and surface waves to surrounding areas and depending on hypocenter location and depth an increase or decrease of 50% in ground motions is possible away from the topography. This indicates that topography can not only act as a funnel to increase seismic energy in some areas, but can also act as a shield to seismic energy in other areas. Later in 2009, Lee et al. (2009b) used a LiDAR generated digital terrain model (DTM) of topography in Taiwan to test their model on real topography.

They concluded that amplifications from crest to flat ground of up to 50% were possible. However, the base to crest amplification was closer to two. The authors also observed unusually high ground motions when high frequency waves impinged upon the small scale topographic features.

In 2012, Maufroy et al. investigated the usefulness of the median reference method (MRM), first introduced by Wilson and Pavlis (2000). This method was originally used to study soil site effects on flat ground using a dense array of sensors, and later by Poppeliers and Pavlis (2002) for measuring topographic effects at a surface coal mine in Indiana. The authors used a shake3D finite element code to perform a comprehensive study of the MRM using both random and known source locations with isotropic and double-couple sources. The authors first compared the amplification factors using the single station reference method (SRM) and the MRM method. They determine that the amplification factors calculated using the SRM are highly dependent on the choice of a reference station and the SRM technique was far more likely to over-estimate or under-estimate the amplification compared to the MRM technique. The authors also determined that the number of stations included in the median reference estimate did not significantly influence the calculated amplification factors and state that to improve the estimate one should place equal numbers of sensors at the base, along the slope, and at the peak of topographic features to obtain a more accurate median amplification factor (see Figure 2.3). When conducting the study with a random source, the authors observed that the amplification factors at different locations were significantly influence by the location of the source and the direction of wave propagation.

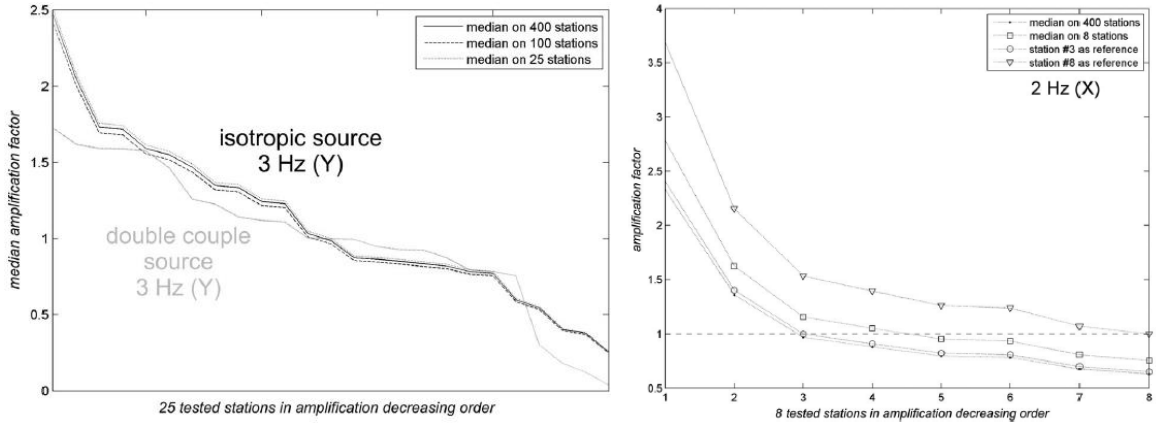

Figure 2.3: MRM amplification factors obtained using a sampling of 25, 100, 400 stations to determine median amplification factors (left), comparison of amplification factors using the SRM and MRM techniques (right) (Maufroy et al. 2012).

2.4 THEORETICAL EVALUATIONS

Simplified theoretical equations are often used in earthquake engineering to evaluate the response of soil deposit and simplified geometric cross sections. These simplified methods reduce the complicated 3D heterogeneous problems of soil mechanics and earthquake engineering to simple homogeneous 1D or 2D problems subjected to simple shear in a single plane. These estimates can provide a good approximation of the response of real world problems under certain circumstances and are used extensively in engineering. Below is a review of the most widely used theoretical methods to evaluate the resonant frequency of topographic features.

Ambraseys (1960) presented a mathematical solution for the shear response of a truncated 2D elastic wedge subjected to an arbitrary disturbance. The wedge is assumed to be elastic and of constant rigidity. Only simple shear was considered, ignoring bending moments. For the analysis, a horizontal disturbance acts perpendicular to the length of the base (L) and in plane with the width (W) and height (H) of the wedge (see Figure 2.4).

Equation 2.1 gives the undamped circular resonance frequencies of the wedge, Wnr in rad/sec.

$$Wnr = \left(\frac{V_S}{H}\right)\left[a_n^2 + \left(\frac{r\pi}{u}\right)^2\right]^{1/2} \quad (2.1)$$

Where Vs is the average shear wave velocity, H is the height of the wedge, a_n are the roots given in Table 2.2, r is the longitudinal mode of vibration (equal to 1), and u is the length divided by the width.

Table 2.2: Roots (a_n) for k'=0 (full height) for the first three modes of vibration (Ambraseys 1960).

k'	n=1	n=2	n=3
0	2.4	5.52	8.65

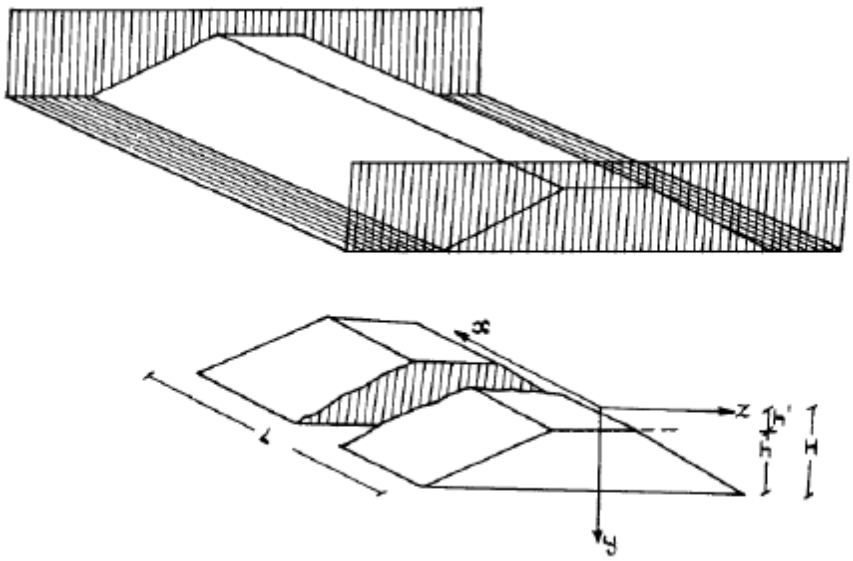

Figure 2.4: Model of a 2D simplified symmetrical wedge with height H and length L. Shear waves act only in the z and y plane (Ambraseys 1960).

In 1985, Sanchez-Sesma (1985) developed a solution using MacDonald's method for the displacement field at the surface of a wedge-shaped medium for incidence harmonic SH waves. The amplification at the vertex of the wedge is given by 2/v, where v is the internal angle of the wedge in radians. The resonant frequency calculated using $kx/\pi=2$, where k is the wavenumber and x is the width of the wedge. The amplification factor is dependent upon the angle of incidence of the shear wave and thus the amplification could be greater if waves reflect within the wedge and interfere constructively.

Dakoulas and Gazetas (1985) derived an exact analytical solution for the free and forced vibrations of a truncated shear wedge using the shear beam approach. The shear beam analysis is one of the earliest approaches to the dynamic analysis of 2D earthen structures including dams and embankments. The method assumes that an earth structure deforms in simple shear in a single plane therefore only producing horizontal displacements and the shear stress or shear strains are uniform across the horizontal planes. The nth circular natural frequency of vibration of a wedge, Wn is given in Equation 2.2.

$$Wn = \frac{V_S}{H}\frac{B_n}{8}(4+m)(2-m) \tag{2.2}$$

Where H is the height of the wedge, Vs is the average shear wave velocity of the wedge, Bn is the nth root of a period relationship (see Table 2.3), and m is a factor of inhomogeneity (0=homogeneous).

Ashford and Sitar (1997) used a numerical modeling method mentioned in section 2.2 to determine the natural frequency of a cliff-type feature empirically. They determined the topographic resonant frequency was equal to the shear wave velocity divided by 5 times the height of the feature. In addition, the 2nd mode resonant frequency

Table 2.3: Values of Bn for the first 3 modes of vibration of an earthen dam (Dakoulas and Gazetas 1985).

m	n=1	n=2	n=3
0	2.404	5.52	8.654
0.5	2.903	6.033	9.171
1	3.382	7.106	9.273

is determined using the coefficients of 1.43 for SH waves and 1.0 for SV waves in place of 5.

Paolucci (2002) derived a closed form solution for estimating the fundamental mode of vibration of a homogenous triangular mountain using Rayleigh's method. The simplified approach is applied to a triangular cross section such as shown in Figure 2.5. The asymmetry of the triangle is accounted for using the H/L_1 and H/L_2 terms where $L_1>L_2$. Using the method, both the anti-plane SH and in-plane SV motions are estimated. In Figure 2.6, the reference drawing is shown in polar coordinates with the origin at the vertex of the feature. The symbol θ is the internal angle of the vertex and R_1 and R_2 are the slope distance of each side of the feature.

For anti-plane SH waves, the fundamental frequency of the feature is:

$$\hat{f}_0 = 0.38\frac{B}{L}\frac{\sin(\theta_1+\theta_2)}{\cos\theta_2}\sqrt{\left[1+ln^2\left(\frac{R_2}{R_1}\right)^{1/(\theta_1+\theta_2)}\right]\frac{2ln(R_2/R_1)}{(R_2/R_1)-1}} \quad (2.3)$$

Where B is the shear wave velocity, L is the width of idealized profile in Figure 2.4, θ_1,θ_2 are vertex internal angles of the idealized profile in the polar coordinate system, and R_1,R_2 are the wedge boundaries of the idealized profile in polar coordinates

The equation is simplified to:

$$\hat{f}_0 = \frac{B}{L}f_{SH}\left(\frac{H}{L_1},\frac{H}{L_2}\right) \quad (2.4)$$

Where H is the height of the feature and H/L_1 and H/L_2 are the shape ratios determined from Figure 2.7a. For most realistic geometries, (i.e., H/L <0.5), the fundamental frequency is approximately $f_0 \sim 0.7$ B/L for SH waves.

For in-plane SV waves, the fundamental frequency is obtained using Equation 2.5:

$$\hat{f}_0 = 0.38\frac{B}{L}\frac{\sin(\theta_1+\theta_2)}{\cos\theta_2}\sqrt{\frac{\alpha}{(R_2/R_1)^2-1}}x\sqrt{(\alpha^2+1)(3+\chi)(\theta_1+\theta_2)+}\,(1+\chi)\{(\alpha^2-$$

$$1)[\sin 2\theta_2+\sin 2\theta_1]/2+\alpha[\cos 2\theta_2-\cos 2\theta_1]\} \quad (2.5)$$

Where B is the shear wave velocity, L is the width of the idealized profile, θ_1,θ_2 are vertex internal angles of the idealized profile in the polar coordinate system, $\alpha = (1/\theta_1+\theta_2)\ln(R_2/R_1)$, R_1,R_2 are the wedge boundaries of the idealized profile in polar coordinates and $\chi = \lambda/\mu$ (where λ and μ are the constants of Lame).

The equation simplifies to:

$$\hat{f}_0 = \frac{B}{L}f_{SV}\left(\frac{H}{L_1},\frac{H}{L_2}\right) \quad (2.6)$$

Where H/L_1 and H/L_2 are the shape ratios determined from Figure 2.7b. For most realistic geometries, (i.e., H/L <0.5), the fundamental frequency is approximately $f_0 \sim 0.7$ B/L for SH waves.

$$f_0 = 1.0\frac{B}{L} \quad (2.7)$$

2.5 EXPERIMENTAL STUDIES

Systematically measuring topographic effects on real topography is a difficult undertaking. Experiments designed to measure topographic effects often require more sensors and have more uncertainty than experiments looking into soil stratigraphy site effects alone. Most experimental studies on topographic effects have used as few as two,

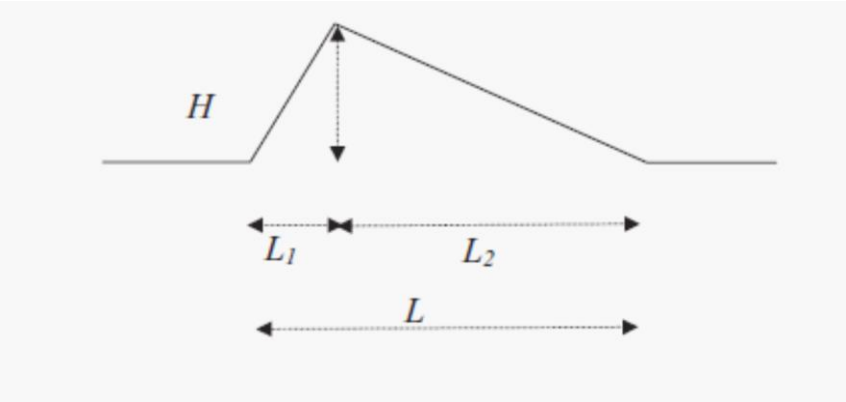

Figure 2.5: Idealized profile of a homogeneous asymmetric mountain (Paolucci 2002).

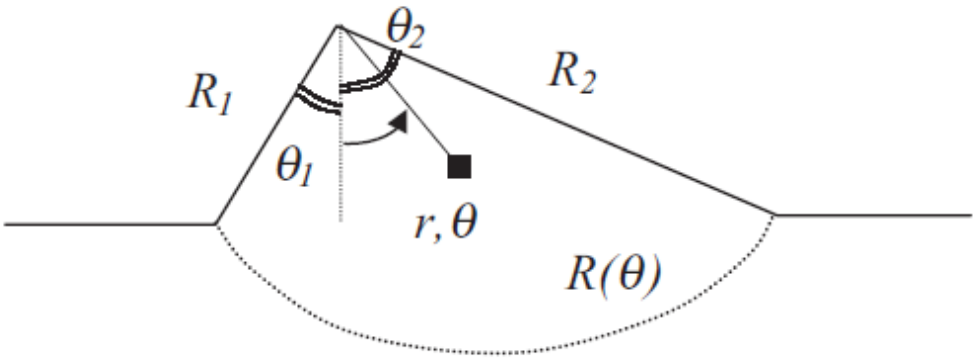

Figure 2.6: Derivation reference system (Paolucci 2002).

but in some cases several dozen sensors at the crest, base, and along the slope of ridges, canyons, and mountains. In early studies, the sensors consisted of 3D low frequency (< 2Hz) geophones. However, as sensor technology advances and long period (> 30 sec period) sensors become more available, studies have become more accurate and have been able to investigate a wider frequency band for topographic effects. Although the experimental studies have advanced in recent years, significant difficulties are still associated with measuring and analyzing topographic effects on real topography. Some of the main problems are listed below:

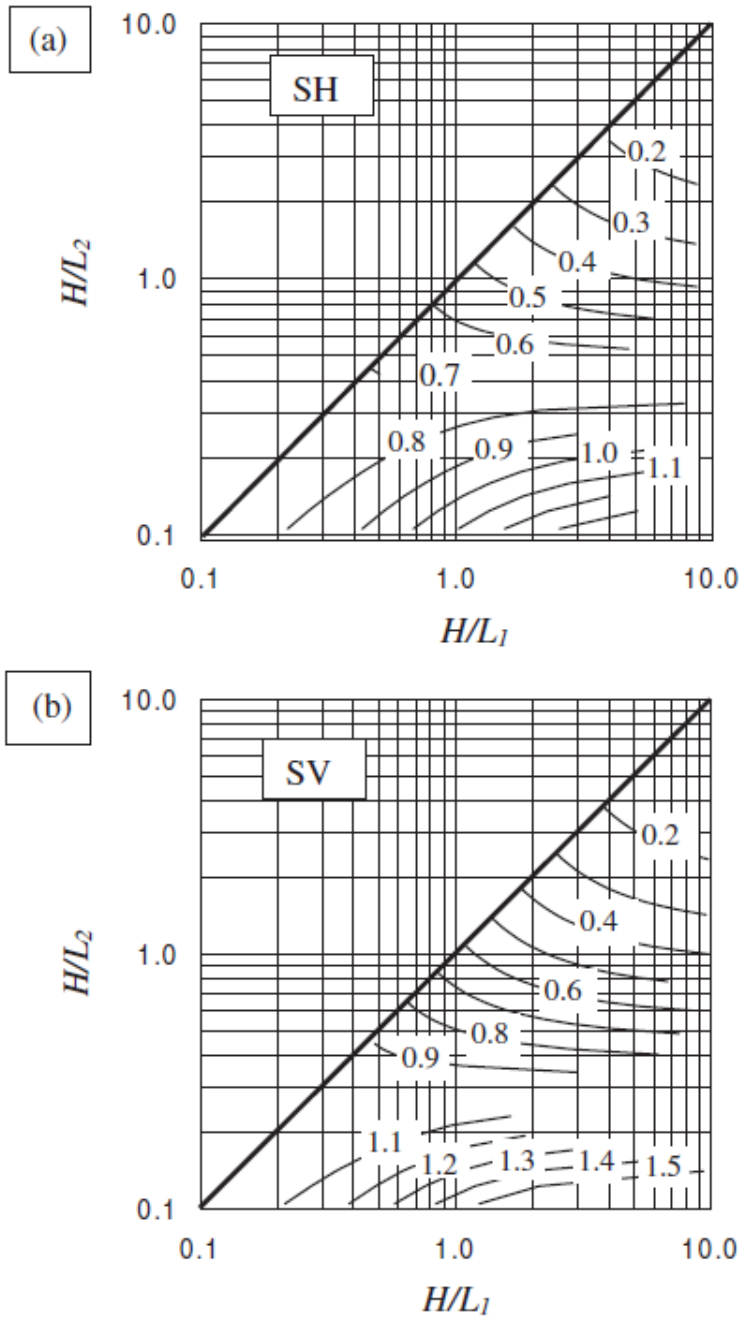

Figure 2.7: Contour levels of the functions f_{SH} and f_{SV} for the estimation of the fundamental resonance frequency of a feature (a) is the SH case and (b) is the SV case (Paolucci 2002).

- There are very few simple 2D isolated ridges to study. Most ridges are 3D features with many sub-ridges with varying geometries. This makes it very difficult to determine the width, height, or slope of the feature. This makes it difficult to simplify the feature into a geometric cross-section that can be easily analyzed using theoretical equations or numerical methods.
- There are very few homogeneous ridges found in nature. Therefore, ground motions measured on topographic features are not only affected by topographic effects, but also by stratigraphy site effects too. This makes it difficult to isolate what part of the ground motion amplification is the result of topographic effects and what part is the result of stratigraphy site effects.
- Knowledge of the soil properties and shear wave velocity profile of the topographic feature is often hard to obtain. Either due to access to the site (i.e., it is difficult to position equipment on a 35 degree slope) or the sheer cost of mobilizing the equipment to the site and drilling or conducted geophysical testing. In addition, differences in the stratigraphy below each sensor can significantly affect the ground motions measured on different parts of the feature, therefore knowledge of the stratigraphy is important.
- The overall unpredictability of earthquakes makes the measurement of topographic effects difficult. Sensors can often be deployed for months or years without measuring significant or strong earthquake activity.
- Finally the sheer cost of deploying numerous broadband sensors over difficult terrain makes these experiments somewhat rare.

These and other difficulties have been realized over time as experiments have been conducted. The overall knowledge of experimental setups, advancements in

instrumentation, and interest in the subject have led to better experiments. Although the experimental datasets have become more plentiful in recent years, data from these experiments is processed using just four general techniques:

- Horizontal to Vertical Spectral Ratio (HVSR) (Nakamura 1989, Lermo and Chavez-Garcia, 1993).
- Standard Spectral Ratio (SSR) (Borcherdt, 1970).
- Median Reference method (MRM) (Wilson and Pavlis (2000), Maufroy et al. 2012).
- Directional analysis of earthquake records (Massa et al. 2010).

These techniques are all based in the frequency domain and have both positive and negative attributes to their application of analyzing topographic effects.

The HVSR technique, otherwise known as the Nakamura technique, uses ambient seismic noise or microtremors produced by wind, ocean tides, urban activity, or other natural and unnatural sources to determine the natural frequency of a site. The technique became popular after being introduced by Nakamura in 1989. Nakamura gave a theoretical explanation to the HVNR technique, where microtremors are mainly caused by Rayleigh waves propagating in the sediment layers overlying bedrock. Fundamental mode Rayleigh wave amplification happens only in the horizontal plane and not in the vertical plane. Therefore, the horizontal component can be divided by the vertical component and a peak in the spectral domain is developed for frequencies experiencing amplification due to stratigraphy. Sanchez-Sesma et al. (2011) provides a different explanation of the theory behind the results of HVSR. They indicate that the intensity of microtremors produced near the surface can be well described by diffusion-like equations

and the energy density in the frequency domain is proportional to the imaginary part of the Green's function. The diffuse wave field theory provides a more comprehensive explanation of the HVSR method compared to Nakamura's theory. The technique has the advantage of being a single station analysis method that requires only one sensor. In 1993, Lermo and Chavez-Garcia applied the HVSR technique to both weak and strong motion records. The authors showed the method was capable of identifying the resonant frequency of topographic features. Other authors have also shown the technique to be promising for determining the fundamental frequency of topographic effects (Bard 1999). However, authors have also cautioned its use due to false amplification peaks and poor estimates of amplification factors (Massa et al. 2010).

The SSR technique was first introduced by Borcherdt (1970) and is one of the most widely used techniques for determining the amplification of seismic waves. The technique uses one sensor (the measurement sensor) located at a site believed to cause amplification of the seismic signal and one sensor (the reference sensor) located on a site close to the measurement sensor but at a location believed to produce no amplification (i.e., a rock flat site). To identify the amplification frequencies, a single component of the measurement sensor (horizontal or vertical) is divided by the same component of the reference sensor for a single event. The SSR technique results in an accurate amplification factor for the measurement sensor only if the reference sensor has zero amplification or de-amplification. In addition, the separation distance between the measurement sensor and reference sensor should be much less than the hypo-central distance to both sensors. Otherwise, a correction should be made that accounts for the geometric spreading of the seismic waves by multiplying the records by their respective hypo-central distance or their P minusS times (Steidl 1996). LuBrun et al. (1999) also

cautions that reference stations should be placed at least one wavelength from a hill in order to avoid waves diffracted by the topography.

The Median Reference Method (MRM) was first introduced by Wilson and Pavlis (2000). The method is similar to the SSR technique; however instead of relying on only one reference station that may be influenced by different factors than the measurement sensor, the MRM technique uses the median of an array of sensors as the reference station. The "median reference station" provides an approximate response of the entire topographic feature to compute amplification factors against. This provides a more stable reference station influenced less by local site conditions. Maufroy et al. (2012), through numerical modeling established the accuracies of MRM compared to SSR techniques. Maufroy et al. (2012) also explain that the median reference is not significantly influenced by the number of stations as long equivalent numbers of sensors are placed at the peak, base and along the slope of the feature.

Directional analysis of seismic waves can be performed to determine if topographic effects have preferential direction of motion for selected frequencies. Several authors have shown topographic effects are polarized in the direction perpendicular to the elongation of the ridge (Davis and West 1973, Chavez and Garcia et al. 1997, Buech 2010 and many others). This phenomenon is very evident on directional or polarity plots. The procedures involve rotating the two horizontal components of a sensor to establish a seismogram for all azimuthal directions. The seismogram of each record is then transformed to the frequency domain and the amplitude at each frequency-azimuth combination is known. Many field experiments have used these methods successfully to analyze topographic effects. A summary of the most influential topographic experiments are summarized below.

In 1973, Davis and West conducted field experiments into topographic effects by deploying instruments at the crest and base of Kagel Mountain and Josephine peak, California and Butler Mountain near Tonopah, Nevada. At the first two sites, aftershock data was recorded from the February 9, 1971 San Fernando earthquake, while ground motions recorded at the Nevada site were generated by a weapons detonations. Using the Standard Spectral Ratio method, the authors observed frequency dependent amplifications at the crest relative to the base of up to 30 for Kagel Mountain, however the other sites recorded much lower amplification (see Figure 2.8). Amplifications were in the frequency range of 2.0-3.3 Hz for Butler Mountain, 2.0-2.5 for Kagel Mountain, and 0.1-1.0 Hz for Joesphine Peak. The authors explain that the amplification and resonant frequencies of the mountains are a function of the dimensions of the relief (i.e., wavelength approximately equal to the width of the feature are amplified and as the slope

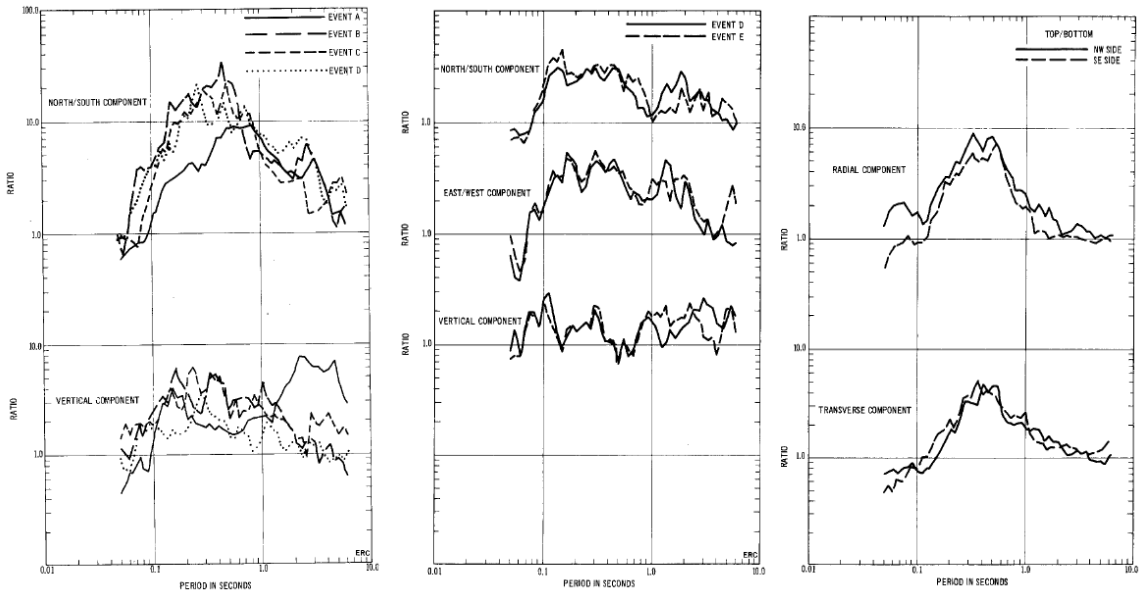

Figure 2.8: Ratios of Pseudo-relative velocity response spectra (PSRV) at Kagel Mountain (left), Josephine Peak (center), and Butler Mountain (right) (Davis and West 1973).

of the feature increases the amplification increases). The authors also determined that larger mountains amplify motions over a broadband of frequencies while smaller mountains amplify motions over a narrower frequency band.

In 1994, Pederson et al. published two experiments looking at topographic amplification in Central Greece and the French Alps. For the first experiment, a hill with a moderate slope (H/L of 0.24) was instrumented with seven 2 Hz 3D geophones (see Figure 2.8). The temporary network recorded 14 local and regional events. The seismograms clearly show amplification at the crest compared to the base of the feature (see Figure 2.9). The authors explain that the amplification measured on the horizontal components exceed those on the vertical component in both the time and frequency domain. Amplification of 1.5 to 3 can be seen on the SSR plots, with the N-S component recording the highest amplification. In addition, an increase in amplification is observed as the elevation increases. Indicating amplification increases as one moves from the base to the crest of a feature. For the second study, five 2-Hz 3D geophones were deployed on a steep limestone hill with stations S1, S4, and S5 placed on sediment deposits (see Figure 2.10). The seismogram in Figure 2.10 clearly shows soft soil amplification for the stations located on sediment deposits. When the records were transformed to the frequency domain, the amplification due to soil site effects was still present. However, the topographic amplification could be identified at 1.5 Hz once numerical modeling of the hill identified the resonant frequencies. From these results, it is clear that soil site effects can induce a much greater broadband amplification than topographic effects. However, topographic effects still produced a significant amplification of up to 3 times the reference station at isolated frequencies. The authors were also able to accurately model the frequency range and amplification of each hill and indicate that the lack of agreement between experimental and numerical results is caused in part by the choice of

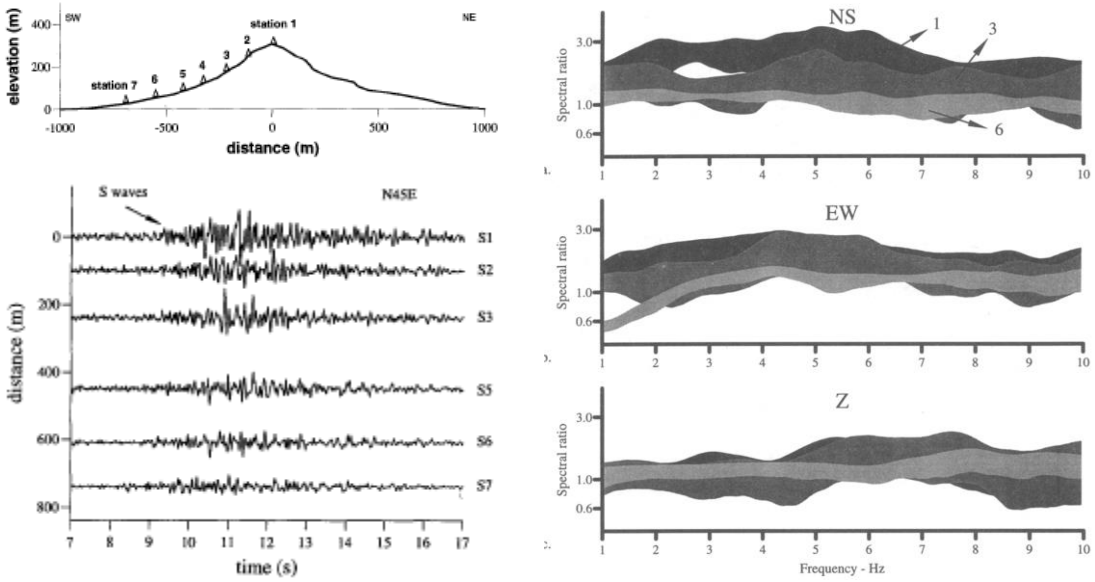

Figure 2.9: Transverse geometry of site 1 (left-top), seismogram for horizontal, transverse component (bottom-left), mean SSR amplitudes relative to station 7 with standard deviation (right) (Pederson et al. 1994).

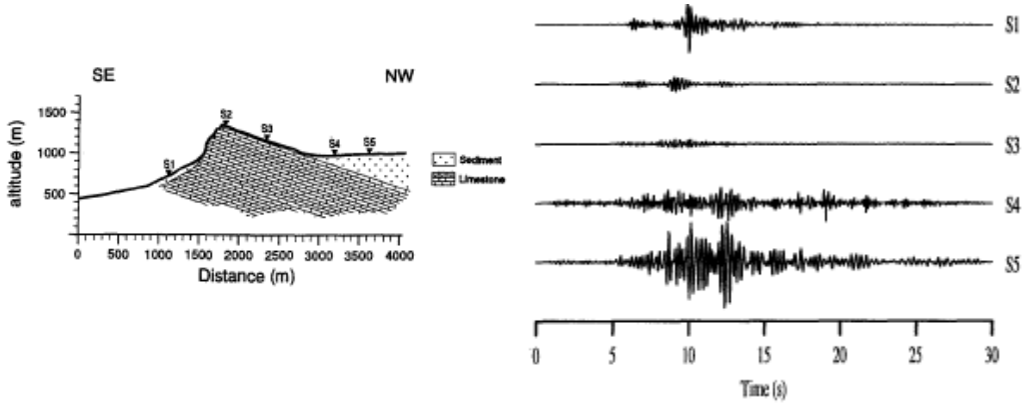

Figure 2.10: Transverse geometry of site 2 (left), Seismogram for horizontal, transverse component (right) (Pederson et al. 1994).

poor reference stations in experimental studies. The authors also indicate de-amplification and other topographic effects influence stations at the base of hills and can led to an overestimate of the amplification at the crest.

In 1994, Hartzell et al. published an experimental study investigating the high structural damage on Robinwood Ridge (H/L=0.61) following the 1989 Loma Prieta earthquake. Sensors were placed along the ridge as shown in Figure 2.11. The time records, as shown in Figure 2.10, show little amplification from base to crest, however the frequency domain results in several amplification peaks across the frequency span of interest. The amplification patterns were determined to be very complicated and variable with general peaks between 1-3 Hz and amplification of 1.5-4.5 times being the result of topographic effects, though sites effects are believed to have played a role in the amplification as well.

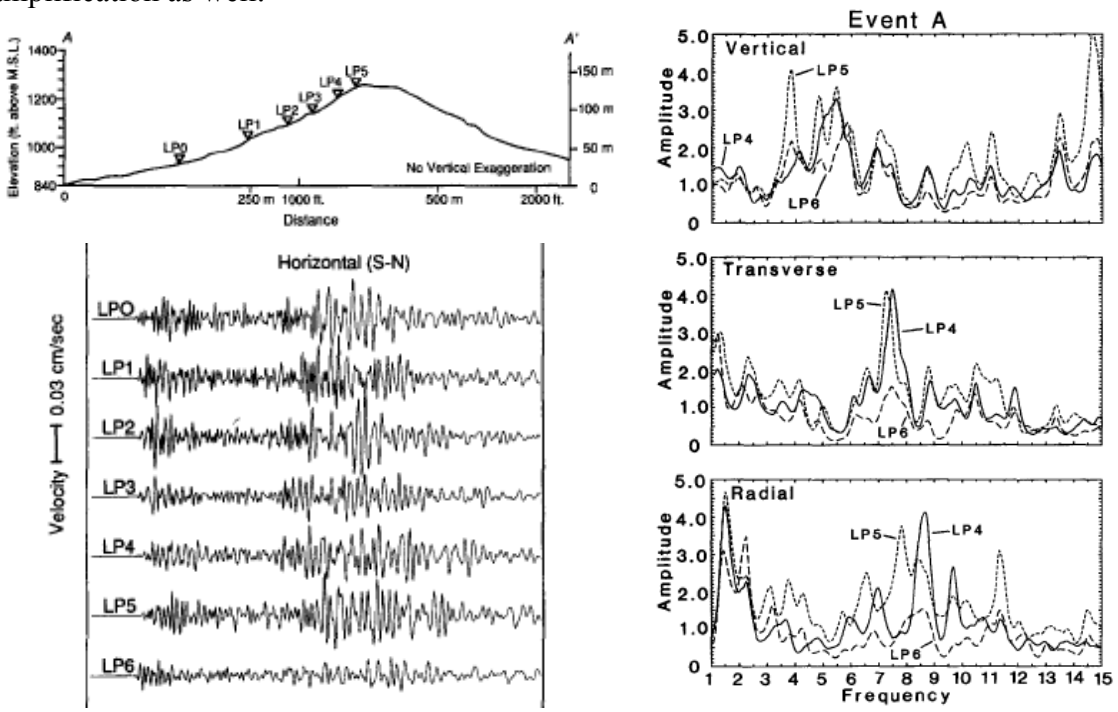

Figure 2.11: Transverse geometry of Robinwood Ridge (left-top), seismogram for horizontal, N-S component (left-bottom), and SSR amplitudes relative to station LP0 (right) (Hartzell et al. 1994).

In 1996, Chavez-Garcia et al. presented a study comparing the HVSR results obtained from sensors deployed in Epire, Northern Greece to HVSR computed from

theoretical transfer functions. The authors obtained the experimental HVSR by analyzing 68 events recorded on 10 seismographs (see Figure 2.11). These were compared to HVSR computed using theoretical transfer functions using P, SV, SH waves. The best results were computed using the response from the SV waves. The comparisons shown in Figure 2.12 indicate relatively good agreement between the experimental and theoretical results, however significant variably still exists. The authors conclude HVSR from earthquake records provide good results when analyzing records for topographic effects and indicate that HVSR for noise records also gives acceptable results.

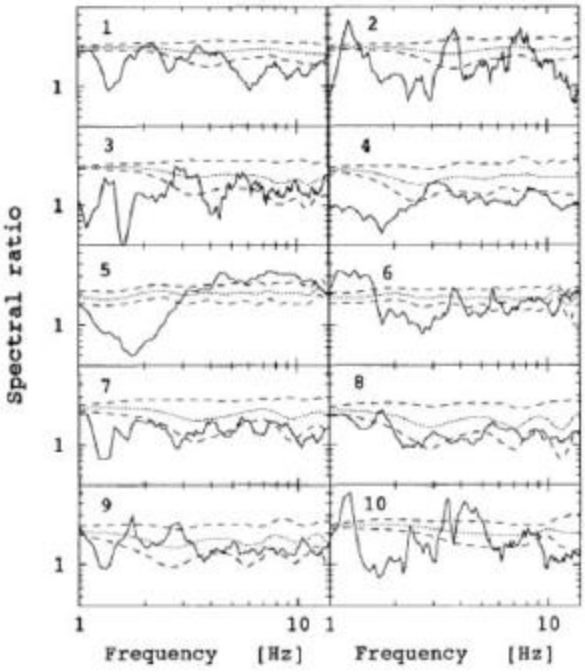

Figure 2.12: HVSR plots where the solid line is the geometric average of the weak-motion data. Dotted line is the geometric mean of the theoretical response and the dashed lines are plus and minus one standard deviation of the theoretical response (Chavez-Garcia et al. 1996).

In 1996, Spudich et al. investigated the seismic response of Tarzana hill in California. Tarzana hill is a small 15m high by 130m wide feature which experienced a ground motion with a PGA of 1.78g during the 1994 Northridge Earthquake. The authors deployed a temporary array of 21 geophones in six radial lines across Tarzana hill (see Figure 2.13). Fifteen aftershocks were recorded following the main shock and were analyzed using the Sources Spectra and Site Effects Inversion method (SSSEI) by inverting aftershock spectra in order to obtain average relative site response at each station as a function of the direction of the ground motion. They identified a resonant frequency of 3.2 Hz with a peak amplification factor of 4.5 for horizontal ground motions transverse to the hill and 2 for ground motions parallel to the hill (see Figure 2.14). The authors explain these amplifications match theoretical predictions of the resonant frequency. However, the measured amplifications do not account for the extremely high ground motions measured during the Northridge Earthquake. To investigate the amplification further Bouchon and Barker (1996) modeled the hill using the discrete wavenumber method. The authors determined that the hill amplified ground motions due to topography in the 2-15 Hz frequency range. However, the crest amplification only ranged from 1.3 to 2.0 times the flat plane ground motion. The large ground motion was not explained until 2009 when Graizer investigated Tarzana Hill using recordings from the Tarzana strong motion station along with a significant site investigation using both drilling and seismic methods. The authors determined that a large amplification does occur at the site in the 3-5 Hz range. However, much of the amplification is attributed to soil site effects due to the layering at the site. The site is underlined by a highly weathered shale formation with a shear wave velocity of 246 m/s in the upper 17 m, this layer is underlined by a 433 m/s layer. The natural frequency of the upper most layer of the profile was determined to be approximately 3.6 Hz, which matches well with the

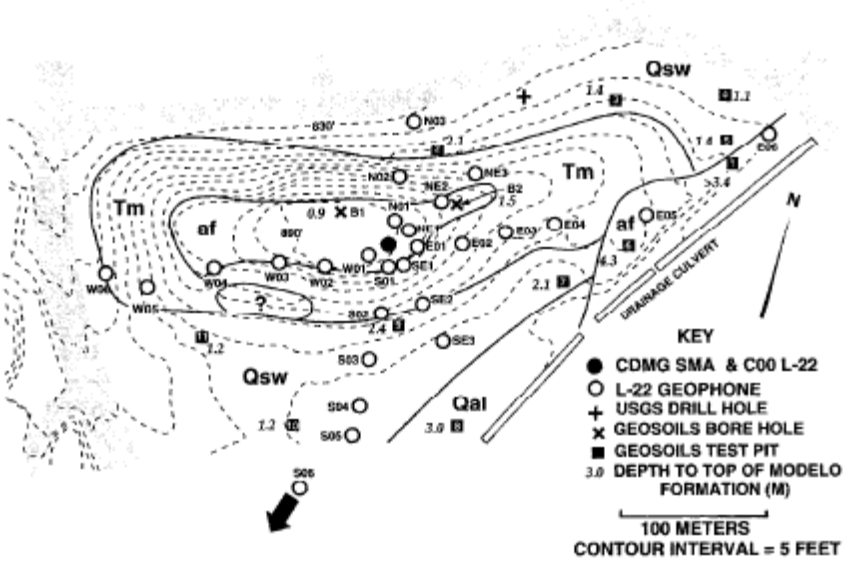

Figure 2.13: Topographic map of Tarzana hill with instrument and borehole locations (Spudich et al. 1996).

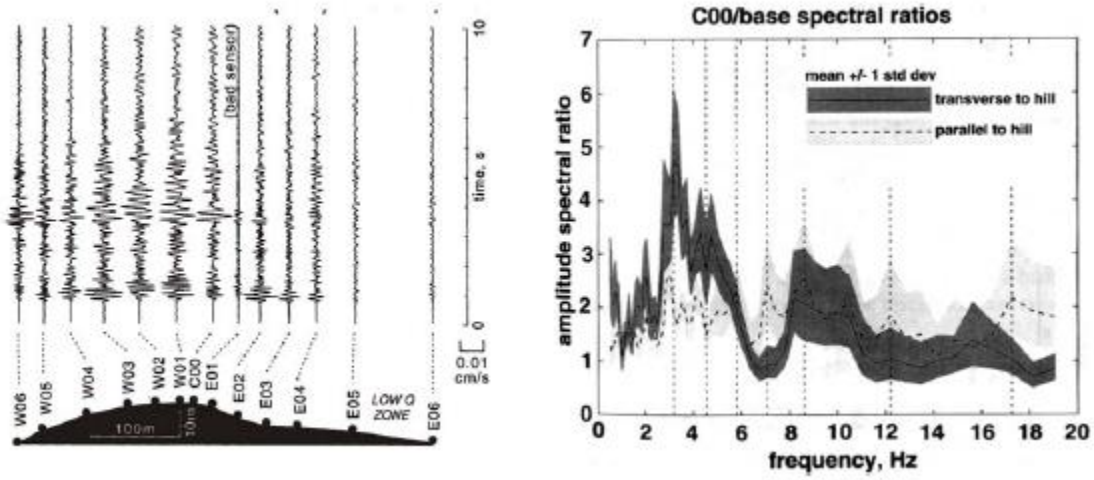

Figure 2.14: North-South seismogram recorded using the East-West array (left) and SSR amplification factors for transverse and parallel directions (right) (Spudich et al. 1996).

measured amplification frequency of Spudich et al. (1996). Therefore, Graizer concluded the extremely high ground motion at Tarzana hill was the result of both topographic and

site amplification, which underscores the need for seismic velocity measurements for topographic amplification experiments.

In 1999, Lebrun et al. published an experimental study conducted on Kitherion Mountain, a large scale feature near Corinth, Greece (see Figure 2.15). The authors used seven seismometers deployed along the mountain to record weak motion earthquake records. Records were analyzed using the SSR, HVSR, and HVNR (i.e., Horizontal to Vertical Noise Ratio) methods. The authors measured only small amplifications less than 3 for a resonant frequency of 0.7 Hz at the crest (see Figure 2.15). However, a significant amplification of up to 10 was measured between 4-5 Hz. This amplification is believed to

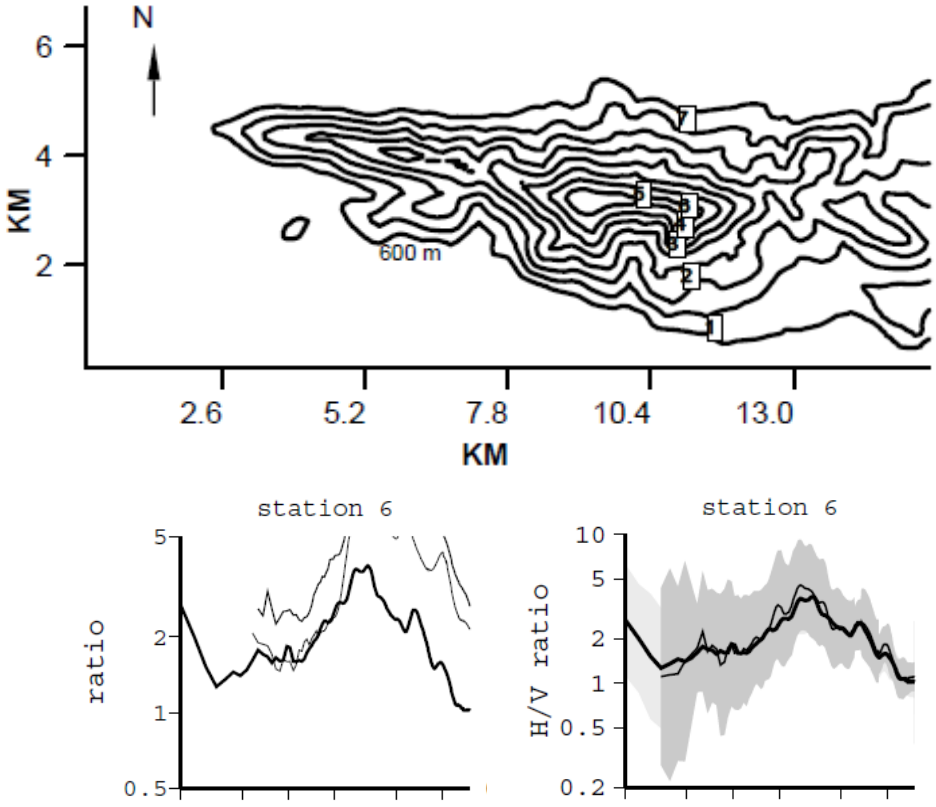

Figure 2.15: Topographic map of Kitheron (top), SSR for crest station (6) (left-bottom), HVSR (thick line) and HVNR (thin line) for crest station (6) (right-bottom) (Lebrun et al. 1999).

be the result of soil site effects; however velocity information was not available to confirm this hypothesis. Overall, the authors believe the analysis techniques matched well over the frequency range of interest and believe HVSR should be further investigated as a useful technique for topographic amplification.

In 2000, Caserta et al. published an experimental study looking at the causes for heavy damage in the historic center of Nocera Umbra, Italy from the M_L 5.6 and 5.8 earthquakes on September 26, 1997. Eight sensors were placed around the city on different geologic and topographic features to capture ground motion amplification from both soil site effects and topographic effects. Data was analyzed using the SSR, HVSR, and HVNR for 87 events (see Figure 2.16). Amplifications at the crest of approximately 2.5 in the frequency range of 2.5 to 5 Hz were measured and attributed to topographic effects. However, additional amplification of up to 10 over a broad frequency range of 4-

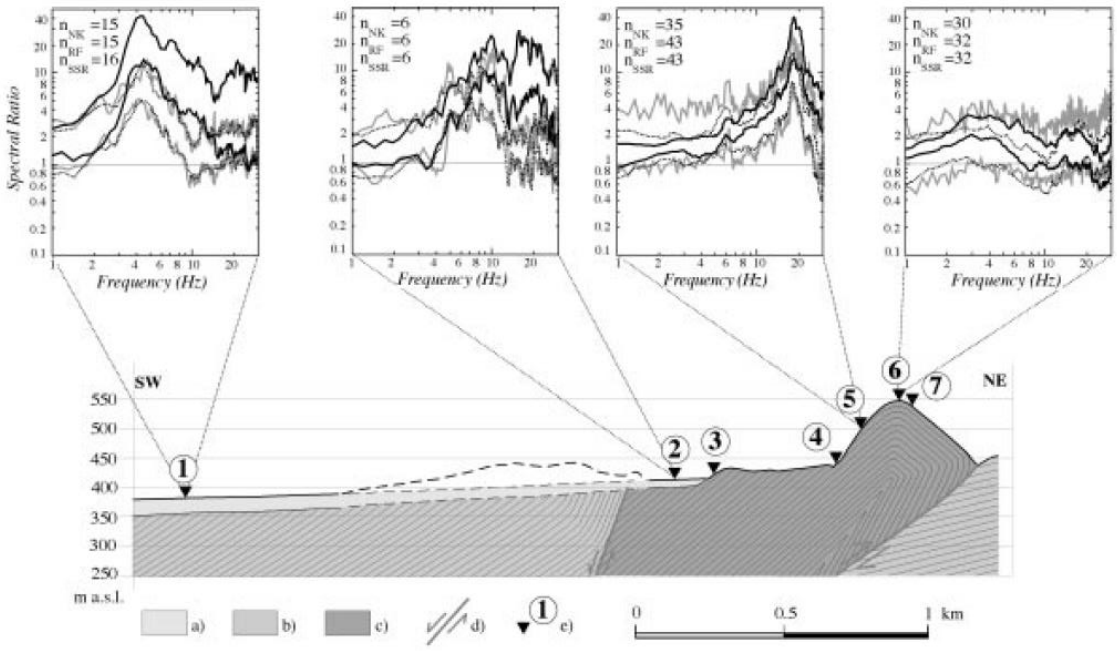

Figure 2.16: Topographic profile of Nocera Umbra with empirical transfer function for SSR (black solid line), HVSR (dotted line), and HVNR (grey solid line). (Caerta et al. 2000).

20 Hz was recorded, which was attributed to soil site effects. Ultimately, the authors concluded that topographic effects only played a small role in the heavy damage in Nocera Umbra and much of the damage was the result of poor building construction and soil site effects. Later in 2010, Pischiutta et al. deployed 8 seismometers across the hill and found good agreement with the results determined by Caserta et al. (2000). In addition, a directional analysis concluded that amplification between 2-4 Hz was polarized in the transverse direction of the hill, further confirming topographic effects.

In 2005, Stewart and Sholtis published an investigation on the difference between recorded ground motions at the base and crest of a 20 m high 3H:1V slope (see Figure 2.17) during the 1983 Coalinga earthquake and aftershocks. The recorded motions, as can be seen in Figure 2.16, are much greater for the switchyard at the crest of the slope than the pumping plant at the base. The authors used a soil-structure interaction model and a 1D site response model to estimate the contribution of each to the recorded ground motions. Conclusions indicate that soil-structure interaction affected short period amplifications while topographic effects were most pronounced for periods between 0.4-1 sec. Overall, half of the measured amplification was attributed to topographic effects and half to soil site effects.

In 2008 Buech, and in 2010 Buech et al., reported a field experiment in New Zealand looking at topographic effects on a bedrock-dominated ridge named Little Red Hill (see Figure 2.18). Seven seismometers were deployed on the ridge to record local and regional seismic events. Records were analyzed by comparing peak ground accelerations, power spectral densities, and standard spectral ratios. Both the time and frequency domain analyses indicated amplification from the crest to base of between 300-1100% for the transverse component, 100-500% for the longitudinal component, and 100%-250% for the vertical component. The resonant frequency of the mountain was

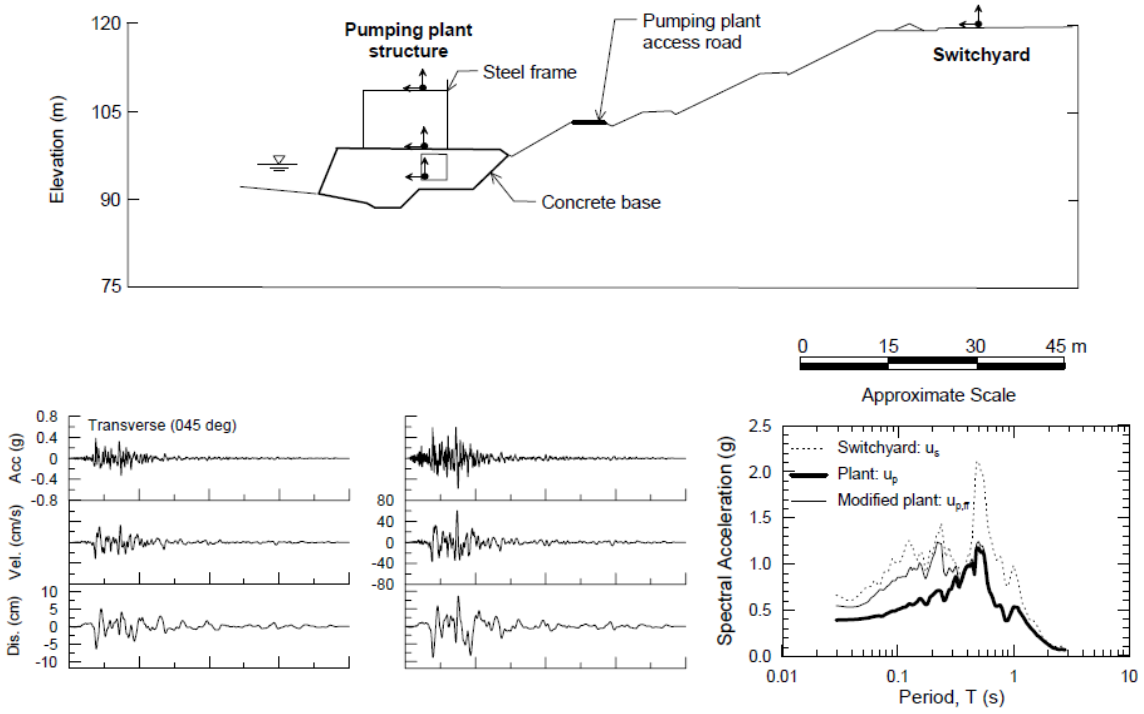

Figure 2.17: Topographic profile of the pumping plant and switchyard (top), time records for pumping plant (bottom-left), time records for switchyard (bottom-center), and spectral acceleration (bottom-right). (Stewart and Sholtis 2005).

determined to be 5 Hz using the SSR method and was consistent with theoretical estimates from Ambraseys (1960) and Gazetas and Dakoulas (1985). Buech et al. (2010) also indicate that nearby earthquakes tended to generate a more broadband amplification than more distant earthquakes, likely due to the frequency content difference between the two types of earthquakes.

In 2010, Massa et al. published an experimental study to determine the effect of topographic amplification on Narni, a small village in central Italy atop a 220 m high limestone ridge (see Figure 2.19). The ridge is characterized by 22-35 degree slopes. Sixty eight earthquake records were analyzed using directional analysis, SSR, and HVSR. The SSR results indicate amplifications due to topography in the frequency range of 4-5

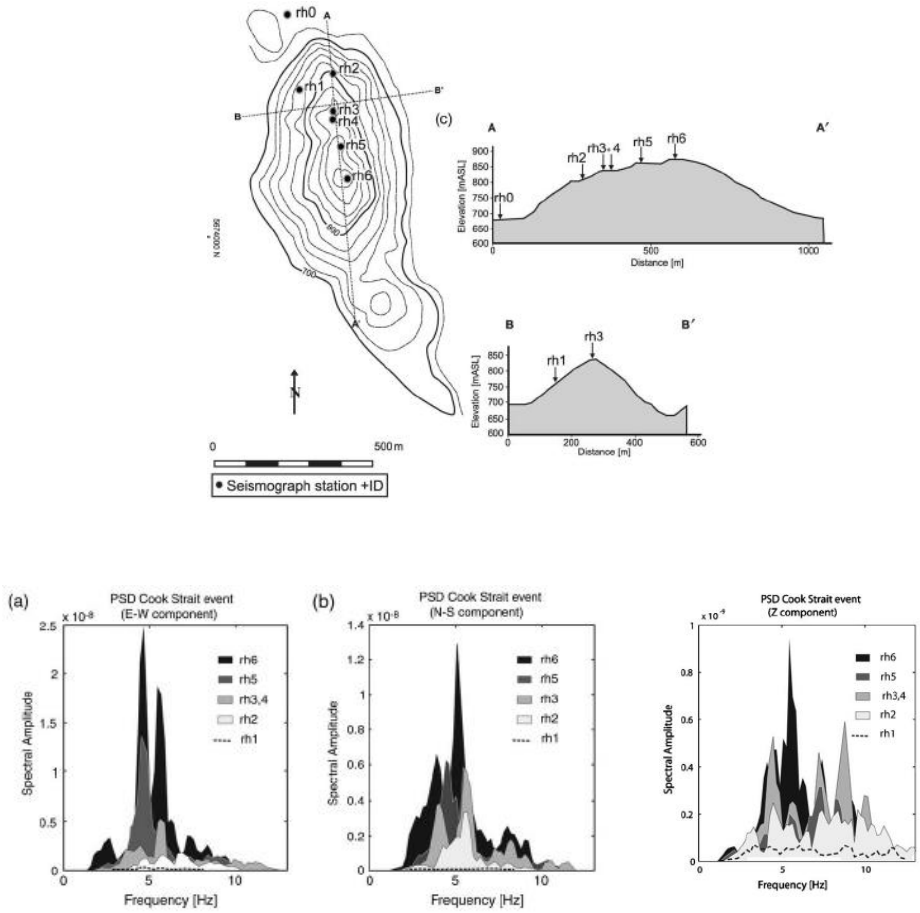

Figure 2.18: Topographic map of Little Red Hill (top), power spectral densities for N-S, E-W, V motions (bottom) (Buech et al. 2010).

Hz with amplification factors up to 4.5 (see Figure 2.19). The amplification is polarized, with greater amplification in the transverse direction. The HVSR technique compared well with the SSR technique for identification of the predominate frequency at 4-5 Hz.

HVSR also indicated amplification peaks that were not related to topographic effects. The authors warn against the use of HVSR for topographic studies due to this observation. Finally, the response spectrum of the events was computed and compared to the amplification factors suggested in Euro Code 8 (i.e., 1.2 or 1.4), an amplification of 3 for frequencies from 4-5 Hz was calculated for the response spectra, which leads to an

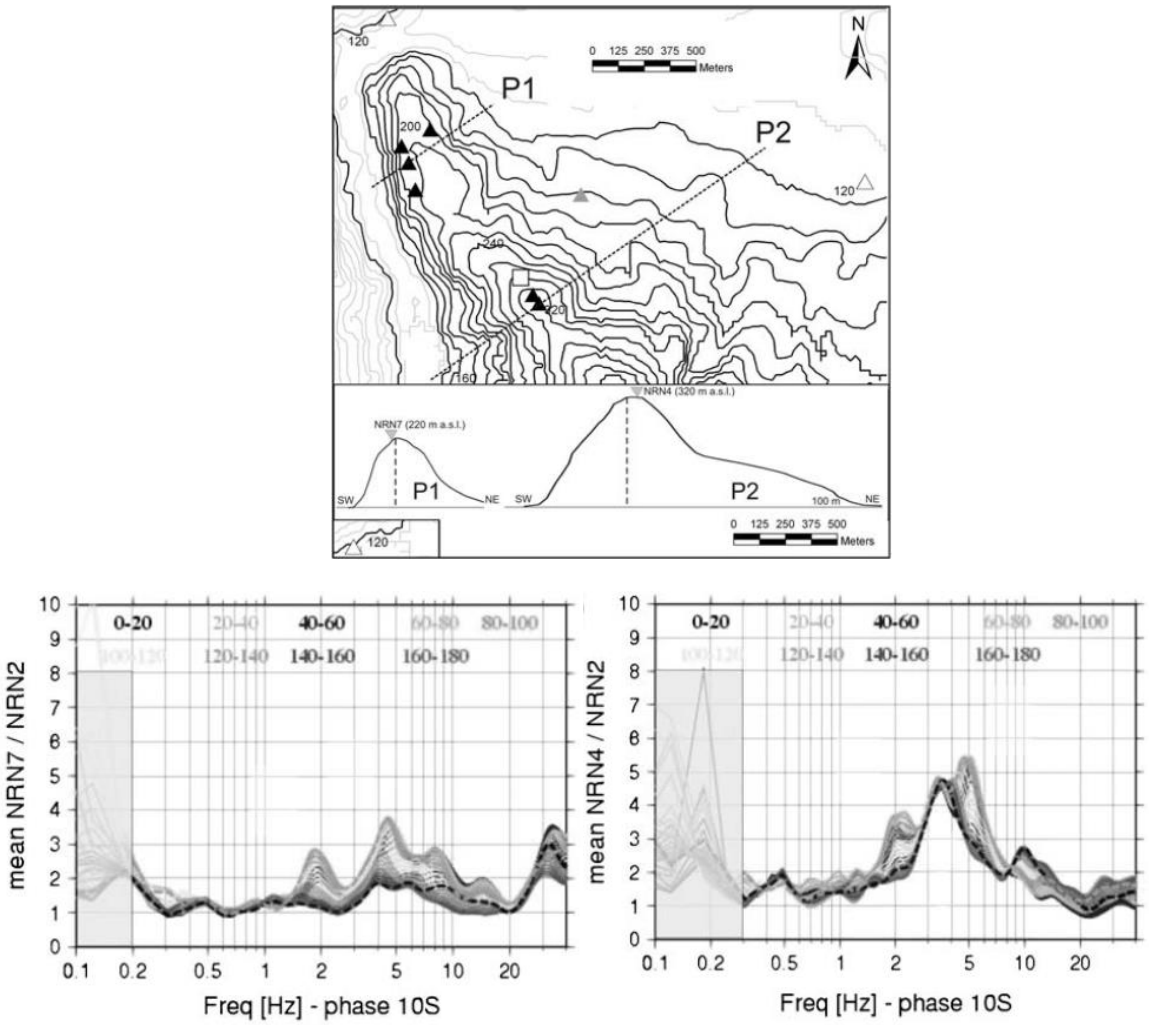

Figure 2.19: Contour map of Narni ridge (top), directional SSR for near field events (bottom) (Massa et al. 2010).

underestimate of amplification at the resonant frequency and an overestimate at other frequencies. The authors criticize the current frequency independent amplification factors used by Euro Code 8 and indicate a higher amplitude, band limited amplification factor would be more appropriate. Later in 2011, Lovati et al. compared the experimental results of Massa et al. (2010) to both 2D and 3D simulations conducted for Narni Ridge. The simulations considered a homogenous, isotropic model using the boundary element

method. The simulations match the frequency response of the ridge well. However, the simulations under estimated the amplification at 4-5 Hz by a factor of 2 relative to the experimental data. The authors attribute this difference to possible soil site effects at Narni Ridge and underscore the need for Vs measurements for topographic amplification sites.

In 2011, Massa et al. published a study comparing the three most commonly used ground motion analysis techniques HVSR, HVNR, and SSR. The techniques were used to analyze ground motions recorded at 5 Italian strong motion sites on various stratigraphy and morphological settings. Results from the article indicate HVNR can be effective at determining the first resonant frequency for sites with simple 1D or 2D configuration and a strong impedance contrast between the upper soil layers and bedrock. However, the amplification factors obtained from HVNR tend to underestimate the amplification compared to those determined from earthquake records at the site. In addition, for complicated setting such as topography, HVNR and HVSR can lead to completely biased results compared to reference stations techniques (e.g., SSR) (see Figure 2.20).

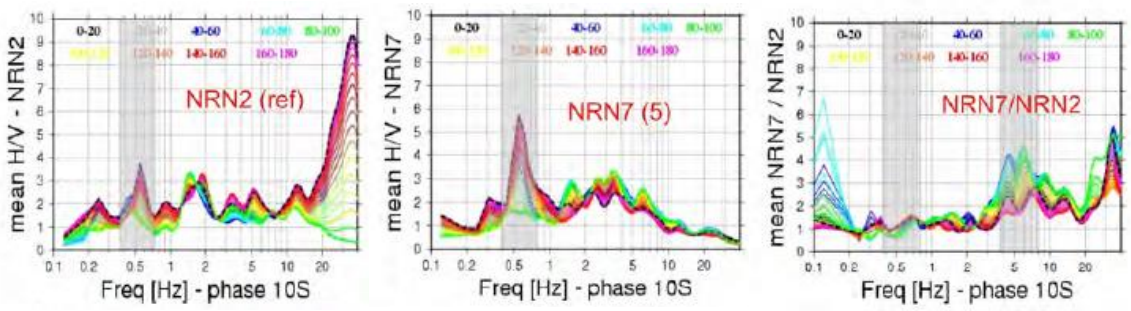

Figure 2.20: Directional HVSR obtained at the reference site (left) and the crest (center) and SSR for reference to crest for 10s coda of the largest aftershock (Massa et al. 2011).

In 2011, Marzorati published an experiment investigating the high levels of damage in Castelvecchio Subequo, Italy following the 2009 L' Aquila earthquake. Castelvecchio Subequo is a small hill in Central Italy (see Figure 2.21). Geophysical investigations, along with geological/structural and geomechanical field surveys, revealed significant surface rock fracturing across the hill. Ground motion HVSR analysis indicates amplification in the 1 to 15 Hz range with amplification factors up to 3. The motions were polarized in the transverse direction of the ridge (see Figure 2.21). This

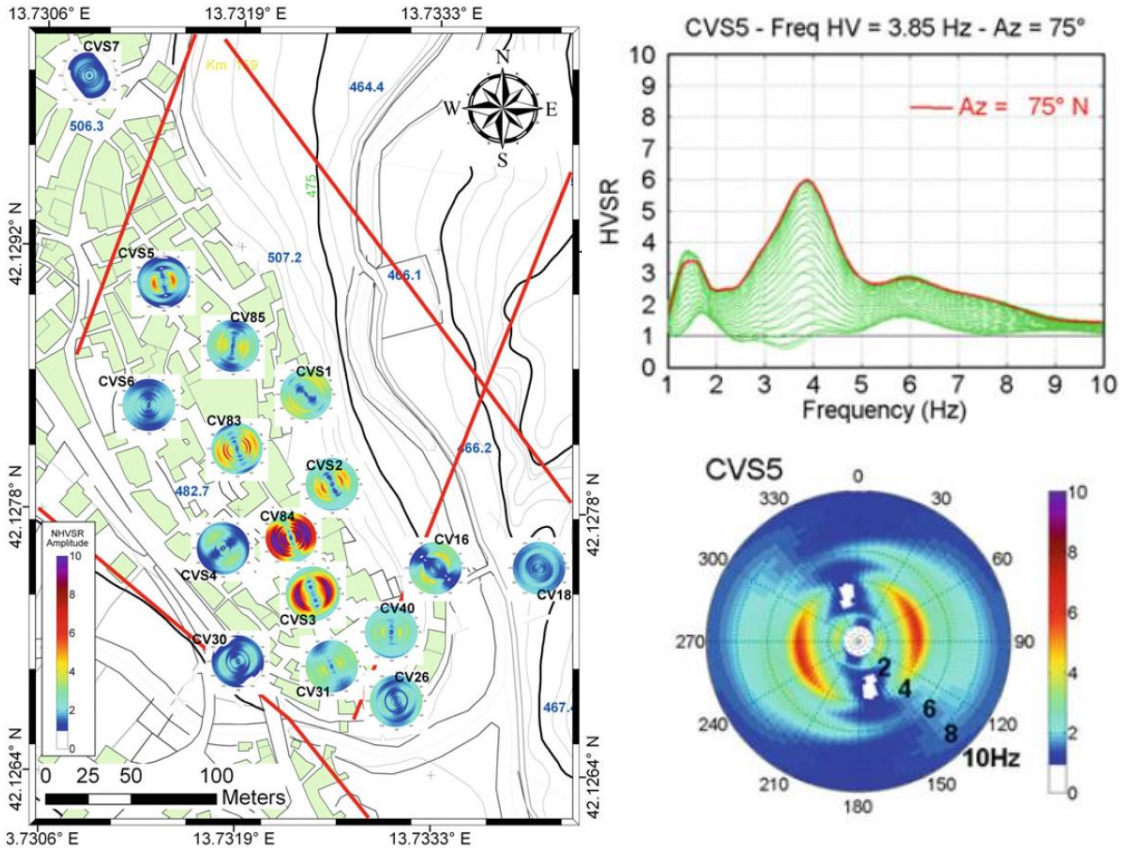

Figure 2.21: Map of Castevelcchio Subequo showing direction analysis of HVNR (left), HVSR for a crest sensor (right-top), and directional analysis of HVSR data (right-bottom) (Marzorati et al. 2011).

corresponds well with the surface rock cracks, which propagate in the direction parallel with the elongation of the ridge. Therefore, the authors indicate that the factures were related to the polarization of the seismic waves on the hills. However, they concluded much of the damage during the earthquake was due to poor building construction.

2.6 SUMMARY AND CONCLUSIONS

Topographic amplification has been studied by many researches using field observations after earthquakes, numerical modeling, theoretical derivations, and experimental studies. All these methods have come to a qualitative agreement about the existence of seismic-motion amplification at ridges and mountain tops and attenuation at the base of hills. Tables 2.4 and 2.5 contain a summary of the experimental and numerical modeling studies over the last several decades. Below is a summary of the key facts determined by these studies.

- The maximum amplification attributed to topographic effects occurs at, or near, the peak of the ridge. The maximum de-amplification occurs near the toe (base) of the feature. Irregular amplification/de-amplification patterns are observed in between (Boore 1972 and Bouchon 1973).
- The amplifications are highly frequency-dependent and seem to occur at wavelengths comparable to a characteristic of the feature, such as width and/or height (Paolucci 2002, Ashford and Sitar 1997).
- Amplifications of particle motion in the direction perpendicular to the direction of elongation of the ridge seem to be larger than the motions parallel to the elongation direction of the ridge.
- The vertical direction of particle motion seems to be affected far less, if any, by topographic amplification.

Table 2.4: Main experimental studies presented in literature about topographic effects (formatted after Lovati 2011).

Site	Geol	Vs (m/s)	Geom	ΔH (m)	W (m)	L (m)	H/ (W/2)	f0(Hz) theo	f exp (Hz)	Amp Factor	Instrum	Analysis method	References
Bays Mountain	L/c	NA	2D rd	260	NA	NA	NA	NA	2.5	0.9-2.0	V2D (1s)	SSR (Sg-Lg)	Griffiths and Bollinger, 1979
Kitherion mt	L	3000	2D rd	700	4000	6000	0.4	0.52-0.75	0.7/ 4.0-5.0	2.0-10.0	V3D (40s)	SSR, HVSR, HVNR	LeBrun et al., 1999
Kagel Mountain	G	3048	3D mt	427	3048	NA	0.3	0.7 - 1	2.0 - 2.5	20.0-30.0	V3D	SSR (PSV)	Davis and West, 1973
Gap Mountain	S/c	NA	2D rd	236	2750	NA	0.2	NA	2.5	0.8-2.5	V2D (1s)	SSR (Sg-Lg)	Griffiths and Bollinger, 1979
Sourpi	L	2800	2D rd	300	2500	5000	0.2	0.78 - 1.12	1.5 - 3.0	<3.0	V3D (0.5 s)	SSR	Pedersen et al., 1994
Mt Saint Eynard	L/M	3000	2D rd	500	2500	7500	0.4	0.84 - 1.2	2.0 - 4.0	<4.0	V3D (0.5 s)	SSR	Pedersen et al., 1994
Powell Mountain	S/c	NA	2D rd	394	2400	NA	0.3	NA	2.0 - 4.0	1.1-3.4	V2D (1s)	SSR (Sg-Lg)	Griffiths and Bollinger, 1979
Mt. Atzmon	L	2100-3200	2D rd	500	2000	NA	0.5	0.74-1.6	1.3- 2.0	4	V3D (1s)	HVSR, HVNR	Zaslavsky and Shapira, 2000
Mt.Berech	L	2400	2D rd	450	1800	NA	0.5	0.9 - 1.3	1.5 - 4.0	3.0-3.5	V3D (1s)	HVSR, HVNR	Zaslavsky and Shapira, 2000
Butler Mountain	D	NA	3D mt	214	1524	NA	0.3	NA	2.0 - 3.3	5.0-6.0	V2D	SSR (PSV)	Davis and West, 1973
Mt.Meron	L	2100-3220	3D hill	250	1500	NA	0.3	0.98-2.15	2.5 - 3.5	4	V 3D (1s)	HVSR, HVNR	Zaslavsky and Shapira, 2000
Robinwood Ridge	v	500	3D hill	460	750	NA	1.2	0.47 - 0.67	1.5 - 3.0	1.5-4.5	V3D (0.58s)	SSR	Hartzell et al., 1994
Narni ridge	L	1000	2D rd	160	500	1300	0.6	1.4 - 2.0	3.0 - 5.0	4.5	V 3D (5s)	HVSR,SSR	Massa et al., 2010
Little Red	S/A	1200	2D rd	210	500	800	0.8	1.68 - 2.4	3.0 - 5.0	3.0-11.0	V 3D (1s)	PSD, SSR	Buech et al., 2010
Nocera Umbra	L/M	2500	3D rd	120	400	NA	0.6	4.38 - 6.25	2.0 - 5	2.0-3.0	V3D (40s)	SSR, HVSR, HVNR	Caserta et al., 2000
Nocera Umbra	L/M	1200	3D rd	144	400	NA	0.7	2.1 - 3.0	2.0 -4.0	<4.0	V3D (40s)	SSR	Pischiutta et al., 2010
Epire	L	2700	2D rd	200	225	NA	1.8	8.4 - 12	1.0 - 5.0	<5.0	V3D (0,5s)	SSR, HVSR, HVNR	Chavez-Garcia et al.,1996
Canal Beagle	G	NA	canyon	20	200	NA	0.2	NA	2.0 -4.0	10.0-15.0	V3D + A3D	SSR	Celebi, 1987
Castelvecchio	L	NA	2D rd	30	150	300	0.4	NA	2.0 - 4.0	4.5	V 3D (5s)	NHVR, HVSR, SSR	Marzorati et al., 2010
Tarzana	v	369	2D rd	15	130	500	0.2	1.99 - 2.84	3.2	<2.0	V3D (0,5s)	SSSEI	Spudich et al., 1996
San Joaquin	s	300	cliff	21	126	NA	0.33	1.67-2.38	1.0-2.5	1.2	A3D	SSR,SSI	Stewart and Sholtis, 2005

column 2: **Geology:** L limestone, S sandstone, A argillite, M marl, G granite, D dacite, c collvial deposits, v various; column 3 **Vs (m/s)** is the shear wave velocity; column 4 **Geom** the geometric characterists of the feature; column 5 **ΔH(m)** is the elevation difference between the base and crest; column 6 **W (m)** width of the feature; column 7 **L (m)** length of the feature; column 8 **H/(W/2)** shape ratio; column 9 **f0 (Hz) Theo** theoretical max and min resonant frequencies determined using Paolucci (2002); column 10 **f exp (Hz)** experimental estimated resonant frequency; column 11 **Amp Factor** Amplifcation factor determined from experimental study; column 12 **Instrum** Intrumentation V velocimeter, A accelerometer

Table 2.5: Main numerical simulations presented in literature about topographic effects (formatted after Lovati 2011).

Site	Geol	Vs (m/s)	Geom	ΔH (m)	W (m)	L (m)	H/ (W/2)	f0(Hz) theo	f model (Hz)	Amp Factor	Method	References
Kitherion mountain	L	3000	2D rd	700	4000	6000	0.4	0.52-0.75	0.7	<3.0	boundary elements	LeBrun et al., 1999
Sourpi	L	2800	2D rd	300	2500	5000	0.2	0.78 - 1.12	1.5 - 3.0	<4.0	boundary elements	Pedersen et al., 1994
Mont Saint Eynard	L/M	3000	2D rd	500	2500	7500	0.4	0.84 - 1.2	2.0 - 4.0	<10.0	boundary elements	Pedersen et al., 1994
M. Titano	L	1500	2D rd	250	1100	NA	0.5	0.95 - 1.36	1	1.2-1.6	spectral elements	Paolucci, 2002
Castellaro	C	800	2D rd	240	600	NA	0.8	0.93 - 1.33	0.93 - 1.33	1.1-1.3	spectral elements	Paolucci, 2002
Irpinia	v	464	2D rd	60	550	NA	0.2-0.24	0.59-0.84	1.5-2.0	1.2-2.0	finite elements	Athanasopoulos et al, 2001
M. Ushibara	NA	1000	3D hill	170	520	NA	0.7	1.34 - 1.93	0.9	<5.0	spectral elements	Paolucci, 1999
Narni ridge	L	1000	2D rd	160	500	1300	0.6	1.4 - 2	4.0 -5.0	<2.2	boundary elements	Lovati et al., 2010
Civita di Bagnoregio	tuff	600	3D hill	110	450	NA	0.5	0.93 - 1.33	1	1.3-1.8	spectral elements	Paolucci, 2002
Nocera Umbra	L/M	2500	3D rd	120	400	NA	0.6	4.37 - 6.25	2.5 - 5.0	2.0-3.0	finite difference	Caserta et al., 2000
Nocera Umbra	L	1200	3D rd	144	400	NA	0.7	2.1 - 3	2.0 - 3.0	<2.0	finite difference/elements	Pischiutta et al., 2010
Altino	L	1000	3D hill	65	300	NA	0.4	2.33 - 3.33	2.6	1.2-1.3	spectral elements	Paolucci, 2002
Epire hill	L	2700	2D rd	200	225	NA	1.8	8.4 - 12	1.0 - 5.0	2.0-3.0	boundary elements	Chavez-Garcia et al.,1996
Tarzana hill	v	369	2D rd	15	130	500	0.2	2 - 2.8	3.0 -5.0	1.3-2.0	boundary elements	Bouchon and Barker, 1996

column 2: **Geology:** L limestone, S sandstone, A argillite, M marl, G granite, D dacite, c collvial deposits, v various; column 3 **Vs (m/s)** is the shear wave velocity; column 4 **Geom** the geometric characterists of the feature; column 5 **ΔH(m)** is the elevation difference between the base and crest; column 6 **W (m)** width of the feature; column 7 **L (m)** length of the feature; column 8 **H/(W/2)** shape ratio; column 9 **f0 (Hz) Theo** theoretical max and min resonant frequencies determined using Paolucci (2002); column 10 **f model (Hz)** resonant frequency estimated through modeling; column 11 **Amp Factor** Amplifcation factor determined from experimental study

- For numerical and theoretical studies, SV waves (in-plane shear waves) produced the highest amplification followed by SH waves (anti-plane shear waves) and finally by P (compression) waves.
- The azimuth and zenith angle of incident waves seems to influence the motions measured spatially across a feature. For zenith angles less than vertical, the maximum amplification shifts from the peak to the "sun" (far) side of the ridge (relative the incoming azimuth angle) and de-amplification occurs on the "shadow" (near) side of the ridge.
- The stratigraphy of a site can significantly influence the level of amplification at a site.
- There is a satisfactory, qualitative agreement between experimental, numerical, and theoretical results for the relationship between a features geometrical and mechanical characteristics and its resonant frequency range. However, difficulties in determining mechanical values, shear wave velocity, and in defining the height and width of real topography make it difficult to compared recorded and estimated values.

Beyond these key facts, review of this literature has revealed several points of contention where authors disagree. Meaning different research approaches have developed differing conclusions. These points are listed below:

- It has been determined that the observed, or computed, amplification is related to the "sharpness" of the topography. Geli (1988) stated that steeper slopes produce higher amplifications. However, Athanasopoulos and Zervas (1993) determined shallower slopes produce higher amplifications than steeper slopes.

- A quantitative discrepancy exists between estimated amplification factors from theoretical equations/numerical modeling and experimental/observational results (see Table 2.3 and 2.4). Experimental and observational results typically report amplification 2 to 10 times higher than those estimated using numerical modeling or theoretical equations. Authors have developed several explanations for this disagreement, including: (1) difficulty of the field experiments to determine a "good" reference station for calculating SSR amplification factors, (2) the effect of cross coupling on the different components of ground motion, (3) source directivity effects, (4) irregularities or difficulties in determining the site stratigraphy or Vs characteristics of the feature, (5) confusion of topographic effects and soil site effects, and (6) over simplification of real topography and material properties by numerical models and theoretical evaluations.
- It is still unknown how recorded and modeled weak motion amplification factors and resonant frequencies correlate to the frequency range and amplification factors expected for strong ground motions. Celebi 1987 reported that the resonant frequency ranges were similar, but weak motion had higher amplification factors than strong motion. However, there is little additional evidence to confirm his findings.

This dissertation details an experimental study using numerous short period and broadband sensors located at various points along steep topography in Central-Eastern Utah. These sensors were deployed to record consistent and predictable mining-induced seismicity on real topographic features. Specifically, the study aims to: (1) record weak motion topographic amplification on various features with a detailed terrain model and (2) provide a significant weak motion data base of topographic amplification for those looking to model real topographic features. It is hoped that this information will allow

engineers to more appropriately account for topographic effects when designing for strong ground motion in seismically active area of the world.

Chapter 3: Topographic Study Phase I

3.1 Introduction

Phase I was the first part of a two part study looking at topographic effects. During Phase I, 11 Mark Products L4-C 3D geophones and two Nanometrics Trillium Compact broadband seismometers were placed in a dense array over a butte in the Manti-La Sal National Forest in Central-Eastern Utah. The 3D array extended nearly 750 m across the butte, spanning a total vertical elevation change of 120 m with slopes angles of 9 to 34 degrees. This area experiences frequent and predictable coal mining induced seismicity, often producing several weak events per day. The array was used to record these microtremors 24 hours a day for 7 days. The microtremors were processed using a standard ground motion processing scheme, followed by three methods of analysis to determine topographic effects. This chapter details the experimental equipment, field deployment, data collection, raw data formats, and analysis schemes for Phase I of the topographic effects field study.

3.2 Site and Geology

The topographic study site is located in Central-Eastern Utah, USA on land dedicated to the Manti-La Sal National Forest. The national forest encompasses over 2900 km^2 in Utah and Colorado and features rugged mountainous terrain with off-road trails. The study area is specifically located in the East Mountain area of the Manti-La Sal National Forest, approximately 39 km South-West of Price, Utah. East Mountain lies within the Wasatch Plateau region in a transition zone between the basin and range province and the Colorado Plateau (see Figure 3.1). The geology of the East Mountain area is summarized below from Arabasz and Julander (1986) and Williams and Arbabasz (1989).

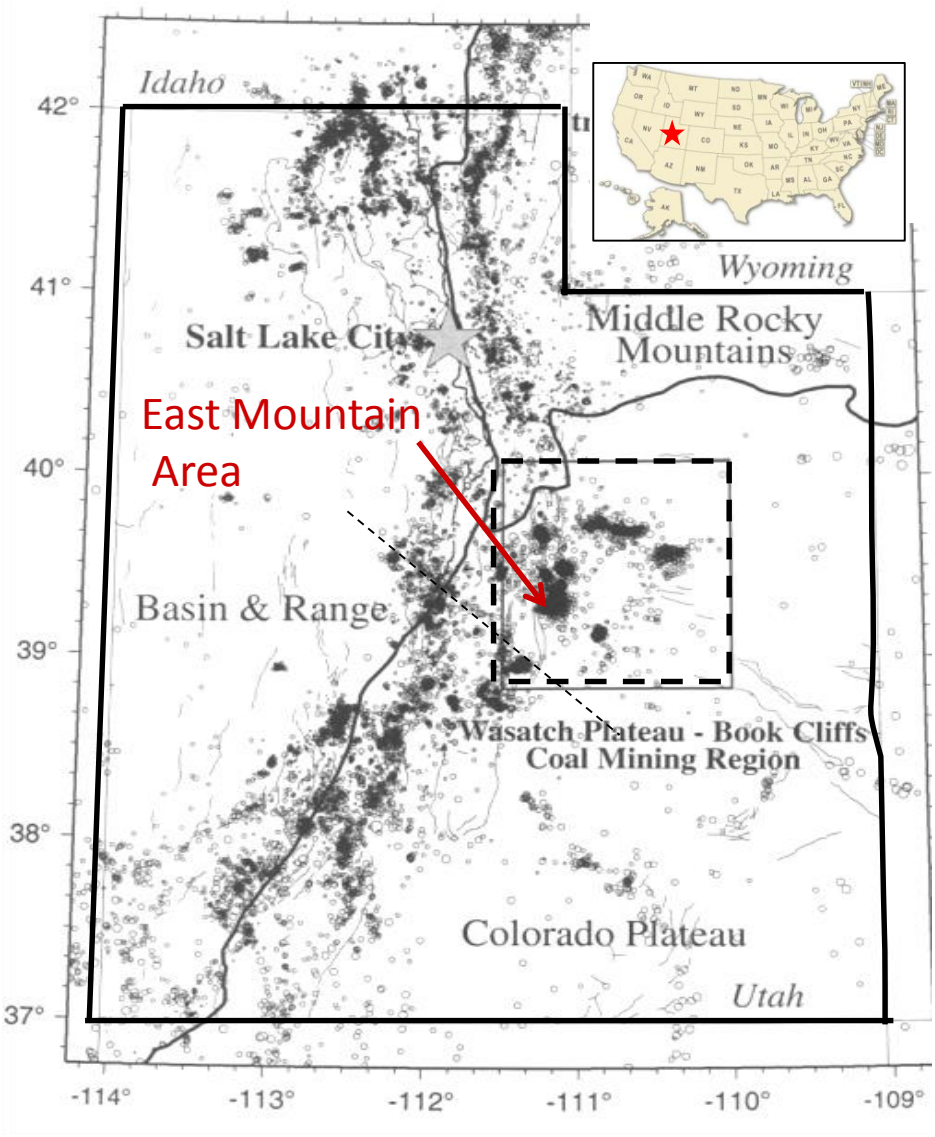

Figure 3.1: Topographic study area showing the East Mountain area in Central-Eastern Utah, USA (Arabasz and Pechmann 2001).

East Mountain is a flat topped incised mountain range that sits at a maximum elevation of just over 3000 m above mean sea level and has approximately 1000 m of relief from peak to valley floor. East mountain is underlined by sedimentary formations consisting of gently dipping (<5°) sandstone and shale of upper Cretaceous to Tertiary age. Two significant coal seams lie within the Blackhawk formation of the Cretaceous

age Mesa Verde Group, approximately 600 m below the crest of East Mountain (see Figure 3.2). Overall, East Mountain is part of a series of North-South trending Grabens formed by relatively young uplift and East-West extension.

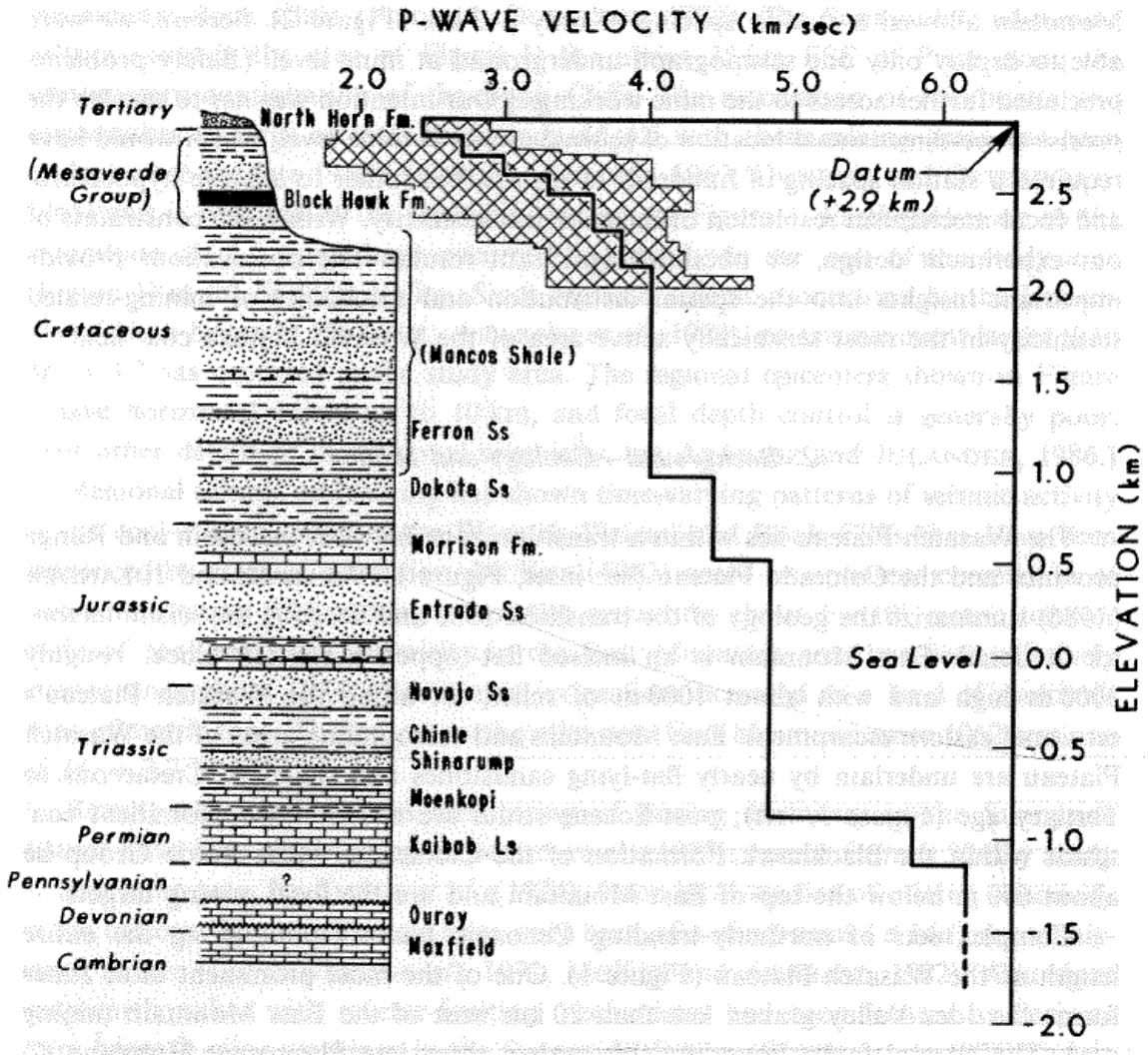

Figure 3.2: P-wave velocity model (right) derived for the East Mountain area and corresponding stratigraphic column (left) after Hintze (1973). Hatched area envelops 14 velocity-depth profiles from seismic surveys on East Mountain (modified from Williams and Arbabsz 1989).

In addition to the geologic profile, a surface geology map was obtained from Deer Creek Coal mine and shown in Figure 3.3. Using the surface geology map, along with boring logs from the United States Geologic Survey and Deer Creek Coal Mine, N-S and E-W geologic cross sections were generated by Deer Creek Coal Mine (see Figure 3.4). These cross sections indicate the feature instrumented in 2010 had a geologic profile with Flagstaff Limestone at the peak of the feature, followed by the North Horn Formation, Upper Price River Formation, Castlegate Sandstone, Blackhawk Formation, Star Point Sandstone, and finally Mancos Shale. Stations in 2010 were located mostly on the

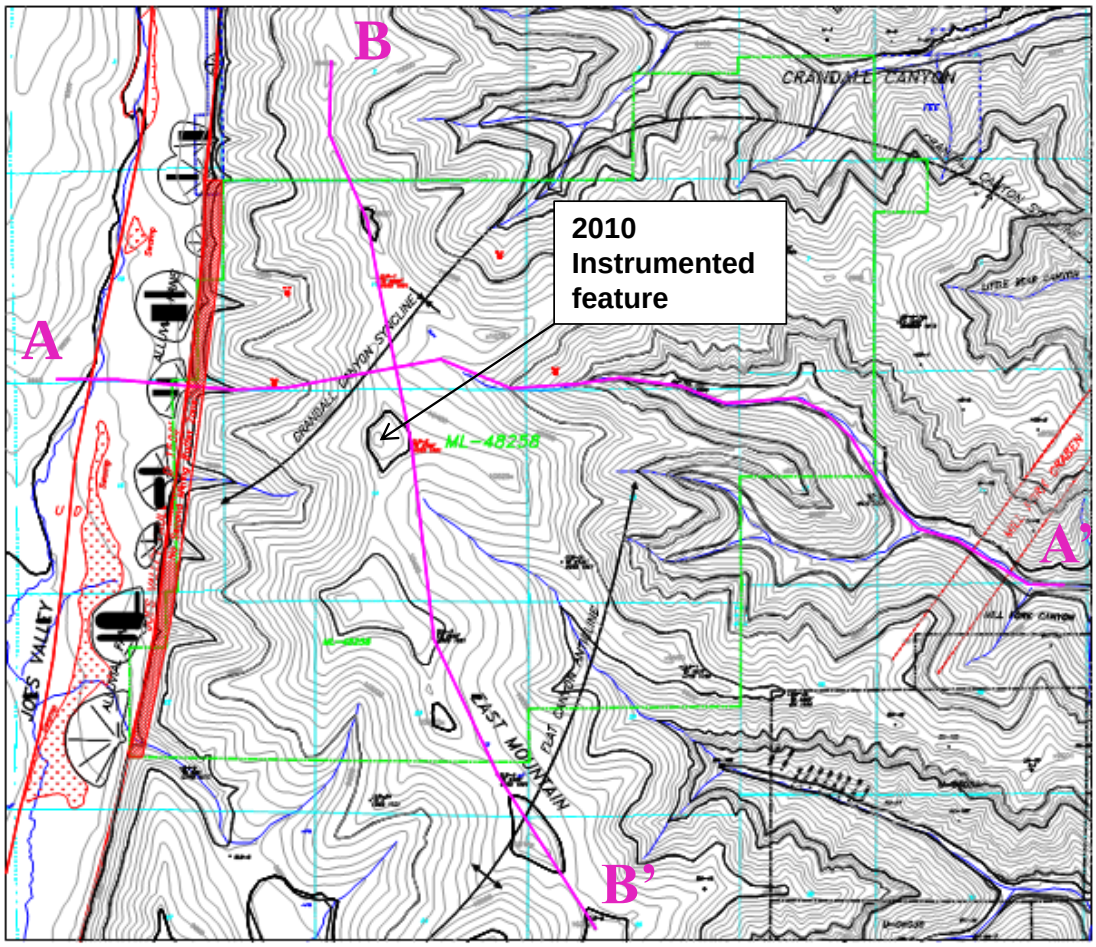

Figure 3.3: Surface geology map of the East Mountain area, Central-Eastern Utah (map provided by Deer Creek Coal Mine).

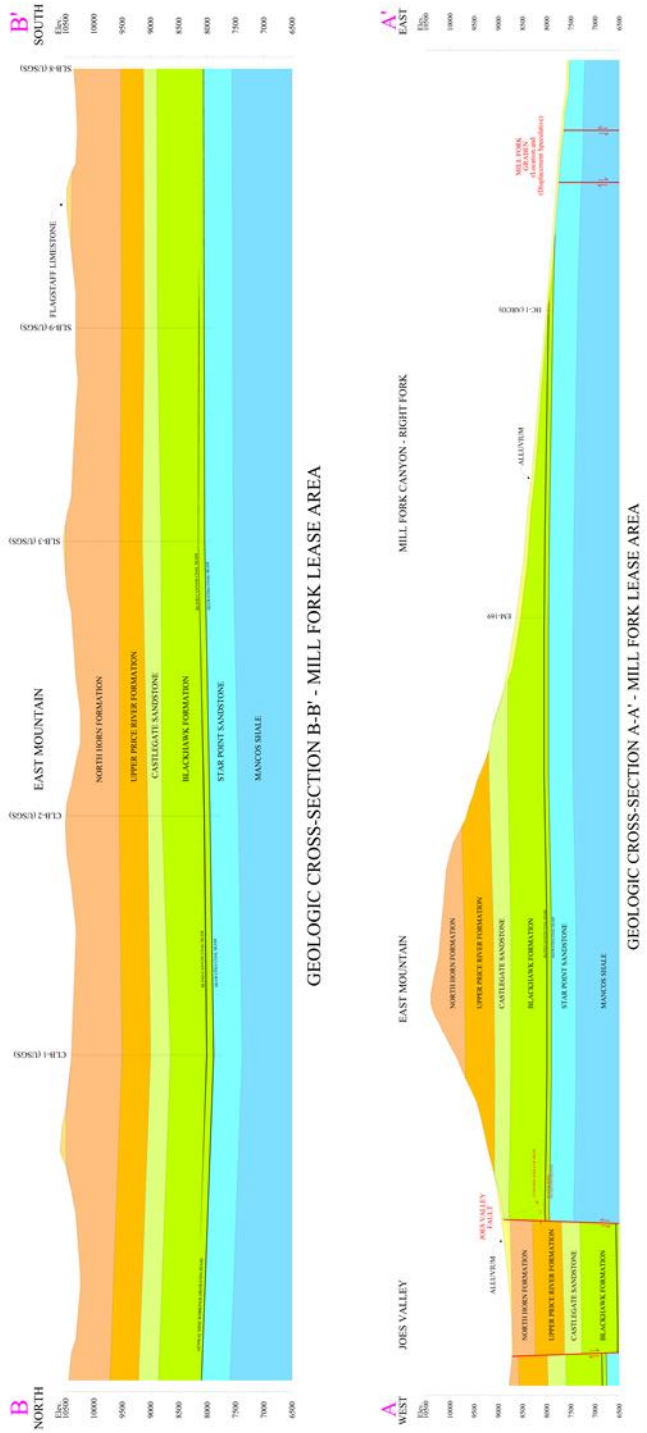

Figure 3.4: Geologic cross sections A-A’ and B-B’ of the East Mountain area, Central-Eastern Utah (from Figure 3.3) (map provided by Deer Creek Coal Mine).

Flagstaff Limestone, North Horn, and Upper Price River Formation.

The East Mountain area is home to intense seismic activity associated with areas of extensive underground coal mining along the arcuate crescent of the Wasatch Plateau and Book Cliffs coal fields (Arabasz et al. 1997 and Arabasz and Pechmann 2001). The Wasatch Plateau and Book Cliffs region is notable as one of two areas in the western United States where mining-induced seismicity is well documented (Wong 1993). Coal mining in the area is conducted via longwall mining, which involves removing nearly horizontal coal seams in blocks hundreds of meters wide by hundreds if not thousands of meters long. Coal is mined by a shear (see Figure 3.5) that moves longitudinally along the coal seam cutting coal from the active face. The coal falls onto a conveyor belt which brings the coal to the outer edge of the longwall called the headgate (the opposite end of the longwall is called the tailgate). The shear and active face are protected by a series of shields (see Figure 3.6). The shields temporarily support the overlying strata via

Figure 3.5: Longwall shear extracting coal from the active face (http://www.cdc.gov/niosh/mining/content/history.html).

Figure 3.6: Longwall shields used to support the roof during longwall mining (http://www.coalleader.com/2005/DBT_shearer_longwall05.htm).

hydraulic rams as the shear moves back and forth shearing coal from the active face. As the shear passes each shield, the shield lowers and steps forward, allowing the roof material behind to collapse behind the advancing longwall. A schematic of the operation is shown in Figure 3.7.

Longwall mining has been shown to produce significant, low magnitude seismic energy due to two main mechanisms: (1) sudden roof failure behind the longwall and (2) triggered seismic slip in geologic structures away from and below the longwall (Arabasz et al. 2005).The seismic activity in the Utah area is primarily tracked by the University of Utah Seismograph Stations (UUSS) ground motion monitoring program. Seismic events recorded by UUSS in the region are deemed to be almost entirely mining induced with two primary event types: (1) Shear-implosional events dominated by Compensated Linear-Vector Dipoles (CLVD) or (2) double-couple shear events that are indistinguishable from tectonic earthquakes.

Seismic events triggered by the mining operations of Deer Creek Coal mine, operated by Energy West Mining Company, were the primary energy source for the

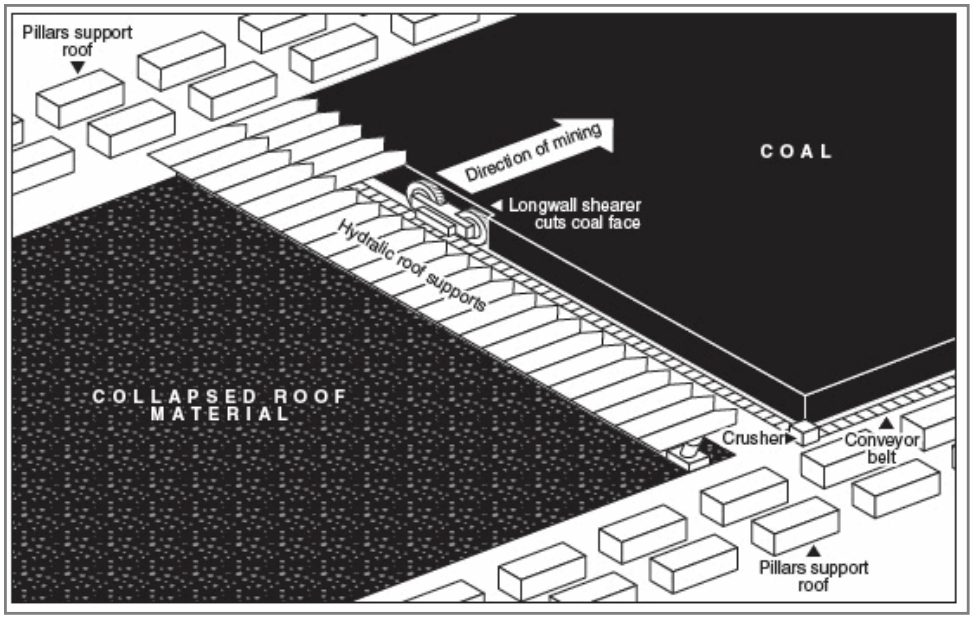

Figure 3.7: Schematic of a longwall panel (http://rajikorba.blogspot.com/2011/06/long-wall-technology-in-coal-mines.html).

topographic study. Figure 3.8 shows the underground structure of Deer Creek mine along with the longwall location during Phase I (2010). The underground location of the longwall is also tabulated in Table 3.1. Deer Creek was extremely cooperative and provided underground drawings in the East Mountain region and provided extensive information regarding longwall timing, location, and underground activity.

Table 3.1: Location of Deer Creek longwall during Phase I (2010).

Date	Location	Event	Latitude	Longitude	Elevation (m)
June 16, 2010	Headgate	Begin Recording	39.44182	-111.194133	2294
June 16, 2010	Tailgate	Begin Recording	39.439814	-111.194142	2294
June 24, 2010	Headgate	Stop Recording	39.441815	-111.192519	2294
June 24, 2010	Tailgate	Stop Recording	39.439811	-111.192528	2294

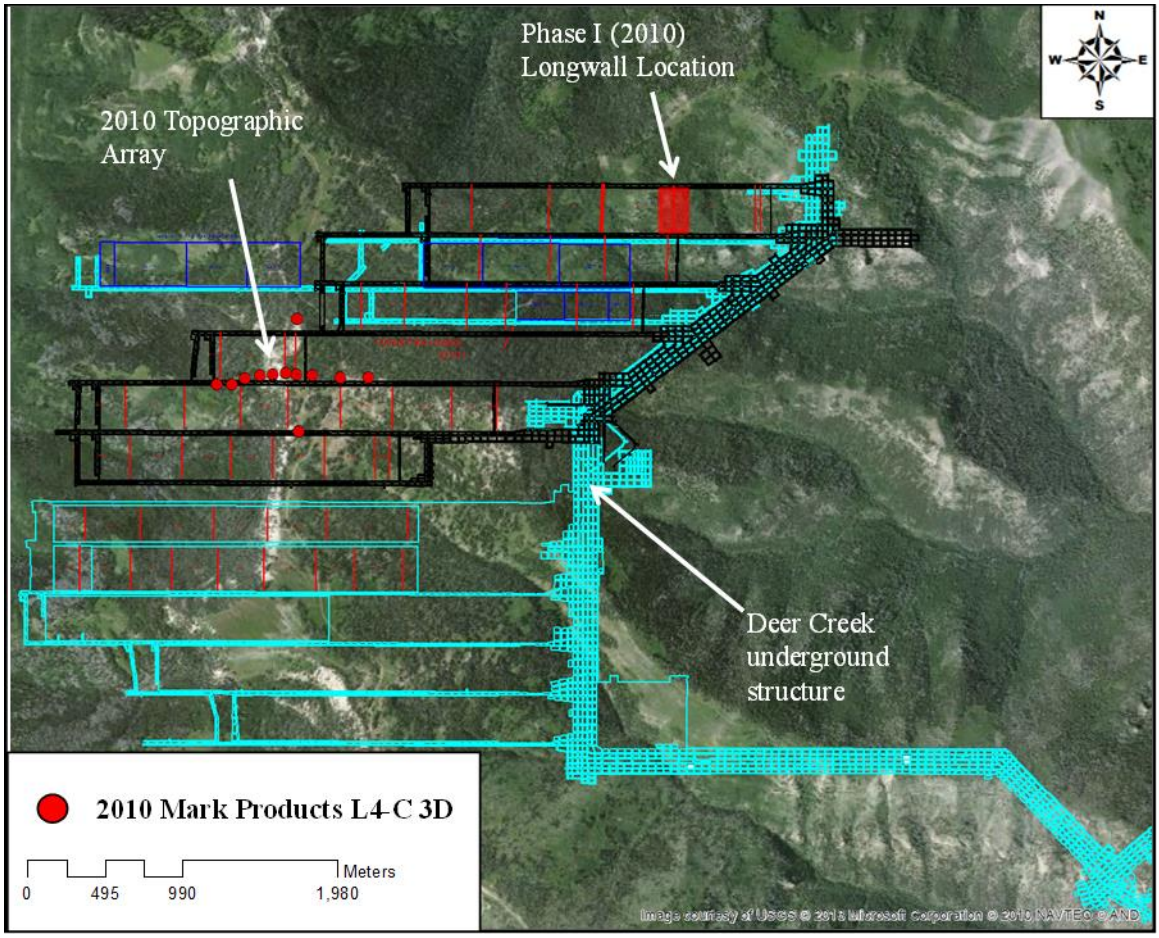

Figure 3.8: East Mountain area showing the underground structure of Deer Creek coal mine along with the location of the topographic array and longwall during Phase I (2010).

3.3 Digital Elevation Model

Airborne laser mapping of the topographic study area was collected by the National Center for Airborne Laser Mapping (NCALM). NCALM is supported by the National Science Foundation (NSF) with a mission to provide research quality airborne light detection and ranging (LiDAR) observations to the scientific community. The LiDAR flown over the topographic study area in Utah was funded by a SEED grant awarded Mr. Clinton Wood by NCALM.

The LiDAR data was collected on July 3, 2010 in a single flight with a total laser-on-time of 1 hour 30 minutes. The area surveyed was an approximately 40-km^2 square with a center point at latitude 39.44228 N and longitude 111.21260 W and sides aligning with true North and East. The survey was performed using an Optech 3100 Airborne Laser Terrain Mapper (ALTM) mounted in a twin-engine Piper PA-31. The system has a horizontal accuracy of 10 cm and a vertical accuracy of between 5 and 30 cm and is capable of measuring up to 4 returns.

In Figure 3.9, the workflow process that NCALM uses to process the raw LiDAR data is shown. The raw GPS and inertial measurement unit coordinates are first used to locate the laser mapping unit during the flight. Next, the laser system is calibrated using the strips of data flown before the main area is surveyed. Next, the LiDAR goes through a series of classification algorithms to separate "bare ground" data points from returns

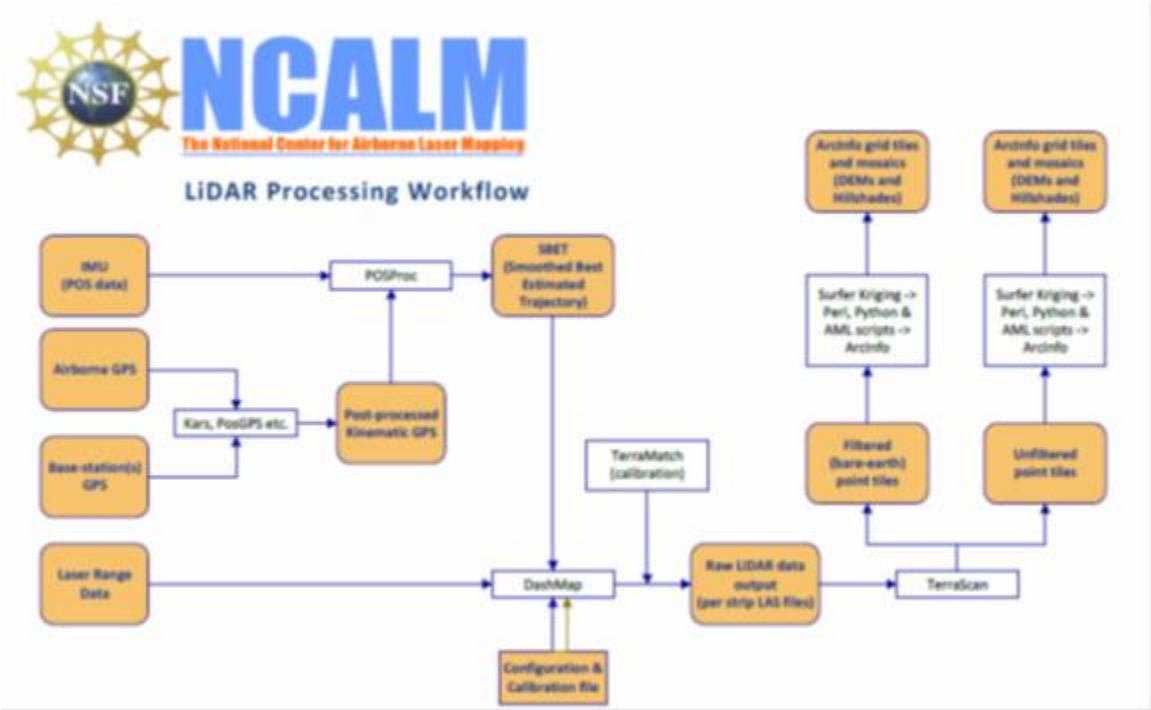

Figure 3.9: NACLM LiDAR data workflow.

associated with trees, houses, power lines, etc. Three deliverables were provided as part of the results: (1) point cloud in LAS format, classified as ground or non-ground returns, (2) ESRI format DEM mosaic and hillshade using default class points at a 1 m node spacing, and (3) ESRI format DEM mosaic and hillshade using only ground class points at a1 m node spacing. An image of the ground class point hillshade is shown in Figure 3.10. All deliverables were processed with respect to NAD83 (CORS96) reference frame. The projection is UTM zone 12N with units in meters. Heights are NAVD88 orthometric heights computed from GRS80 ellipsoid heights using NGS GEOID09 model.

3.4 SEISMIC EQUIPMENT

In Phase I, two different seismic sensors, the Mark Products L4C-3D geophone and the Nanometrics Trillium Compact broadband seismometer were used to record seismic ground motions. These sensors and other equipment for Phase I were provided by NEES@UTexas through the Network for Earthquake Engineering Simulation (NEES) program. These sensors were recorded using a single data acquisition system (DAS), the VTI Instruments, VXI dynamic signal analyzer. Further information on each system is given below.

3.4.1 Mark Products L4-C 3D

The Mark Products L4-C 3D (see Figure 3.11) is a 1-Hz geophone with three component of measurement. The L4-C is a passive sensor that requires no external power to operate. The dimensions of the sensors are approximately 30-cm high by 30-cm in diameter with a mass of approximately 12 kg. The three vibration components include one vertical sensor (V) and two orthogonal horizontal sensors (H1 and H2). The sensors are oriented so that a positive voltage output on the DAS represents ground movement in the up direction for the vertical component, North for the H1 component, and East for the

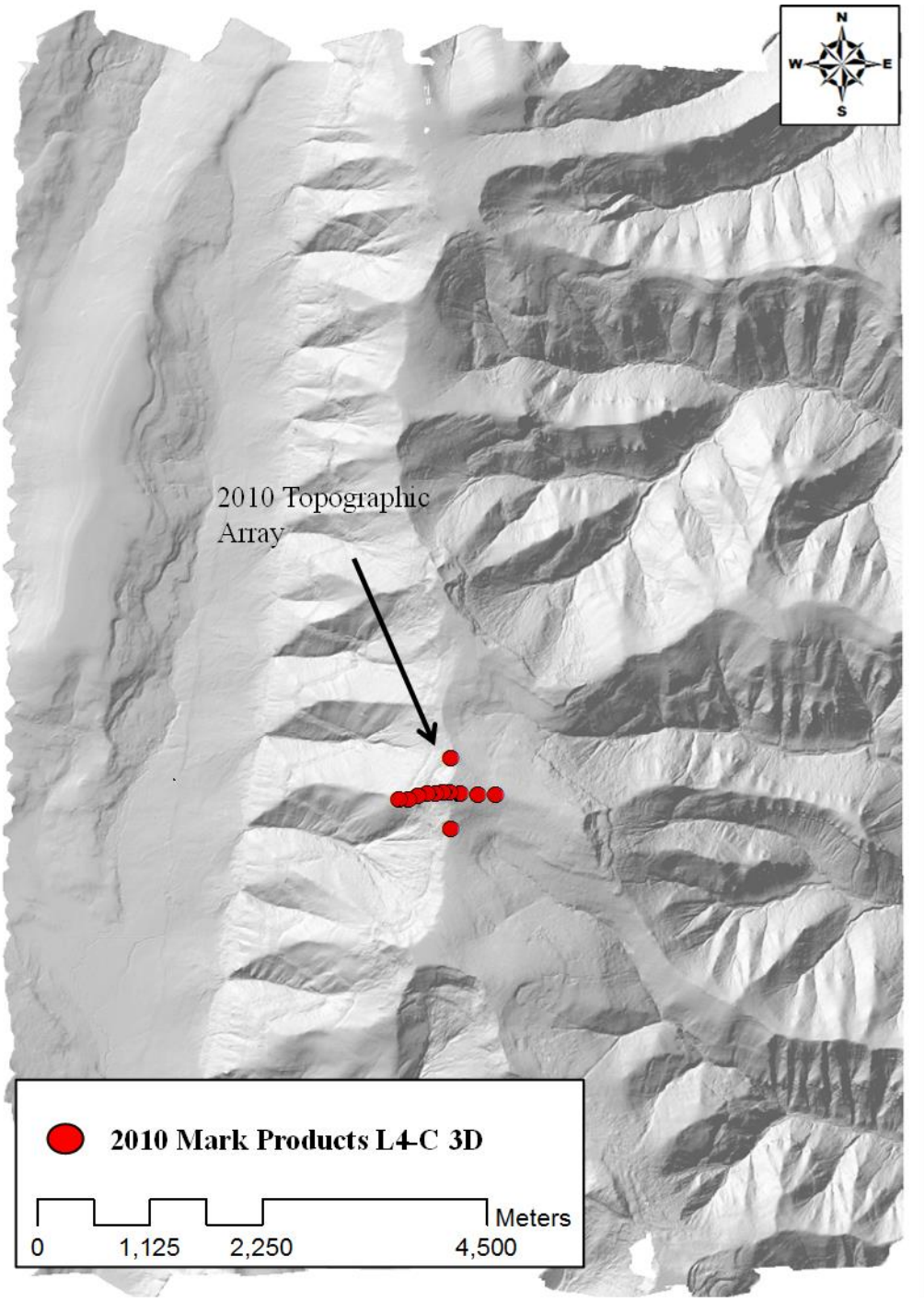

Figure 3.10: NACLM LiDAR derived hillshade of the topographic study area showing the Phase I (2010) topographic array.

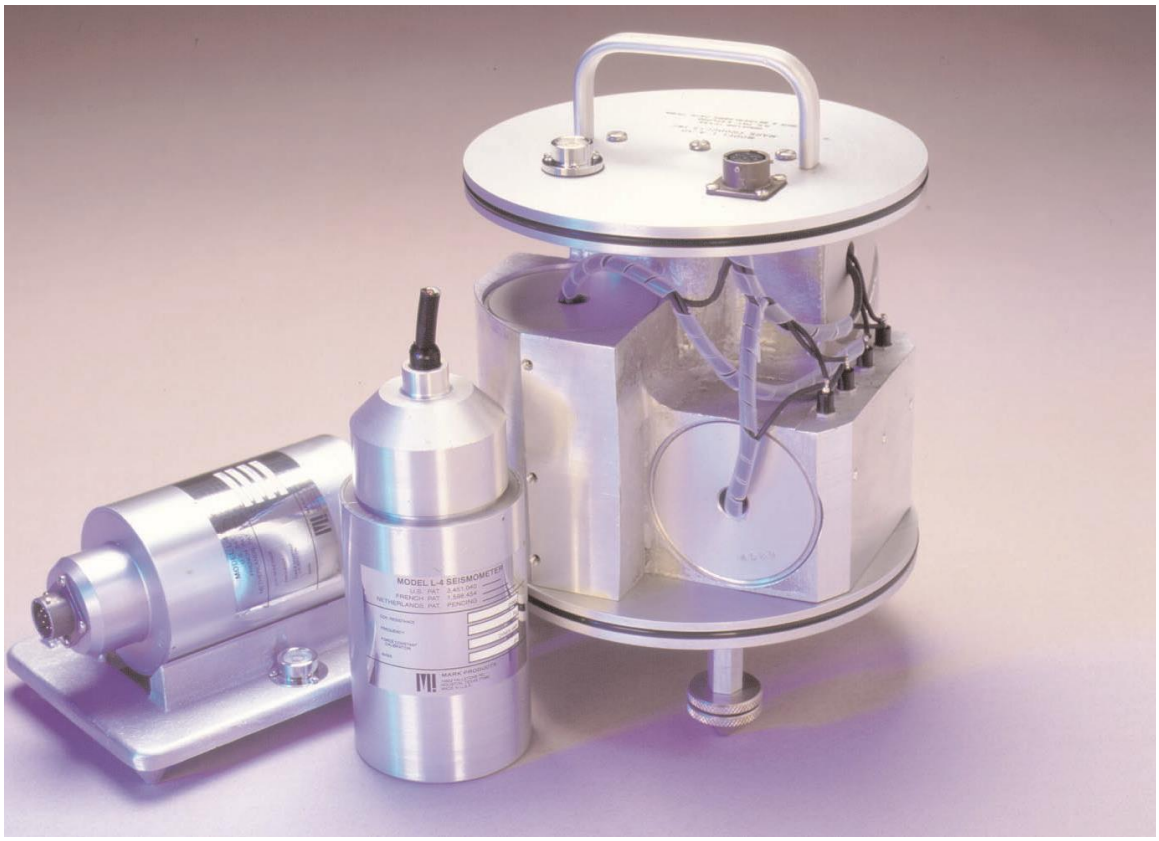

Figure 3.11: Mark Products L4-C 3D 1 Hz geophone (right, with outer case removed for visualization) (http://www.ligo.caltech.edu/~coyne/AL/SEI/L4C/L4.pdf).

H2 component. The response of each individual geophone is non-linear and varies as a function of frequency. A typical set of calibration curves for a L4C are shown in Figure 3.12. The calibration curve is defined using Equation 1 as a function of frequency (F) where FRF is the Frequency Response Function, S is the calibration factor, fn is the natural frequency, and D is the damping ratio. Typical values for the L4-C are S=282 V/m/sec (7.16 V/in/sec), fn=1 Hz, and D=0.28.

During Phase I, 11 L4-C 3D geophones, owned by NEES@UTexas, were used to measure seismic signals. These sensors were calibrated between 0.7 and 30 Hz by

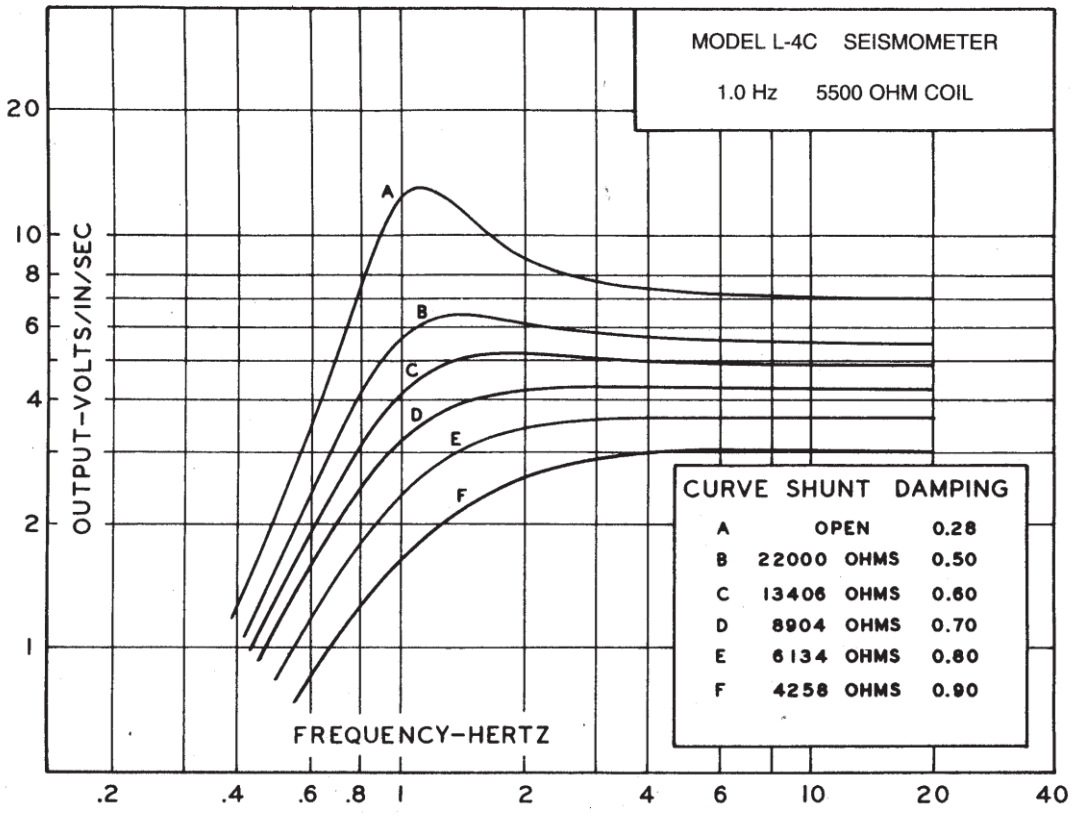

Figure 3.12: Typical calibration curve for Mark Products L4-C 1-Hz geophone (http://www.ligo.caltech.edu/~coyne/AL/SEI/L4C/L4.pdf).

$$FRF = \frac{SF^2}{\sqrt{(f_n^2 + F^2)^2 + (2Df_nF)^2}} \tag{3.1}$$

NEES@UTexas prior to deployment. NEES@UTexas conducted the calibration using an electro-mechanical shaker and a dynamic signal analyzer. A proximitor and accelerometer were both used as calibration references. Calibration values for each of the 11 sensors are provided in Table 3.2.

Table 3.2: Mark Products L4-C 3D geophone calibration values.

	Vertical			H1 (North-South)			H2 (East-West)		
Serial #	**S**	**fn**	**D**	**S**	**fn**	**D**	**S**	**fn**	**D**
770907	266.9	0.96	0.29	282.3	1.01	0.28	278.7	0.97	0.30
770908	263.8	0.97	0.30	282.3	0.98	0.29	282.7	1.03	0.29
770911	283.5	0.97	0.27	280.7	0.98	0.28	289.4	0.96	0.30
770910	287.4	1.02	0.28	275.6	0.97	0.29	277.6	1.00	0.29
770909	287.8	0.96	0.28	278.3	0.98	0.30	281.1	1.04	0.27
770913	292.1	0.98	0.29	282.7	1.01	0.28	267.7	0.98	0.29
770914	273.2	1.00	0.28	283.5	1.00	0.29	280.3	1.05	0.28
770915	281.5	0.98	0.29	275.6	0.97	0.29	293.3	0.98	0.28
770916	294.5	0.98	0.29	288.2	0.97	0.29	287.4	0.99	0.29
770917	285.4	0.99	0.29	284.3	0.97	0.29	283.5	1.01	0.28
770918	292.1	0.98	0.29	275.6	0.99	0.28	257.9	0.97	0.28

S, Calibration Factor (V/m/sec)
fn, Natural Frequency (Hz)
D, Damping

3.4.2 Nanometrics Trillium Compacts

The Trillium compact sensors (see Figure 3.13) are a broadband seismometer capable of measure seismic energy from 100 Hz to 120 sec period. The sensors use an active force balance system with capacitive transducer to accurately measure over this wide frequency band. The dimensions of the sensor are approximately 90-mm diameter and 100-mm tall. The sensor has three measurement outputs (vertical, North-South, and East-West), and have an output polarity so that ground movement in the down, North, and East directions produce a positive voltage. Normally the sensor is wired so that case movement up produces a positive voltage; however these units were wired backward for the vertical component. The calibration curves for the Trillium compacts are much simpler than those for the L4-C geophones, with have a flat response over the frequency measurement range. Therefore, the sensors only have a single calibration factor of 750 V/meter/sec (provided by Nanometrics). Only two Trillium compacts were used during Phase I.

Figure 3.13: Nanometrics Trillium Compact broadband seismometer.

3.4.3 VTI Instruments VXI Analyzer

The VXI is a 72 channel dynamic signal analyzer (see Figure 3.14) with a maximum sampling rate of 50 kHz. The system has anti-aliasing filters with 24 bit A-D converters. The system is controlled by SignalCalc software manufactured by Data Physics Corporation and has a selectable digitization input range of either 1 or 10 volts maximum. The software is capable of outputting signals in a variety of formats including ASCII and Matlab.

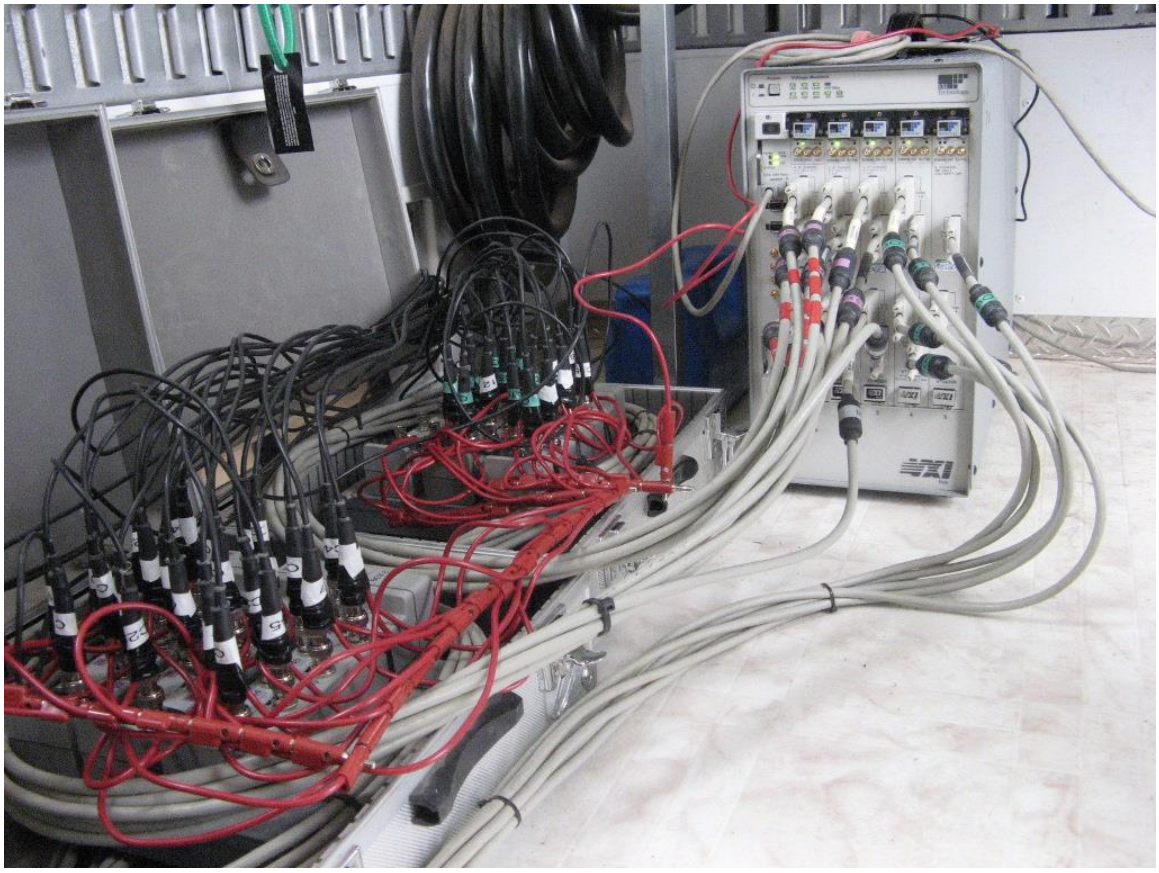

Figure 3.14: VTI Instruments, VXI Analyzer shown with two breakout boxes.

3.5 Deployment and Data Collection

Once the number of instruments available for the experiment was set, the placement of those instruments was chosen based on the location of Deer Creek Mine, the topographic features in the area, and access to the terrain. The sensors were installed and cabled to the DAS and recorded continuously for 7 days.

3.5.1 Sensor Deployment and Mine Location

For Phase I (2010), an array of sensors was placed along a section of the East Mountain Ridge in the Manti-La Sal National Forest in Central-Eastern Utah. In Figure 3.15, the location of the topographic array is shown along with the location of the

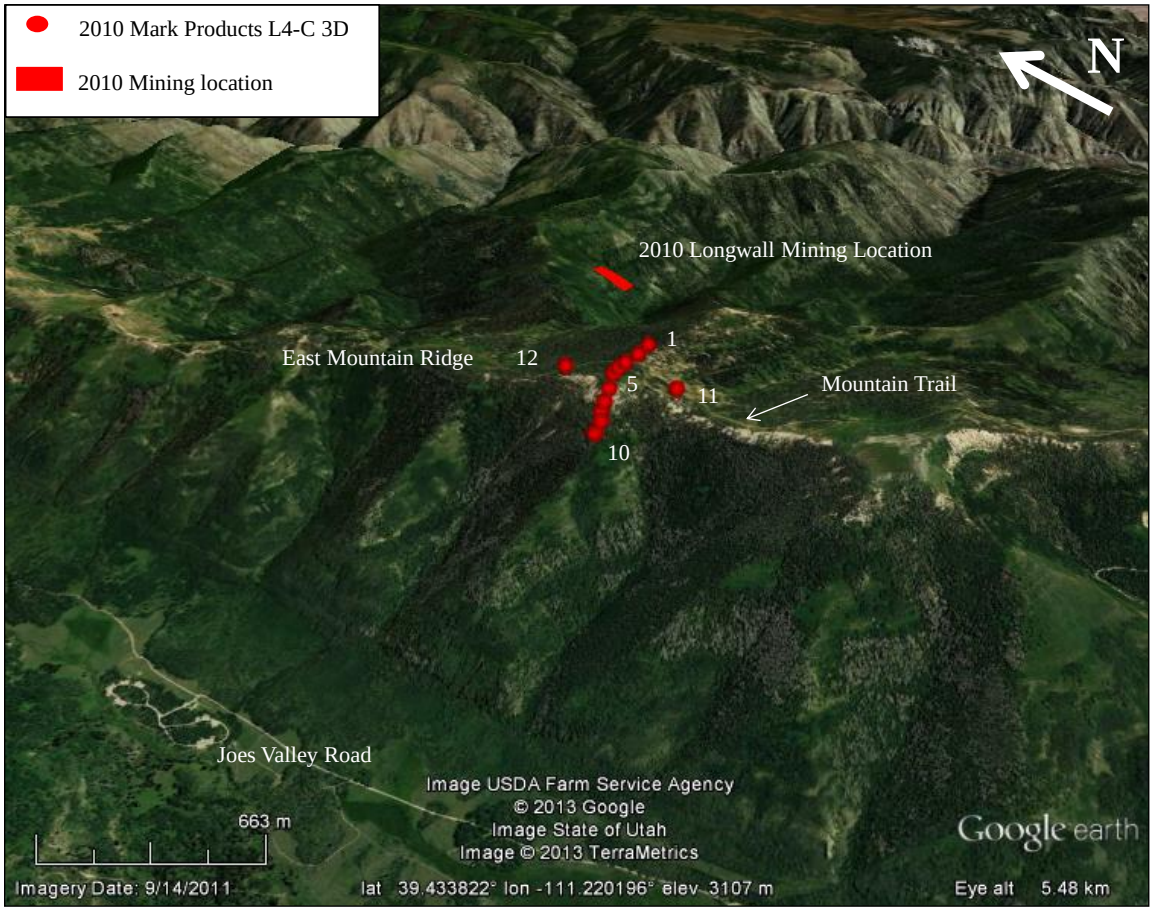

Figure 3.15: Overview of East Mountain Ridge, longwall mining location, and the topographic array.

longwall operated by Deer Creek Mine. The location of the topographic array was chosen based on three main parameters: (1) proximity to the current longwall mining operations of Deer Creek Coal Mine, (2) the overall feasibility of placing the sensors over the terrain, and (3) the steepness, shape, and size of the topographic feature.

The underground location of Deer Creek Coal Mine longwall was provided before deployment of the array, and was used to insure that significant seismic energy could reach the array. During Phase I, the longwall was approximately 600 m directly below the local ground surface and 900 m below the elevation of Sensor 1. At the surface, the

longwall was approximately 2000 m from the center of the topographic array. The longwall was mining coal from West to East during Phase I, and removed a section of coal approximately 140 m by 230 m by 3 m during the seven days of seismic recording (see Figure 3.15).

Figures 3.15 and 3.16 show the terrain in the Manti-La Sal National Forest as very rugged, with steep slopes, dense tree cover and often significant dead fall to complicate the placement of sensors. In addition, the US forest service does not allow motorized vehicles to leave the designated mountain trails. This limited the possible locations of the topographic array to areas that are close to the trail and did not require packing the equipment kilometers back into the wildness. The mountain peak that was chosen was the tallest and steepest peak in the area. It was approximately 400 m from the mountain trail making it the best topographic feature to instrument.

A total of 12 sensor locations were occupied by 13 sensors during Phase I of the topographic study. These positions are shown in Figure 3.17 and the sensor coordinates are provided in Table 3.3. The positions were determined in the field using standard handheld GPS units with accuracy of between 3-10 m. The elevation of the sensors were determined from the LiDAR DEM using the sensors x and y positions. The main array (sensors 1-10 and 13) was oriented in an East-West direction with two sensors (11 and 12) placed in a North-South orientation. The array extended approximately 750 m from East to West and 550 m from North to South. Sensors 1-11 were Mark Products L4-C 3D geophones and sensors 12 and 13 were Trillium Compacts. The Trillium Compacts were used during testing for two reasons: (1) one L4-C geophone was damaged prior to shipment of the equipment to Utah and (2) the Trillium compacts were new instruments for NEES@UTexas and required validation before being used in a full-scale experiment.

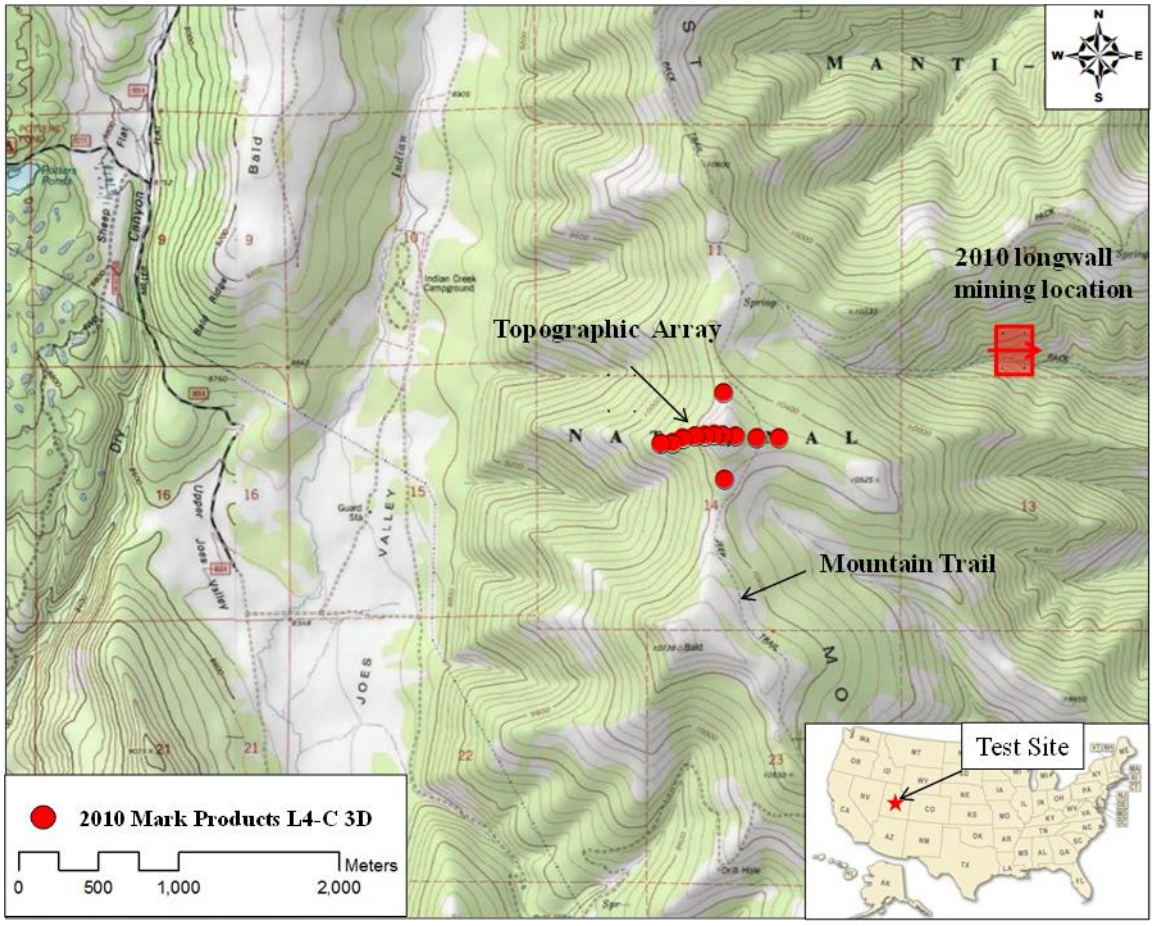

Figure 3.16: Overview of East Mountain Ridge, Showing the direction of longwall mining compared to the topographic array.

For that reason, Sensor 13 (a Trillium Compact) was collocated with Sensor 4 (a L4C 3D) to compare the response of the two instruments.

In Figure 3.18, the approximate locations of Sensors 1-9 are shown in a picture looking from South-to-North. Sensor 5 was located at the peak of the feature at an elevation of 3256 m, while Sensors 4-1 and 13 were on the East side of the feature and Sensors 6-10 were on the West side of the feature. Sensor 11 was located on the North-side and Sensor 12 was located on the South side of the feature. Sensor 1 was the closest

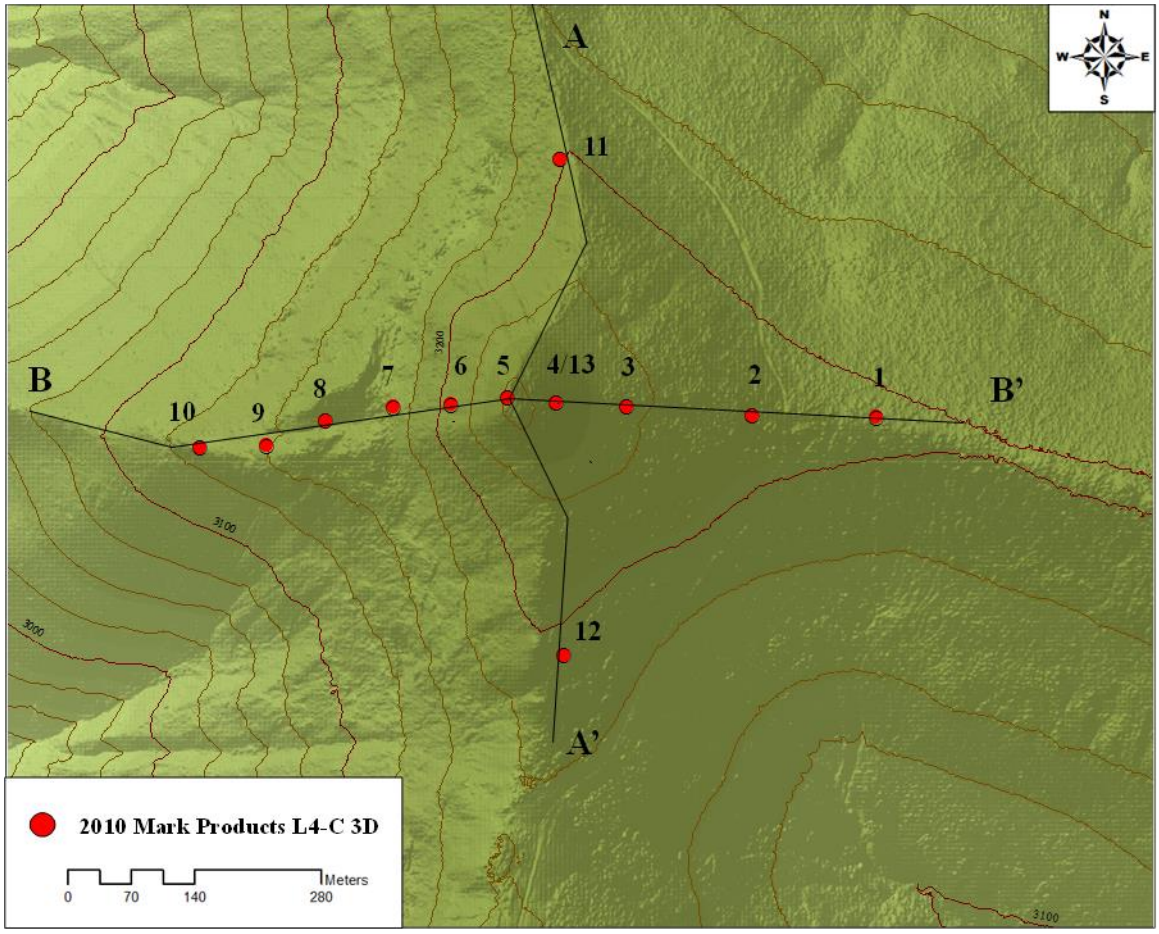

Figure 3.17: Topographic array for Phase I (2010) with Sensor positions shown and feature cross sections (A-A' and B-B') identified.

sensor to the underground longwall mining activates of Deer Creek Coal Mine, which was approximately 2 km North-East.

A North-South 2D cross section of the peak (profile A-A' in Figure 3.17) is shown in Figure 3.19. This cross-section runs along the main mountain ridge and is approximately perpendicular to the orientation of the main sensor array. In this direction, the peak is nearly a perfect triangular feature with a height of 78 m and a width of 800 m. On average, the northern slope is approximately 11^{o} and southern slope is approximately 12^{o}. The West-East 2D cross section of the peak (profile B-B' in Figure 3.17) is shown in

Table 3.3: Sensor locations and DAS channels for the Phase I (2010) topographic array.

Sensor Type	Serial #	Sensor Location/#	DAS Channel #	Latitude	Longitude	Elev (m)
L4-C 3D	770907	1	1-3	39.43376	-111.21069	3202
L4-C 3D	770908	2	4-6	39.43377	-111.21228	3216
L4-C 3D	770911	3	7-9	39.43387	-111.21390	3235
L4-C 3D	770910	4	10-12	39.43390	-111.21481	3246
L4-C 3D	770909	5	13-15	39.43395	-111.21544	3256
L4-C 3D	770913	6	16-18	39.43388	-111.21616	3226
L4-C 3D	770914	7	19-21	39.43385	-111.21690	3188
L4-C 3D	770915	8	22-24	39.43371	-111.21776	3163
L4-C 3D	770916	9	25-27	39.43346	-111.21853	3172
L4-C 3D	770917	10	28-30	39.43344	-111.21937	3147
L4-C 3D	770918	11	31-33	39.43633	-111.21476	3200
Trillium Compact	788500	12	34-36	39.43137	-111.21470	3192
Trillium Compact	788501	13	37-39	39.43390	-111.21481	3246

Notes: (1) Coordinates are based on a WGS 1984 Datum

(2) Elev was determined from the Lidar DEM

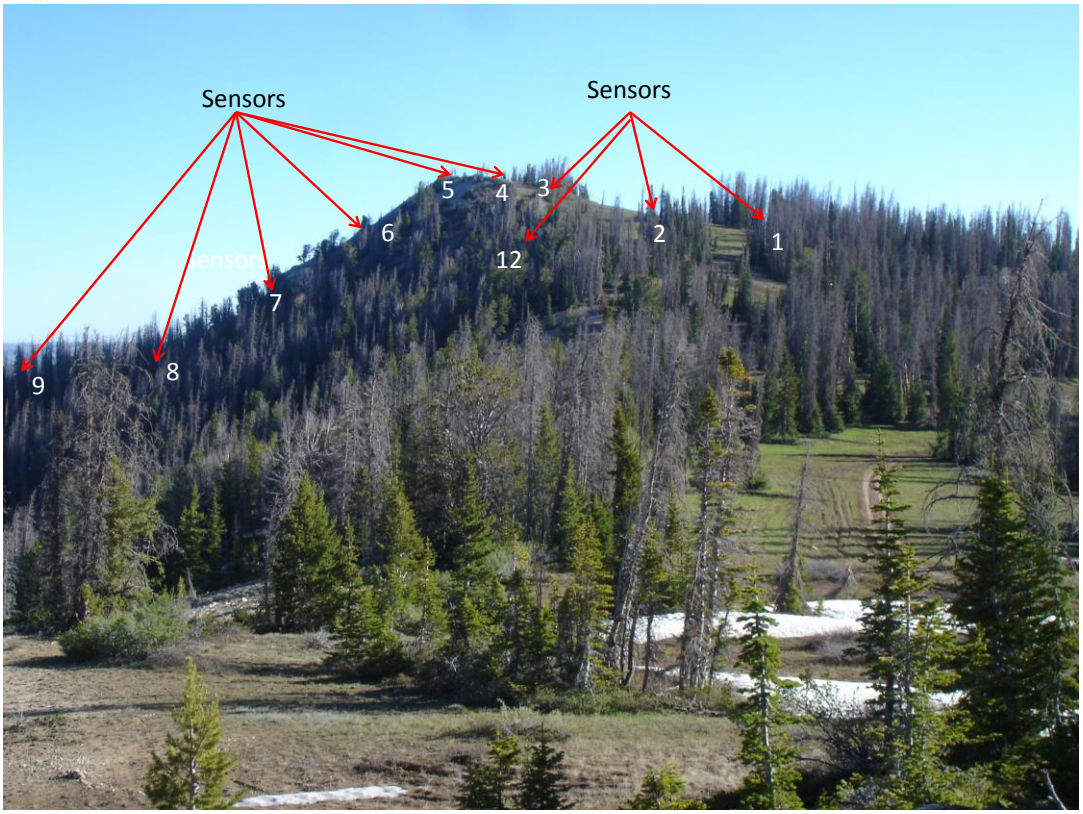

Figure 3.18: Topographic array for Phase I (2010). Positions of Sensors 1-9 and 12 shown in profile view (photo taken by Brady Cox, south of the topographic array).

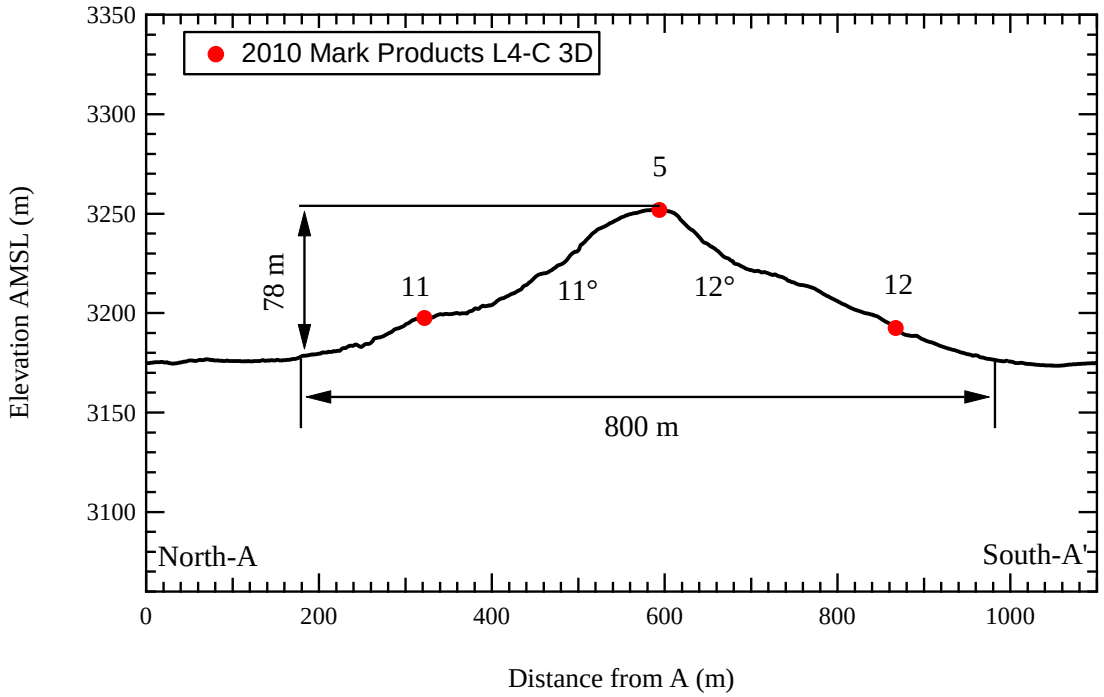

Figure 3.19: North-South 2D profile from A-A', Phase I (2010).

Figure 3.20. The feature is much more irregular in this direction and defining a height and width is more challenging/subjective. The peak west of the crest (Sensor 5) consists of two distinct slopes: a somewhat consistent slope of 10^{o} on the far west-side (i.e., west of Sensor 7) and a steep 34^{o} slope between sensors 7 and 5. The peak east of the crest has a more gradual and consistent slope of approximately 9^{o} between sensors 5 and 2, which levels out between sensors 2 and 1. Using the height of the peak defined in Figure 3.19, and a continuation of the slope between Sensors 9 and 8, the approximate width of the peak in the West-East direction is estimated at 470 m (140 m west of the crest and 330 m east of the crest).

To layout the sensors, a basecamp was established near Sensor 2 (see Figure 3.21). From the basecamp, sensors 1-4 were placed, and all other equipment was brought to the location of Sensor 4, where the data acquisition system (VXI analyzer) was setup

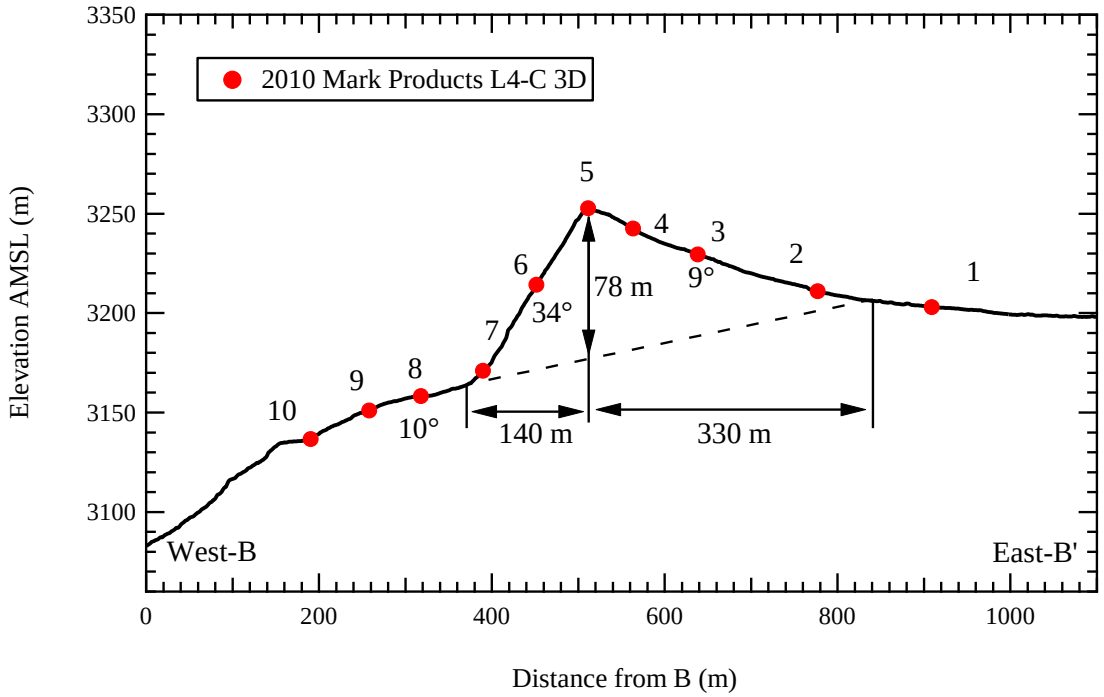

Figure 3.20: West-East 2D profile from B-B', Phase I (2010).

Figure 3.21: Basecamp for Phase I (2010) near Sensor 2.

in a tent (see Figure 3.22). All sensors were cabled to the VXI via twisted shielded pair cable. Over 7600 m of cable was used to connect each of the 13 sensors to the VXI. The VXI was powered 24 hours a day for 7 day via a generator located approximately 20 m from the acquisition tent.

The sensors used during Phase I were installed by first digging a hole approximately 30-cm deep, then placing the sensor in the hole, orienting the sensor so that the H1 component was pointed North, and then compacting soil around the sensor to insure good coupling between the ground and the sensor (see Figure 3.23). Once the sensor was installed, a bucket was placed over the top of the sensor with large rocks on top to reduce wind noise measured by the sensor (see Figure 3.24). The sensors were connected to the VXI using the setup in Table 3.3, where the vertical component was the

Figure 3.22: Central Data Acquisition system near Sensor 4.

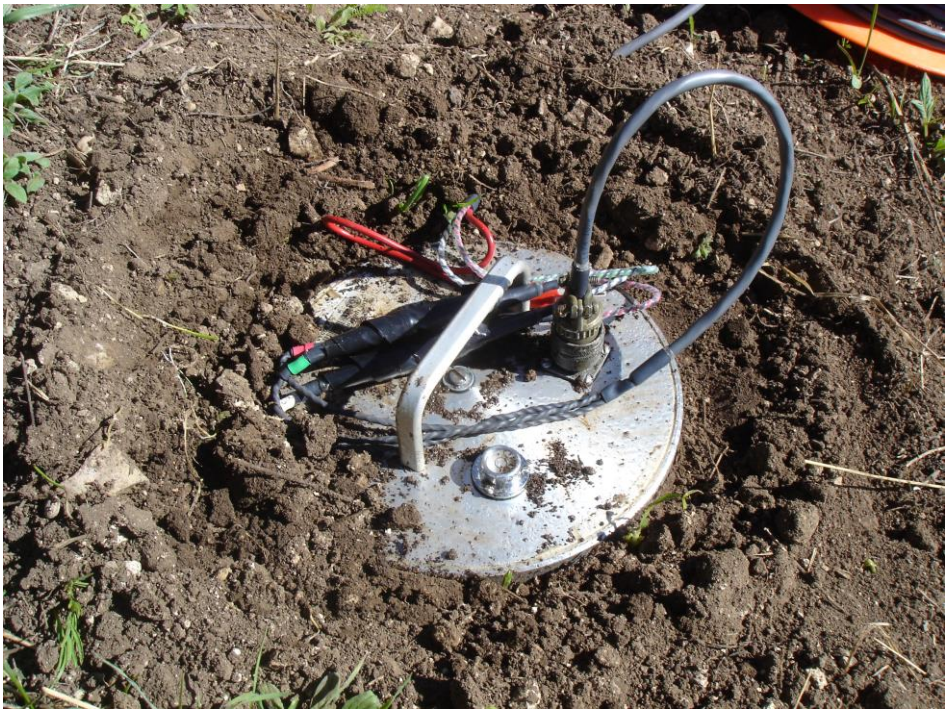

Figure 3.23: L4-C 3D installed below the surface during Phase I.

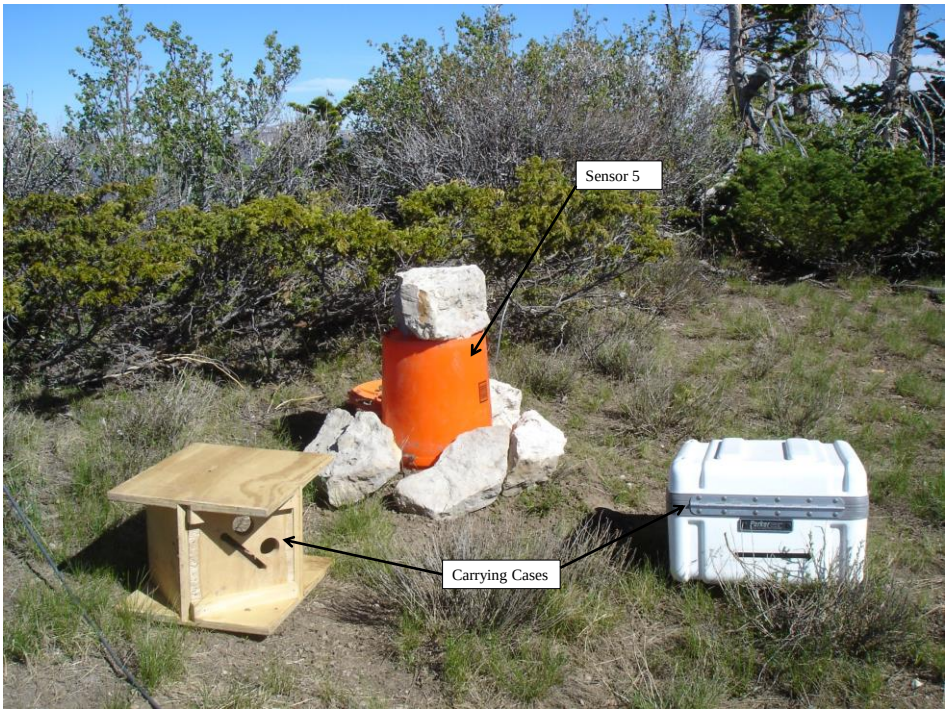

Figure 3.24: Sensor 5 (L4-C 3D) installed with bucket during Phase I.

first channel, North-South component was the sec channel, and the East-West component was the third channel.

3.5.2 Seismic Recording and Output Format

The seismic signals were collected in Phase I from June 16, 2010 to June 23, 2010. Due to the many unknowns associated with mine seismicity (such as intensity and frequency of occurrence) and the limited time frame of the experiment, a continuous recording scheme was determined to provide the most reliable method to capture the events. The other option of choosing a threshold intensity to trigger the recording systems was determined to be too unreliable to successfully capture all the seismic events of interest and would lead to gaps in the data. Though the continuous scheme would create significantly more data, it would provide a more useful dataset from which events could be chosen based on multiple methods, ultimately leading to the best collection of seismic events possible.

To accomplish the continuous recording scheme, the SignalCalc software was used to interface with the VXI. Since the VXI is a dynamic signal analyzer made to record and save data primly in the frequency domain and not in the time domain, it is limited to combinations of sampling rate and time window lengths that produce 2^n number of time domain points. Additionally, the anti-aliasing filters require the system to sample in the time domain 2.56 times faster than the desired frequency span (i.e., the maximum frequency of interest). As such, a sampling rate of 128 Hz was chosen along with a window length of 32 sec, which results in 4096 time domain points per window, or 2^{12}. This limitation of the VXI analyzer prevents continuous sampling of seismic signals because as the system captures one 32 sec window and prepares to capture the next, several milliseconds of time is lost to delays in the system before the new 32 sec window

can be captured. However, this gap would be unacceptable in the data processing and therefore a ThruPut to disk option for data recording can be used to sample continuously. The ThruPut option allows the system to continuously sample the seismic signals and push the data to disk. For Phase I, ThruPut recording was started at 15:00 hours on June 16, 2010 and allowed to run for 24 hours before being stopped to download the single continuous ThruPut file and restart the system. During this time approximately 10 minutes of recording was lost during data download. This process was continued for 7 days until the system was shut down on June 23, 2010.

Once the ThruPut file was downloaded, it could be played back using the SignalCalc software to process and create continuous 32-sec windows of data over the entire 24 hour period. It was chosen to export the 32-sec window from the SignalCalc software to Matlab format with one Matlab file representing one 32-sec time window. Therefore, a 24 hour period results in 2700 Matlab files with a total size of 6.75 GB of data.

The data recorded during Phase I (2010) was archived as part of the Network for Earthquake Engineering's data achieving plan. The data can be downloaded free of charge at www.neeshub.org under Project 977 "Topographic Effects in Strong Ground Motion-From Physical and Numerical Modeling to Design" Experiment 1 contains the data associated with the Phase I (2010) topographic array.

3.6 DATA PROCESSING

To process the raw Matlab data, the seismic events were first identified using several methods. Then, the events were pulled out from the larger data set. Each event was processed using a standard ground motion processing scheme. Finally, the sensors

responses for different parts of the mountain were compared using three analysis methods.

3.6.1 Event Identification

The first step in processing the seismic events was to identify points in time where "earthquakes" occurred during the recording period of Phase I. As a first means to identify points, the catalog of events from the University of Utah seismograph stations (UUSS) was examined. Events identified by the UUSS network only consist of earthquakes over a local magnitude (M_L) of 1.0. These events are likely the largest ones recorded by the temporary topographic array. All other events are too small to accurately determine their magnitude, but can still be excellent events for accessing topographic effects. Once the events on the UUSS network were identified, all other events were identified based on three criteria: (1) The ground velocity of the event has to exceed 0.005 mm/sec on the horizontal components, (2) the duration of the event has to be at least 2 sec from P arrival to S coda, and (3) the event has to be clearly measured on all sensors in the array. A total of 52 events meet these criteria for Phase I (2010). The events will be further discussed in Chapter 7.

To accomplish this, a Matlab m-file was written to open and organize 225, 32-sec long Matlab files into one single file two hours long. This single file was then used to generate 8 sets of 3 plots. The sets of plots contained consecutive 15-min windows of all 13 sensors for the vertical, H1 (North-South), and H2 (East-West) component (see Figure 3.25). Once an acceptable "earthquake" was identified, the event was "isolated" by starting at the P-wave arrival and stitching together three 32 sec windows on each side of the arrival time. Next, a 16 sec time window or 2048 points, centered on the highest amplitude of the vertical component of Sensor 1 was isolated. Corresponding time

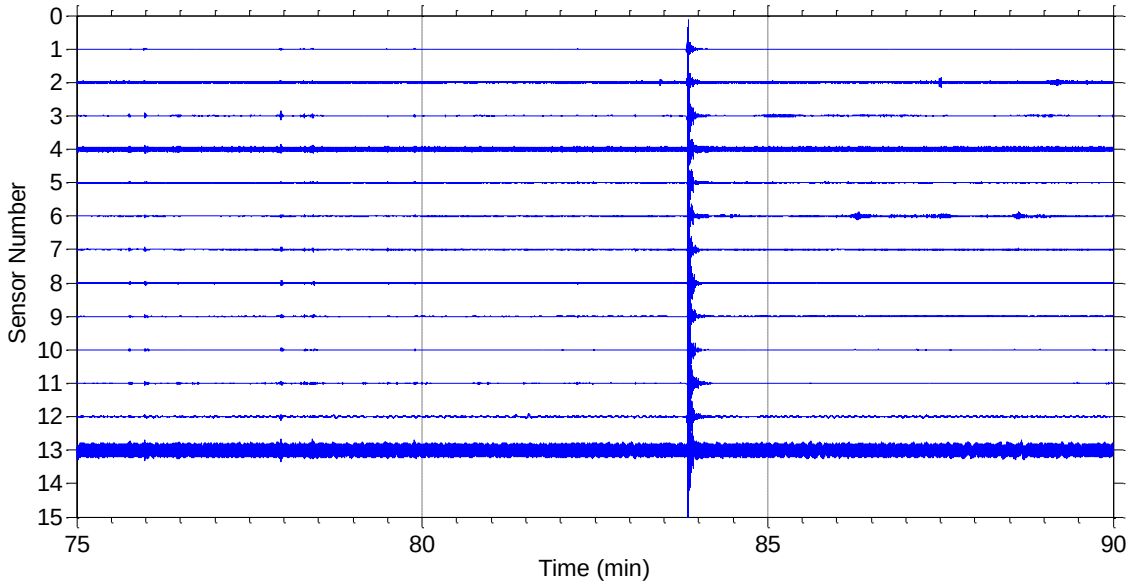

Figure 3.25: Phase I event identification plot (15 mins occurring at 5 hours and 15 mins from the start of recording June 17, 2010) (Event 17606).

periods were taken for all other sensors and components resulting in 39, 16 sec windows. Each event was named based on the day of recording in which it occurred and the Matlab file number corresponding to the P-wave arrival (i.e., 17606 for file 606 out of 2700 occurring on June 17, 2010).

After the events were identified, attempts were made to locate the hypocenter of each event. However, due to the limited extend of the Phase I topographic array, the fact that all sensors were located to the south-east of the presumed energy source, and the fact that the distances between sensors was several times smaller than the distance to the source, the hypocenter could not be reliably located using only the topographic array. Therefore, it was simply assumed that the energy recorded in Phase I originated from the underground location of the Deer Creek Coal Mine longwall.

3.6.2 Event Processing

Once all the events were identified, they were run through a ground motion processing scheme that corrected and prepared the individual seismograms so that the effects of topography could be analyzed. In general, recommendation from Boore and Bommer (2004) were followed in the ground motion processing. In Figure 3.26, a raw seismogram of event 17606 is shown. The ground motion was centered in the record and all of the P and S wave energy is captured. The first step in the process is to baseline correct the signal using the "detrend" command in Matlab. Detrend fits a linear least squares line of best fit to the seismogram then removes that line from the seismogram, which corrects for DC offset, drift, and/or other sensor and digitizer errors. Figure 3.27 shows the detrended seismogram for event 17606 along with the raw signal. A 1 sec cosine tapper is then applied to the front and back of the signal to prevent ripples when the signal is transformed to the frequency domain (see Figure 3.28). Next, to increase the frequency domain resolution of the seismogram, the 2048 point record is padded with 3072 zeros on the front and back to form an 8192 point vector with the seismogram in the

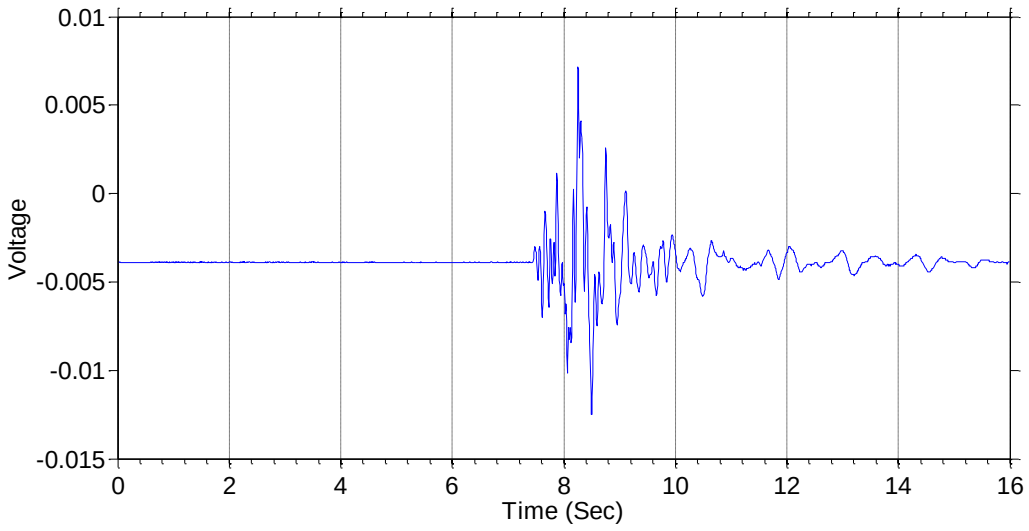

Figure 3.26: Phase I, raw seismogram from event 17606.

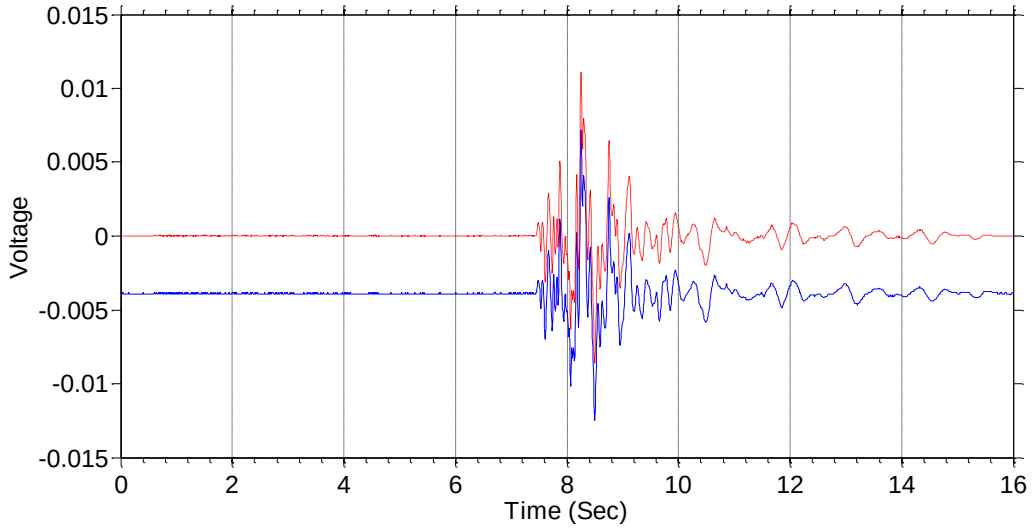

Figure 3.27: Phase I, raw seismogram (blue) and detrended seismogram (red) from event 17606.

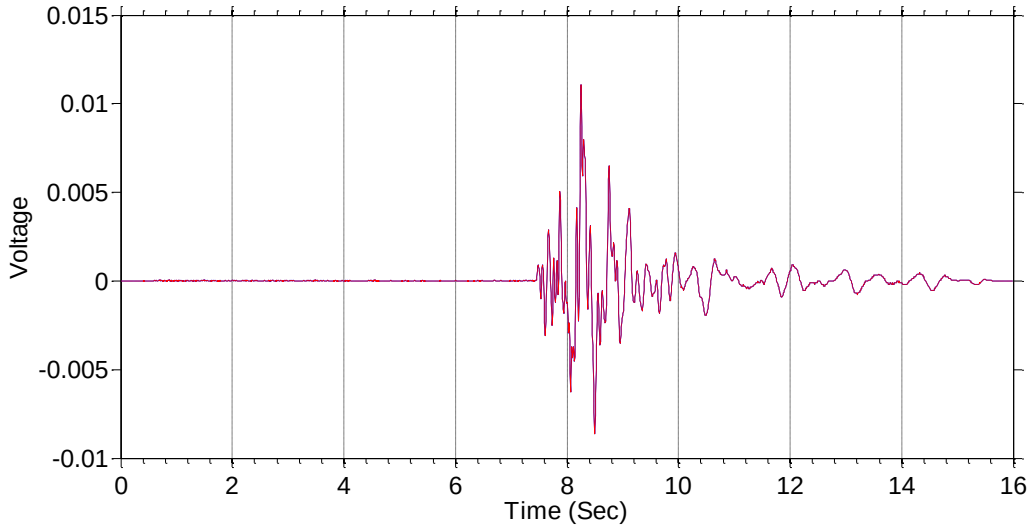

Figure 3.28: Phase I, detrend seismogram (blue) and seismogram with 1 sec cosine taper (red) from event 17606.

center (see Figure 3.29). Next, the data is filtered with a 5th order Butterworth zero phase shift high pass filter. The filter was set at 0.5 Hz because of three reason: (1) the output (i.e., V/m/sec) of the L4-C geophones at 0.5 Hz (92 V/m/sec) is less than a third of the

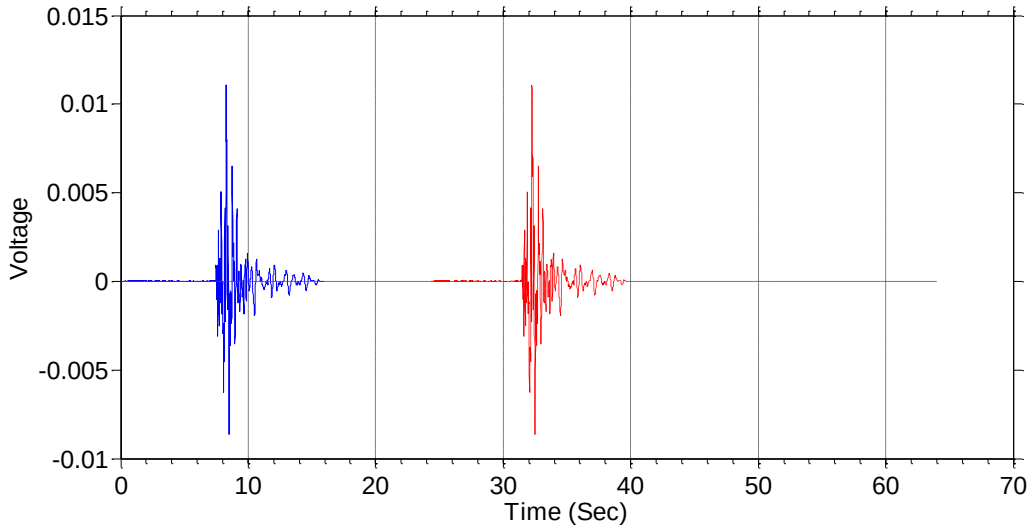

Figure 3.29: Phase I, seismogram with 1 sec cosine taper (blue) and front-and-back zero padded seismogram (red) from event 17606.

nominal output of the sensor (282 V/m/sec), (2) the sensors were not calibrated below 0.7 Hz and due to the steep drop in output below the natural frequency of the geophone (i.e., 1-Hz), the calibration factor cannot be trusted, and (3) for the small feature instrumented, frequencies below 1 Hz were not expected to contribute to the topographic frequency range. A low pass filter of 40 Hz, similar to the high pass filter with characteristics described above, was also applied to the data. A frequency of 40 Hz was considered well above the frequencies of interest to engineers and outside the calibration range of the instruments. The effect of filtering can be seen in Figure 3.30.

Once the time domain processing was complete, the signals were transformed to the frequency domain using the Fast Fourier Transform (FFT) in Matlab. The calibration factors are next applied to the signals in the frequency domain. For the L4-C sensors, the calibration factors are applied using the values in Table 3.2 and Equation 3.1. The calibration values above 10 Hz are simply equal to the listed sensitivity, but below 10 Hz

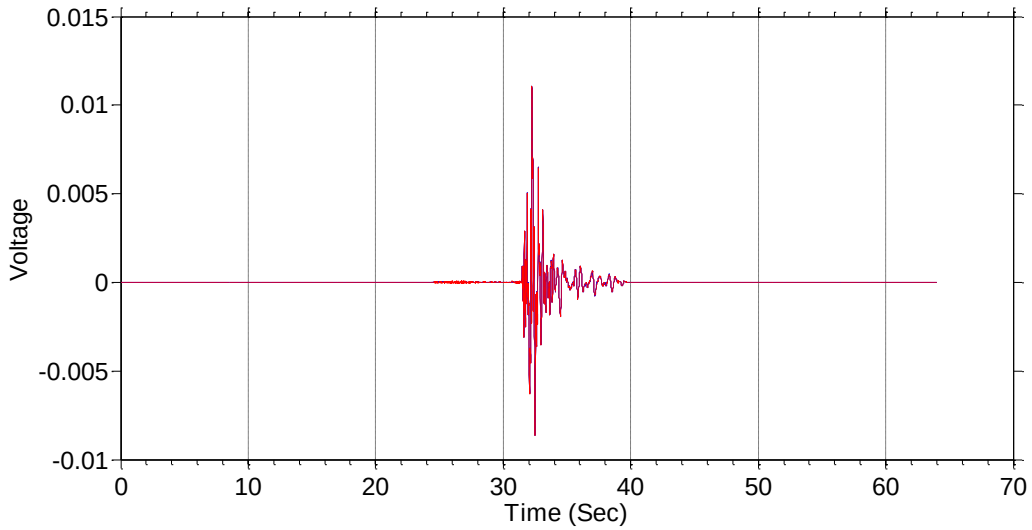

Figure 3.30: Phase I, zero padded seismogram (blue) and filtered seismogram (red) from event 17606.

the factors change rapidly as a function of frequency. The largest sensitivity value occurs at the natural frequency of the instrument and the lowest sensitivity value occurs at a frequency near zero. For the Trillium compacts, a single calibration factor of 750 V/m/sec can be applied due to the flat frequency response of the instrument. In Figure 3.31, an example spectral amplitude plot is shown. To reduce the spikes in the frequency response and provide a more stable spectral estimate, a Konno and Ohmachi (Konno and Ohmachi, 1998) smoothing function is applied to data (see Figure 3.32). A b value of 60 was chosen for the smoothing function because it reduced the erratic spikes in the frequency domain without significantly impacting the overall amplitude and frequency response. This processing results in refined signals from each sensor that are ready to be used for estimating topographic effects.

To estimate topographic effects, three methods were used: (1) the Standard Spectral Ratio (SSR) (Borcherdt, 1970), (2) the Median Reference Method (Wilson and Pavlis (2000), Maufroy et al. 2012), and (3) the Horizontal to Vertical Spectral Ratio

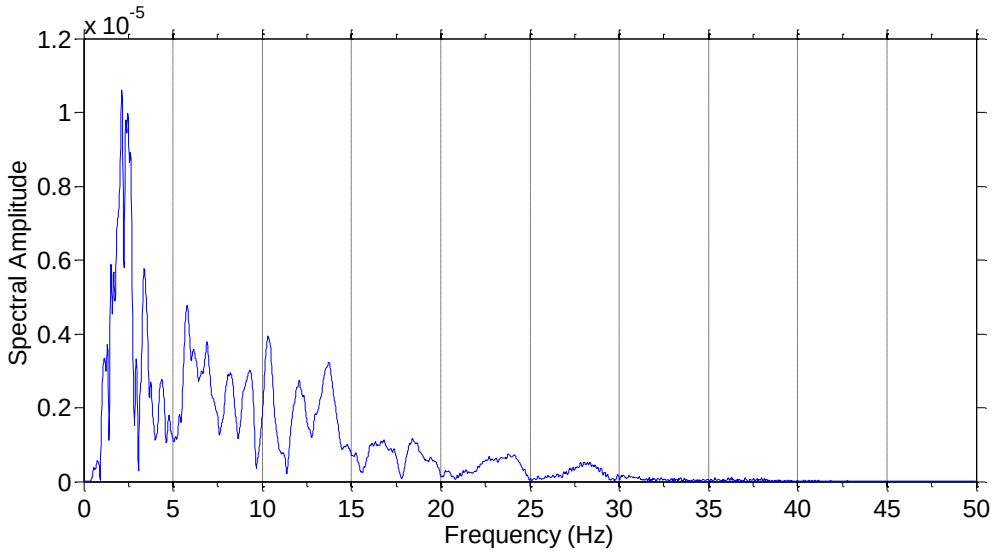

Figure 3.31: Phase I, example spectral amplitude plot for event 17606.

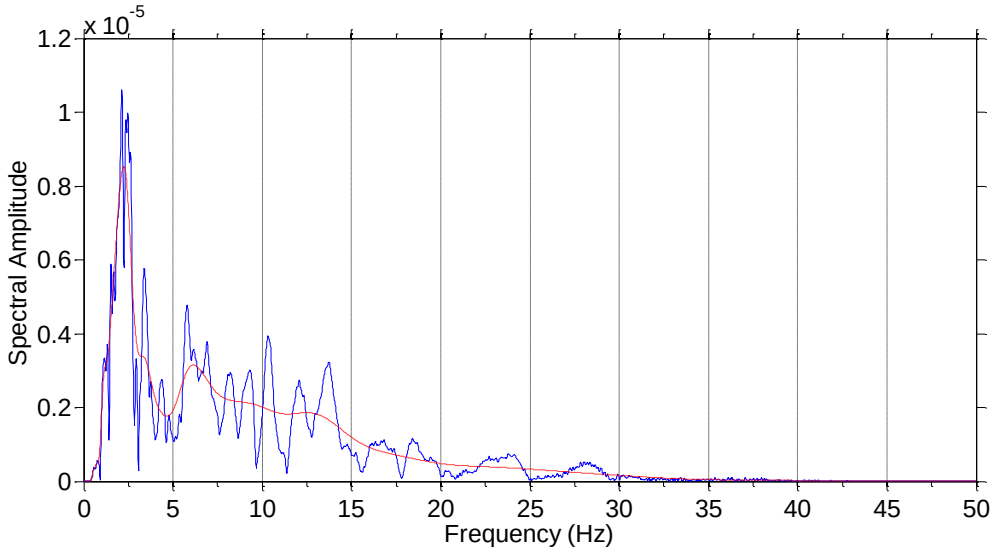

Figure 3.32: Phase I spectral amplitude plot of raw amplitude (blue) and KO smoothed (b=60) amplitude (red) for event 17606.

Method (HVSR) (Nakamura 1989, Lermo and Chavez-Garcia, 1993). Directional analysis of the results of each method was also performed. Each method has advantages and disadvantages, which are explained in Chapter 2. These methods were used to

process each individual event, however to reduce the number of figures and increase the practicality of the dataset, a log-normal median was taken for the entire catalog of events as a function of frequency, sensor number, and component.

To compute the SSR, a single reference station must be chosen to represent a response that is free of site or topographic effects, but remains an approximately equal distance from the source and has the same geology as the measurement sensor. For Phase I, Sensor 1 was chosen as the reference station. It was the closest sensor to Deer Creek Mine (see Figure 3.16) and therefore, all things being equal would have the largest amplitude if there were no site or topographic effects compared to other sensors in the array. In addition, Sensor 1 is located on a relatively flat area of the mountain, although it may still be influenced by some low frequency topographic effects. An example of an SSR for Sensor 5-to-1 North-South component for event 17801 is shown in Figure 3.33. The response is computed by dividing the smoothed spectral amplitude frequency by frequency of Sensor 5 North-South component by the North-South component Sensor 1

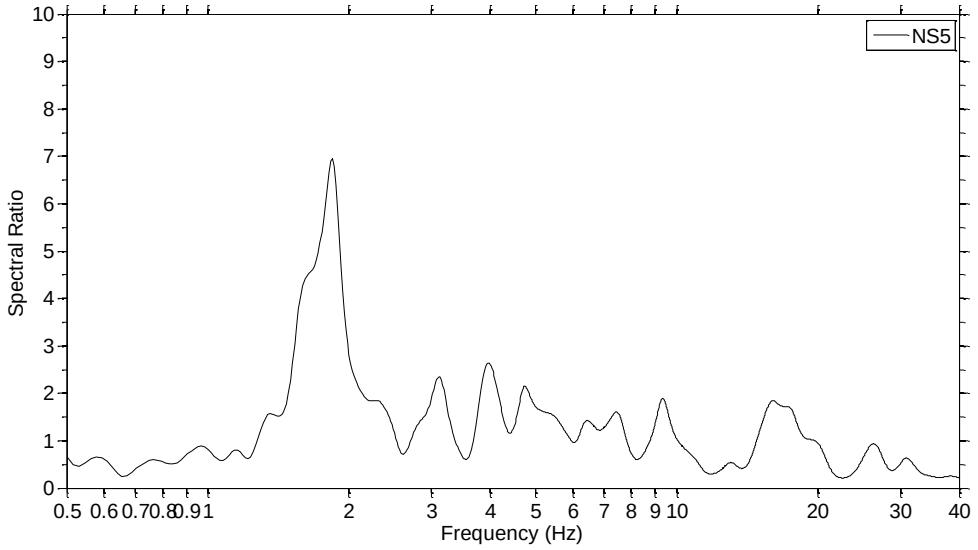

Figure 3.33: Phase I example SSR for Sensor 5, North-South component event 17801 (reference Sensor 1).

for event 17801. This process is repeated for all components, all sensors, and all events. To compute the median response of the entire event catalog, the SSR for each event is computed then the log-normal median and plus and minus one standard deviation (1-sigma) are computed. In Figure 3.34, the median, plus and minus 1 sigma, and all individual events are shown for SSR 5/1.

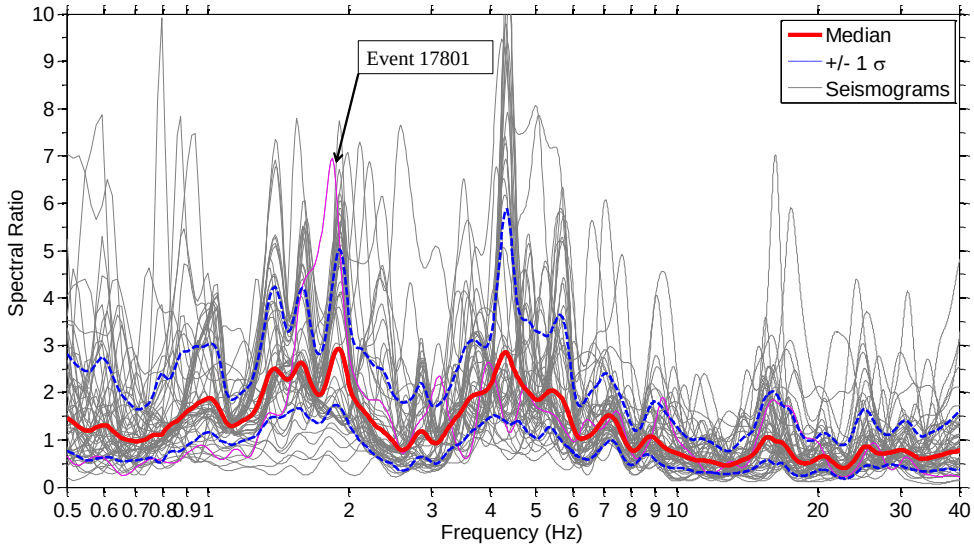

Figure 3.34: Phase I example SSR for Sensor 5, North-South component median, plus and minus one sigma (1σ), and all seismograms in the event catalog (event 17801 shown in pink) (reference Sensor 1).

To compute the MRM, locations/stations 1-12 in the array (note that Sensor 13 was used for station 4) were used to calculate a log-normal median for each component (Vertical, North-South, and East-West) for the entire array. The median reference was computed event by event by calculating the log-normal median Fourier Amplitude Spectra (FAS) for stations 1-12. The individual FAS of each station is then divided by the median reference FAS calculated earlier, resulting in a spectral ratio for the MRM. In Figure 3.35, an example MRM spectral ratio for the North-South component of Sensor 5 in event 17801 is shown. Similar to the SSR, a median and plus and minus one sigma

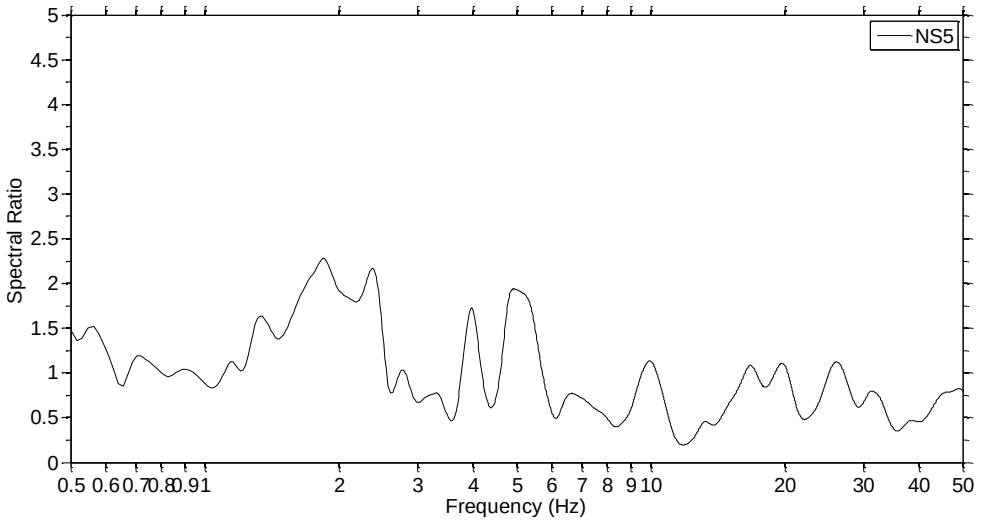

Figure 3.35: Phase I example MRM for Sensor 5, North-South component event 17801 (median reference).

response for the entire event catalog is computed, an example of which is shown in Figure 3.36.

The HVSR was computed separately for both horizontal components (North-South and East-West) by dividing the FAS of the horizontal components by the FAS of the vertical component of each sensor. This calculation results in two HVSR estimates for each sensor (one for each horizontal component) and each event. An example HVSR is shown in Figure 3.37 for Sensor 5, North-South component, event 17801. Just as for the SSR and MRM methods, a log-normal median is calculated for each sensor and horizontal component for the entire event catalog. An example is shown in Figure 3.38.

A directional analysis of the frequency domain results can be computed for any of the methods above. The process takes the time records from the North-South and East-West components and rotates them in 1 degree increments through 360 degrees (using vector rotation) to get a single time record for each azimuth. Each record is then analyzed according to any of the methods above. The amplitudes of the plot are normalized by the

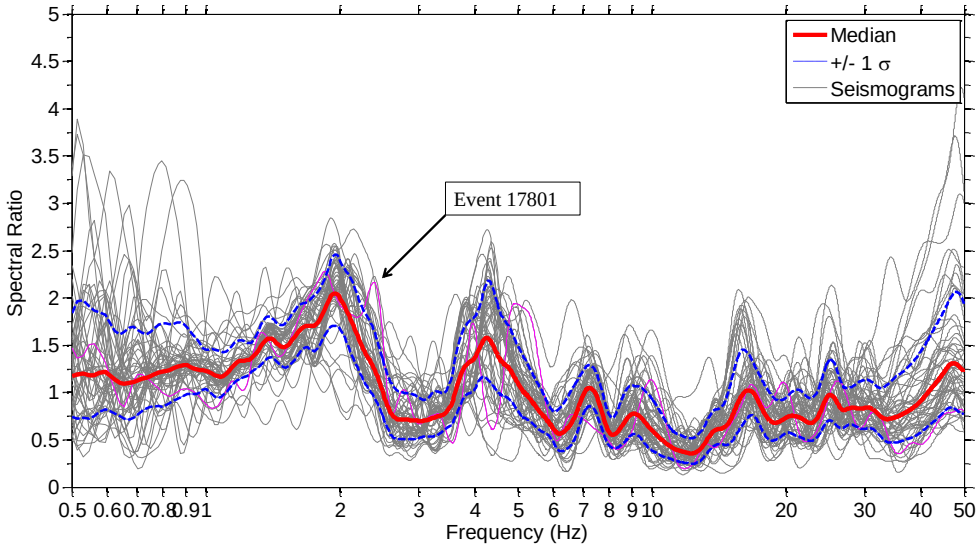

Figure 3.36: Phase I example MRM for Sensor 5, North-South component median, plus and minus one sigma, and all seismograms in the event catalog (event 17801 shown in pink) (median reference of stations 1-12).

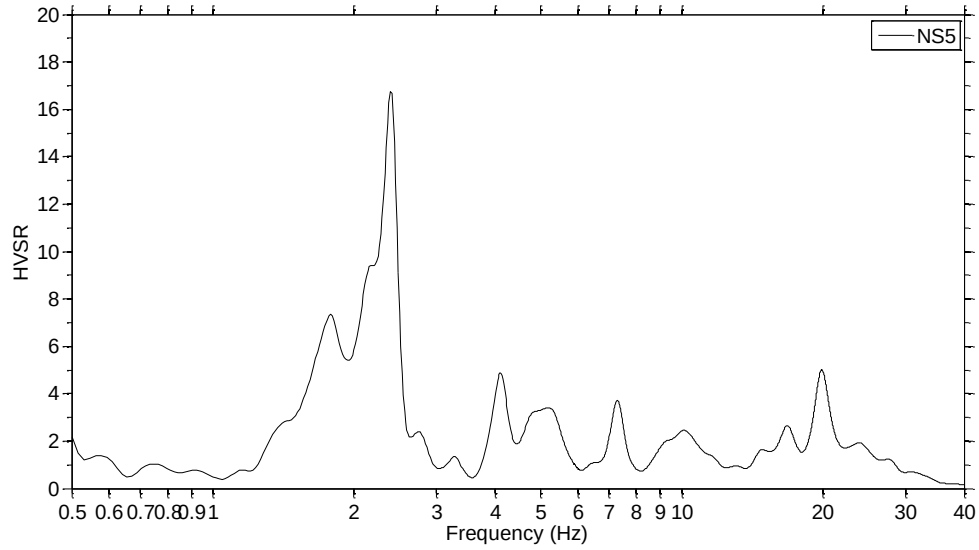

Figure 3.37: Phase I example HVSR for Sensor 5, North-South component event 17801.

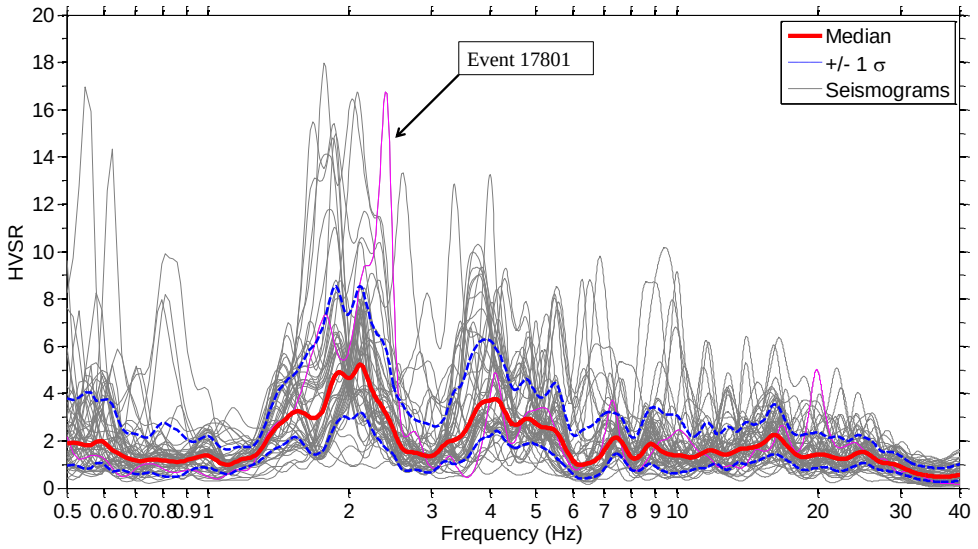

Figure 3.38: Phase I example HVSR for Sensor 5, North-South component median, plus and minus one sigma, and all seismograms in the event catalog (event 17801 shown in pink).

maximum amplitude for any azimuth for frequencies between 1 and 5 Hz. Normalizing makes the color scheme equivalent for all the stations in the array. The results are plotted as a polar plot with cardinal directions and frequencies bands moving from low frequency in the center to high frequency on the outside (see Figure 3.39). The amplitude at a particular frequency-azimuth combination is given as a color with hot colors representing higher amplitudes.

3.7 SUMMARY

This chapter detailed the experimental equipment, deployment, data collection, raw data formats and data processing scheme for Phase I (2010) of the topographic effects field study. Phase I included the deployment of 11 1-Hz geophones and two broadband seismometers in 12 locations across a topographic butte in Central-Eastern Utah. The butte is characterized by 9 to 34 degree slopes with a total of 120 m vertical

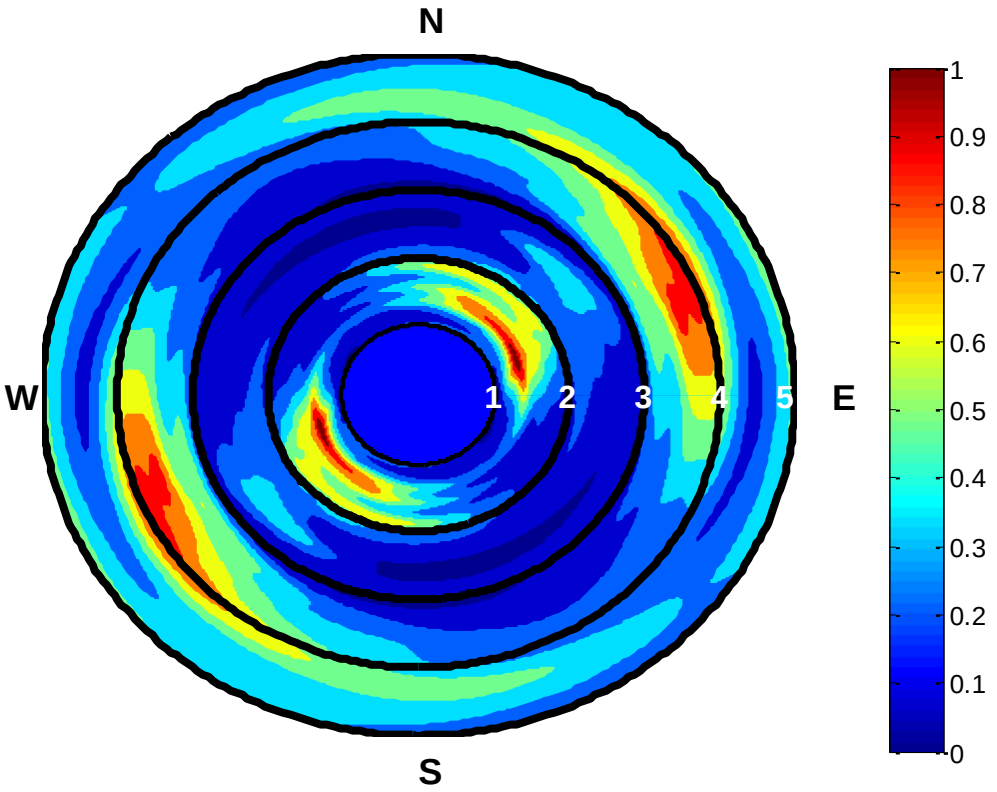

Figure 3.39: Phase I example directional plot for Sensor 5, SSR median of all catalog events (reference Sensor 1).

elevation change. The array was used to record frequent and predicable coal mining inducted seismicity which was recorded 24 hours a day for 7 days by the topographic array. Each event was processed in the time and frequency domain according to standard ground motion processing schemes. Four separate methods to determine topographic effects were detailed and examples of each were given.

Chapter 4: Topographic Study Phase II

4.1 INTRODUCTION

Phase II is the second part of a two part study looking at topographic effects. In Phase II (2011), 22 broadband and intermediate period sensors, along with 5 short period geophones were deployed in a dense array over significant topography in Central-Eastern Utah. The array encompasses an area of approximately 25 km^2 and instruments two features using three linear arrays and one large circular array. The seismicity recorded during Phase II was associated with underground longwall coal mining directly under the topographic array. Data was recorded for approximately 10 continuous days using independent dataloggers. The data was processed using a standard seismic signal processing scheme and the hypocenters for each event were located. This chapter details the sensors, dataloggers, station layout, and event processing for Phase II (2011) of the topographic effects field study.

4.2 SEISMIC EQUIPMENT

In Phase II, three seismic sensors and two dataloggers were used to record ground motions with three separate sensor and datalogger combinations. The Trillium Compact and CMG-40T sensors were broadband and intermediate period sensors while the L-22 3D was a 2-Hz geophone. These sensors were recorded using the Reftek RT130 and Nanometrics Taurus dataloggers.

4.2.1 Guralp CMG-40T 30 Sec

The Guralp CMG-40T is a true force feedback instrument with no internal mass locks (see Figure 4.1). The instrument is approximately 168-mm in diameter, 210-mm tall, and has a mass of 5-kg. It measures three components of motion: vertical, North-

Figure 4.1: Guralp CMG-40T 30 sec intermediate period sensor (http://www.passcal.nmt.edu/content/instrumentation/sensors/intermediate-period-sensors/cmg-40t-int-sensor).

South, and East-West. The polarity of these components corresponds to the seismology standard (i.e., positive is case movement up, North, and East). The instrument has a flat dynamic response from 50 Hz to 30-sec period and a nominal output of 809 V/m/s. The instrument response is checked by placing the sensors on a controlled pier and comparing the passive response of the sensor against other reference sensors. The CMG-40T instruments used in this study were provided by the Program for Array Seismic Studies of the Continental Lithosphere (PASSCAL) instrument program, through the National

Science Foundation (NSF) sponsored Incorporated Research Institutions for Seismology (IRIS) program. PASSCAL provides instruments at low cost to researchers conducting seismology related experiments, and provides support and training for the use of the instruments.

4.2.2 Nanometrics Trillium Compacts

The Trillium compact sensors were the same sensors used in Phase I with one exception. The polarity of the sensor component was changed to the seismologic standard of up, North, and East case movement results in a positive departure on the seismogram. These sensors were again provided by NEES@UTexas. Please refer to Section 3.4.2 for further information on the Trillium Compact sensors.

4.2.3 Mark Products L-22 3D

The L-22 3D is a three component geophone with a natural frequency of 2.0 Hz (see Figure 4.2). The L-22 is approximately 130-mm in diameter, 76-mm tall and has a mass of 2.5-kg. The instrument is a passive sensor with a damping ratio of 0.707 and a sensitivity of 88 V/m/s. The dynamic range of the instrument is limited by its natural frequency similar to the L4-C geophones used in Phase I (i.e., the output drops off significant below the natural frequency). Unlike the L4-C geophones, the L-22 sensors were not calibrated using a shake table. Therefore, the instruments were only used for hypocenter location and not for calculating topographic amplification. The polarity of the L-22 was different from traditional seismometers, a positive polarity on the DAS represents case movement in the down, North, and East directions. These instruments were provided by the PASSCAL instrument program.

Figure 4.2: Mark Products L-22 3D low frequency geophone (http://www.passcal.nmt.edu/content/instrumentation/sensors/short-period-sensors/l-22-sp-sensor).

4.2.4 RefTek RT130

The RefTek RT130 is a high resolution 3 channel datalogger (see Figure 4.3). The system is a low power unit, which is configurable to control a wide variety of sensors. The system is approximately 135-mm high by 185-mm wide by 343-mm long with a mass of 2-kg. It is housed in a nearly waterproof, shock-resistant plastic shell. The datalogger has a modulated, 24-bit A-D converter, whose dynamic range changes as a function of sampling rate, and has an input range of either 40 volts peak-to-peak or 1.25 volts peak-to-peak depending on the gain chosen (i.e., 1 or 32 times). The system has a sampling rate of between 1 and 1000 samples per second and draws approximately 1 watt of power during operation. The timing of the system is obtained via a GPS antenna, and

Figure 4.3: RefTek RT 130 Datalogger (http://www.passcal.nmt.edu/content/instrumentation/dataloggers/3-channel-dataloggers/reftek-rt-130-datalogger).

is accurate within +/- 10 microseconds. The system saves data in the PASSCAL recording format on up to two 32 GB compact flash cards.

The RT130 was used with both the CMG-40T and L-22 sensors. To determine the combined calibration factor of the datalogger and the instrument, one multiplies the calibration factor of the sensor, the gain of the datalogger, and the dynamic range of the instrument together. In Table 4.1, the calibration factors for the datalogger and sensor combinations are provided.

Table 4.1: Calibration factors for the RT130 datalogger and the CMG-40T or L-22 sensor.

Sensor	Datalogger	Sensor Cal F (V/m/s)	DAS Gain (V/c)	DAS dyn range (c/c)	Final Cal F (c/m/s)
CMG 40T	RT130	809.153	1	629330	509224257.5
L-22	RT130	87.8286	32	629330	1768741531

Notes: c=counts,Cal=Calibration, F=Factor

4.2.5 Nanometrics Taurus

The Taurus is a 3 channel low power, high resolution datalogger (see Figure 4.4). The unit is approximately 264-mm by 147-mm by 60-mm with a mass of 1.8-kg. The system is housed in an aluminum case that is nearly waterproof and shock proof, and has a power consumption of only 650 mW, when in ultra-low power mode. The digitizer is a 24-bit A-D converter with a sampling rate of between 2 and 500 samples per second, and an input range of 40 volts peak-to-peak. A hardware high pass filter can be applied to the data before recording to reduce the low frequency drift. The system uses GPS timing similar to the Reftek datalogger. The Taurus is capable of saving in Miniseed format

Figure 4.4: Nanometrics Taurus datalogger.

Table 4.2: Calibration factors for Taurus and Trillium Compact combination.

Sensor	Datalogger	Sensor Cal F (V/m/s)	DAS input P-P (V)	DAS dyn range (c/c)	Final Cal F (c/m/s)
Trillium Compact	Taurus	750	40	16777216	314572800

Notes: c=counts,Cal=Calibration, F=Factor

along with Nanometrics store format on dual compact flash cards.

The Taurus datalogger was used in the field with the Trillium Compact sensors. To compute the combined calibration factor, the dynamic range of the digitizer is divided by the peak-to-peak input range and then multiplied by the sensor calibration factor. In Table 4.2, the calibration factor for the combination of datalogger and sensor is provided.

4.3 Deployment and Data Collection

In Phase II (2011), a locally-dense array of seismic stations was setup over several natural topographic features above the underground coal mining activities of Deer Creek Coal Mine in Central-Eastern Utah, with the goal of recording ground motions from frequent and predictable mining-induced seismicity. Phase II was designed as the main topographic study, focused on recording ground motions on various topographic features, with varying slope angles, and 2D and 3D geometries. This section details the array deployment, data collection, and data processing associated with Phase II (2011).

4.3.1 Sensor Deployment and Mine Location

Similar to Phase I (2010), the topographic array for Phase II (2011) was located along East Mountain Ridge in the Manti-La Sal National Forest in Central-Eastern Utah, USA. Using the knowledge obtained from Phase I (2010), and the new sensors from NEES@UTexas and IRIS/PASSCAL, the topographic array for Phase II (2011) was deployed to encompass three separate cross sections, and to instrument a large enough area to properly locate the hypocenters of each “earthquake”. The location of the

topographic arrays during Phase I (2010) and Phase II (2011) are shown in Figure 4.5. The Phase II array was significantly larger than the Phase I array and encompassed more than 25 km^2 compared to Phase I, which only encompassed 0.3 km^2. In addition, the underground longwall was located much closer to the topographic array in Phase II (directly under) than in Phase I (2 km NE).

The features instrumented in Phase II (2011) are shown in plan-view in Figure

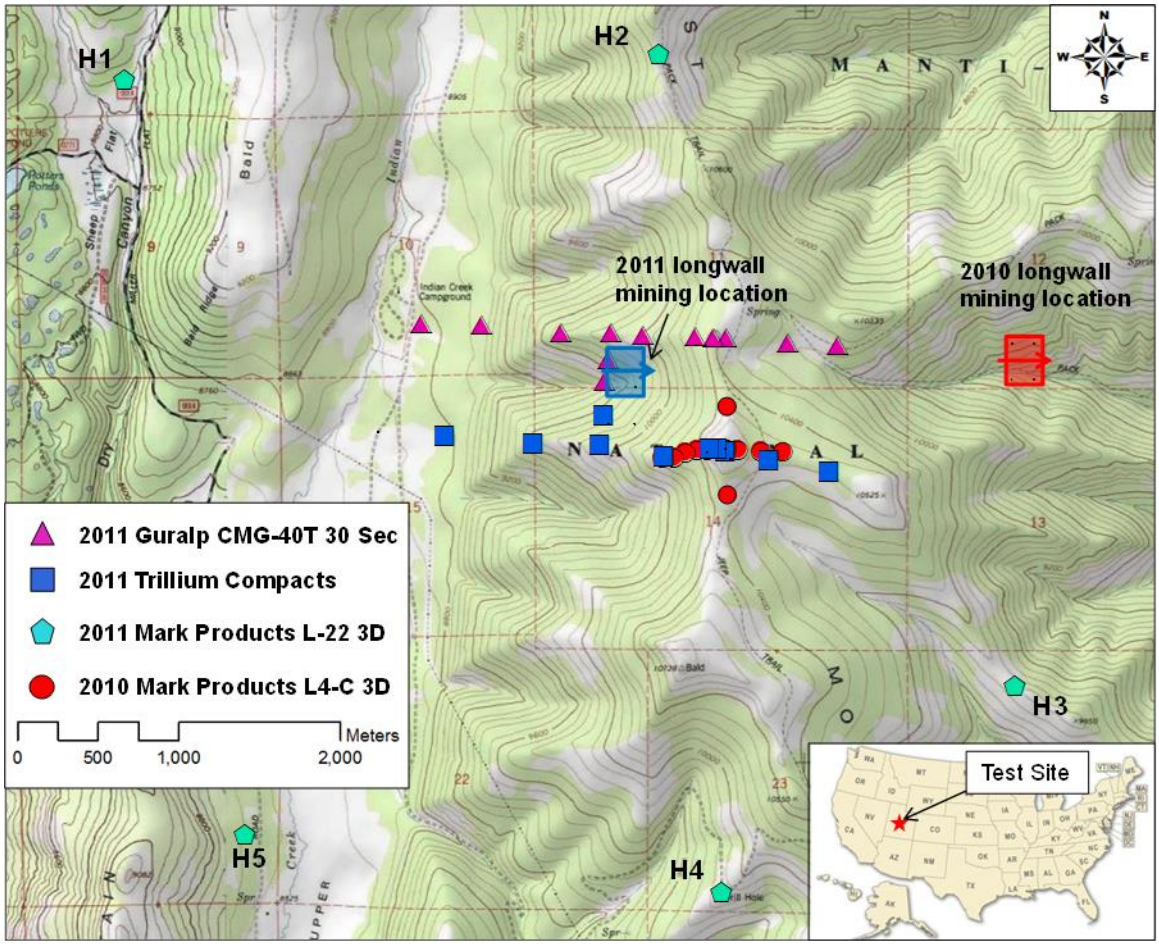

Figure 4.5: Phase I (2010) and Phase II (2011) topographic arrays and longwall mining locations.

4.5, 3D view in Figure 4.6 and a zoomed-in view of main topographic array is shown in Figure 4.7. During Phase II, the active longwall for Deer Creek Coal Mine was located directly under the main topographic array (see Figures 4.5 and 4.6). Due to the steep terrain, the longwall was operating under soil cover that varied between 500 and 600 meters in thickness. It was approximately 850 meters below the highest elevation sensor, but only 275 meters below the lowest elevation sensor. As with Phase I, the longwall was moving from West to East during Phase II. During the 10 day recording period of Phase II, the longwall removed a section of coal approximately 170 m by 230 m by 3 m.

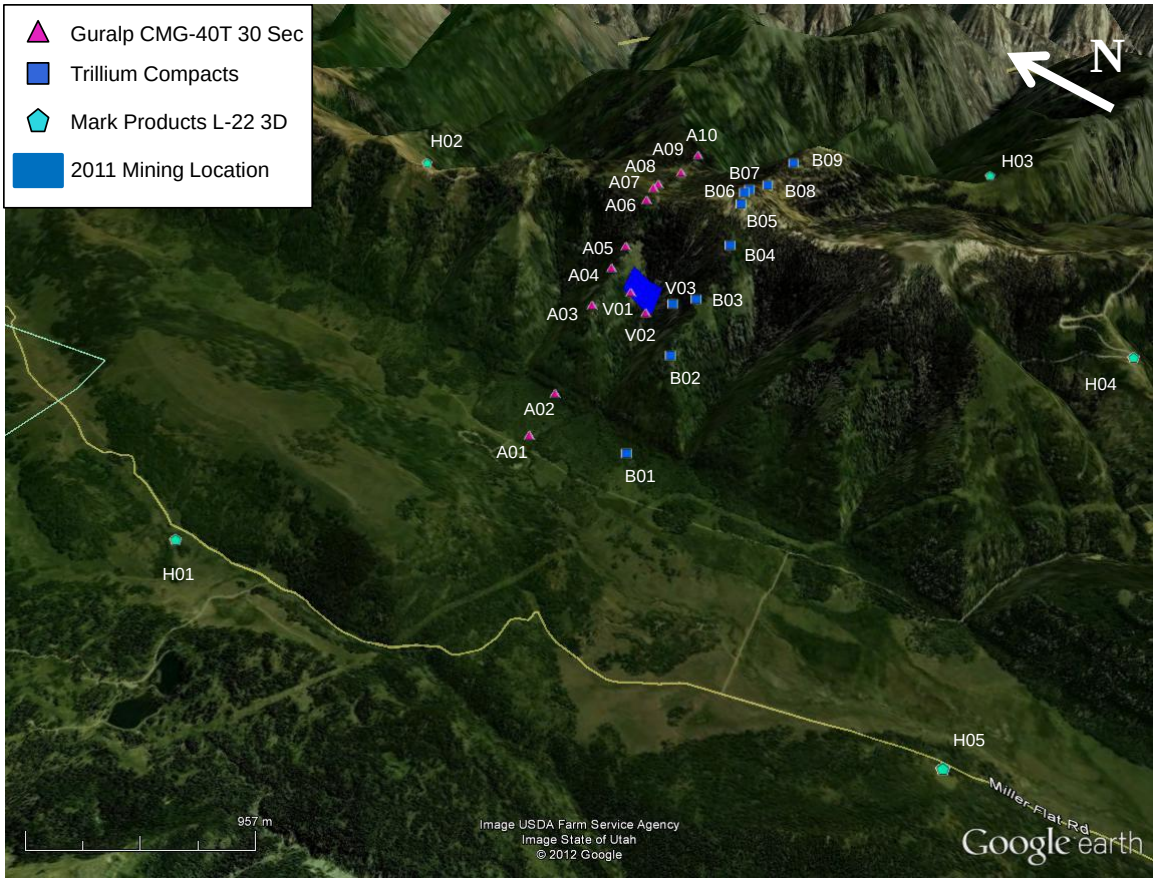

Figure 4.6: Phase II (2011) topographic array and longwall mining location (3D view).

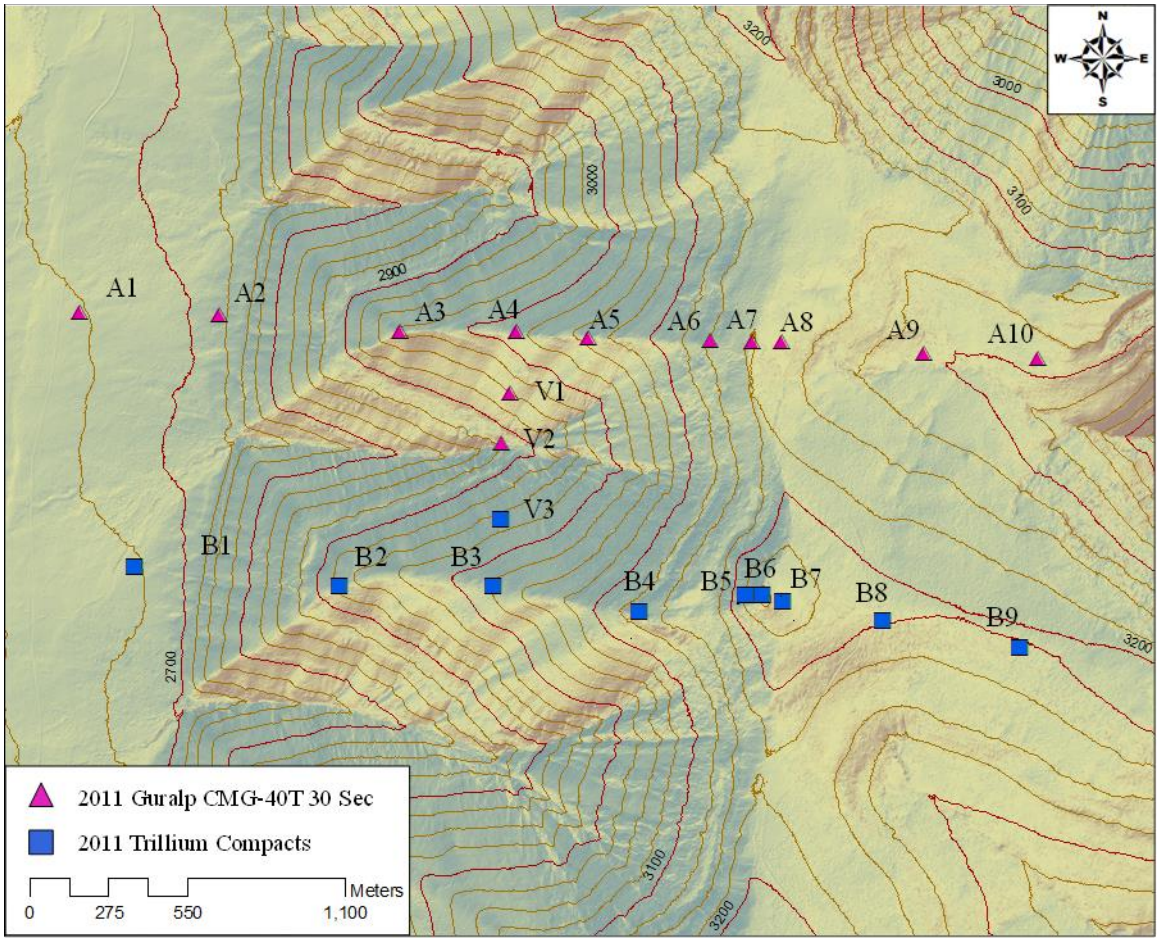

Figure 4.7: Phase II (2011) main topographic array.

A total of 27 stations were used during Phase II, with 22 main topographic stations and 5 stations only used for hypocenter location. There were three main station configurations: (1) Guralp CMG40T-30 sec sensors combined with Reftek RT130 dataloggers (denoted as magenta triangles in figures), (2) Nanometrics Trillium Compact sensors combined with Nanometrics Taurus dataloggers (denoted as blue squares in figures), and (3) Mark Products L-22 3D sensors combined with Reftek RT130 dataloggers (denoted as cyan pentagons in figures). To deploy the stations, type 1 and 2 stations were placed in two parallel and one perpendicular line to form an "H" over the

steep topography. These lines were identified as lines “A”, “B”, and “V” according to their placement. Stations A1-A10 were part of the “A” line, which was the northern most line running from West to East. Stations B1-B9 formed the “B” line, which was the southernmost line running from West to East. Stations A4, V1-V3, and B3 formed the “V” line, which ran from North to South. The type 3 stations were used at locations H1-H5 to form the H (Hypocenter) array, which encircled the main topographic array, and was used for azimuthal control, when locating the event hypocenters. In Table 4.3, the latitude, longitude, and elevation of each station is tabulated along with the DAS and sensor used for each station. The latitude and longitude of each station were determined using a Trimble GeoXH GPS unit with post-corrected sub-meter accuracy (see Figure 4.8). The elevation of each station was determined using the Lidar DEM elevation and the latitude and longitude from the GPS unit.

In Figure 4.9, the topographic array is shown with cross sections A-A’, B-B’, C-C’. West-East cross section A-A’ is shown in Figure 4.10, along with the location of each station in line A, and the location of the longwall during recording. The feature is nearly symmetric about the peak with just slightly more area on the East side of the peak. Stations A1-A2 were deployed at the base of the feature on a 6 degree slope to be reference stations for the rest of the array. Station A3 was located at the intersection of a 28 degree and 15 degree slope. Stations A4-A6 were located to the West of Station A3 along a 15 degree slope. Station A7 was located at the crest of the feature. Stations A8-A9 were located on a 9 degree slope just off the East side of the feature, and finally, Station A10 was located on a level area near the edge of a 22 degree slope. The feature in cross section A-A’ had a total width of 3705 m at the base and a total height of 480 m. In addition, the feature can be divided up into two smaller features with widths of 2224 m

Table 4.3: Phase II (2011) station locations and equipment list for each station.

Station #	Station Name	DAS Type	DAS Serial #	Sensor Type	Sensor Serial #	Latitude	Longitude	Elevation (m)
1	A01	Ref-Tek 130	9811	Guralp CMG40T	T4901	39.440724	-111.236722	2673.8
2	A02	Ref-Tek 130	9459	Guralp CMG40T	T4D86	39.440666	-111.232382	2716.4
3	A03	Ref-Tek 130	9876	Guralp CMG40T	T4873	39.440250	-111.226710	2978.1
4	A04	Ref-Tek 130	91F6	Guralp CMG40T	T4E83	39.440262	-111.223083	3018.7
5	A05	Ref-Tek 130	947E	Guralp CMG40T	T4624	39.440099	-111.220820	3066.4
6	A06	Ref-Tek 130	92CF	Guralp CMG40T	T4484	39.440048	-111.217008	3155.8
7	A07	Ref-Tek 130	9801	Guralp CMG40T	T4891	39.440024	-111.215715	3180.0
8	A08	Ref-Tek 130	989D	Guralp CMG40T	T4897	39.440000	-111.214771	3166.4
9	A09	Ref-Tek 130	944A	Guralp CMG40T	T4892	39.439743	-111.210336	3111.9
10	A10	Ref-Tek 130	955C	Guralp CMG40T	T4906	39.439621	-111.206779	3111.3
11	B01	Taurus	2794	Trillium Compact	861	39.434611	-111.235025	2672.9
12	B02	Taurus	2775	Trillium Compact	856	39.434146	-111.228598	2933.7
13	B03	Taurus	2778	Trillium Compact	722	39.434148	-111.223811	3028.7
14	B04	Taurus	2780	Trillium Compact	854	39.433510	-111.219222	3137.0
15	B05	Taurus	2781	Trillium Compact	785	39.433927	-111.215917	3226.3
16	B06	Taurus	2783	Trillium Compact	863	39.433930	-111.215384	3253.1
17	B07	Taurus	2785	Trillium Compact	864	39.433774	-111.214745	3240.3
18	B08	Taurus	2786	Trillium Compact	859	39.433299	-111.211604	3206.6
19	B09	Taurus	2795	Trillium Compact	865	39.432662	-111.207313	3197.6
20	V01	Ref-Tek 130	92B4	Guralp CMG40T	T4880	39.438769	-111.223277	2949.9
21	V02	Ref-Tek 130	92E4	Guralp CMG40T	T4E33	39.437556	-111.223528	2881.2
22	V03	Taurus	2777	Trillium Compact	703	39.435741	-111.223542	2965.3
23	H01	Ref-Tek 130	933A	Mark Products L-22 3-D	493L	39.454384	-111.258083	2691.6
24	H02	Ref-Tek 130	9960	Mark Products L-22 3-D	458L	39.455834	-111.219673	3126.2
25	H03	Ref-Tek 130	9465	Mark Products L-22 3-D	734L	39.420773	-111.193947	3015.5
26	H04	Ref-Tek 130	980F	Mark Products L-22 3-D	0241L	39.409271	-111.214953	3006.7
27	H05	Ref-Tek 130	980B	Mark Products L-22 3-D	1496L	39.412435	-111.249268	2628.6

and 890 m, and corresponding heights of 202 m and 68 m, respectively. During recording, the longwall was moving parallel with the cross section, in a West to East direction, 200 m south and alongside Station A4, but just over 600 m below it.

West-East cross section B-B' is shown in Figure 4.11 along with the location of each station in line B and the location of the longwall during recording. Similar to cross section A-A', cross section B-B' was nearly symmetric about the peak with just slightly more area on the East side of the peak. Station A1 was located at the base of the feature to act as a reference station. Station B2 was located well above B1 at the intersection of a 28 degree and 14 degree slope. Stations B3-B4 were evenly spaced along a 14 degree slope above Station B2. Station B4 was at the western edge of the Phase I (2010) topographic array. Station B5 was placed at the middle of a 34 degree slope leading up to

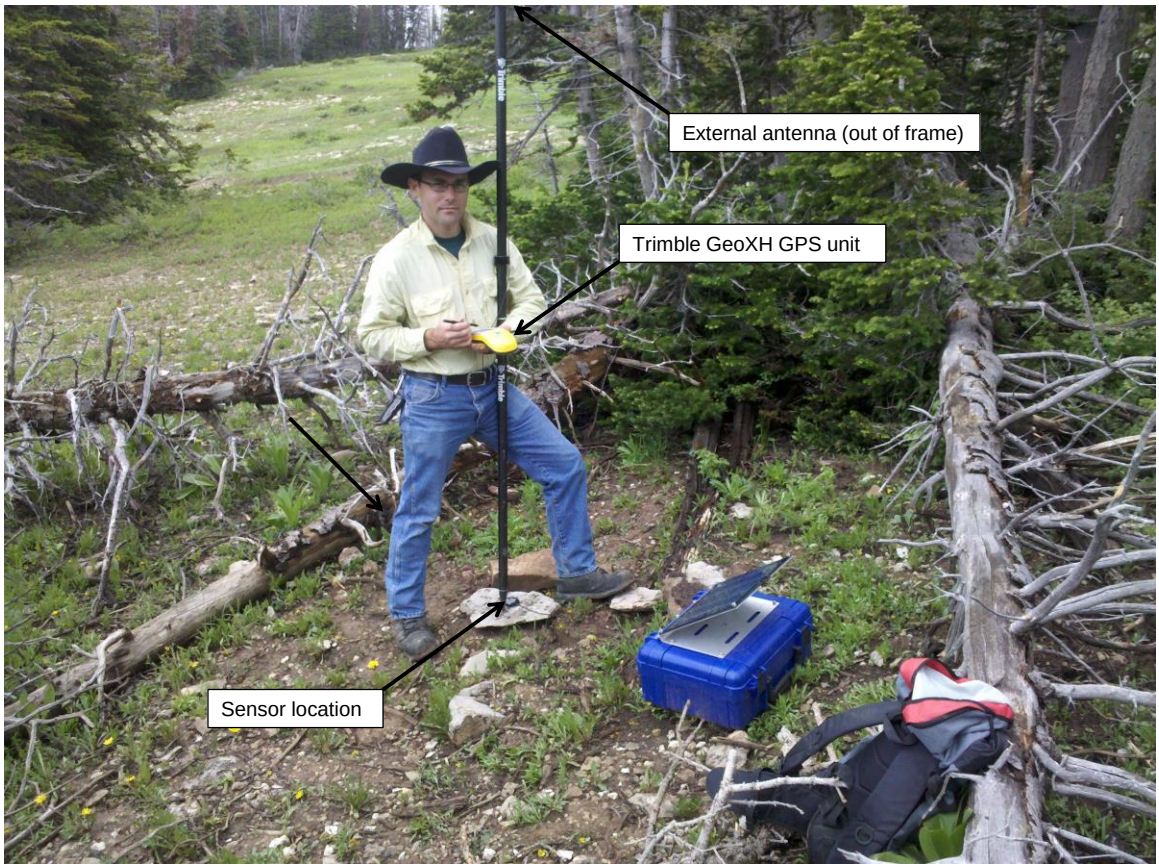

Figure 4.8: Phase II (2011) Trimble GeoXH GPS unit used to locate the topographic stations.

Station B6 at the crest of the feature. Stations B7 and B8 were located on the East side of the feature, on a 9 degree slope, and just within the boundary of the Phase I array.

Finally, Station B9 was located on a flat area on the East side of the feature. Overall, the feature in cross section B-B' is 41% larger in area than the feature in cross section A-A', with a width of 4295 m and a total height of 585 m. In addition, the feature was further divided up into smaller features, with widths of 2765 m and 470 m, and corresponding heights of 305 m and 78 m, respectively. The latter was the same feature defined in Phase I (2010). As with cross section A-A', the longwall was moving parallel

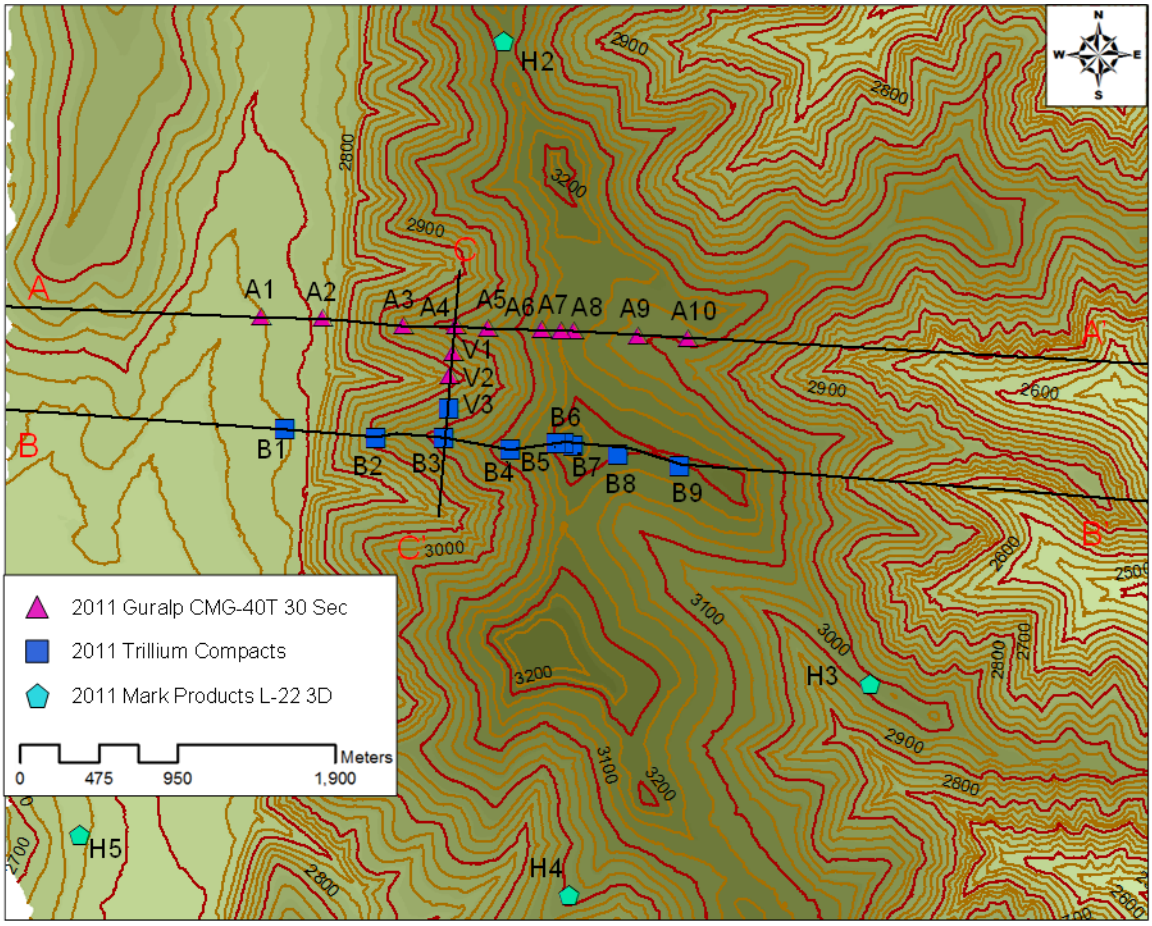

Figure 4.9: Phase II (2011) topographic array showing array cross sections A-A', B-B', and C-C'.

with cross section B-B'. The center of the longwall was approximately 450 m due North of station B3, and just over 600 m below the station.

North-South cross section C-C' is shown Figure 4.12, along with the stations in line V, and the location of the longwall during recording. Cross section C-C' was unique, and formed two nearly triangular shapes in the North-South direction. The cross section formed two nearly 2D features, with a significant elevation change in only one dimension. Station A4, which was also part of the A line, was located at the peak of the northernmost feature. Station B3, which was also part of the B line, was located at the

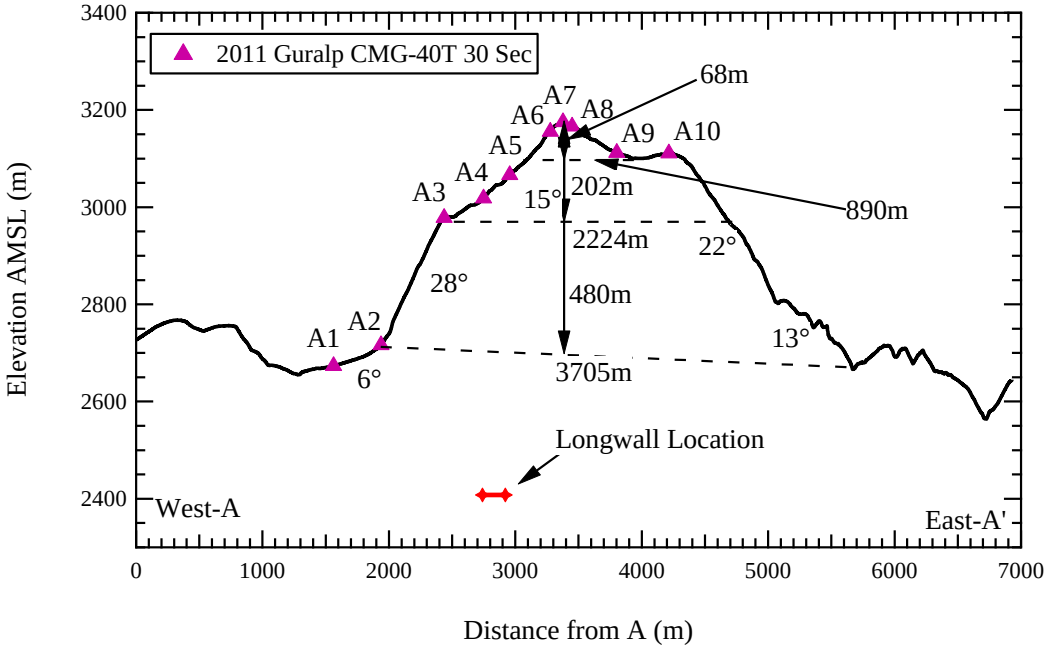

Figure 4.10: Phase II (2011) cross section A-A' showing station and longwall location during recording.

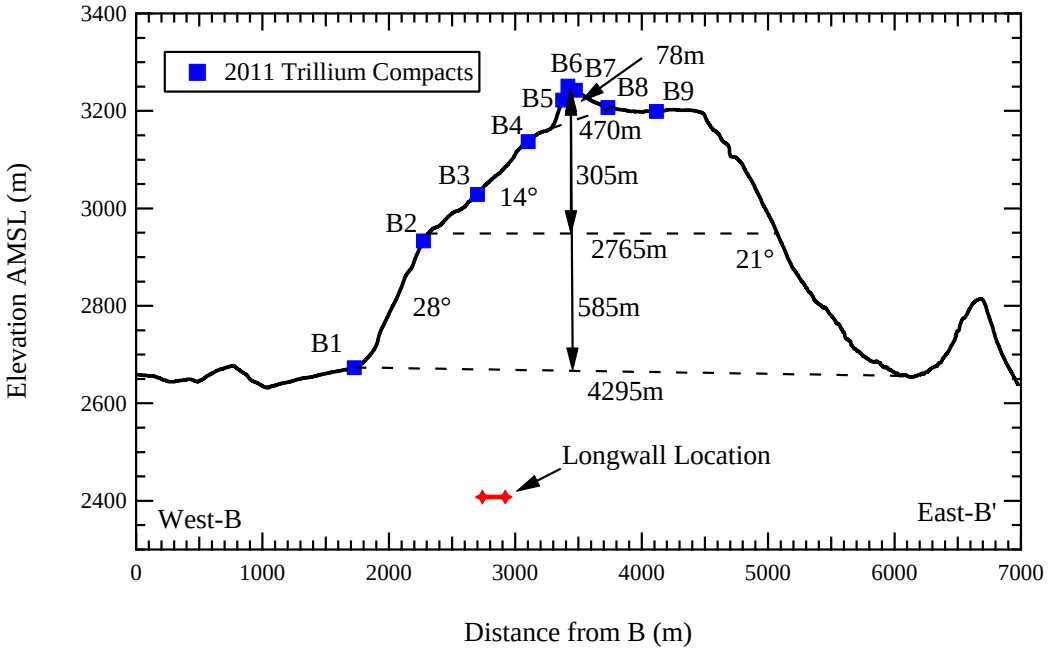

Figure 4.11: Phase II (2011) cross section B-B' showing station and longwall location during recording.

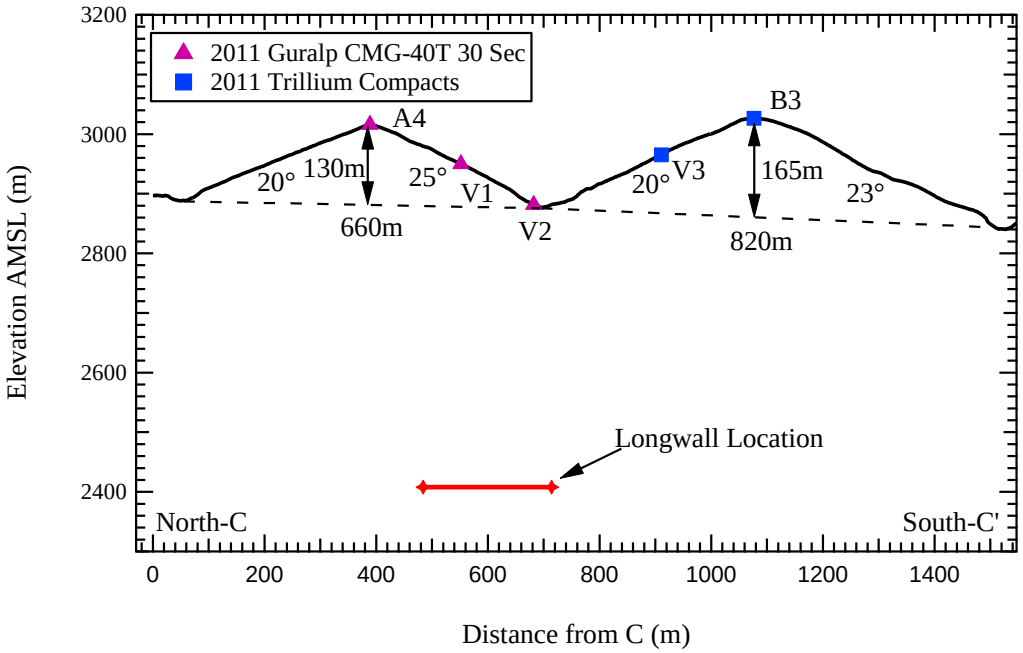

Figure 4.12: Phase II (2011) cross section C-C' showing station and longwall location during recording.

peak of the southernmost feature. Stations V1 and V3 were located half way down the northern and southern slopes, respectively, while Station V2 was located in the valley of the cross section, to act as a reference station. The slopes in cross section C-C' varied between 20 and 25 degrees, with the northern most feature being slightly steeper. The total width of the two features was 660 m and 820 m, with heights corresponding to 130 m and 165 m, respectively. Unlike cross sections A-A' and B-B', the longwall was moving perpendicular to cross section C-C' just east of Stations V1 and V2. The longwall during recording was less than 500 meters below Station V2.

To deploy the seismic stations, access to the mountain was along the 4x4 trail shown in Figure 4.5. However, due to heavy rains and snow drifts on the mountain, the road could only be accessed using all-terrain vehicles (ATV), which were used to move all the equipment along the trail (see Figure 4.13). With the help of about a dozen people,

Figure 4.13: All-terrain vehicles (ATV) used to deploy the seismic stations due to poor road conditions during Phase II (2011).

each station was carried by hand from the trail to its recording location. Stations were also deployed using Miller Flat Road, which was just west of the main array. Station types 1 (CMG 40T and RT130) and 3 (L-22 and RT130) are shown in Figures 4.14 and 4.15, respectively. These stations consisted of a sensor, datalogger, charge controller, solar panel, car battery, GPS unit, and cables to connect each component. Each system had a mass of approximately 32 kg. Station type 2 (Trillium compact and Taurus) is shown in Figure 4.16. These systems were much smaller in overall size, and use lightweight lithium polymer batteries. The systems fit within the blue case shown in Figure 4.16 and had a total mass of 12 kg. Prior to deployment, a huddle test (see Figure 4.17) was performed with several stations to confirm the systems were working correctly before they were deployed.

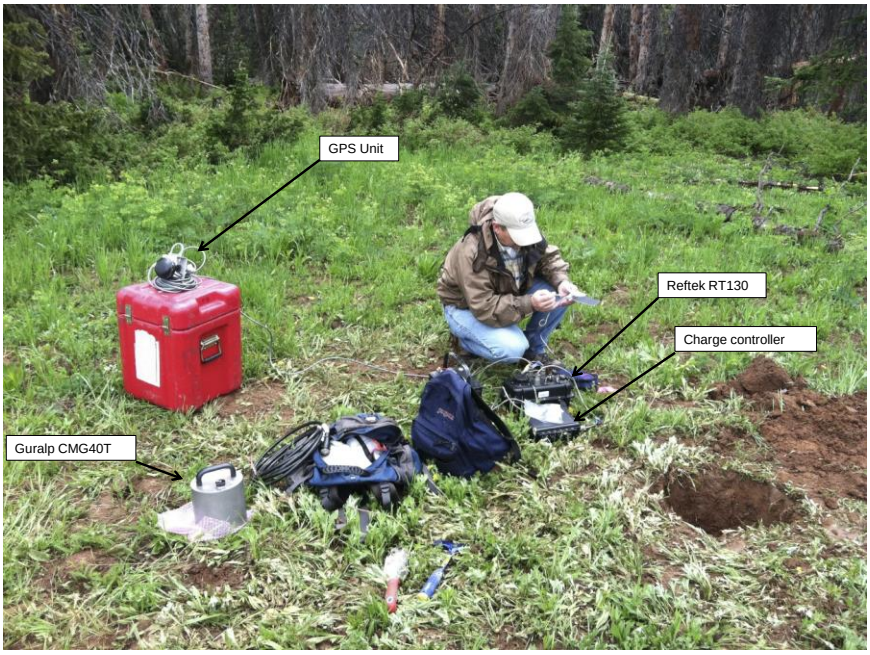

Figure 4.14: Phase II (2011) station type 1 (Guralp CMG40T 30sec and Reftek RT130).

Figure 4.15: Phase II (2011) station type 3 (Mark Products L-22 and Reftek RT130).

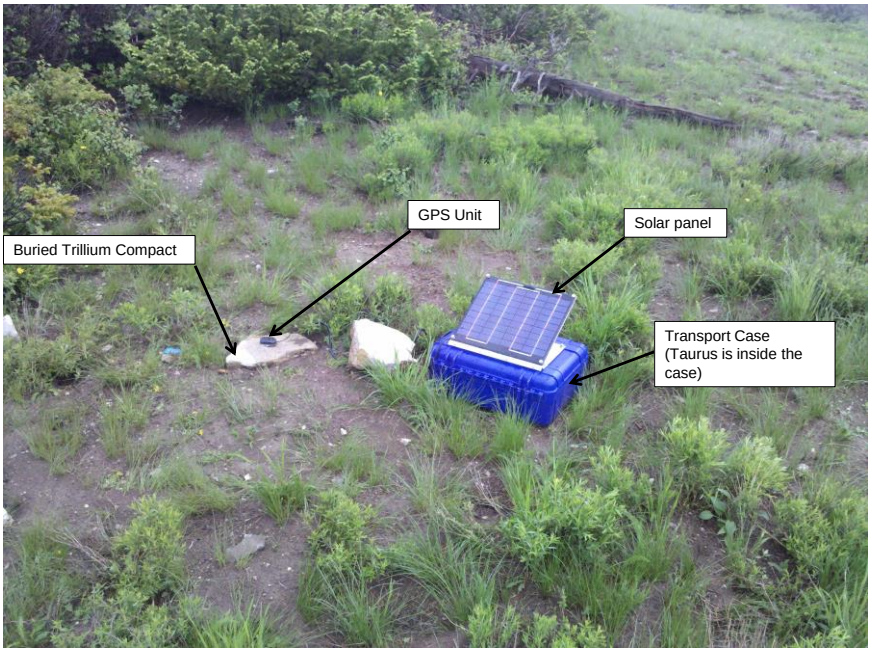

Figure 4.16: Phase II (2011) station type 2 (Nanometrics Trillium Compact and Taurus).

To install the stations, a hole was dug with a depth approximately twice the height of the sensor (60 cm) and the sensor was placed in the bottom of the hole inside a plastic bag. The sensor was leveled and oriented toward magnetic North. Soil was then compacted around the sensor to couple it to the ground (see Figure 4.18). The datalogger and other station components were placed in a garbage sack or the blue transport case to protect them from the weather.

4.3.2 Seismic Recording and Output Format

In Phase II (2011), seismic stations started recording data on 7-8-2011 at 18:04 GMT. However, the entire array was not operation until 7-10-11 at 20:47 GMT. Once completely operational, the entire array of stations recorded data continuously until 7-21-2011 at 15:55 GMT, when the sensors were systematically shutdown. In Figure 4.19, the activation and deactivation times of each station used in Phase II (2011) is shown. The

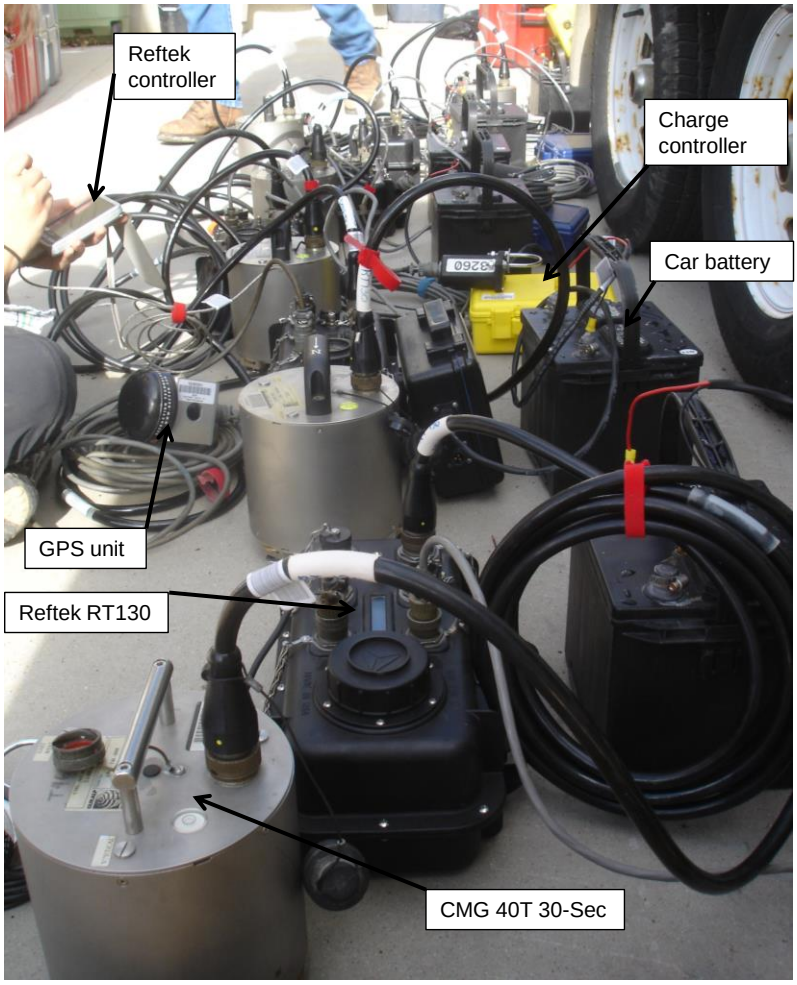

Figure 4.17: Huddle test of station type 1 (CMG 40T 30-sec and Reftek RT130) prior to deployment during Phase II (2011).

values are also tabulated in Table 4.4. Most of the seismic stations were operational on 7-10-11 at 00:00 am. However, the "H" stations were not activated until later in the day. All the stations were taken offline on 7-21-11. Each station in the array was set to record at a sampling rate of 200 Hz, and to record data continuously. For the Taurus dataloggers, a high pass hardware filter was applied at a frequency of 0.1 Hz, to reduce the low frequency drift in the data.

Figure 4.18: Example of station installation during Phase II (2011).

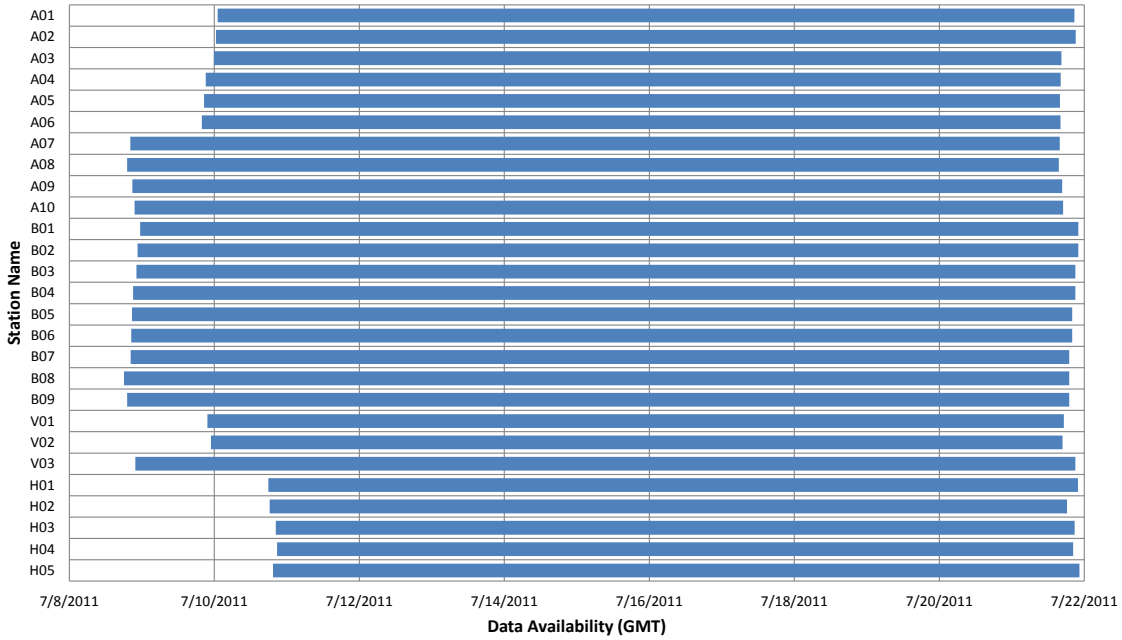

Figure 4.19: Phase II (2011) seismic recording station activation and deactivation times.

Table 4.4: Phase II (2011) tabulated activation and deactivation times for each seismic recording station.

Station #	Station Name	Time on (GMT)	Time off (GMT)
1	A01	7/10/2011 1:06	7/21/2011 20:42
2	A02	7/10/2011 0:30	7/21/2011 21:10
3	A03	7/9/2011 23:52	7/21/2011 16:26
4	A04	7/9/2011 21:10	7/21/2011 16:11
5	A05	7/9/2011 20:34	7/21/2011 15:55
6	A06	7/9/2011 19:50	7/21/2011 16:07
7	A07	7/8/2011 20:11	7/21/2011 15:50
8	A08	7/8/2011 19:06	7/21/2011 15:34
9	A09	7/8/2011 20:52	7/21/2011 16:40
10	A10	7/8/2011 21:34	7/21/2011 16:58
11	B01	7/8/2011 23:27	7/21/2011 22:00
12	B02	7/8/2011 22:35	7/21/2011 22:00
13	B03	7/8/2011 22:13	7/21/2011 21:00
14	B04	7/8/2011 21:06	7/21/2011 21:00
15	B05	7/8/2011 20:43	7/21/2011 20:00
16	B06	7/8/2011 20:29	7/21/2011 20:00
17	B07	7/8/2011 20:17	7/21/2011 19:00
18	B08	7/8/2011 18:04	7/21/2011 19:00
19	B09	7/8/2011 19:09	7/21/2011 19:00
20	V01	7/9/2011 21:41	7/21/2011 17:14
21	V02	7/9/2011 22:53	7/21/2011 16:47
22	V03	7/8/2011 21:51	7/21/2011 21:00
23	H01	7/10/2011 17:54	7/21/2011 21:53
24	H02	7/10/2011 18:18	7/21/2011 18:14
25	H03	7/10/2011 20:19	7/21/2011 20:48
26	H04	7/10/2011 20:47	7/21/2011 20:18
27	H05	7/10/2011 19:23	7/21/2011 22:23

At the end of recording, the data from each station was downloaded from the compact flash cards. The data from station type 2 (Trillium and Taurus) was downloaded in 1 hour long files, in Miniseed format (http://www.passcal.nmt.edu/content/all-about-seed-format). The Miniseed format is a sub-format of the SEED data format, and contains

only data from the station and no location information, or other metadata about the station. Each 1 hour file contained the response of all three components of the sensor and starts at the top of each hour. The data for station type 1 and 3 (Reftek dataloggers) was downloaded in Reftek format. The data was then converted to Miniseed format, finally to Seed format using PASSCAL and Antelope software. In Figure 4.20, a diagram is shown

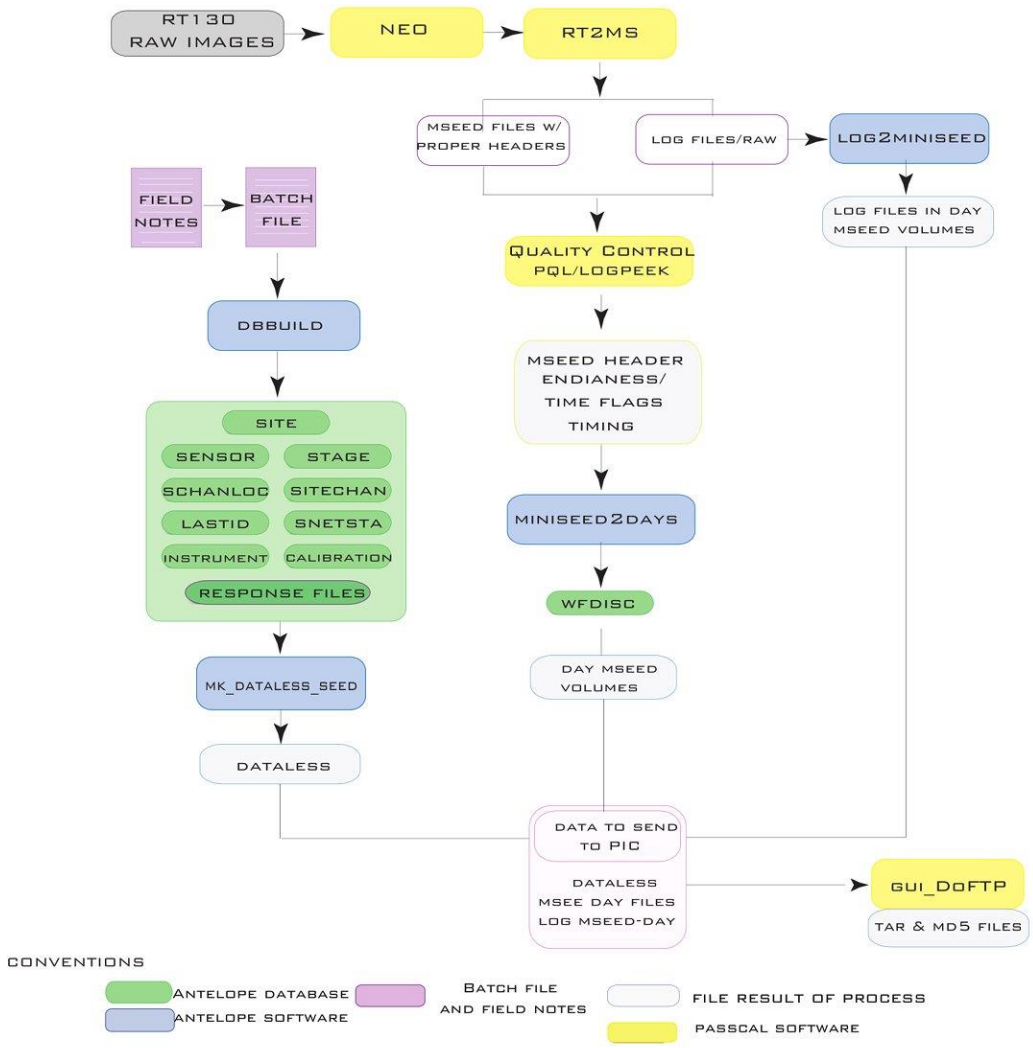

Figure 4.20: PASSCAL data reduction flowchart for station type 1 and 3 (Reftek datalogger).

explaining the process flow of converting the raw Reftek records into SEED format. The SEED files are divided into separate files according to day, component, and station.

4.4 DATA PROCESSING

To process the seismic events classified during Phase II (2011), the SEED and MiniSeed files were first converted to Matlab format and then the seismic events were identified. The hypocenters were located for each event and sensor amplitudes were corrected for geometric attenuation. The events were then processed using the standard ground motion processing scheme used in Phase I. The sensors responses were then compared using the four methods described in Section 3.6.2.

4.4.1 Event Identification

As with Phase I, the first step in processing the seismic events is to identify the points in time at which "earthquakes" occurred during Phase II. Similar to Phase I, events were first identified using the UUSS earthquake catalog and then events were identified visually using time record plots (see Figure 4.21). Only a select number of stations were included in the plot to reduce the overall complexity of the plot, but still provide good coverage of the entire array. Each plot contains the time records for Stations H1-H5, A1, A7, A10, B1, B6, B9, and V2, East-West components, and plots one hour of time. The amplitude of the time traces were normalized by 10,000 counts to decrease overlap between traces. Events were chosen from the plots based on 3 criteria: (1) The raw amplitude of the event has to exceed .005 mm/sec on station types 1 and 2 (station type 3 was not included because the calibration factor was significant different than station types 1 and 2), (2) the duration of the event has to be at least 2 seconds from P arrival to S coda, and (3) the event has to be clearly measured on all sensors in the array. As with Phase I (2010), 52 events were identified in Phase II (2011).

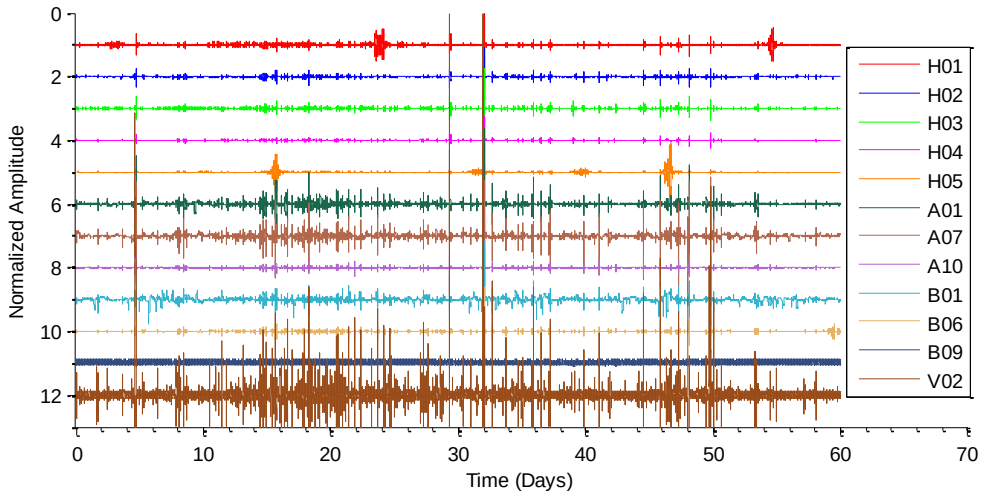

Figure 4.21: Phase II (2011) event identification plot for 1:00-2:00 am, July 20, 2011 GMT (East-West component).

Once an acceptable "earthquake" was identified, a 20 second window was used to "isolate" the event from the main record. To determine the center of the 20 second window, the maximum amplitude of the vertical component of station A01 was identified, and 10 seconds on either side of this point were taken to create the 20 second window. The same window in time was then taken from the records of each station and each component. This operation resulted in 4000 point vectors with a total of 81 traces for 3 components of 27 stations. The events were named based on the day of the year, hour, and minute of the event (i.e., event 201.1.29 was recorded in 2011 on day of year 201 (July 20), hour 1, and minute 29).

4.4.2 Hypocenter Location

For each of the recorded events, the hypocenter was located using the Hypoellipse software program. Hypoellipse was developed by the United States Geological Society (USGS) for locating the hypocenters of local and regional earthquakes. Hypoellipse along with Hypoinverse have been used extensively by the USGS and UUSS to locate

hypocenter with both densely and sparsely spaced seismic arrays. Many of the parameters and methods used in locating the hypocenters for Phase II (2011) were obtained from previous projects in the Trail Mountain, East Mountain, and the Crandall Canyon areas of Central-Eastern Utah, along with personal communications with UUSS personnel (Ababasz et al. 2002, Williams and Arbabasz 1989, and Pechmann et al. 2008).

A velocity model for the East Mountain area was created by modifying the crustal velocity model from the Trail Mountain Study (Arabasz et al. 2002), similar to what was done in Pechmann et al. (2008) for the Crandall Canyon Study. The main modification to the Trail Mountain velocity model was adjusting the elevation of the top of the model to 3300 meters to account for the higher surface elevations and stratigraphic of the East Mountain area. The crustal model used in Phase II is shown in Table 4.5. The P wave velocity of the upper 700 meters was set at 4000 m/sec with the next layer increasing to 4300 m/sec, with a thickness of 1280 meters. The rest of the crustal model increases incrementally to a maximum velocity of 7900 m/sec at a depth of 4500 meters below the surface.

The P-wave arrivals for each event were picked from the vertical component of each station. Next, the event hypocenters were located using the P wave arrival times only. The accuracy and acceptability of the results was based on the difference between the measured travel times and the estimated travel times of the model, called the residual times. After several analysis runs using different numbers of stations, it was determined that the location estimates using only P wave arrivals had reached the accuracy of the program. The Hypoellipse program only accounts for timing accuracies of 0.01 sec or greater and most residual times were already less than 0.01 sec. Therefore, the S wave travel times were not used in the analysis. Moreover, due to the short travel time, picking S wave arrivals would have been very ambiguous due to interference from the P-wave

Table 4.5: Phase II (2011) crustal model used in Hypoellipse.

Layer	Velocity km/sec	Depth km	Thickness km	Vp/Vs
1	4	0	0.7	1.96
2	4.3	0.7	1.28	1.96
3	4.4	1.98	0.44	1.74
4	4.84	2.42	1.4	1.74
5	5.81	3.82	0.26	1.74
6	6.2	4.08	26.62	1.74
7	6.8	30.7	14.3	1.74
8	7.9	45	1000	1.74

arrival, and would have only increased the overall uncertainty of the problem.

The magnitude of each event was not determined in the analysis because many of the events were believed to be less than M_L 1.0, and current magnitude estimates are not calibrated correctly for magnitudes less than M_L 1.0.

4.4.3 Event Processing

The events recorded in Phase II (2011) were processed using the same ground motion processing scheme used in Phase I (2010). In Phase II, the raw signals were baseline corrected, a cosine taper of 1 sec was applied to the front and back of the signal, and zeros were padded to the front and back of the signal, to create a vector the same length as Phase I (64 seconds). Due to the difference in sampling rates during Phase I and II, the time traces for Phase II contained 12800 points in the time domain (compared to 8192 points for Phase I). This was done to achieve the same frequency resolution in both Phase I and II. The calibration factors for each type of station were then applied to the data in the time domain.

In Phase II, the seismic source (i.e., the longwall) was much closer to the recording stations than in Phase I, and the distances between the stations were greater than the distances to the source for many of the stations in Phase II. Therefore, geometric

attenuation likely had a large influence on the amplitude difference between stations. To assess the effect of geometric attenuation on the topographic array, the PGV values from all 52 events are plotted versus the ray path distance from the average hypocenter (see Table 4.6) to each station in Figure 4.22. Geometric attenuation clearly had an effect on the records as evidence from the clear negative trend in Figure 4.22. Attenuation factors between 1.36 and 1.71 were calculated, when a power function was fit to the data from the three components; however, due to errors and unknowns in estimating the hypocenters, it was chosen to correct the data based on the standard attenuation factor one over the ray path distance (i.e., 1/R). This correction was not applied in Phase I because the size of the topographic array was much smaller than the distance from the longwall location. The geometric attenuation correction was applied by multiplying the time signal from each component and each station by the ray travel path distance from source to the receiver in kilometers. Due to inaccuracies in the estimated location of the events (i.e., some events were located outside of the topography), an average hypocenter location was used instead of each individual hypocenter, to correct for geometric attenuation. For the majority of the events, the average hypocenter location was less than 50 meters from the estimate hypocenter for each event. Table 4.6 contains the ray path distances from the average hypocenter location to each station. The closest station to the average hypocenter was V02 at a distance of 0.19 km, while the farthest station (H05) was at a distance of 3.68 km. In Figure 4.23, the uncorrected and corrected PGV values for event 200.19.5 are plotted against their hypocenter distances. The plot clearly indicates a negative trend for the uncorrected values and a more flat line trend for the corrected values, which is more appropriate.

After geometric attenuation correction, the signals were filtered with a 0.1 Hz high pass and 40 Hz low pass filter. The high pass cutoff frequency was chosen because

Table 4.6: Phase II (2011) geometric attenuation correction values for each station.

Station #	Station Name	Ray Distance (km)
1	A01	1.25
2	A02	0.89
3	A03	0.49
4	A04	0.37
5	A05	0.43
6	A06	0.67
7	A07	0.77
8	A08	0.82
9	A09	1.13
10	A10	1.41
11	B01	1.15
12	B02	0.72
13	B03	0.56
14	B04	0.72
15	B05	0.90
16	B06	0.94
17	B07	0.98
18	B08	1.19
19	B09	1.52
20	V01	0.24
21	V02	0.19
22	V03	0.38
23	H01	3.54
24	H02	2.01
25	H03	3.14
26	H04	3.30
27	H05	3.68

the Taurus digitizers used in Phase II (station type 2) were setup with a 0.1 Hz analog high pass filter, therefore for comparison purposes all the records were filtered at that frequency. The high pass filter frequency was chosen at 40 Hz to coincide with Phase I and because frequencies above 40 Hz were not considered useful for the experiment. The signals were then transformed to the frequency domain using the FFT and the Konno and

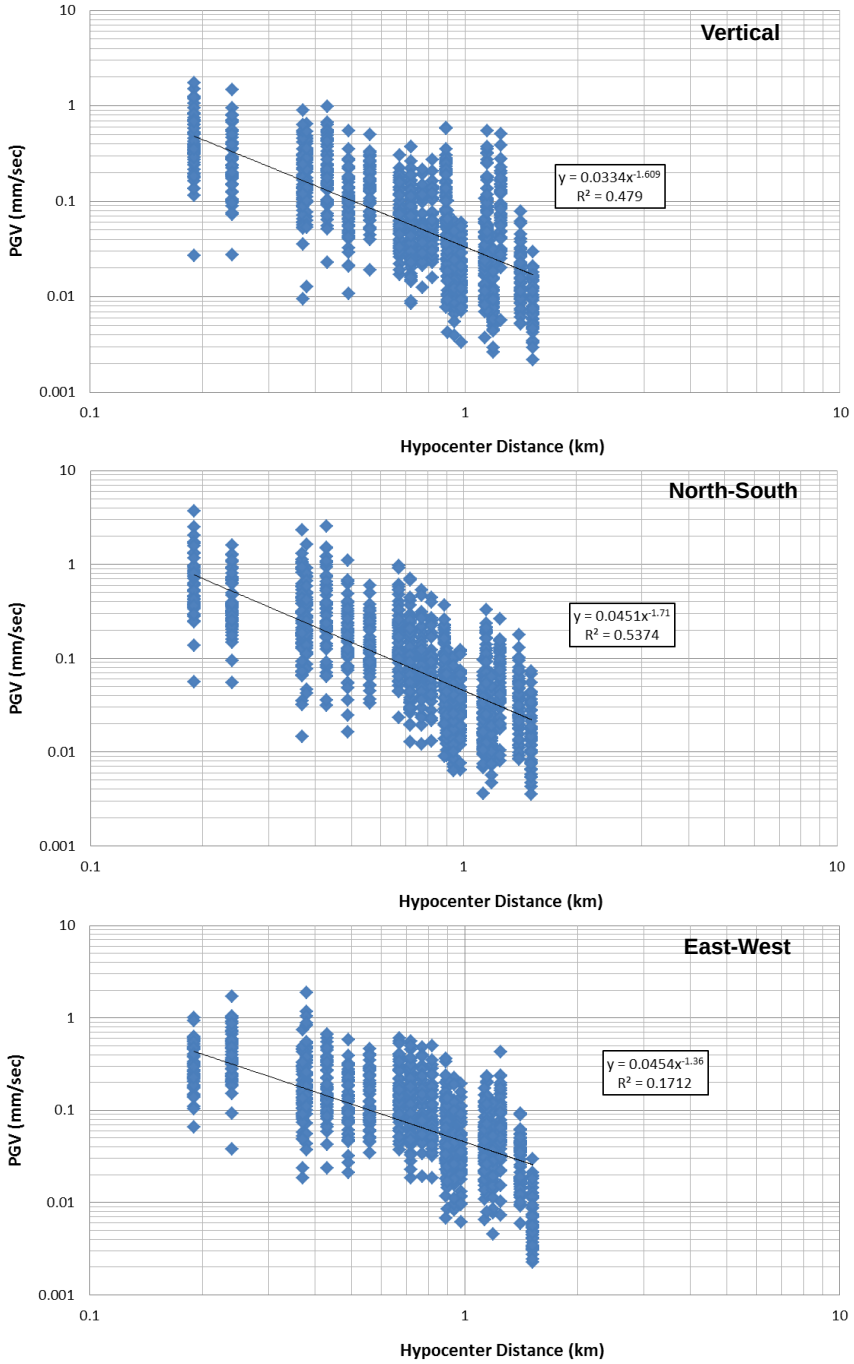

Figure 4.22: PGV values for all 52 events versus station hypocenter distance for Phase II (2011).

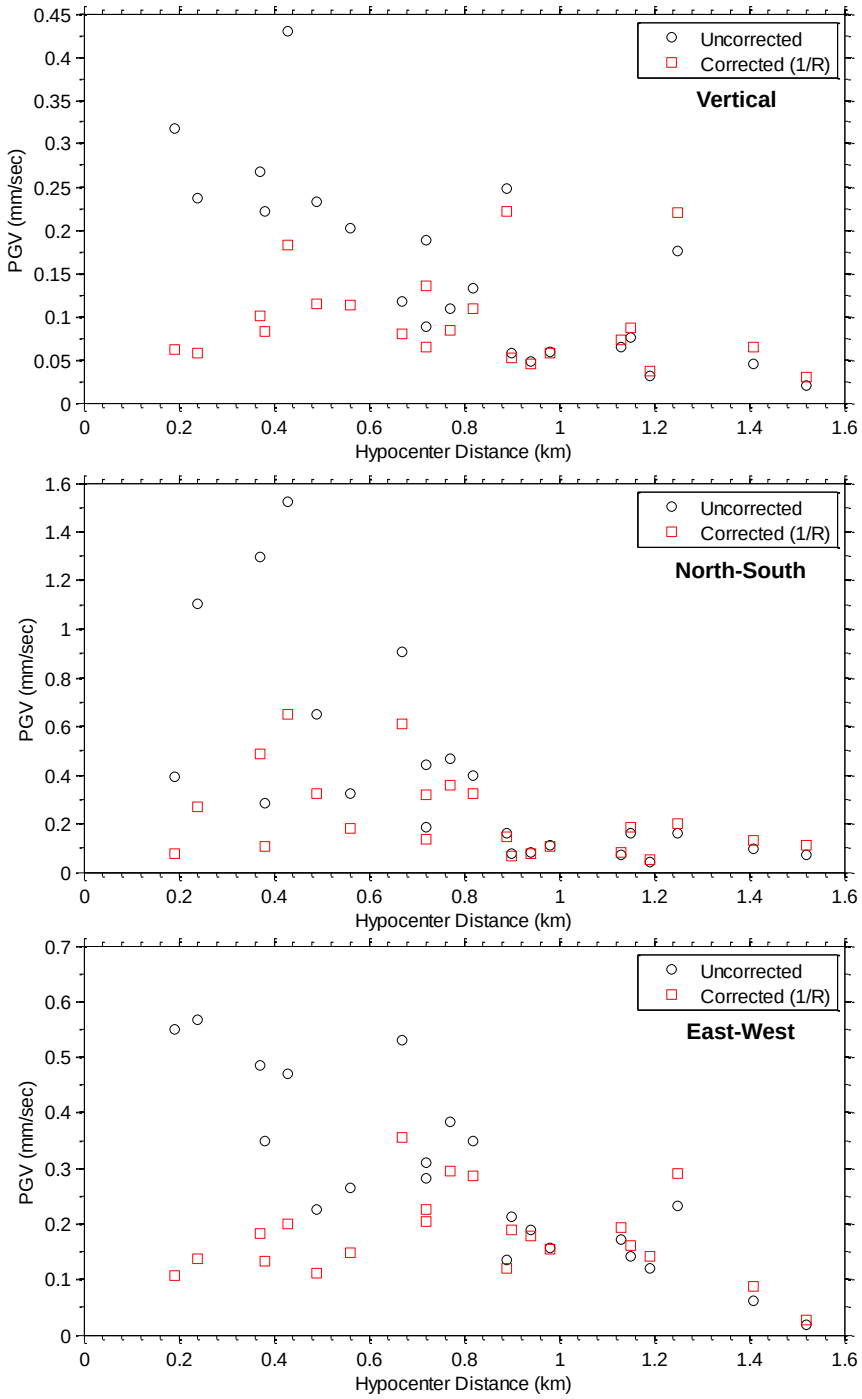

Figure 4.23: Raw PGV values and PGV values corrected for geometric attenuation for event 200.19.5.

Ohmachi smoothing function was applied to the Fourier Amplitude Spectrum (FAS). Similar to Phase I, a "b" value of 60 was used with the smoothing algorithm.

The effect of topography on the ground motions in Phase II was estimated using the same three methods as Phase I, namely the Standard Spectral Ratio (SSR), the Median Reference Method, the Horizontal to Vertical Spectral Ratio Method (HVSR). Directional analysis was once again used to visualize the polarity of the horizontal results for each method. For the SSR analysis, a reference station was chosen for each cross section or station line. For line A, Station A01 was chosen as the reference station because it was on the flattest topography and was least likely to be affected by topographic effects. For line B, Station B01 was chosen and for line V, V02 was chosen for the same reasons discussed for line A. For the MRM analysis, the median reference response was calculated based on the response of only the main topographic array stations, and not the hypocenter stations (H1-H5). Therefore, only one reference value was computed for the entire array. The hypocenter stations were not used to compute the median because the amplitude response of the geophones was considered inaccurate compared to the intermediate and broadband sensors in the array. The HVSR and directional analyses were computed in same way as Phase I.

4.5 SUMMARY

This chapter detailed the sensors, dataloggers, station layout, and event processing for Phase II (2011). Phase II deployed 22 broadband and intermediate period sensors, along with 5 short period geophones in a dense array over sharp topographic features in central-eastern Utah. The array encompassed an area of approximately 25 km^2 and instrumented two main features using three linear arrays and one large circular array. The seismicity recorded during Phase II was associated with underground longwall coal

mining directly under the topographic array. Data was recorded for approximately 10 continuous days using independent dataloggers. The data was processed using a standard seismic signal processing scheme, and the hypocenters for each recorded event were located. The hypocenter distances were then used to correct for geometric attenuation.

Chapter 5: Surface Wave Testing and Results

5.1 INTRODUCTION

Multi-channel Analysis of Surface Waves (MASW) testing was conducted in the vicinity of the topographic array during Phase I (2010). A total of 16, 1 Hz vertical geophones were placed in a linear array with a total length of 115 meters. A 12 kg rock was used as the surface wave source and signals from each geophone were recorded in the frequency domain. The MASW data was analyzed using the frequency domain beamformer method. Forward modeling using the 3-D effective mode solution in the software WinSASW was used to generate the shear wave velocity profile. This chapter details the equipment, data collection, data processing, and results of surface wave testing to determine the small strain shear stiffness of the mountain.

5.2 SURFACE WAVE EQUIPMENT

For surface wave testing, the L4-C 1 Hz geophones were used to measure seismic waves. The seismic signals were sampled and recorded by the mobilyzer dynamic signal analyzer. This section details the equipment used to conduct surface wave testing.

5.2.1 Sercel L4-C (Vertical)

The Sercel L4-C (see Figure 5.1) is a 1 Hz geophone with one vertical component of measurement. The geophone is a velocity transducer that requires no external power. The sensor is approximately 9 cm in diameter and 20 cm in height with a mass of approximately 1.7 kg. Coil resistance for each sensor is 500 Ohm with a sensitivity of approximately 282 V/m/sec. A total of 16 L4-C were used for surface wave testing during Phase I each sensor has similar output and natural frequency. Therefore, the

Figure 5.1: Sercel L4-C vertical 1 Hz geophone.

sensors were used without applying the calibration factors. The sensors were provided by NEES@UTexas.

5.2.2 Data Physics Mobilyzer

The Mobilyzer (see Figure 5.2) is a full-function dynamic signal analyzer manufactured by Data Physics Corporation. The system has 32-input channels and 2-output channels with a 105 kHz simultaneous sampling rate, 120 Gb internal hard drive, 24 bit ADC, 120 dB dynamic range, and 110 dB anti-aliasing filter. The system has a variable input range from 1 to 10 volts. It is controlled using a windows-based software package produced by Data Physics (SignalCalc) that has measurement capabilities in both the time and frequency domain. The system was owned by the University of Arkansas.

Figure 5.2: Data Physics Mobilyzer 32 channel dynamic signal analyzer.

5.3 DEPLOYMENT AND DATA COLLECTION

A linear array of 16, 1 Hz geophones was deployed along a mountain trail just South of the main topographic array in Central-Eastern Utah (see Figure 5.3). This area was chosen for three reasons: (1) the road provides easy access to layout the sensors, (2) this was the closest flat area to the topographic array, (3) the soil in this area was likely thicker than other locations on the mountain, but still has the same geologic structure at depth. The array was deployed parallel to the mountain trail closest to the eastern edge (see Figure 5.4). The center line of the array was located at approximately 39.42876 Latitude by -111.21516 Longitude. A uniform receiver spacing of 7.62 meters was used with a total array length of 115 meters. Each geophone was buried approximately 10 cm deep in order to reduce wind noise and increase the coupling between the geophone and

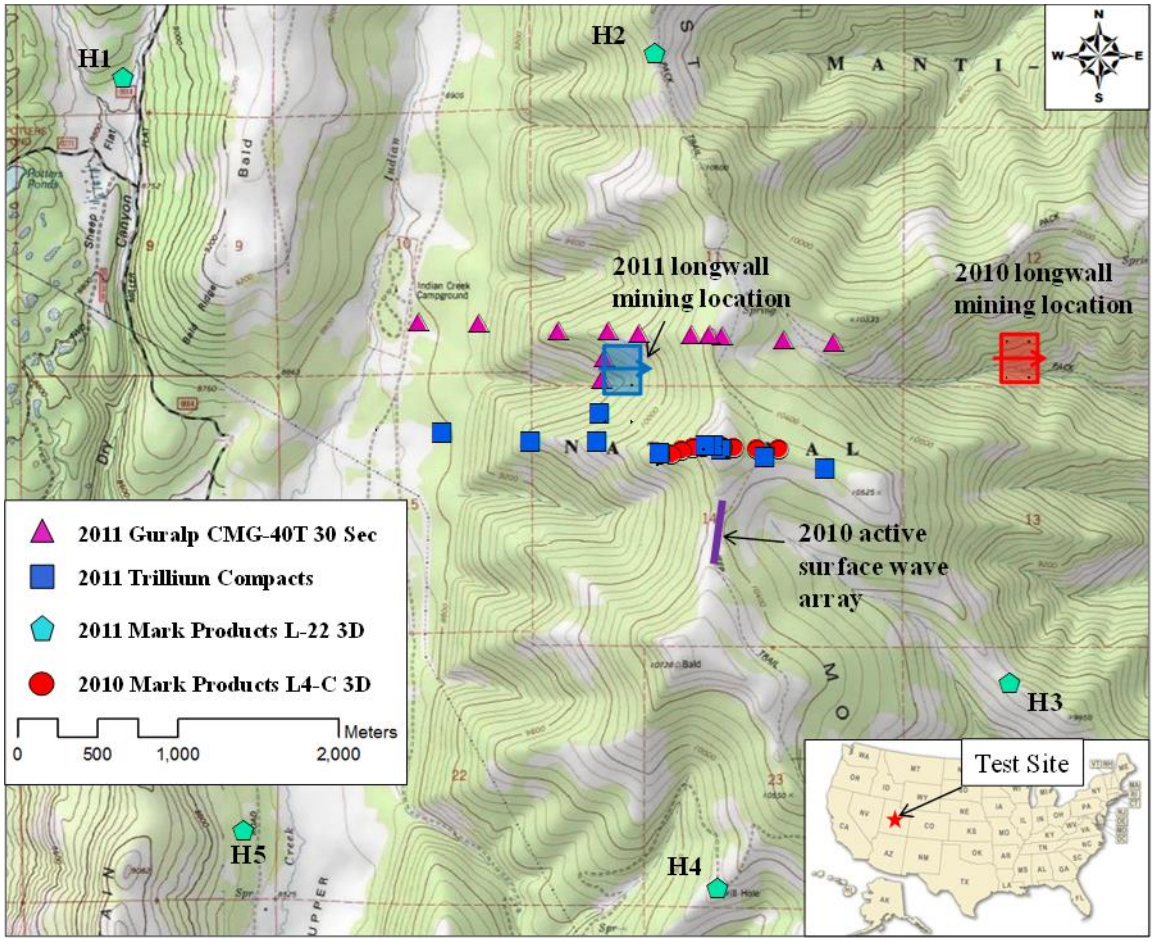

Figure 5.3: Surface wave array location Phase I (2010).

ground surface. Spools of single pair cable were run to each receiver and the sensors and cables were grounded to the Mobilyzer case (See Figure 5.4).

To collect data, the multi-source offset method was used. For this method, the array is left stationary and data is collected at multiple source offset locations. Source to first receiver distances of 4.6 m, 9.2 m, and 18.3 m were used, which resulted in array center distances of 62.1 m, 66.7 m, and 75.8 m, respectively (Yoon and Rix 2009). A large 12 kg rock was used to produce surface waves. For each source location, the rock was lifted above the head and thrown down. Five shots were taken at each of the source

Figure 5.4: Geophone array used to conduct surface wave testing during Phase I.

location and staked in the frequency domain to increase signal to noise ratio. The seismic signals were recorded in the frequency domain with a frequency span of 150 Hz and a total of 1600 frequency domain points. Seismic data was saved in Matlab format.

5.4 SURFACE WAVE DATA PROCESSING AND RESULTS

The MASW data from each shot was analyzed using the frequency domain beamformer method (Zywicki 1999). A 3-D dispersion curve was generated for each source-offset and the maximum spectral peak for each frequency was picked

automatically using a Matlab code. The dispersion data from each source-offset was then combined to form a composite dispersion curve as a means to: (1) identify potential near-field effects, (2) aid in selecting the fundamental mode of surface wave propagation, and (3) provide a robust means for estimating dispersion uncertainty. Dispersion points clearly displaying near field effects, higher modes, or obvious inconsistencies were manually removed after combining the data from all offsets. However, much of the "normal" dispersion scatter was left intact to provide a better estimate of the uncertainty in the dispersion data. The composite experimental dispersion curve was then divided into 30 wavelength bins using a log distribution. The mean phase velocity and associated standard deviation was then calculated for each bin, resulting in an experimental dispersion curve with associated uncertainty. The shear wave velocity profile was determined using forward modeling by fitting a 3D theoretical solution to the mean experimental dispersion curve using the software WinSASW (Figure 5.5). The 3D solution uses the superposed-mode dynamic stiffness matrix method to solve for the surface displacements generated by all Rayleigh wave modes and body waves (Joh 1996). The solution is the most appropriate solution for the Spectral Analysis of Surface Waves (SASW) method, but can also be used to account for the smearing/superposition of modes that can exist in MASW dispersion data at longer wavelengths due to a lack of spatial resolution. The shear wave velocity profile obtained from the forward model was limited to the maximum experimental wavelength divided by two (i.e., $\lambda max/2$).

In Figure 5.5, the experimental dispersion curve and theoretical fit are shown. Experimental wavelengths were resolved from 15 m to 134 m (22 Hz to 7.5 Hz) and the dispersion curve appears to be normally dispersive with positive increases in Rayleigh wave velocity with wavelength. The shear wave velocity profile associated with the theoretical dispersion curve is shown in Figure 5.6. The forward modeling parameters used to obtain the

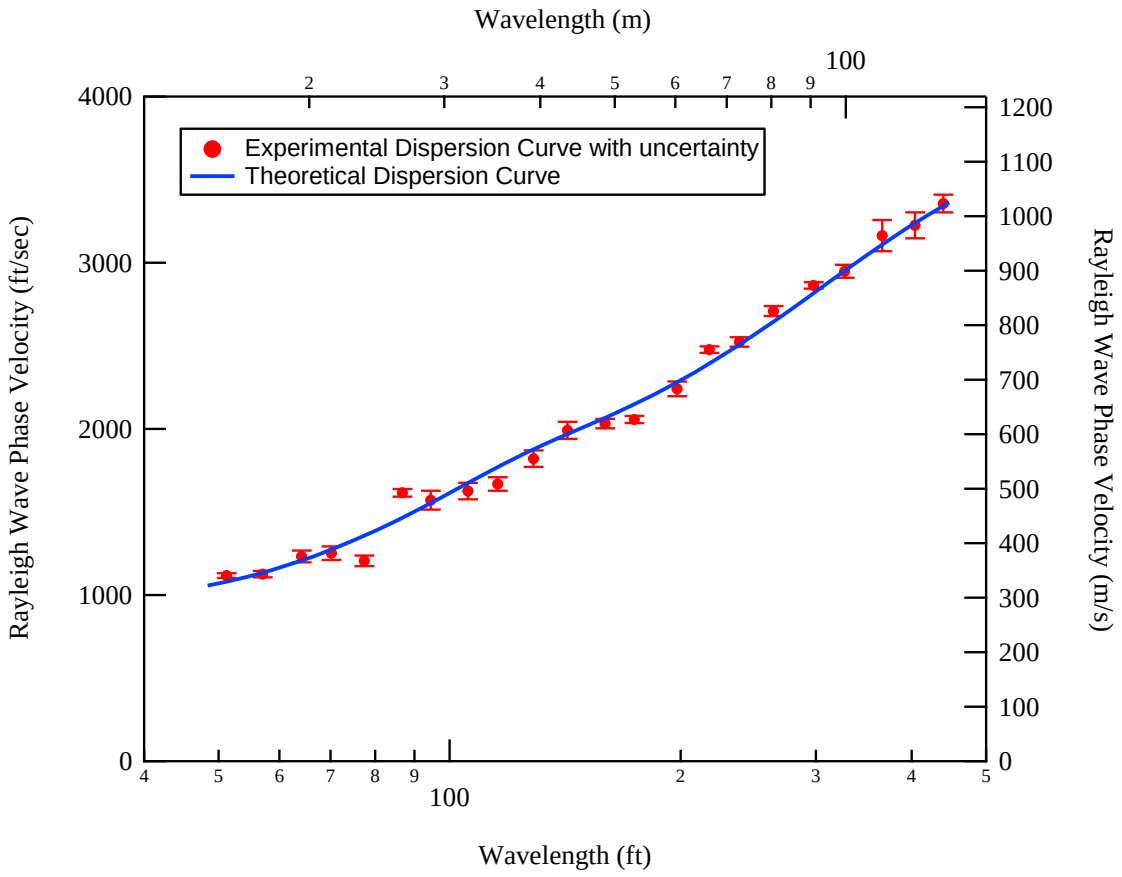

Figure 5.5: MASW experimental dispersion curve with uncertainty and associated theoretical dispersion curve.

shear wave velocity profile are shown in Table 5.1. The shear wave velocity profile starts off at the surface with a velocity of 300 m/s, which represents stiff soil, but quickly transitions to 790 m/s, which represents soft rock, at a depth of 7.6 meters. Firm rock is encountered at 27.4 meters below the surface with a velocity of 1400 m/s. This layer extends to the maximum depth of the profile of 67 meters. Overall, the shear wave velocity profile matches well with the shallow bedrock geology presented in Section 3.2 and represents a much more localized velocity structure than those presented early.

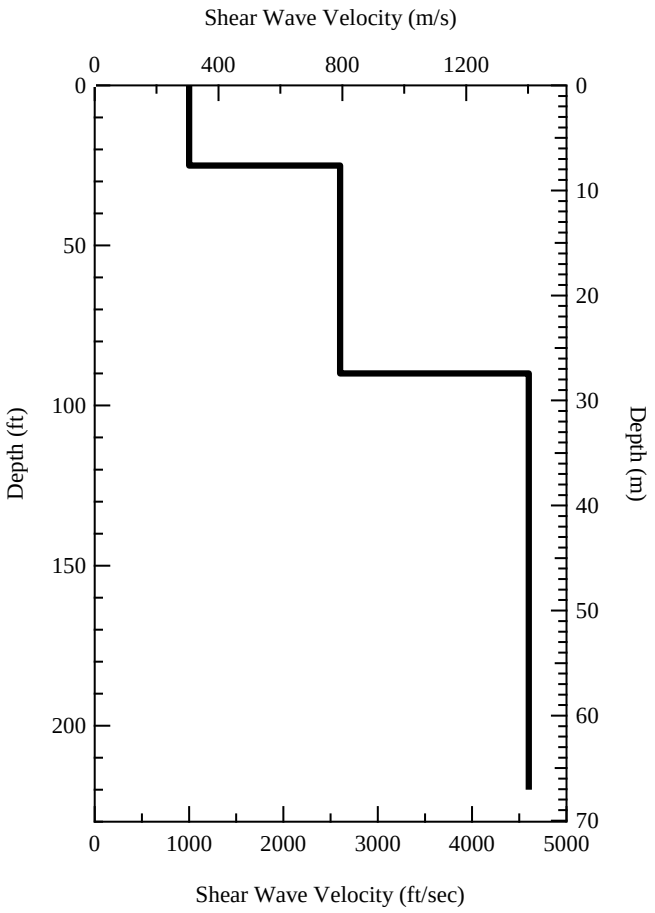

Figure 5.6: MASW shear wave velocity profile corresponding to the theoretical dispersion curve.

Table 5.1: Final forward modeling soil profile corresponding to the theoretical dispersion curve.

Layer No.	Thickness (m)	Depth to bottom (m)	P-wave velocity (m/s)	Shear wave velocity (m/s)	Poisson's Ratio	Unit Weight (kN/m^3)	Vs 30 Site Class (m/s)
1	7.6	7.6	570	300	0.30	19	584
2	19.8	27.4	1480	790	0.30	22	
3	39.6	67.0	2570	1400	0.30	24	C

Note: maximum depth of profile is approximately equal to maximum experimental wavelength/two.

5.5 SUMMARY

This chapter detailed the equipment, data collection, data processing, and results of surface wave testing to determine the small strain shear stiffness of the study area in Central-Eastern Utah. A linear array of 16, 1 Hz geophones was used to conduct MASW testing on a mountain trail near the topographic array. The data was analyzed using the frequency domain beamformer method and fit using a forward model. The analysis results in a shear wave velocity profile that indicates a thin layer of soil overlies weathered bedrock which is underlined at a depth of approximately 28 meters with solid unweathered bedrock.

Chapter 6: Theoretical Estimates of Topographic Frequencies

6.1 Introduction

Topographic amplification has been shown to be a fairly band limited phenomenon, meaning only select frequencies are amplified (i.e., those that have wavelengths comparable (approximately equal) to the characteristic width or height of a feature). To help insure that amplification patterns recorded during Phase I and II of the topographic study are properly identified as topographic amplification, soil site effects amplification, or other amplitude altering phenomenon (e.g., path effects), calculations were made to estimate the frequency range of topographic and soil site effects. A 1-D site response/transfer function was first computed for the soil profile developed in Chapter 5. Second, the topographic frequencies of each of the cross sections in both Phase I and II were estimated using methods developed by Ashford and Sitar (1997) and Paolucci (2002). These estimates are detailed in the current chapter and expected frequency ranges for each phenomenon are given.

6.2 1-D Site Response

A 1D, linear strain range site response analysis was conducted for the test site using the shear wave velocity profile presented in Chapter 5. The velocity profile obtained through surface wave testing is believed to be the most representative stiffness profile of the study area. In addition, the shear wave velocity profile was taken in an area that is believed to have the thickest soil deposit relative to the soil profiles directly under each of the seismic stations in Phase I and most of the stations in Phase II (i.e., the thicker the given soil layer the lower the amplified frequency). The 1-D site response was conducted to insure that the amplification caused by the soil layering (i.e., soft soil effects) is not confused with the amplification caused by topographic effects.

The software package DEEPSOIL was used to conduct the site response analysis. The most appropriate analysis given ground motions from underground mining is a linear, small strain analysis or transfer function. The linear transfer function represents the ratios of the Fourier amplitude spectra between the input motion at the half space and the output motion at the surface. This ratio identifies frequencies that will be amplified due to the soil column layering and stiffness. This analysis uses the in-situ maximum value of shear modulus (Gmax) and small strain damping values for each layer and determines the frequencies at which the soil column resonates. The shear wave velocity profile presented in Chapter 5 was input into DEEPSOIL as a two layer system with a half space velocity of 1400 m/s. Damping values to 1.2% were used for the soil layers, while damping of 0.2% was used for the half space rock. A ground motion was introduced at the top of the half space and propagated up through the soil column using a linear analysis (i.e., linear, small strain). The ground motion used during the analysis does not affect the transfer function output because only the linear strain range is considered. In addition, the damping ratios only affect the amplitude of the transfer function and not which frequencies are amplified.

The transfer function associated with the shear wave velocity profile presented in Chapter 5 is shown in Figure 6.1. This soil profile produces peak amplification at approximately 7 Hz and 12.5 Hz. Higher harmonics occur at 27 Hz and 32.5 Hz with slightly less amplitude due to soil damping. Since engineers are typically only interested in frequencies less than 10-20 Hz, we will only consider the fundamental mode of soil vibration. To select a frequency band where we can expect soft soil amplification, frequencies with transfer function amplitudes greater than 2.0 were presumed to produce the most noticeable amplification. Therefore, frequencies from approximately 5-15 Hz were determined to be affected by soft soil amplification. Due to the location of the shear

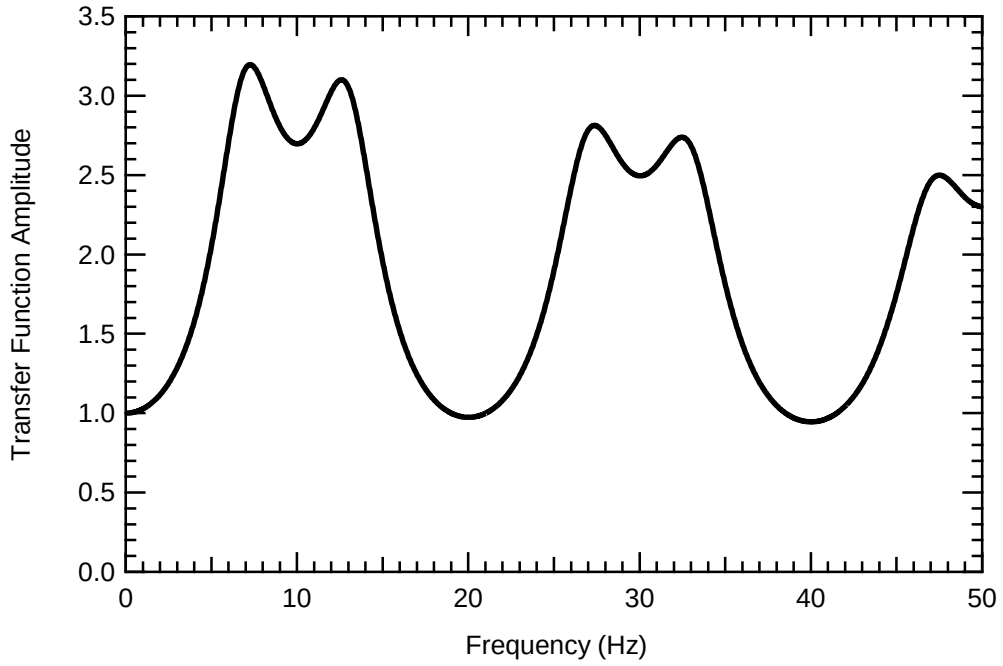

Figure 6.1: Transfer function associated with the Vs profile presented in Chapter 5.

wave velocity profile (i.e., flat ground off of the predominant topographic features), the soil/weather bedrock thickness is believed to be thicker than the same deposits on the topographic features, which means the resonant frequencies of the topographic feature will be higher than that of the measured Vs profile. Therefore, any frequencies less than 5 Hz that are amplified on topographic features are believed to be caused by topographic amplification and not soil site effects amplification.

6.3 ESTIMATES OF TOPOGRAPHIC AMPLIFICATION FREQUENCIES

To estimate the frequency at which topographic amplification is expected, two different relationships were used: (1) Ashford and Sitar (1997) and (2) Paolucci (2002). Both methods are explained in depth in Chapter 2 and are summarized below. The first method, developed by Ashford and Sitar (1997) is for a cliff type slope arrangement. The authors tested slope angles from 30-90 degree with wave incident angles from +30 to -30

degrees. The model uses the height of the feature to estimate the fundamental mode of vibration. To estimate the fundamental topographic frequency of a feature, the average shear wave velocity of the feature is divided by five times the height of the feature.

The second method, developed by Paolucci (2002), uses the width of an asymmetrical wedge feature to estimate the topographic frequency of the wedge. The method was derived using a closed form solution for the fundamental mode of vibration of a homogenous asymmetrical wedge using Rayleigh's method. The complex geometric equations to estimate the fundamental frequency can be reduced to approximately 0.7 or 1.0 times the average shear wave velocity divided by the representative width of the feature for SH and SV waves, respectively.

These calculations seem rather simple; however the difficult part is not making the calculations, but determining the average shear wave velocity and representative height or width of a feature. Real 3D topographic features do not make clean 2D cross sections that can be easily divided into triangular shapes or slopes such as those used in the equations above. Typically, there is significant ambiguity in determining a representative height and width. In addition, shear wave velocity measurements are often very difficult to obtain at the peak of a feature and Vs profiles obtained off slope cannot always be presumed to be equivalent to those taken at the crest.

To estimate an approximate average shear wave velocity (Vs) of each feature, the shear wave velocity profile presented in Chapter 5 is used. The shear wave velocity profile, however, only extends to a depth of 67 m and the height of many of the cross sections exceeds this depth. To combat this short coming, two separate shear wave velocity profiles (shown in Table 6.1) were used to compute the average Vs for each cross section. These profiles represent an upper and lower bound of velocities in the deeper material and therefore will provide an upper and lower bound estimate of

Table 6.1: Shear wave velocity profiles used to estimate the fundamental topographic frequencies.

Layer	Thickness (m)	PF1 (m/s)	PF2 (m/s)
1	7.6	300	300
2	19.8	790	790
3	39.6	1400	1400
4	NA	1400	2040

topographic frequencies. The first profile (PF1) uses the surface wave Vs profile presented in Chapter 5 and simply extends the final 1400 m/s layer to the depth of the feature resulting in a lower bound Vs profile. The second profile (PF2), attaches the velocity model used to locate the hypocenters to the surface wave Vs profile. This results in a profile with a final layer velocity of 2040 m/s starting at a depth of 67 m. These two profiles should encompass the range of possible Vs values on the mountain. To calculate the average Vs over the entire height of the feature, the two way travel time method is used. This method, often used in Vs30 site classification calculations, sums the shear wave velocity of each layer divided by its thickness and divides that summation by the total thickness of the soil profile, which results in the average Vs over the height of the feature.

6.3.1 Phase I (2010)

In Phase I (2010), a small 3D peak (see Figure 6.2) was instrumented with a dense array in the East-West direction and a limited array in the North-South direction (see more information on the array and setup for Phase I in Chapter 3). To break this feature up into discrete 2D cross sections for analysis, cross sections were chosen in both the North-South and East-West directions, as shown in Figure 6.2. The North-South cross section A-A' is shown in Figure 6.3. The cross section is nearly symmetric about the

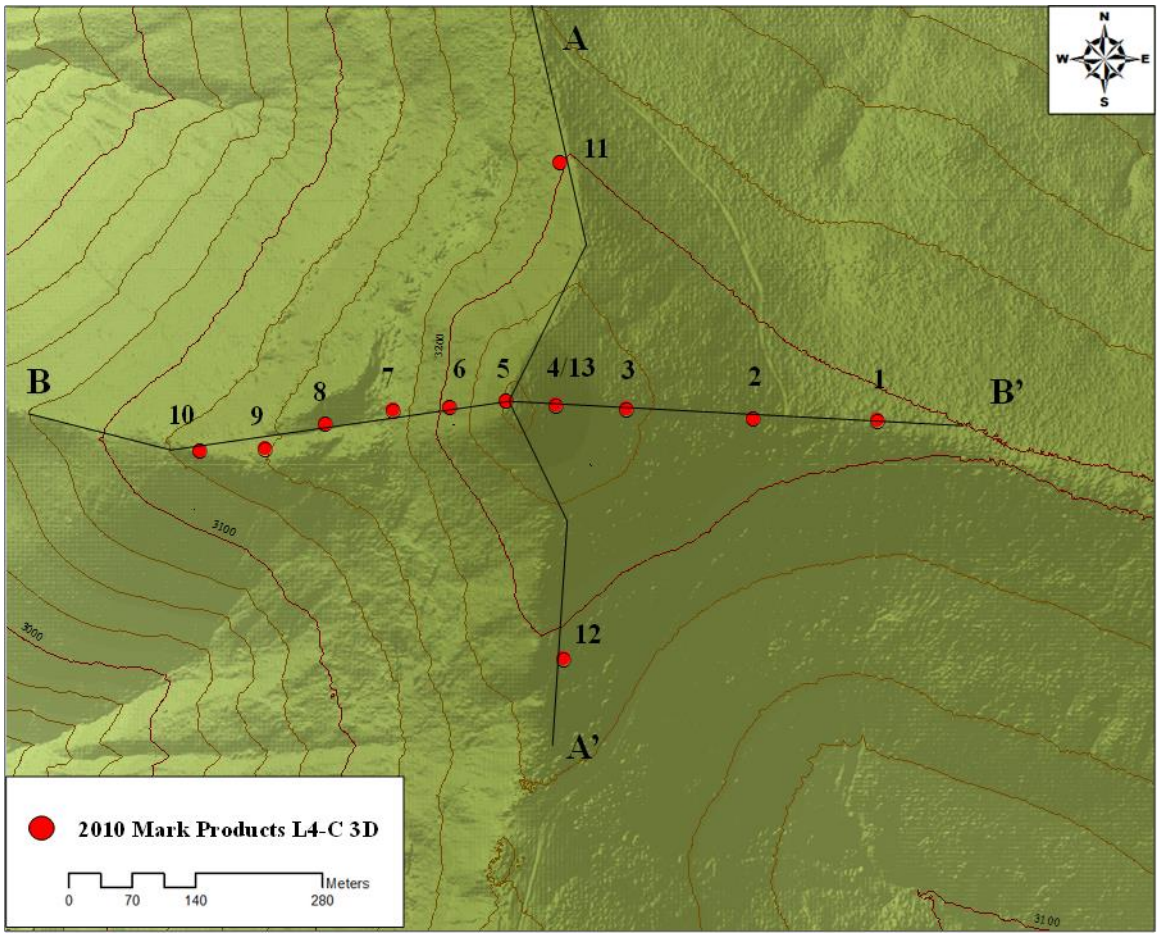

Figure 6.2: Topographic array and site map for Phase I (2010) showing 2-D cross sections A-A' and B-B'.

peak and forms a fairly simple cross section with a width of approximately 800 m and a height of 78 m. The characteristics of cross section A-A', along with the average shear wave velocities (Vs1 and Vs2) for the PF1 and PF2 profiles, are provided in Table 6.2. The average shear wave velocity over the 78-m height of the feature (Vs78) for both the PF1 and PF2 Vs profiles is 907 m/s and 934 m/s, respectively. The estimated fundamental topographic frequencies for cross section A-A' are shown in Table 6.3. The fundamental frequencies were calculated using both Ashford and Sitar (1997) and Paolucci (2002).

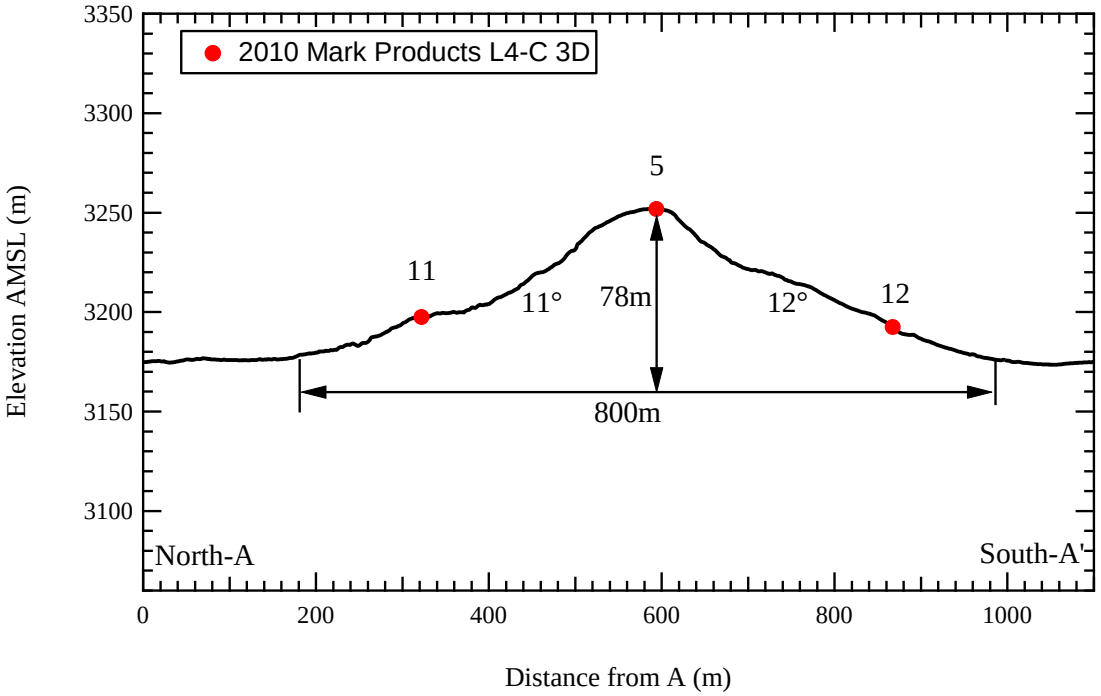

Figure 6.3: North-South topographic cross section A-A' for Phase I.

Table 6.2: Characteristics of North-South cross section A-A' for Phase I.

Feature	H (m)	W (m)	Vs1 (m/s)	Vs2 (m/s)
A1	78	800	907	934

Table 6.3: Fundamental topographic frequency estimates for North-South cross section A-A' for Phase I.

	PF1 Estimates			PF2 Estimates		
Feature	f0-1 (Hz)	f0-2a (Hz)	f0-2b (Hz)	f0-1 (Hz)	f0-2a (Hz)	f0-2b (Hz)
A1	2.33	0.79	1.13	2.39	0.82	1.17

f0-1 Ashford and Sitar (1997)
f0-2a Paolucci (2002) SH
f0-2b Paolucci (2002) SV

The frequencies range from 2.33 Hz to 0.79 Hz for the Vs1 average velocity and 2.39 Hz to 0.82 Hz for the Vs2 average velocity.

The 2D West-East cross section B-B' taken from Figure 6.2 is shown in Figure 6.4. This cross section presents a more complex geometry that is harder to subdivide into a triangular geometric shape. To discretize the feature, the height from the previous cross section (A-A') was first used to establish the height under the peak of the feature in the West-East direction. Then, the shallow slope on the west side of the feature was extended eastward to intersect the eastern slope, while maintaining a depth below the center of the peak of 78 m. This results in a cross section with a total width of 470 m and height of 78 m. In Table 6.4, the characteristics of cross section B-B' are provided. The average shear wave velocities (Vs1 and Vs2) for the PF1 and PF2 profiles are 907 m/s and 934 m/s,

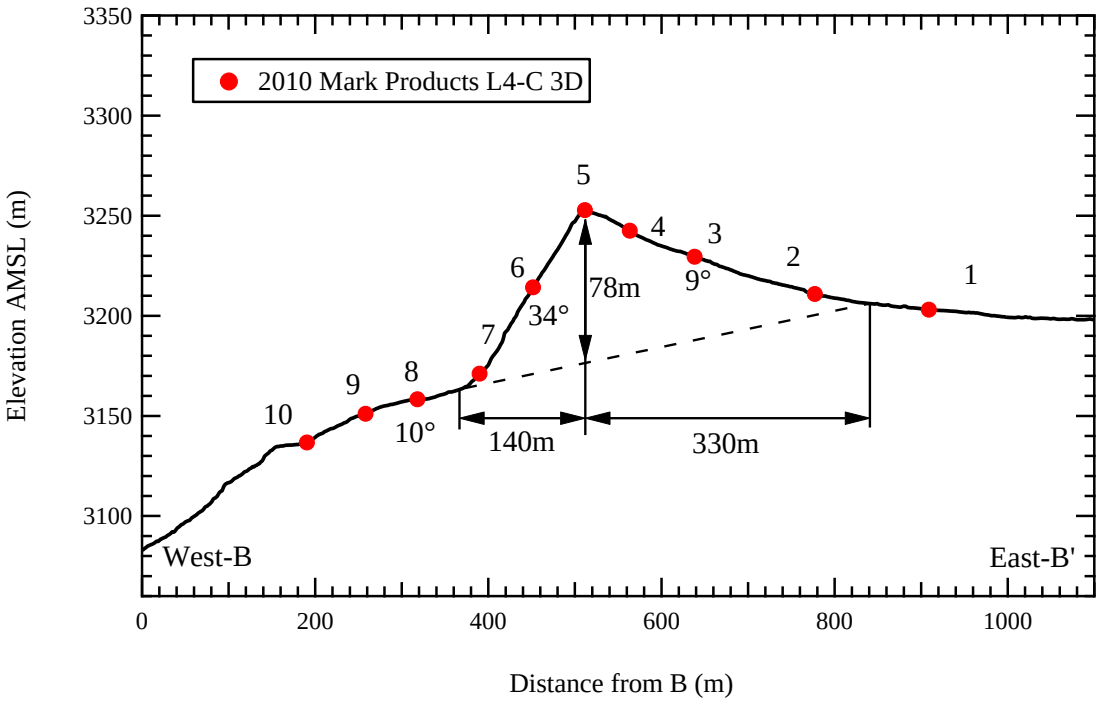

Figure 6.4: West-East topographic cross section B-B' for Phase I.

respectively. These result in fundamental topographic frequencies of between 2.33 Hz to 1.35 Hz for Vs1 average velocity and 2.39 Hz and 1.39 Hz for Vs2 average velocity (see Table 6.5).

Therefore, for Phase I of the topographic experiment, one should expect topographic amplification for frequencies between approximately 2.39 Hz and 0.79 Hz. In addition, one should expect soft soil amplification at frequencies between 5 Hz and 15 Hz. This provides a good frequency separation between those expected to be amplified by topography and those expected to be amplified by soft soil effects.

Table 6.4: Characteristics of West-East cross section B-B' for Phase I.

Feature	H (m)	W (m)	Vs1 (m/s)	Vs2 (m/s)
B1	78	470	907	934

Table 6.5: Fundamental topographic frequency estimates for West-East cross section B-B' for Phase I.

	PF1 Estimates			PF2 Estimates		
Feature	f0-1 (Hz)	f0-2a (Hz)	f0-2b (Hz)	f0-1 (Hz)	f0-2a (Hz)	f0-2b (Hz)
B1	2.33	1.35	1.93	2.39	1.39	1.99

f0-1 Ashford and Sitar (1997)
f0-2a Paolucci (2002) SH
f0-2b Paolucci (2002) SV

6.3.2 Phase II (2011)

In Phase II (2011), the topographic array was expanded significantly to include much larger features and to instrument multiple cross sections throughout East Mountain ridge (see more information on the array and setup for Phase II in Chapter 4). A site overview of the array deployed in Phase II (2011) along with discrete 2-D cross sections is shown in Figure 6.5. The array is broken up into three primary 2-D cross sections A-

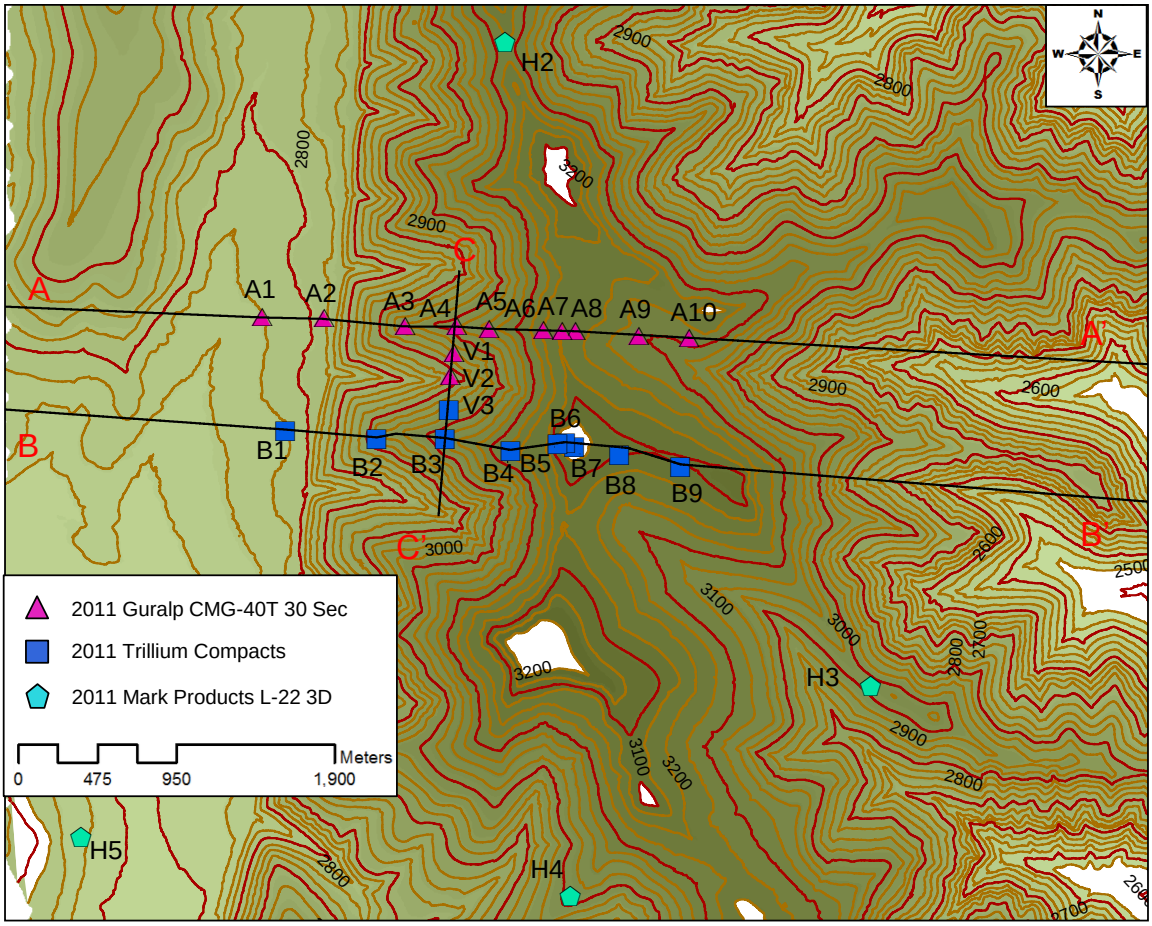

Figure 6.5: Phase II (2011) topographic array with 2-D cross sections (A-A', B-B', and C-C') shown.

A', B-B', and C-C'. West-East cross section A-A' from Figure 6.5 is shown in Figure 6.6. The cross section has a nearly uniform triangular shape, which was broken up into three separate triangles along natural breaks in the slope. The smallest feature (A1) is approximately 890 m wide with a height of 68 m, while feature (A2) is 2224 m wide with a height of 202 m. The final feature (A3) has a width of 3705 m and a height of 480 m. These geometries, along with the average shear wave velocities (Vs1 and Vs2) calculated using profiles PF1 and PF2 for each feature are provided in Table 6.6. The average Vs values vary from 862 m/s for the smallest feature to 1711 m/s for the largest feature. The

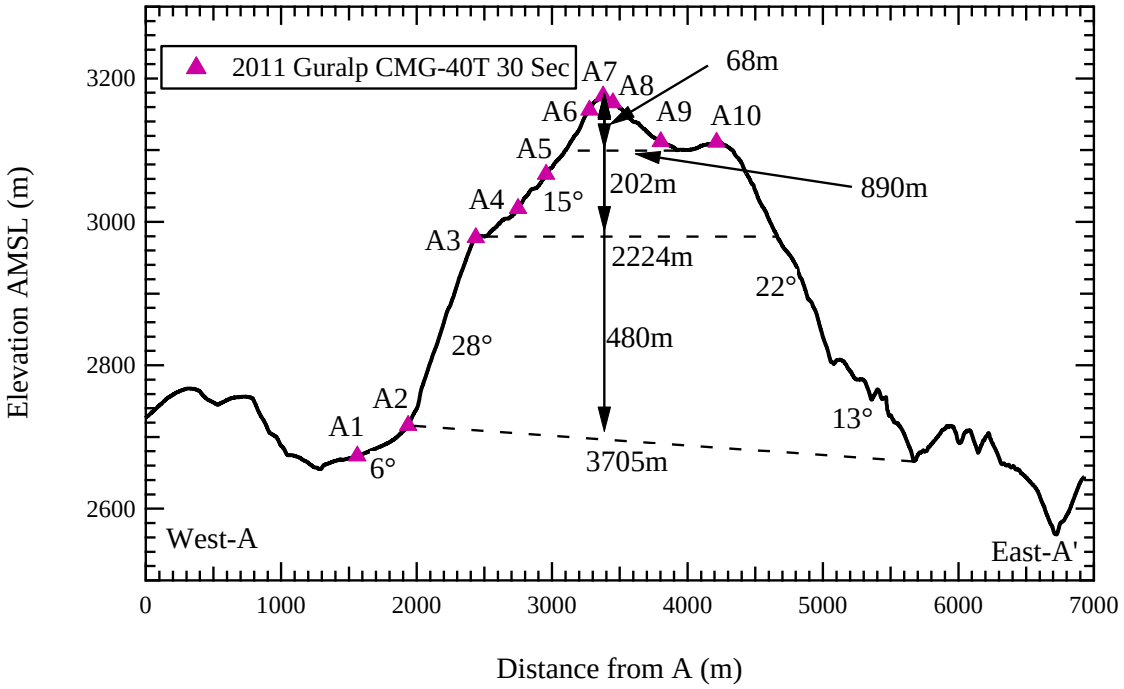

Figure 6.6: West-East topographic cross section A-A' for Phase II.

Table 6.6: Characteristics of West-East cross section A-A' for Phase II.

Feature	H (m)	W (m)	Vs1 (m/s)	Vs2 (m/s)
A1	68	890	862	865
A2	202	2224	1158	1400
A3	480	3705	1288	1711

fundamental topographic frequencies estimated for the three features in cross section A-A' are provided in Table 6.7. The topographic frequencies are fairly broadband for the overall cross section, varying from 2.54 Hz to 0.24 Hz, but are still below those expected to be amplified by soft soil effects (i.e., 5-15 Hz).

West-East cross section B-B' is shown in Figure 6.7. Cross section B-B' is over the same feature instrumented in Phase I, however the cross section is extended over a much larger area to encompass the entire feature and all stations used in Phase II. The B-B' cross section is similar in shape to cross section A-A'; however cross section B-B' is

Table 6.7: Fundamental topographic frequency estimates for West-East cross section A-A' for Phase II.

	PF1 Estimates			PF2 Estimates		
Feature	**f0-1 (Hz)**	**f0-2a (Hz)**	**f0-2b (Hz)**	**f0-1 (Hz)**	**f0-2a (Hz)**	**f0-2b (Hz)**
A1	2.54	0.68	0.97	2.54	0.68	0.97
A2	1.15	0.36	0.52	1.39	0.44	0.63
A3	0.54	0.24	0.35	0.71	0.32	0.46

f0-1 Ashford and Sitar (1997)
f0-2a Paolucci (2002) SH
f0-2b Paolucci (2002) SV

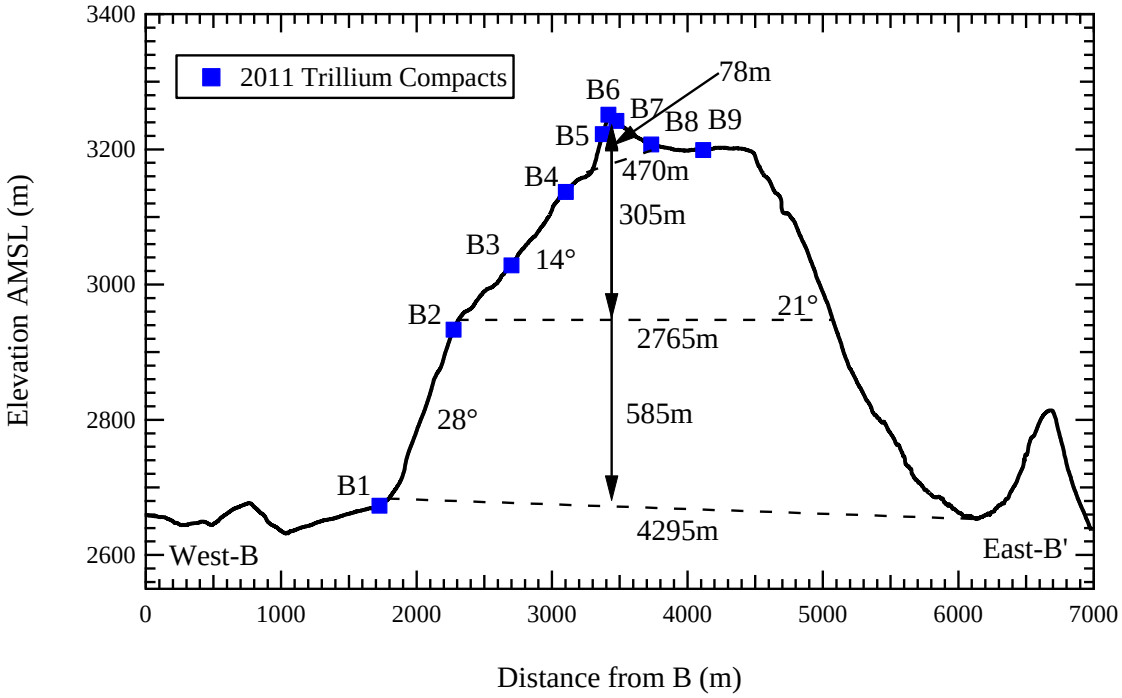

Figure 6.7: West-East topographic cross section B-B' for Phase II.

slightly larger in both overall width and height. As with cross section A-A', B-B' is spilt into three main features. The smallest feature (B1) is the exact cross section used during Phase I and is again approximately 470 m wide with a height of 78 m, while feature (B2) is 2765 m wide with a height of 305 m. The final feature (B3) has a width of 4295 m and

a height of 585 m. These properties, along with the average shear wave velocities (Vs1 and Vs2) calculated using profiles PF1 and PF1 for each feature are provided in Table 6.8. The average Vs values vary from 907 m/s for the smallest feature to 1762 m/s for the largest feature. The fundamental topographic frequencies estimated for the three features in cross section B-B' are provided in Table 6.9. The expected topographic frequencies are fairly broadband and compare well with those for cross section A-A', only varying from 2.39 Hz to 0.21 Hz.

North-South cross section C-C' is shown in Figure 6.8. Cross section C-C' is perpendicular to cross sections A-A' and B-B', but is located between each profile on the West-side of the main mountain ridge. This North-South cross section forms double triangular peaks with the North feature having a width of 660 m and height of 130 m. The

Table 6.8: Characteristics of West-East cross section B-B' for Phase II.

Feature	H (m)	W (m)	Vs1 (m/s)	Vs2 (m/s)
B1	78	470	907	934
B2	305	2765	1230	1566
B3	585	4295	1307	1762

Table 6.9: Fundamental topographic frequency estimates for West-East cross section B-B' for Phase II.

	PF1 Estimates			PF2 Estimates		
Feature	f0-1 (Hz)	f0-2a (Hz)	f0-2b (Hz)	f0-1 (Hz)	f0-2a (Hz)	f0-2b (Hz)
B1	2.33	1.35	1.93	2.39	1.39	1.99
B2	0.81	0.31	0.44	1.03	0.40	0.57
B3	0.45	0.21	0.30	0.60	0.29	0.41

f0-1 Ashford and Sitar (1997)
f0-2a Paolucci (2002) SH
f0-2b Paolucci (2002) SV

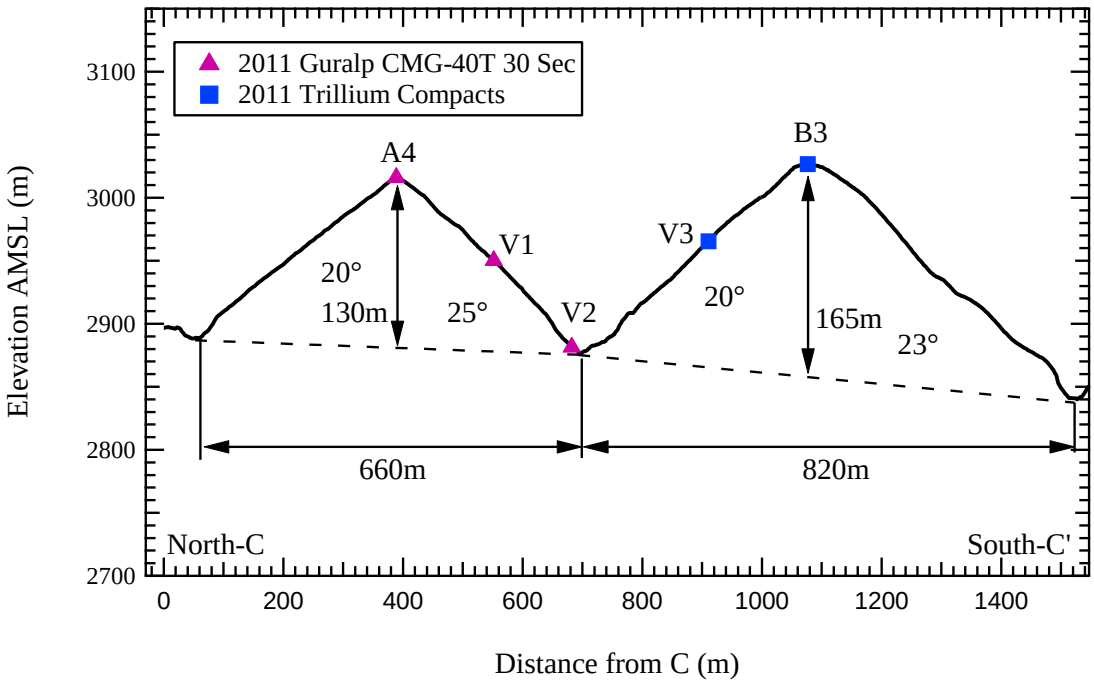

Figure 6.8: North-South topographic cross section C-C' for Phase II.

South feature has a slightly larger width of 820 m and a corresponding height of 165 m. These features both have uniform cross sections that do not need to be broken up into smaller features, as was done for cross sections A-A' and B-B'. The geometries for cross section C-C' are given in Table 6.10 along with the average shear wave velocities (Vs1 and Vs2) calculated using profiles PF1 and PF2 for each feature. The average Vs values vary from 1056 m/s for Vs1 and feature 1 (North) to 1308 m/s for feature 2 (South). The fundamental topographic frequencies estimated for both features in cross section C-C' are shown in Table 6.11. The topographic frequencies are fairly narrow banded for cross section C-C' when compared to previous estimates for cross section A-A' and B-B', only vary between 0.95 Hz and 1.83 Hz.

Table 6.10: Characteristics of North-South cross section C-C' for Phase II.

Feature	H (m)	W (m)	Vs1 (m/s)	Vs2 (m/s)
C1	130	660	1056	1193
C2	165	820	1115	1308

Table 6.11: Fundamental topographic frequency estimates for North-South cross section C-C' for Phase II.

	PF1 Estimates			PF2 Estimates		
Feature	f0-1 (Hz)	f0-2a (Hz)	f0-2b (Hz)	f0-1 (Hz)	f0-2a (Hz)	f0-2b (Hz)
C1	1.63	1.12	1.60	1.83	1.26	1.81
C2	1.35	0.95	1.36	1.59	1.12	1.59

f0-1 Ashford and Sitar (1997)
f0-2a Paolucci (2002) SH
f0-2b Paolucci (2002) SV

6.4 SUMMARY

This chapter detailed frequency range estimates for of both soil site effects and topographic effects for the East Mountain area and the geometric features instrumented during Phase I and II of the topographic effects study. The soil site effects were estimated from a 1D site response/transfer function analysis using the Vs profile presented in Chapter 5. This analysis resulted in estimated frequency amplification in the range of 5-15 Hz. Topographic amplification frequencies were then estimated for each of the cross sections in Phase I and II. The estimated frequencies for Phase I were limited to 0.87 Hz to 2.33 Hz due to the smaller feature instrumented, which is well below those expected for soft soil effects (i.e., 5-15 Hz). For Phase II, estimates were made for all three of the main cross sections instrumented, resulting in topographic frequency ranges for cross section A-A' of 0.24 Hz to 2.54, cross section B-B' of 0.21 Hz to 2.39 Hz and cross section C-C' of 0.95 to 1.83 Hz. Like Phase I, these estimated topographic frequencies are less than those estimated for soil site effects. Therefore, it is presumed that

amplification patterns recorded in the lower topographic frequency range of approximately 0.2-2.5 Hz are likely caused by topographic effects and not soil site effects.

Chapter 7: Topographic Study Results: Phase I (2010)

7.1 INTRODUCTION

In Phase I (2010), an array of 12 stations (13 sensors) deployed over a 3D mountain peak recorded 52 seismic events ("earthquakes") produced by underground longwall coal mining. These seismic events were processed using a standard ground motion processing scheme and analyzed for topographic effects using three methods: Standard Spectral Ratio (SSR), Median Reference Method (MRM), and Horizontal to Vertical Spectral Ratio (HVSR). A directional analysis was also performed on the results of each method to assess the polarity of the amplification. To assess the usefulness and accuracy of each analysis method, along with determining the effect of topographic amplification on the mountain, a single M_L 1.2 seismic event (17801) was first analyzed using all three methods, resulting in spectral ratios and horizontal energy polarity plots for each station in the array for each method. The analysis was then extended to include all 52 events. The spectral ratios for each event were compared for Station 5 (the crest station) using each of the three methods and a log-normal median and +/- 1 sigma are calculated for the entire event catalog. Finally, the median response of all 12 stations is compared for each of the three methods and the results are compared with Station 5.

7.2 RECORDED EVENTS

In Phase I (2010), seismic signals were recorded continuously from June 16, 2010 until June 23, 2010. During that time many small, medium, large events were recorded by the instrumentation. However, only 52 of the largest events were identified as meeting all the criteria established in Chapter 3. These 52 events are included in the recorded events catalog. The recorded seismic events for Phase I are identified in Table 7.1 in UTC time, and in Table 7.2 in local time (Mountain daylight savings time). As mentioned in Chapter

Table 7.1: Seismic events identified during Phase I (2010) in UTC.

Event #	Filename	UTC Date	UTC Time	Event #	Filename	UTC Date	UTC Time
1	17172	6/17/2010	22:31	27	192686	6/20/2010	20:52
2	17278	6/17/2010	23:28	28	201449	6/21/2010	9:52
3	17585	6/18/2010	2:12	29	21810	6/22/2010	4:12
4	17606	6/18/2010	2:23	30	21920	6/22/2010	5:10
5	17801	6/18/2010	4:07	31	21991	6/22/2010	5:48
6	171045	6/18/2010	6:17	32	211180	6/22/2010	7:29
7	171295	6/18/2010	8:30	33	211405	6/22/2010	9:29
8	171516	6/18/2010	10:28	34	211522	6/22/2010	10:31
9	171638	6/18/2010	11:33	35	212218	6/22/2010	16:42
10	171953	6/18/2010	14:21	36	212295	6/22/2010	17:24
11	172468	6/18/2010	18:56	37	22140	6/22/2010	22:14
12	172497	6/18/2010	19:11	38	22215	6/22/2010	22:54
13	1857	6/18/2010	21:30	39	22245	6/22/2010	23:10
14	18294	6/18/2010	23:36	40	22753	6/23/2010	3:41
15	18363	6/19/2010	0:13	41	221057	6/23/2010	6:23
16	18515	6/19/2010	1:34	42	221318	6/23/2010	8:42
17	181418	6/19/2010	9:36	43	221691	6/23/2010	12:01
18	181952	6/19/2010	14:21	44	222028	6/23/2010	15:01
19	181992	6/19/2010	14:42	45	222533	6/23/2010	19:30
20	182548	6/19/2010	19:38	46	23140	6/23/2010	22:30
21	182602	6/19/2010	20:07	47	23346	6/24/2010	0:20
22	19519	6/20/2010	1:36	48	231190	6/24/2010	7:50
23	191252	6/20/2010	8:07	49	231436	6/24/2010	10:01
24	191441	6/20/2010	9:48	50	231620	6/24/2010	11:40
25	191677	6/20/2010	11:54	51	231906	6/24/2010	14:12
26	192563	6/20/2010	19:46	52	231955	6/24/2010	14:38

3, the times listed in Tables 7.1 and 7.2 are approximate and believed to accurate to within 10 minutes of absolute time, but are certainly not GPS accurate. Of the 52 events classified in Phase I, only two events were identified by the University of Utah Seismograph Stations (UUSS). These events are 17801 and 22140, which have estimated magnitudes of M_L 1.2 and M_L 1.6, respectively. All other events are believed to have local magnitudes of less than 1.0.

Table 7.2: Seismic events identified during Phase I (2010) in local time (Mountain daylight savings time).

Event #	Filename	Local Date	Local Time	Event #	Filename	Local Date	Local Time
1	17172	6/17/2010	16:31	27	192686	6/19/2010	14:52
2	17278	6/17/2010	17:28	28	201449	6/20/2010	3:52
3	17585	6/17/2010	20:12	29	21810	6/21/2010	22:12
4	17606	6/17/2010	20:23	30	21920	6/21/2010	23:10
5	17801	6/17/2010	22:07	31	21991	6/21/2010	23:48
6	171045	6/17/2010	0:17	32	211180	6/21/2010	1:29
7	171295	6/17/2010	2:30	33	211405	6/21/2010	3:29
8	171516	6/17/2010	4:28	34	211522	6/21/2010	4:31
9	171638	6/17/2010	5:33	35	212218	6/21/2010	10:42
10	171953	6/17/2010	8:21	36	212295	6/21/2010	11:24
11	172468	6/17/2010	12:56	37	22140	6/22/2010	16:14
12	172497	6/17/2010	13:11	38	22215	6/22/2010	16:54
13	1857	6/18/2010	15:30	39	22245	6/22/2010	17:10
14	18294	6/18/2010	17:36	40	22753	6/22/2010	21:41
15	18363	6/18/2010	18:13	41	221057	6/22/2010	0:23
16	18515	6/18/2010	19:34	42	221318	6/22/2010	2:42
17	181418	6/18/2010	3:36	43	221691	6/22/2010	6:01
18	181952	6/18/2010	8:21	44	222028	6/22/2010	9:01
19	181992	6/18/2010	8:42	45	222533	6/22/2010	13:30
20	182548	6/18/2010	13:38	46	23140	6/23/2010	16:30
21	182602	6/18/2010	14:07	47	23346	6/23/2010	18:20
22	19519	6/19/2010	19:36	48	231190	6/23/2010	1:50
23	191252	6/19/2010	2:07	49	231436	6/23/2010	4:01
24	191441	6/19/2010	3:48	50	231620	6/23/2010	5:40
25	191677	6/19/2010	5:54	51	231906	6/23/2010	8:12
26	192563	6/19/2010	13:46	52	231955	6/23/2010	8:38

A rate of occurrence plot is shown in Figure 7.1, where the cumulative number of recorded events is plotted versus the time each event was recorded. The rate of occurrence taken as events per day has four clear sections. The first section, starting at the beginning of recording (6/17), has a rate of 10 events per day. However, the rate drops off to around 6 events per day on 6/19 and then drops off to only 1.5 events per day on 6/20. On 6/21, the rate returns to just below 10 events per day. The decrease in the

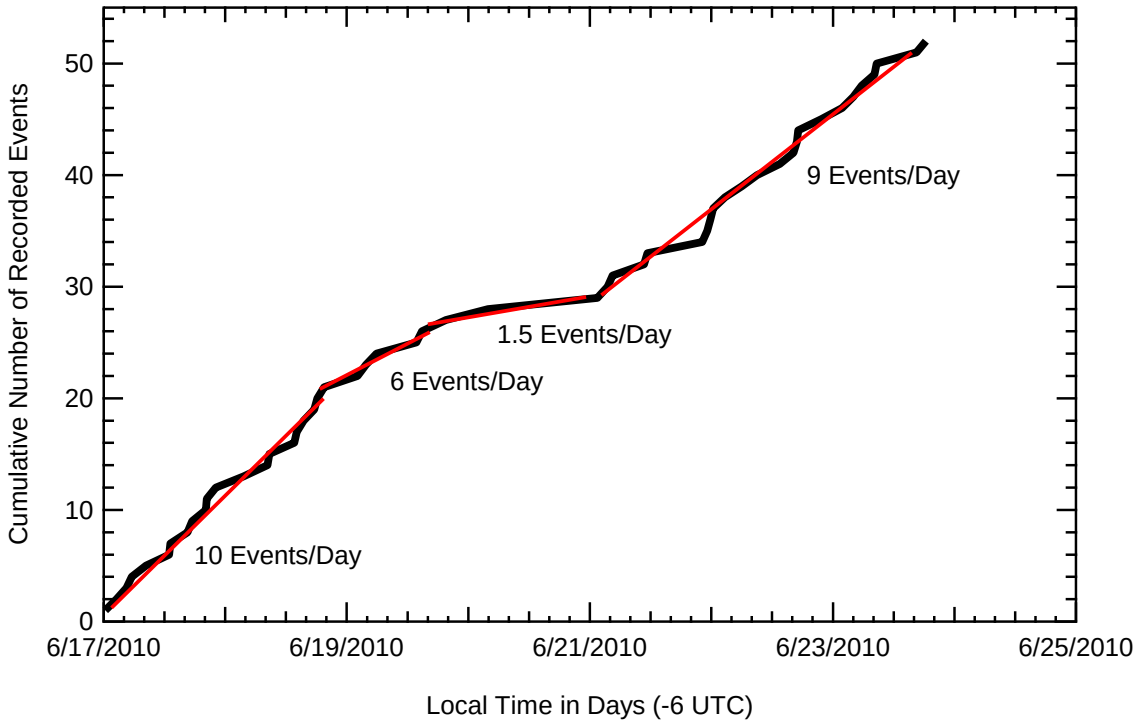

Figure 7.1: Rate of occurrence of seismic events during Phase I (2010).

occurrence rate from 6/19 to 6/21 is interesting, but can be explained by examining a calendar for 2010. In 2010, 6/19 was a Saturday and 6/20 was a Sunday, and both are non-working days for Deer Creek Mine. Therefore, the longwall was not operating during this time, quieting the development of seismic energy. Overall, the occurrence and frequency of mining seismicity is a very interesting topic, but is beyond the scope of this research. Therefore, the events will not be discussed further beyond their use in the estimation of topographic effects.

7.3 Single Event Results (17801)

Event 17801 was recorded on June 17, 2010 at 22:07 local time. The UUSS classified the event as a shallow M_L 1.2 "earthquake". The event was located by UUSS just north of the topographic array. However, attempts to locate the event using the

topographic array showed the event was located closer to the location of Deer Creek Mine's longwall. The event was processed using the standard ground motion processing scheme laid out in Chapter 3, which resulted in the time records for event 17801 for the vertical, North-South, and East-West components (refer to Figure 7.2). In the plots, Sensor 5 is at the peak of the feature, sensors 4-1 are on the East side of the peak, and sensors 6-10 are on the West side of the peak (see Figure 7.2). Sensor 11 is on the North side of the peak and Sensor 12 is on the South side of the peak. Sensor 13 is collocated with Sensor 4 at station location 4.

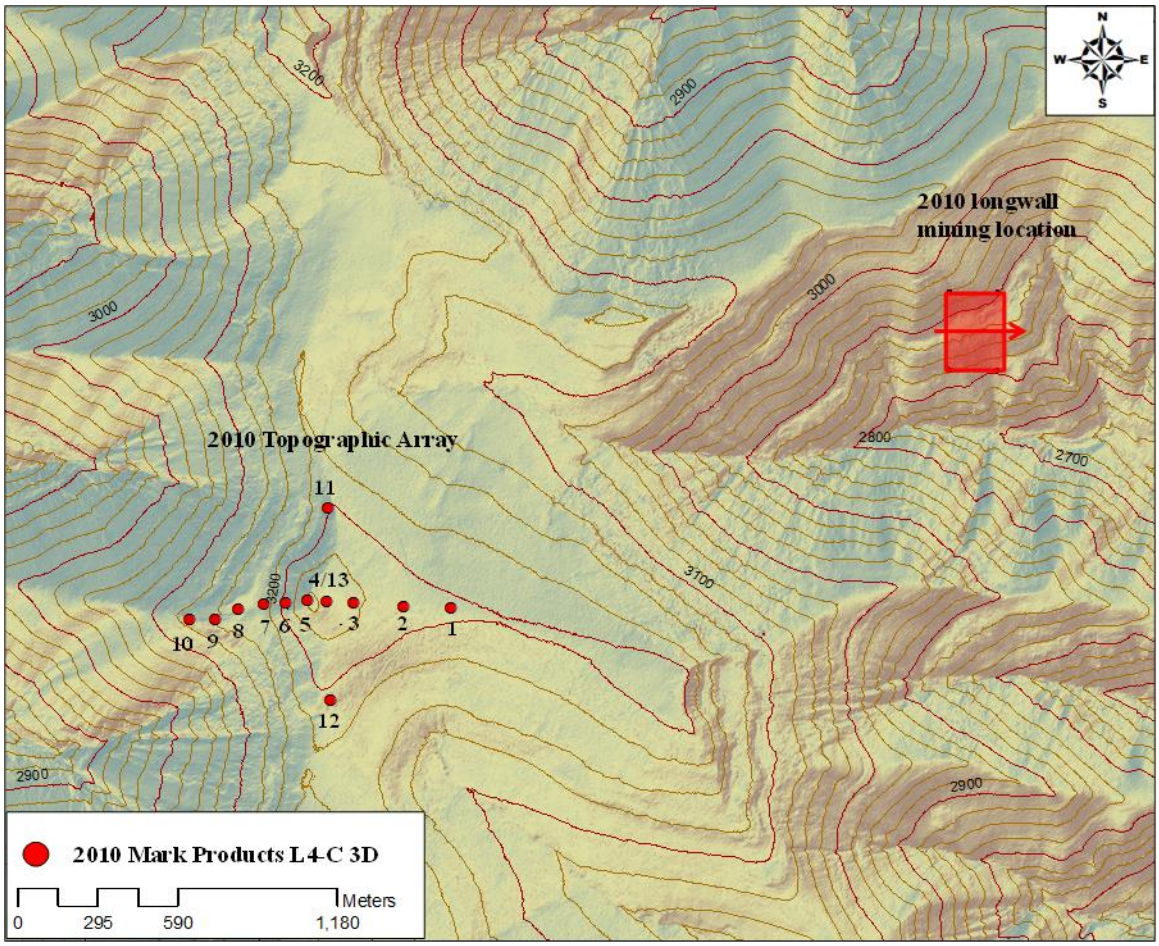

Figure 7.2: Phase I (2010) topographic array and longwall mining location.

Comparing the time domain amplitudes of each sensor in Figure 7.3, sensor 4, and sensors 7-9 have the largest amplitudes, while sensors 5 and 6 have the lowest amplitudes on each of the components. This does not correspond well with literature observations of topographic effects (presented in Chapter 2), where we would expect the highest amplitude at the peak of the feature (i.e., Sensor 5) (Bouchon 1973). The peak ground velocity of each sensor is then compared in Figure 7.4. For each of the components and similar to the time records there is no correlation between the topography and the PGV values of each sensor. Sensor 5 for all three components has the lowest PGV values, while sensors 4, 7, 8, and 9 have the highest PGV values. Even though there is no evidence of topographic effects in the time domain, topographic effects have been shown to be highly frequency dependent phenomenon. Therefore, the analysis was transferred to the frequency domain.

To determine the frequency response differences between Sensor 13 (a Trillium compact sensor) and Sensor 4 (a 1-Hz geophone) a plot of the Fourier amplitude spectra for both sensors and each component of motion are shown in Figure 7.5. Throughout the frequency range of the plots, the two spectra are virtually identical in amplitude, and only in a small band around 10 Hz can the spectral differences even be recognized. Therefore, sensors 12 and 13 (both trillium compacts) can be accurately compared to the 1 Hz geophones in the topographic array. In addition, and due to problems with Sensor 4 during the final days of the experiment, Sensor 13 will be used to represent the response of Station 4 in the topographic array.

The Fourier amplitude spectra for event 17801, for the vertical, North-South, and East-West components of motion for Sensors 1-13 are shown in Figure 7.6. For all three components, two separate high energy frequency bands can be seen. The first band occurs at 1 to 3 Hz and the second band occurs at 5-15 Hz. At frequencies less than

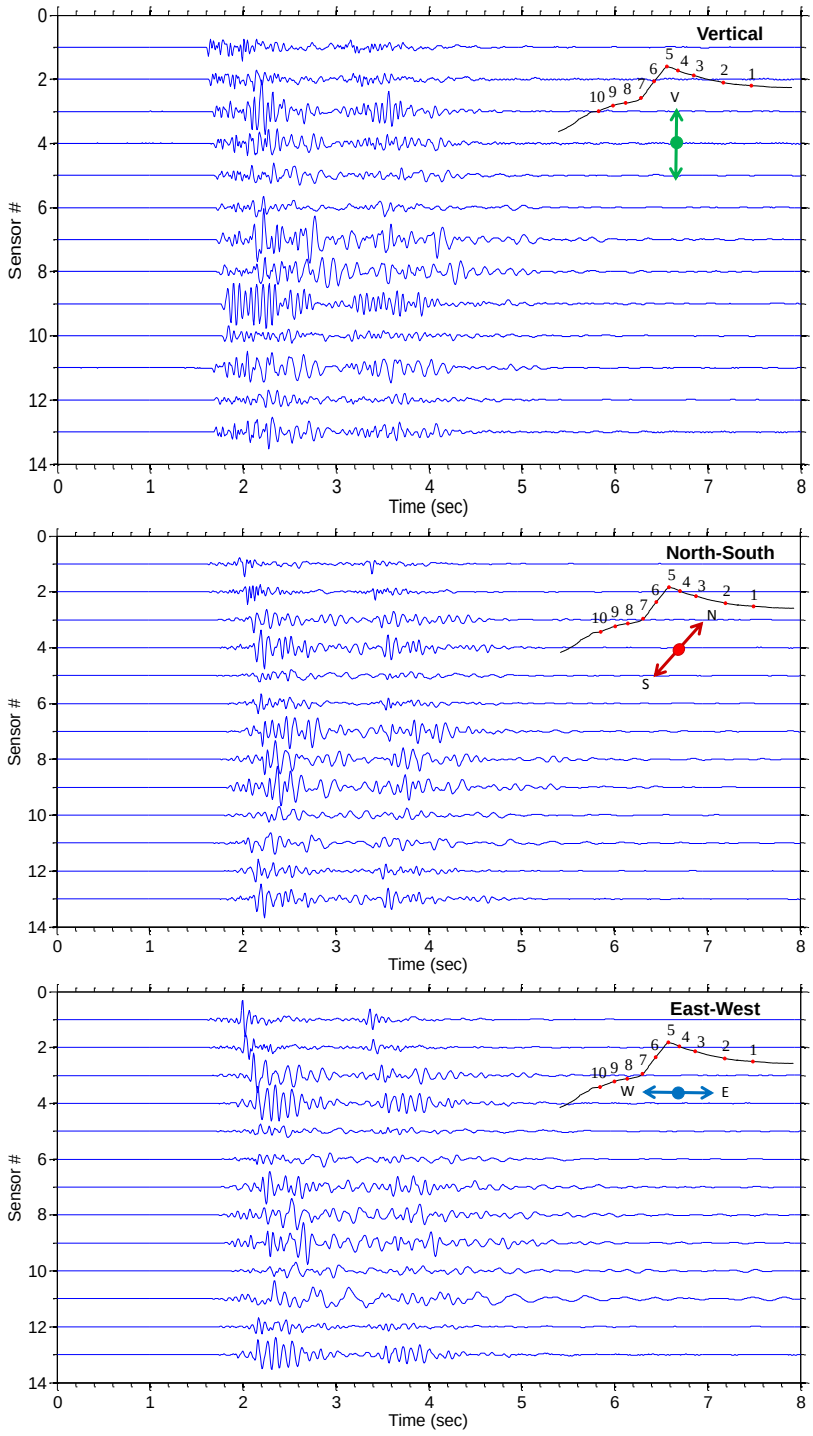

Figure 7.3: Time record plot for event 17801 for the vertical, North-South, and East-West component of motion.

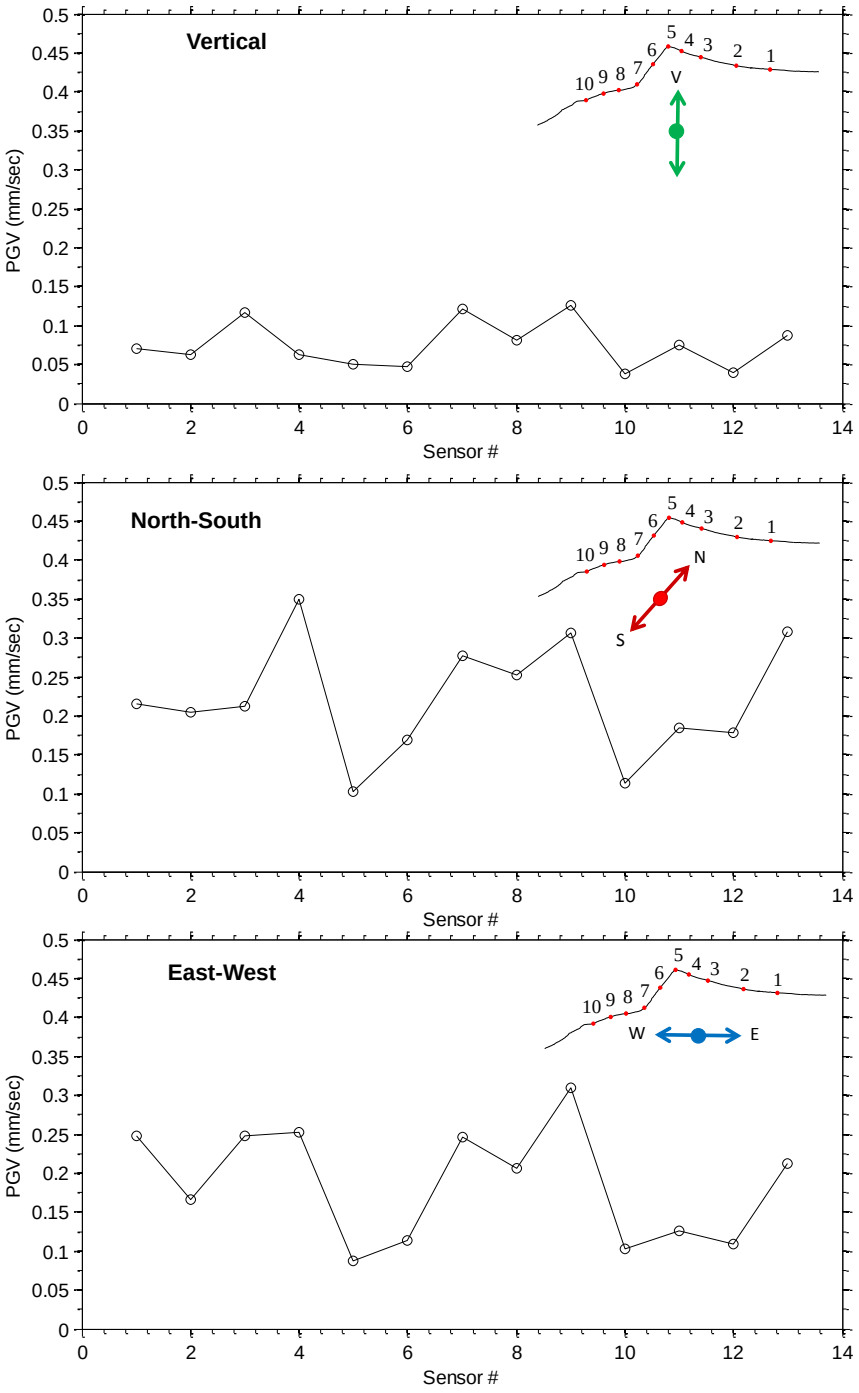

Figure 7.4: Peak ground velocity (PGV) for event 17801 for the vertical, North-South, and East-West component of motion.

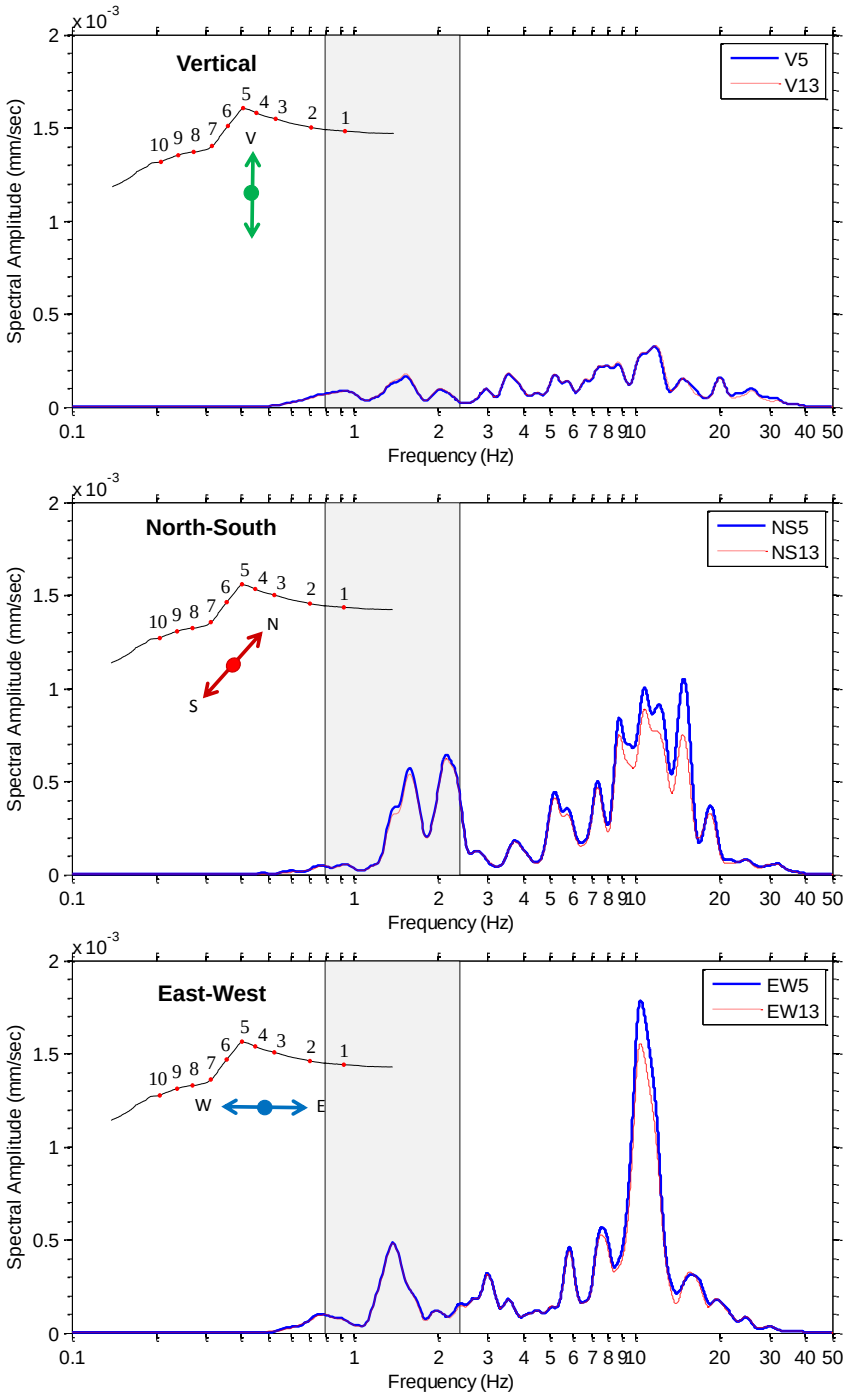

Figure 7.5: Spectral amplitude plots of sensors 4 and 13 for event 17801 for the vertical, North-South, and East-West components of motion. The estimated topographic frequency range based on cross-section geometry and average shear wave velocity is shaded.

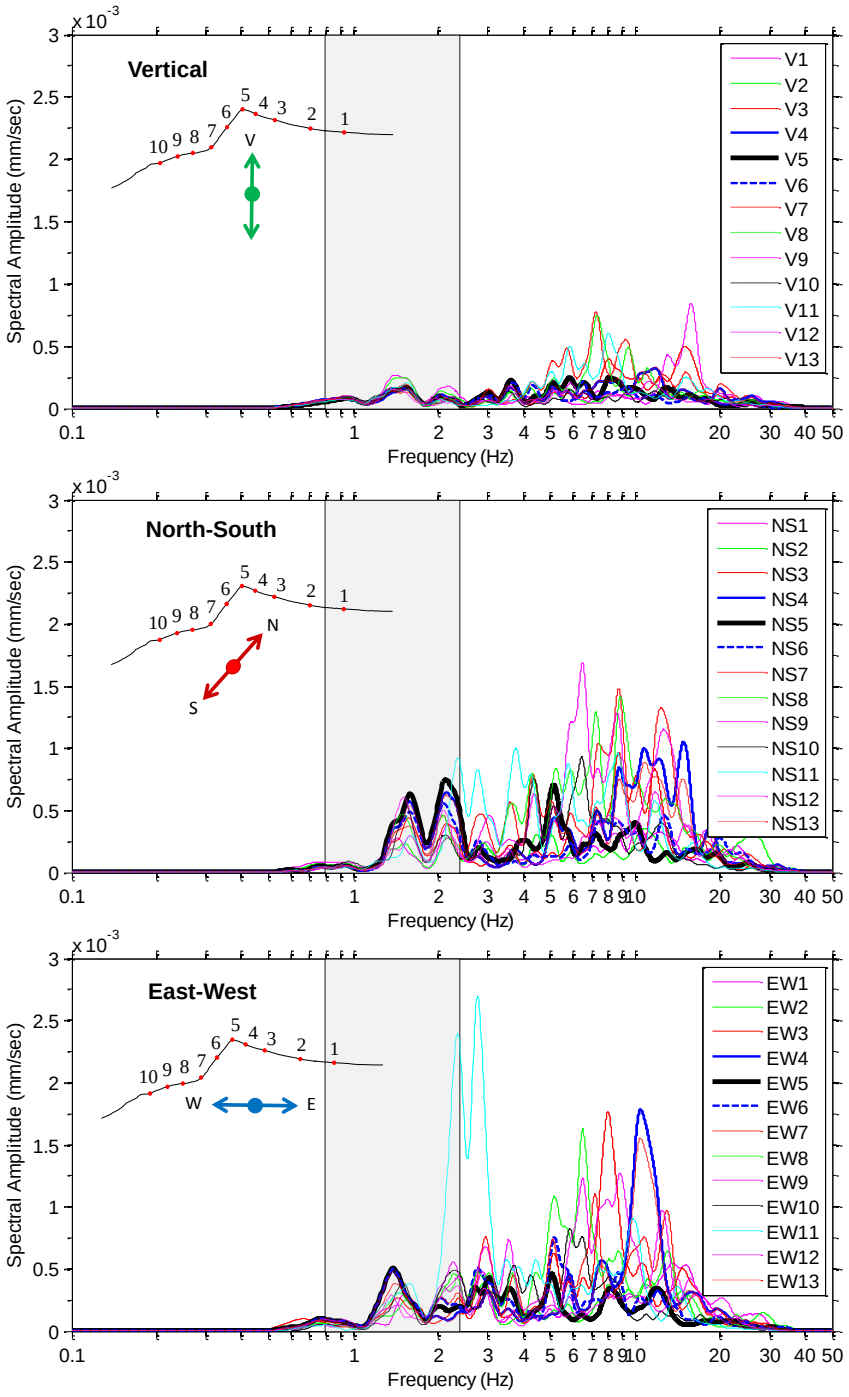

Figure 7.6: Spectral amplitude plots for event 17801 for the vertical, North-South, and East-West components of motion at Sensors 1-13. The estimated topographic frequency range based on cross-section geometry and average shear wave velocity is shaded.

approximately 1 Hz, and greater than 20 Hz, the amplitude of each of the sensors drops off significantly compared to frequencies between 1-20 Hz. The 1-20 Hz range seems to be the energy band output contained within these mining induced events after they have propagated approximately 2 km from the presumed hypocenter location. This limits the low frequency analysis that can be conducted on the data, but topographic amplification was predicted in Chapter 6 between the frequencies of 0.87 to 2.39 Hz, which is directly in one of the main energy bands of the data. The other energy band (5-15 Hz) can be attributed to soil site effects amplification and fits very well with the estimates in Chapter 6. The amplitudes in the 5-15 Hz range are much higher for sensors on the back side of the slope (i.e., 6-10), which may be the result of a sun/shadow effect mentioned in Chapter 2, where sensors on the slope opposing the direction of wave propagation have higher motions than those on the incoming side of the slope. The higher amplitudes in the 5-15 Hz range can explain why Sensor 5 has a lower time domain amplitude compared to other sensors in the array. Overall, the events seem to provide energy in the necessary frequency range (~1-2.4 Hz) to assess the effects of topography on the recorded ground motions.

7.3.1 Standard Spectral Ratio (SSR) Analysis

To determine the amplification at a station, the baseline amplitude has to be established that represents a response similar to a station whose amplification is of interest, but not affected by soil site effects or topographic amplification. The first method used to accomplish this task is the Standard Spectral Ratio (SSR) method. This method (described in detail in Chapters 2 and 3) uses a single reference station that is believed to be free of amplification, but is close enough to the measurement stations to not be overly influenced by geometric attenuation. This reference station is compared to

other measurement stations in the same vicinity to determine amplification or de-amplification at various frequencies. For Phase I, Station 1 was chosen as the reference station for the SSR method for two reasons: (1) Station 1 is located closest to the presumed hypocenter of the recorded events (i.e., the longwall), and therefore should have the highest amplitude of all the stations, all other things being equal and (2) Station 1 is located on the flattest topography in the area and is least likely to be affected by topographic amplification.

In Figure 7.7, the SSR for vertical (V), North-South (N-S), and East-West (E-W) components of Stations 2-12 are shown with respect to Station 1. For the vertical component, amplification peaks can be seen at 3.5 and 6.25 Hz. For the lower frequency peak (3.5 Hz), the station at the peak of the ridge (#5) has the highest spectral ratio/amplification (5.0) followed by Stations 4 and 6 on the East and West side of the ridge, respectively. However, this amplification peak is outside the estimated topographic frequency band (~1-2.4 Hz), but still could be the result of topographic amplification. The higher frequency peak (6.25 Hz) is directly in the estimated soil site effects band (5-15 Hz), and is likely the result of soil site effects as the stations do not follow a regular pattern of top-down amplification. In the estimated topographic frequency band, only a small peak at 1.1 Hz was measured and the amplification pattern does not match the assumption of maximum amplification at the peak. Overall, amplification at frequencies higher than the estimated topographic frequency range were measured on the vertical component of event 17801, and were likely caused by soil site effects and/or path effects.

For the N-S component, a significant amplification peak of 7 was measured on Station 5 at 1.8 Hz. In addition, a strong amplification pattern is present at that frequency, in which Station 5 (the crest station) has the highest amplification followed,

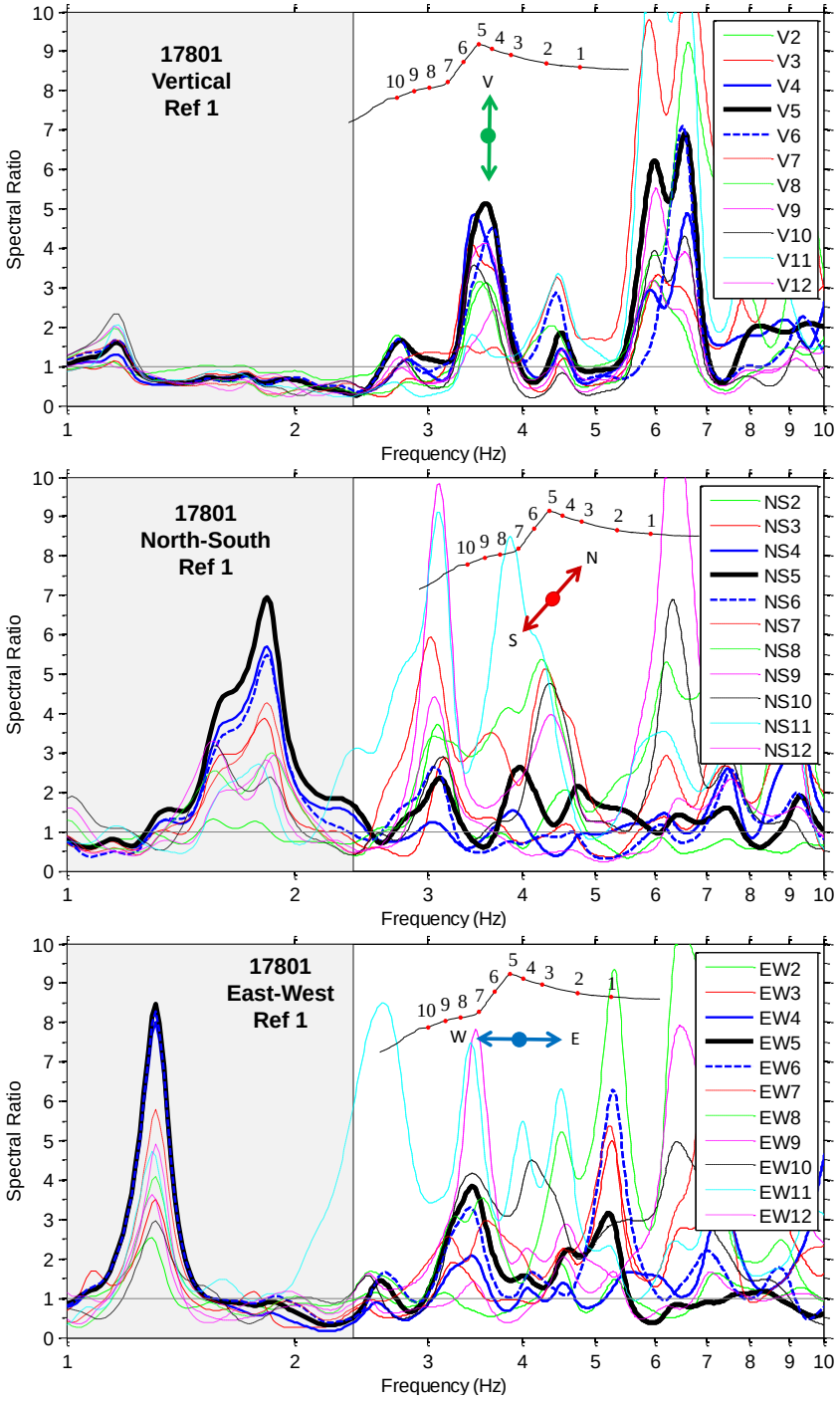

Figure 7.7: Standard spectral ratio (SSR) for event 17801 vertical, North-South, and East-West components of motion. Station 1 used as the reference station. The estimated topographic frequency range based on cross-section geometry and average shear wave velocity is shaded.

by Stations 4 and 6 on either side of the peak of the feature, with amplifications of 5.7. Stations 4 and 6 are followed by Stations 3 and 7 with amplifications of approximately 4 in the same frequency range. These stations are also just lower in elevation than Stations 4 and 6. After Stations 3 and 7, most other stations in the array, excluding Station 2, have an amplification of approximately 2.5. In addition to the amplification pattern, the maximum frequency amplification is directly in the center the estimated topographic frequency range. These two facts provide strong evidence that the amplification measured at 1.8 Hz is the result of topographic effects. At frequencies greater than 2.4 Hz (outside the estimated topographic frequency range), amplifications were measured on Stations 7-10 and 11, which have large spectral ratios of over 10. Most of these stations, excluding 11, are on the back side of the ridge and may be affected by the source path effects and/or soil site effects. In addition, the higher frequency amplifications (greater than 2.3 Hz) have a random pattern of amplification, and do not have a clear pattern of top-down amplification.

Similar to the N-S component, a significant amplification peak was measured on the E-W component in the estimated topographic frequency range. This frequency peak also has an excellent pattern of amplification. In contrast to the N-S component, the amplification peak was measured a 1.3 Hz on the E-W component, which is a lower frequency than the peak measured in the N-S direction (1.8 Hz), though both are within the estimated topographic frequency range. This difference in the peak amplification frequency does not match well with the topography size in the N-S and E-W directions (i.e., the topographic width is greater in the N-S direction than the E-W direction, therefore the amplification peak for the N-S component should be lower than for the E-W.) However, this is not the case and it reinforces the fact that defining a characteristic height or width of a topographic feature can be very difficult and subjective. In addition

to differences in the peak frequency, the 1.3 Hz E-W peak is much narrower than the 1.8 Hz N-S peak, varying from only 1.1 to 1.4 Hz compared to 1.5-2.1 Hz for the N-S component. The maximum amplification is also greater for the E-W component at 8.5 compared to 7 for the N-S component. This observation matches well with literature that states that steeper slopes should produce higher amplification compared to shallower slopes. Similar to the V and N-S components, significant amplifications were measured at frequencies higher than the estimated topographic frequency range, this amplification is attributed to soil site effects and/or path effects. However, Station 11 has a large amplification peak at 2.6 Hz, which could be topographic amplification, but since it is isolated, it is very difficult to discern a pattern of amplification.

In Figure 7.8, a plot of the horizontal polarity of Stations 2-12 for frequencies from 1-5 Hz based on the SSR method is shown. The horizontal polarity plot helps one visualize the amplification present at each azimuthal direction in the horizontal plane and is valuable to help determine the most intense direction of shaking for a given frequency. In Figure 7.8, Stations 3-10 have a singular direction of energy in the 1 to 2 Hz range, with a N-E to S-W polarity. This polarity matches well with the azimuth direction of the presumed energy source (the underground longwall). In addition to the main energy peak, Stations 2, and 7-10 all have significant energy at frequencies between 3 and 5 Hz, but this energy seems to be more multidirectional indicating that it may be the result of soil site effects and not topographic effects.

Overall, the SSR analysis of event 17801 demonstrated significant topographic amplification at 1.8 and 1.3 Hz in the N-S and E-W directions, respectively, with SSR ratios of 7 and 8.5, respectively. This amplification also has a primary polarity, which is common for topographic effects. Possible topographic amplification was also measured on the vertical component at a frequency of 3.5 Hz.

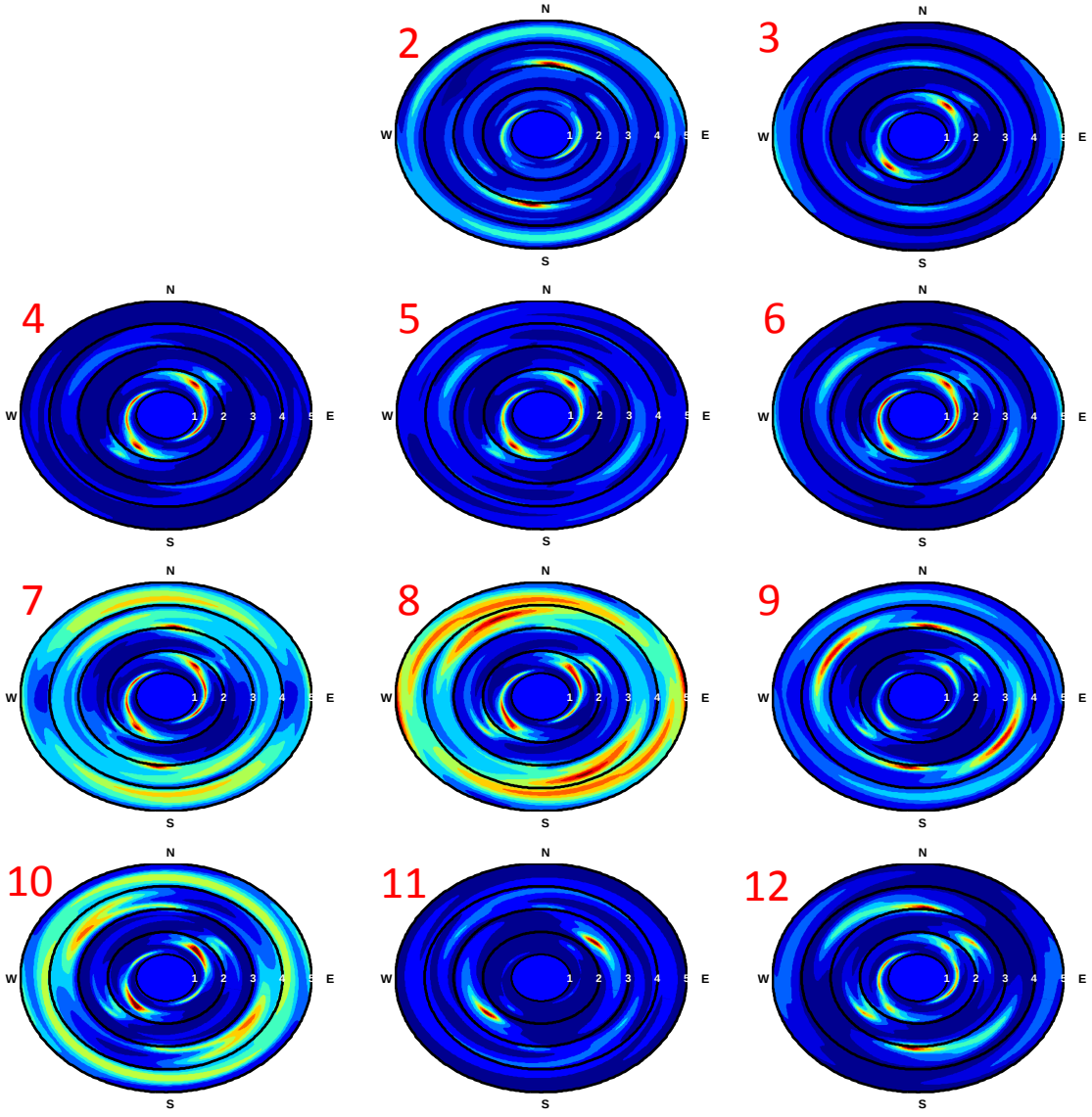

Figure 7.8: Horizontal polarity plots from the SSR method for event 17801. Station 1 used as the reference station.

7.3.2 Median Reference Method (MRM) Analysis

The Median Reference Method (MRM) is an update to the classical SSR method that eliminates the short comings of only having a single reference station. The MRM uses the entire array of stations to create a reference amplitude by calculating the median

response as a function of frequency for all the stations in the array (MRM is detailed in Chapters 2 and 3). The method has been shown in numerical simulations to be very stable, regardless of the number of sensors in the array and fits well with the geometric setup in Phase I (Maufroy et al. 2012). For the data in Phase I, Stations 1-12 were used to compute the median response of the instrumented portion of the mountain.

The MRM results for event 17801 for the vertical (V), North-South (N-S), and East-West (E-W) components are shown in Figure 7.9. The V component of motion has little amplification at the crest (Station 5) in the estimated topographic frequency range. Stations 1 and 2, on the other hand, have up to a 2.5 times amplification in the estimated topographic frequency range. However, no significant pattern can be discerned from the stations being amplified. Large amplifications for Stations 7, 8 and 11 were calculated using the MRM for frequencies above 5 Hz, which is within the range judged to be caused by soil site effects and/or path effects.

Unlike the vertical component, the N-S component of motion has a wide frequency band amplification of up to 2.25 from 1.5 to 2.5 Hz for the crest station (#5). This amplification frequency band is characterized by double peaks at 1.8 and 2.4 Hz. A consistent pattern of lower and lower amplification is measured by Stations 4 and 6 and then 3 and 7, similar to the pattern observed using the SSR method. Additional amplifications were measured at higher frequencies (4 and 5 Hz), but no significant pattern of amplification can be discerned in this frequency range from the array of stations. Significant amplifications were also measured at Station 11 and may be the result of topographic effects; however, as with the SSR, this cannot be confirmed with the limited station geometry in Phase I. In addition to Station 11, several other Stations (7-10) have amplification greater than 2.5. However, these amplifications do not have a

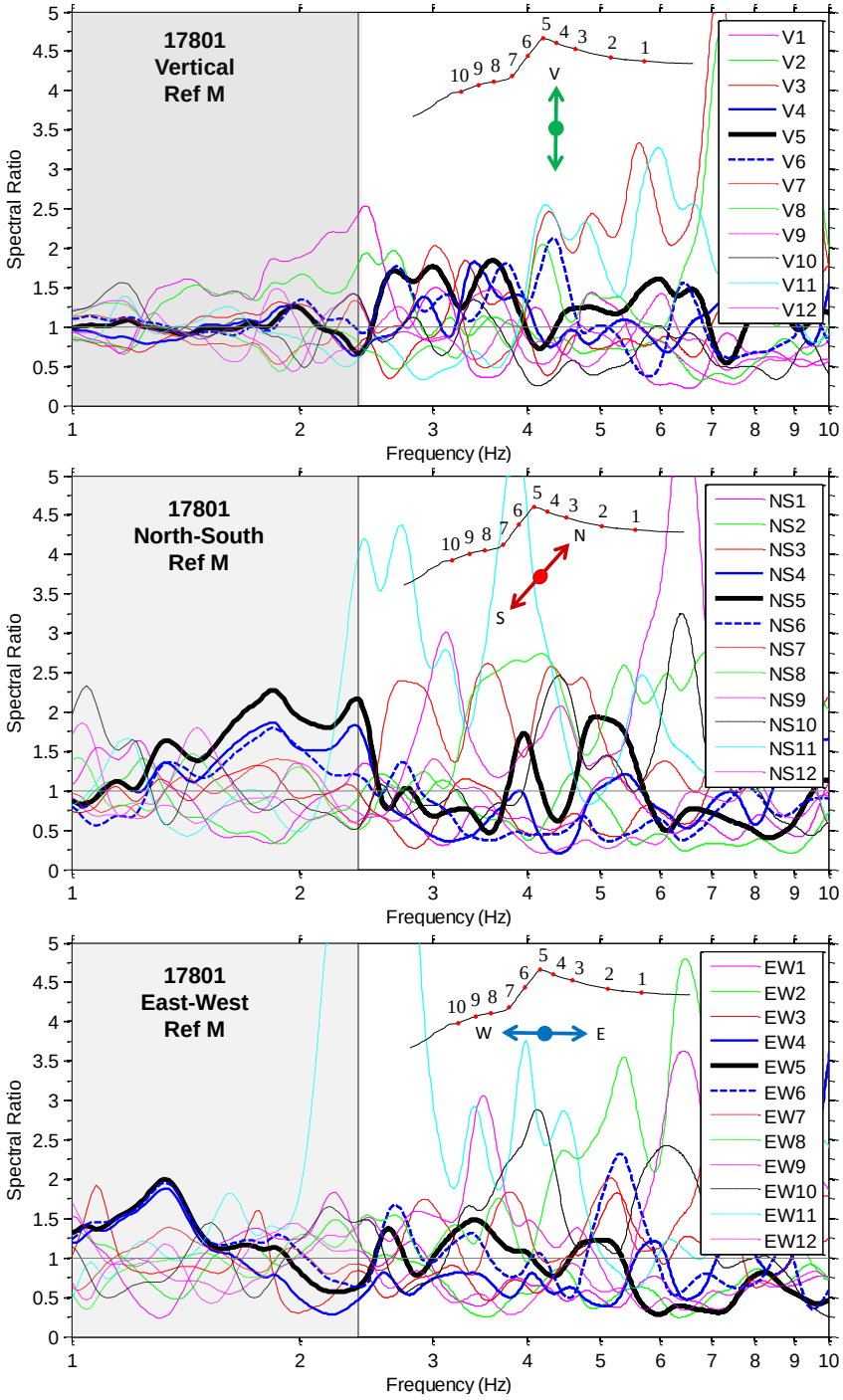

Figure 7.9: Median Reference Method (MRM) for event 17801 vertical, North-South, and East-West components of motion. The estimated topographic frequency range based on cross-section geometry and average shear wave velocity is shaded.

significant pattern of amplification and maybe due to site or path effects, but likely not topographic effects.

For the E-W component, an amplification peak of 2 was measured on Station 5 at a frequency of 1.3 Hz, with a 1.9 times amplification on Stations 4 and 6. A significant pattern is not indicated at elevations lower than Stations 4 and 6, but these stations still form a good pattern of amplification and the peak is directly within the estimate topographic frequency range. Similar to the SSR analysis, the topographic amplification peak for the E-W component is at a lower frequency than the N-S component, which again doesn't match the expected trend based on the geometry of the feature. Other stations in the array also show amplification; however these are believed to be caused by soil site effects or path effects.

A plot of the horizontal polarity using MRM for event 17801 is shown in Figure 7.10 for all 12 stations from 1 to 5 Hz. Stations 4-6 all have a significant band of energy in the 2.5 to 1 Hz range, with the lower part of the band having a E-W polarity and the higher frequencies having a N-S polarity. Stations 7-10 seems to have energy concentrated in the 3-5 Hz range, but has little to no polarity to the signal.

Overall, almost no topographic amplification was calculated using the MRM for the vertical component, but topographic amplification was measured on both horizontal components. Amplification of up to 2.25 were measured on the N-S component within the estimated topographic frequency range from 1.5 to 2.5 Hz, while topographic amplifications up to 2.0 were measured on the E-W component over a narrower frequency range from 1.15 to 1.45 Hz. Other strong amplifications were measured by stations on the West side of the ridge on all components, however these are not believed to be the result of topographic effects.

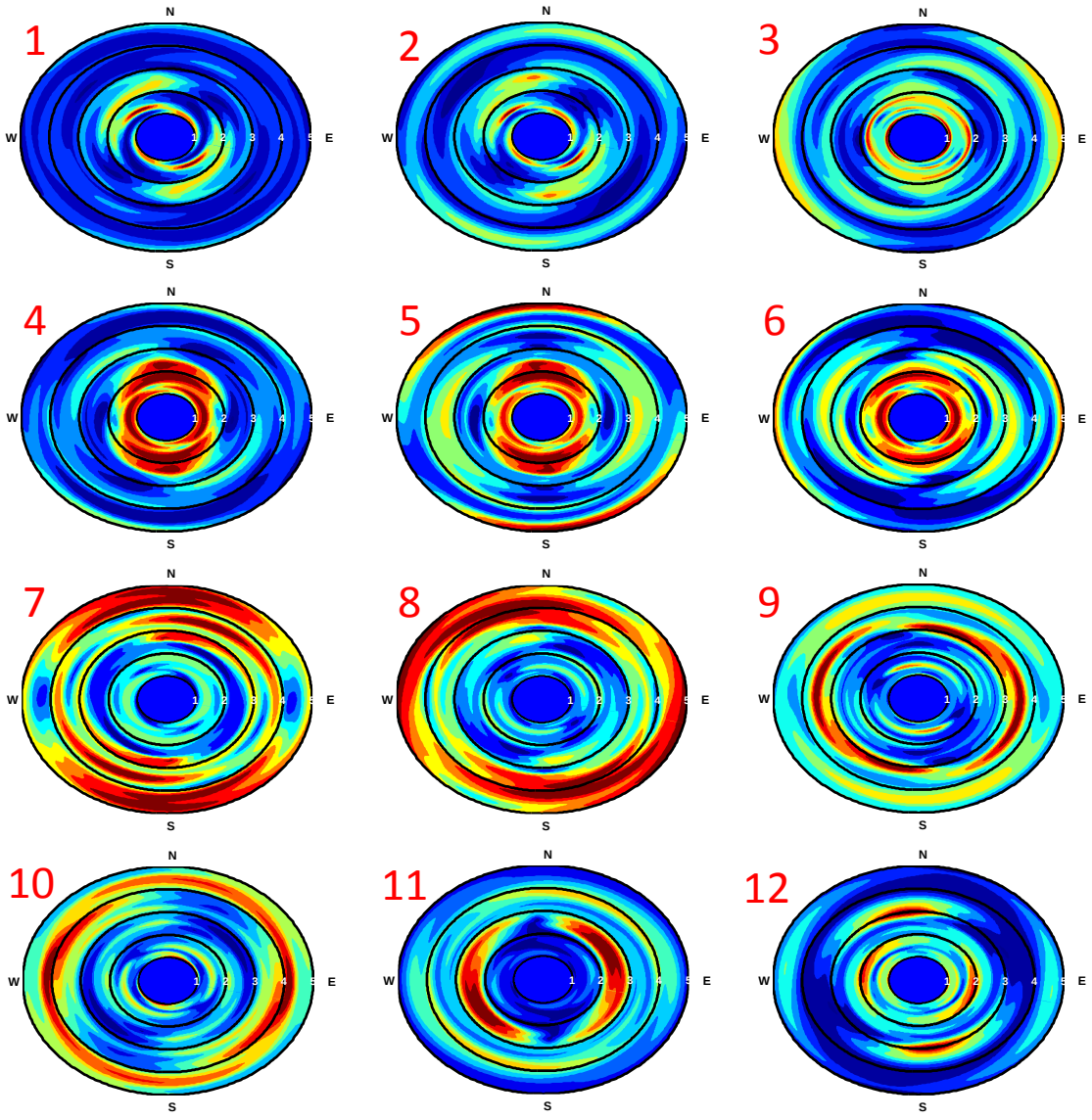

Figure 7.10: Horizontal polarity plots from the MRM for event 17801.

7.3.3 Horizontal to Vertical Spectral Ratio (HVSR) Analysis

Horizontal to Vertical Spectral Ratio (HVSR) was originally used to estimate a sites natural resonant frequency or the frequency where soil site effect amplification may be possible. In recent years researchers have shown that the method may be used to estimate topographic effects. A HVSR is calculated by dividing the horizontal component

of motion for a given sensor by the vertical component of that same sensor. This method has the advantage of only requiring one station for the calculations, compare with 2 to 10 stations for the SSR and MRM methods. For further details on the HVSR method, please refer to Chapters 2 and 3.

The North-South and East-West HVSR plots for event 17801 are shown in Figure 7.11. For the N-S HVSR, a significant peak is measured at Station 5 at a frequency of 2.4 Hz. This peak has a maximum amplification of almost 17. Station 4 follows Station 5 and has a very similar amplification pattern. However, the other stations in the array do not follow this amplification pattern. In addition to the HVSR peak at 2.4 Hz for Station 5, a smaller amplification peak was measured at a frequency of 1.8 Hz. This peak has a maximum amplification of 7.4 (60% less), however both Stations 4 and 6 follow a predictable amplification pattern of Station 5. Both HVSR peaks are within the estimated topographic frequency range for the feature, however significant patterns of amplification do not exist beyond Stations 4-6. Other stations in the array have significant HVSR peaks at frequencies of 2.8, 4.2, and 8 Hz, which likely indicate differences in the near surface velocity structure below each station.

For the E-W HVSR, a peak for Station 5 was measured at a frequency of 2.4 Hz, with a maximum amplification of 8. This frequency is at the upper edge of the estimated topographic effects range. However, the peak is significantly over-shadowed by many of the other stations in the array with amplification at some stations greater than 8 (up to 102 times amplification was measured by Station 11). A smaller amplification peak at 1.3 Hz matches well with the estimated topographic frequency range and has a maximum amplification of 3.2. At this frequency, Stations 4 and 6 have broken pattern of amplification, with Station 4 having a 20% higher spectral ratio than Station 5 and Station 6 having an 8% lower amplification than Station 5. Station 7

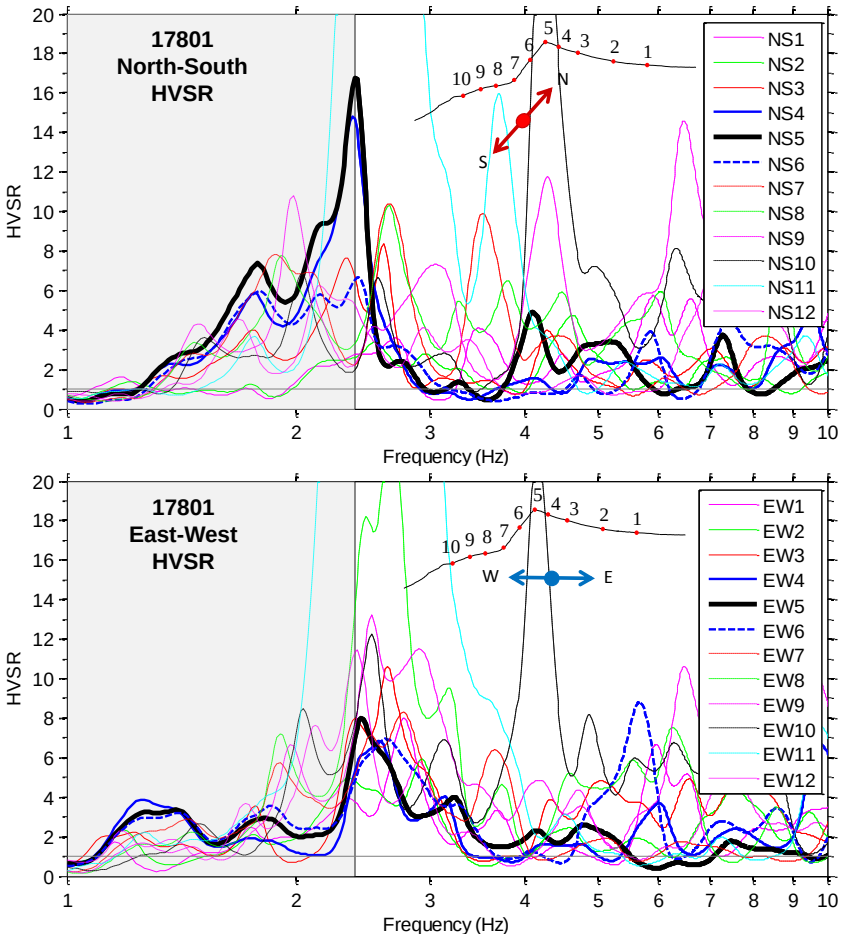

Figure 7.11: Horizontal to Vertical Spectral Ratio (HVSR) for event 17801 North-South, and East-West component. The estimated topographic frequency range based on cross-section geometry and average shear wave velocity is shaded.

also fits the topographic amplification pattern well, with a 12% reduction in amplification compared to Station 5. Stations at lower elevations did not form a good pattern of amplification, but this peak may still represent topographic amplification in the 1.3 Hz range.

A plot of the horizontal polarity of the HVSR for event 17801 is shown in Figure 7.12 for all 12 stations over a frequency range from 1 to 5 Hz. Stations 4-5 all have a strong N-S directionality in the 2.5 Hz range. Many of the other stations, excluding 10,

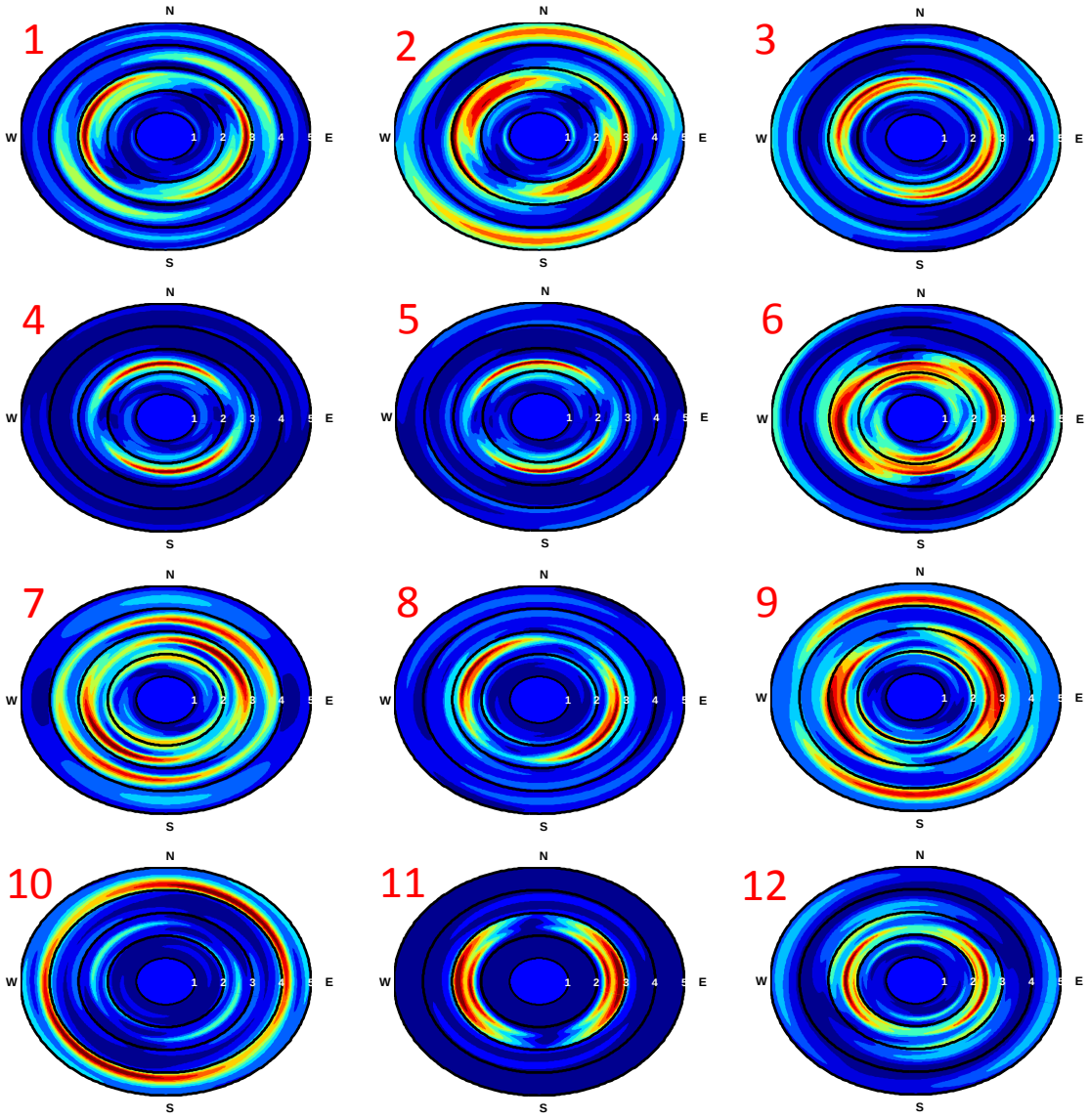

Figure 7.12: Horizontal polarity plots for the HVSR method for event 17801.

7.3.4 Method Comparison

Event 17801, a M_L 1.2 "earthquake", was processed using three separate methods to assess the effects of topography on the seismic response of the mountain. Each analysis method indicated amplification in the topographic frequency range estimated using Ashford and Sitar (1997) and Paolucci (2002). The spectral ratios calculated using

each method for the crest station (Station 5) are shown in Figure 7.13 for the vertical, North-South, and East-West components of motion. Comparing the vertical components of motion over the estimated topographic frequency range (~1-2.4 Hz), the SSR method has a spectral ratio of around 0.65, which indicates de-amplification at the peak. On the other hand, the MRM has a spectral ratio of around 1.0, which indicates no amplification of the vertical component. The only major difference between the SSR and MRM methods are at frequencies of 3.5 and 6.25 Hz, where an amplification of approximately 5 is calculated using the SSR method, while amplification of 1.75 is calculated using the MRM method.

For the North-South component, a peak is calculated at 1.7-1.8 Hz for each of the three methods. The SSR and HVSR methods have an amplification of approximately 7, while the MRM only has an amplification of 2.25. The amplifications of the three methods match well for frequencies between 1.4 and 2.6 Hz. Though, a significantly greater amplification (850%) is calculated using the HVSR method compared to the SSR and MRM methods between 2.0 and 2.6 Hz. This difference in calculated amplification between the HVSR and SSR/MRM methods has been reported by other authors, and confirms that the calculated Horizontal to Vertical Spectral Ratio cannot be directly related to the amplification measured at a site (Massa et al. 2010).

For the East-West component, maximum amplification was calculated over a uniform frequency range of 1.1 to 1.5 Hz using each method. The maximum amplification over this frequency range (9) was calculated using the SSR method, while amplification of 3 and 2 were calculated using the HVSR and MRM methods, respectively. An 8 times amplification was also calculated using the HVSR method at a frequency of approximately 2.5 Hz, while no amplification was calculated at

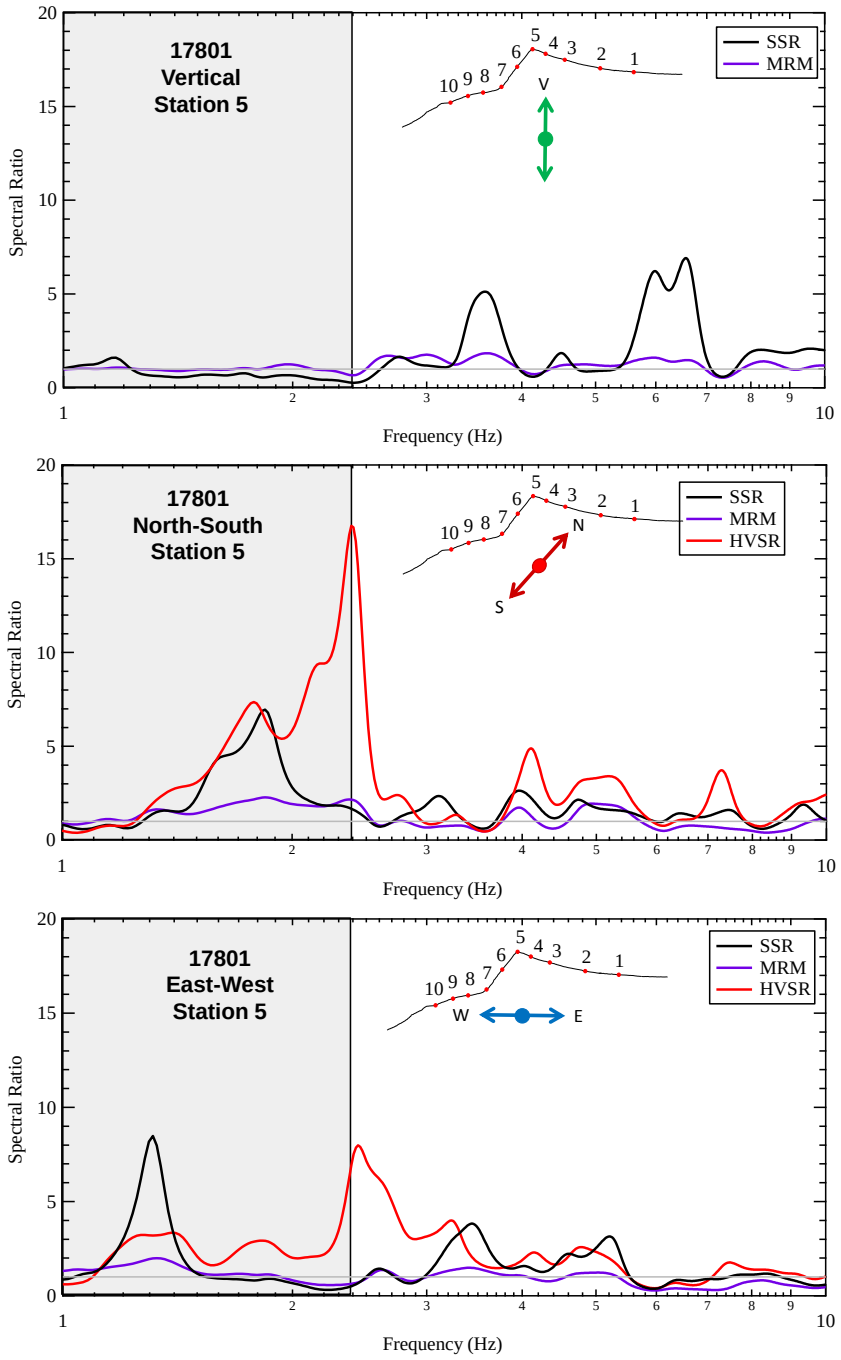

Figure 7.13: Comparison of the SSR, MRM, and HVSR results the vertical, North-South, and East-West components of Sensor 5for event 17801 . The estimated topographic frequency range based on cross-section geometry and average shear wave velocity is shaded.

the same frequency using the SSR and MRM methods. These false amplification peaks have been reported by other authors using the HVSR method (Massa et al. 2010).

Overall, each method predicted a similar topographic amplification frequency range; however, the amplification values calculated using each method vary wildly (up to an 850% difference). To investigate the differences in the amplification values calculated using the SSR and MRM methods, the spectral ratios for event 17801 were compared for Station 5 using the SSR method and Stations 1 and 5 using the MRM method (see Figure 7.14). Comparing the response of Stations 1 and 5 calculated using the MRM, the spectral ratios of the two stations were almost always polar opposites at each frequency (i.e., when Station 5 has a spectral ratio greater than 1, Station 1 has a spectral ratio less than 1, and vice versa). Consequently, to calculate the response at the crest of the feature using the SSR method, Station 5 (an amplification station in the estimated topographic frequency range) is divided by Station 1 (a de-amplification station in the estimated topographic frequency range). This calculation using the SSR method resulted in a large amplification peak in the estimated topographic frequency range.

To explain this large amplification peak, the location of each station is examined. Station 5 is located at the crest of the feature, and from the literature in Chapter 2 is expected to amplify ground motions due to topography. In contrast, Station 1 is located on flat terrain near the base of the feature, which has been shown in the literature to typically attenuate motions due to topography. Therefore, when a SSR between Stations 5 and 1 is calculated, an unrealistically high amplification results in the topographic frequency range, which is greater than the "free-field" amplification value typically measured using numerical modeling or theoretical estimation methods. This observation explains the quantitative bias reported in Chapter 2 between amplifications measured experimentally using the SSR method and those calculated using numerical methods.

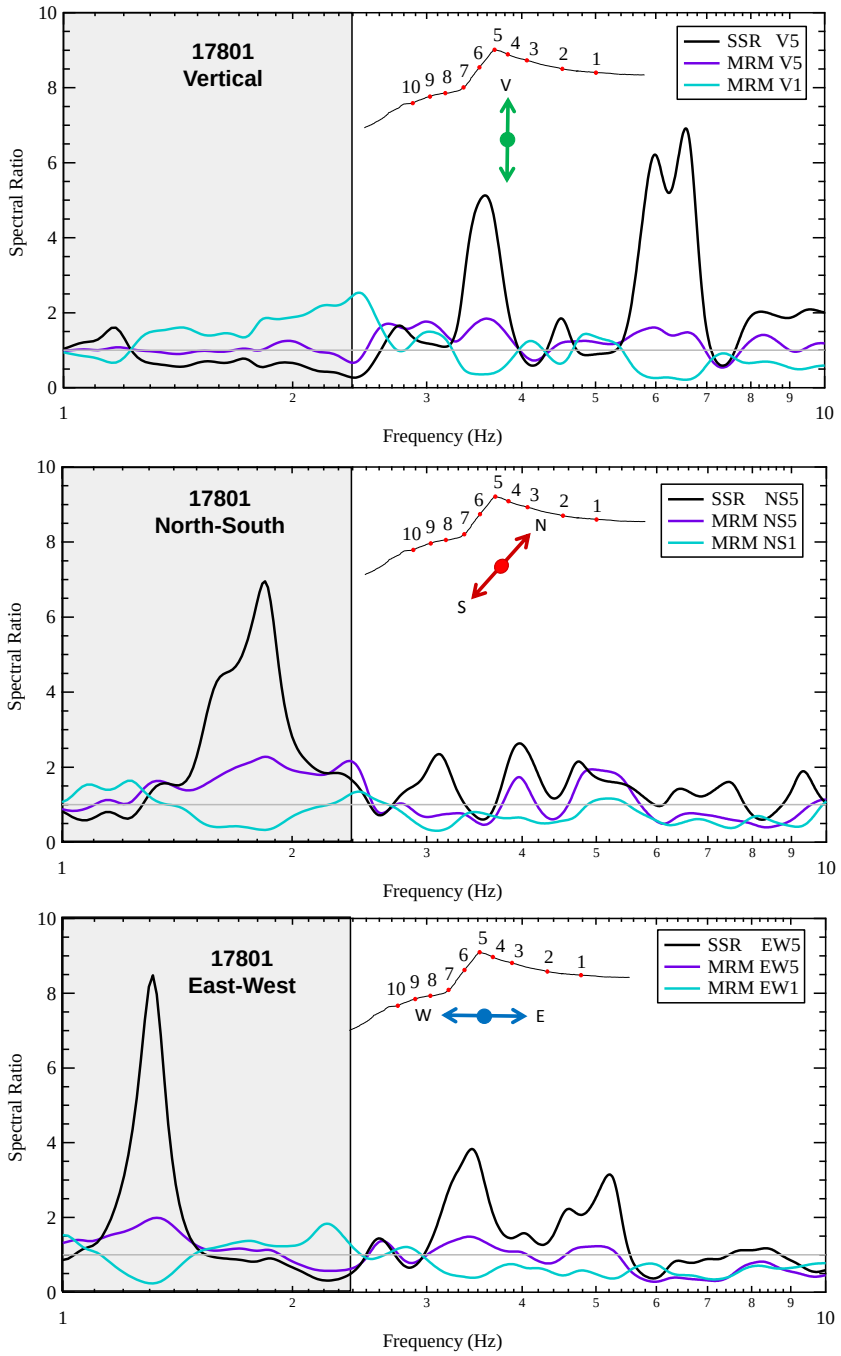

Figure 7.14: Comparison of the SSR for Station 5 with the MRM for Stations 5 and 1 for the vertical, North-South, and East-West components for event 17801. The estimated topographic frequency range based on cross-section geometry and average shear wave velocity is shaded.

Overall, similar topographic amplification frequencies were calculated using each of the three methods used to analyze event 17801. The calculated topographic frequency range (1.1-2.6 Hz) and also match very well with the combined frequency range estimated using both Ashford and Sitar (1997) and Paolucci (2002) (0.87-2.4 Hz), although the calculated frequencies were slightly higher than the estimated frequencies. However, major differences in the estimated amplification (up to 850%) were seen between methods, with the MRM method resulting in the most reasonable amplification of the three methods. In general, event 17801 resulted in topographic amplification at the peak (Station 5) of the instrumented feature and slightly less amplification as one moved down the slope (Stations 3, 4, 6, and 7) of the feature, ultimately switching to de-amplification at the base of the feature (Stations 1 and 2).

7.4 Multiple Event Processing (52 Events) for Station 5

In Phase I (2010), 52 events were recorded by the topographic array. Each of these events represents a singular look at how topographic amplification affects the response of the instrumented feature. Because looking at each individual event would be repetitive, the events were processed individually and a log-normal median and +/- 1 sigma were calculated for each station in the array. This section examines the variation in PGV and spectral ratio of the entire event catalog (52 events) for the crest station (#5).

The peak ground velocity (PGV) values for all 52 recorded events are shown in Figure 7.15 for Stations 1-12. As with the PGV values for event 17801, no correlation could be determined between PGV and the topographic location of each station. Stations 3, 4, 7, 8, and 9 had the highest PGV values for each component, while the crest Station (5) had one of the lowest PGV values for each component. In comparison to other events, Event 17801 had one of the largest PGV's of the stations in the topographic array, and

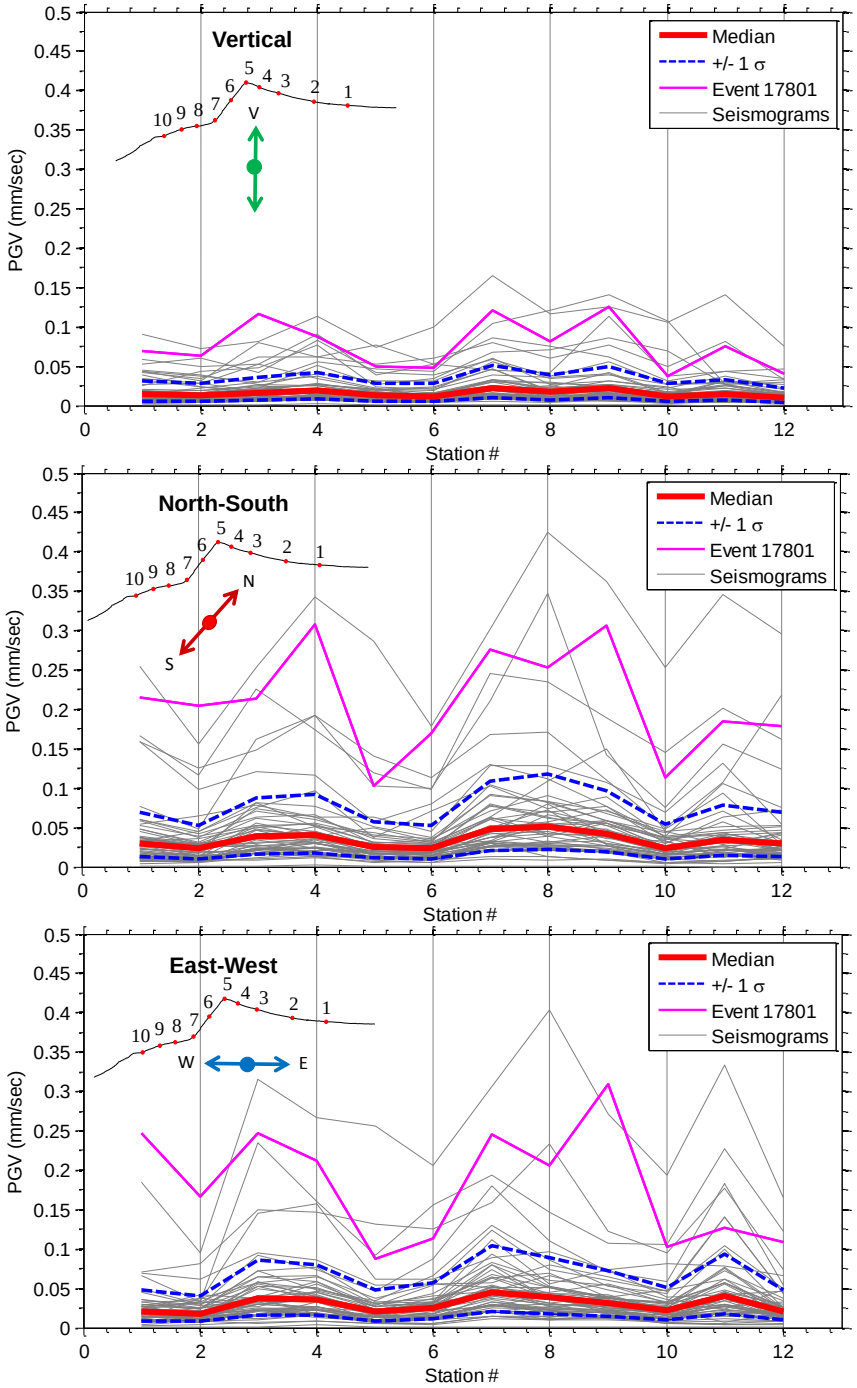

Figure 7.15: PGV's for all 52 events recorded during Phase I, V, N-S, and E-W components with log-normal median and +/- 1 sigma shown.

was an order of magnitude greater for each station than the log-normal median PGV of all 52 events.

The Fourier amplitude spectra for each event are shown in Figure 7.16 for Station 5, along with the log-normal median of the events and +/- 1 sigma. For all three components, the median spectral amplitude has corner frequencies of 1-2 Hz on the low frequency side and 10-20 Hz on the high frequency side. The amplitude of the individual events varies within the frequency range of interest (1-10 Hz) by over 3 log cycles, but all the ground motions are still below the level that can be felt by humans (~1 mm/sec) (Wald et al. 1999).

7.4.1 Standard Spectral Ratio (SSR)

All 52 events in the ground motion catalog were analyzed using the SSR method for Station 5. The SSR spectral ratios for all 52 events are shown for Station 5 in Figure 7.17, along with the log-normal median, and +/- 1 sigma of all 52 events. For the vertical component, the calculated spectral ratios for each event indicate significant variations in the location and amplification values of spectral peaks within the 1-10 Hz frequency range. Although significant variations in calculated spectral response exist between events, the median of the events indicates no significant amplification in the estimated topographic frequency range.

For the North-South component, significant variations in spectral ratio also exist from event to event, but unlike the vertical component, a measurable amplification peak is indicated on the median response of the events in the estimated topographic frequency range. The median response has a maximum amplification of 3.0 with a +/- 1 sigma of at the peak frequency of 5.0 and 1.7, and results in a coefficient of variation (COV), in

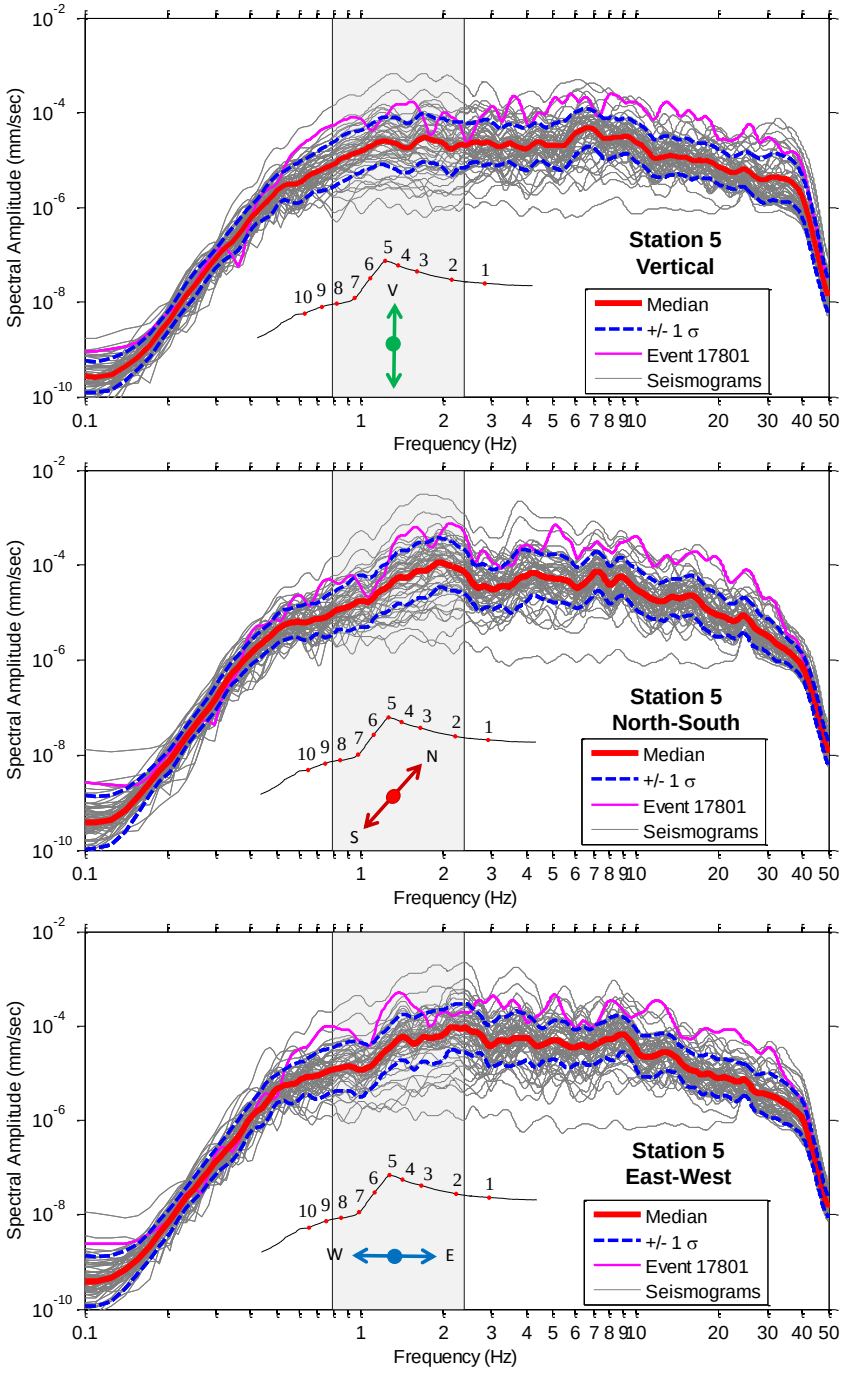

Figure 7.16: Fourier amplitude spectra for all 52 events recorded during Phase I for the vertical, North-South, and East-West components of Station 5 with the log-normal median and +/- 1 sigma shown. The estimated topographic frequency range based on cross-section geometry and average shear wave velocity is shaded.

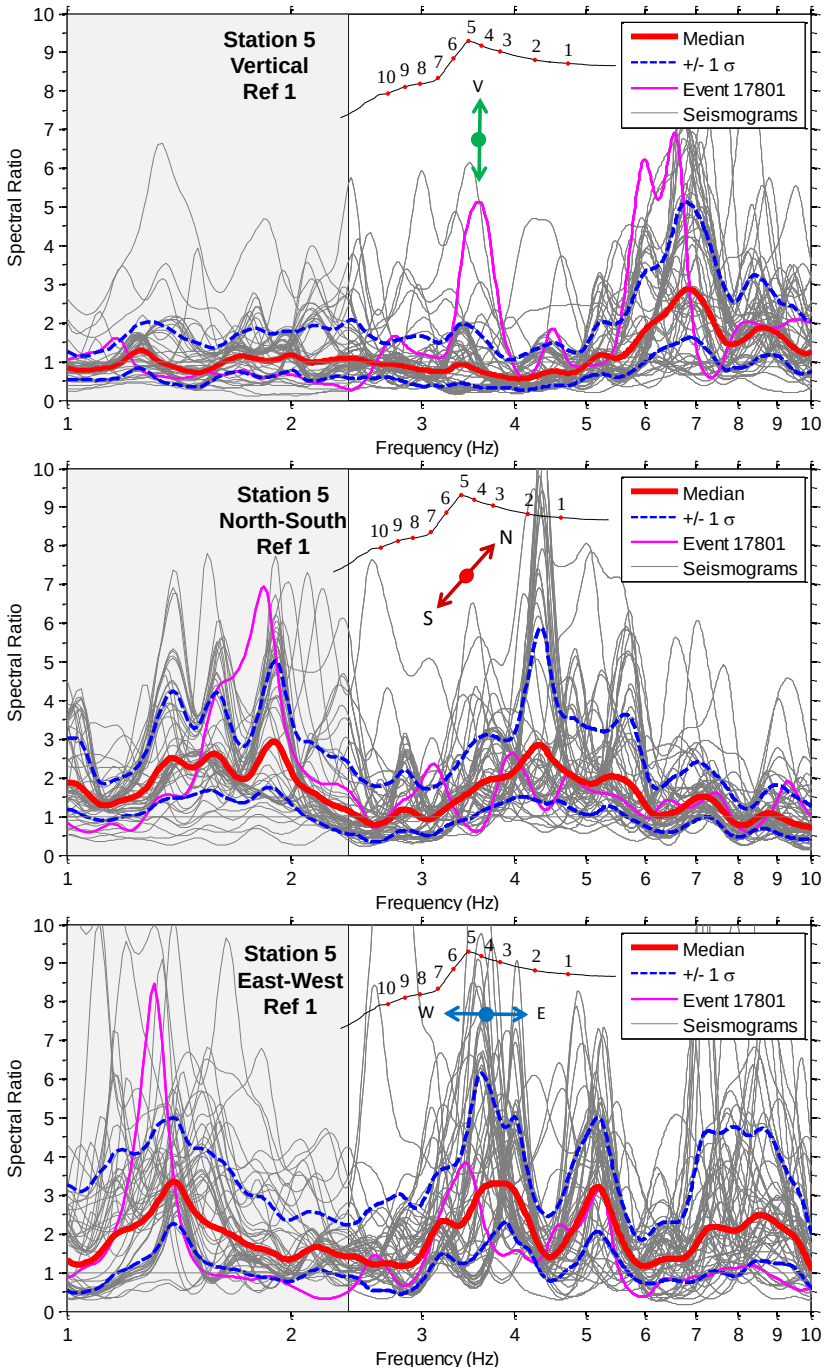

Figure 7.17: Standard Spectral ratio (SSR) for all 52 events recorded during Phase I for vertical, North-South, and East-West components of Station 5 with log-normal median and +/- 1 sigma shown. The estimated topographic frequency range based on cross-section geometry and average shear wave velocity is shaded.

the amplification frequency range, of 0.38-0.60. Moreover, the amplification for individual events varied from 0.25-8 within the estimated topographic frequency range. Other amplification peaks exist for the median response at frequencies above 2.5 Hz, but those amplifications are likely caused by soil site effects and/or path effects.

Similar to the N-S component, an amplification peak for the median was calculated on the E-W component, within the estimated topographic frequency range. A maximum amplification of 3.4 was calculated for the median with +/- 1 sigma values at the peak frequency of 5.0 and 2.2, and results in a COV, in the amplification frequency range, of 0.42-0.63. Moreover, the amplification for individual events varied from 0.5-11times within the estimated topographic frequency range. For each of the components, the calculated spectral peaks within the estimated topographic frequency range varied significantly in terms of both amplification factors and the location of the peak frequency. These large variations indicate that the SSR method does not provide a stable spectral estimate of the amplification at the crest of feature for Phase I.

7.4.2 Median Reference Method (MRM)

All 52 events in the ground motion catalog were analyzed using the MRM for Station 5. The MRM spectral ratios for all 52 events are shown for Station 5 in Figure 7.18, along with the log-normal median, and +/- 1 sigma of all 52 events. For the V component, the individual spectral ratios are more consistent with the median than observed using the SSR method. However, there are still some outliers that don't conform to the median trend. The response of the median indicates virtually no amplification over the entire frequency band and only a slight amplification seen at a frequency of 7 Hz, which is likely caused by path effects and/or soil site effects.

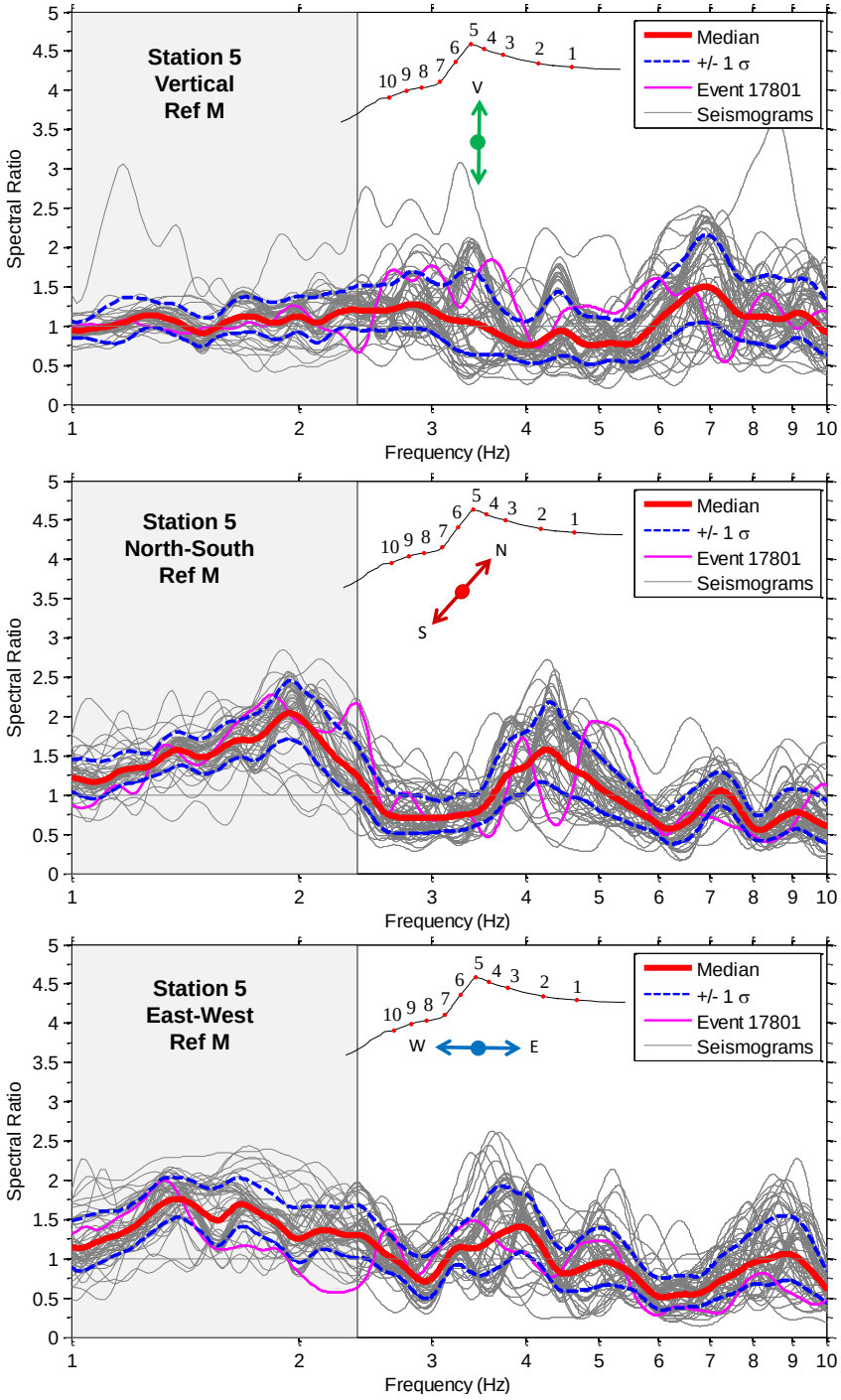

Figure 7.18: Median Reference Method (MRM) for all 52 events recorded during Phase I for vertical, North-South, and East-West components of Station 5 with median and +/- 1 sigma shown. The estimated topographic frequency range based on cross-section geometry and average shear wave velocity is shaded.

For the North-South component, a clear amplification peak is indicated, in the estimated topographic frequency range, by the median response and the majority of the individual spectral ratios emulated the median trend. A maximum amplification of 2.0 is calculated for the median response with a +/- 1 sigma of 2.4 and 1.7, and results in a COV, in the amplification frequency range, of 0.13-0.18. Moreover, the amplification for individual events varied from 0.6-2.8 within the estimated topographic frequency range. Similar to the N-S component, an amplification peak for the median was calculated on the E-W component, within the estimated topographic frequency range. A maximum amplification of 1.8 was calculated for the median with +/- 1 sigma values at the peak frequency of 2.0 and 1.5, and results in a COV, in the amplification frequency range, of 0.14-0.19. Moreover, the amplification for individual events varied from 0.8-2.3 within the estimated topographic frequency range. For of the three components, the spectral ratios of the individual events had a similar amplification and shape as the median of all the events, which indicates the MRM calculates a stable spectral estimate from event to event. Therefore, the median response can calculated using few events compared to the SSR method.

7.4.3 Horizontal to Vertical Spectral Ratio (HVSR)

All 52 events in the ground motion catalog were analyzed using the HVSR method for Station 5. The HVSR for all 52 events are shown for Station 5 in Figure 7.19, along with the log-normal median, and +/- 1 sigma of all 52 events. For the North-South component, a clear amplification peak is indicated, in the estimated topographic frequency range, by the median response. A majority of the individual events indicate a similar amplification frequency range; however the estimated amplifications factors vary significantly between events. A maximum amplification of 5.2 is calculated for the

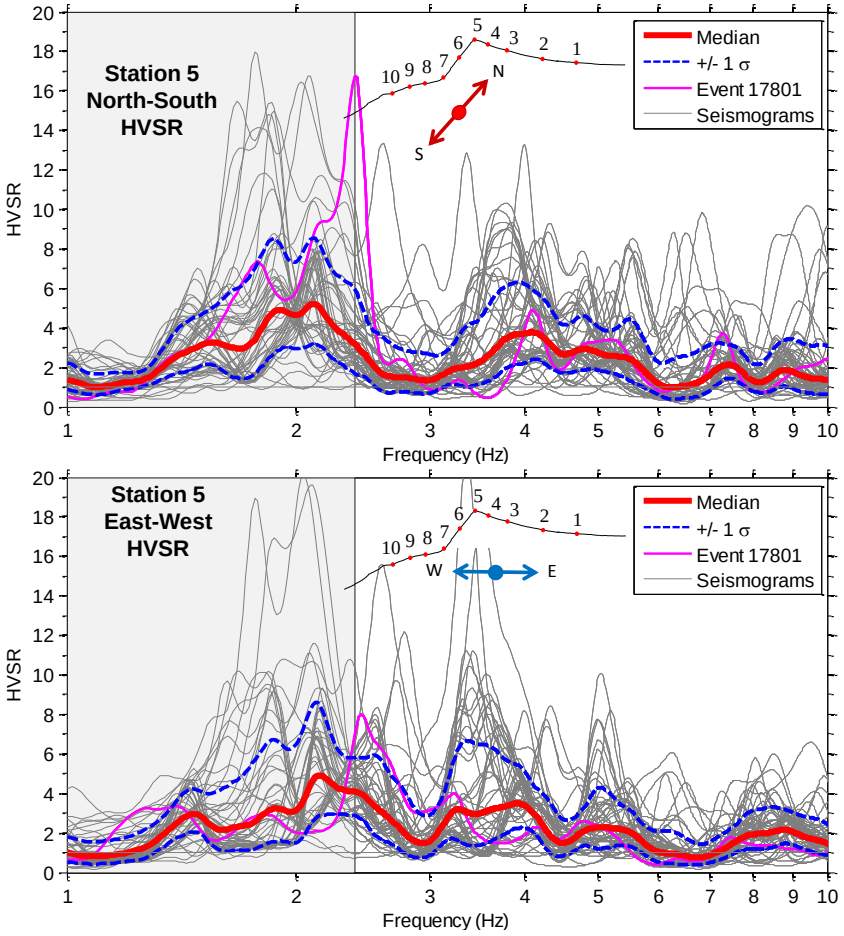

Figure 7.19: Horizontal to Vertical Spectral Ratio (HVSR) for all 52 events recorded during Phase I for Station 5 North-South, and East-West components with median and +/- 1 sigma shown. The estimated topographic frequency range based on cross-section geometry and average shear wave velocity is shaded.

median response with a +/- 1 sigma of 8.5 and 3.2, and results in a COV, in the amplification frequency range, of 0.44-0.85. Moreover, the amplification for individual events varied from 1.0-17 within the estimated topographic frequency range.

Similar to the N-S component, an amplification peak for the median was calculated on the E-W component, within the estimated topographic frequency range. However, the amplification peak for the E-W component was not as clear and uniform as

calculated on the N-S component. A maximum amplification of 4.9 was calculated for the median with +/- 1 sigma values at the peak frequency of 8.6 and 2.9, and results in a COV, in the amplification frequency range, of 0.39-0.93. Moreover, the amplification for individual events varied from 1.1-20 within the estimated topographic frequency range. For of the three components, the spectral ratios of the individual events had similar amplification ranges, but the amplification factors varied significantly from event to event.

7.4.4 Summary of Multiple Event Processing

In this section, all 52 events recorded during Phase I were processed using the SSR, MRM, and HVSR methods for Station 5. The results indicated significant variability from event to event when the catalog of events was processed using the SSR and HVSR methods. The two methods had large variations in both the frequency of the peak amplification and the calculated amplification factor from event to event. Using the SSR method, maximum amplification factors on the N-S and E-W components of 3.0 and 3.4 were calculated for the median response, respectively. The COV was quite significant for the SSR method varying between 0.38 and 0.63. The HVSR method had similar COV's of between 0.39 and 0.93, but the maximum amplification for the median was much higher, varying between 5.2 and 4.9 for the N-S and E-W components, respectively. The variability using the MRM was much lower than either the SSR or HVSR methods, with COV's of only 0.13-0.19, and it calculated lower maximum amplifications for the median of 2.0 and 1.8 for the N-S and E-W components. For all three methods, the MRM methods calculates the most stable spectral estimate and likely calculates the most reliable amplification factors.

7.5 Median Results for the Entire Event Catalog

For Phase I of the topographic study, 52 events were record during a 7 day period. These 52 events varied in amplitude, but all the events remained in the linear strain range and below the threshold felt by humans. To combine all the events together and estimate a collective response, a log-normal median was calculated for all 52 events using the SSR, MRM, and HVSR methods. Therefore, each Station (1-12) and component (V, N-S, and E-W) can be represented by a single spectral response for a given method. Overall, this section looks at the median response of the entire event catalog for all three topographic analysis methods.

7.5.1 Standard Spectral Ratio (SSR)

For the Standard Spectral Ratio (SSR) method, Station 1 was used as the reference station for the analysis of each event in the catalog. A comparison of the SSR median response of all 12 seismic stations is shown in Figure 7.20. Comparing the vertical component of each station, no significant amplification peak was measured in the topographic frequency range (~1-2.4 Hz). Though there was no amplification in the estimated topographic frequency range (i.e., a spectral ratio of 1.0 or less), Station 5 had the highest spectral ratio in the estimated topographic frequency range, indicating a slight amplification may exist. In the soil site effects frequency range (5-15 Hz), an amplification peak was observed at 6.8 Hz, but it is likely not caused by topographic effects due to the no pattern of amplification.

For the North-South component, an amplification peak was calculated in the estimated topographic frequency range for Station 5 (the crest station) from 1.2-2.4 Hz, with a maximum amplification of 3. An excellent pattern of amplification was measured by Station 4 and 6, which have about a 15% reduction in amplification compared to Station 5. Stations 3 and 7 (the next stations off the peak) also had a good

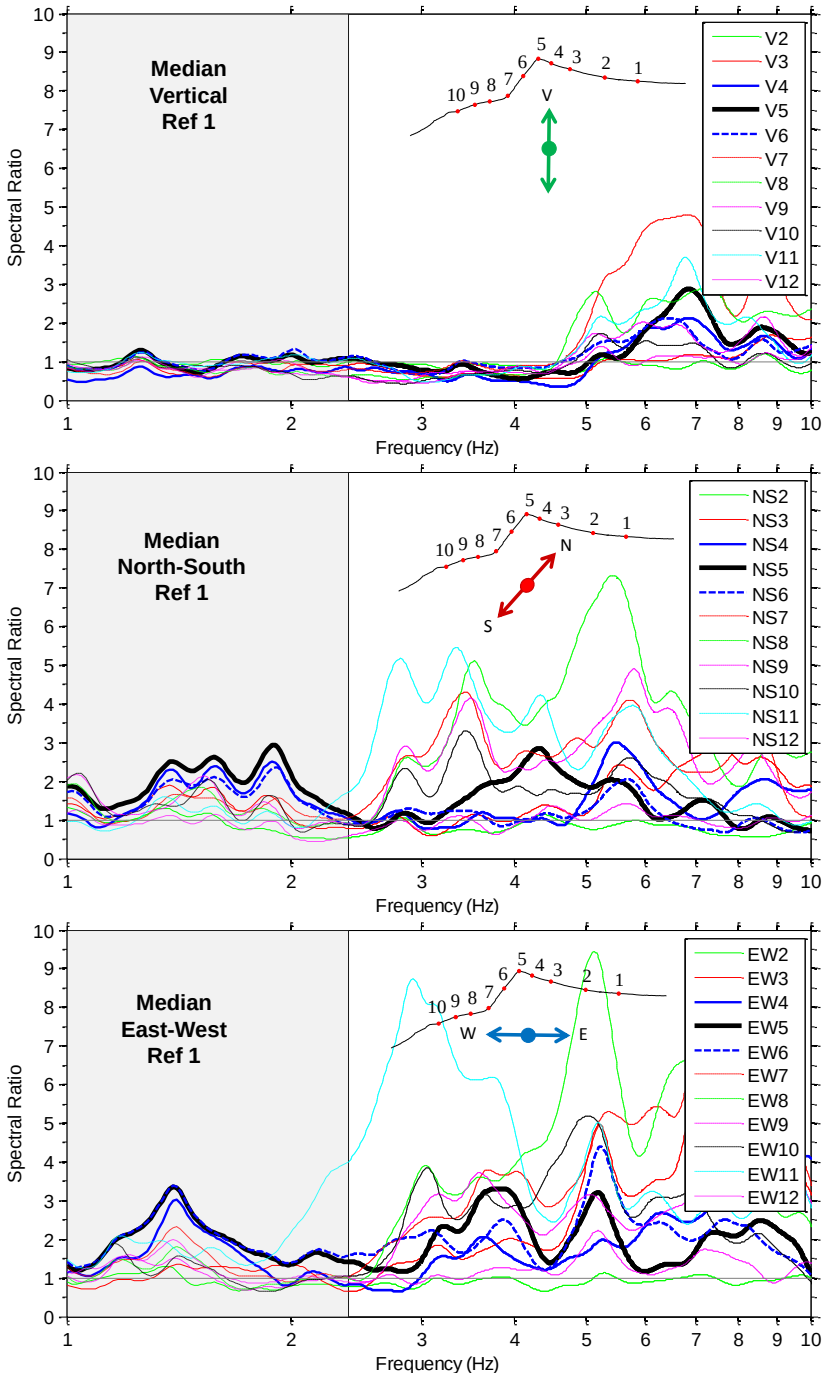

Figure 7.20: Standard spectral ratio (SSR) for the median of the Phase I event catalog (52 events) for the vertical, North-South, and East-West components of motion. Station 1 used as the reference station. The estimated topographic frequency range based on cross-section geometry and average shear wave velocity is shaded.

pattern of amplification, with a 35% reduction in amplification over the amplification frequency range. At frequencies above 2.5 Hz, amplification peaks on Stations 7-11 were estimated, but no significant pattern of amplification was noted. However, Stations 7-10 were located on the opposing side of the ridge from the energy source (i.e., the longwall). Therefore, these stations may be affected by path effects from the waves striking the West slope of the feature at a nearly perpendicular angle to the ground surface.

As with the N-S component, an amplification peak was measured on Station 5 in the East-West direction. The amplification peak extends from 1.1 Hz to 1.9 Hz, and had a maximum amplification of 3.4 times Station 1. The peak is centered at a frequency of 1.4 Hz, which was slightly lower frequency than the amplification peak measured in the N-S direction. In addition, the E-W direction had a higher overall amplification (13%) in the topographic frequency range compared to the N-S direction. A good pattern of top-down amplification was also measured for this topographic amplification peak, with Station 6 having almost an identical amplification to Station 5, and Station 4 having about a 10% reduction in amplification. Stations 3 and 7 have the next lowest amplification with a 35% reduction compared to Station 5. At frequencies above 2 Hz, amplifications were measured by all station, excluding Station 2. These amplifications seem to follow little to no pattern, and are believed to be a function of soil site effects, and not topographic effects.

In Figure 7.21, a plot of the horizontal polarity of Stations 2-12 from 1 to 5 Hz for the SSR method is shown. The horizontal polarity plot helps one visualize the amplification present at each azimuthal direction in the horizontal plane, and is valuable to help determine the most intense direction of shaking for a given frequency. Stations 2-10 had a very polarity in the NE-SW direction for frequencies in the estimated topographic frequency range, this polarity matches well with the azimuth direction (NE)

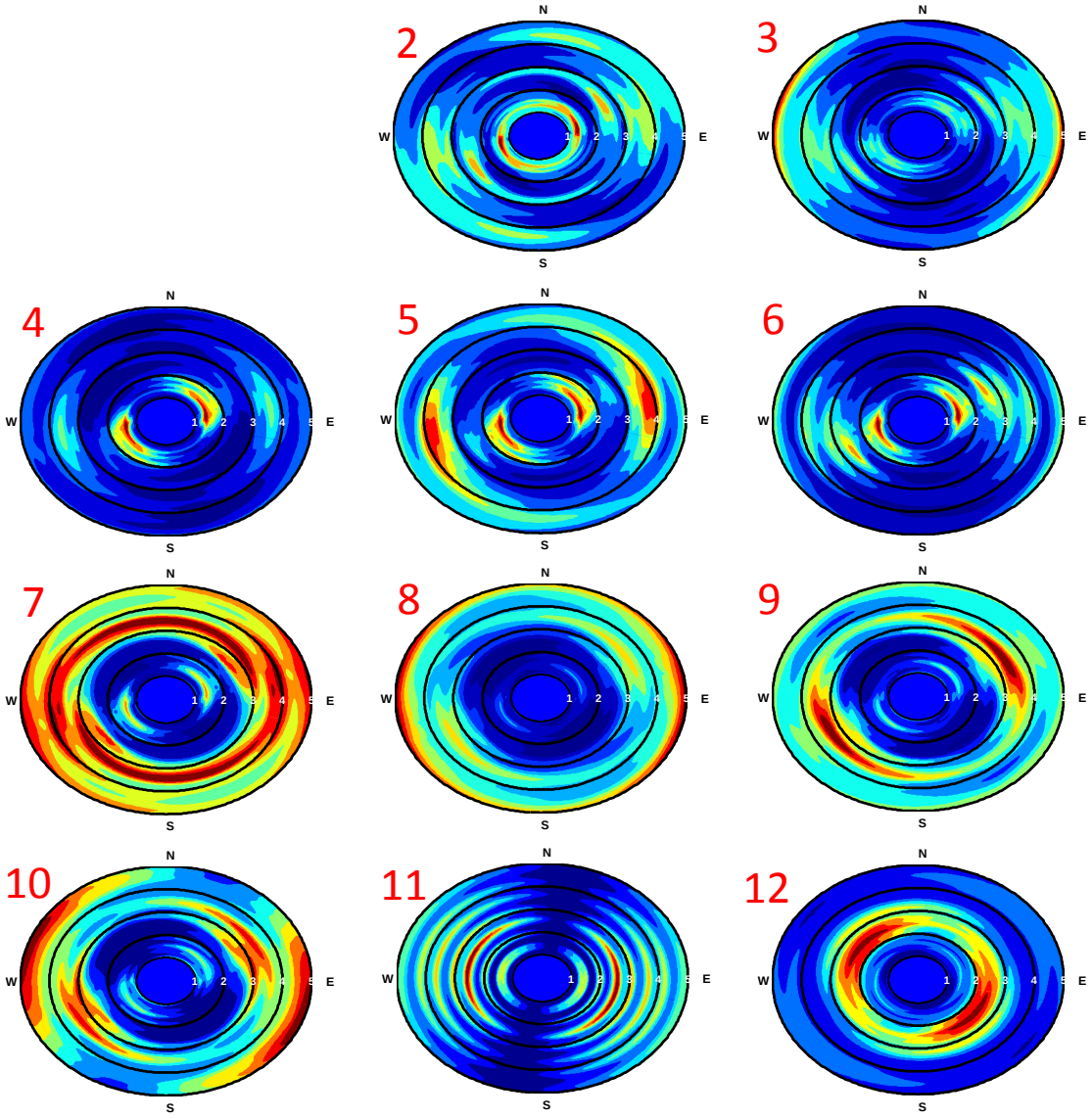

Figure 7.21: Horizontal polarity plots for the SSR method using the median response of the event catalog for Phase I (52 events). Station 1 used as the reference station.

of the presumed energy source (the underground longwall). Stations 11-12 had strong polarity in the opposite direction (SE-NW).

Overall, amplifications at the peak were calculated using the SSR method on both the N-S and E-W component in the estimated topographic frequency range. The

horizontal components of stations near the crest had a polarity that matched well with the direction of wave propagation from the presumed energy source. Topographic amplifications, in the N-S direction, occurred at 1.2-2.4 Hz, with a maximum amplification of 3. The E-W direction had amplifications in the estimated topographic frequency range from 1.1-1.9 Hz with a maximum amplification of 3.4. However, no significant amplifications were measured in vertical direction within the estimated topographic frequency range.

7.5.2 Median Reference Method (MRM)

The Median Reference Method (MRM) was used to analyze each recorded seismic event. The log-normal median spectral ratio of these events was then calculated for all 12 stations in the topographic array. A comparison of the log-normal medians for each station using MRM is shown in Figure 7.22. Comparing the vertical component of each station, no significant amplification peak was estimated in the topographic frequency range (~1-2.4 Hz). In the soil site effects frequency range (5-15 Hz), an amplification peak at 6.9 Hz was measured. However, it was likely caused by soil site effects and/or path effects.

For the North-South component, an amplification peak was measured from 1.2-2.4 Hz from the crest station (#5), with a maximum amplification of 2.0. A good pattern of amplification was seen on Stations 4 and 6, which had a 15% reduction in spectral ratio compared to Station 5. Stations 3 and 7 were also part of the pattern of amplification with a amplification of approximately 1.0. The other stations, in the topographic array, measured de-amplification (i.e., a spectral ratio less than 1.0) in the estimated topographic frequency range. Therefore, we can conclude that stations at the crest of the feature recorded amplification, while stations at the base of the feature

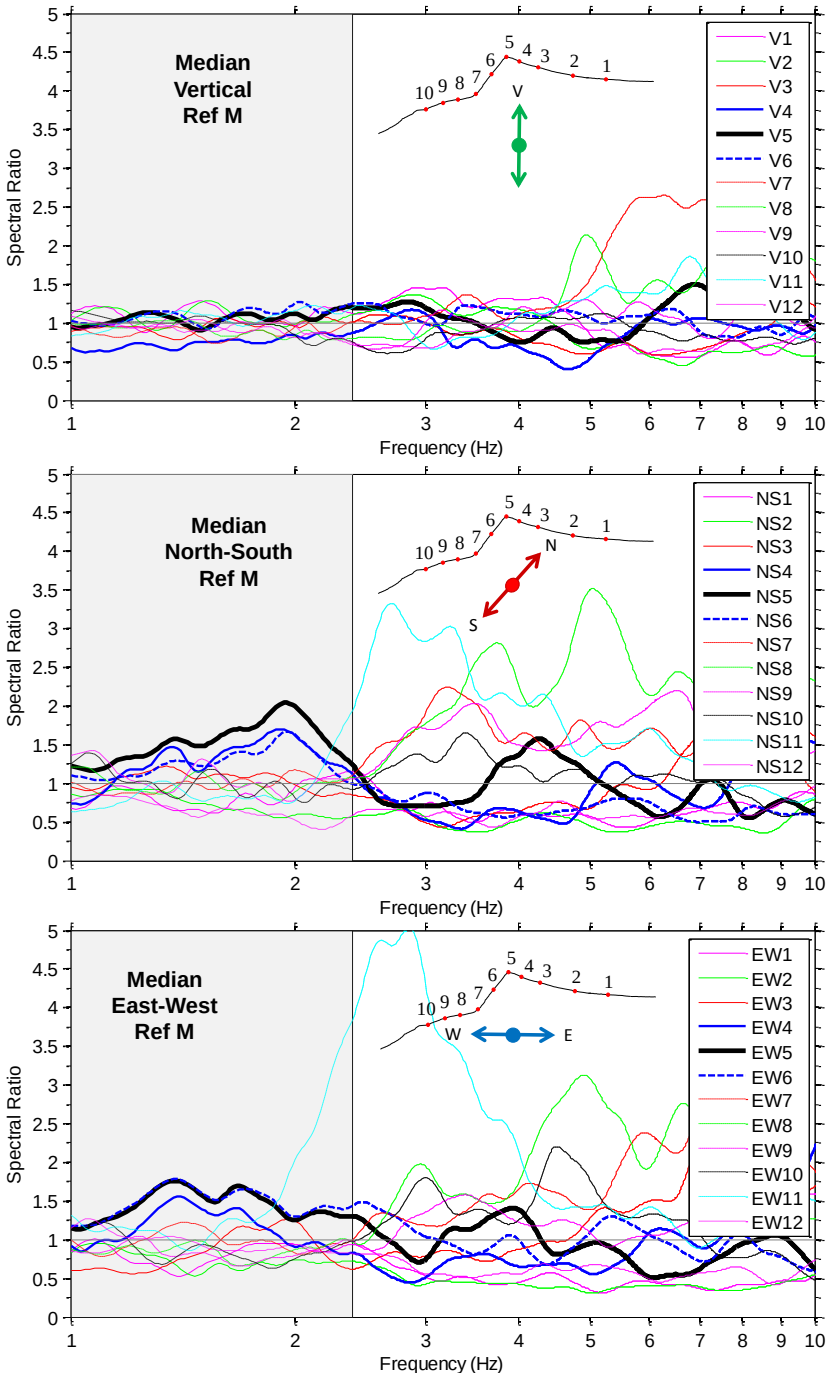

Figure 7.22: Median Reference Method (MRM) for the median of the Phase I event catalog (52 events) for the vertical, North-South, and East-West components of motion. The estimated topographic frequency range based on cross-section geometry and average shear wave velocity is shaded.

recorded de-amplification, and likely at some point along the slope, a cross over point was reached, where zero amplification occurred. At frequencies higher than the estimated topographic frequency range, stations on the back side of the ridge (i.e., 6-10) had amplifications, possibly due to path effects, and similar to that calculated using the SSR method.

For the East-West component, an amplification peak was calculated for Station 5, in the estimated topographic frequency range, from 1.1 to 1.9 Hz, with a maximum amplification of 1.8. Station 6 had an almost identical response compared to Station 5, in the estimated topographic frequency range, while Station 4 only had an 8% reduction in amplification compared to Station 5. Stations 3 and 7 had a poor pattern of amplification, but were still lower than that in amplification than Stations 4-6. The other stations in the array had a de-amplification, in the estimated topographic frequency range, similar to that calculated in the N-S direction. Station 11 had a large amplification at a frequency of 2.8 Hz, but as stated when analyzing event 17801, the cause of this amplification cannot be determined using the available data. At frequencies higher than the estimated topographic frequency range, random patterns of amplification occurred on all stations in the array except Stations 1 and 2, which indicated a de-amplification at all frequencies.

In Figure 7.23, a plot of the horizontal polarity of Stations 1-12 from 1 to 5 Hz for the MRM method is shown. Station 5 had a slight polarity in the NE-SW direction, while Station 4 had an N-S polarity, and Station 6 had an E-W polarity in the estimated topographic frequency range. Stations 1 and 2 had a slight NW-SE polarity and Station 11 had a strong E-W polarity. The other stations in the array do not have a significant polarity from 1-2.4 Hz.

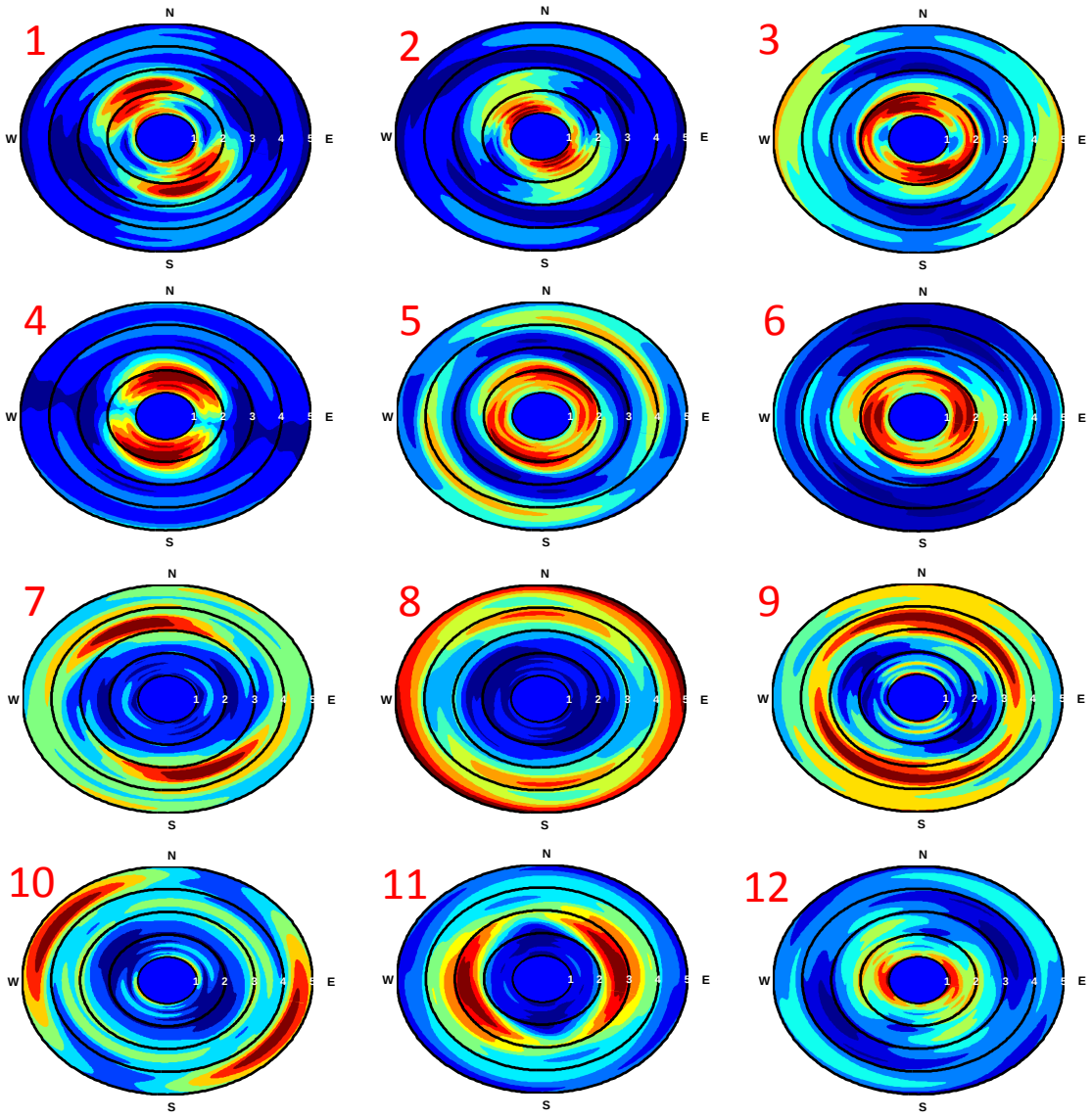

Figure 7.23: Horizontal polarity plots for the MRM method using the median response of the event catalog for Phase I (52 events).

Overall, amplifications at the crest were calculated using the MRM method, on both the N-S and E-W components in the estimated topographic frequency range. The horizontal components of the crest stations indicated only a slight polarity in NW-SE direction; however, other stations in the array did not have that polarity. Amplifications

occurred in the N-S direction at frequencies of 1.2-2.4 Hz, with a maximum amplification of 2.0. For the E-W direction, amplifications were measured from 1.1-1.9 Hz with a maximum amplification of 1.8. However, no amplifications were measured in vertical direction within the estimated topographic frequency range.

7.5.3 Horizontal to Vertical Spectral Ratio (HVSR)

The Horizontal to Vertical Spectral Ratio (HVSR) was used to analyze each recorded seismic event. The log-normal median spectral ratio of these events was then calculated for all 12 stations in the topographic array. A comparison of the log-normal medians for each station using HVSR method is shown in Figure 7.24.

For the North-South component of Station 5, an amplifications peak was measured, in the estimated topographic frequency range, from a frequency of 1.2 to 2.6 Hz, with a maximum amplification of 5.2. In the amplification range (i.e., 1.2 to 2.6 Hz), a major and minor amplification peak were measured, not just a single amplification peak. A good pattern of amplification was observed, for both peaks, on Station 4, with a 10-15% reduction in spectral ratio compared to Station 5. Station 6 had a 15-30% reduction, Station 7 a 20-40% reduction, and Station 2 with a 30-50% reduction in amplification compared to Station 5, which combined to produce a good pattern of amplification. At frequencies greater than 2.5 Hz, stations on the back side of the ridge (7-10) and Station 11 have significant H/V peaks at frequencies of 3-4 Hz, but a good pattern of amplification was not observed, and therefore the amplification is likely the result of path and/or soil site effects and not topographic effects.

Similar to the N-S component of Station 5, an amplification peak was measured in the E-W direction at frequencies of 1.3-2.9 Hz, with a maximum amplification of 4.9. Also like the N-S component, major and minor amplification peaks were observed in this

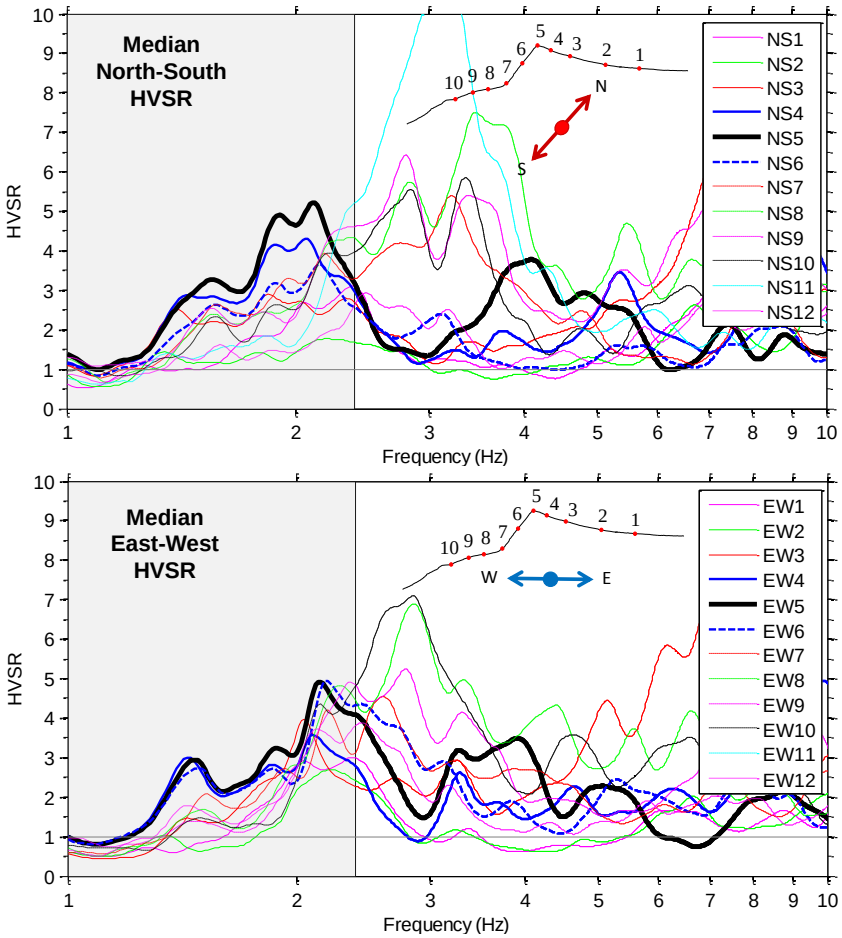

Figure 7.24: Horizontal to Vertical Spectral Ratio (HVSR) for the median of the Phase I event catalog (52 events) for the North-South, and East-West components of motion. The estimated topographic frequency range based on cross-section geometry and average shear wave velocity is shaded.

amplification range (i.e., 1.3-2.9 Hz). A good pattern of amplification was formed for the lower frequency amplification peak, with Station 4 and 6 having similar amplification values as Station 5. In addition, Stations 3 and 7 had a 40% and 20% reduction in amplification compared to Station 5, respectively. For the higher frequency amplification peak at approximately 2.1 Hz, Stations 6 had a similar spectral ratio to Station 5, and Station 4 had a 30% reduction in amplification compared to Station 5. Other stations in the array did not conform to the amplification pattern of the crest station. Therefore, the

higher frequency amplification peak may have been influenced by more than topographic effects.

In Figure 7.25, a plot of the horizontal polarity of Stations 1-12 from 1 to 5 Hz for the HVSR method is shown. Stations 1-3 and 5-6 had a strong polarity in the NW-SE direction, which is perpendicular to the presumed direction of propagation. Station 4 had a N-S polarity, while Stations 11 and 12 had a E-W to NE-SW polarity.

Overall, amplifications peaks were calculated at the crest of the feature using the HVSR method on both the N-S and E-W components, in the estimated topographic frequency range. Both directions indicated dual amplification peaks in the estimated topographic frequency range. For both components, the higher frequency peak had the highest amplification, but the lower frequency peak had the more defined pattern of amplification.

7.5.4 Method Comparison

All 52 events recorded in Phase I of the topographic effects study were analyzed using three separate methods to assess the effects of topography on the seismic response of the mountain. The log-normal medians of the 52 events for each station were then compared to assess whether amplifications measured in the frequency domain were caused by topographic effects. In Table 7.3, a summary of the topographic amplification range measured using each analysis method, along with the maximum amplification observed at the crest station in that same frequency range are provided. In addition, a comparison of the spectral ratios of Station 5 (the crest station) for the three methods is shown in Figure 7.26. Comparing the vertical components over the estimated topographic frequency range (~1-2.4 Hz), neither the SSR or MRM methods had a strong amplification in the vertical direction. The only amplification peak for both methods occurred at approximately 6.

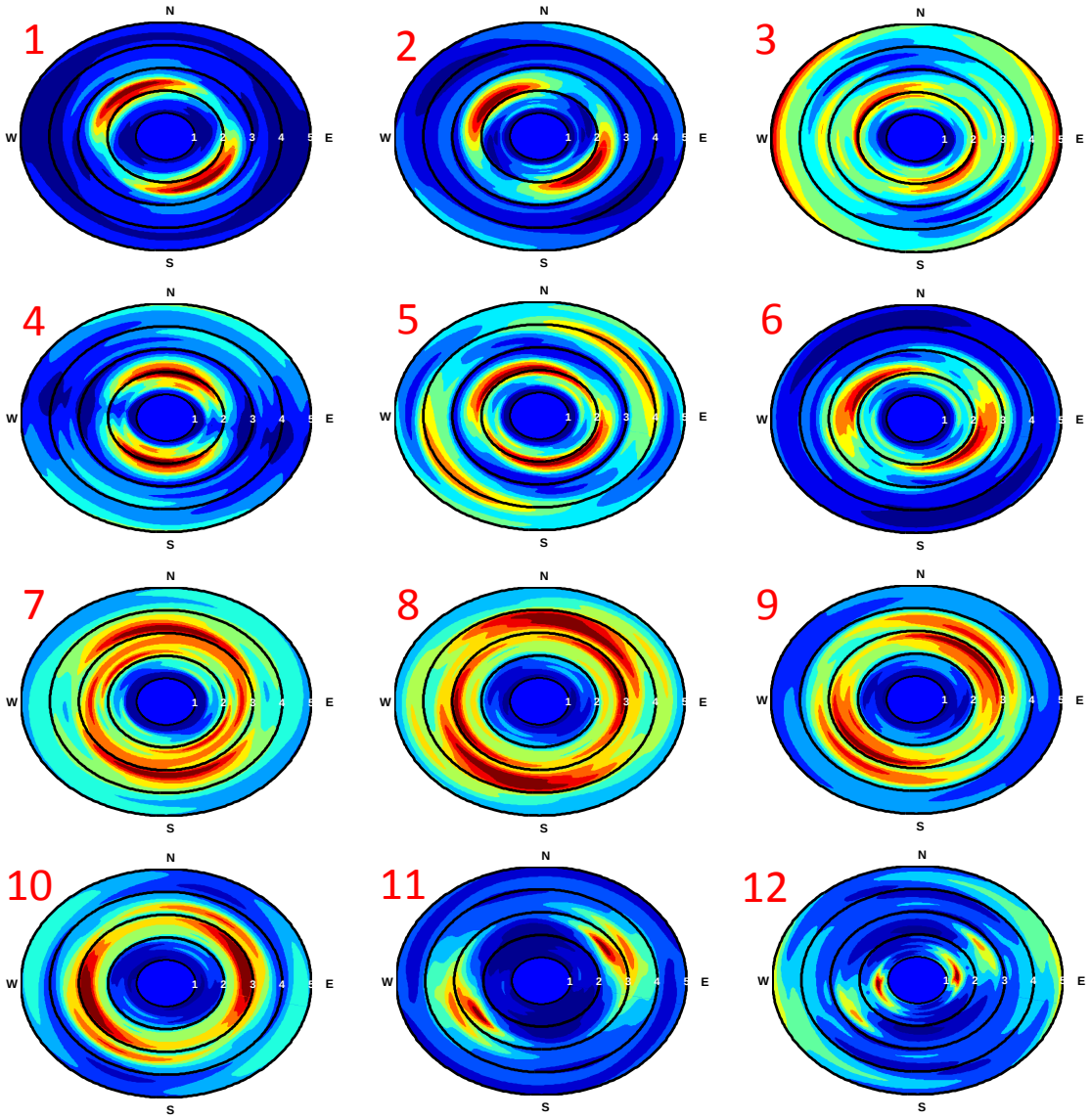

Figure 7.25: Horizontal polarity plots for the HVSR method using the median response of the event catalog for Phase I (52 events).

Hz, but this amplification is likely the result of soil site effects and not topographic effects.

Table 7.3: Summary of the topographic amplification frequency ranges for the median analysis of all three methods, and the maximum amplifications measured on the crest station within the same frequency range.

	Amplification Range (Hz)			Max Amplification		
Method	**V**	**N-S**	**E-W**	**V**	**N-S**	**E-W**
SSR	NA	1.2-2.4	1.1-1.9	NA	3	3.4
MRM	NA	1.2-2.4	1.1-1.9	NA	2	1.8
HVSR	NA	1.2-2.6	1.3-2.9	NA	5.2	4.9

For the North-South component, an amplification peak was identified using all three methods in the estimated topographic frequency range (~1-2.4 Hz). However, the shape and spectral ratio of the amplification peaks differed between methods. The amplification range for the three methods was approximately 1.2 Hz to between 2.4 and 2.6 Hz. The HVSR method had the highest spectral ratio at almost all frequencies, followed by the SSR method, and then the MRM method with the lowest amplification. Spectral ratios at 1.5 Hz for the HVSR, SSR, and MRM methods are 3.2, 2.6, and 1.6, respectively. The difference is even greater in the 1.9-2.1 Hz range, where each method has the highest amplification. The HVSR, SSR, and MRM methods had amplifications of 5.2, 2.9, and 2.0, respectively. An additional amplification peak was measured using each method at approximately 4 Hz. However, this peak is outside the estimated topographic frequency range, and acceptable patterns of amplification were not observed in early sections, where the response of the entire array of stations was compared. Therefore, the peaks at 4 Hz are likely the result of soil site effects or path effects and not topographic effects.

For the East-West component, a peak in the estimated topographic frequency range was measured using the SSR, MRM, and HVSR methods. An amplification peak

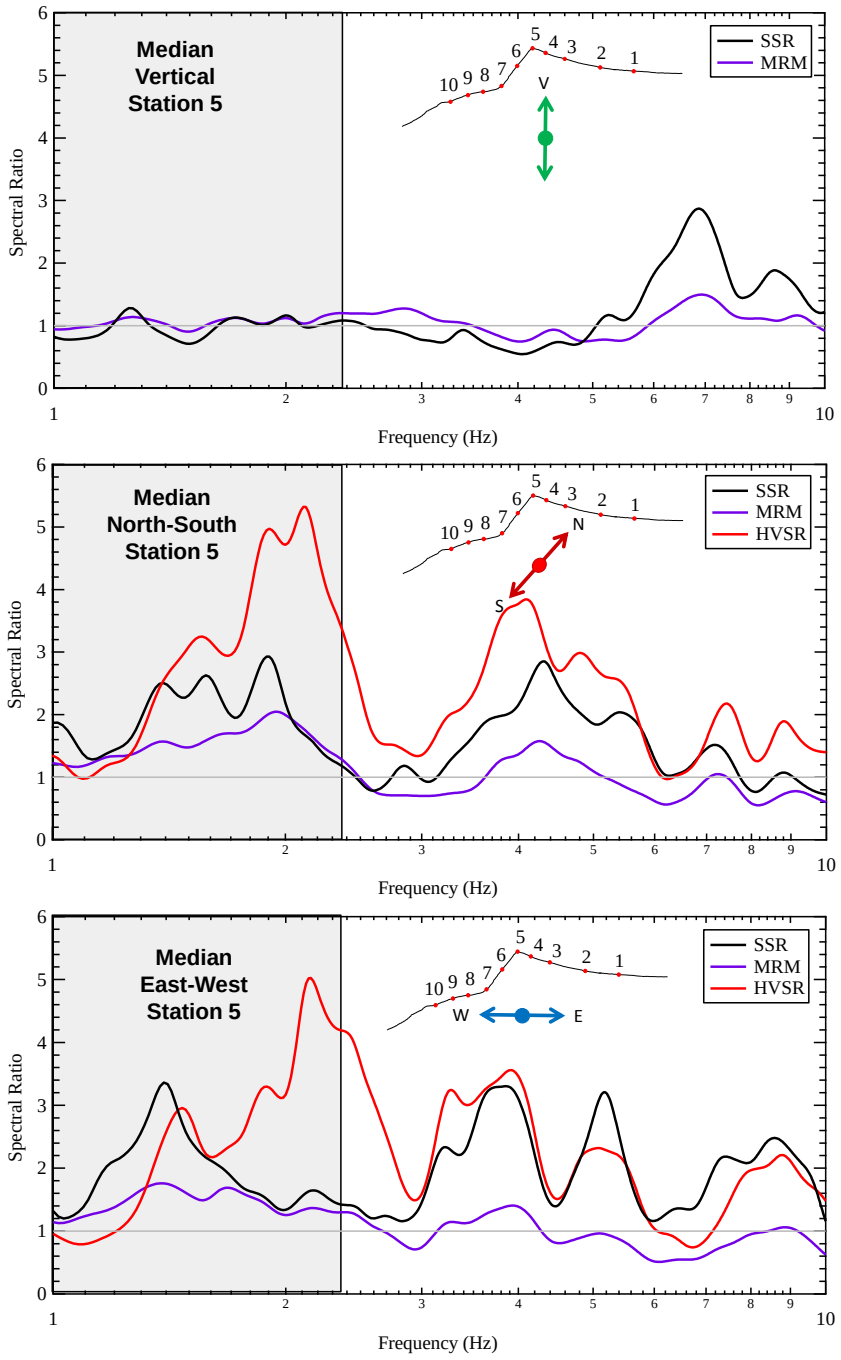

Figure 7.26: Comparison of the SSR, MRM, and HVSR results for the median response of all 52 events recorded during Phase I for the vertical, North-South, and East-West components of Station 5. The estimated topographic frequency range based on cross-section geometry and average shear wave velocity is shaded.

was measured using the SSR and MRM methods between 1.1 and 1.9 Hz, while the amplification peak was measured between 1.3 and 2.9 Hz for the HVSR method. The lower frequency peak (1.1-1.9 Hz) identified using the SSR and MRM methods was also identified using the HVSR method; however, a amplification peak was calculated using the HVSR method at between 1.8 and 2.9 Hz, which over shadowed the lower frequency peak. For the lower frequency peak, maximum amplifications of 3.4, 3.0, and 1.8 were calculated using SSR, HVSR, and MRM methods. However for the higher frequency peak, maximum amplifications of 4.9, 1.7, and 1.4 were calculated using the HVSR, SSR, and MRM methods. Therefore, for both peaks the MRM method had the lowest estimated amplification; however the overall maximum amplification for the two frequency peaks changed from the SSR method for the lower frequency peak to the HVSR method for the higher frequency peak. The higher frequency peak was only identified originally using the HVSR method and not on the SSR and MRM methods, even though the two methods still indicate an amplification at the crest of the feature. The reason the higher frequency peak was not identified using the SSR and MRM methods was because the pattern of amplification using both methods was poor above a frequency of 1.9 Hz. It is still unclear if the amplification should extend to frequencies above 1.9 Hz for the SSR and MRM methods, but given the evidence currently available the higher frequency amplification of the HVSR method was likely influenced at least in some part by soil site effects.

As with the analysis of event 17801, the log-normal median of all 52 events using the SSR method for Station 5 is plotted along with the log-normal median of all 52 events using the MRM method for Stations 5 and 1 (see Figure 7.27). For the vertical component, each curve shows little to no amplification from 1 to 2.4 Hz. For the North-South and East-West components from 1-2.4 Hz, a clear pattern emerges similar to that

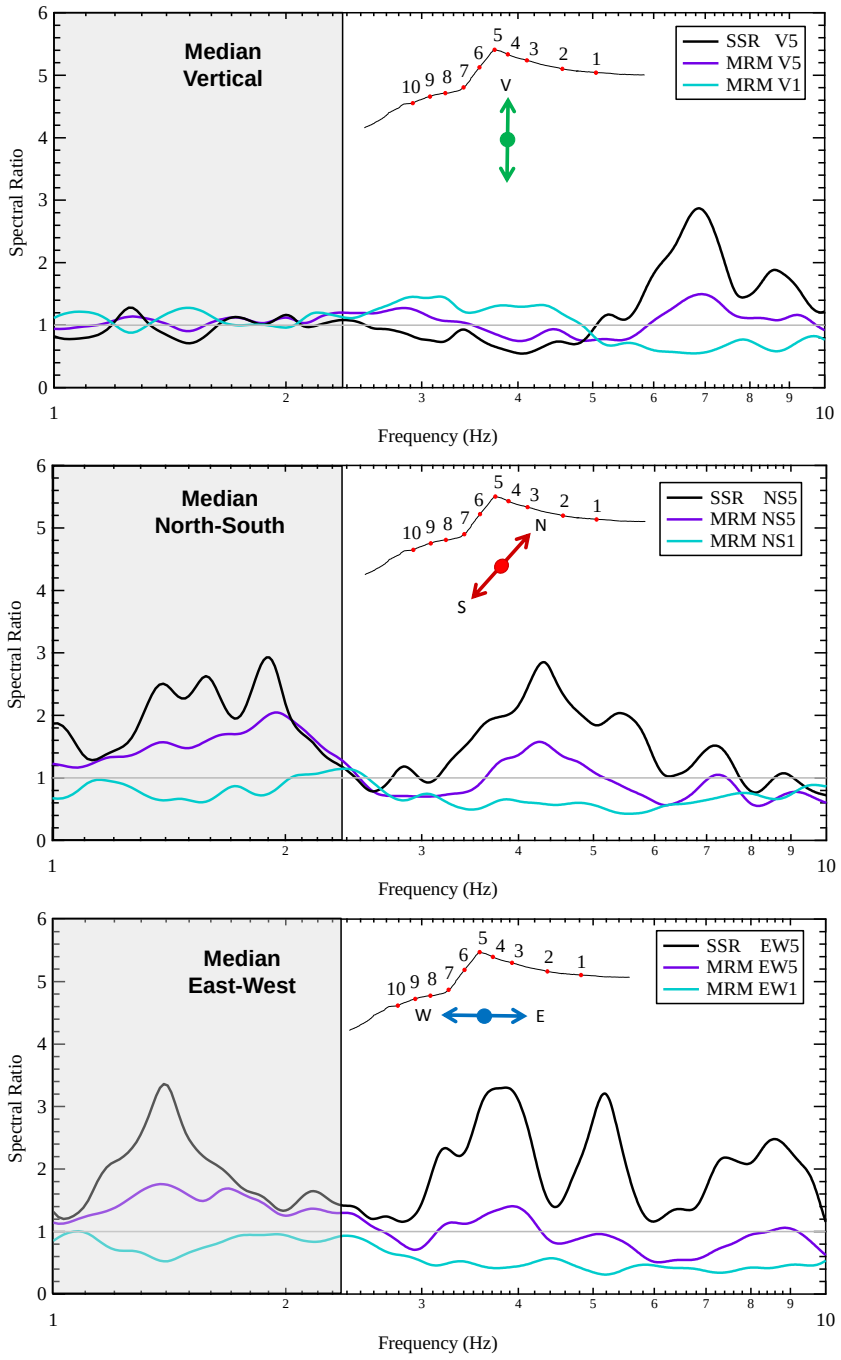

Figure 7.27: Comparison of SSR Station 5 with MRM from Station 5 and 1 results for median response of all 52 events recorded during Phase I for the vertical, North-South, and East-West components. The estimated topographic frequency range based on cross-section geometry and average shear wave velocity is shaded.

explained for event 17801, where Station 5 SSR has the highest spectral ratio followed by Station 5 MRM and final with a spectral ratio less than 1.0 for Station 1 MRM. If we assume that the MRM results in an amplification compared to the "average" response of the ridge, Station 5 is considered an amplification station and Station 1 a de-amplification station compared to the average ridge response. Therefore, when calculating the SSR at Station 5, an amplification station is divided by a de-amplification station thereby exaggerating the amplification of Station 5 to an unrealistic value. As a result the MRM method is believed to estimate the most accurate amplification factors for the experimental data.

7.6 SUMMARY AND DISCUSSION

In Phase I (2010), 52 seismic events were recorded by the topographic array in Central-Eastern Utah. To assess the effects of topographic amplification and the usefulness and accuracy of the SSR, MRM, and HVSR analysis methods, a single event (17801; M_L 1.2) was analyzed using the three analysis methods. The results from this single event were used to determine at what frequency range (s) a clear pattern of topographic amplification was apparent. The determinations of topographic amplification were aided by comparing the measured topographic frequencies against analytically estimated topographic frequencies calculated using methods Paolucci (2002) and Ashford and Sitar (1997). Within the estimated topographic frequency range (~1-2.4 Hz), each method resulted in amplification peaks at the crest of the feature in both the North-South (N-S) and East-West (E-W) directions for Event 17801. In addition, amplifications were calculated over the same frequency range for stations down the slope from the crest, ultimately forming a pattern of amplification, starting with the highest amplification at the crest and lower and lower amplification as elevation decreases. Although

amplifications were measured in the horizontal directions, no significant amplifications were observed in the vertical direction.

After Event 17801 was analyzed, each of the 52 events was analyzed together to determine if any time domain amplifications were apparent, and to assess the variability in the spectral estimates from event to event produced by each of the three spectral analyzes methods. In the time domain, no clear correlation could be established between the PGV calculated for each station and the station's topographic location. For the frequency domain, the events range in spectral amplitude over 3 log cycles, but the amplitudes stayed well within the linear strain range. Using all 52 events, a log-normal median and +/- 1 sigma were calculated for the results of the SSR, MRM, and HVSR methods. The individual events, the median, and the +/- 1 sigma values were compared, over the estimated topographic frequency range, for the crest station (#5) for the results of each method. For the SSR and HVSR methods, significant variability existed from event to event in terms of both the peak amplification frequency and the maximum amplification value. For the peak topographic amplification frequency, COV's from 0.38 to 0.93 were observed for the horizontal components of the SSR and HVSR methods. However, for the MRM method the variability from event to event was far lower, with many of the events having a very similar response as the median. As a result, COV's for the MRM were much lower, and varied from 0.13 to 0.19. This clearly indicated the spectral estimates of the MRM method were more stable than the SSR and HVSR methods and less prone to poor results if only a small number of events were available.

A comparison of the median values for each station (calculated using all 52 events) was then conducted using the SSR, MRM, and HVSR methods. Similar to the results of Event 17801, no significant amplifications were noticed in the topographic frequency range for the vertical components. However, amplifications were calculated for

crest station on both horizontal components. For the N-S component, similar amplification frequency ranges (1.2-2.4 Hz) were calculated for the SSR and MRM methods; however the maximum amplification at the crest varied from 3.0 to 2.0, respectively. A slightly higher amplification frequency range was observed using the HVSR method of 1.2-2.6 Hz, with a maximum amplification at the crest of 5.2. For the E-W component, the SSR and MRM methods again had similar topographic amplification frequency ranges (1.1-1.9 Hz), with a maximum amplification at the crest of 3.4 and 1.8, respectively. However, a wider amplification range was predicted using the HVSR method from 1.3 to 2.9 Hz, with a maximum amplification of 4.9. The higher frequency part of the amplification range of the HVSR method was likely influenced by soil site effects.

From analyzing the results from Phase I, the East Mountain ridge and instrumented peak were affected by topographic effects in a narrow frequency range, when seismic energy, from underground longwall coal mining, impinged upon the ridge. The mining seismicity provided enough energy in the narrow frequency band to produce topographic effects and provided a frequent source of energy to record many events within a short period of time. By using the results from the array of stations, it was clear that topographic effects were not only present at the crest of the feature, but along the slope and base of the feature. Typically, the highest amplification factors were measured at the peak of the feature and amplifications decreased as one moved down the slope. At some point down the slope, the amplification should reach a value equal to the "free-field" amplification, and as one moved lower in elevation the ground motions would be further and further attenuated until a minimum was reached at the base of the feature.

Overall, the empirical and analytical methods of Ashford and Sitar (1997) and Paolucci (2002) proved to be successful at estimating the topographic amplification

frequency. However, neither method was superior to the other. The Ashford and Sitar (1997) method typically predicted the higher range of amplified frequencies (i.e., 2.3-2.4 Hz), while Paolucci (2002) method typically predicted the lower frequency range of amplification (i.e., 0.87-1.99). Therefore, when used together the methods bracket the measured topographic effects frequency range.

The comparisons of the SSR, MRM, and HVSR methods indicated the MRM provided the most accurate and stable topographic amplification factors. Amplification factors of up to 2.0 were calculated over the narrow frequency range predicted by Ashford and Sitar (1997) and Paolucci (2002). Although the MRM method provided the best topographic amplification factors, similar amplification frequencies were calculated using the SSR method and in most cases the HVSR method. However, the amplification factors of these methods were significantly higher than those calculated using the MRM. In addition, the intra-event variability of the SSR and HVSR methods were greater than that of the MRM. Moreover, the HVSR method calculated amplification peaks in the topographic frequency range that the other two methods did not calculate leading to possible errors in identifying the topographic frequency range.

Chapter 8: Topographic Study Results: Phase II (2011)

8.1 INTRODUCTION

In Phase II (2011), an array of 22 broadband and intermediate period sensors, along with 5 short period geophones, were deployed in a dense array over significant topography. The instruments recorded 52 seismic events ("earthquakes") produced by underground longwall coal mining directly under the topographic array. These seismic events were processed using a standard ground motion processing scheme, and analyzed for topographic effects using three methods: Standard Spectral Ratio (SSR), Median Reference Method (MRM), and Horizontal to Vertical Spectral Ratio (HVSR). A directional analysis was also performed on the results of each method to assess the polarity of the amplification. To assess the usefulness and accuracy of each analysis method, along with determining the effect of topographic amplification on the mountain, a single M_L 1.6 seismic event (200.19.5) was first analyzed, using all three methods. Each topographic cross section/line (A, B, and V) was analyzed independently using each method, resulting in spectral ratios and horizontal energy polarity plots for each station in the array. The analysis was then extended to include all 52 events. The calculated spectral ratios for each event were compared for crest stations (A7, B6, and B3) of each cross section/line (A, B, and V), using each of the three methods. In addition to the spectral ratios for each event, a log normal median and +/- 1 sigma were calculated for the entire event catalog. Finally, the median response of the stations in lines A, B, and C were compared for each of the three methods, and the results from each method were compared.

8.2 RECORDED EVENTS

In Phase II (2011), seismic signals were recorded continuously from July 8, 2011 until July 21, 2011. During that time, many small, medium, and large events were recorded by the instrumentation. However, only 52 of the largest events were identified as meeting all the criteria established in Chapter 4. These 52 events were included in the recorded events catalog for Phase II. The recorded seismic events for Phase II are identified in Table 8.1 in UTC time, and in Table 8.2 in local time (Mountain Daylight Savings time). The times listed in Tables 8.1 and 8.2 do not represent the origin time of the events, but the time of the Peak Ground Velocity (PGV) for the vertical component of Station A1. However, the listed event times are likely within 5 seconds of the origin time of each event. Of the 52 events classified in Phase II, only two events were identified by the University of Utah Seismograph Stations (UUSS) as earthquakes. These events were 197.18.50 and 200.19.5, which had estimated magnitudes of M_L 1.3 and M_L 1.6, respectively. All other events are believed to have local magnitudes of 1.0 or less.

A rate of occurrence plot is shown in Figure 8.1, where the cumulative number of recorded events is plotted versus the time each event was recorded. The rate of occurrence, plotted as events per day, has five clear sections. The first section, starting just after the beginning of recording (7/11), has a rate of occurrence of only one event per day. However, the rate picks up on 7/13 to seven events per day, and stays at this rate until 7/17. On 7/17, the rate drops to 1.5 events per day for approximately one and half days, then picks back up to approximately 12 events per day, and finally levels off to 5 events per day on 7/20. As with Phase I, these increases and decreases in the occurrence rate can be tied to the activity of the longwall during recording. However, the connection between the calendar days and occurrence rate is not as conclusive during Phase II as noticed in Phase I. In 2011, weekend days (Saturday and Sunday) occurred on July 9, 10,

Table 8.1: Seismic events identified during Phase II (2011) in UTC.

Event #	Filename	UTC Date	UTC Time	Event #	Filename	UTC Date	UTC Time
1	192.19.3	7/11/2011	19:03	27	198.7.25	7/18/2011	7:25
2	193.8.59	7/12/2011	8:59	28	199.16.38	7/18/2011	16:38
3	194.18.37	7/13/2011	18:37	29	199.19.26	7/18/2011	19:26
4	194.21.19	7/13/2011	21:19	30	199.19.54	7/18/2011	19:54
5	195.2.31	7/14/2011	2:31	31	200.0.2	7/19/2011	0:02
6	195.3.33	7/14/2011	3:33	32	200.0.47	7/19/2011	0:47
7	195.7.5	7/14/2011	7:05	33	200.3.23	7/19/2011	3:23
8	195.17.47	7/14/2011	17:47	34	200.4.10	7/19/2011	4:10
9	195.19.59	7/14/2011	19:59	35	200.5.58	7/19/2011	5:58
10	196.3.41	7/15/2011	3:41	36	200.6.36	7/19/2011	6:36
11	196.3.53	7/15/2011	3:53	37	200.6.44	7/19/2011	6:44
12	196.4.22	7/15/2011	4:22	38	200.6.52	7/19/2011	6:52
13	196.7.53	7/15/2011	7:53	39	200.8.58	7/19/2011	8:58
14	196.11.26	7/15/2011	11:26	40	200.16.58	7/19/2011	16:58
15	196.17.6	7/15/2011	17:06	41	200.19.5	7/19/2011	19:05
16	196.18.54	7/15/2011	18:54	42	200.19.15	7/19/2011	19:15
17	196.21.49	7/15/2011	21:49	43	200.20.45	7/19/2011	20:45
18	196.22.51	7/15/2011	22:51	44	201.1.29	7/20/2011	1:29
19	197.0.31	7/16/2011	0:31	45	201.1.32	7/20/2011	1:32
20	197.2.33	7/16/2011	2:33	46	201.3.22	7/20/2011	3:22
21	197.8.35	7/16/2011	8:35	47	201.8.43	7/20/2011	8:43
22	197.18.50	7/16/2011	18:50	48	201.14.18	7/20/2011	14:18
23	197.21.27	7/16/2011	21:27	49	201.21.13	7/20/2011	21:13
24	197.23.14	7/16/2011	23:14	50	201.21.45	7/20/2011	21:45
25	198.0.25	7/17/2011	0:25	51	202.3.44	7/21/2011	3:44
26	198.7.15	7/17/2011	7:15	52	202.4.15	7/21/2011	4:15

16, and 17. The decrease in the rate of events for Phase II seems to be delayed, and occurs approximately a day after mining is stopped for the weekend and doesn't pick back up until approximately a day after mining has been resumed. With the limited data set and without further investigation, it is unclear why the delay is occurring, but it does not affect the results of this experiment. Therefore, the delay will not be investigated any further.

Table 8.2: Seismic events identified during Phase II (2011) in local time (Mountain daylight savings time).

Event #	Filename	Local Date	Local Time	Event #	Filename	Local Date	Local Time
1	192.19.3	7/11/2011	13:03	27	198.7.25	7/18/2011	1:25
2	193.8.59	7/12/2011	2:59	28	199.16.38	7/18/2011	10:38
3	194.18.37	7/13/2011	12:37	29	199.19.26	7/18/2011	13:26
4	194.21.19	7/13/2011	15:19	30	199.19.54	7/18/2011	13:54
5	195.2.31	7/13/2011	20:31	31	200.0.2	7/18/2011	18:02
6	195.3.33	7/13/2011	21:33	32	200.0.47	7/18/2011	18:47
7	195.7.5	7/14/2011	1:05	33	200.3.23	7/18/2011	21:23
8	195.17.47	7/14/2011	11:47	34	200.4.10	7/18/2011	22:10
9	195.19.59	7/14/2011	13:59	35	200.5.58	7/18/2011	23:58
10	196.3.41	7/14/2011	21:41	36	200.6.36	7/19/2011	0:36
11	196.3.53	7/14/2011	21:53	37	200.6.44	7/19/2011	0:44
12	196.4.22	7/14/2011	22:22	38	200.6.52	7/19/2011	0:52
13	196.7.53	7/15/2011	1:53	39	200.8.58	7/19/2011	2:58
14	196.11.26	7/15/2011	5:26	40	200.16.58	7/19/2011	10:58
15	196.17.6	7/15/2011	11:06	41	200.19.5	7/19/2011	13:05
16	196.18.54	7/15/2011	12:54	42	200.19.15	7/19/2011	13:15
17	196.21.49	7/15/2011	15:49	43	200.20.45	7/19/2011	14:45
18	196.22.51	7/15/2011	16:51	44	201.1.29	7/19/2011	19:29
19	197.0.31	7/15/2011	18:31	45	201.1.32	7/19/2011	19:32
20	197.2.33	7/15/2011	20:33	46	201.3.22	7/19/2011	21:22
21	197.8.35	7/16/2011	2:35	47	201.8.43	7/20/2011	2:43
22	197.18.50	7/16/2011	12:50	48	201.14.18	7/20/2011	8:18
23	197.21.27	7/16/2011	15:27	49	201.21.13	7/20/2011	15:13
24	197.23.14	7/16/2011	17:14	50	201.21.45	7/20/2011	15:45
25	198.0.25	7/16/2011	18:25	51	202.3.44	7/20/2011	21:44
26	198.7.15	7/17/2011	1:15	52	202.4.15	7/20/2011	22:15

As detailed in Chapter 4, the hypocenter for each event recorded during Phase II was located using the software package Hypoellipse. The locations (x, y, and z) for each of the 52 events recorded during Phase II are tabulated in Table 8.3 and shown in Figure 8.2. Events highlighted in Table 8.3 were not used to calculate the average hypocenter location because the events were located outside/above the topography or at some other clearly incorrect location. The vast majority of the events were located directly above the

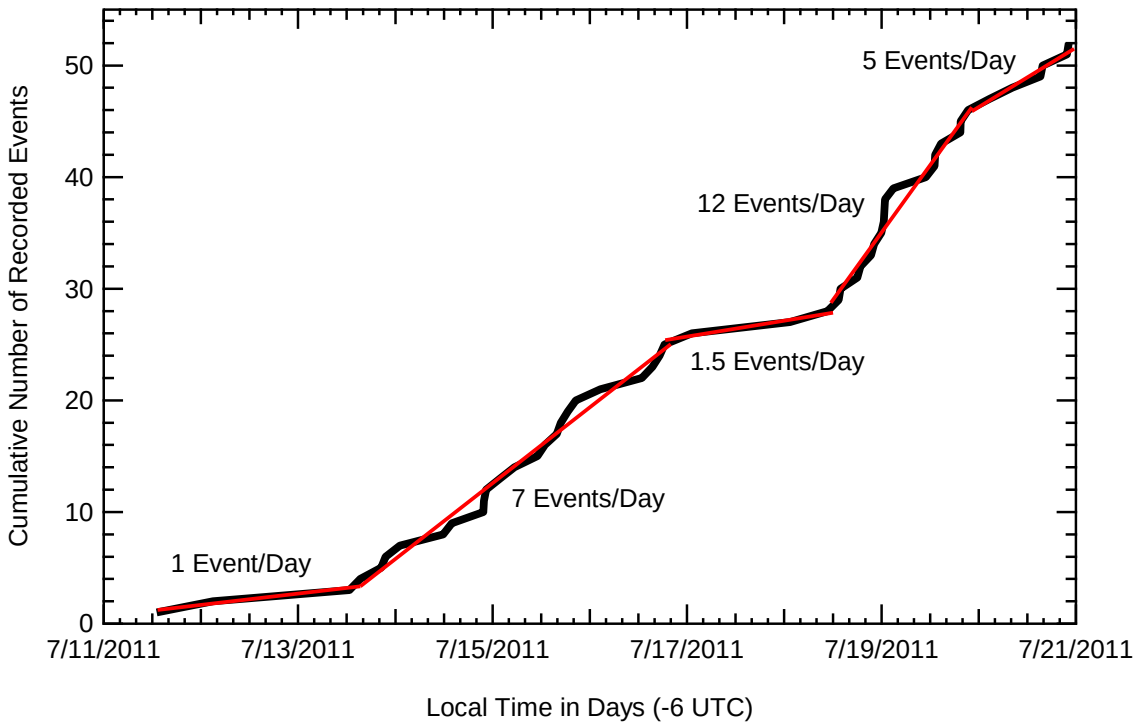

Figure 8.1: Rate of occurrence of seismic events during Phase II (2011).

location of the longwall during recording. Two tails of events extended out from the longwall to the West. These tails lined up well with the previous location of the longwall before recording was initiated. The events are color coded in Figure 8.2 according to when the events were recorded (i.e., lighter events occurred earlier in time and darker events occurred later in time). As presumed, the events got darker from West to East, due to the longwall moving from West-East during recording, and the event hypocenters being located further and further to the East as time passed. An average hypocenter for the recorded events was calculated to be in the center of the main cluster of events. The location of the average hypocenter is provided in Table 8.4. For further information about the average hypocenter refer to Chapter 4.

Table 8.3: Hypocenter location for all 52 events recorded during Phase II (2011). Events highlighted were not used to determine the average hypocenter location.

Event #	Filename	Latitude	Longitude	Elevation (m)	Event #	Filename	Latitude	Longitude	Elevation (m)
1	192.19.3	39.4393	-111.2228	2740	27	198.7.25	39.4405	-111.2262	2670
2	193.8.59	39.4373	-111.2230	2710	28	199.16.38	39.4403	-111.2252	2700
3	194.18.37	39.4373	-111.2233	3020	29	199.19.26	39.4373	-111.2233	2720
4	194.21.19	39.4372	-111.2233	2960	30	199.19.54	39.4373	-111.2222	2730
5	195.2.31	39.4398	-111.2227	2710	31	200.0.2	39.4375	-111.2218	2710
6	195.3.33	39.4373	-111.2232	2700	32	200.0.47	39.4398	-111.2220	2710
7	195.7.5	39.4375	-111.2227	2710	33	200.3.23	39.4395	-111.2220	2700
8	195.17.47	39.4402	-111.2243	2710	34	200.4.10	39.4382	-111.2215	2720
9	195.19.59	39.4397	-111.2225	2730	35	200.5.58	39.4373	-111.2245	2740
10	196.3.41	39.4397	-111.2227	2760	36	200.6.36	39.4372	-111.2228	2710
11	196.3.53	39.4375	-111.2225	2730	37	200.6.44	39.4383	-111.2217	2720
12	196.4.22	39.4382	-111.2223	2710	38	200.6.52	39.4387	-111.2215	2730
13	196.7.53	39.4398	-111.2233	2720	39	200.8.58	39.4373	-111.2218	2710
14	196.11.26	39.4373	-111.2223	2730	40	200.16.58	39.4380	-111.2218	2780
15	196.17.6	39.4373	-111.2225	2770	41	200.19.5	39.4373	-111.2222	2760
16	196.18.54	39.4360	-111.2220	2880	42	200.19.15	39.4372	-111.2255	2750
17	196.21.49	39.4373	-111.2225	2770	43	200.20.45	39.4393	-111.2213	2730
18	196.22.51	39.4375	-111.2225	2710	44	201.1.29	39.4375	-111.2217	2720
19	197.0.31	39.4362	-111.2223	2810	45	201.1.32	39.4397	-111.2220	2720
20	197.2.33	39.4407	-111.2282	2680	46	201.3.22	39.4373	-111.2223	2710
21	197.8.35	39.4398	-111.2230	2730	47	201.8.43	39.4372	-111.2215	2700
22	197.18.50	39.4405	-111.2182	3220	48	201.14.18	39.4375	-111.2120	2670
23	197.21.27	39.4372	-111.2225	2670	49	201.21.13	39.4375	-111.2233	2720
24	197.23.14	39.4397	-111.2225	2710	50	201.21.45	39.4373	-111.2217	2720
25	198.0.25	39.4373	-111.2227	2720	51	202.3.44	39.4387	-111.2300	2730
26	198.7.15	39.4402	-111.2257	2700	52	202.4.15	39.4393	-111.2215	2740

In Figure 8.3, a map view of the Phase II (2011) array is shown with cross sections A-A', B-B', and C-C' indicated. Cross sections A-A' and B-B' extend from West to East across the topography and cross section C-C' extends from North to South. The location of the average hypocenter and the longwall are also indicated. The average hypocenter location and longwall location during recording are also indicated in Figures 8.4, 8.5, and 8.6 for cross sections A-A', B-B', and C-C', respectively. The average hypocenter is approximately 325 meters above the longwall and near the western edge of the working longwall. Station V2 was only 150 m above (190 m ray path) the average hypocenter, while Station B6 was approximately 530 m above the average hypocenter

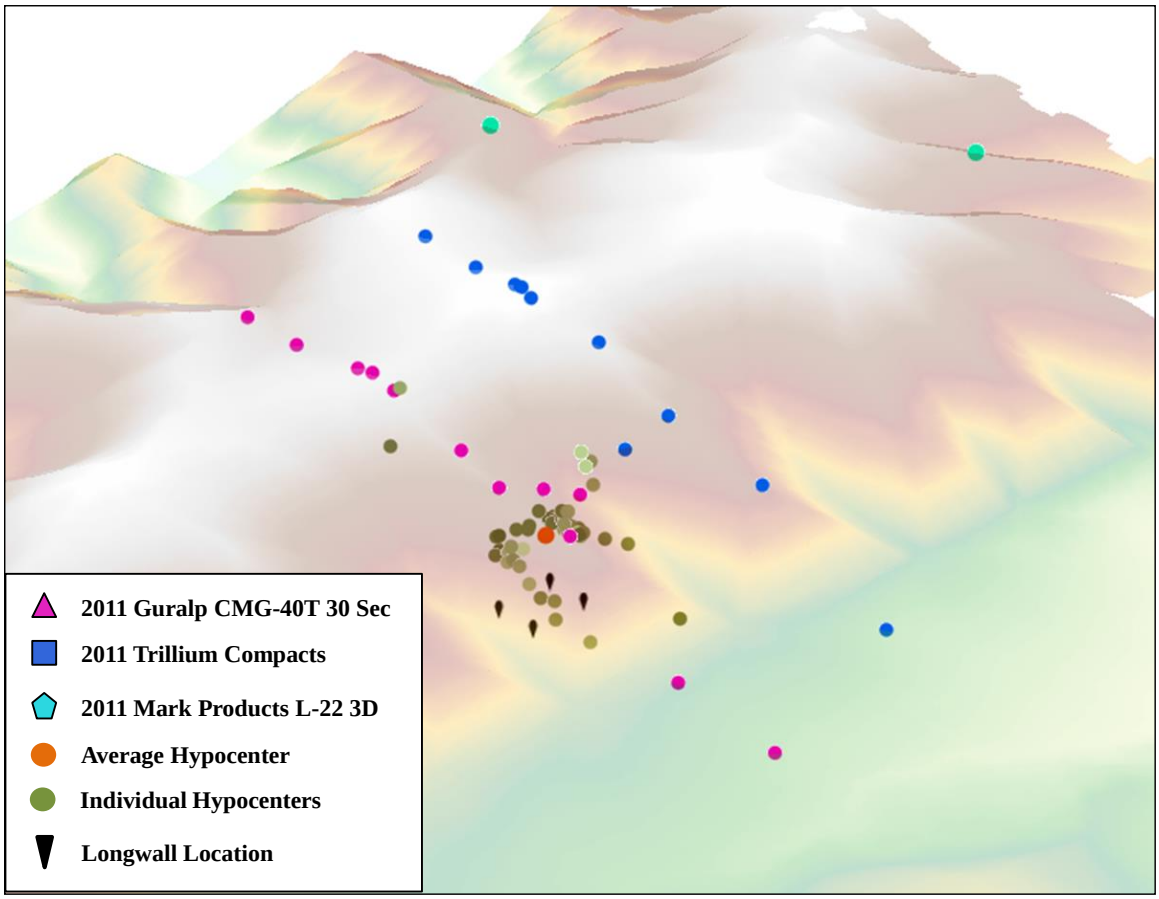

Figure 8.2: Hypocenter locations during Phase II (2011) showing both individual hypocenters and the average hypocenter. For individual hypocenters, light green represents early events and dark green represents later events.

location. This large difference in hypocenter distances highlights the need to correct for geometric attenuation to insure proper estimation of amplification factors for various stations in the array.

For cross sections A-A', B-B', and C-C' (lines A, B, and C) topographic amplification is expected at the crest of the topographic features. Therefore for the A-line, topographic amplifications are expected for Stations A7, and possibly other stations

Table 8.4: Average hypocenter location for events recorded in Phase II (2011).

Event	Latitude	Longitude	Elevation (m)
Average	39.4382	-111.2225	2724

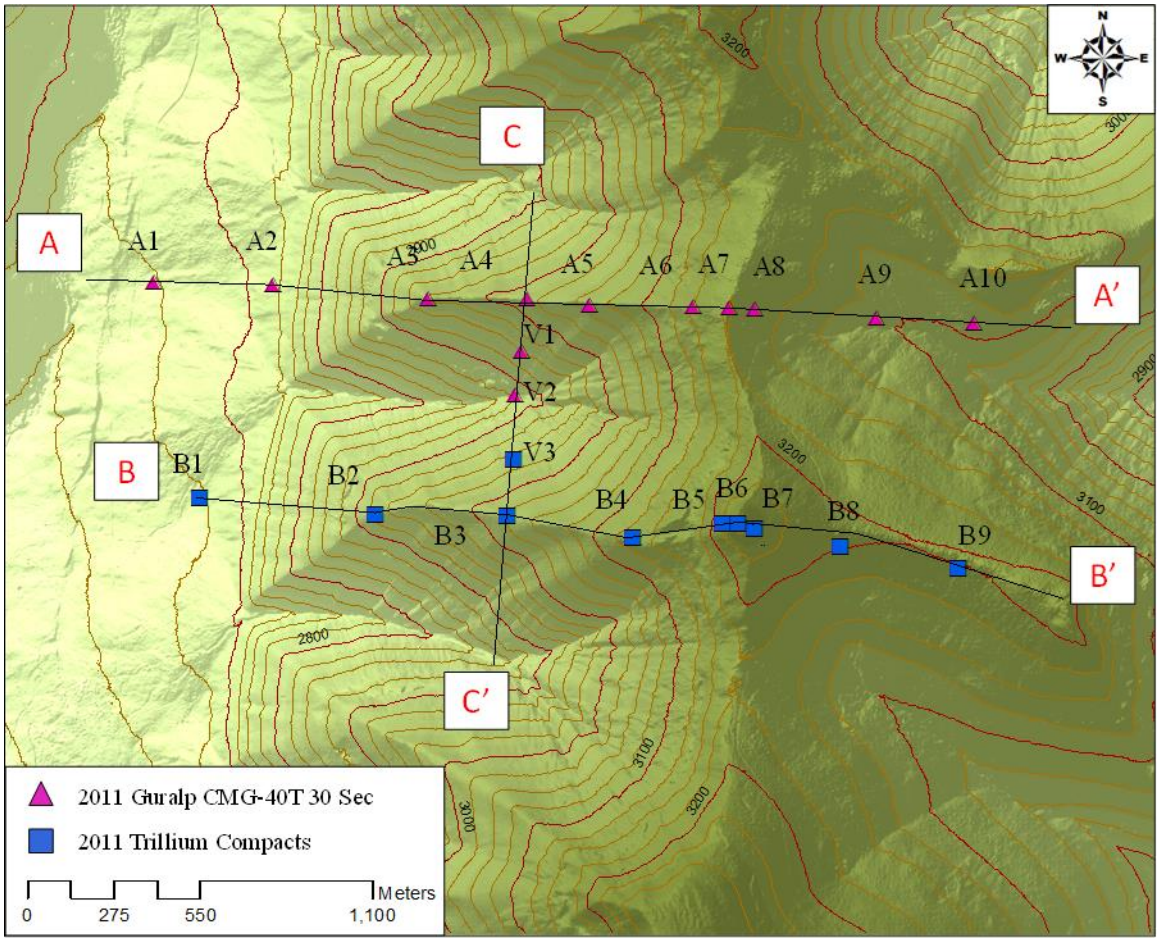

Figure 8.3: Map view of topographic array during Phase II (2011) with cross sections A-A', B-B', and C-C' along with the average hypocenter location.

down the slope from Station A7 (i.e., Stations A5-A6 and A8-A9). For line B, topographic amplifications are expected for Station B6 at the crest, and possibly stations down the slope from Station B6 (i.e., Stations B4-B5 and B7-B8). For the V line,

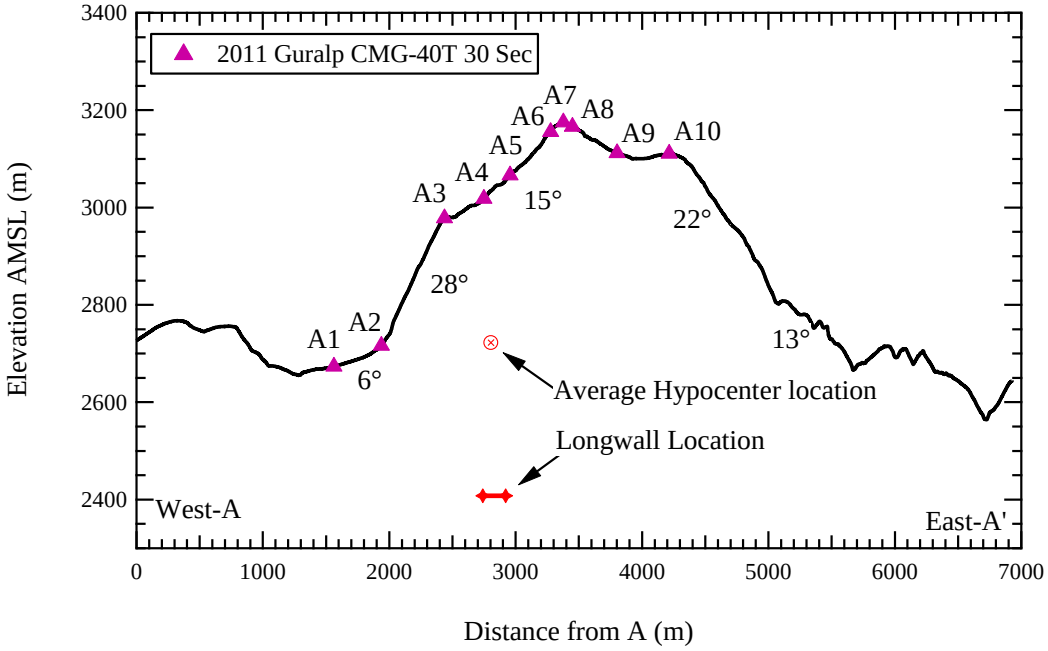

Figure 8.4: Cross section A-A' for Phase II (2011) with longwall and average hypocenter location shown.

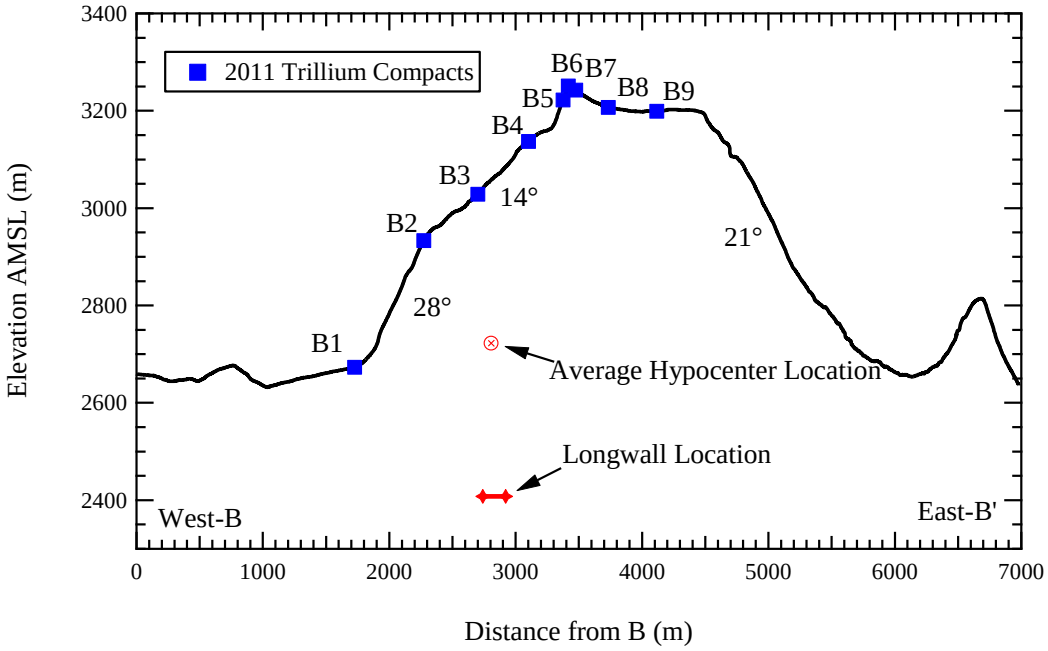

Figure 8.5: Cross section B-B' for Phase II (2011) with longwall and average hypocenter location shown.

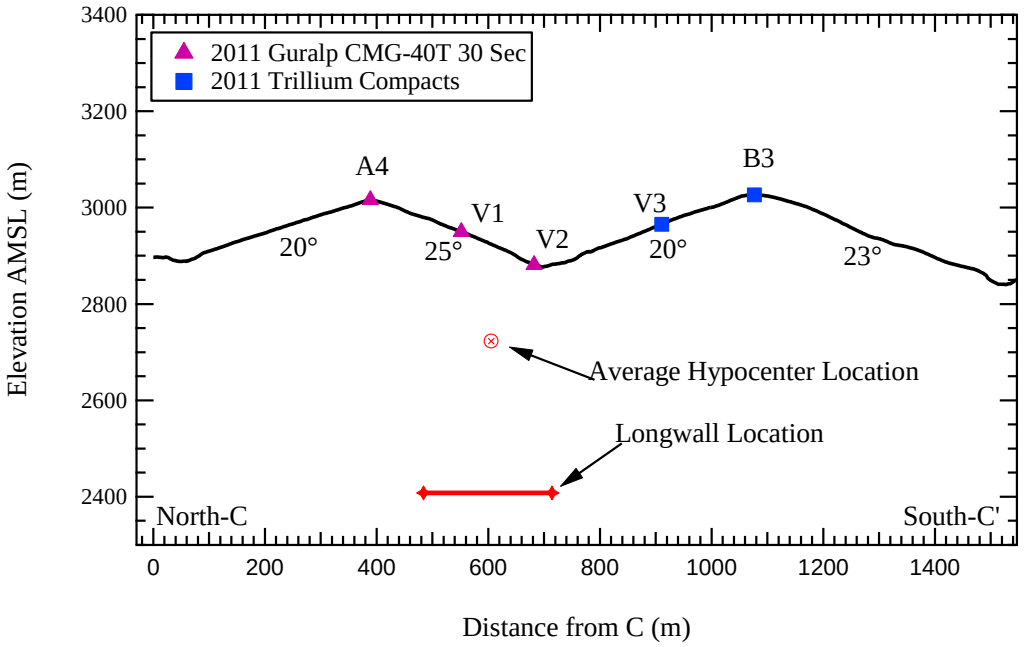

Figure 8.6: Cross section C-C' for Phase II (2011) with longwall and average hypocenter location shown.

topographic amplifications are expected for Stations A4 and B3, and possibly Stations V1 and V3, which are located along the slope under Stations A4 and B3, respectively.

In addition to cross sections A-A', B-B', and C-C', smaller cross sections were taken in the direction perpendicular to the three main cross sections for each station. Those cross sections are shown in Figure 8.7. The sub-cross sections are paired together according to their associated main cross section (i.e., sub-cross sections for stations A1-A10 are paired together as part of the A-line cross sections). North-South sub-cross sections for line A (A1-A10) are shown in Figure 8.8. Each sub-cross section is started at the same Northing value and continues due South, for a total horizontal distance of 900 m. The N-S sub-cross sections for Stations A3-A5 indicate steep N-S topographic relief under the stations, while the other stations in line A are relatively flat in the N-S direction. Therefore, topographic amplification can be expected for Stations A3-A5 in the

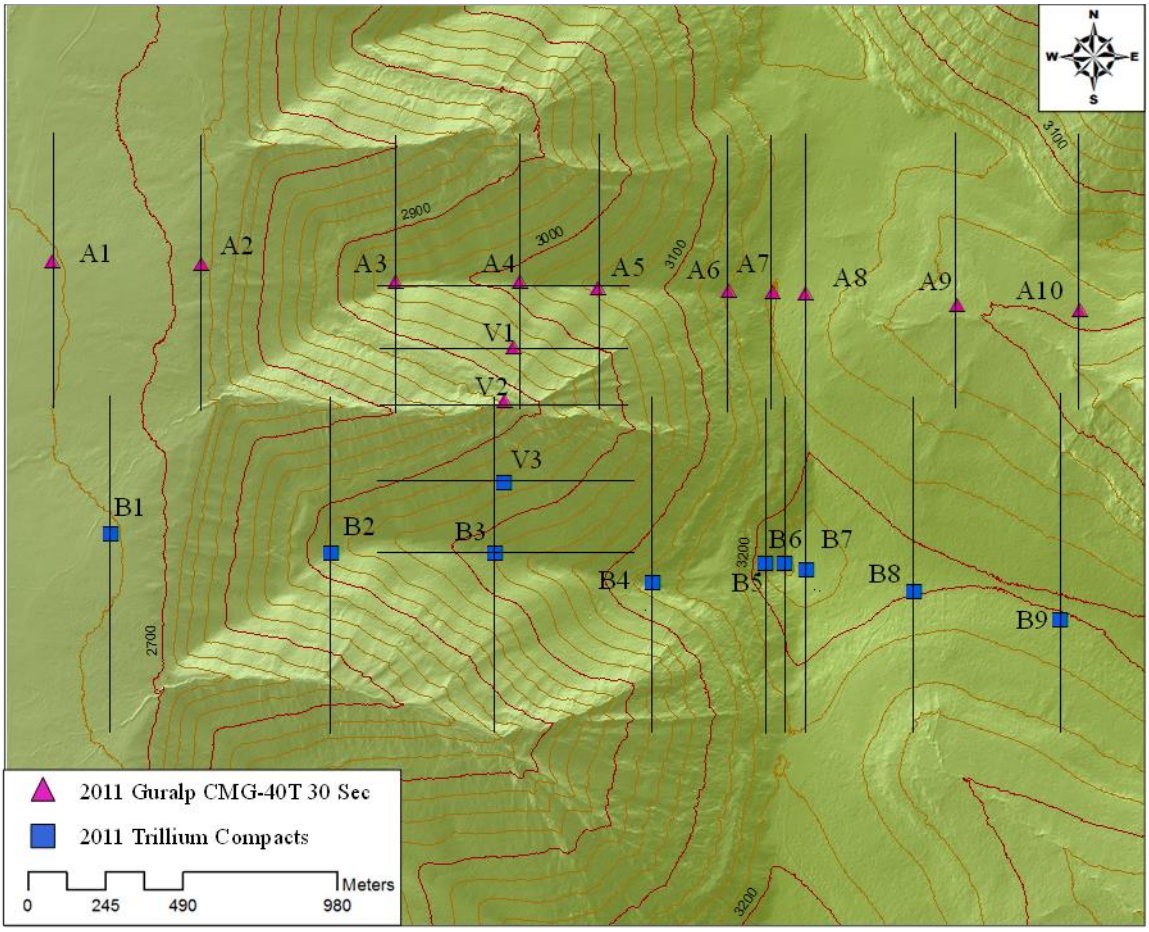

Figure 8.7: Map view of topographic array during Phase II (2011) with sub-cross sections for the A, B, and C lines shown.

N-S direction. As with sub-cross sections for the A line, North-South sub-cross sections for line B (B1-B9) are shown in Figure 8.9. Each sub-cross section of the B line is started at the same Northing value and continues due South, for a total horizontal distance of 900 m. The N-S sub-cross sections for Stations B2-B4 indicate steep N-S topographic relief under Stations B2-B4, similar to Stations A3-A5 in the A line. Stations B5-B9 have some N-S topographic relief, but the slope angles are approximately 10 degrees compared to the 20 degree slopes for the N-S topographic relief under Stations B2-B4. Therefore, topographic amplification can be expected for Stations B2-B4 in the N-S direction with

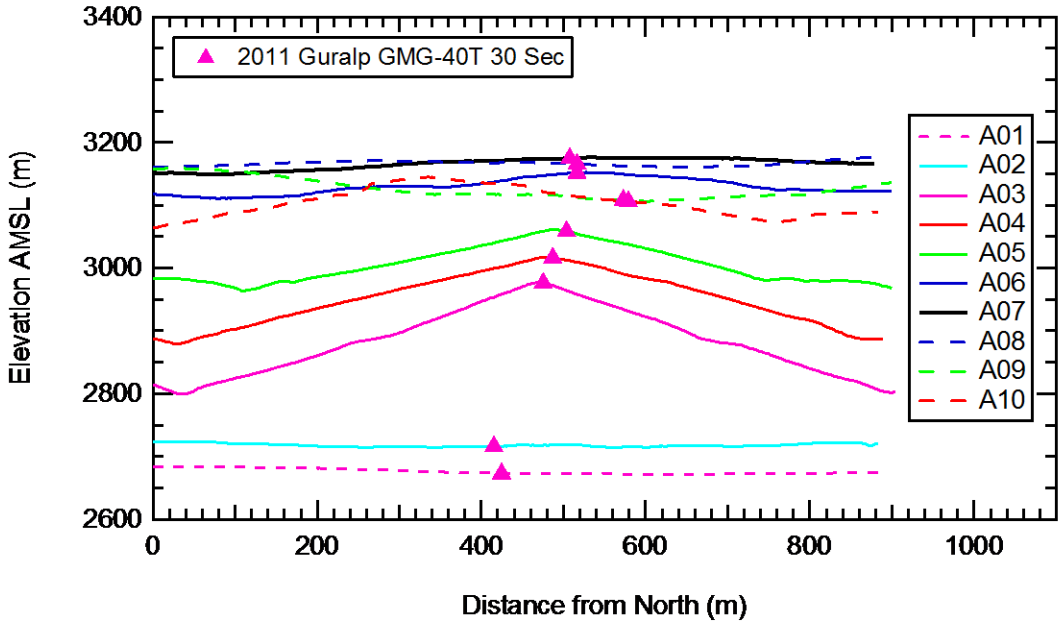

Figure 8.8: North-South sub-cross sections perpendicular to line A (Stations A1-A10) for Phase II (2011).

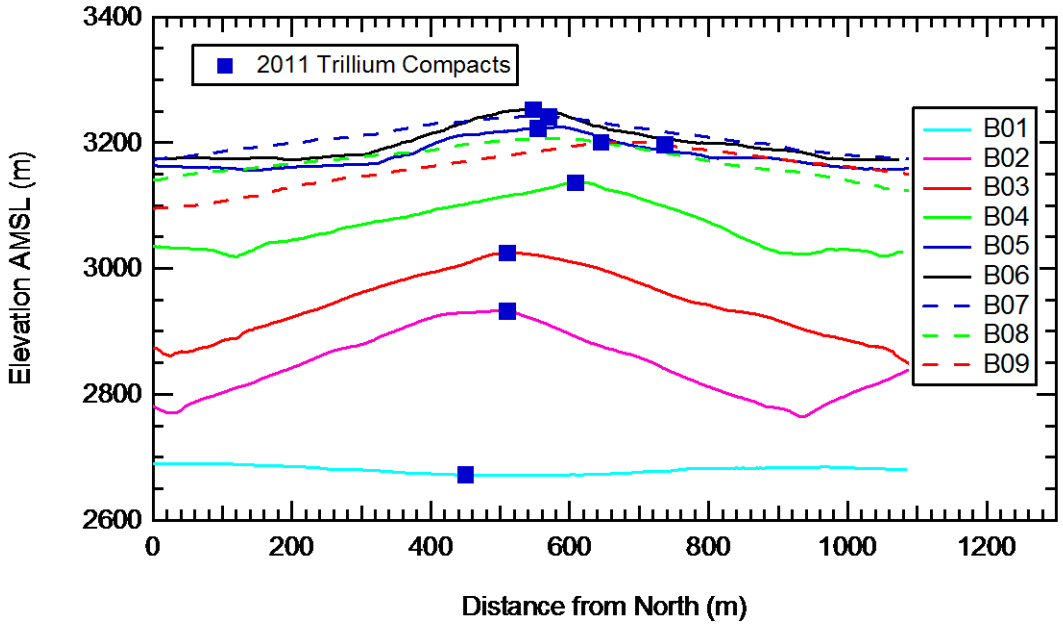

Figure 8.9: North-South sub-cross sections perpendicular to line B (Stations B1-B9) for Phase II (2011).

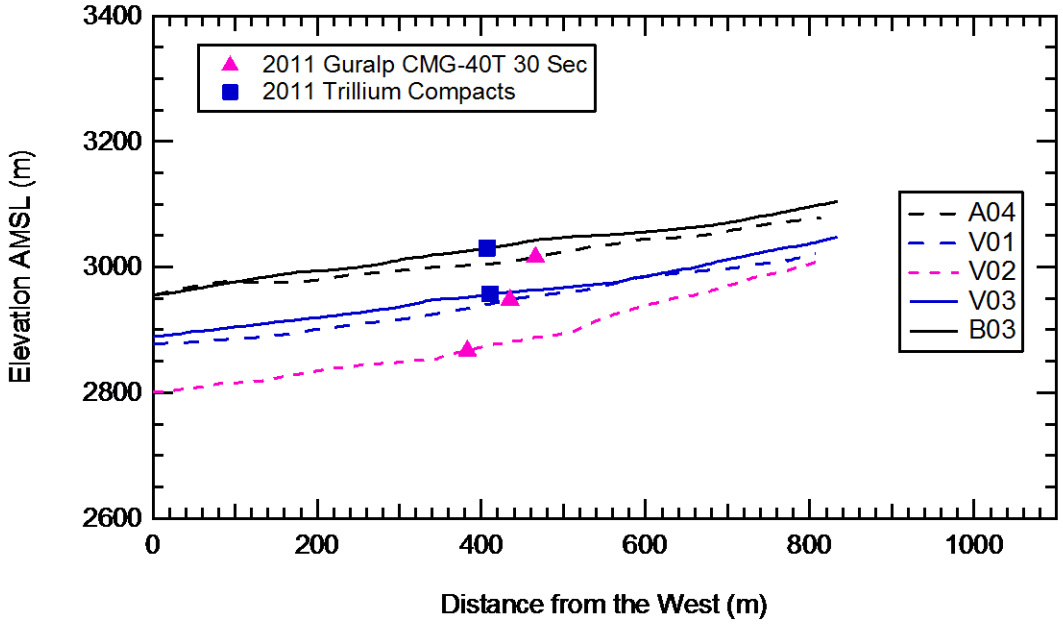

Figure 8.10: East-West sub-cross sections perpendicular to line V (Stations A4, V1-V2, and B3) for Phase II (2011).

some possible N-S topographic amplification for Stations B5-B9. West-East sub-cross sections for line V (A4, V1-V3, and B3) are shown in Figure 8.10. Each sub-cross section of the V line is started at the same Easting value and continues due East, for a total horizontal distance of 800 m. The E-W sub-cross sections for all the stations in the V line have little topographic relief in the E-W direction, and certainly are not located at the crest of any E-W topographic features. Therefore, topographic amplification is not expected in the E-W direction for the V-line stations.

8.3 Single Event Results (200.19.5)

Event 200.19.5 was recorded on July 19, 2011 at 19:05 Greenwich Mean Time (GMT). The UUSS classified the event as a shallow M_L 1.6 "earthquake". The event was located approximately 350 meters above the tailgate of the longwall. The event was

processed using the standard ground motion processing scheme laid out in Chapters 3 and 4, which resulted in the time records in Figure 8.11 for the vertical (V), North-South (N-S), and East-West (E-W) components. In this figure, each time record has been normalized by the highest overall peak ground velocity (PGV) of any station in the array for plotting purposes only. Since it was difficult to determine amplification from the time records alone, the PGV for each station was calculated, and plotted in Figure 8.12 for the V, N-S, and E-W components. For each component, the records have been corrected for geometric attenuation as explained in Chapter 4. The PGV's of the N-S component were the highest for the three components, followed by the E-W component, and finally the V component. All the PGV values indicate the vibrations were below the level perceivable by humans (1 mm/sec) (Wald et al. 1999). For the V component, high PGV values were recorded on Stations A1, A2, A5, and B2. None of these stations correspond with peaks in the topography (i.e., crest stations A7 and B6 do not have high vertical PGV values), or distance from the hypocenter of the event (see Figure 8.3). Therefore, the vertical PGV values were determined to be randomly distributed and not affected by topography.

For the N-S component, Stations A5 and A6 had the highest PGVs for the A line, while Stations B2 and V1 had the highest PGV's for the B and V lines. As with the vertical component, the highest PGV values did not correspond with stations at the crest of topographic features (i.e., Stations A7 and B6). Interesting, the A stations, in general, had higher PGV values than other stations in the array. The A stations were slightly closer to the average hypocenter than other stations, but if geometric attenuation was completely controlling the pattern, Stations V1, and V2 should have had the largest PGV values. However, these stations had lower PGV's than most of the A-line stations. Overall, there might be a slight distance influence on the PGV values, even after

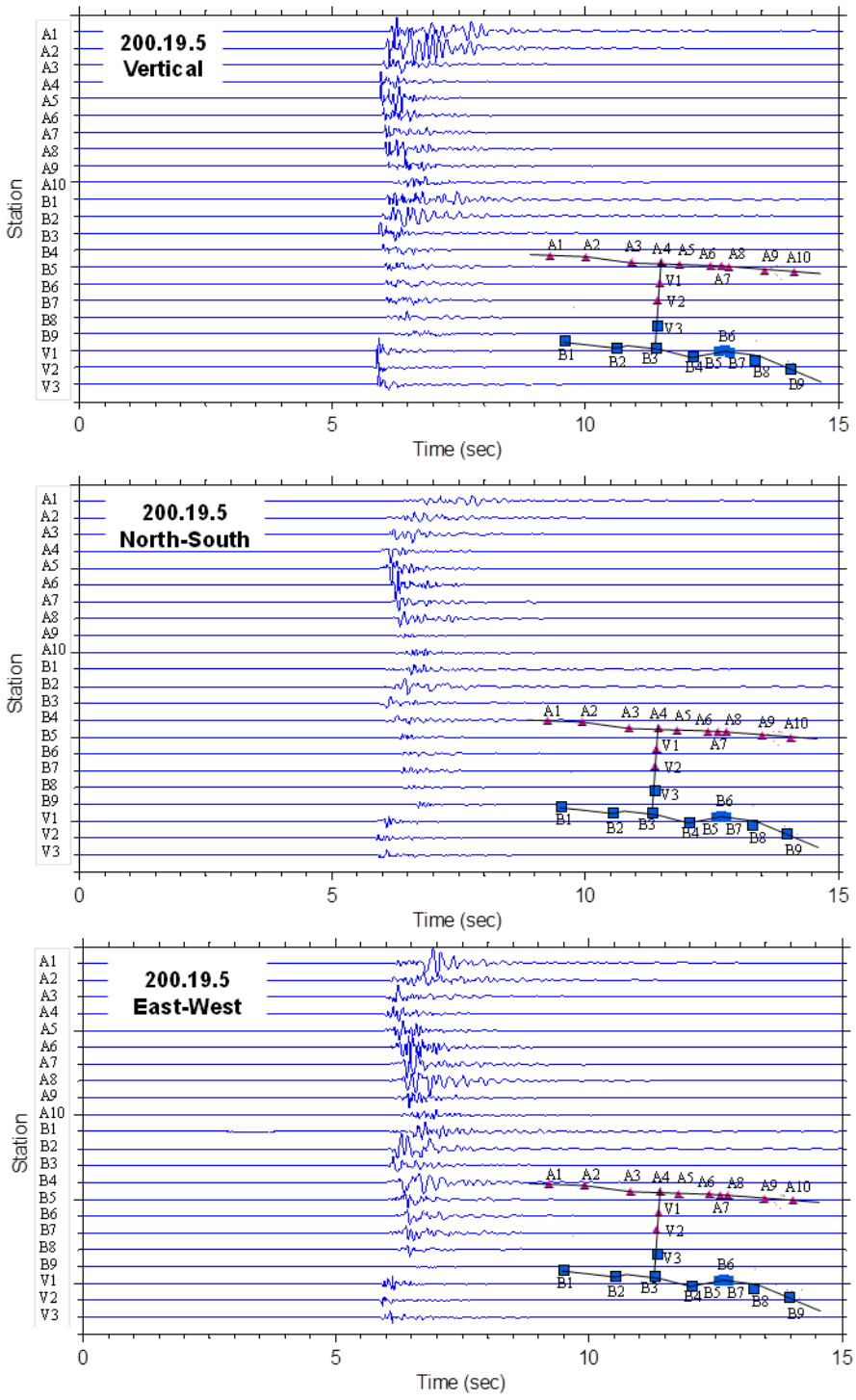

Figure 8.11: Time record plot for event 200.19.5 for the vertical, North-South, and East-West component of motion. Records normalized by the highest overall PGV at any station.

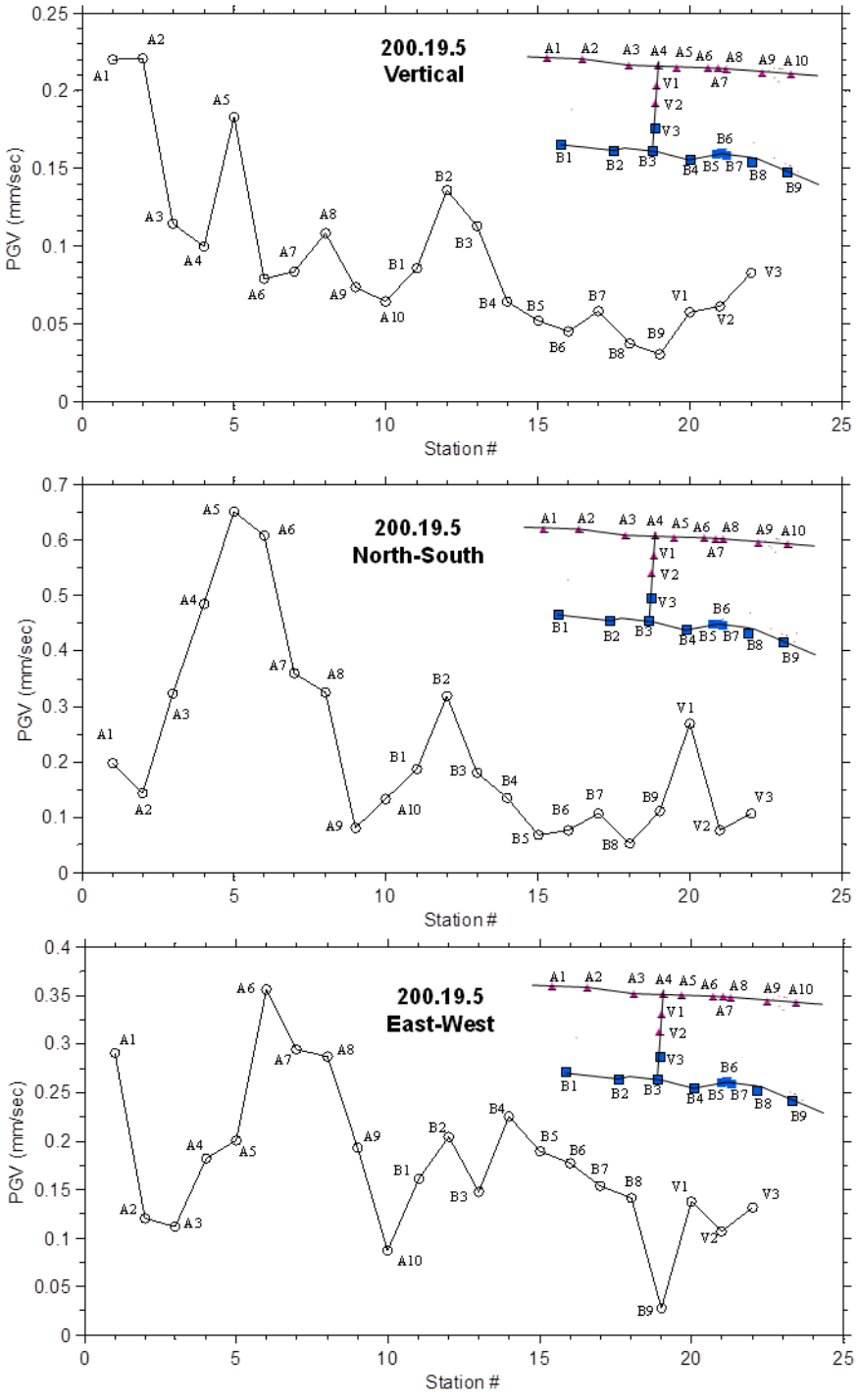

Figure 8.12: PGV's for event 200.19.5 for the vertical, North-South, and East-West component of motion.

correcting for geometric attenuation, but no significant topographic amplification patterns were observed from the N-S PGV values.

For the E-W component, Stations A1, A6-A8, and B4 all had high PGV values. Station A1 was at the base of the feature and Station A6 was at the crest; therefore, a significant amplification was expected from Station A6 to A1, but almost no amplification was observed in the PGV values. As with the V and N-S components, the A-line stations seemed to have greater PGV values (50% on average) than B- or V-line stations, but no pattern can be established as to why. The E-W component showed no pattern of topographic amplification in terms of PGV values (i.e., maximum PGV at the crest and lowest PGV at the base). Therefore, the PGV values for event 200.19.5 did not indicate the mountain was affect by topographic effects.

Since no topographic amplification was identified in the time domain by observation of PGV, event 200.19.5 was transformed to the frequency domain using the Discrete Fourier Transform (DFT) (detailed in Chapters 3 and 4). To make visualization easier, and identification of topographic effects simpler, the stations will be plotted and analyzed based on the three cross sections presented in Chapters 4, 6, and 8, which were: (1) Line A (cross section A, Stations A1-A10), (2) Line B (cross section B, Stations B1-B9), and (3) Line V (cross section C, Stations A4, V1-V3, and B3). The Fourier amplitude spectra (FAS) of the A-line stations for event 200.19.5 are shown in Figure 8.13. Though the energy bands and overall amplitude of each component vary, the main energy band is concentrated from a frequency of 1 Hz to 20 Hz for all three components. Below 1 Hz and above 20 Hz, the spectral amplitude drops off fairly sharply resulting in little energy at those frequencies. For the V and N-S components, no crest-down amplifications were observed. However, for the E-W component, Stations A6-A8 had the highest amplitude at most of the frequencies of interest, indicating possible topographic

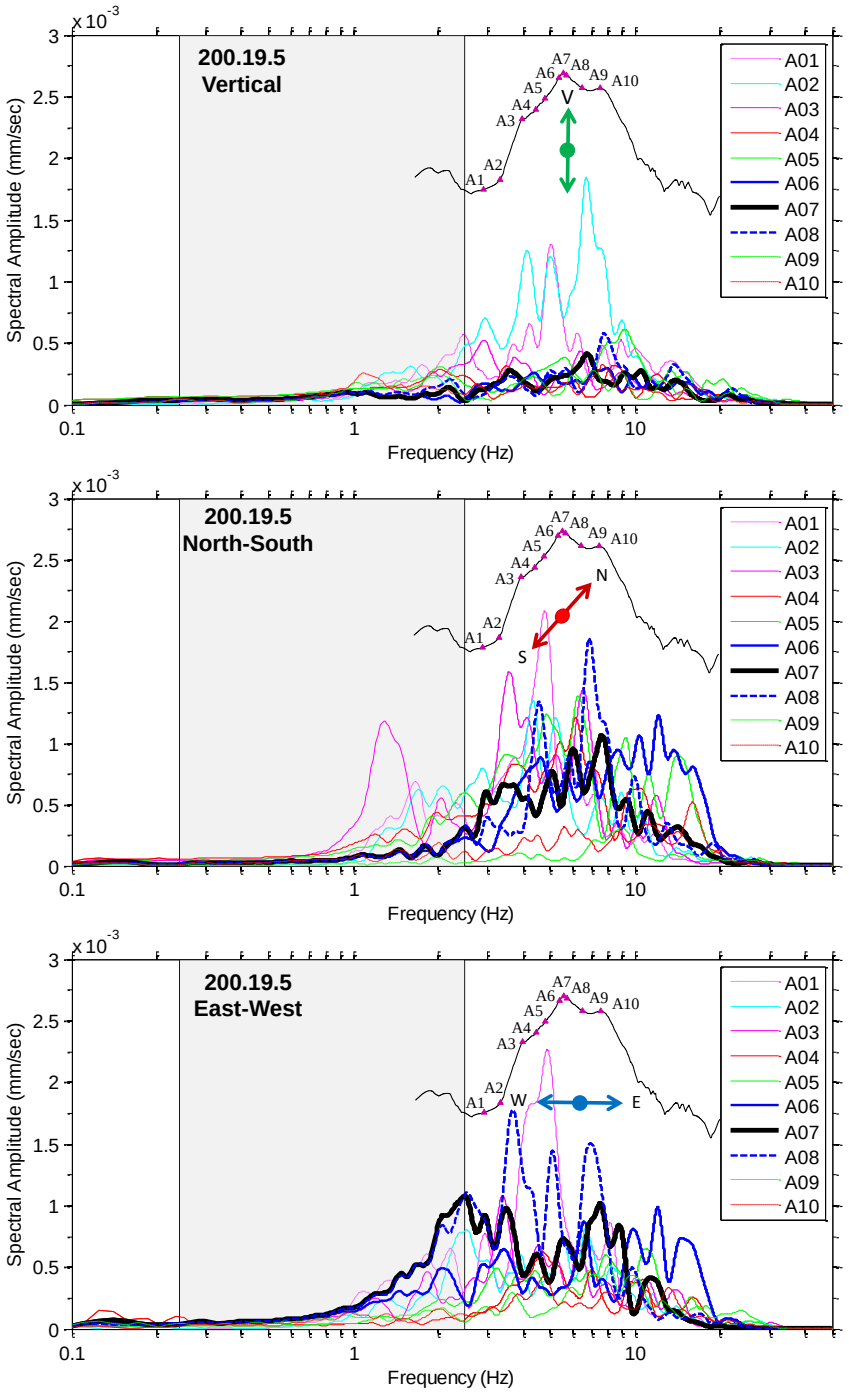

Figure 8.13: Spectral amplitude plot for event 200.19.5 (A-line stations) for the vertical, North-South, and East-West components of motion. The estimated topographic frequency range based on cross-section geometry and average shear wave velocity is shaded.

effects in the E-W direction. The FAS of the B-line stations for event 200.19.5 are shown in Figure 8.14. As with the A-line stations, the main energy band was concentrated from a frequency of 1 Hz to 20 Hz, though the E-W component does have a slightly lower energy band extending to approximately 0.7 Hz. For all the components, no top-down amplifications can be seen from a visual inspection of the spectral amplitudes. The FAS of the V-line stations for event 200.19.5, are shown in Figure 8.15. Unlike the other two lines, the energy bands of the three components for the V line did not match well. The V component had a fairly wide energy band extending from 0.1 Hz to 20 Hz. The N-S component had a standard energy band from 1 Hz to 20 Hz, while the E-W component only had energy from 2 Hz to 20 Hz. The largest amplitudes were recorded in the N-S direction, which makes sense given the steep 2D cross section in the N-S direction for the V line. Overall, each station in the array has energy from approximately 1 Hz to 20 Hz for event 200.19.5. However, less energy exist above and below those frequencies, and additional analysis methods (SSR, MRM, and HVSR) are needed to compare the response of each station.

8.3.1 Standard Spectral Ratio (SSR) Analysis

To determine the amplification at a station, a baseline amplitude has to be established that represents a response similar to the measurement station (whose amplification is of interest), but not affected by soil site effects or topographic amplification. The first method investigated to accomplish this task is the Standard Spectral Ratio (SSR) method. This method (described in detail in Chapters 2-4) uses a single reference station that is believed to be free of soil site effects or topographic effects, but is close enough to the measurement station to not be overly influenced by geometric attenuation. This reference

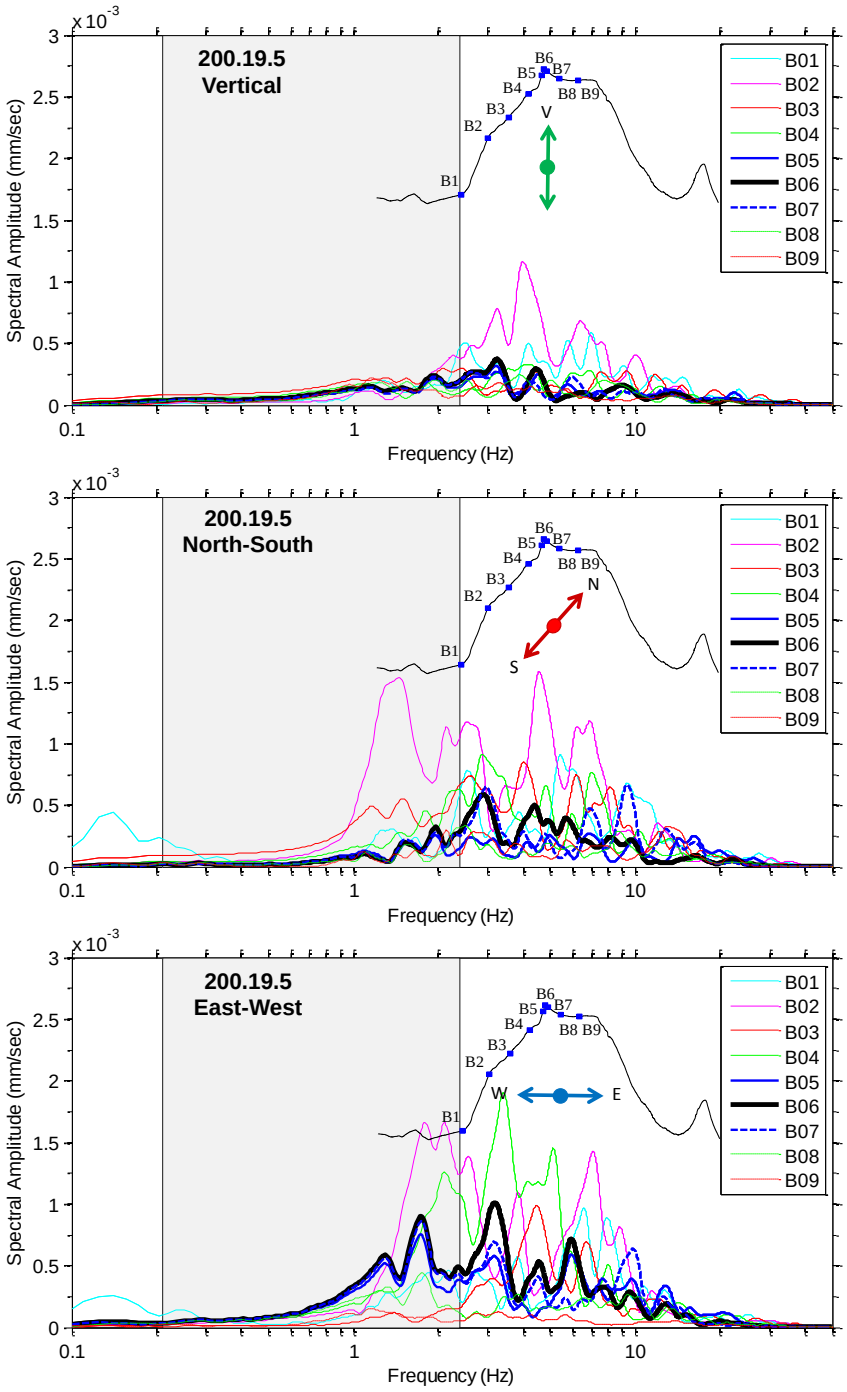

Figure 8.14: Spectral amplitude plot for event 200.19.5 (B-line stations) for the vertical, North-South, and East-West components of motion. The estimated topographic frequency range based on cross-section geometry and average shear wave velocity is shaded.

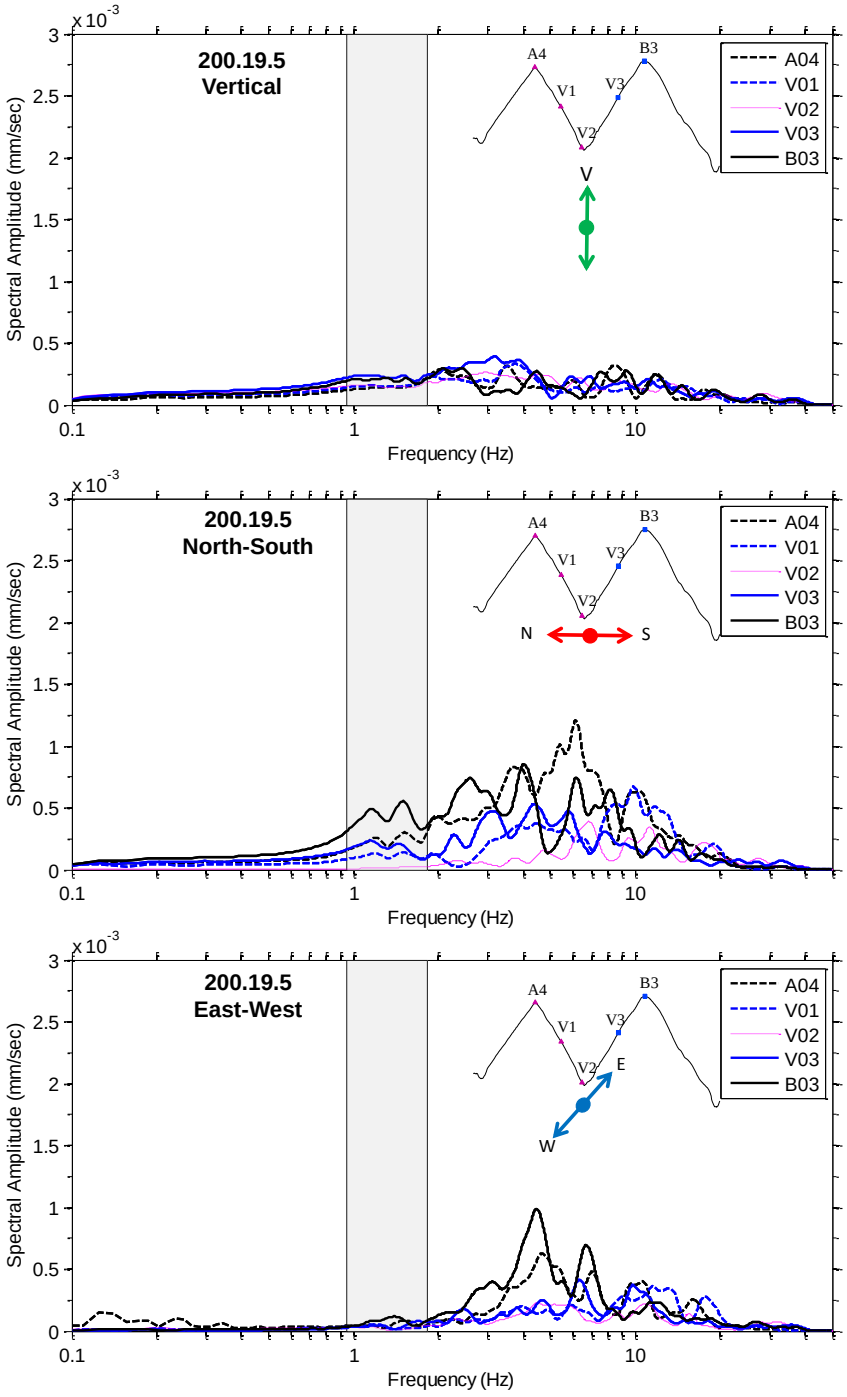

Figure 8.15: Spectral amplitude plot for event 200.19.5 (V-line stations) for the vertical, North-South, and East-West components of motion. The estimated topographic frequency range based on cross-section geometry and average shear wave velocity is shaded.

station is compared to other measurement stations in the same vicinity to determine the amplification or de-amplification at various frequencies. For Phase II, three different stations were chosen as reference stations for the three lines of sensors (A, B, and V). For the A line, A1 was chosen as the reference station because the station was off the topography on relatively flat ground, but was still relatively close to the other stations. For the B line, B1 was chosen as the reference station because like A1, it was off the topography and on relatively flat ground. For the V line, V2 was chosen because it was in the valley and off the topographic feature. The V line reference station was the hardest to choose because there was no flat ground in the vicinity of the V line, but V2 provided the closest approximation to a flat ground station for the V line. Refer to Figures 8.3-8.10 for maps, cross sections of the array, and station locations. As with the FAS plots, the SSR analyses will be conducted on the three cross sections separately to make data visualization easier and the results clearer.

In Figure 8.16, the SSR for line A (Stations A1-A10) are shown with respect to Station A1. For the V component, strong amplification peaks were measured at a frequency of 0.3 Hz and 0.16 Hz, with amplifications of up to 12 and 10, respectively. The higher frequency peak was just within the estimated topographic frequency range (0.24-2.54 Hz; refer to Chapter 6). However, Stations A4-A5 had the highest amplitude followed by Stations A3 and A6-A10, which did not correspond well with the geometry of the feature (i.e., top-down amplification). Beyond these two peaks, no other area of the curve had significant amplifications.

For the N-S component, three significant amplification peaks were measured inside of the estimated topographic frequency range from 0.24 Hz to 0.85 Hz. The crest station, A7, had a maximum amplification of 6 with a good pattern of top-down amplification from Stations A6 and A8; however, it did not have the highest

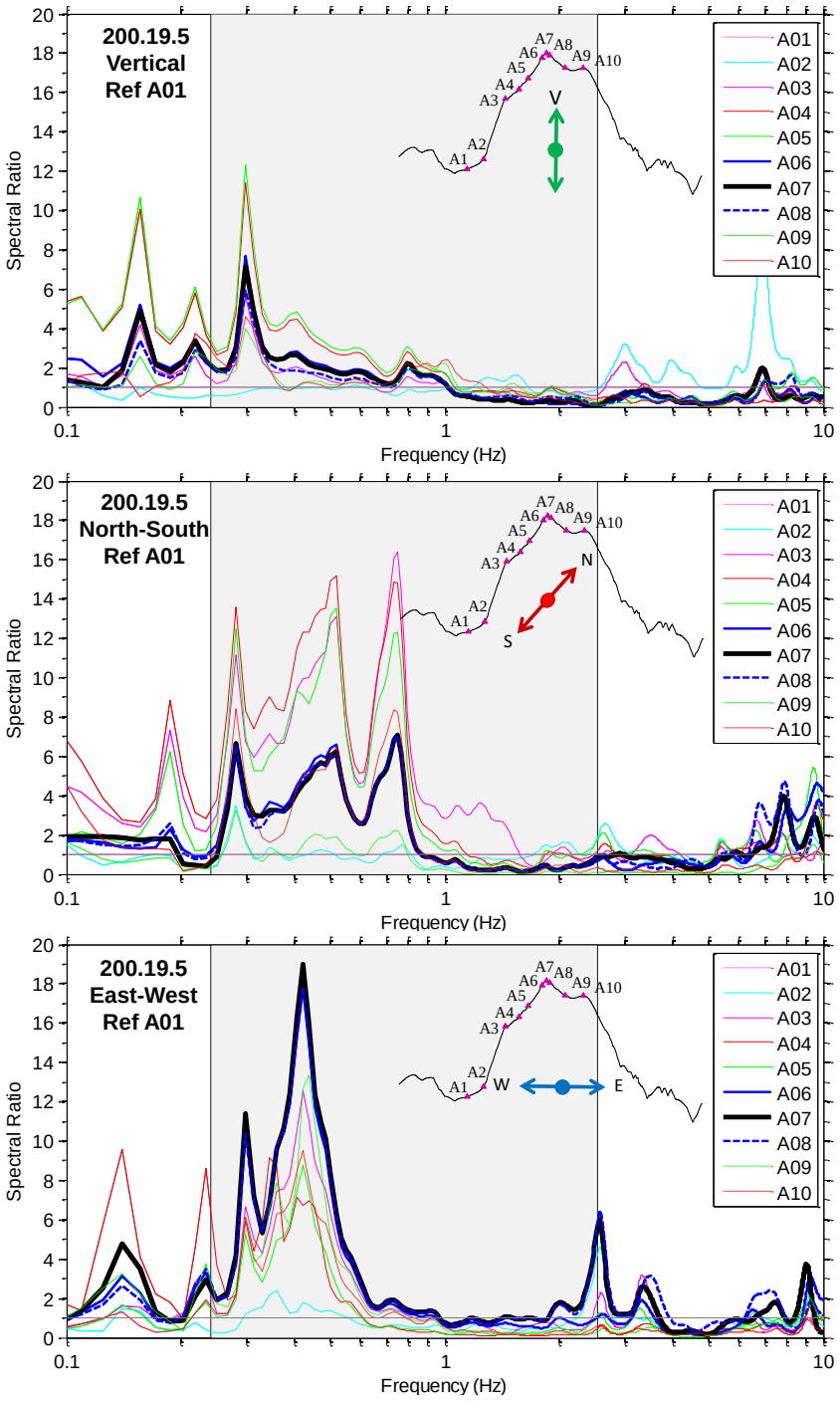

Figure 8.16: Standard spectral ratio (SSR) for event 200.19.5, line A vertical, North-South, and East-West components of motion. Station A1 was used as the reference station. The estimated topographic frequency range based on cross-section geometry and average shear wave velocity is shaded.

amplification for the N-S direction. The highest amplifications (16) were measured on Stations A3-A5, which are located on a minor N-S oriented feature connected to the larger E-W feature in cross section A (see Figure 8.3, 8.4, 8.7 and 8.8). This N-S oriented sub-feature under Stations A3-A5 likely produced topographic amplifications in the N-S direction, which were greater than that produced by the larger E-W oriented feature shown in the A line cross section in Figure 8.4. This N-S feature, under Stations A3-A5, is a smaller feature than the larger A line feature; however, the N-S feature is connected to the larger A line feature, and forms a ridge and valley system in the N-S direction. Even though the N-S feature is part of the larger topographic system, this smaller topographic feature is still capable to generating topographic amplifications, particularly in the N-S direction. Therefore, even though the main A line cross section is being examined, other smaller sub-features can generate amplifications exceeding those of the larger feature. The N-S feature will be further analyzed as part of the V line of stations. The amplifications measured in the N-S direction by Stations A6-A8 and A10 have spectral ratios up to 6, but have little topographic relief in the N-S direction (see Figure 8.8). It is not clear whether the amplifications in the N-S direction for these stations were caused by the E-W topography under each station or by possible problems with the reference station, A1. Outside of the estimated topographic frequency range (0.24-2.54) amplifications were measured on Stations A3-A5 at 0.19 Hz, but no clear top-down amplification pattern could be identified using the stations. However, the amplifications are likely connected to the N-S sub-feature mentioned earlier, and will be investaged further as part of the V line.

For the East-West component, a major and minor amplification peak were measured inside the estimated topographic frequency range at frequencies of 0.3 Hz and 0.4 Hz, respectively. Maximum amplifications of 19 and 11 were measured on the crest

station, A7. These peaks had good top-down amplification patterns from the crest station, A7, with the highest amplification, followed by Stations A6 and A8 (stations just off the crest). After which, amplifications were measured on all other stations in the A line excluding Station A02, which is at the base of the E-W feature, similar to the reference Station A1. Therefore, Stations A1 and A2 could both be used as the reference station, and no significant difference in the spectral estimates would be noticed. A smaller amplification of 6 was measured at 2.5 Hz, but the amplification pattern only included Station A7, with the highest amplification, and Station A8. Therefore, this amplification may not be caused by topographic effects.

Horizontal polarity plots depicting the response of event 200.19.5 recorded by Stations A2-A10 based on the SSR method applied over the frequency range of 0.1 to 5 Hz, are provided in Figure 8.17. Based on the results presented in Figure 8.16, topographic effects are expected at frequencies less than 1 Hz. The horizontal polarity plots help one visualize the amplification present at each azimuthal direction in the horizontal plane, and are valuable to determine the most intense direction of shaking for a given frequency. Stations A6-A10 had a strong directional response at less than 1 Hz in the nearly E-W direction, which agrees with the strong SSR amplification peak resolved in the E-W direction of Figure 8.13. Stations A3-A5 had more of a multi-directional response with strong energy in all directions. This amplification may be caused by those stations being on both N-S and E-W trending topographic features, while Stations A6-A10 were only positioned on a primarily E-W trending feature.

Overall, the SSR analysis for event 200.19.5 along line A resulted in significant amplification in the E-W direction for stations near the crest of the A line feature of up to 19 in the estimated topographic frequency range, and with good top-down amplification patterns. Amplifications were also measured in the N-S direction for the

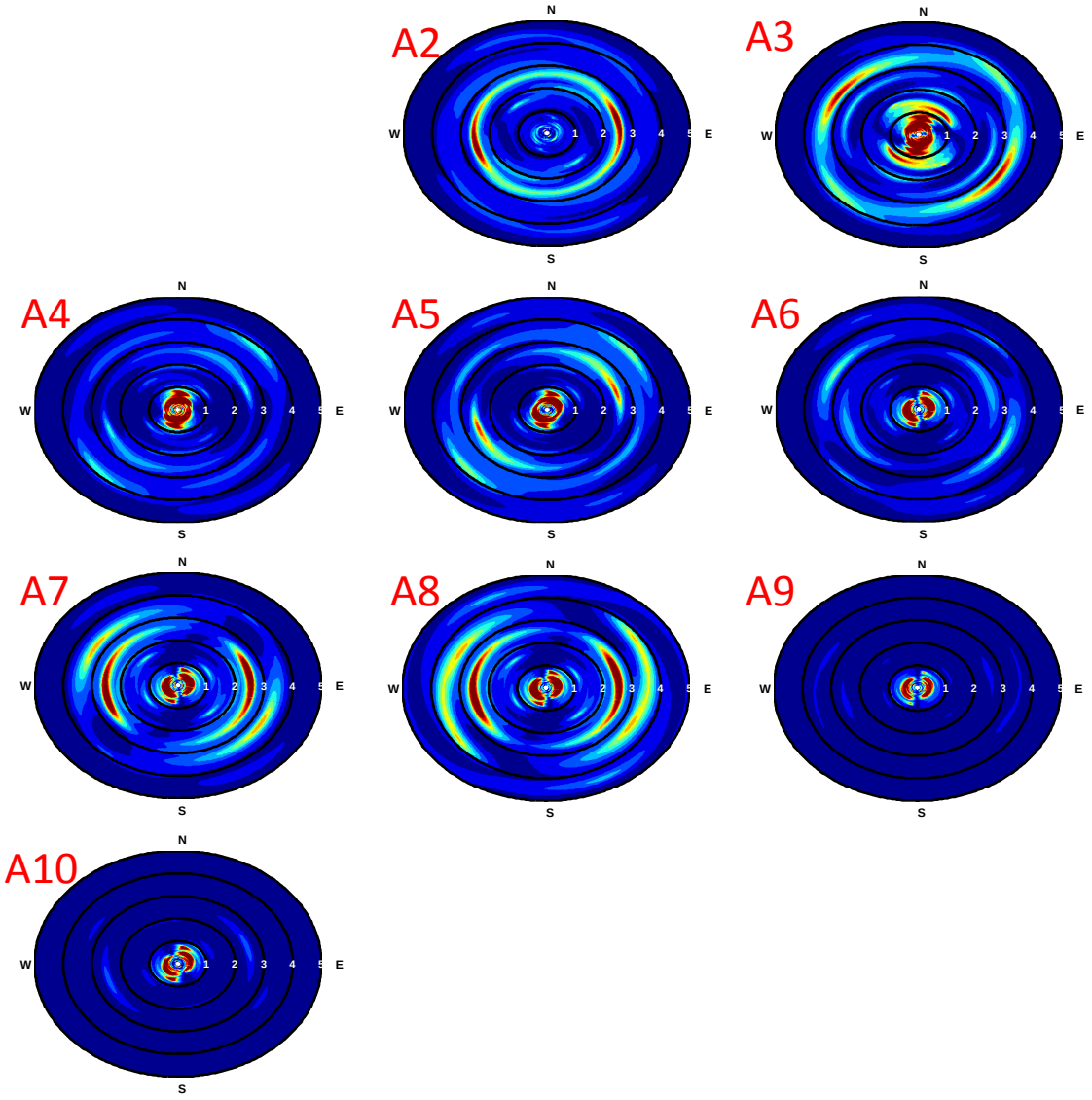

Figure 8.17: Horizontal polarity plots for the SSR method for event 200.19.5, line A. Station A1 was used as the reference station.

crest stations (A6-A8). However, Stations A3-A5 had larger amplifications than the crest stations in the N-S direction, likely due to strong N-S topographic relief near each station. Narrow banded amplifications were measured in the vertical direction, but no significant pattern of topographic amplification was observed.

In Figure 8.18, the SSR for line B (stations B1-B9) are shown with respect to Station B1. For the vertical component, a major amplification peak was measured at 0.16 Hz, with amplifications from over 100 to 18, with Stations B3 and B4 having the highest amplification. This amplification was slightly less than the estimated topographic frequency range, and may be caused by an error in the reference station. Other smaller amplification peaks occurred at higher frequencies, with Stations B3-B4 still having the greatest amplification.

For the N-S component, amplification occurred between 0.4-2.0 Hz, which is within the estimated topographic frequency range for the E-W trending feature. The crest station of the E-W trending feature (Station B6) only had a slight amplification over this frequency range. However, stations B2-B4 had much greater amplifications in the N-S direction. These stations were located on a minor N-S trending feature, much like Stations A3-A5 in the A line (see Figure 8.9). Therefore, these stations were likely influenced by topographic effects from the N-S trending feature. Without other stations placed in a consistent N-S pattern along the feature, it cannot be determined if the amplification was truly the result of topographic effects. However, stations in the V line will be used to further investigate these amplifications in the N-S direction.

For the East-West component, amplifications were measured from a frequency of 0.35-2.0 Hz, which is directly within the estimated frequency range for the E-W trending feature in cross section B (0.21-2.39 Hz, refer to Chapter 6). A maximum amplification of 5 times the reference station was recorded on the crest station, B6. A good pattern of top-down amplification was alsoobserved at Stations B5 and B7, with slightly lower amplifications. Stations B4 and B8 also have an amplification of 3.5 in the same frequency range, which is a 30% reduction in amplification from the crest station. This pattern indicates the amplification trends are likely caused by topographic effects

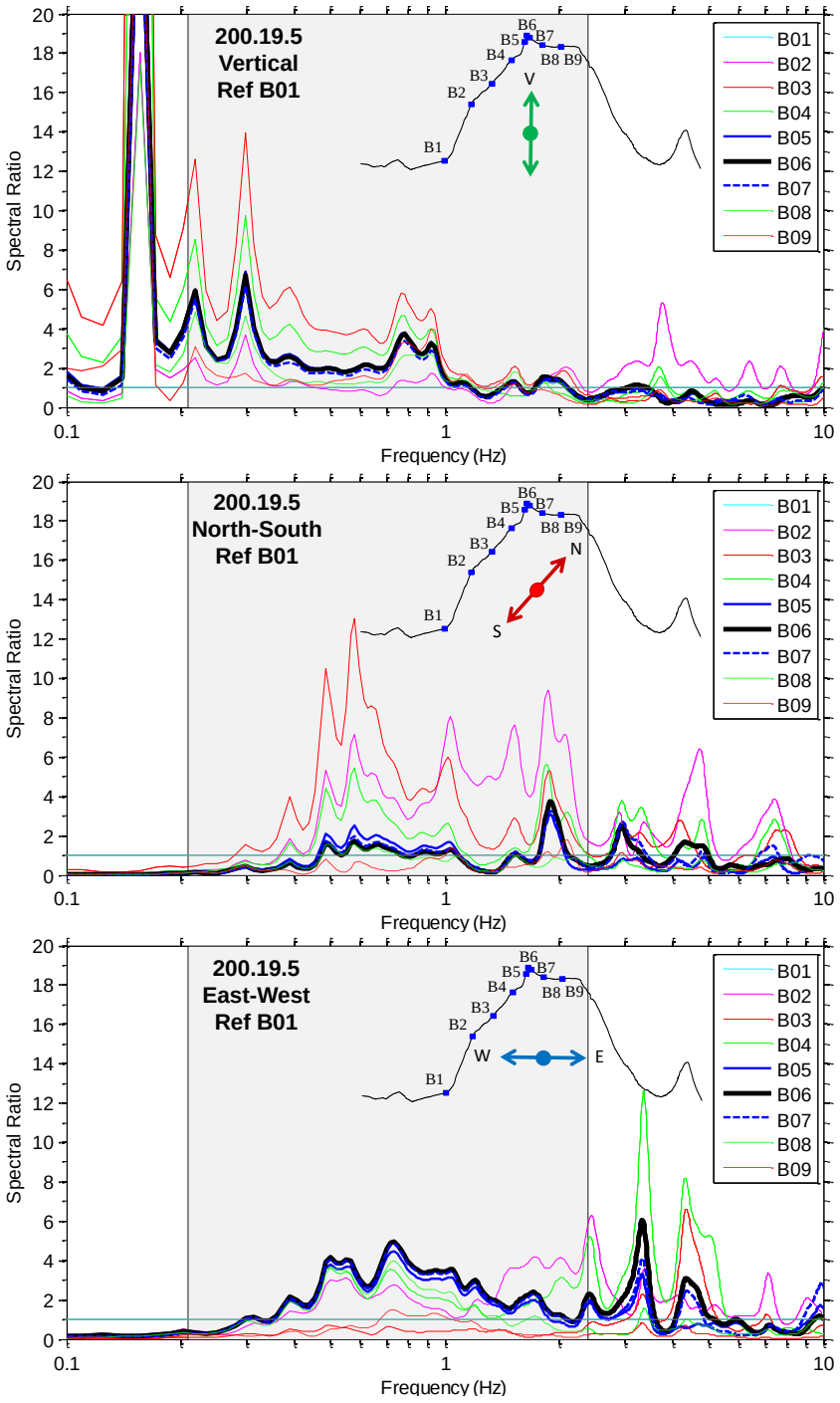

Figure 8.18: Standard spectral ratio (SSR) for event 200.19.5, line B vertical, North-South, and East-West components of motion. Station B1 was used as the reference station. The estimated topographic frequency range based on cross-section geometry and average shear wave velocity is shaded.

resulting from the E-W trending feature. A narrow amplification peak was also measured at a frequency of 3.3 Hz, with an amplification of 6 for Station B6. However, this peak is outside the estimated topographic frequency range, despite having a limited pattern of amplification at Stations B5 and B7. Therefore, topographic amplification cannot be completely ruled out, but the main topographic amplification peak occurred at a frequency range of 0.35-2 Hz.

Horizontal polarity plots depicting the response of event 200.19.5 recorded by Stations B2-B9 based on the SSR method applied over the frequency range of 0.1 to 5 Hz, are provided in Figure 8.19. Based on the results presented in Figure 8.18, topographic effects are expected at frequencies less than 2 Hz. Stations B4-B8 all had strong E-W to NW-SE polarity for energy around a frequency of 1 Hz, which was in the direction of the steep E-W topographic relief under the stations. Station B3 had a N-S polarity at around 1 Hz, which corresponds well with the steep N-S topographic relief and lack of E-W topographic relief under the station. Stations B2 and B9 have less directionality than previously mentioned stations; however, their amplifications seem to also be oriented in the NW-SE direction. Overall, the amplification seem to oriented in-line with steep topographic feature under each station indicating topographic amplifications.

Overall, the SSR analysis of event 200.19.5 along line B resulted in significant amplification for the crest station (B6) in the East-West direction of 5 times the reference station. Stations B2-B4 recorded strong amplification of up to 12 in the N-S direction, while Station B6 experienced little to no amplification in the N-S direction. Large amplifications were also measured on the V component in a narrow frequency range, but outside the estimated topographic frequency range.

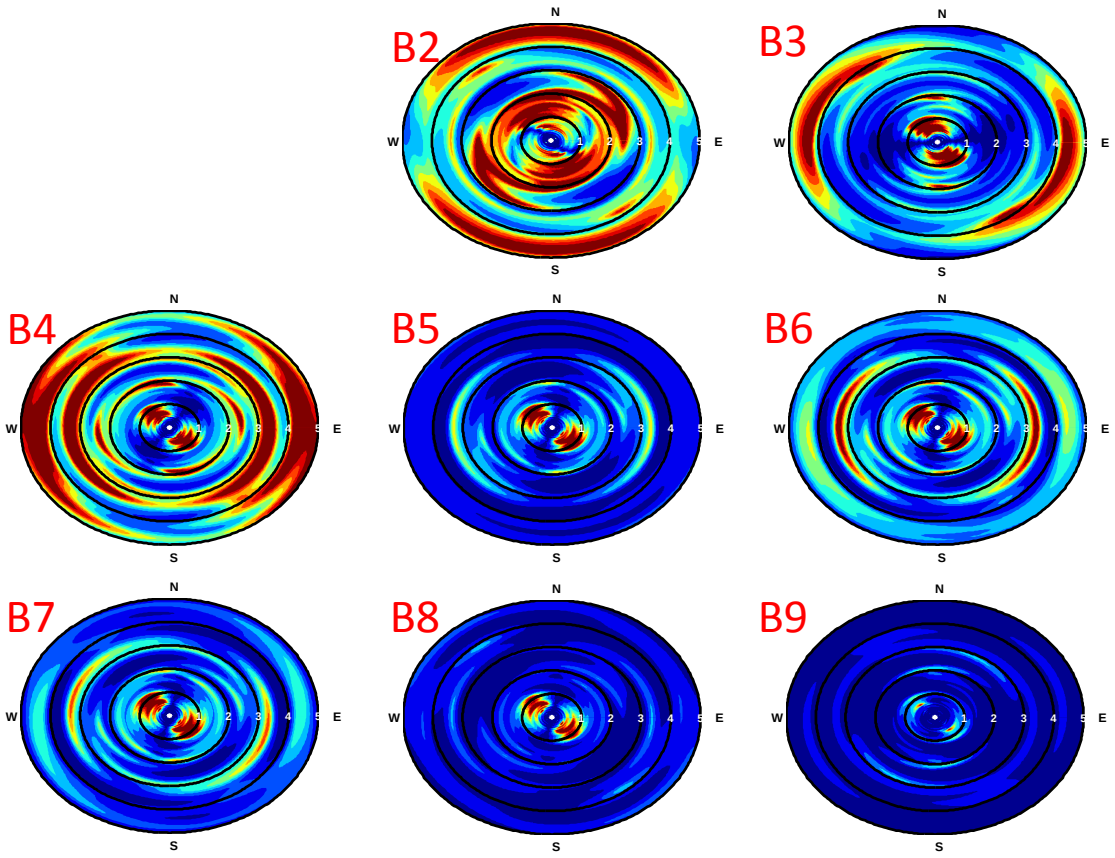

Figure 8.19: Horizontal polarity plots for the SSR method for event 200.19.5, line B. Station B1 was used as the reference station.

In Figure 8.20, the SSR for line V (Stations A4, V1-V3, and B3) are shown with respect to Station V2. For the vertical component, a slight amplification of up to 2 was measured on several stations, but no strong pattern of top-down amplification was observed.

For the N-S component, very large amplifications (up to 50) were recorded on Station B3 over almost the entire frequency range (0.1 to 5 Hz). The next highest amplifications were recorded on Stations V3 and A4, with a 40% reduction in amplification compared to station B3. Station V1 also recorded a large amplification of up to 15 times the reference station. These are very large amplifications that have a good

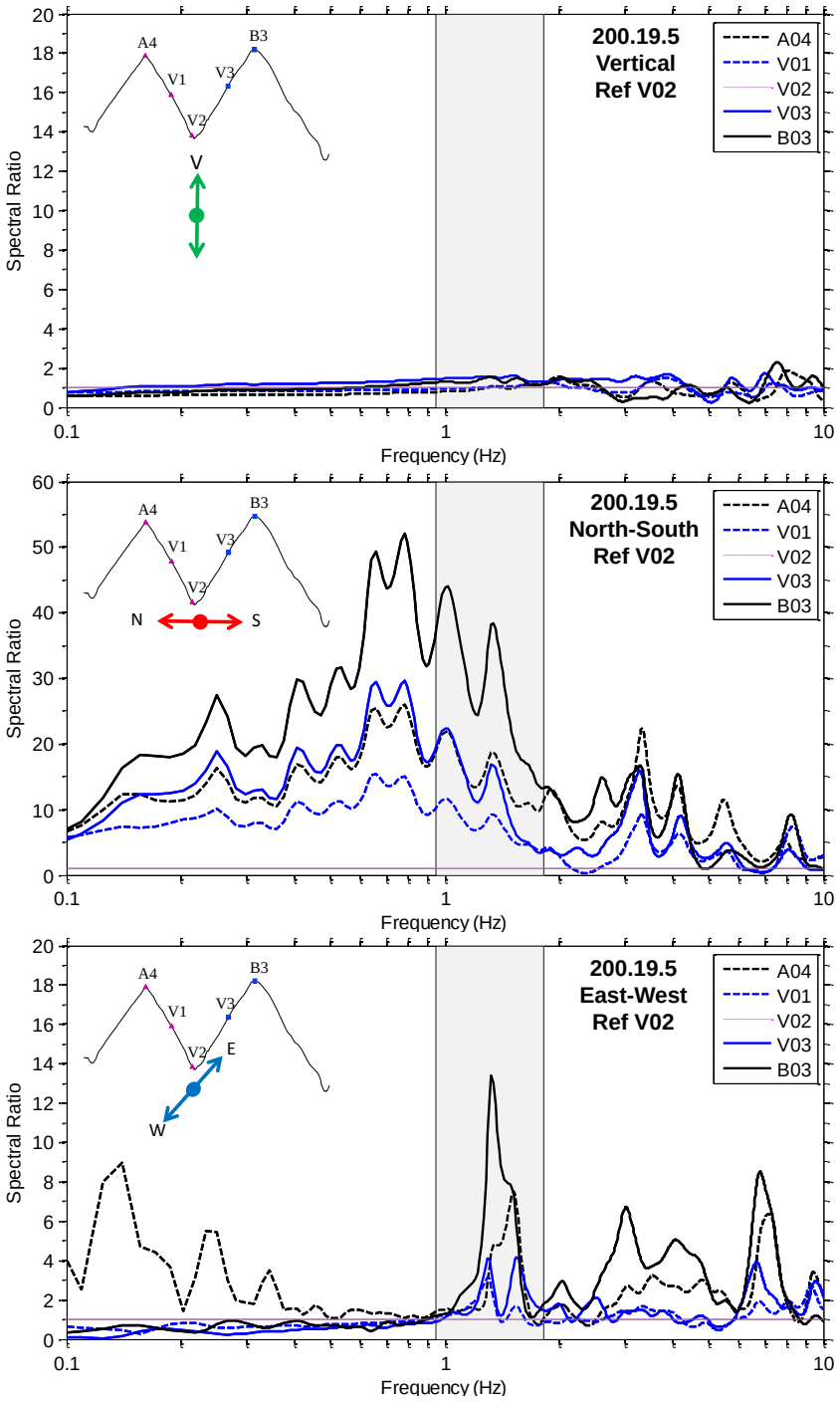

Figure 8.20: Standard spectral ratio (SSR) for event 200.19.5, line V vertical, North-South, and East-West components of motion. Station V2 was used as the reference station. The estimated topographic frequency range based on cross-section geometry and average shear wave velocity is shaded.

top-down pattern of amplification. However, the estimated topographic frequency range of 0.95 to 1.83 Hz only encompassed a small part of the amplification range recorded by each of the stations. Much of the lower frequency amplifications (less than 1 Hz) were not predicted using the relationships by Ashford and Sitar (1997) and Paolucci (2002). Normally, this disagreement could be blamed on the velocity model or irregularity in the topographic feature. However, in order to properly predict the low-frequency amplification recorded in the N-S direction, one would have to reduce the average velocity of the feature from 1000-1300 m/s to less than 500 m/s over the assumed height of the features (see Tables 6.10 and 6.11). This velocity reduction is very unlikely to be true, given the geologic setting. Moreover, even if the velocities changed that significantly, the models would no longer predict the higher frequency amplification range correctly. As for the correct geometry, the overall size of the feature would have to increase 2 or 3 fold to accurately predict the frequency amplification measured on the V line if the average velocity were to remain the same. Therefore, this lower frequency amplification that appears to be tied to topographic effects is one example where the analytical equations do not correctly predict the measured frequency range of topographic effects.

For the East-West component, much smaller amplifications than in the N-S direction were measured over the estimated topographic frequency range (0.95-1.83 Hz) for the crest stations (A4 and B3). The largest amplification of 14 was measured on Station B3, followed by Station A4 with an 8 times amplification. It is not well understood why amplification occurred in the E-W direction because no topographic relief exists in that direction (see Figure 8.10), but it may be related to the A and B line topographic features in the E-W direction or due to the sensors not being oriented directly in-line with the N-S topographic feature. Amplifications also occurred above a frequency

of 3 Hz. These amplification did have a top-down pattern of amplification similar to that seen for topographic amplifications, but those amplifications are directly in the soil site effects amplification frequency range (i.e., 5-15 Hz; refer to Chapter 6). Therefore, it is not clear what is causing these amplifications.

Horizontal polarity plots depicting the response of event 200.19.5 recorded by Stations A4, V1, V3, and B3 based on the SSR method applied over the frequency range of 0.1 to 5 Hz, are provided in Figure 8.21. Based on the results presented in Figure 8.20, topographic effects are expected at frequencies less than 2 Hz. Stations A4 and B3 (the crest stations) had a strong N-S polarity (refer to Figure 8.20) that was difficult to visualize in the polarity plots due to relatively high amplitudes over wide range of frequencies. Nonetheless, the lower frequency (i.e., < 3 Hz) N-S polarity is still obvious. Stations V1 and V3 had a significant polarity in the NE-SW direction for frequencies greater than 2 Hz, and a more of N-S polarity for frequencies less than 2 Hz (the likely topographic amplification frequencies). Therefore, the polarity of the Stations in the V line are oriented in-line with the minor N-S trending features indicating topographic effects.

Overall, the SSR analysis of event 200.19.5 along line V resulted in significant amplification for all stations in the N-S direction, with maximum amplifications of up to 50. However, the amplification frequency range in the N-S direction was not estimated correctly using the analytical approximations of Ashford and Sitar (1997) and Paolucci (2002), which only estimated the higher frequency part of the amplified frequency range. Amplifications were also measured in the estimated topographic frequency range in the E-W direction, with amplification of around 14 times the reference station. No strong amplifications were measured by the vertical components.

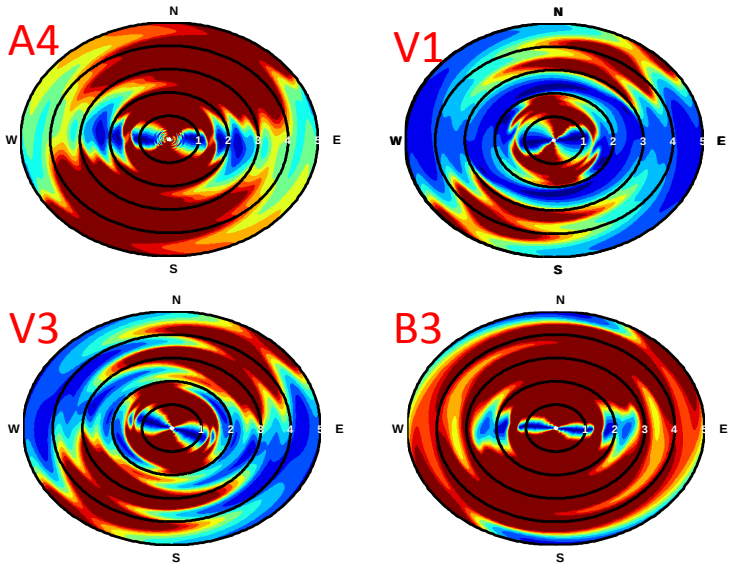

Figure 8.21: Horizontal polarity plots for the SSR method for event 200.19.5, line V. Station V2 was used as the reference station.

8.3.2 Median Reference Method (MRM) Analysis

The Median Reference Method (MRM) is an update to the classical SSR method that eliminates the short comings of only having a single reference station. The MRM uses the entire array of sensors to create a reference amplitude by calculating the median response as a function of frequency for all the sensors in the array (MRM is detailed in Chapters 2, 3, and 4). The method has been shown in numerical simulations to be a very stable tool for investigating topographic amplification, regardless of the number of sensors in the array, and fits well with the geometric setup in Phase II (Maufroy et al. 2012). For the data in Phase II, Stations 1-22 (A1-A10, B1-B9, and V1-V3) were used to compute the median response of the entire mountain. As with the SSR method, the individual responses at each station are compared using three separate cross sections/lines of Stations (i.e., A, B, and V).

The MRM results for event 200.19.5 along the line A stations are shown in Figure 8.22. The V components had no amplifications for the majority of stations in the estimated topographic frequency range. However, Stations A4 and A5 have a slight amplification of up to 2.5 from 0.1-1.0 Hz. The amplification does not seem to be related to any of the topographic features. However, these stations were directly over the hypocenter location (see Figure 8.4), and may be affected by direct ray path effects from vertical propagating P-waves. Some amplifications were also measured at frequencies greater than 2.5 Hz, but these amplification do not follow a top-down pattern and are likely caused by soil site effects.

For the N-S component, the crest station, A7, had no amplification in the estimated topographic frequency range (0.24-2.54), which was expected because the cross section in the N-S direction near Station A7 was reality flat (see Figure 8.8). However, a small amplification was measured between 0.1-0.2 Hz. This amplification peak showed a limited pattern of top-down amplification for stations off the slope, and was likely not the result of topographic effects. Amplification also occurred at frequencies above 2.5 Hz, but these were likely caused by soil site effects. Unlike the lack of amplification on Station A7, Stations A3-A5 had strong amplification over the entire frequency band. Station A3 had the largest amplification of just less than 9, while Stations A4 and A5 had amplifications of between 1.5 and 3. These amplifications are likely caused by topographic amplification from the N-S trending topographic features (see Figure 8.4 and 8.8). These amplifications will be discussed further in reference to line V.

For the E-W component, amplifications occurred at the crest station, A7, over the entire frequency band. In the estimated topographic frequency range (0.24-2.54 Hz), a constant amplification of approximately 2.0 was measured from 0.24-1.2 Hz, and a larger

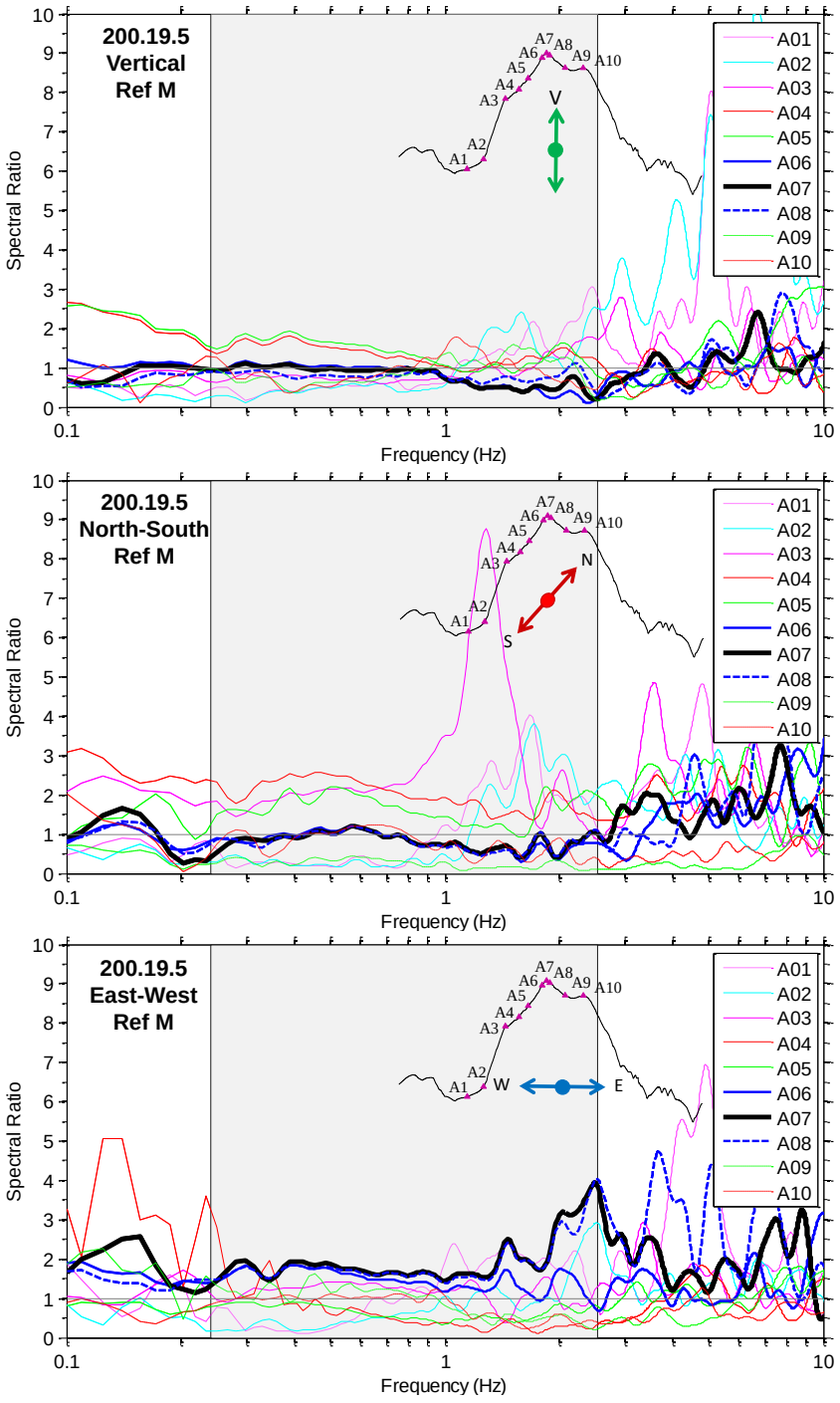

Figure 8.22: Median Reference Method (MRM) for event 200.19.5, line A vertical, North-South, and East-West components of motion. The estimated topographic frequency range based on cross-section geometry and average shear wave velocity is shaded.

amplification was measured at the upper edge of the estimate topographic frequency range of 4 for Station A7. From a frequency of 0.24-1.2 Hz, a good pattern of amplification was formed with Stations A6 and A8. However, only Station A8 and not Station A6 continued to follow the amplification pattern of Station A7 above a frequency of 1.2 Hz. Therefore, it was unclear whether the higher frequency amplification (1.2-4 Hz) was solely due to topographic effects. Other stations showed some amplifications at frequencies greater than 3 Hz. However, these amplifications were very erratic, and no significant patterns could be determined from the spectral ratios. Therefore, the amplifications at higher frequencies were likely not caused by topographic effects.

Horizontal polarity plots depicting the response of event 200.19.5 recorded by Stations A1-A10 based on the MRM method applied over the frequency range of 0.1 to 5 Hz, are provided in Figure 8.23. Based on the results presented in Figure 8.22, topographic effects are expected at frequencies less than 4 Hz. Stations A6-A9 all have a strong E-W polarity for the low frequency range, which is likely caused by topographic effects from the E-W trending feature. Stations A2-A5 all have fairly strong N-S polarities, likely caused by the topographic amplification from the N-S trending topography near the stations. The polarity of the different stations indicates that topographic amplifications are polarized in the direction of steep topographic relief for stations located near the crest of topographic features.

Overall, the MRM calculated almost no topographic amplification on the vertical component, but did predict clear patterns of topographic amplification in the E-W direction. Maximum amplifications of up to 4.0 were measured for the crest station A7. However, no amplifications were measured in the N-S direction for Station A7, which was expected given the lack of topographic relief in the N-S direction. Though,

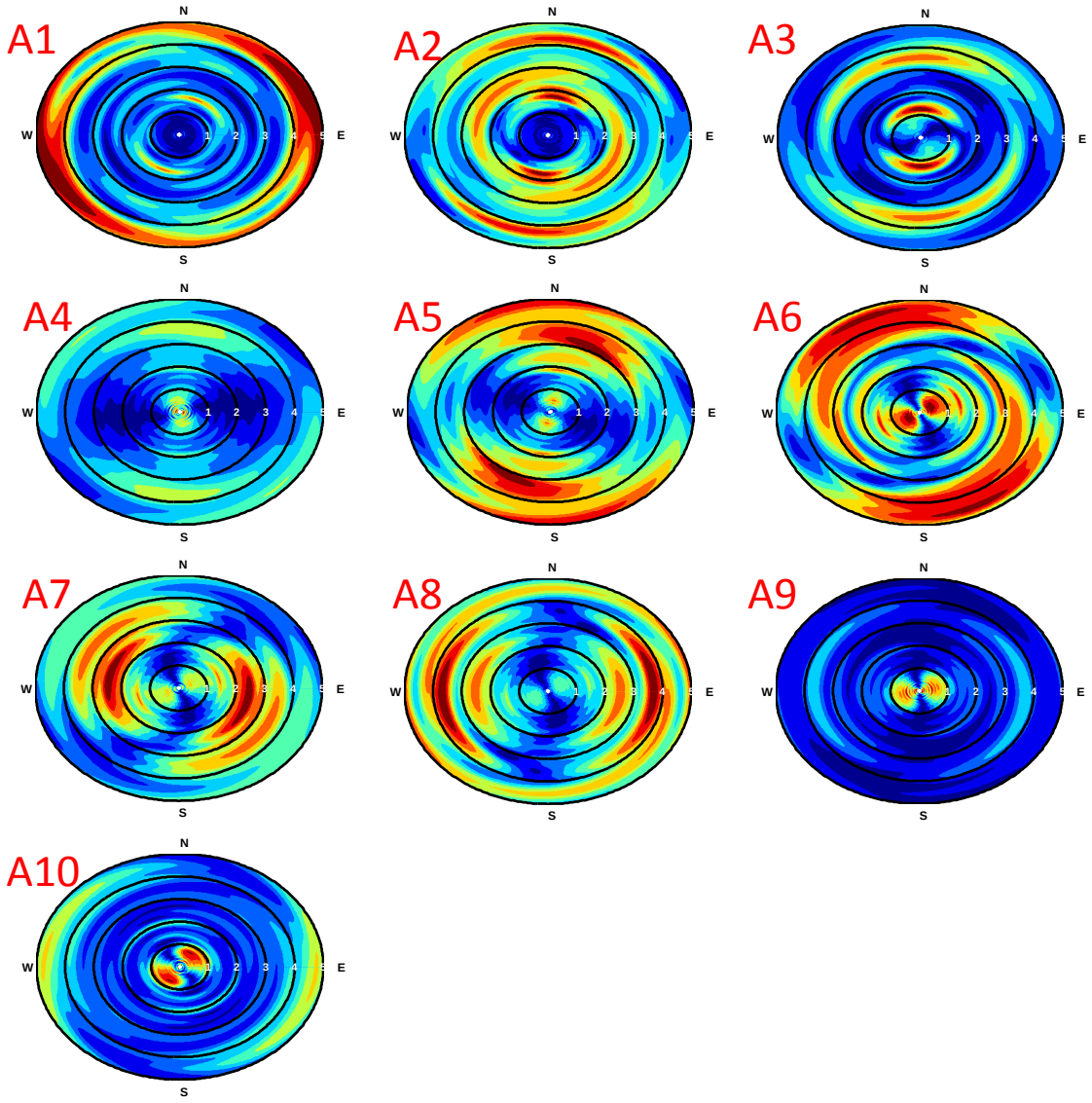

Figure 8.23: Horizontal polarity plots for the MRM method for event 200.19.5, line A.

strong amplifications were measured on Stations A3-A5, which were located on steep N-S trending topographic relief (see Figure 8.8).

The MRM results for event 200.19.5 along line B are shown in Figure 8.24. The V component had no amplification for the majority of stations in the estimated topographic frequency range. Similar to the A-line stations, Stations B3 and B4 had a

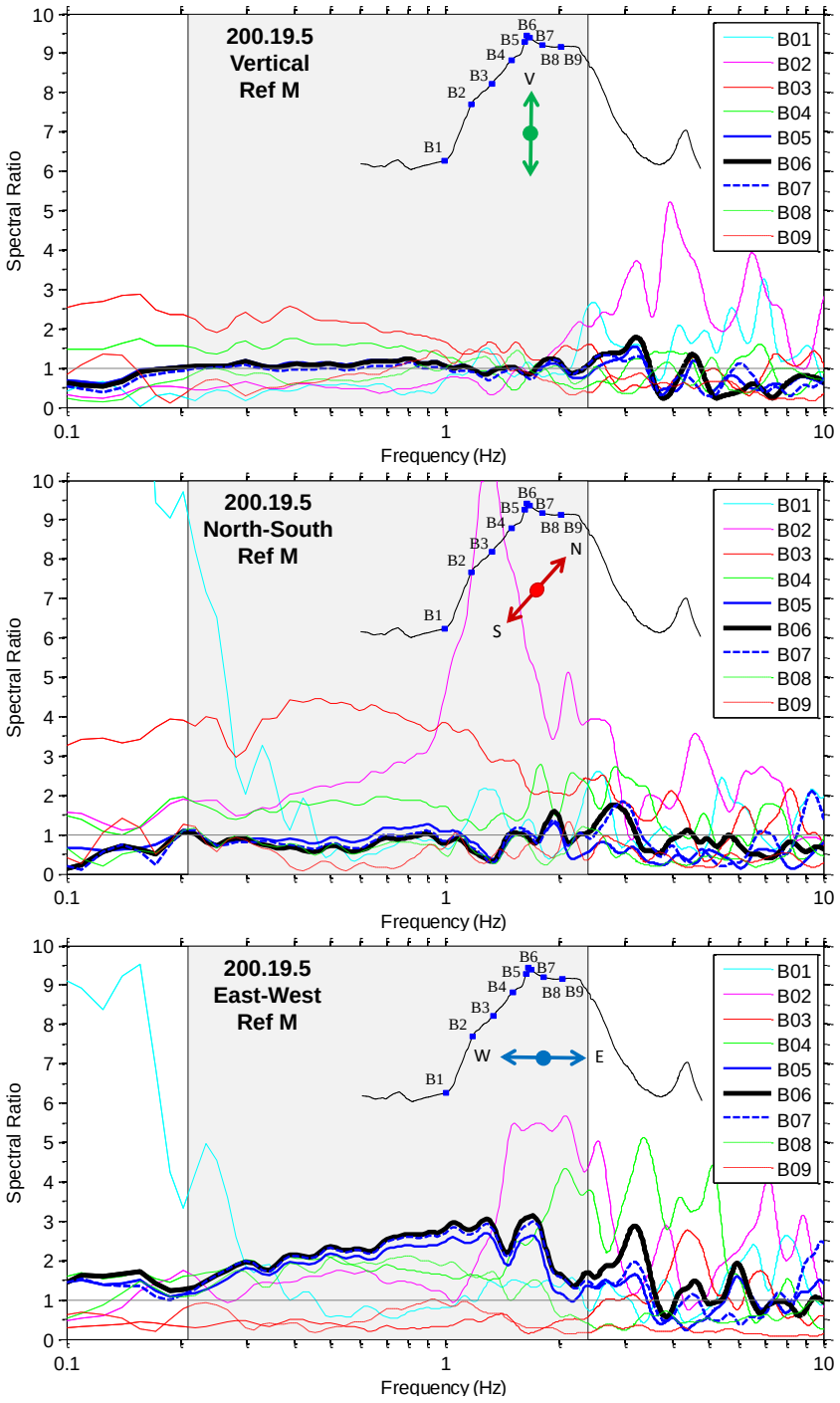

Figure 8.24: Median Reference Method (MRM) for event 200.19.5, line B vertical, North-South, and East-West components of motion. The estimated topographic frequency range based on cross-section geometry and average shear wave velocity is shaded.

slight amplification of up to 2.5 from 0.1-2.0 Hz. As with the A line, the amplifications did not seem to be related to any of the topographic features. However, the stations were directly over the average hypocenter location (see Figure 8.5), and may have been affected by direct ray path effects. Some amplifications were measured at frequencies greater than 2.5 Hz, but these amplifications were likely caused by something other than topographic effects.

For the N-S component, the crest station B6 had little to no amplification over the entire frequency range, with only a small amplification at approximately 2 Hz (similar to what was recorded during Phase I for this feature; see Chapter 7). Although Station B6 had a small amplification, Stations B2-B4 had large amplifications in the estimate topographic frequency range, which were likely caused by the steep N-S trending topographic relief under Stations B2-B4. Station B2 had over a 2 times amplification from 0.4 to 3.0 Hz, with the main amplification peak centered at 1.3 Hz, and a maximum amplification of just over 10. This peak (1.3 Hz) matched well with the estimated topographic frequency range for the V line cross section (i.e., 0.95-1.83 Hz), and was likely caused by topographic effects resulting from the N-S trending feature under Station B2. Station B3 also had significant amplifications over a broad frequency range from 0.1 Hz to 1.5 Hz, with an average amplification of 4. Station B4 also had amplifications over the same frequency range, although it only had an average amplification of 1.75. Low frequency amplifications were measured by Station B1 (which is off the topography), which were likely caused by either basin effects or more likely instrument error (low frequency drift).

For the E-W component, amplifications over 2 occurred at the crest station, B6, from 0.4 to 2 Hz, with a maximum amplification of 3. A good pattern of top-down amplification was measured in the same frequency range with Stations B5 and B7 having

a 5-10% reduction in amplification compared to the crest, and Stations B4 and B8 having between a 5-40% reduction in amplification compared to the crest. Therefore, this amplification was likely the result of topographic effects. Station B2 had an amplification of up to 5.5 from 1.2 to 3 Hz. This amplification did not match well with any estimated frequencies from cross sections B or C. Even when the E-W cliff-face from B1 to B2 (see Figure 8.5) was analyzed using Ashford and Sitar (1997), the resulting topographic frequencies were 0.85-1.46, which was still below the main amplification range recorded on Station B2. Therefore, the amplification was likely caused by some other effect or the 3D topography under Station B2 was causing amplification accounted for in the 2D topographic estimation methods. As with the N-S feature, Station B1 had a large low frequency amplification likely due to instrument errors.

Horizontal polarity plots depicting the response of event 200.19.5 recorded by Stations B1-B9 based on the MRM method applied over the frequency range of 0.1 to 5 Hz, are provided in Figure 8.25. Based on the results presented in Figure 8.24, topographic effects are expected at frequencies less than 2 Hz. Station B2 had a NW-SE polarity at frequencies less than 2 Hz, which indicative of the 3D feature under the station. Station B3 had a strong N-S polarity, likely related to the N-S trending feature under the station, while Stations B4-B8 all had very strong E-W polarities in-line with the main E-W trending topographic feature under the stations. Similar to previous cross sections, the polarity of the amplifications seem to be in-line with the steep topographic relief under the station.

Overall using the MRM, only small amplifications on stations directly over the hypocenters (B3-B4) were measured on the vertical component. Large amplifications were measured by Stations B2 and B3 in the N-S direction, but no amplifications were measured on the crest station, B6, in the N-S direction. However, Station B6 had

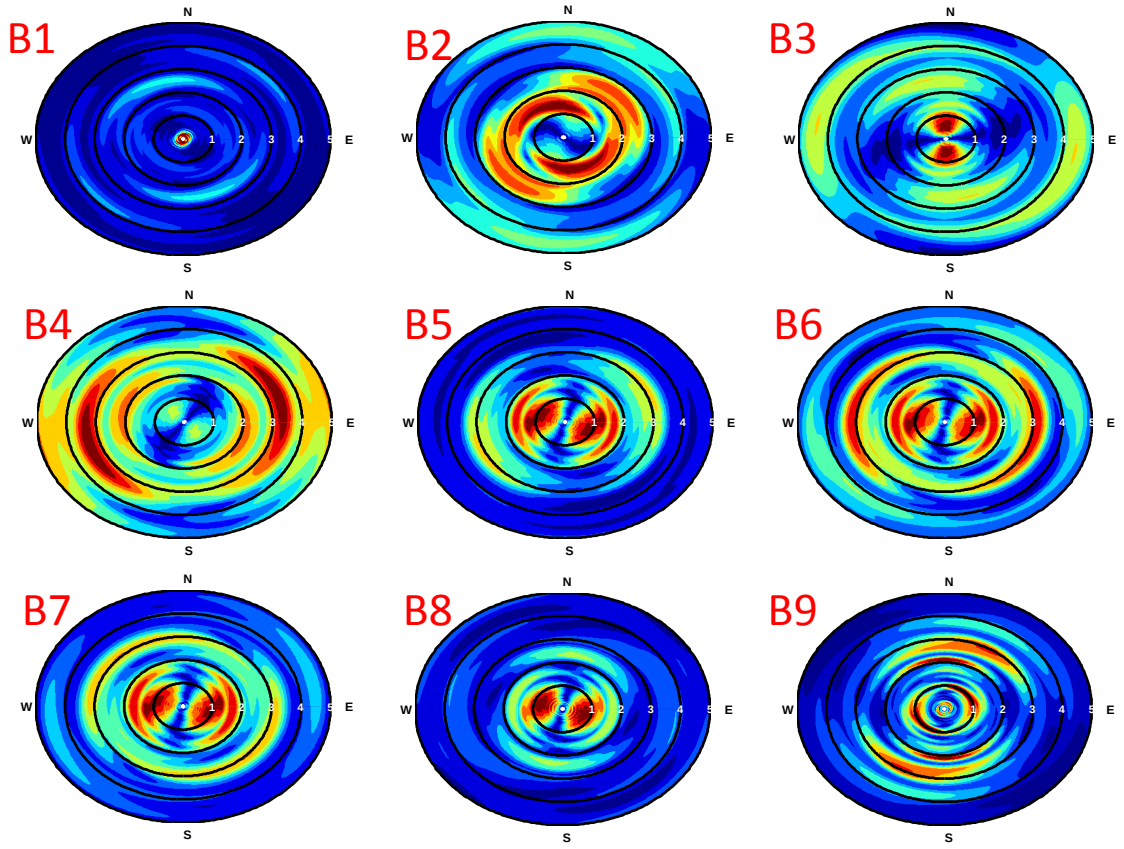

Figure 8.25: Horizontal polarity plots for the MRM method for event 200.19.5, line B.

amplifications of up to 3.0 within the estimated topographic frequency range in the E-W direction. A good pattern of top down amplification was also measured by Stations B4-B5 and B7-B8 within the same frequency range. This indicates that topographic effects were likely the cause for the measured amplification in the E-W direction for Stations B4-B8, and possibly for Stations B2-B4 in the N-S direction.

The MRM results for event 200.19.5 along line V are shown in Figure 8.26. For the V component, all the stations had random amplifications at frequency greater than 2 Hz, but for frequency less than 2 Hz, the V-line stations have a large low frequency

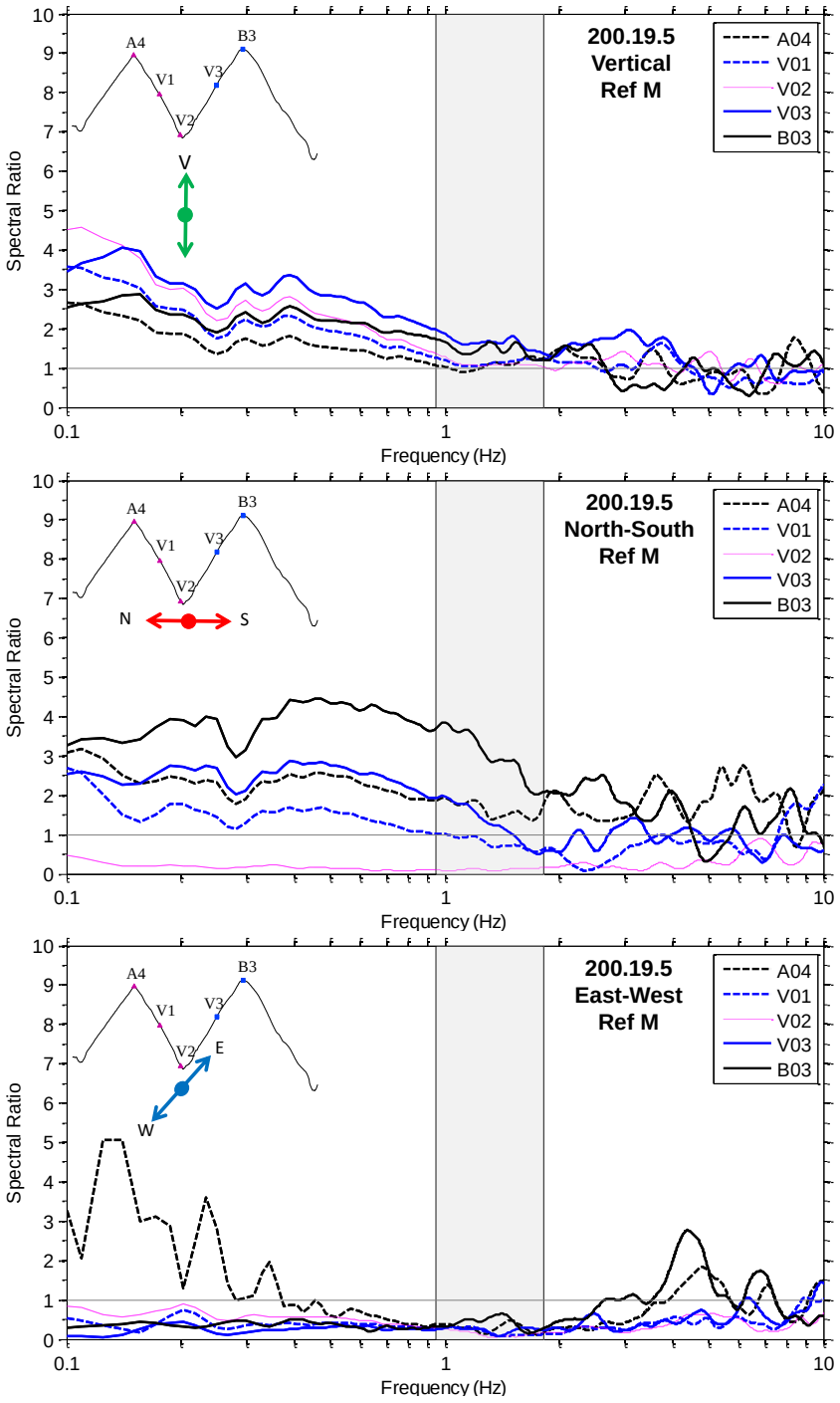

Figure 8.26: Median Reference Method (MRM) for event 200.19.5, line V vertical, North-South, and East-West components of motion. The estimated topographic frequency range based on cross-section geometry and average shear wave velocity is shaded.

amplification that increases in spectral ratio at lower frequencies. Since, all these stations were at varying elevations on the topography (i.e., they were at the crest, base, and along the slope) and have a poor pattern of amplification, it is unlikely that topographic effects caused this amplification. The one thing that all these stations had in common was they were located almost directly above the hypocenter of event 200.19.5. The vertically propagating P-wave would arrive directly in-line with the vertical component possibly causing a higher than normal vertical ground. Large vertical ground motions on stations directly under the hypocenter have also been observed in some large earthquakes such as the M6.3 Christchurch Earthquake (Bradley and Cubrinovski 2011). This could explain the high vertical amplification on stations in the V line, along with other stations in the A and V lines.

For the N-S component, amplifications were measured on all stations expect Station V2, which was located in the valley of the feature. Station B3 had the largest amplification of up to 4.5 over a frequency range from 0.1-3.0 Hz. Station V3 (just down the hill from Station B3) had a 30% lower amplification than Station B3, and has an amplified frequency range from 0.1-1.5 Hz. Station A4 had a very similar response to Station V3 with about a 30% lower amplification than Station B3. Station V1 had about a 30% lower amplification than the Northern crest station, A4. These amplifications formed an excellence top-down pattern of amplification that indicated topographic effects. However, the amplification frequency range for each of the stations was far wider (0.1-3.0 Hz) than the range predicted by Ashford and Sitar (1997) and Paolucci (2002) (0.95-1.83 Hz) for the geometry of the cross section and the average shear wave velocity of the material. It is unknown whether or not the wider amplification frequency range recorded on the V line was caused by the poor performance of the 2D analytical methods

when applied to 3D features or if other ground motion effects were influencing the ground motions recorded on this part of the feature.

For the E-W component, no amplifications were measured in the estimated topographic frequency range (0.95-1.83 Hz). Stations A4 and B3 measured a small amplification peak at approximately 5 Hz. However, this was directly in the soil site effects band (i.e., 5-15 Hz), and was likely the result of soil site effects. Station A4 also had a large amplification a low frequencies (<0.4 Hz), but this was likely the result of instrument error/low frequency drift.

Horizontal polarity plots depicting the response of event 200.19.5 recorded by Stations A4, V1-V3, and B3 based on the MRM method applied over the frequency range of 0.1 to 5 Hz, are provided in Figure 8.27. Based on the results presented in Figure 8.26, topographic effects are expected at frequencies less than 2 Hz. Stations A4, V1, V3, and B3 all have a strong N-S polarity, especially below 1 Hz, which matches well with the N-S trending topography around each station and the high location of each station on the topography. Station V2 has a more E-W polarity aligning more with the valley and E-W trending topography.

Overall, low frequency amplifications were calculated on the vertical components using the MRM, but these amplifications were not believed to be the sole result of topographic effects, but rather the result of being directly above the hypocenter of the event. Significant amplifications were calculated in the N-S direction for all the stations expect V2. N-S amplifications of up to 4.5 were measured over a wide frequency range of 0.1-3 Hz for stations excluding V2. The N-S amplifications had a good pattern of top-down amplification, but did not match well with the estimated topographic frequency range. No significant amplifications were recorded in the E-W direction, which

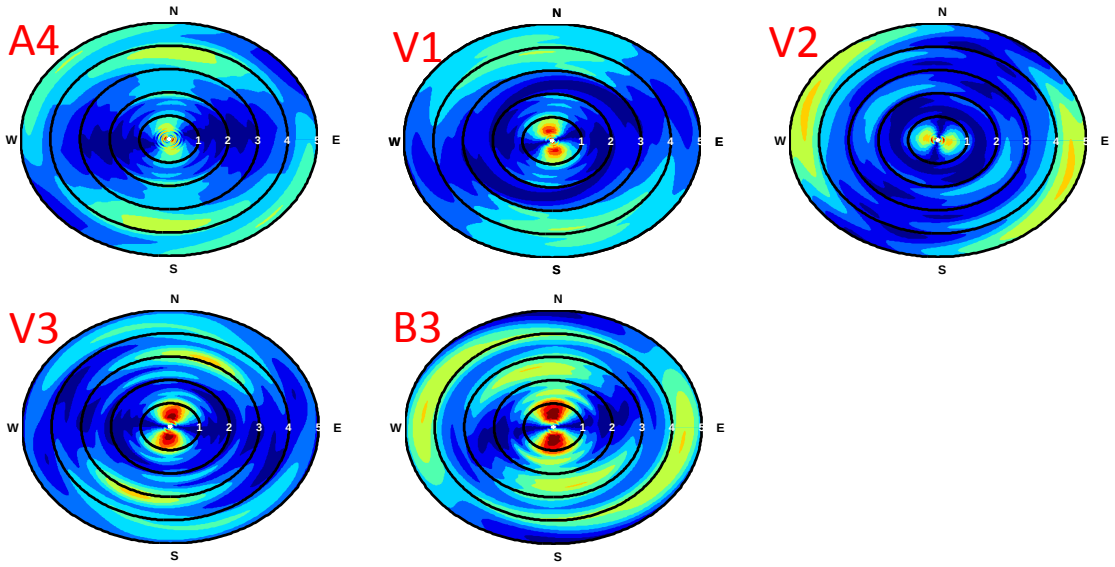

Figure 8.27: Horizontal polarity plots for the MRM method for event 200.19.5, line V.

corresponded well with the strong N-S trending topography and weak E-W trending topography.

8.3.3 Horizontal to Vertical Spectral Ratio (HVSR) Analysis

Horizontal to Vertical Spectral Ratio (HVSR) was originally used to estimate a sites natural resonant frequency or the frequency where soft soil amplification may be possible. In recent years, researchers have shown that the method may be used to estimate topographic effects (Lermo and Chavez-Garcia 1993, Bard 1999, and Lebrun et al. 1999, Massa et al. 2010). HVSR is calculated by dividing the horizontal component for a given sensor by the vertical component of that same sensor. This method has the advantage of only requiring one station for the calculations, compared with to 2 to 10 stations for the SSR and MRM methods. For further details on the HVSR method, please refer to Chapters 2, 3, and 4.

The North-South and East-West HVSR plots for event 200.19.5 along A line are shown in Figure 8.28. For the N-S spectral ratio, an amplification peak was measured at 2.5 Hz on the crest station, A7. Stations A6 and A8 also had an amplification peak at 2.5 Hz. The three stations each have similar amplification factors of 8-11, with no strong top-down amplification pattern, but all three stations had the same amplification indicating that the response may be driven by topographic effects. Station A3 had an amplification peak at between 1-1.8 Hz of approximately 10, which matched well with the estimated N-S topographic frequency range calculated from the N-S trending feature under Station A3, indicating topographic amplification. Other amplifications were measured at frequencies above 4 Hz. However, these amplifications were likely caused by soil site effects (i.e., 5-15 Hz soil site effects range; refer to Chapter 6).

For the E-W component, an amplification peaks for Stations A7 (32), A8 (27) and A6 (15) were measured at 2.5 Hz. The amplification frequency range recorded on the E-W components match amplification frequency range recorded on the N-S components for the majority of the stations in the A line, but the E-W components recorded a much higher amplification than the N-S components. This difference in the amplification factors indicates the E-W components were more affected by topographic effects than the N-S components, which matches well with large E-W trending topographic feature (i.e., larger amplifications for components in-line with steep topographic features). The amplification peaks show a pattern of top-down amplification, but only includes Stations A6 and A8 and not stations further down the slope. Moreover, the peak is at the high frequency edge of the estimated topographic frequency range, which brings into question whether the amplification peak is the result of topographic amplification or some other effect.

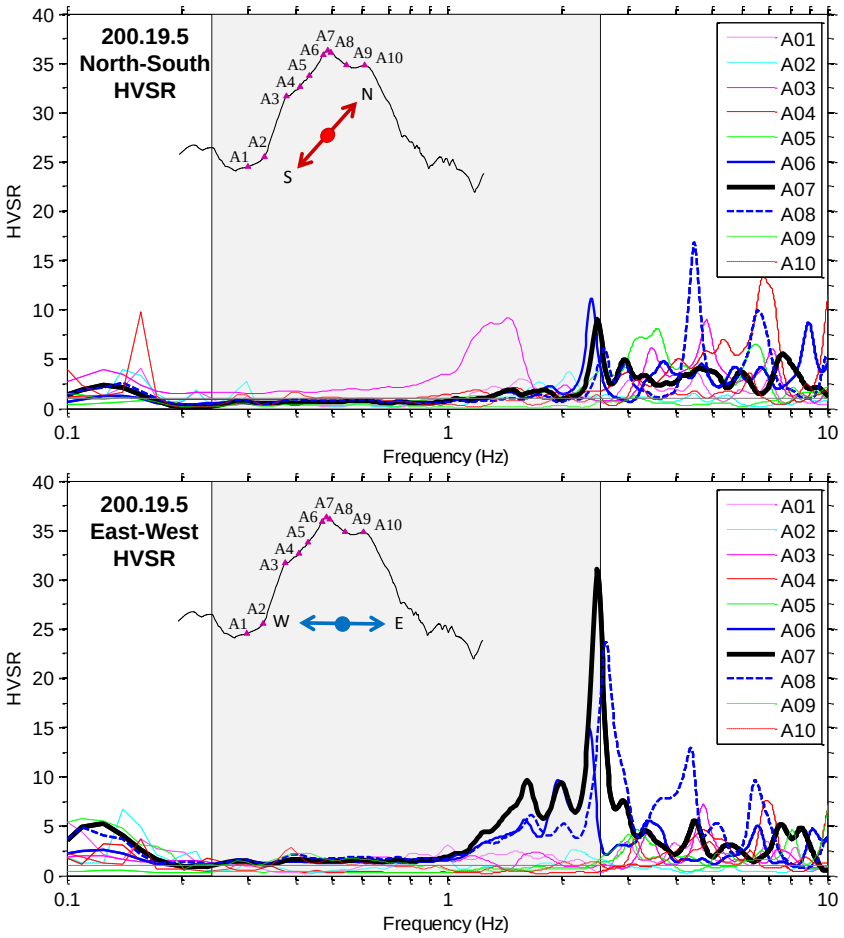

Figure 8.28: Horizontal to Vertical Spectral Ratio (HVSR) for event 200.19.5, line A vertical, North-South, and East-West components of motion. The estimated topographic frequency range based on cross-section geometry and average shear wave velocity is shaded.

Horizontal polarity plots depicting the response of event 200.19.5 recorded by Stations A1-A10 based on the HVSR method applied over the frequency range of 0.1 to 5 Hz, are provided in Figure 8.29. Based on the results presented in Figure 8.28, topographic effects are expected at frequencies less than 4 Hz. Stations A7-A8 had a strong E-W polarity, which matches the steep E-W trending feature under the stations. Station A6 had a strong NW-SE amplification peak. Stations A3-A4 had a slight polarity in the N-S direction, which corresponds well with the N-S trending topography under those stations.

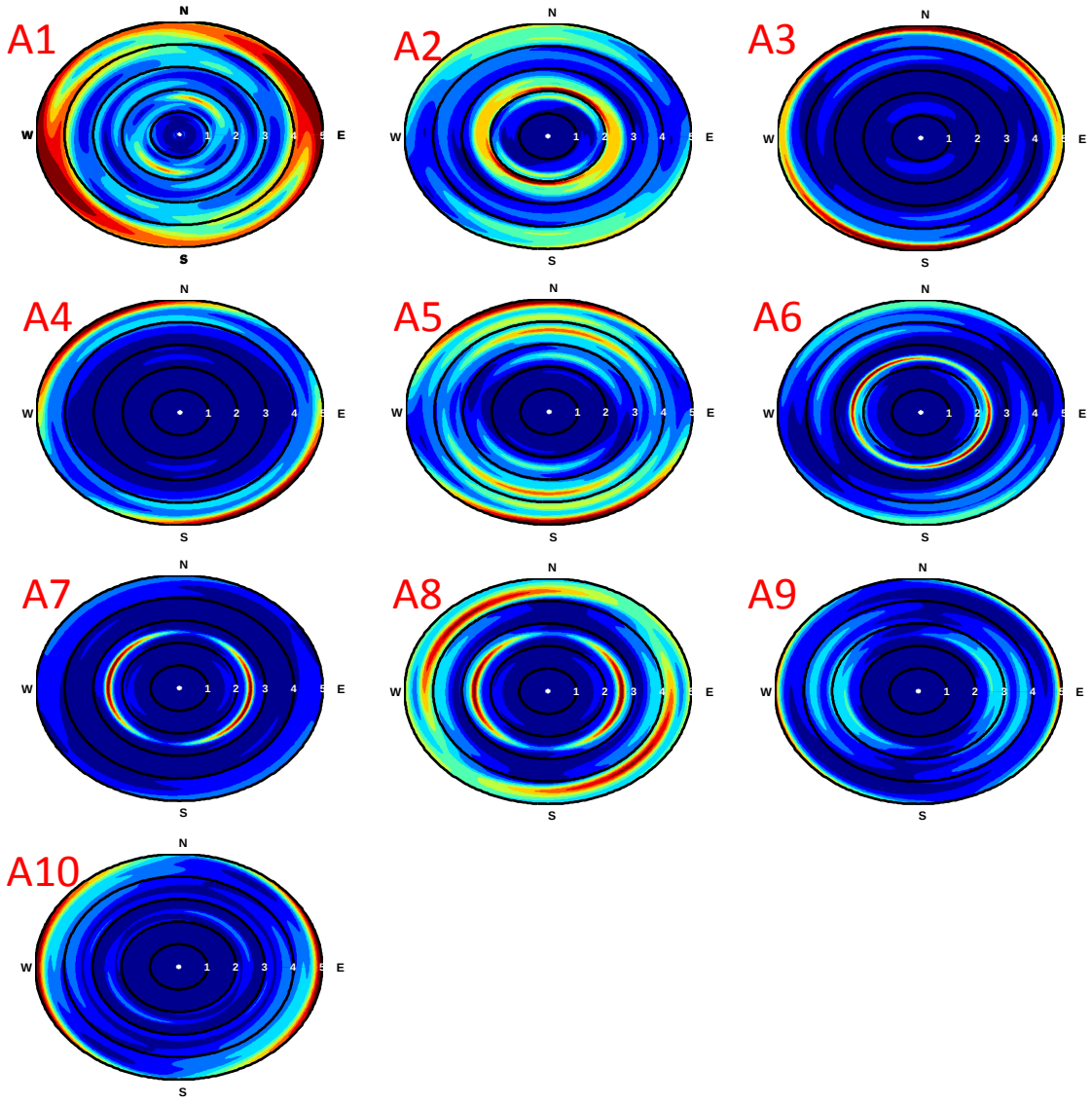

Figure 8.29: Horizontal polarity plots for the HVSR method for event 200.19.5, line A.

As with the other methods, the polarity of topographic effects seems to be orientated in the direction of steep topography for the HVSR method.

Overall, the HVSR method calculated amplifications in both horizontal directions at approximately the same frequency of 2.5 Hz. However, the E-W peak was much

stronger for Stations A6-A8 with HVSR spectral ratios of up to 32. The amplification peaks showed a good pattern of amplification for frequency less than 2.5 Hz. However, for frequency greater than 2.5 Hz and outside the estimated topographic frequency range, the amplification pattern starts to fall apart, raising question as to whether the peaks were caused by topographic effects.

The North-South and East-West HVSR plots for event 200.19.5 along B line are shown in Figure 8.30. For the N-S component, Station B2 had the only significant amplification, over the estimated topographic frequency range, at 1.4 Hz with an spectral ratio of 35. This peak corresponded well with the estimated topographic frequency range for line V, which is approximately the same as the topographic frequencies for the N-S topographic under Station B2 (see Figure 8.9), and may be the cause of the amplifications at Station B2. Amplifications at frequencies greater than the estimated topographic frequency range were likely caused by soil site effects, and the low frequency amplification measured by Station B1 was likely due to instrument error (low frequency drift).

For the E-W component, amplifications were measured by Stations B5-B7 from 1.2-2.0 Hz of up to 8. A fairly good pattern of amplification was formed around the crest station, and amplifications were within the estimated topographic frequency range. Therefore, the amplifications were likely caused by topographic effects. Stations B2 and B4 have amplifications in the same frequency range. The amplifications of Station B2 were likely caused by the cliff-type westward-facing slope between B1 and B2. Ashford and Sitar (1997) predicts a topographic frequency of 1.46 Hz for the height and average Vs of the cliff face (computed similar to those discussed in Chapter 6), which is very close to the center topographic frequency. The cause for the amplification on Station B4 is not known, but may be the result of topographic effects on the E-W cross section.

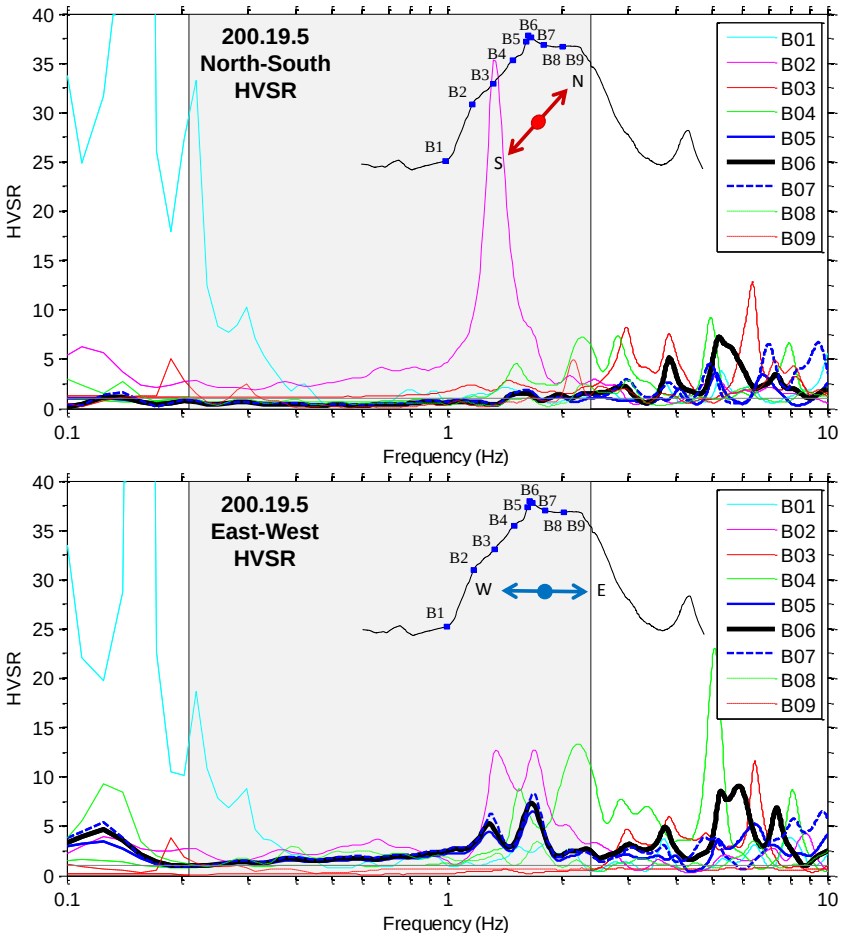

Figure 8.30: Horizontal to Vertical Spectral Ratio (HVSR) for event 200.19.5, line B vertical, North-South, and East-West components of motion. The estimated topographic frequency range based on cross-section geometry and average shear wave velocity is shaded.

Horizontal polarity plots depicting the response of event 200.19.5 recorded by Stations B1-B9 based on the HVSR method applied over the frequency range of 0.1 to 5 Hz, are provided in Figure 8.31. Based on the results presented in Figure 8.30, topographic effects are expected at frequencies less than 2 Hz. Stations B5-B7 all have a weak E-W polarity in-line with the E-W cross section. Stations B1-B2 and B8-B9 all have a stronger N-S polarity.

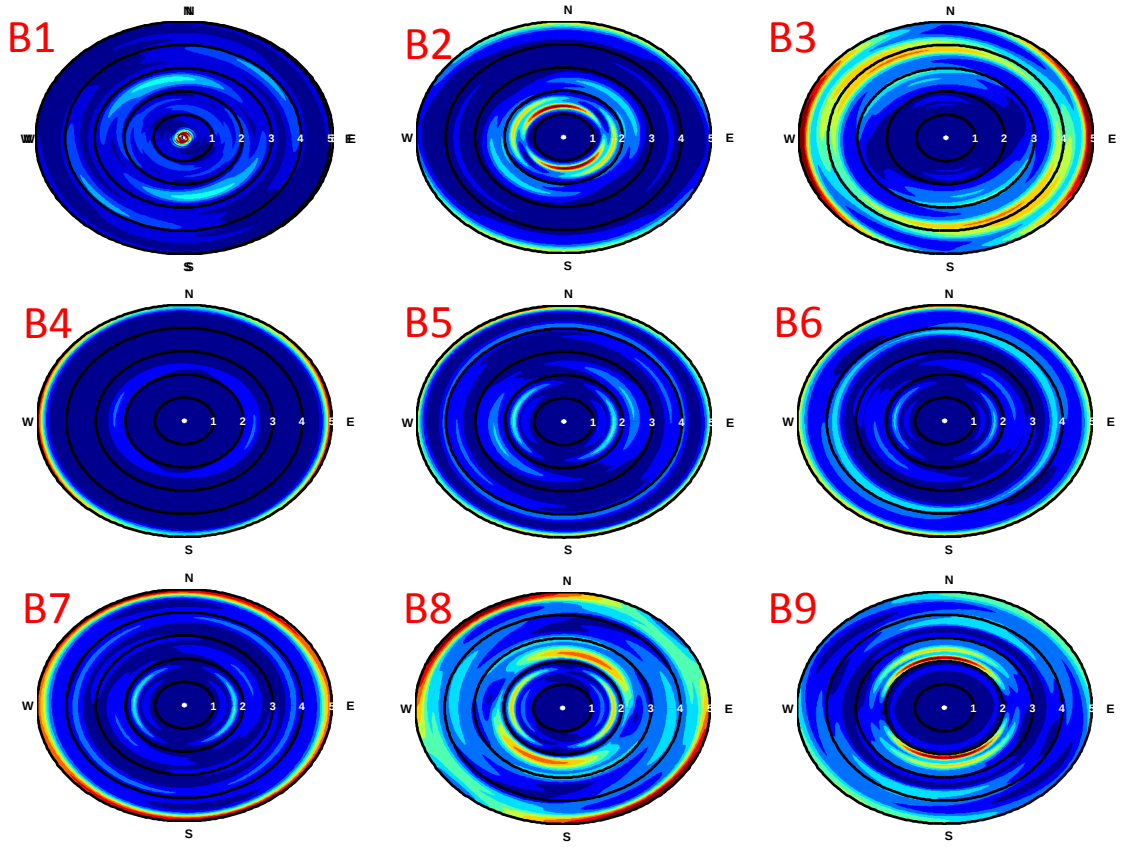

Figure 8.31: Horizontal polarity plots for the HVSR method for event 200.19.5, line B.

Overall, the HVSR method calculated amplifications for the crest stations, B5-B7, in the E-W direction from 1.2-2.0 Hz frequency range, which matched well with the estimated topographic frequency range for the E-W direction (0.21-2.39 Hz). No amplifications were calculated for the crest stations in the N-S direction. Station B2 measured amplification in both the N-S and E-W direction at approximately 1.4 Hz, with the N-S direction having the highest amplification. The peak frequency in both directions matched well with estimates for the N-S feature and the Westward-looking face.

The North-South and East-West HVSR plots for event 200.19.5 along V line are shown in Figure 8.32. For the N-S spectral ratio, a small amplification peak was

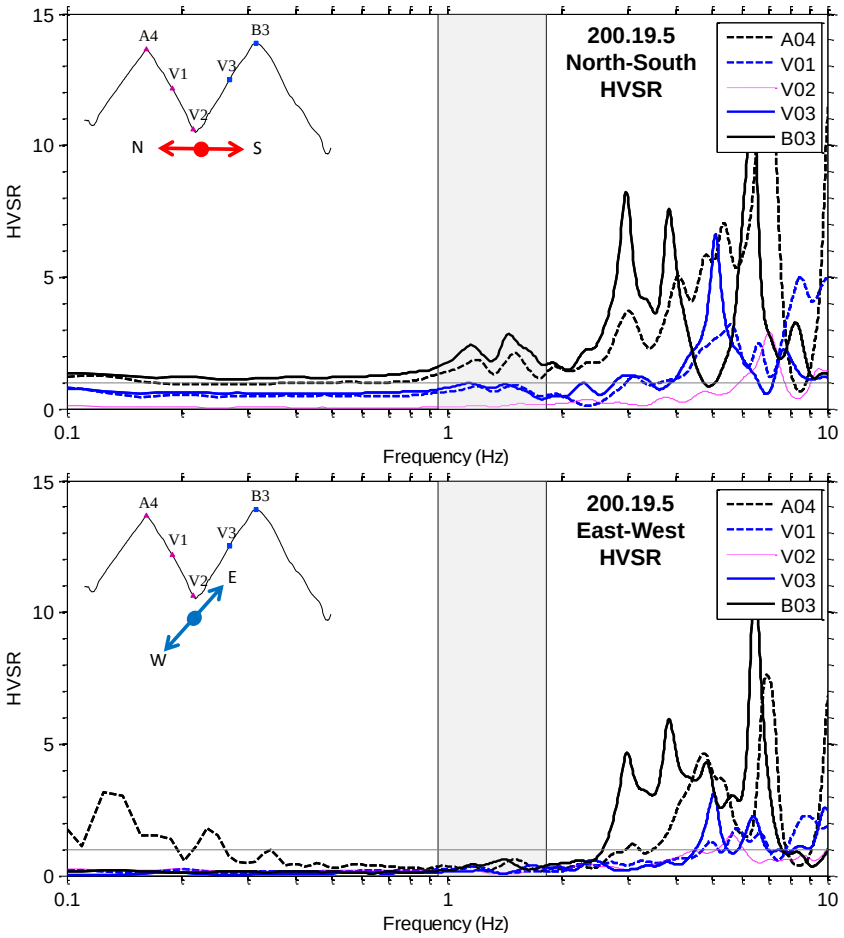

Figure 8.32: Horizontal to Vertical Spectral Ratio (HVSR) for event 200.19.5, line V vertical, North-South, and East-West components of motion. The estimated topographic frequency range based on cross-section geometry and average shear wave velocity is shaded.

measured in the estimated topographic frequency range (0.95-1.84 Hz) for the crest stations. A maximum amplification of 3.0 was measured on Station B3 (south crest station), followed by Station A4 (north crest station) with an amplification of 2.0. Station V1 and V3 had no amplification with spectral ratios of 1.0, while Station V2 measured a spectral ratio less than 1.0. At frequencies above the estimated topographic frequency range, large spectral ratios were measured. However, these amplifications are directly in

the soil site effects frequency band and no pattern of amplification could be established. Therefore, the amplifications were likely caused by soil site effects.

For the E-W spectral ratio, no amplifications were measured in the estimated topographic frequency range, which matches well with the lack of E-W topographic relief under the V line. Some amplification occurred at higher frequencies, but like the N-S direction, these were believed to be the result of soil site effects.

Horizontal polarity plots depicting the response of event 200.19.5 recorded by Stations A4, V1-V3, and B3 based on the HVSR method applied over the frequency range of 0.1 to 5 Hz, are provided in Figure 8.33. Based on the results presented in Figure 8.32, topographic effects are expected at frequencies less than 2 Hz. Station V1 had a fairly strong polarity in the N-S direction. However, the other stations in the array did not have a strong polarity in any horizontal direction because the amplifications at frequencies greater than 2 Hz mask the lower frequency topographic amplifications.

Overall, the HVSR method only calculated a small amplification peak in the N-S direction. This amplification had a maximum amplification of 3 and 2 for crest Stations B3 and A4, respectively. A good top-down amplification pattern was form by the stations in the array, and the measured amplification frequencies matched well with the estimated topographic frequencies.

8.3.4 Method Comparison

Event 200.19.5, a M_L 1.6 “earthquake”, was processed using three separate methods to assess the effects of topography on the seismic response of the mountain. Each analysis method indicated amplification in the topographic frequency range estimated using Ashford and Sitar (1997) and Paolucci (2002), for the three lines of stations. The spectral ratios calculated using each method for only the crest stations of

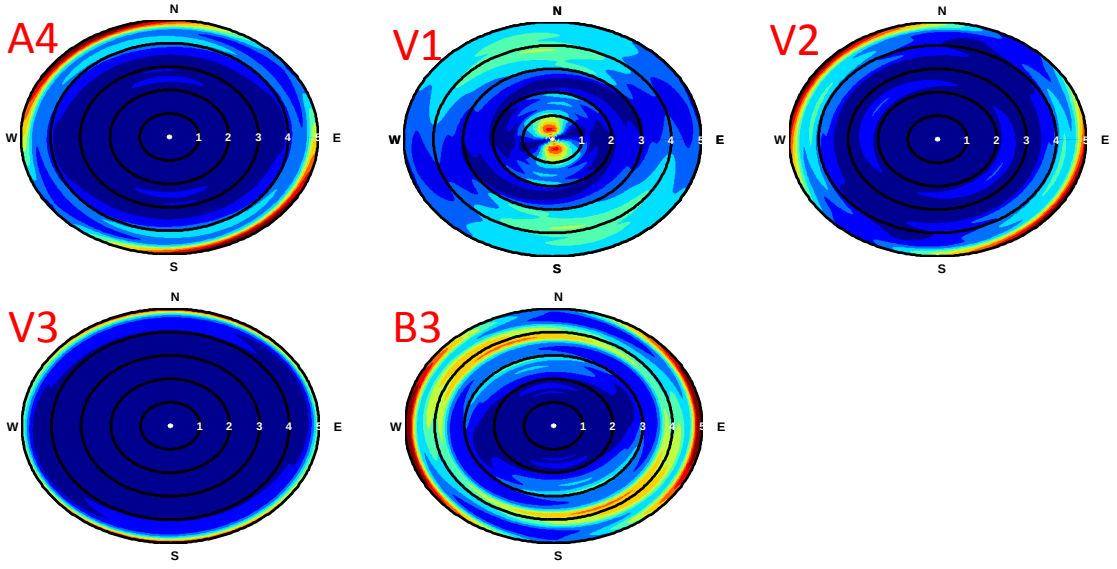

Figure 8.33: Horizontal polarity plots for the HVSR method for event 200.19.5, line V.

each cross section are compared in this section to assess the differences and similarities between the methods.

The spectral ratios for the SSR, MRM and HVSR for Station A7 (the crest station in line A) are shown in Figure 8.34. Comparing the V components over the estimated topographic frequency range (0.24-2.54 Hz), the SSR method had a spectral ratio of around 7.0 at a frequency of 3 Hz. The MRM, on the other hand, had a spectral ratio of around 1.0, which indicates no amplification of the vertical component. The two methods compare well over many of the higher frequencies; however, an amplification at lower frequencies was predicted using the SSR method, while zero amplification was predicted using the MRM.

For the North-South component from 0.25 to 0.85 Hz, the SSR method predicts a 3-7 times amplification. However, the MRM and HVSR methods do not indicate amplification in that same frequency range. Due to limited topographic relief in the N-S

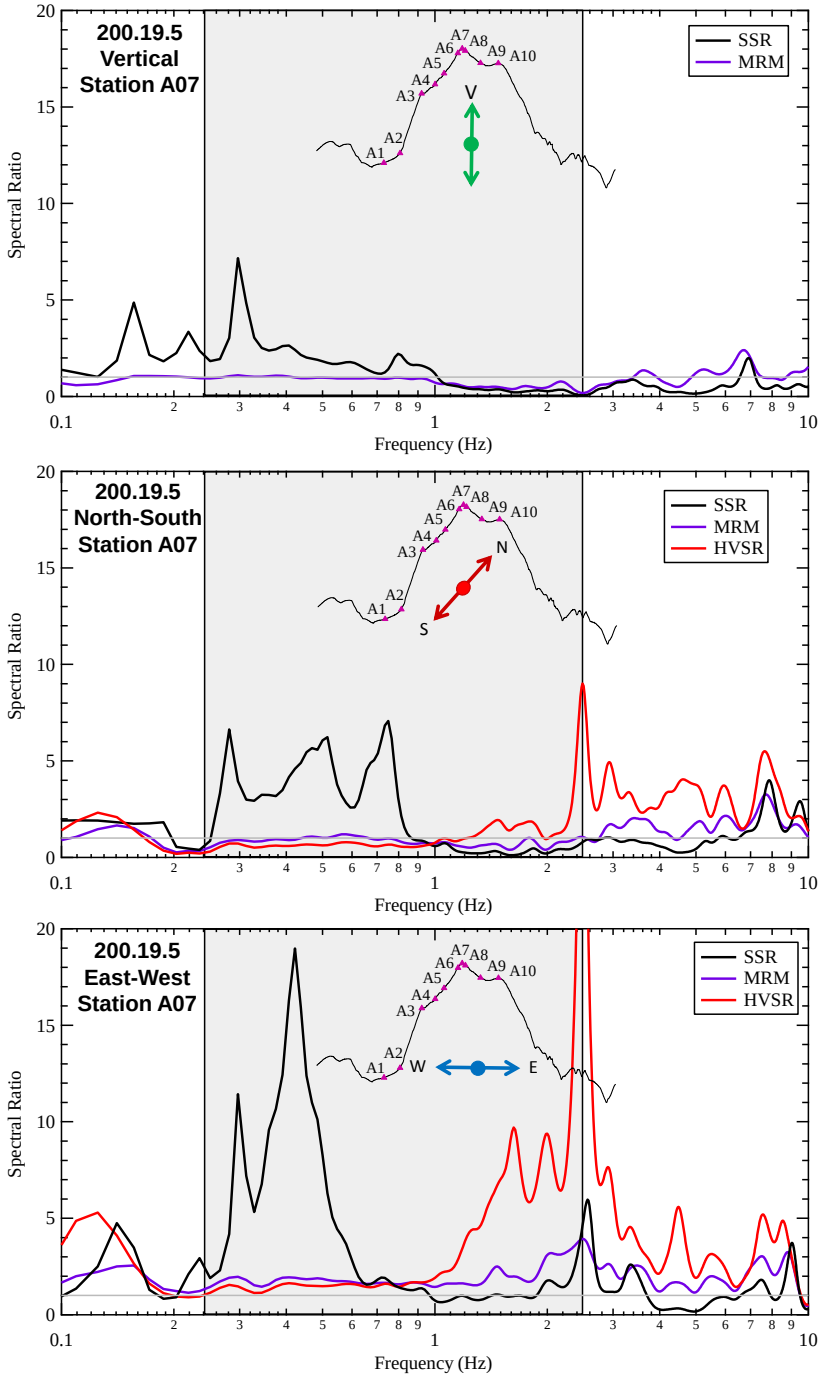

Figure 8.34: Comparison of A line SSR, MRM, and HVSR results for event 200.19.5 Station A7 vertical, North-South, and East-West components. The estimated topographic frequency range based on cross-section geometry and average shear wave velocity is shaded.

direction near Station A7, one would likely not expect amplification in the N-S direction. Therefore, the SSR method has likely mis-predicted an amplification peak in this range. The HVSR has the same mis-prediction at a frequency of 2.5 Hz where the method predicts amplification of up to 10, while the other two methods predict zero amplification.

For the East-West component, a strong amplification peak was predicted between 0.25 Hz and 0.65 Hz using the SSR method, with a maximum amplification of 19. However, only a slight amplification of 2.0 or less was predicted using the MRM and HVSR methods for the same frequencies. An amplification peak was also measured at 2.5 Hz for each method. This peak was identified as topographic effects diven using the pattern of amplification for each method. The HVSR method had the highest spectral ratio (over 30), while the SSR and MRM method had spectral ratios of 6 and 4, respectively.

Overall, the methods had similar amplification frequency ranges for the E-W component, although the spectral ratios were quite different. For the V and N-S directions, the methods disagreed across many frequencies, with some amplification predicted using the SSR and HVSR methods, while the MRM predicted very little or no amplification for many of the frequencies. To investigate the differences between the SSR and MRM methods, the spectral ratio for event 200.19.5 was plotted for Station A7 (the crest) using the SSR method and Stations A7 and A1 using the MRM method (see Figure 8.35). Comparing the MRM response of Stations A7 and A1 for each component, the amplitudes of the two stations were almost always polar opposites at each frequency (i.e., when Station A7 has a ratio greater than 1, Station A1 has a ratio less than 1, and vice-versa). Therefore, to calculate the response at the crest of the feature using the SSR method, Station A7 (an amplification station in the estimated topographic frequency

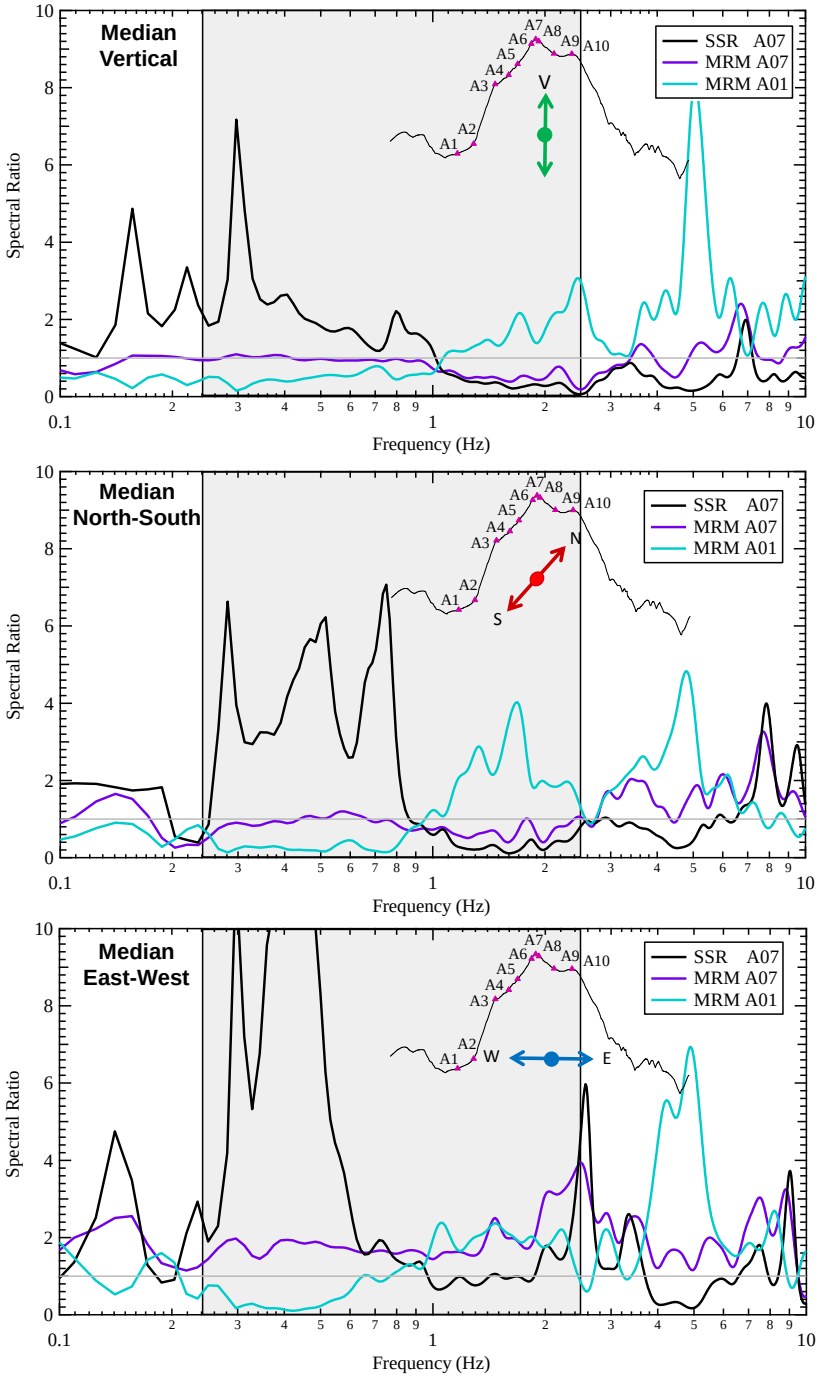

Figure 8.35: Comparison of A line SSR Station A7 with MRM from Stations A7 and A1 for event 200.19.5 vertical, North-South, and East-West components. The estimated topographic frequency range based on cross-section geometry and average shear wave velocity is shaded.

range) was divided by Station A1 (a de-amplification station in the estimated topographic frequency range). This calculation resulted in a large amplification peak for Station A7 using the SSR method. Combining a de-amplified station with an amplified station was explained in Chapter 7, and often resulted in either false amplification peaks or significantly overestimating the amplification factor.

The spectral ratios for the SSR, MRM and HVSR methods for Station B6 (the crest station in line B) are shown in Figure 8.36. For the V component, amplifications significantly over 10 were estimated using the SSR method for frequencies less than 1 Hz. However, the MRM method has a flat amplification of 1.0 over the same frequency range. No topographic amplifications were identified in the previous sections. Therefore, the amplifications on the SSR method are likely errors.

For the North-South component, the methods produced similar spectral responses, a slight amplification from 0.45-0.8 Hz was calculated using the SSR method, while the other two methods indicated de-amplification in the same frequency range. All three methods indicated a small amplification peak at 2 Hz. The SSR method had a spectral ratio of 4.0, but the MRM and HVSR methods had a much smaller amplification factor of less than 2.0.

For the East-West component, all three methods predicted amplification between 0.4 Hz and 2 Hz. A lower frequency peak amplification of 0.7 Hz was calculated using the SSR method, while the maximum amplification was closer to 1.7 Hz for the MRM and HVSR methods. The HVSR and MRM methods gave very similar responses over the estimated topographic frequency range, while the SSR method was quite different. Maximum amplifications of 7, 5, and 3 were calculated for the HVSR, SSR and MRM methods, respectively.

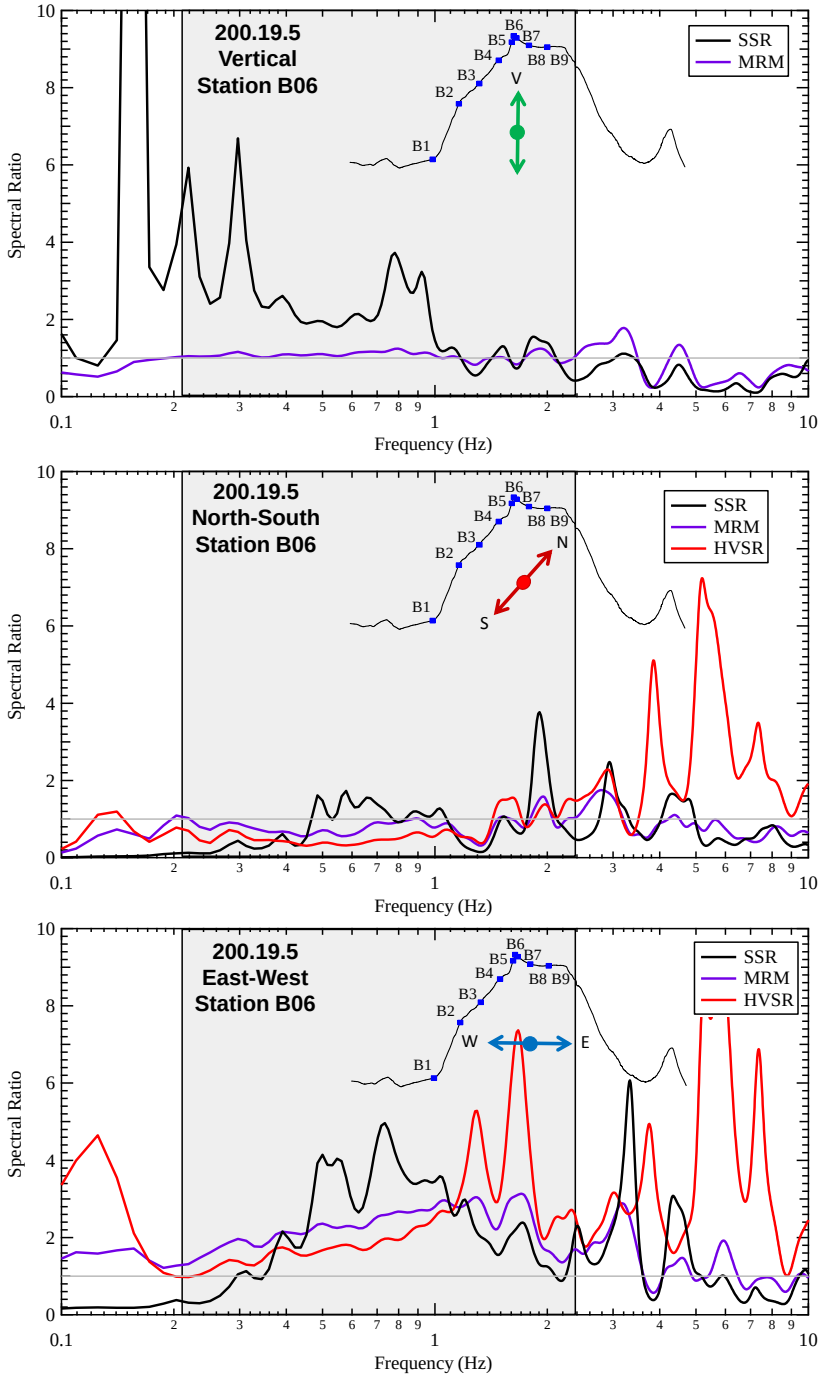

Figure 8.36: Comparison of B line SSR, MRM, and HVSR results for event 200.19.5 Station B6 vertical, North-South, and East-West components. The estimated topographic frequency range based on cross-section geometry and average shear wave velocity is shaded.

Overall, the methods have similar amplification frequency ranges for the N-S and E-W components. The methods were much closer for the E-W component, but had significant difference for the vertical component. The spectral ratio for event 200.19.5 was plotted for Station B6 (the crest) using the SSR method and Stations B6 and B1 using the MRM method (see Figure 8.37). As with the A line, the B line of stations produce the same trend, where the MRM for Stations B6 and B1 mirror each other for each component and each frequency, leading to an exaggeration of the spectral ratio for the SSR method.

The spectral ratios for the SSR, MRM and HVSR methods for Station B3 (North crest station in line V) are shown in Figure 8.38. For the V component, the SSR and MRM methods both indicated a slight amplification of less than 2.0 in the estimated topographic frequency range, and matched well in that frequency range, and at higher frequencies. At frequencies less than the 1 Hz, the MRM method predicted an amplification of up to 3.0, while the SSR method predicted de-amplification over the same frequency range. This MRM amplification may be the result of the vertically propagating P-waves mentioned early. The SSR, with reference V2, would result in flat-line amplification because both the measurement and reference stations are directly under the hypocenter, resulting in an equal vertical ground motion.

For the North-South component, the SSR method indicated a very large amplification range from 0.1-4.5 Hz, with a maximum amplification of over 50. The MRM method, however, only indicated a small amplification of 4.0 from 0.1-1.0 Hz, and HVSR method predicted de-amplification in the same frequency range. In the estimate topographic frequency range (0.95-1.83 Hz), the MRM and HVSR methods predict an amplification of approximately 3.0 compared to the SSR amplification of 35.

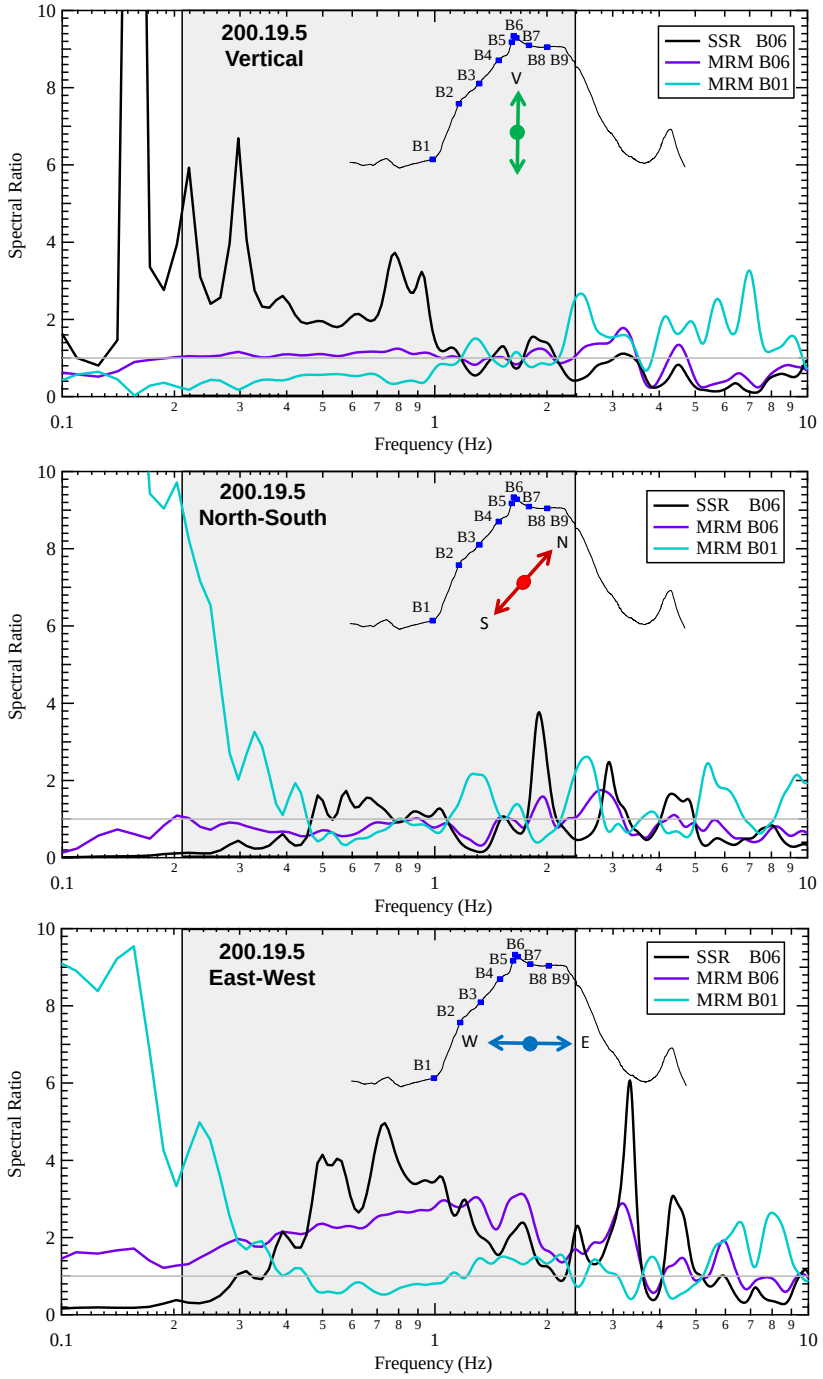

Figure 8.37: Comparison of B line SSR Station B6 with MRM from Stations B6 and B1 for event 200.19.5 vertical, North-South, and East-West components. The estimated topographic frequency range based on cross-section geometry and average shear wave velocity is shaded.

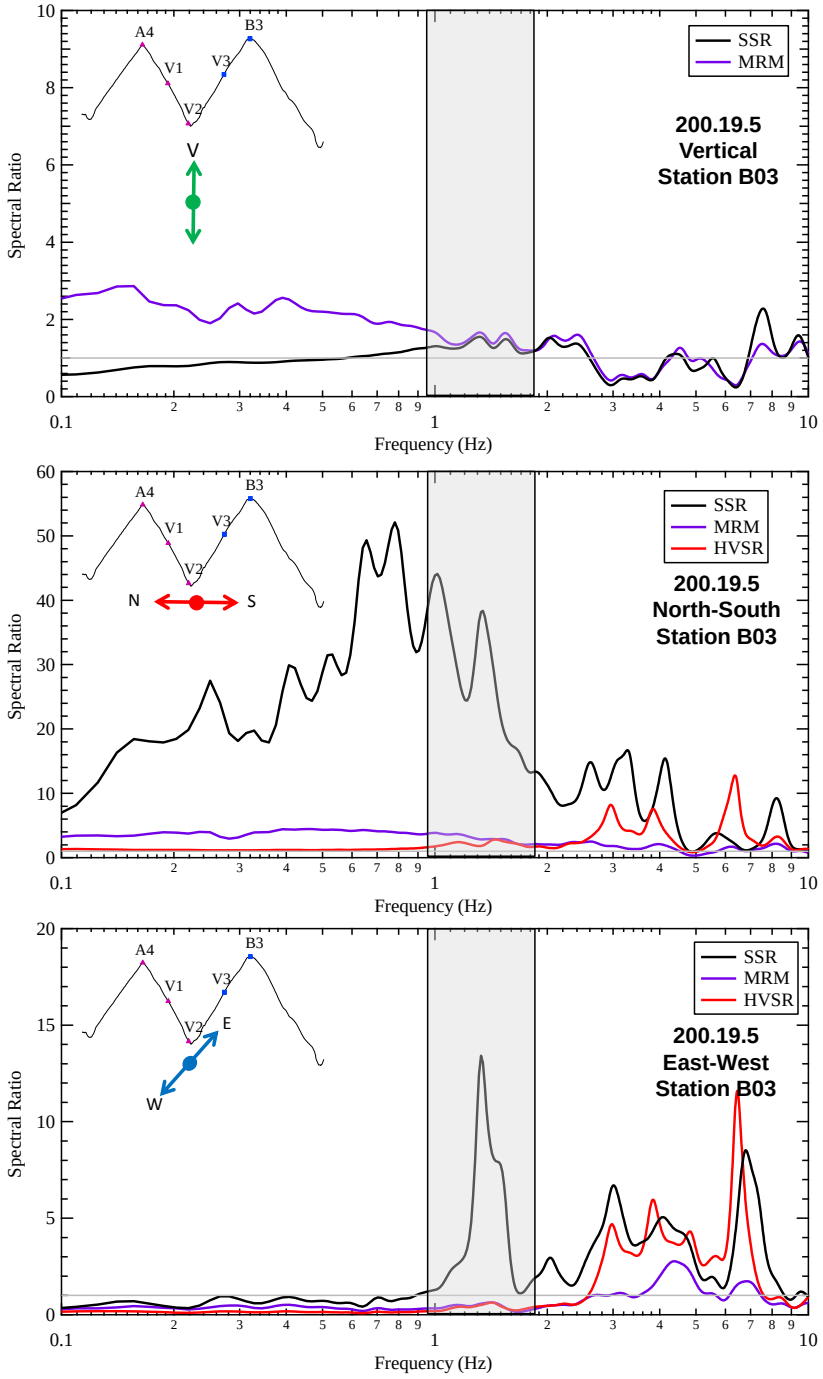

Figure 8.38: Comparison of V line SSR, MRM, and HVSR results for event 200.19.5 Station B3 vertical, North-South, and East-West components. The estimated topographic frequency range based on cross-section geometry and average shear wave velocity is shaded.

For the East-West component, the SSR method was the only method to predict amplification in the estimated topographic frequency range. The other methods predicted de-amplification in the same frequency range. Given the lack of E-W topographic relief near Station B3, an amplification in the E-W direction should not have been predicted. All three methods predicted amplifications above 3 Hz, but there was no pattern of top-down amplification associated with the methods. Therefore, the amplifications were likely due to soil site effects.

Overall, the methods had different topographic frequency ranges, and the maximum amplifications varying wildly according to the method used in the analysis. The spectral ratio for event 200.19.5 was plotted for Station B3 (the North crest) using the SSR method and Stations B3 and V2 using the MRM method (see Figure 8.39). As with the A and B lines of stations, the amplifications of the SSR method at many of the frequencies were more due to the attenuation of the reference station (V2) than the amplification of the crest station (B3). This has been the story of all three lines, and indicates the problems with using a single reference station at the base of topographic features to estimate the amplification and frequency range for topographic effects.

After comparing the three different methods and the results from each of the cross sections (A, B, and V), each of the three methods calculated amplifications in the direction of steep topographic relief (i.e., E-W for line A, E-W for line B, and N-S for line V). The frequency ranges for each method were similar, and often corresponded to the same minimum and maximum frequencies that were associated with topographic amplification for each method. However, the amplifications measured in the direction in-line with steep topography varied fairly significantly between the methods, with over a 200% difference between the methods common, and up to a 1200% maximum difference observed. The major differences in amplification values were observed for each cross

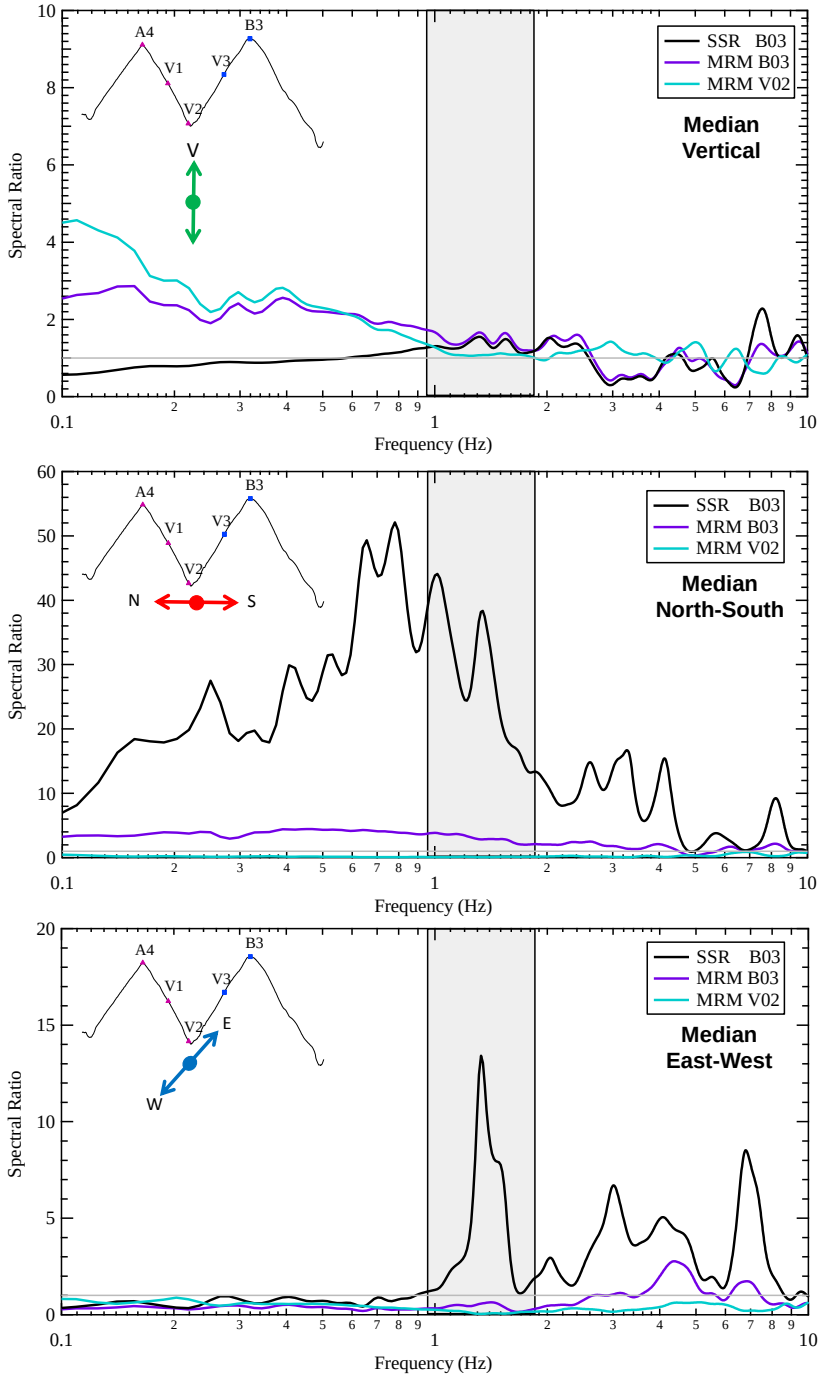

Figure 8.39: Comparison of V line SSR Station B3 with MRM from Stations B3 and V2 for event 200.19.5 vertical, North-South, and East-West components. The estimated topographic frequency range based on cross-section geometry and average shear wave velocity is shaded.

section. The extremely large amplifications calculated using the SSR method were shown to have been the result of dividing an amplification station at the crest by a de-amplification station at the base, resulting in an abnormally high amplification factor. As for the HVSR, the spectral ratios calculated using HVSR have been shown by other authors (Massa et al. 2010) to be a poor indicator of the amplification potential at a site. Therefore, the MRM method likely yields the most accurate amplification factors for the mountain, but since most the stations are located on the topography, and very irregular patterns of amplification were record along different parts of the topography, the MRM method's amplification factors may be biased high or low, although the method likely still provided the best amplification factors.

For station components measuring the particle motion in the opposing direction (cross-line) of steep topographic relief (i.e., N-S for line A, N-S for line B, and E-W for line V), the MRM and HVSR method resulted in very similar spectral ratios with values of 1.0 or less over the frequency band of interest. However, the SSR method typically indicated large amplifications in that direction, which was likely a false amplification peak that was the result of the SSR reference station affect that was explained previously. For the vertical component, the MRM method showed little to no topographic amplification, but did indicate possible amplification of stations directly under the hypocenter and subject to vertically propagating P-waves.

8.4 Multiple Event Processing (52 Events) for Crest Stations A7, B6, and B3

In Phase II (2011), 52 events were recorded using the topographic array over a 10 day period. Each of these events represents a singular look at how topographic amplification affects the response of the instrumented features. Because looking at each individual event would be repetitive, the events were processed individually and a log-

normal median and +/- 1 sigma were calculated for each station in the array. The events are first examined in terms of the peak ground velocity (PGV) for all 52 events. In Figure 8.40, the PGV for each station for all 52 events is shown, along with the log normal median and +/- 1 sigma. For the vertical component, the PGV values were relatively flat over the entire array of stations. Station A1, B1, and V2 had the highest vertical PGV (and the largest standard deviations), but there was no correlation between the topography and the recorded PGV values (i.e., highest PGV at the crest and lowest PGV at the base).

For the North-South component, Stations A5, B2, and V2 have the largest median PGV values, along with the largest variation in PGV over the catalog of events. The PGV values for Station A5 varied from 0.1512 to 1.093 mm/sec, which was over a 70 times difference between the smallest and largest PGV values for that station. The crest Stations A4, A7, B3, and B6 all had lower PGV values, which is counterintuitive to the crest down amplification pattern that is expected from topographic effects. For the East-West component, Stations A6 and V1 had the highest median PGV's, but just like the N-S component, no correlation could be developed between the measured PGV values and the topographic location of the stations.

For all three components, no topographic amplification could be measured using the PGV values. This fits well with the idea that topographic effects is a frequency based phenomenon that only affects select frequencies. Though time domain topographic amplifications were not measured in this study, it does not mean that time domain amplifications are not possible. The combination of topography size and earthquake energy input may have restrict the effect of topography in the time domain. For example, the energy of the events recorded in Phase II had a main energy band from approximately 1 Hz to 20 Hz, which was on the edge to outside the estimated topographic frequency

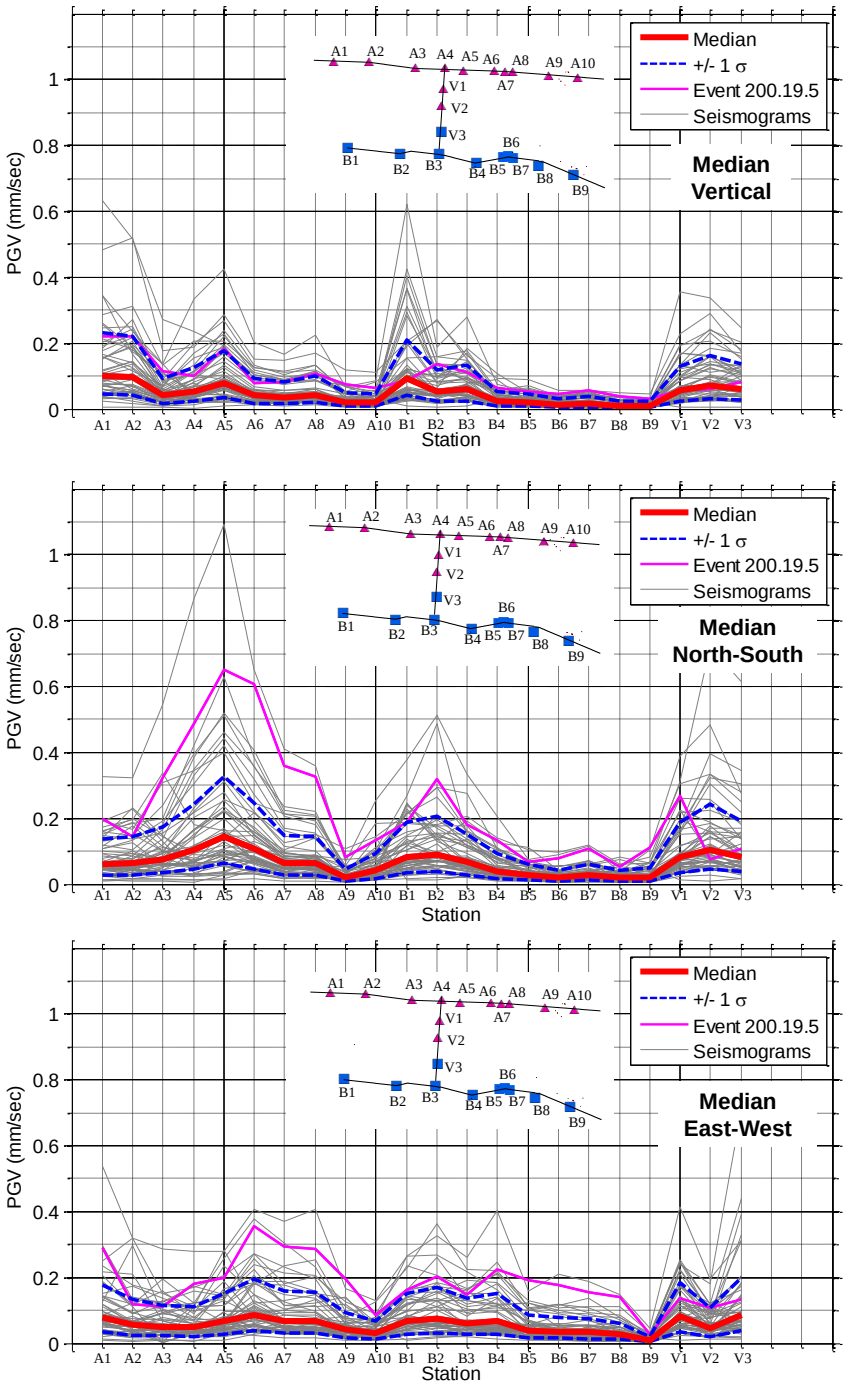

Figure 8.40: PGV's for all 52 events recorded during Phase II, V, N-S, and E-W components with log normal median and +/- 1 sigma shown.

range for the instrumented features (~0.2-2.5 Hz). Therefore, even if the topographic frequencies were amplified above 5, the energy at the topographic frequencies may still not have exceeded the energy at higher frequencies (5-20 Hz), which had significantly more energy to start with. Therefore, given the correct match of earthquake energy at the correct frequencies and topography size, amplifications in the time domain are possible.

After the time analysis, the Fourier amplitude spectra (FAS) for each event were calculated, and the FAS for Station B6 for all 52 events are plotted in Figure 8.41 along with the log normal median of the events and +/- 1 sigma. For the V component, the median spectral amplitude for each event was relatively flat over a frequency range of 1 Hz to 10 Hz. Over this same frequency range, the ground motions varied in amplitude over 3 log cycles from 2.1E-4 to 8.7E-6 mm/sec, but all the ground motions were significantly below the level that could be felt by humans (~1 mm/sec) (Wald et al. 1999). Event 200.19.5 (highlighted in magenta) was one of the highest ground velocities in the event catalog, and often had amplitudes greater than one standard deviation above the median. Many of the other events are clustered within the +/- 2E-5 standard deviation with only a few outliers.

For the N-S component, the ground motions were relatively flat from 3-10 Hz, but drop off beyond those frequencies. At a frequency of 0.5 Hz, the spectral amplitude was an order of magnitude lower than at 3 Hz. At frequencies less than 0.5 Hz, the spectral amplitude was relatively flat to a frequency of 0.1 Hz (the high pass filter frequency). At frequencies greater than 10 Hz, the spectral amplitude of the N-S component dropped off very rapidly and was two orders of magnitude lower than the peak spectral amplitude at a frequency of 40 Hz (which is the low pass filter frequency). The E-W component spectral amplitude had a similar shape to the N-S. However, the flat amplitude response extends

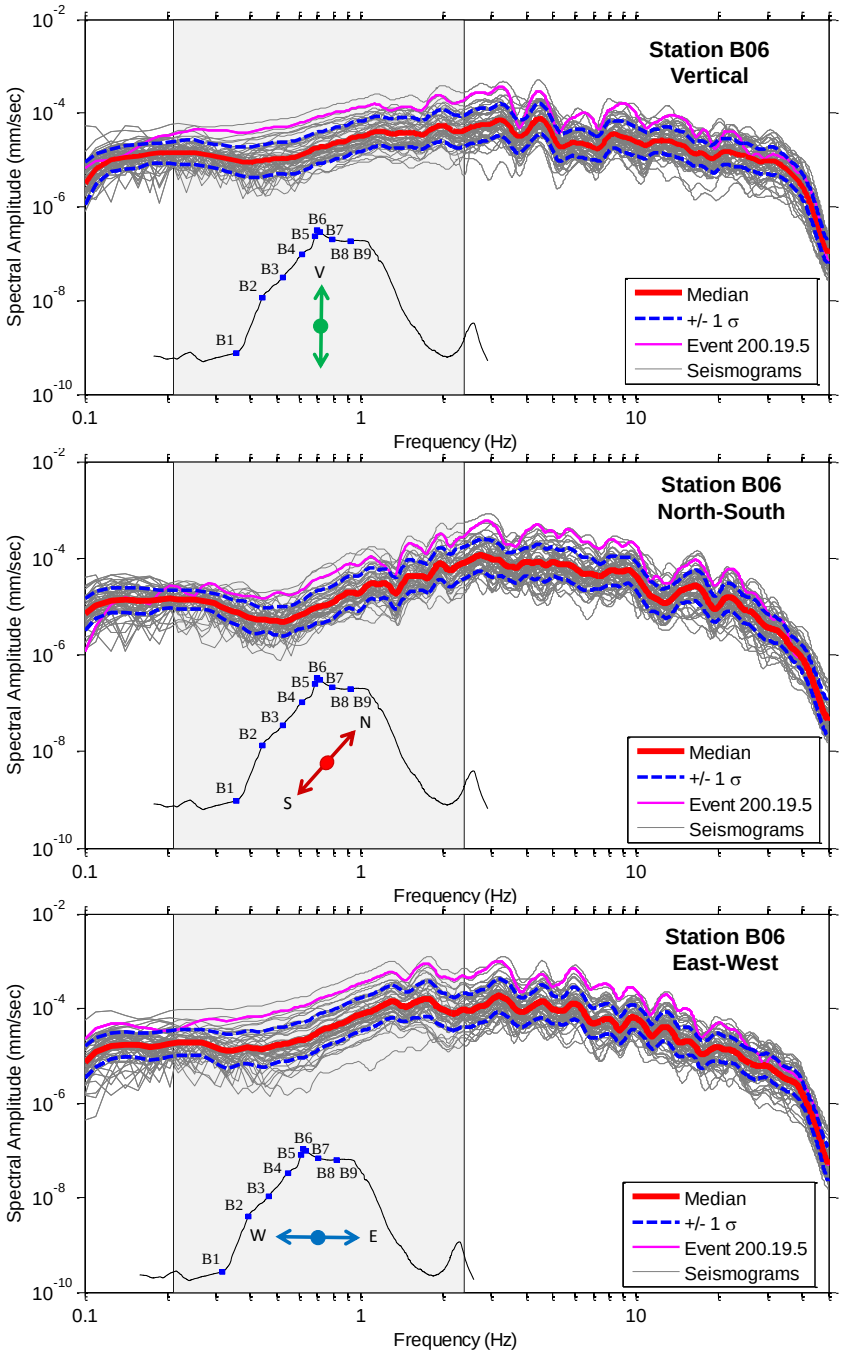

Figure 8.41: Fourier amplitude spectra for all 52 events recorded during Phase II for Station B6 vertical, North-South, and East-West components with log normal median and +/- 1 sigma shown. The estimated topographic frequency range based on cross-section geometry and average shear wave velocity is shaded.

to slightly lower frequencies (1.5 Hz to 7.0 Hz). The spectral amplitude of the E-W component still dropped off after 0.4 Hz, and leveled off. A rapid drop in amplitude was also recorded above 10 Hz. Overall, the 52 events in the ground motion catalog had a good variation in amplitude; however, all the ground motions were well below what could be felt by humans, and within the linear strain range for soils deposits.

8.4.1 Standard Spectral Ratio (SSR)

All 52 events in the ground motion catalog for Phase II were analyzed using the SSR method for the vertical, North-South, and East-West components of motion for all stations in the array. The events were analyzed similar to event 200.19.5, and the SSR for the V, N-S, and E-W components are shown in Figure 8.42 for Station A7 (crest station of the A line) along with the log normal median, and +/- 1 sigma for the 52 recorded events. In addition, event 200.19.5 is highlighted in magenta for reference. For the vertical component, the spectral ratio for frequencies greater than 1 Hz was less than 1.0 for almost all the events indicating a de-amplification of frequencies greater than 1 Hz for the vertical component. For frequencies less than 1 Hz, the median of the events had a spectral ratio very near 1.0. However, the spectral ratios of the individual events vary over almost 2 log cycles from 0.06 to 8.

For the North-South component, the spectral ratio was very flat for frequencies greater than 1.0 Hz with amplification values less than one for the majority of frequencies and events. For frequencies less than 1 Hz, the median of the events had a small section of frequencies from 0.3 to 0.8 Hz, which had a spectral ratio greater than 1.0 with a maximum amplification of 2.0. The spectral ratio for the individual events in that same section varied significantly from a maximum spectral ratio of 12 to a minimum of 0.3. The +/- 1 sigma values varied from 1 to 4 in the same section of frequencies. At

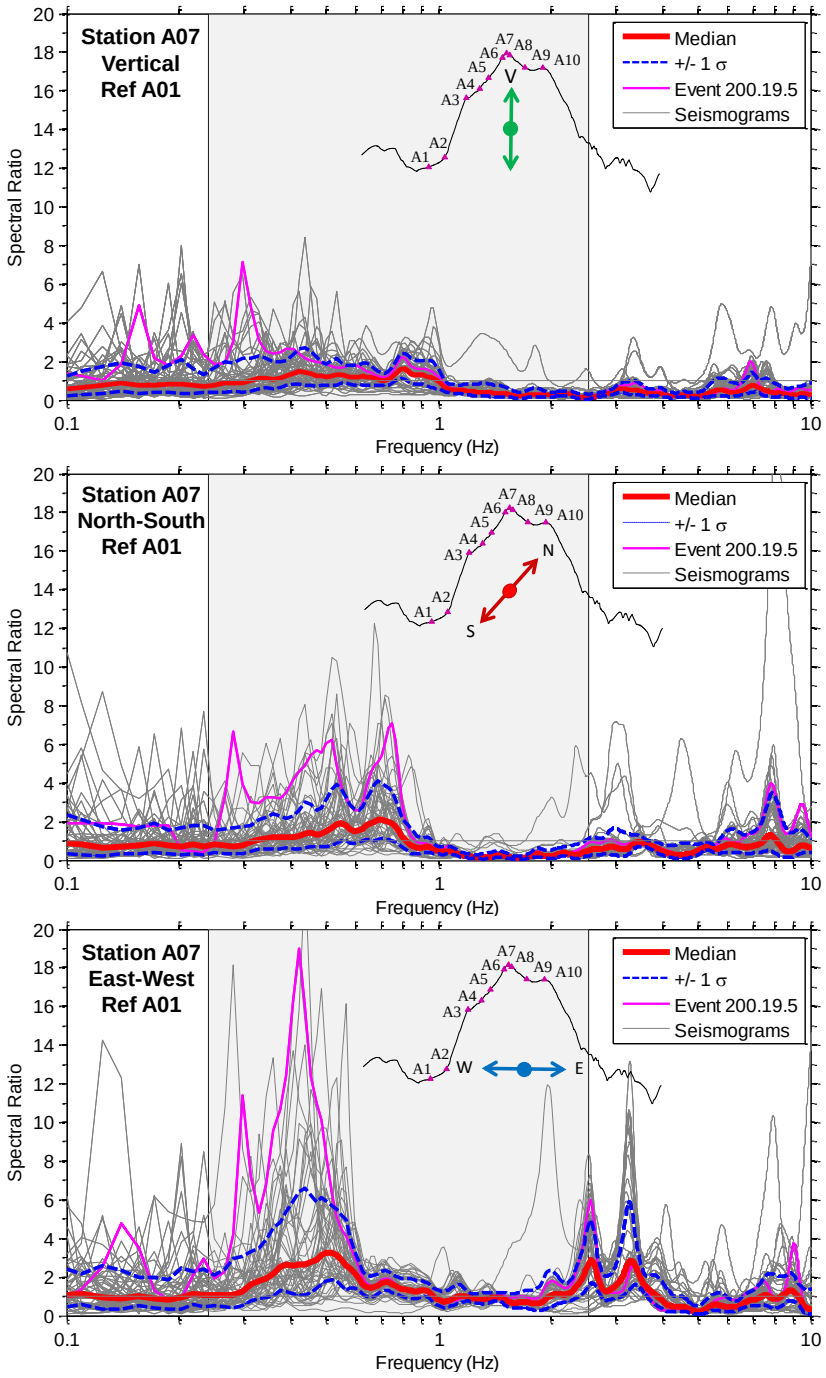

Figure 8.42: Standard Spectral ratio (SSR) for all 52 events recorded during Phase II for Station A7 vertical, North-South, and East-West components with log normal median and +/- 1 sigma shown. The estimated topographic frequency range based on cross-section geometry and average shear wave velocity is shaded.

frequencies less than 0.3 Hz, the spectral ratios were less than 1.0 indicating de-amplification of most of the events compared to the reference station.

For the East-West component, two separate frequency sections had spectral ratios greater than 1.0. The first amplification section was from a frequency of 2.4 Hz to 3.7 Hz, and had a maximum spectral ratio of 2.8 at two separate peaks. The two peaks are just at the edge of the topographic frequency range and may be related to the smallest cross section at the crest of the feature. The lower frequency amplification occurs at a frequency of 0.3-0.65 Hz, and has a maximum amplification of 3.25 for the median response. The standard deviations for the peak varied from 6.6 to 1.1, and results in COVs of 0.61-1.10. The individual events varied in spectral ratio over a very large range from over 20 to 0.3, which is over a 500% difference between the highest amplification event and the median spectral ratio.

The Standard Spectral Ratios (SSR) for Station B6 (crest station of the B line) for all 52 recorded events are shown in Figure 8.43 along with the log normal median, and +/- 1 sigma for the 52 recorded events. For the V component, a small amplification peak on the median response was calculated from 0.7-1.0 Hz, with an amplification of around 2.0. The strong amplification at 0.16 Hz, which was recorded on each of the stations for event 200.19.5 using the SSR method in the previous section, was not repeated by any of the other recorded events. Therefore, there was likely an error at that frequency for the reference station when event 200.19.5 was recorded. This major difference in the spectral ratio between events emphases the instability of the SSR method. The median spectral ratio for other frequencies were 1.0 or less, but vary more significantly below 1 Hz than above 1 Hz, which may be caused by the lower energy for frequencies less than 1 Hz (see Figure 8.41).

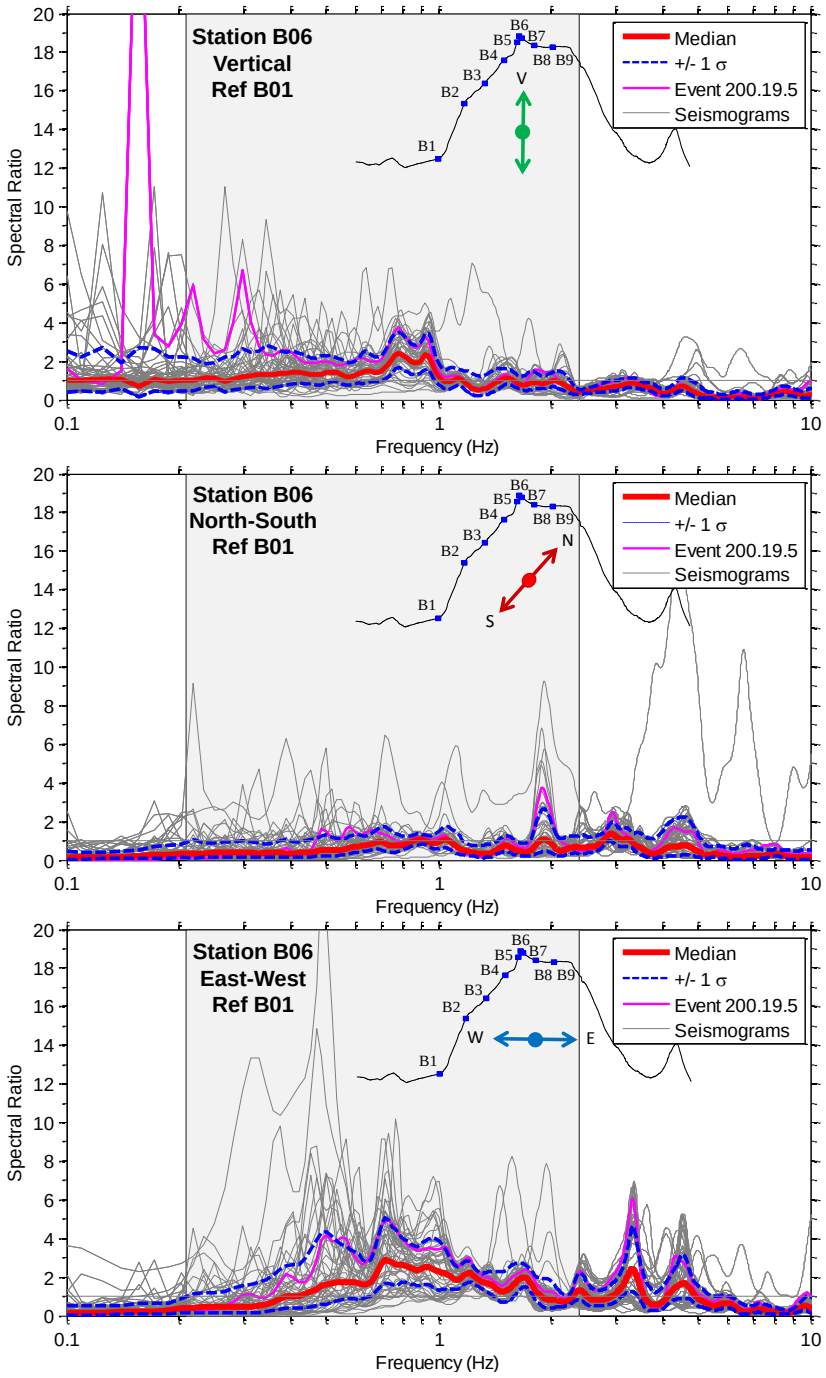

Figure 8.43: Standard Spectral ratio (SSR) for all 52 events recorded during Phase II for Station B6 vertical, North-South, and East-West components with log normal median and +/- 1 sigma shown. The estimated topographic frequency range based on cross-section geometry and average shear wave velocity is shaded.

For the North-South component, the median spectral ratio was below 1.0 for the entire frequency span, indicating a de-amplification of waves compared to the reference station. The median response mirrors that of event 200.19.5 over much of the frequency span. Only at a frequency of 2 Hz did event 200.19.5 indicate a slight amplification of 4, which was not replicated on the median response. For the East-West component, a main amplification peak at 0.4-1.5 Hz was calculated for the median response with a peak spectral ratio of 2.9. The standard deviations in that range varied from approximately 1.65-5, and results in COVs of 0.43-0.61. The spectral ratios of individual events in the amplification frequency range vary significantly from 0.5 to 10, but vary less than those recorded on Station A7 presented earlier.

The Standard Spectral Ratios (SSR) for Station B3 (a crest station for the V line) for all 52 recorded events are shown in Figure 8.44 along with the log normal median, and +/- 1 sigma for the 52 recorded events. For the vertical component, the calculated spectral ratio for both the median and event 200.19.5 had a value near or below 1.0 for the entire frequency range. The spectral ratios of individual events varied from 12 to 0.3 over the frequency range.

For the North-South component, a major amplification peak was calculated for the median response from 0.1 Hz to 5 Hz, with a maximum spectral ratio of 16.75. The standard deviations for the topographic amplification peak varied from 34 to 7, and results in COVs of 0.55-1.0. The spectral ratios in the N-S direction were significantly larger (over an order of magnitude i.e., 50 vs 5) than spectral ratios recorded on other lines (A and B). The spectral ratios for the individual events varied from over 100 to 0.86, which was significantly greater than the other cross sections, and was just over 2 log cycle.

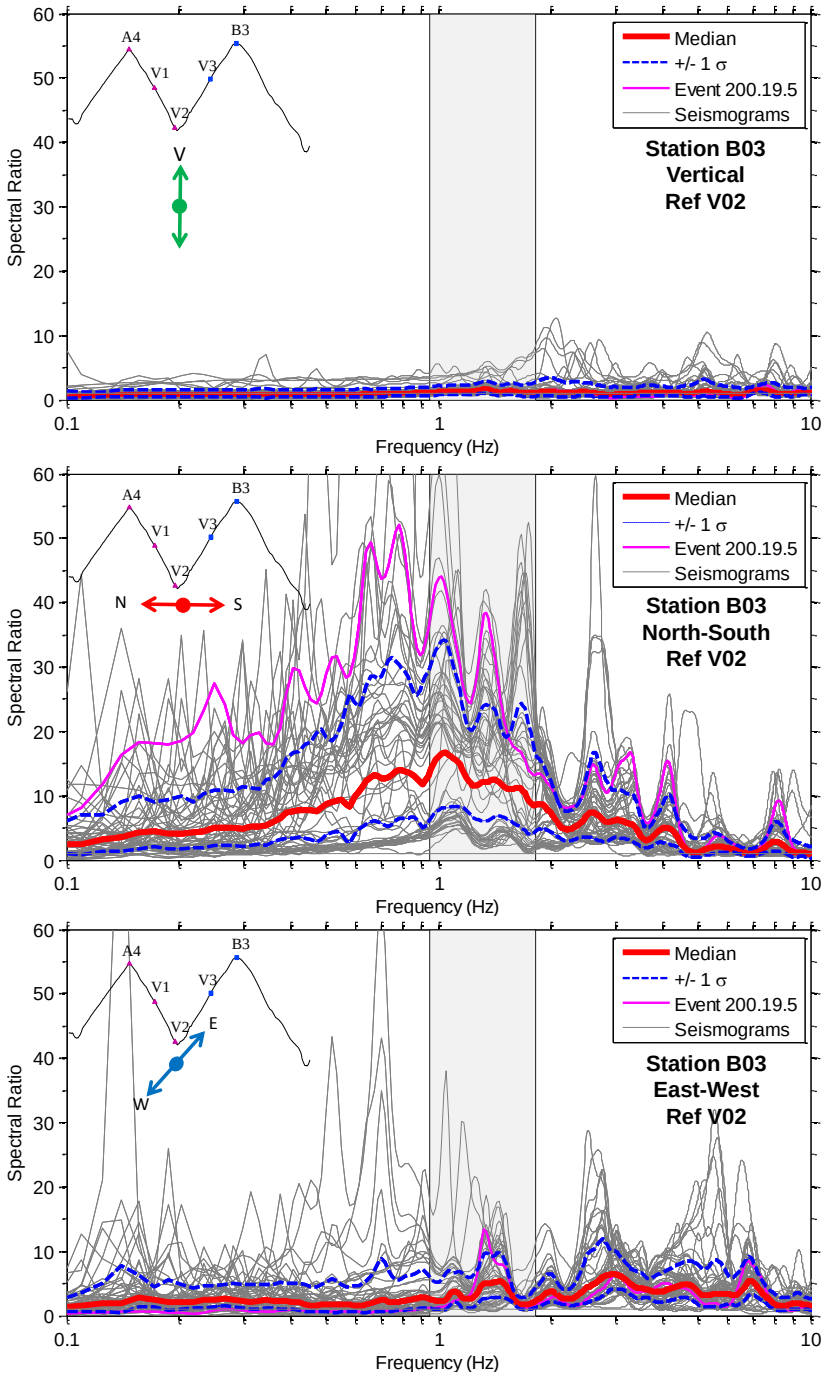

Figure 8.44: Standard Spectral ratio (SSR) for all 52 events recorded during Phase II for Station B3 vertical, North-South, and East-West components with log normal median and +/- 1 sigma shown. The estimated topographic frequency range based on cross-section geometry and average shear wave velocity is shaded.

For the East-West component, the median had a spectral ratio of 2.0 for frequencies less than 1 Hz and a spectral ratio of 3-4 for frequencies greater than 1 Hz. As with the other components for Station B3, the E-W component had a large variation in the spectral ratio estimates varying between 60 and 0.2. However, the standard deviation is still between 1 and 3, which was similar to previous lines.

For the SSR method, the A line (A7) and B line (B6) resulted in similar standard deviations for the main topographic frequencies of the E-W component. The A line had +/- 1 sigma of between 6.6-1.1 for a peak amplification for the median response of 3.25, and resulted in COVs of 0.65-1.10. The B line had +/- 1 sigma values of between 5.0-1.65 for a peak amplification for the median response of 2.9, which resulted in slightly lower COVs of 0.43-0.61. The V line had by far the largest spectral ratio for the median line of 16.75, and had large differences in the +/- 1 sigma spectral ratios of 7.0-34. However, the COVs were still around 0.55-1.0 for the V line. The individual events for each line also had significant variation in spectral ratio, and varied between 1-2 orders of magnitude difference between the highest and lowest spectral ratios for the peak amplification frequency. This indicates the SSR method produces a poor measure of the true amplification of a site, especially when the amplification factor is based on just a few select events without the benefit of a large catalog of events.

8.4.2 Median Reference Method (MRM)

The Median Reference Method (MRM) was used to analyze all 52 events in the ground motion catalog in Phase II (2011). The analysis of each event was conduct in the same manner as the previous analysis of event 200.19.5, and detailed in Chapters 2, 3 and 4. The MRM results are presented for the crest stations (A7, B6, and B3) in lines A, B, and C. The MRM results for all 52 events for Station A7, along with the log normal

median and +/- 1 sigma for all the events are shown in Figure 8.45. For the V component, the spectral ratios were more consistent than observed using the SSR method, with far fewer seismograms that exceeded the median by more than 1 standard deviation. The response of the median showed virtually no amplification below 5 Hz, and amplification above 5 Hz were likely caused by soil site effects (i.e., soil site effects band 5-15 Hz; refer to Chapter 6).

For the North-South component, the median response has a spectral ratio of 1.0 over the estimated topographic frequency range (0.24-2.54 Hz), indicating no topographic amplification in the North-South direction. For the East-West component, a uniform flat amplification of 1.70 was calculated on the median response for frequencies less than 1.3 Hz, which included a majority of the estimated topographic frequency range. Over this range, the +/- 1 sigma lines were approximately 2.26 and 1.25 respectively, and resulted in COVs of 0.22-0.38. A larger amplification peak for the median response was calculated from about 1.3 Hz to 5.0 Hz, with a maximum spectral ratio of 3.25. This main amplification peak was located at the upper frequency range for topographic effects, but almost all the events had the same response in this region. The +/- 1 sigma values for the main peak were 4.0 and 2.6 respectively, which resulted in COVs of 0.21-0.35. Overall, the individual events varied from a maximum of 6.0 to a minimum of 0.7 for the main amplification peak.

The MRM results for all 52 events for Station B6, along with the log normal median and +/- 1 sigma for all the events are shown in Figure 8.46. For the V component, the spectral ratios were similar to those measured by Station A7 in terms of amplification, and variation in the calculated spectral ratio. The response of the median showed virtually no amplification over the entire spectra.

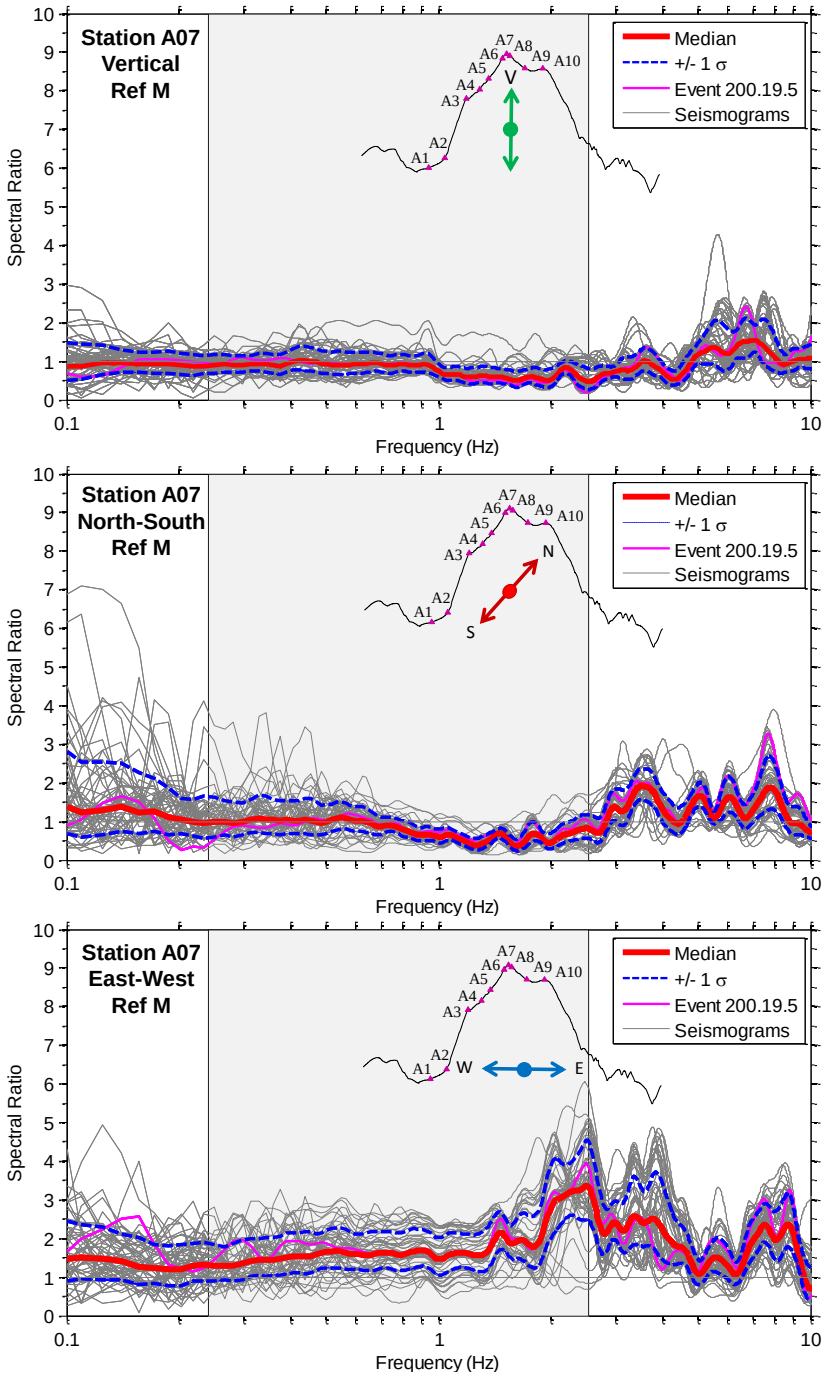

Figure 8.45: Median Reference Method (MRM) for all 52 events recorded during Phase II for Station A7 vertical, North-South, and East-West components with log normal median and +/- 1 sigma shown. The estimated topographic frequency range based on cross-section geometry and average shear wave velocity is shaded.

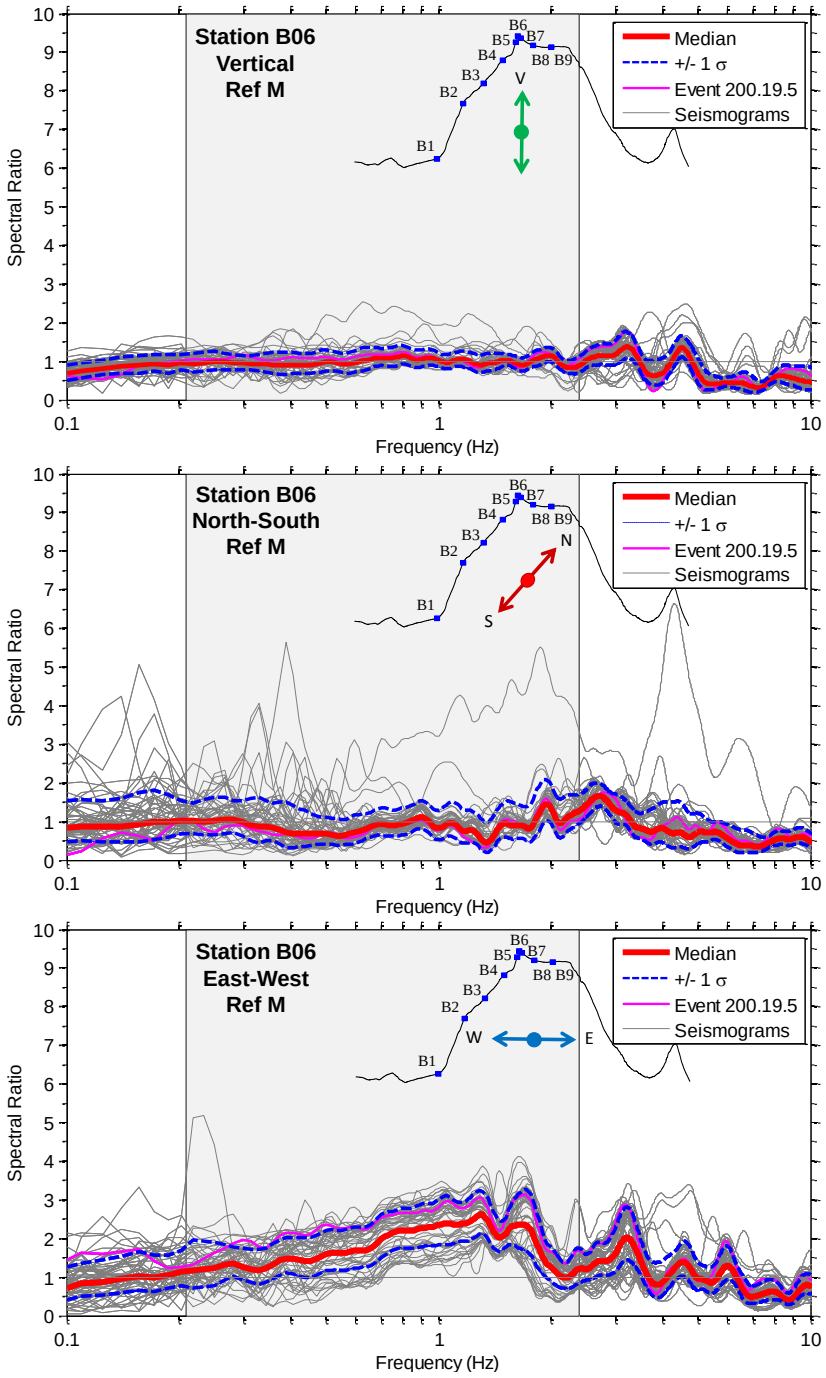

Figure 8.46: Median Reference Method (MRM) for all 52 events recorded during Phase II for Station B6 vertical, North-South, and East-West components with log normal median and +/- 1 sigma shown. The estimated topographic frequency range based on cross-section geometry and average shear wave velocity is shaded.

For the North-South component, the median response had a spectral ratio of 1.0 over the estimated topographic frequency range (0.21-2.39 Hz), which indicated no topographic amplification in the North-South direction. At frequencies above the topographic frequency range, small amplifications of 1.5 or less were calculated mainly at a frequency of 2.8 Hz. The individual seismograms for each event varied more significantly than measured on Station A7, with variations in spectral ratio of over 5 when the median response is 1.0 or less. These variations were more in-line with the ones measured using the SSR method for Station B6.

For the East-West component, a large amplification peak was calculated for the median component from a frequency of 0.3-2.0 Hz, which was directly within the estimated topographic frequency range (0.21-2.39 Hz). The maximum amplification (spectral ratio) at 1.3 Hz calculated for the median response was 2.6, with +/- 1 sigma values of 3.2 and 2.1, which corresponded to COVs of 0.18-0.23. The individual events spectral ratios varied between 3.82 and 1.1 for the peak amplification. This variation was much lower than that measured using the SSR for Station B6, but the median peak amplification was only slightly higher for the SSR method than the MRM method. Overall, the amplifications measured on the E-W component were believed to be the result of topographic effects.

The MRM results for all 52 events for Station B3, along with the log normal median and +/- 1 sigma for all the events are shown in Figure 8.47. For the V component, the median response had a slight amplification of 1.5 or less over a frequency range from 0.25-1.3 Hz. This range was slightly lower than the estimated topographic frequency range (0.95-1.83), and there were large variations in the estimate amplification factors

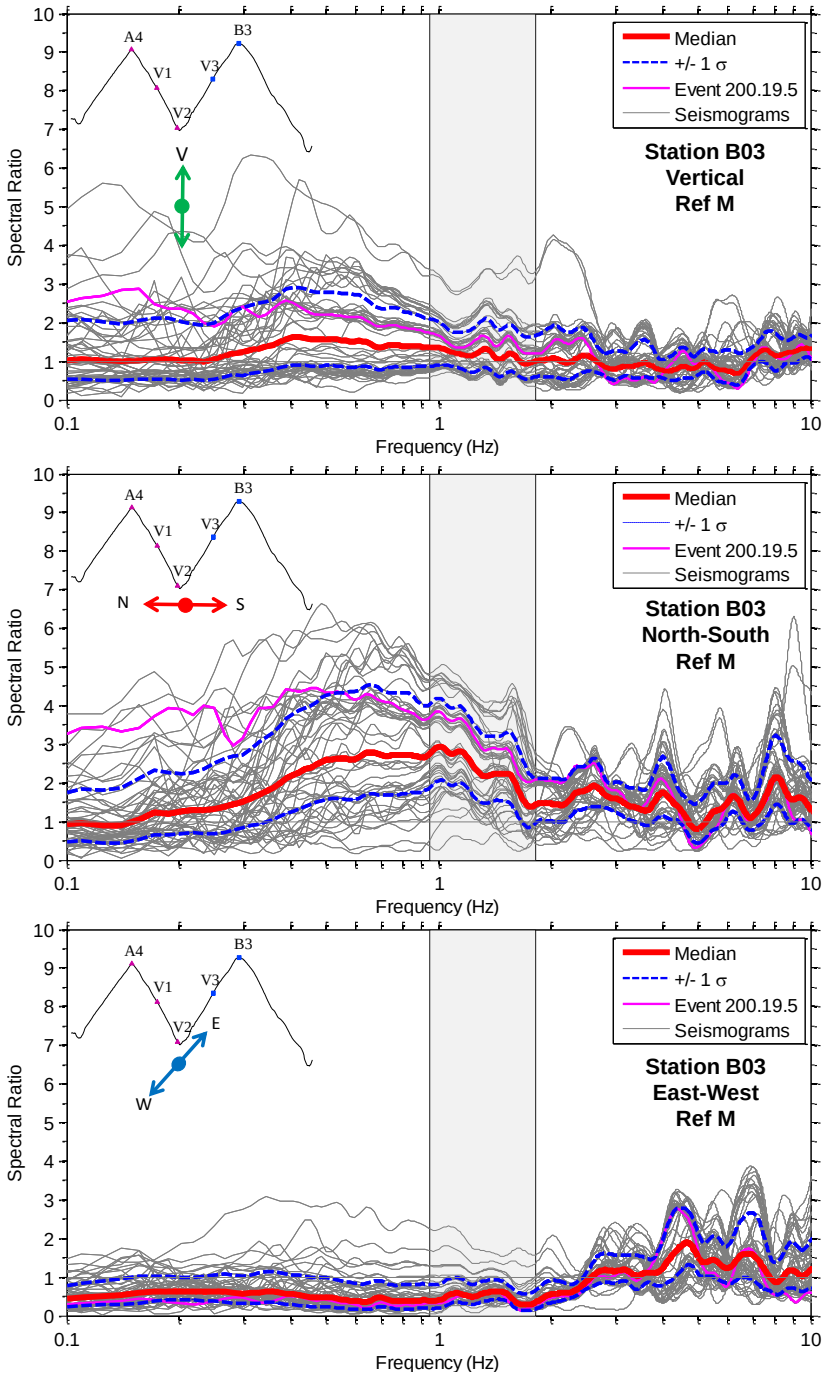

Figure 8.47: Median Reference Method (MRM) for all 52 events recorded during Phase II for Station B3 vertical, North-South, and East-West components with log normal median and +/- 1 sigma shown. The estimated topographic frequency range based on cross-section geometry and average shear wave velocity is shaded.

varying from almost 6 to 0.25. Further investigation is needed to determine if this peak was the result of topographic amplification or the vertical propagation of P-waves from the hypocenter.

For the North-South component, the median response had a wide amplification peak from 0.3 Hz to 1.8 Hz. This amplification range was much larger than the estimated topographic frequency range of 0.95-1.83 Hz. The maximum amplification for the median was approximately 3.0 with a +/- 1 sigma of 4.3 and 1.7. This resulted in COVs of 0.36-0.52. This percent increase or decrease was almost double that seen on lines A and B for the MRM method, and closer to those measured using the SSR method. The individual events also varied significantly, with a maximum of 6 and a minimum of 0.22 (over log cycle difference).

For the East-West component, a flat de-amplification of 0.5 was measured at frequencies less than 2.5 Hz, indicating a lower ground motion in the E-W direction than the rest of the array. A slight amplification was measured at frequencies above 4 Hz, but that was likely caused by soil site effects and not topographic effects.

For the MRM method, the A line (A7) and B line (B6) resulted in similar standard deviations for the main topographic frequency for the E-W component. The A line had +/- 1 sigma values of between 2.6-4 for a peak amplification for the median line of 3.25, and resulted in COVs of 0.21-0.35. The B line had +/- 1 sigma of between 2.1-3.2 for a peak amplification for the median line of 2.6, which results in slightly lower COVs of 0.18-0.24. The V line had by far the largest +/- 1 sigma values on the N-S component varying from 4.3 to 1.7 for a median response of 3.0, and results in COVs of 0.36-0.52. The maximum amplification values of the median of each line varied from 3.25 to 2.6 with the B line having the lowest amplification and the A line having the highest amplification. Overall, the standard deviation and uncertainty was lower using the MRM

compared to the SSR method, which results in a more stable spectral estimate and more accurate amplification factors.

8.4.3 Horizontal to Vertical Spectral Ratio (HVSR)

The Horizontal to Vertical Spectral Ratio (HVSR) method was used to process the 52 events in the ground motion catalog for Phase II (2011). The events were processed similar to event 200.19.5, and in accordance with the methods discussed in Chapter 4. The HVSR for all 52 events is shown in Figure 8.48 for Station A7 (A line) along with the log normal median and +/- 1 sigma. For the N-S component, the median spectral ratio was less than or equal to 1.0 from a frequency of 0.2 Hz to 2 Hz, which was almost the entire estimated topographic frequency range (0.24-2.54). A slightly higher median spectral ratio of 3.0 was measured for frequencies greater than 2 Hz, but the flat amplification band was unlikely caused by topographic effects due to its higher frequency. Within the estimated topographic frequency range, the ground motions had little variation between the median spectral ratio, and individual event spectral ratios, meaning that all the events indicated no amplification in the estimated topographic frequency range for the N-S direction.

For the E-W component, a large amplification peak of 12 was calculated for the median response in a frequency range from 1 and 5 Hz with the main peak at 2.5 Hz. Much smaller amplifications were measured at frequencies outside this range, with larger variation in the spectral ratios for the individual events occurring at lower frequencies. For the main amplification peak at 2.5 Hz, the individual events spectral ratios varied somewhat significant with a maximum of 45 and a minimum of 1.0 (over 1.5 orders of magnitude). The standard deviation values in this range were also quite large, and varied

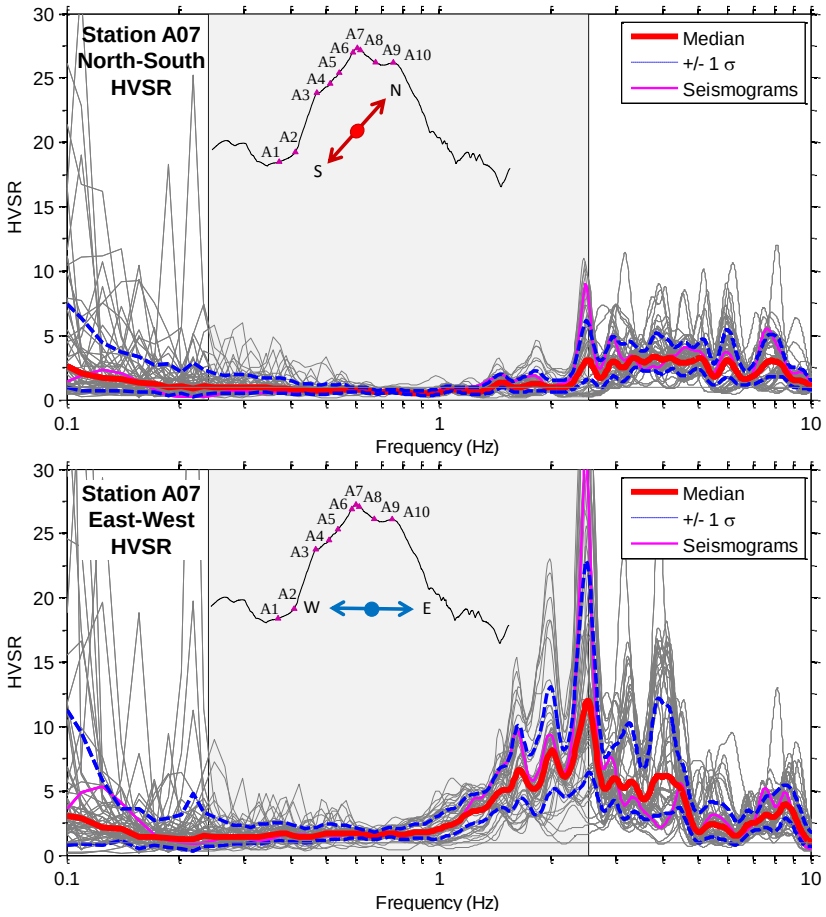

Figure 8.48: Horizontal to Vertical Spectral Ratio (HVSR) for all 52 events recorded during Phase II for Station A7 vertical, North-South, and East-West components with log normal median and +/- 1 sigma shown. The estimated topographic frequency range based on cross-section geometry and average shear wave velocity is shaded.

from a minimum of 6 to a maximum of 23, and results in COVs of 0.30-0.76.

The HVSR for all 52 events is shown in Figure 8.49 for Station B6 (B line) along with the log normal median and +/- 1 sigma. The response for the N-S component of Station B6 was very similar to the response of the previous Station, A7, with an amplification of 1.0 or less over the estimated topographic frequency range (0.21-2.39

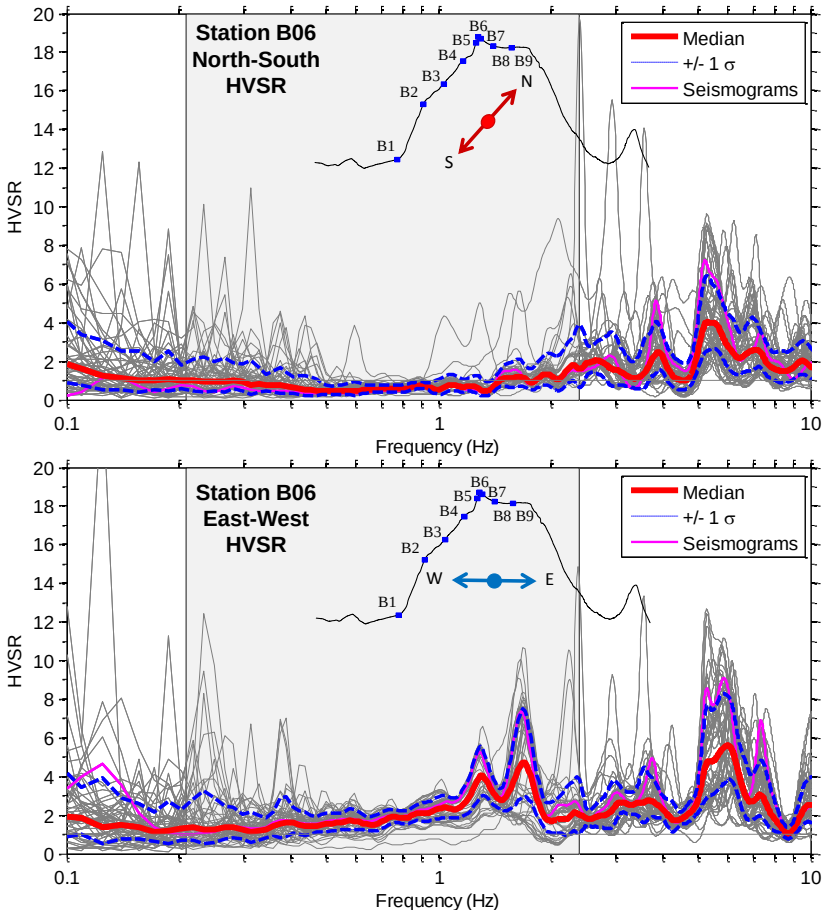

Figure 8.49: Horizontal to Vertical Spectral Ratio (HVSR) for all 52 events recorded during Phase II for Station B6 vertical, North-South, and East-West components with log normal median and +/- 1 sigma shown. The estimated topographic frequency range based on cross-section geometry and average shear wave velocity is shaded.

Hz). For frequencies greater than the estimated topographic frequency range, spectral ratios up to 4 were measured. The spectral estimates from individual events had large variations for frequencies less than 0.5 Hz and greater than 1.5 Hz (up to 150%), but was lower (30-40%) for frequencies between 0.5 Hz and 1.5Hz.

For the E-W component, a small amplification peak was calculated for the median response between frequencies of 0.7-2.0 Hz, with a maximum amplification of 4.4. The

standard deviation for the main amplification peak at 1.7 Hz varied between 3.0 and 7.4, resulting in COVs of 0.31-0.49. The median response was flat below 0.7 Hz with a spectral ratio between 1 and 2. Above 2 Hz, an amplification peak was measured at 6 Hz, but this peak was directly in the soil site effects range (5-15Hz).

The HVSR for all 52 events is shown in Figure 8.50 for Station B3 (V line) along with the log normal median and +/- 1 sigma. For the N-S component, a small amplification peak was calculated in the estimated topographic frequency range for line V (0.95-1.83Hz) with a maximum amplification of 2.5. The standard deviations for the topographic amplification peak at 2.5 Hz varied from 1.7 to 3.9, resulting in COVs of 0.28-0.50. At frequencies greater than the topographic frequency range, large amplifications of up to 5 were calculated.

For the E-W component, an amplification of 1.0 or less was calculated for frequencies less than 2 Hz. For frequencies greater than 2 Hz, amplifications of up to 5 were measured, which was very similar to the spectral ratio and frequency band of the N-S component likely indicating that soil site effects were the cause for the amplification and not topographic effects.

For the HVSR method, the three Stations A7, B6, and B3 from the A, B, and V lines resulted in different amplification factors for the median response varying from 2.5 for B03 to 12 for A7, with B6 having a amplification factor of 4.4, for the direction in which topographic amplification was expected (i.e., E-W for A7 and B6 and N-S for B3). The standard deviations (+/- 1 sigma) for each station were similar for Stations B3 and B6 with COVs of 0.21-0.50. However, Station A7 had slightly higher COVs of 0.30-0.76 at the peak topographic frequency. Station components not in-line with a topographic cross section, including the vertical component showed little to no amplification in the estimated topographic frequency range as would be expected.

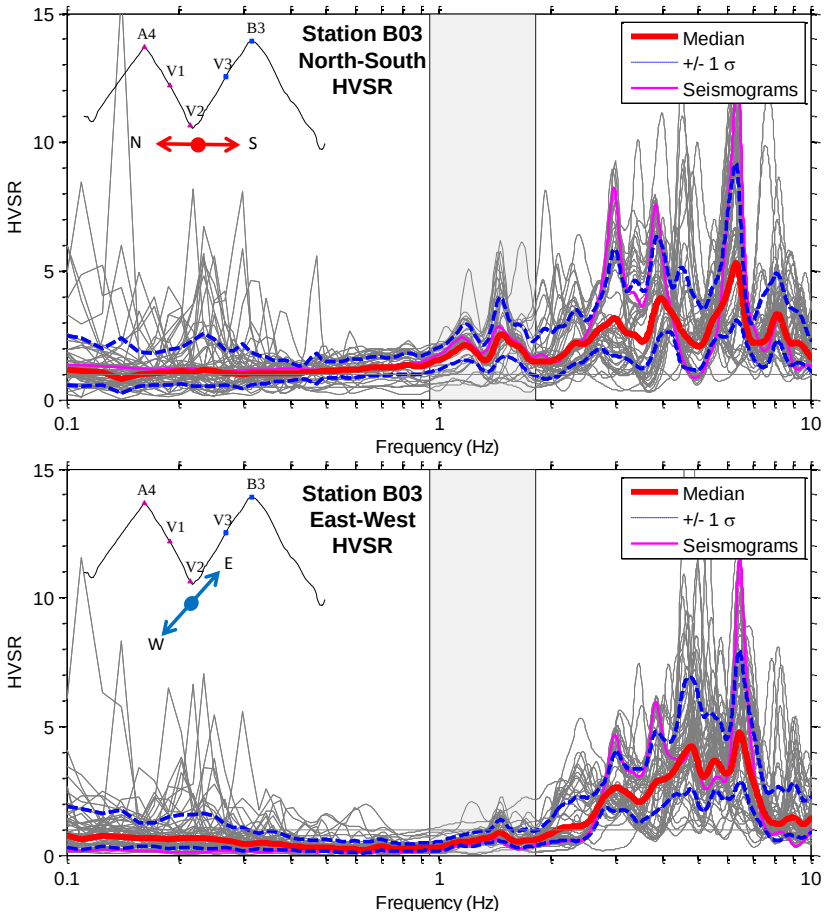

Figure 8.50: Horizontal to Vertical Spectral Ratio (HVSR) for all 52 events recorded during Phase II for Station B3 vertical, North-South, and East-West components with log normal median and +/- 1 sigma shown. The estimated topographic frequency range based on cross-section geometry and average shear wave velocity is shaded.

8.4.4 Summary of Multiple Event Processing

In this section, all 52 events recorded during Phase II were processed using the SSR, MRM, and HVSR methods. The results indicate that the SSR and HVSR methods had the largest variation in the estimated amplification at the topographic amplification peak for each station. The SSR COVs often varied between 0.50 and 1.0, while the HVSR had lower COVs only varying from 0.30-0.85. However, the MRM method had by far the lowest variability with COVs varying between 0.20 and 0.45. Although the

stability of the methods is important to correctly predict the amplification, an analysis methods overall ability to calculate accurate amplification factors is just as important. For the SSR method, amplification factors of approximately 3.0 were calculated for Stations A7 and B6, but an extremely high amplification of 16.75 was calculated for Station B3. This was not surprising given the problems with the SSR method explained in Section 8.3.4. The HVSR method also had problems calculating good amplification factors indicating a 4.4 and 12 amplification for Stations A7 and B6, but did calculate an acceptable factor for B3 of 2.5. The problems with the HVSR method were also expected because as stated before, the HVSR spectral ratios cannot be accurately equated to the potential amplification of a site (Massa et al. 2010). The MRM did a much better job of measuring good amplification factors of between 2.5 and 3.25 for each crest station, which was similar to the results of event 200.19.5. Overall, the MRM method is believed to have performed the best with the lowest variability between individual events and the most stable amplification factors.

8.5 Median Results for the Entire Event Catalog

For Phase II (2011) of the topographic study, 52 events were record during a 10 day period. These 52 events varied in amplitude, but all the events remained in the linear strain range, and below the threshold felt by humans. To combine all the events together and estimate a collective response, the log normal median was calculated for all 52 events using the SSR, MRM, and HVSR methods. Therefore, each station and component (V, N-S, and E-W) can be represented by a single spectral response for all 52 events. Overall, this section looks at the median response of the entire event catalog for all three topographic analysis methods and cross sections.

8.5.1 Standard Spectral Ratio (SSR)

For the Standard Spectral Ratio (SSR) method, Stations A1, B1, and V2 were used as the reference stations for the A line, B line, and V lines, respectively. A comparison of the SSR median response of the A-line Stations, A1-A10, is shown in Figure 8.51. Comparing the vertical component of each station, a slight amplification of up to 1.5 was measured on the crest station, A7, from 0.3 to 1.0 Hz. In the same frequency range, Stations A4 and A5 had a higher amplification of up to 2.9, but given the pattern of amplification, topography was likely not the cause of the amplifications. As mentioned for other analyses, the amplifications could be the result of vertically propagating P-waves recorded by sensors directly over the hypocenter. Outside of the 0.3 to 1.0 Hz range, little or no amplification occurs at any of the stations in line A.

For the North-South component of motion, an amplification peak was measured from 0.3 to 1.0 Hz for Stations A3-A8 and A10. The crest station, A7, had an amplification of 2.1, and Stations A6 and A8 (just off the crest) had amplifications up to 2.0, indicating a good pattern of top-down amplification. However, Station A3-A5 and A10 all had higher spectral ratios in the same frequency band. Station A3 had the highest amplification of 6.5, which was over 300% greater than the spectral ratio of Station A7. This amplification on the N-S component is likely the result of a ridge and valley pattern that exists in the N-S direction (i.e., perpendicular to the main A-line cross section). This amplification will be further explored in line V.

As with the N-S component, an amplification peak was estimated from 0.3 Hz to 1 Hz in the E-W direction, but for the E-W component, Station A7 had the largest amplification with a spectral ratio of 3.25 at 0.5 Hz. Stations A6 and A7 had a 10% decrease in spectral ratio with a maximum amplification of 2.9. Station A9 also followed

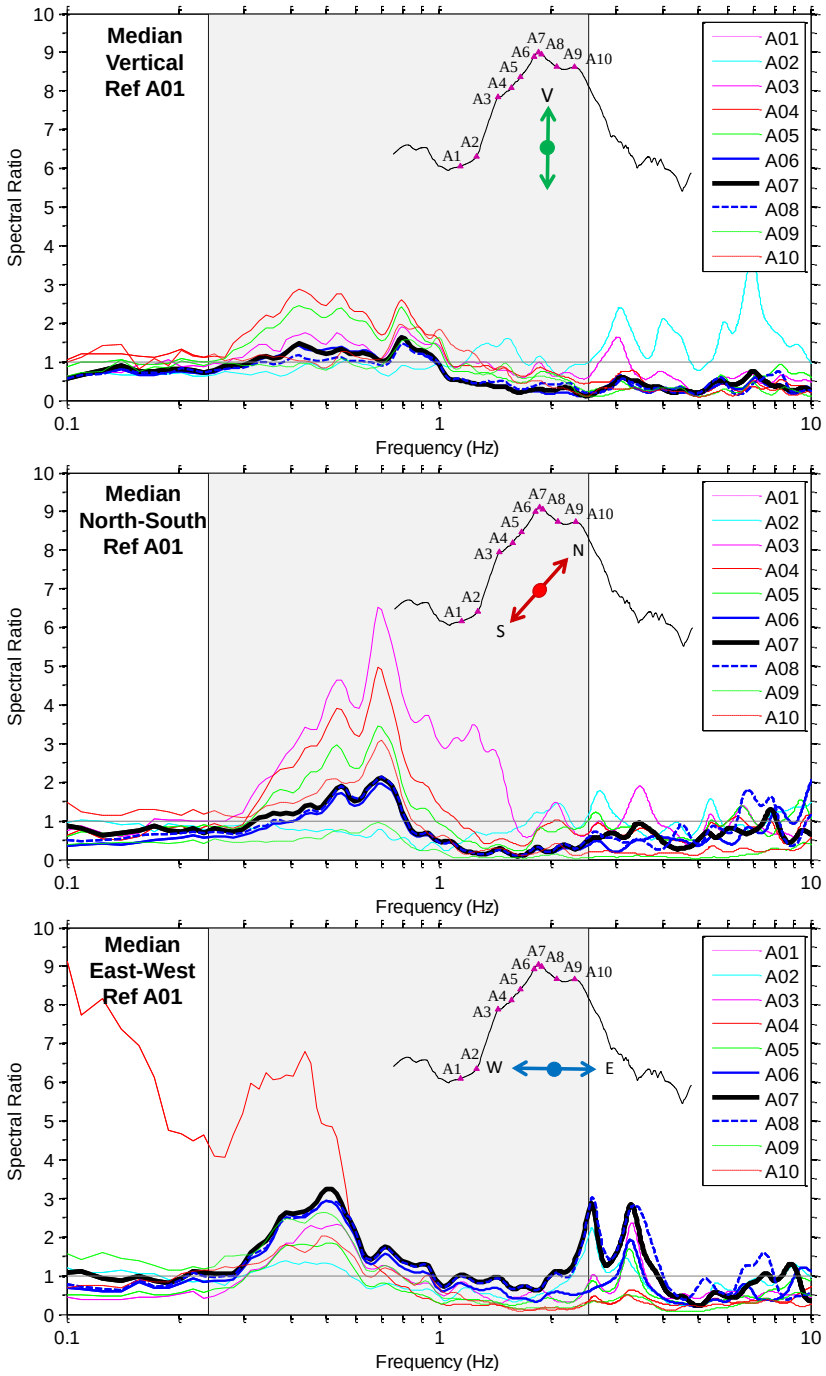

Figure 8.51: Standard spectral ratio (SSR) for the median of the Phase II event catalog (52 events) line A for the vertical, North-South, and East-West components of motion. Station A1 used as the reference station. The estimated topographic frequency range based on cross-section geometry and average shear wave velocity is shaded.

the top-down amplification pattern with an 18% reduction in spectral ratio. This frequency peak was also directly in the estimated topographic frequency range, providing good evidence that it was the result of topographic effects. Station A4 had a large low frequency amplification that was likely caused by an error with the sensor, and was not included in the consideration of potential topographic effects for the A line. In addition to the 0.5 Hz peak, two higher frequency amplification peaks were calculated at frequencies of 2.6 Hz and 3.3 Hz, with amplifications of 3.0 and 2.8, respectively. Stations A7 and A8 both have the highest amplitude for the higher frequency peaks, but no other stations consistently follow the top-down amplification pattern. The higher frequency peaks are also at the upper limit of the estimated topographic frequency range. Therefore, these peaks were possibly caused by topography, but the evidence is not as strong as for the 0.5 Hz peak.

Horizontal polarity plots depicting the median response for all 52 events recorded by Stations A2-A10, based on the SSR method applied over the frequency range of 0.1 to 5 Hz, are provided in Figure 8.52. Based on the results presented in Figure 8.51, topographic effects are expected at frequencies less than 1 Hz. Stations A5-A8 and A10 had a strong NE-SW polarity for frequencies less than 1 Hz, indicating a combined response from both the N-S and E-W directions. However, since there was not strong topographic relief in the N-S direction for most of these stations, the directionality was likely being affected by some other unknown phenomenon (such as effects on the reference station). Stations A4 and A9 had a much stronger E-W polarity, and Station A3 has a strong N-S polarity, matching the steep N-S topographic relief near Station A3.

Based on the SSR method, amplifications at the crest were observed on all three components across frequencies of 0.3 to 1 Hz. For the E-W component, the maximum amplification peak was measured at the crest station, A7, with a maximum amplification

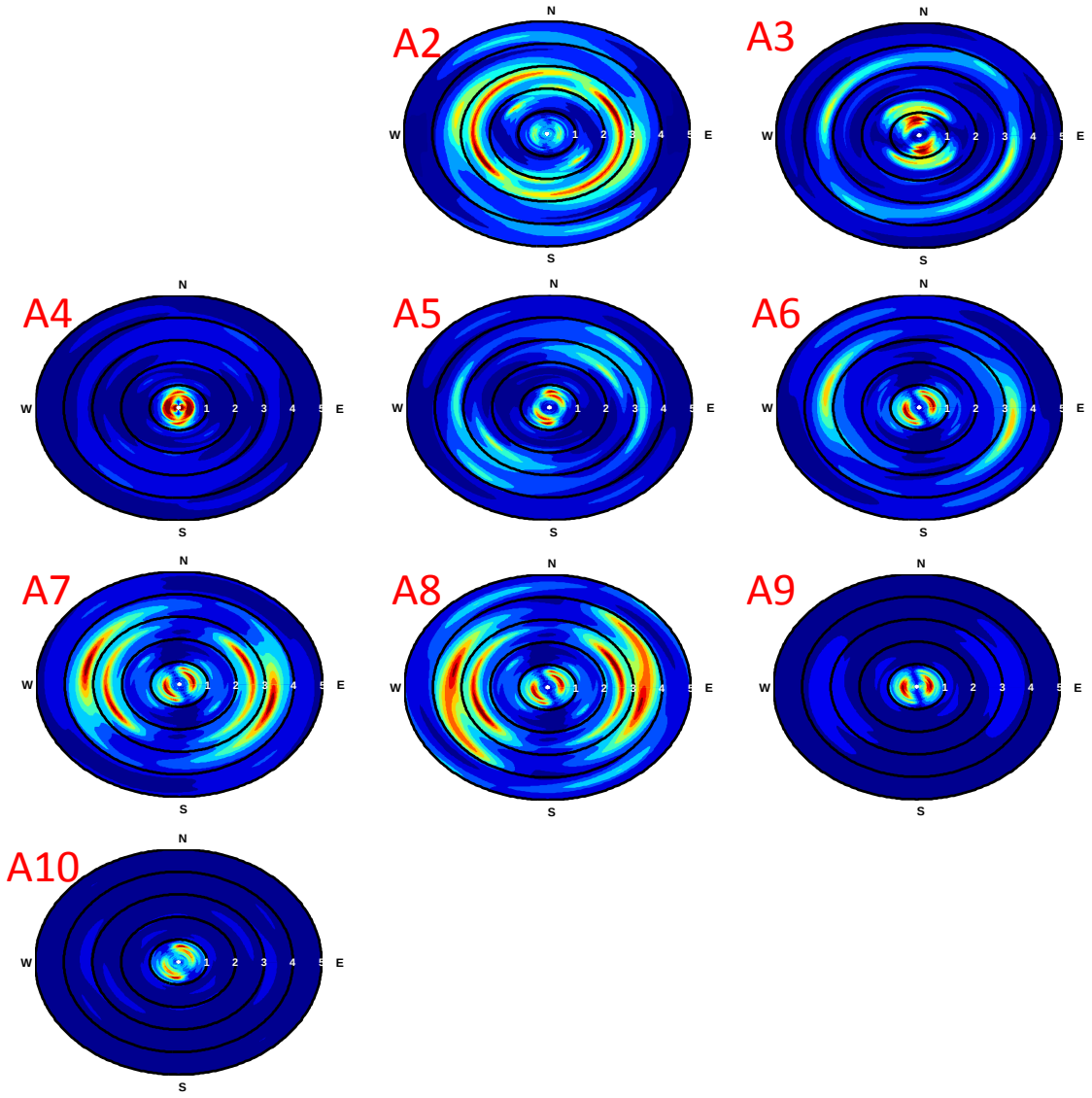

Figure 8.52: Horizontal polarity plots for the SSR method line A using the median response of the event catalog for Phase II (52 events). Station A1 was used as the reference station.

of 3.25. A good pattern of top-down amplification was also measured by stations just off the crest of the feature, providing strong evidence of topographic-driven effects. On the other hand, for the V and N-S components, Stations A3-A5 had higher amplifications

than the crest station, A7, likely indicating influence from other topographic relief perpendicular to the orientation of the A-line.

A comparison of the SSR median response of the B-line Stations, B1-B9, is shown in Figure 8.53. Comparing the V component of each station, a slight amplification of up to 2.3 was measured on the crest station A7 from 0.3 to 1.0 Hz. In the same frequency range and similar to line A, stations down the west slope from the crest (A3 and A4) had a higher amplification of up to 3.1, but given the pattern of amplification, topography was likely not the cause of the higher ground motion.

For the North-South component, the crest station, A7, had no amplification peaks across the entire frequency band. However, Stations B2-B4 had amplifications from 0.4 Hz to approximately 2-3 Hz, with maximum amplifications of 6.7 for Station B2 and 3.6 for Station B3. The amplifications measured by these stations were likely related to the topography in the N-S direction under each station. To confirm this belief, the theoretical topographic frequencies from Station B2 and B3 were calculated using Ashford and Sitar (1997) and Paolucci (2002). The frequency range for those stations in the North-South direction was calculated to be 0.95-1.84 Hz, which matches very well with the main amplification peak of Station B2. However, this frequency range only covers part of the amplification range for Station B3, and it is unknown what was driving the lower frequency range amplification from 0.4-0.95 Hz. Possible differences in soil layering or 3D effects not accounted for in the 2D models could be the cause of the error.

For the E-W component, amplifications for the crest station, A7, were measured from 0.4 Hz to 1.8 Hz with a maximum amplification of 2.9, which was also directly within the estimated topographic frequency band. Stations A6 and A8 established a good pattern of top-down amplification with a 10% reduction in spectral ratio compared to the

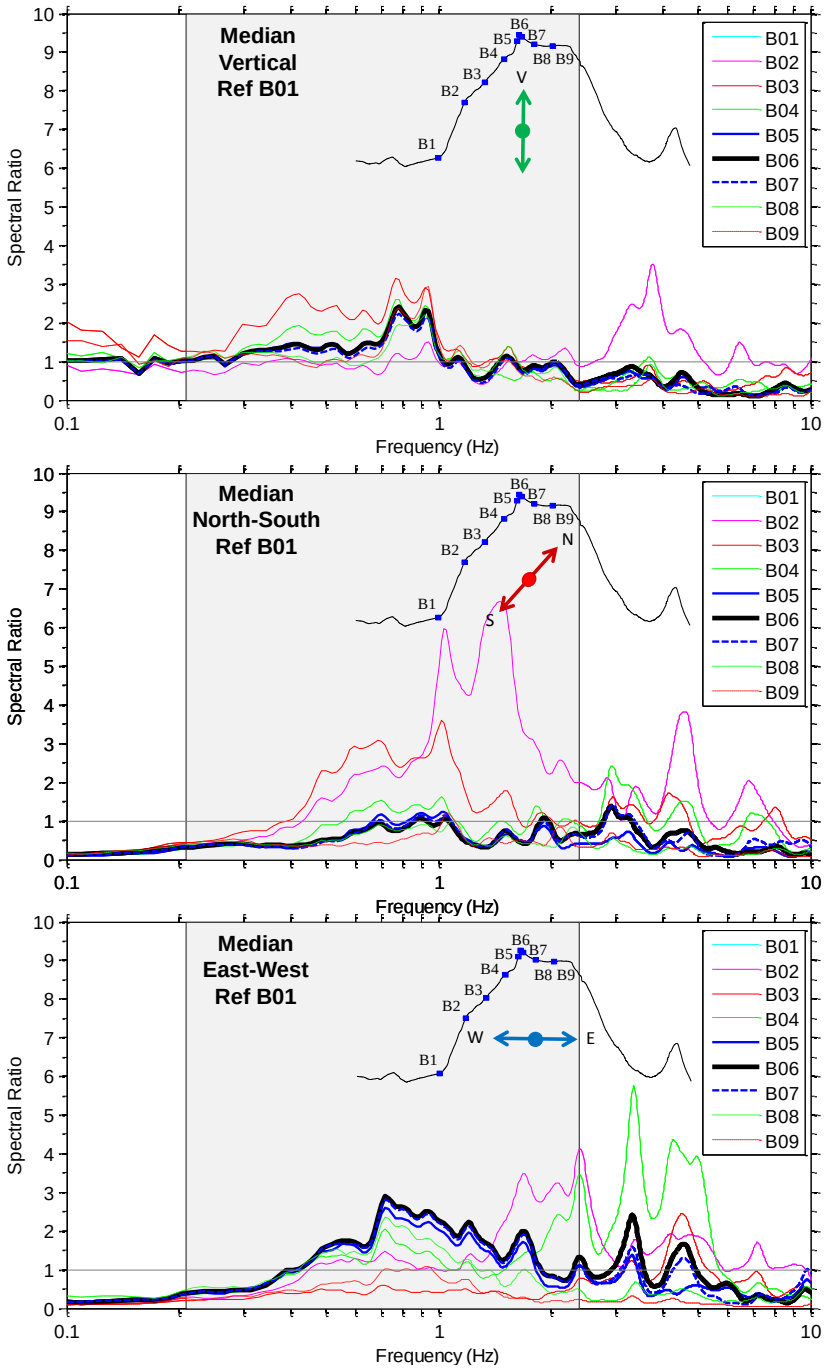

Figure 8.53: Standard spectral ratio (SSR) for the median of the Phase II event catalog (52 events) line B for the vertical, North-South, and East-West components of motion. Station B1 was used as the reference station. The estimated topographic frequency range based on cross-section geometry and average shear wave velocity is shaded.

crest. Stations B8 and B4 also followed the amplification pattern with 17% and 31% reductions in spectral ratio compared to the crest. This provided good evidence to the fact that the amplifications from 0.4-1.8 Hz were driven by topography. Other amplifications were measured at higher frequencies on Station B2 from 1.2-3.0 Hz. At first thought, the amplifications at B2 were driven by the cliff face from B1 to B2, but the theoretical frequency range for this feature was 0.87-1.46, which was lower than the amplification frequency range measured on Station B2. Therefore, it was not fully understood what was driving the amplification, but as with the N-S component presented earlier, the amplification range difference may be related to 3D effects versus a 2D model.

Horizontal polarity plots depicting the median response for all 52 events recorded by Stations B2-B9, based on the SSR method applied over the frequency range of 0.1 to 5 Hz, are provided in Figure 8.54. Based on the results presented in Figure 8.53, topographic effects are expected at frequencies less than 1 Hz. All the stations in the array have a strong NW-SE polarity, which indicates some amplification in both the N-S and E-W directions.

Overall, amplifications at the crest station, B6, were calculated using the SSR method for the E-W component. An amplification of up to 2.9 was measured by the E-W component from a frequency of 0.4-1.8 Hz, which is directly in the topographic frequency range. Stations off the crest also formed a good pattern of amplification around the crest. Therefore, the amplifications measured in the E-W direction were likely caused by topographic effects. In the N-S direction, amplification were not measured at Station B6, but stations that were located on features with steep topographic relief in the N-S direction measured amplification that were likely driven by topographic effects. The vertical component also calculated a slight amplification for some stations, but these were likely not caused by topographic effects.

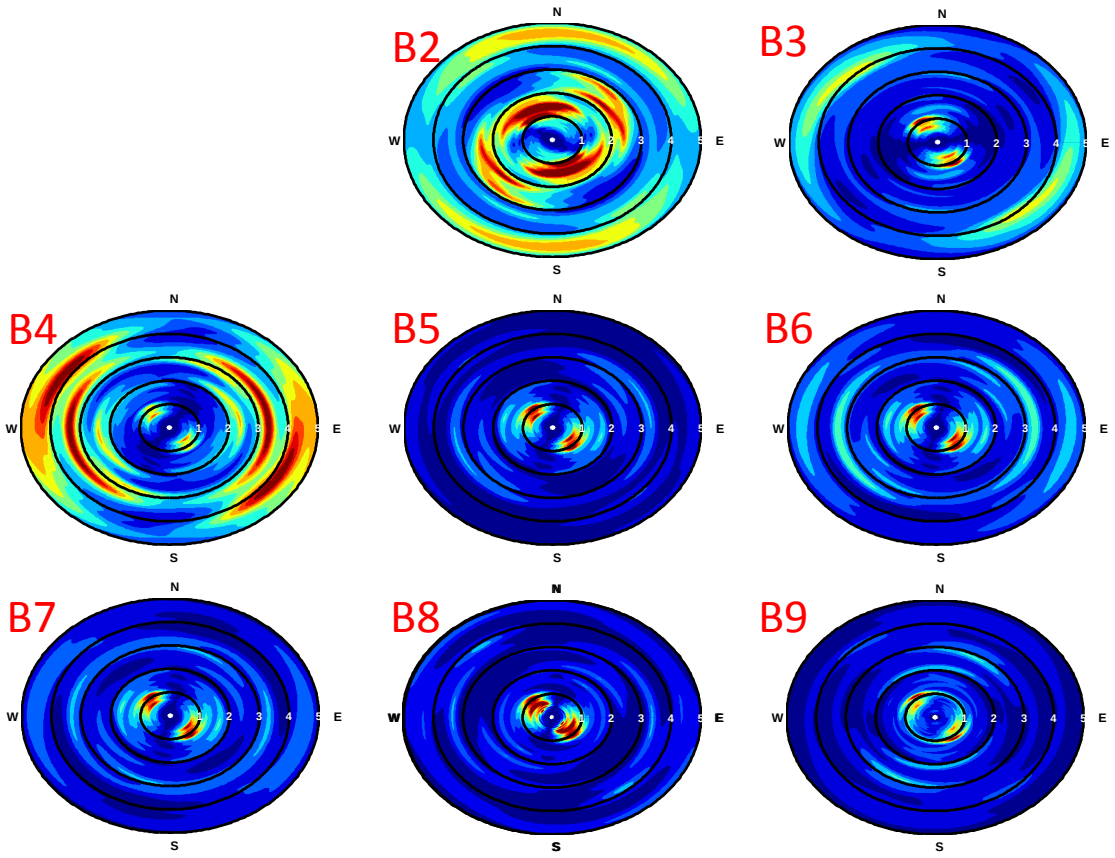

Figure 8.54: Horizontal polarity plots for the SSR method line B using the median response of the event catalog for Phase II (52 events). Station B1 was used as the reference station.

A comparison of the SSR median response of the V-line Stations A4, V1-V3, and B3 is shown in Figure 8.55. Comparing the vertical component of each station, only a slight amplification of less than 1.5 was measured for the stations in the V line. These amplifications did not form a good top-down pattern of amplification with other stations in the array. Therefore, the higher spectral ratios were likely caused by other effects and not topographic effects.

For the North-South component of motion, a large amplification peak of 16.75 was measured on Station B3 at a frequency of 1 Hz. In addition, the other crest station A4

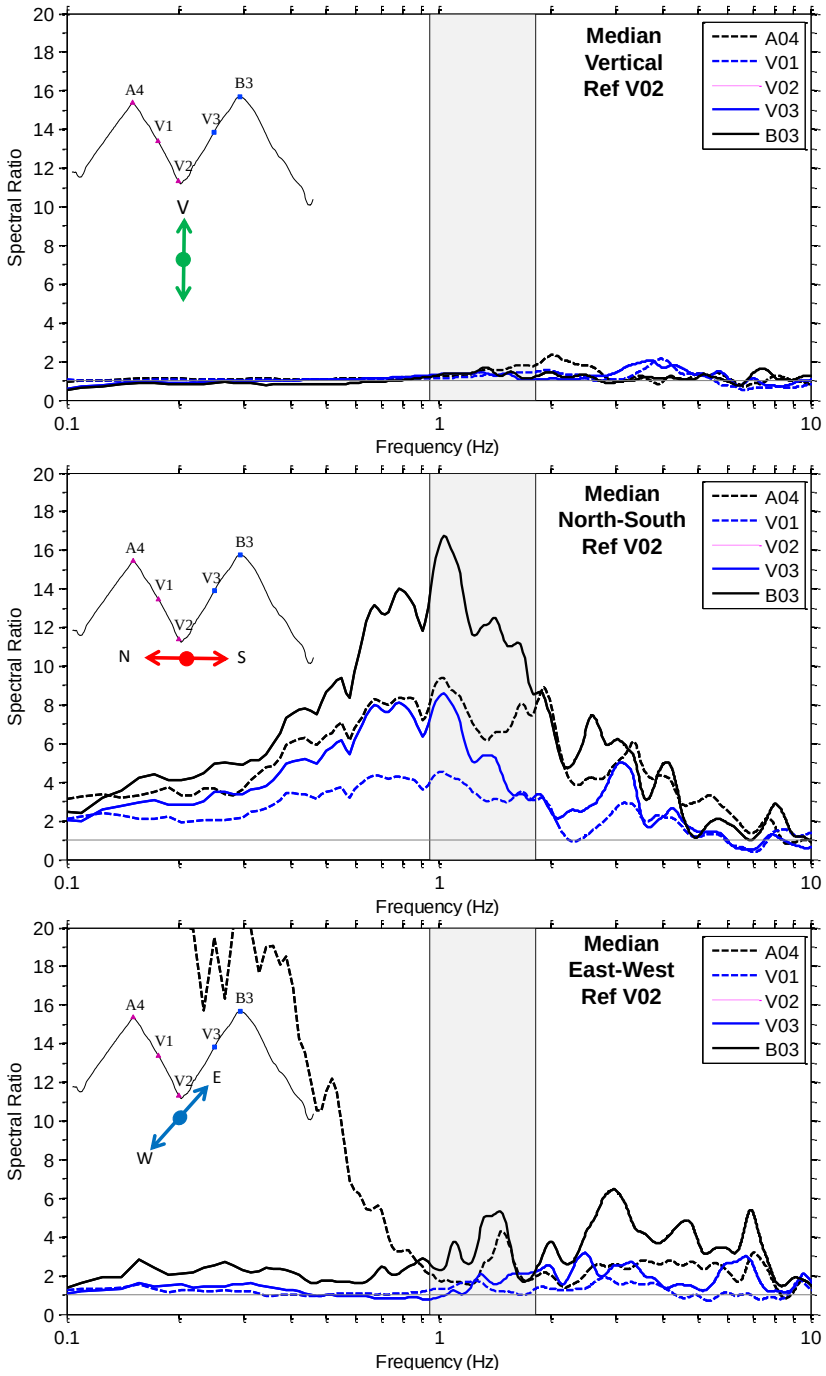

Figure 8.55: Standard spectral ratio (SSR) for the median of the Phase II event catalog (52 events) line V for the vertical, North-South, and East-West components of motion. Station V2 was used as the reference station. The estimated topographic frequency range based on cross-section geometry and average shear wave velocity is shaded.

measured an amplification of 9.5 at the same frequency. Stations V1 and V3, which were in the middle of the slope on the North and South topographic features, respectively had amplifications of 8.6 and 4.5, which was approximately a 50% reduction in spectral ratio from their respective crest stations. This formed a good pattern of top down amplification for the V line. The 1.0 Hz amplification was also directly in the topographic frequency range. However, the measured amplifications on each station extended over a much wider frequency band than estimated for each topographic feature (0.95-1.83 Hz). Indicating the estimates were not able to correctly predict the measured topographic amplification frequency range for the V line features. It is unknown why the errors occurred, but possible errors in the estimated topography size or stiffness cannot be blamed, because no adjustments in the models parameters (that are within reason) could correctly predict the wide band amplification measured by line V.

For the E-W component, an amplification of 5.1 was measured by Station B3 within the estimated topographic frequency range at 1.5 Hz. Station A4 also had an amplification at the same frequency of 4.3. Stations V1 and V3 had slight amplification at the same frequency of 1.1 and 1.7, respectively, which formed a good pattern of amplification for each feature. Amplifications at higher frequencies (greater than 2 Hz) were also calculated for each station, and formed a good pattern of top-down amplification similar to the pattern at 1.5 Hz. These amplifications are near the soil site effects frequency band (5-15 Hz), therefore it is unclear whether these amplifications are the result of topographic effects or soil site effects.

Horizontal polarity plots depicting the median response for all 52 events recorded by Stations A4, V1, V3, and B3, based on the SSR method applied over the frequency range of 0.1 to 5 Hz, are provided in Figure 8.56. Based on the results presented in Figure 8.55, topographic effects are expected at frequencies less than 2 Hz. All the stations in

the array have a strong N-S polarity, which is directly in-line with the strong topographic relief under each station. Therefore, the N-S amplifications are likely caused by topographic effects.

Overall, amplifications at the crest stations B3 and A4 were measured on each of the components in the estimated topographic frequency range. However, the N-S component, which is in-line with the topographic relief, had the highest amplification of 16.75 and 9.5, respectively, but the true frequency amplification range extended beyond the estimated range, and could not be explained using the current height and width estimation methods. The amplifications in the E-W direction were much lower than the N-S, but still significant in terms of overall amplification values.

8.5.2 Median Reference Method (MRM)

The Median Reference Method (MRM) was used to analyze each recorded seismic event. The log normal median spectral ratio of these events was then calculated for stations 1-22 (not including the H stations) in the topographic array. A comparison of the log normal medians for each station in line A (A1-A10) using the MRM is shown in Figure 8.57. Comparing the V component of each station, no significant amplification peak was estimated in the topographic frequency range (0.24-2.54 Hz) for the crest station A7. Amplifications were calculated for Stations A3-A5 at approximately 0.5 Hz, but no pattern of amplification was observed. These stations are directly over the hypocenter of the events, and the amplification is believed to be caused by vertically propagating P-wave arriving in-line with the vertical component of the stations, which results in a higher ground motion. Amplifications also occurred on Stations A1-A2 forhigher frequencies (> 2 Hz), but those amplifications are likely linked to the soil layering under the stations.

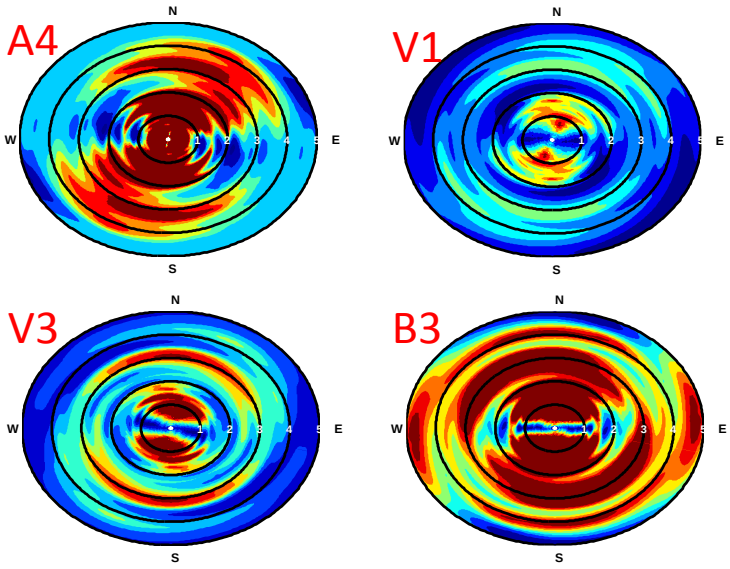

Figure 8.56: Horizontal polarity plots for the SSR method line V using the median response of the event catalog for Phase II (52 events). Station V2 was used as the reference station.

For the North-South component of motion, amplifications were measured on Stations A3-A5 in the topographic frequency range, with amplifications up to 8.5. As with the SSR method for line A, these amplification were likely driven by the steep topographic relief in the N-S direction under the stations. The amplification peak measured on Station A3 matches well with the estimated topographic frequency range (0.95-1.84) for the N-S trending topography under the station. It is still unknown why the amplification for this station was so much greater than the median response of all the other stations in the array, but it could be the result of the Westward facing cliff combined with the N-S topographic relief creating a double amplification (see Figures 8.3-8.10).

For the East-West component, a wide band amplification was measured for the crest station, A7, from 0.1 Hz to 5 Hz. For frequencies less than 1.8 Hz, a flat amplification of 1.5 was measured, but for a narrow band from 1.8-2.8 Hz, the amplification was higher at 3.25. This narrow band was right on the edge of the estimated

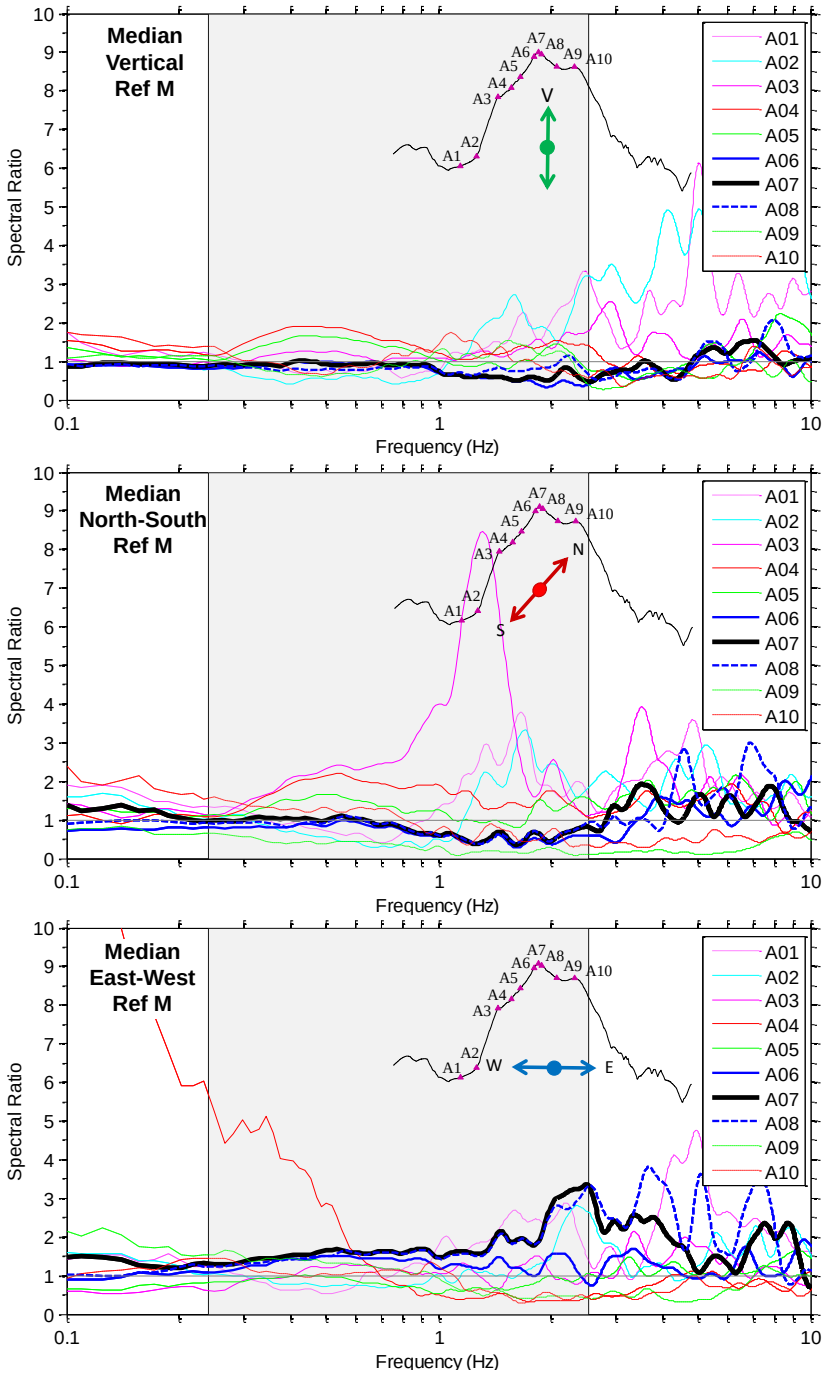

Figure 8.57: Median Reference Method (MRM) for the median of the Phase II event catalog (52 events) line A for the vertical, North-South, and East-West components of motion. The estimated topographic frequency range based on cross-section geometry and average shear wave velocity is shaded.

topographic frequency band (0.24-2.54 Hz), and only Station A8 forms a good pattern of amplification with Station A7. In addition Station A8 had almost the same spectral ratio for frequencies less than 3 Hz as Station A7. Therefore, it cannot be said conclusively if the amplifications at A7 and A8 were driven by topographic effects, but topographic effects likely at least contributed to the measured amplifications.

Horizontal polarity plots depicting the median response for all 52 events recorded by Stations A1-A10, based on the MRM method applied over the frequency range of 0.1 to 5 Hz, are provided in Figure 8.58. Based on the results presented in Figure 8.57, topographic effects are expected at frequencies less than 5 Hz. Stations A6-A9 had a strong E-W polarity driven by the E-W trending topographic relief. Stations A3-A5 had a strong N-S polarity due to the steep N-S trending topography under those stations. Therefore for the line A, the polarity of the ground motions seemed to be connected to the direction of the steepest topographic relief.

Overall, amplifications were measured for the crest station A7 in the estimated topographic frequency range for only the E-W component. The E-W amplifications for Station A7 occurred over a wide frequency band, and were highest from 1.8-2.8 Hz, with a maximum amplification of 3.25. Amplifications in N-S direction occurred for Stations A3-A5, which all have strong N-S topographic relief. The amplifications of Station A3 were calculated to be up to 8.5, much larger than measured on other stations using the MRM. As stated above, this may be caused by double amplification due to amplification in the E-W direction, caused by the cliff face between Stations A2-A3, and amplification in the N-S direction, caused by the steep N-S topographic feature. Both these features have estimated topographic frequency ranges from approximately 1-2 Hz, which could cause the superposition of topographic amplifications from the two features resulting in a much larger amplification.

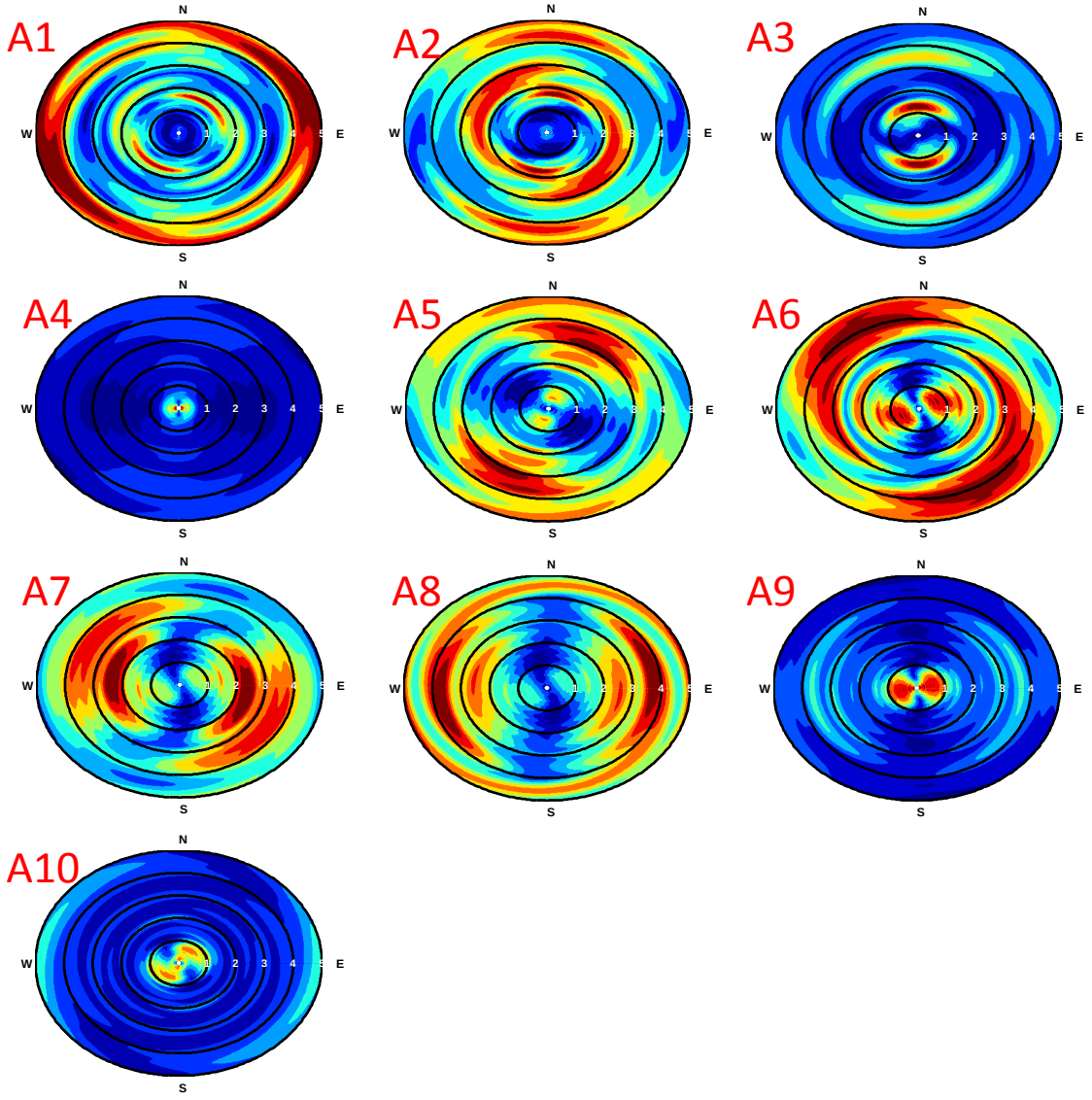

Figure 8.58: Horizontal polarity plots for the MRM method line A using the median response of the event catalog for Phase II (52 events).

A comparison of the log normal medians for each station in line B (B1-B9) using the MRM is shown in Figure 8.59. Comparing the vertical component of each station, no significant amplification peak was measured in the estimated topographic frequency

range (0.21-2.39 Hz) for the crest station B6. Slight amplifications, less than 1.5, were calculated for Stations B3-B4 at approximately 0.5 Hz, which were directly over the hypocenter of the events, and may be affected by vertically propagating P-wave similar to line A in the previous section. Amplifications also occurred on Stations B1-B2 for higher frequencies (> 2 Hz), but the amplification cannot be tied to any topographic feature. Therefore, the amplifications were likely caused by soil site effects.

For the North-South component of motion, amplifications were measured on Stations B2-B4 in the topographic frequency range, with amplifications up to 10 from 0.2 to 3 Hz, but more concentrated between 0.8 and 2 Hz. As with the SSR method for line B and the MRM for line A, these amplifications were likely driven by the steep topographic relief in the N-S direction. In addition, the amplification may have been influenced by the Westward facing cliff between Station B1 and B2. Amplifications on Station B3 have a broadband frequency range from 0.2-2 Hz with amplifications of up to 3. As with the A and B lines for the SSR method, lower frequency amplification are measured on Station B3 than predicted using the available height and width prediction methods on the N-S topographic feature. This poor prediction by the analytical method may be the result of using the 2D methods on a clearly 3D topographic feature.

For the East-West component of motion, a wide band amplification was measured for the crest station B6 from 0.2 Hz to 2 Hz. This frequency range amplification matched the estimated topographic frequency range (0.21-2.39 Hz) very well. Stations B7, B5, B8, and B4 formed a good top-down amplification pattern with maximum amplification values of 2.5, 2.3, 1.7, and 1.2, respectively, that resulted in amplification reduction of 3%, 11%, 35%, and 55% compared to Station B6, respectively. Amplifications were also measured on Station B2 in the E-W direction from 1.1-3.3 Hz with a maximum amplification of 4.3. As discussed for line B using the SSR method, this amplification

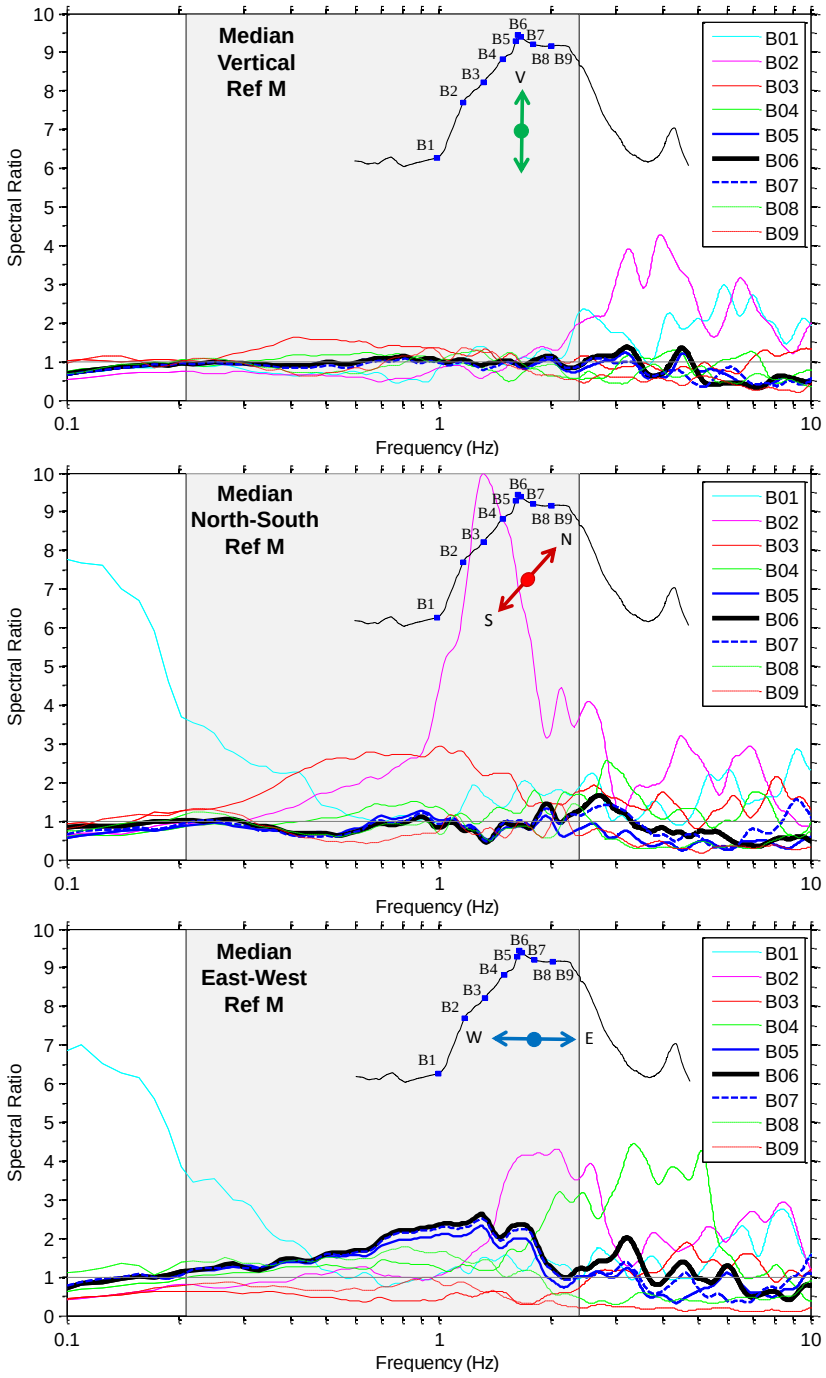

Figure 8.59: Median Reference Method (MRM) for the median of the Phase II event catalog (52 events) line B for the vertical, North-South, and East-West components of motion. The estimated topographic frequency range based on cross-section geometry and average shear wave velocity is shaded.

could be the result the cliff face from B1 to B2, but estimated topographic frequencies for this feature do not match the measured amplification range.

Horizontal polarity plots depicting the median response for all 52 events recorded by Stations B1-B9, based on the MRM method applied over the frequency range of 0.1 to 5 Hz, are provided in Figure 8.60. Based on the results presented in Figure 8.59, topographic effects are expected at frequencies less than 2 Hz. Stations B5-B8 had a strong E-W polarity driven by the steep E-W trending topographic relief. Stations B2-B3 had a strong N-S polarity due the steep N-S topography under those stations. Therefore, similar to line A, the polarity of the ground motions seemed to be connected to the direction of the steepest topography for line B.

Overall, amplifications were measured for the crest station, B6, in the estimated topographic frequency range for only the E-W component. The amplifications for E-W component of Station B6 occurred over a wide frequency band from 0.2-2.0 Hz, which matched the estimate topographic frequency band well. Maximum amplifications of 2.6 were measured for Station B6, and stations just off the crest (Stations B4-B5 and B7-B8) had lower and lower amplification as one moved down the slope away from the crest. Amplifications occurred in the N-S direction for Stations B2-B3, which all have steep N-S topographic relief. The amplification of Station B2 was calculated to be 10, which was much larger than measured on other stations using the MRM. As stated for line A, this may be caused by superposition of the amplifications of the cliff face in the E-W direction at Stations B2, and amplification in the N-S direction caused by the steep N-S trending topographic feature.

A comparison of the log normal medians for each station in line V (A4, V1-V3, and B3) using MRM are shown in Figure 8.61. Comparing the V component of each

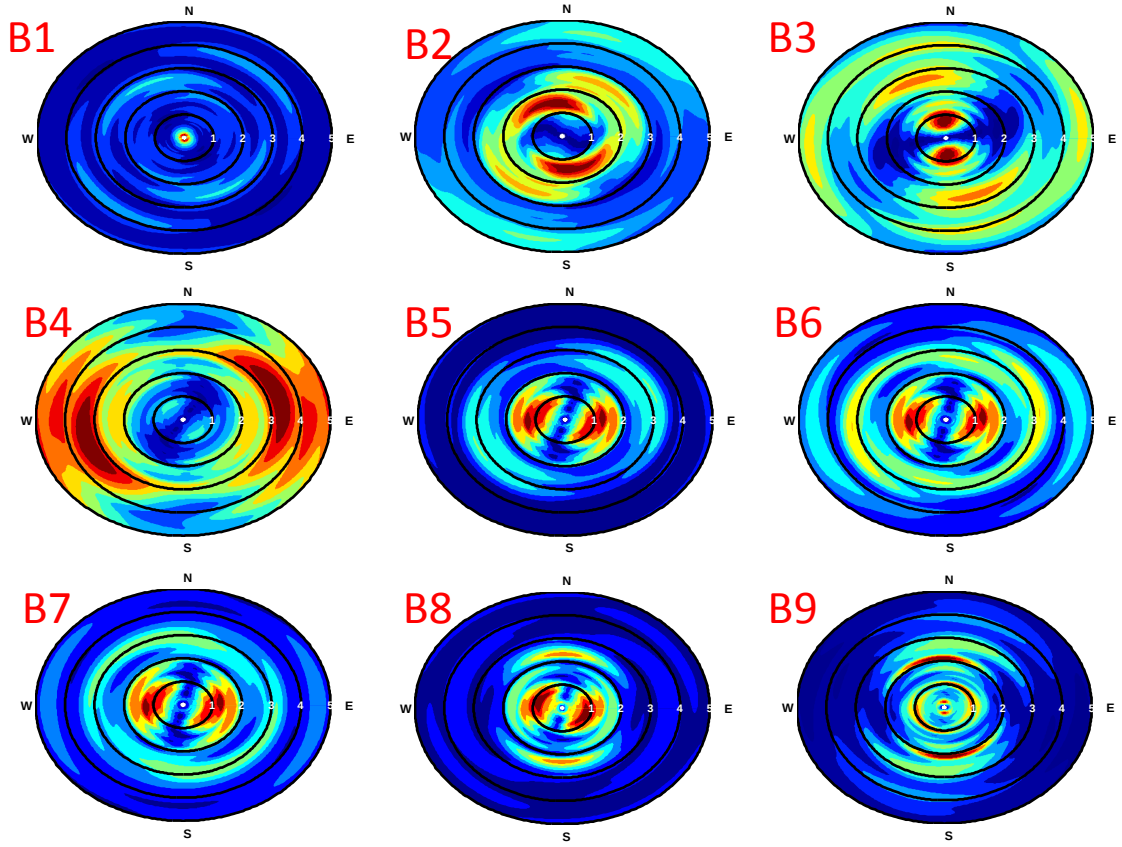

Figure 8.60: Horizontal polarity plots for the MRM method line B using the median response of the event catalog for Phase II (52 events).

station, an amplification of 1.5-2 was measured on all the stations in the V line from 0.25-1 Hz. No pattern of amplification was noticed from the stations. Therefore, topography was likely not the cause, but the amplification may be related to the stations being directly over the hypocenter of the events and P-wave energy propagating in-line with the vertical components. Amplifications were measured, in the same frequency range, on stations in the A and B lines that were also directly over the hypocenters (A3-A5, and B2-B4).

For the North-South component, amplifications were measured on the crest stations B3 and A4 from 0.3-1.9 Hz, with maximum amplifications of 3.0 and 2.2,

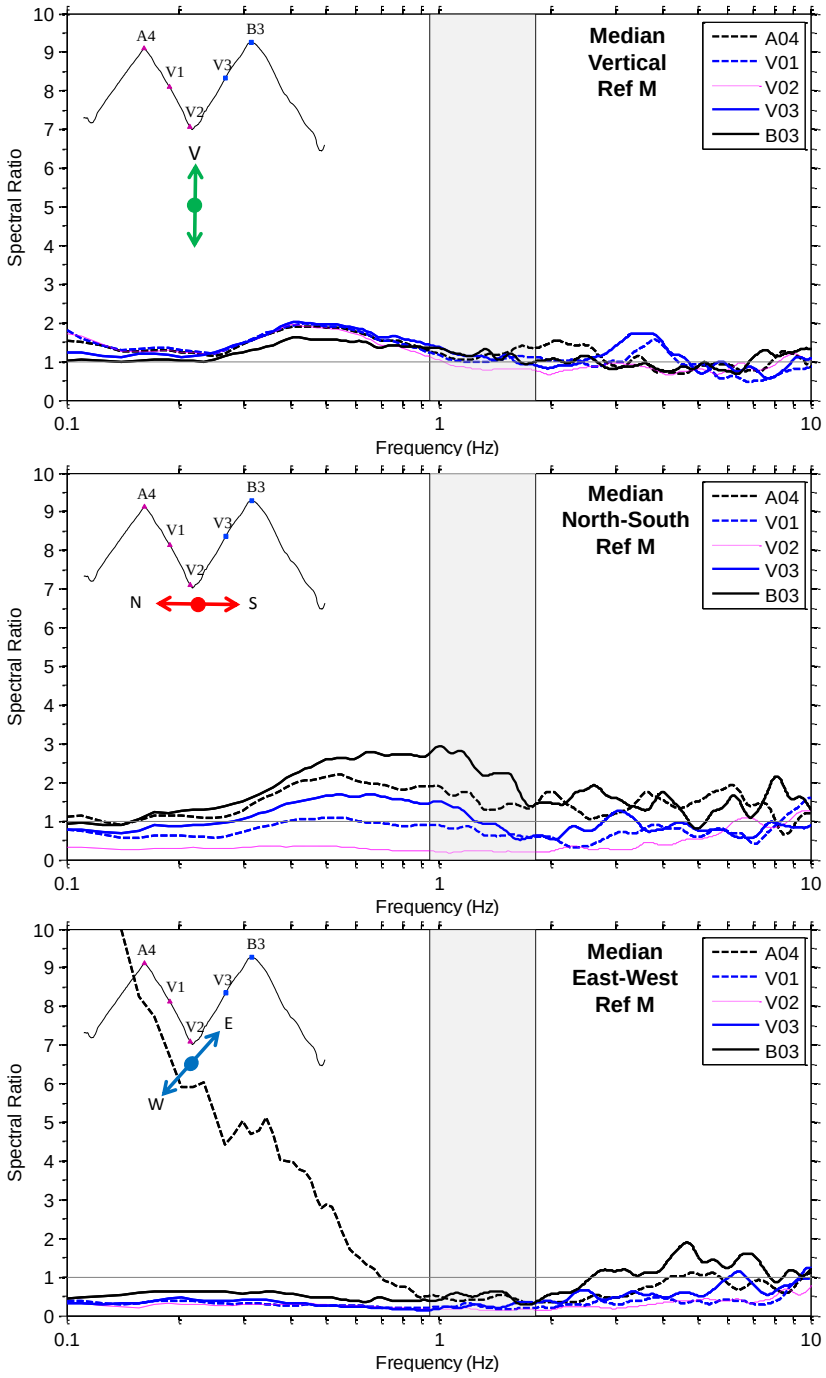

Figure 8.61: Median Reference Method (MRM) for the median of the Phase II event catalog (52 events) line V for the vertical, North-South, and East-West components of motion. The estimated topographic frequency range based on cross-section geometry and average shear wave velocity is shaded.

respectively. The upper part of the amplification range (>0.95 Hz) matches well with the estimated topographic frequency range (0.95-1.83 Hz), but a large portion of the low frequency amplification is not predicted by the height or width based estimation methods of Ashford and Sitar (1997) and Paolucci (2002). A good top-down amplification pattern was formed by Stations V1 and V2, with about a 50% reduction in spectral ratio when compared to their respective crest stations. The pattern of amplification provides good confidence that topographic effects were driving the amplifications.

For the East-West component of motion, amplifications were only measured on Station B3 at a frequency of 5 Hz, which is believed to be caused by soil site effects and not topographic effects (i.e., soil site effects band is 5-15 Hz). A low frequency amplification was calculated for Station A4, but as mentioned before it was likely due to sensor errors and not ground motion amplification.

Horizontal polarity plots depicting the median response for all 52 events recorded by Stations A4, V1-V3, and B3, based on the MRM method applied over the frequency range of 0.1 to 5 Hz, are provided in Figure 8.62. Based on the results presented in Figure 8.61, topographic effects are expected at frequencies less than 2 Hz. All the stations in the array had a strong N-S polarity in-line with the topographic relief under the station. With the low frequency problems with A4 in the E-W direction it made the station appear E-W polarized, but the E-W amplification was likely caused by the sensor error.

Overall, topographic amplifications were measured in only the N-S direction for crest stations A4 and B3. The amplifications were measured over a wider frequency band than estimated using the height or width estimation methods. The maximum amplification for Station A4 and B3 in the N-S direction were 2.2 and 3.0, respectively with the larger feature under Station B3 producing the higher amplification. A slight

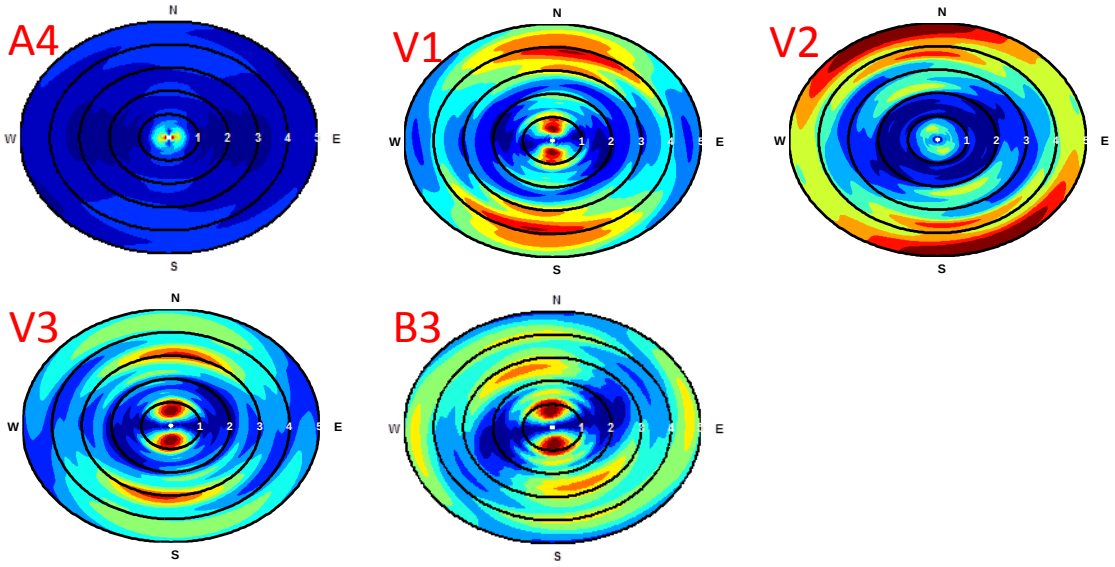

Figure 8.62: Horizontal polarity plots for the MRM method line V using the median response of the event catalog for Phase II (52 events).

amplification of less than 2.0 was measured on the vertical component for all the station, which may be related to P-wave arriving nearly vertically from the hypocenter.

8.5.3 Horizontal to Vertical Spectral Ratio (HVSR)

The Horizontal to Vertical Spectral Ratio (HVSR) was used to analyze each recorded seismic event. The log normal median spectral ratio of these events was then calculated for all stations in the topographic array. A comparison of the log normal medians for each station in line A using the HVSR method is shown in Figure 8.63 for the N-S, and E-W components of motion.

For the North-South component, no amplifications were measured on the crest station A7 for frequencies less than 2 Hz. For frequencies greater than 2 Hz, a flat band amplification of 3 was measured, but no strong pattern of top-down amplification, with any of the stations in the array, was measured. An amplification of up to 7 was measured on Station A3 over a frequency range from 1.0-1.8 Hz, which corresponded well with the

estimated N-S topographic frequencies under Station A3 of ~1-2 Hz. Amplifications were also measured on a majority of stations for frequencies greater than 2 Hz, but these were likely caused by soil site effects due to the frequency range and lack of amplification pattern.

For the E-W component, a large amplification of up to 12 was measured on Station A7, over a frequency range from 1.0-5.0 Hz. The main amplification peak occurred at a frequency of 2.5 Hz, which put half of the amplification range in the estimated topographic frequency range, and half higher than the estimate topographic frequency range. For the half within the estimate topographic frequency band, a good pattern of amplification is formed with Station A6 and A8, with approximately 30% reductions in spectral ratio compared to Station A7. For the higher frequency half, the amplification pattern falls apart, which may indicate the amplification were no longer driven by topographic effects.

Horizontal polarity plots depicting the median response for all 52 events recorded by Stations A1-A10, based on the HVSR method applied over the frequency range of 0.1 to 5 Hz, are provided in Figure 8.64. Based on the results presented in Figure 8.63, topographic effects are expected at frequencies less than 5 Hz. Stations A6-A9 had a strong E-W polarity matching the steep E-W topography in those locations. Station A3 had a strong N-S polarity matching the steep N-S topography under that station. Other stations in the array do not have a strong polarity in any direction.

Overall, a large amplification peak of up to 12 was measured in the E-W direction for the crest station at a frequency of 2.5 Hz. The amplification range extended from a frequency of 1.0-5.0 Hz; however, only the low frequency part matched with the estimated topographic frequency range. The peak was likely at least partially driven by topographic effects, but some other effects may have played a role at higher frequencies

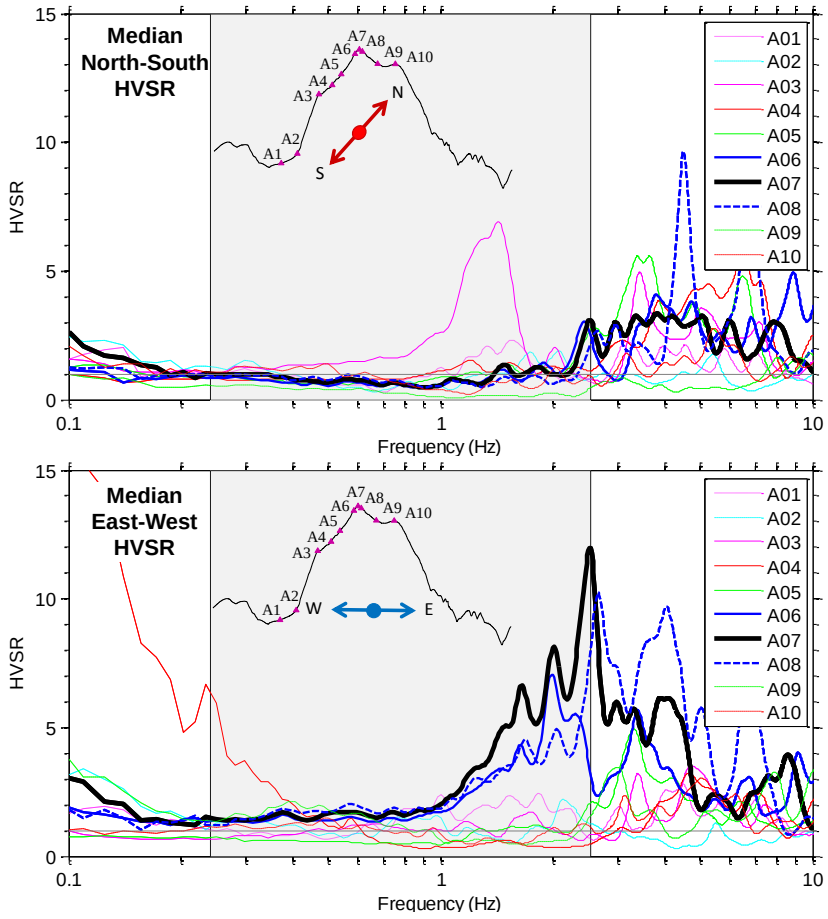

Figure 8.63: Horizontal to Vertical Spectral Ratio (HVSR) for the median of the Phase II event catalog (52 events) line A for the vertical, North-South, and East-West components of motion. The estimated topographic frequency range based on cross-section geometry and average shear wave velocity is shaded.

(>2.5 Hz). Amplifications were also measured on Station A3, and matched well with N-S estimated topographic frequencies.

A comparison of the log normal medians for each station in line B using the HVSR method is shown in Figure 8.65. For the North-South component, no amplifications were measured at the crest station, B6, for frequencies less than 2 Hz. For frequencies greater than 2 Hz, an amplification of up to 4 was measured, but no strong pattern of top-down amplification with any of the stations in the array was measured. An

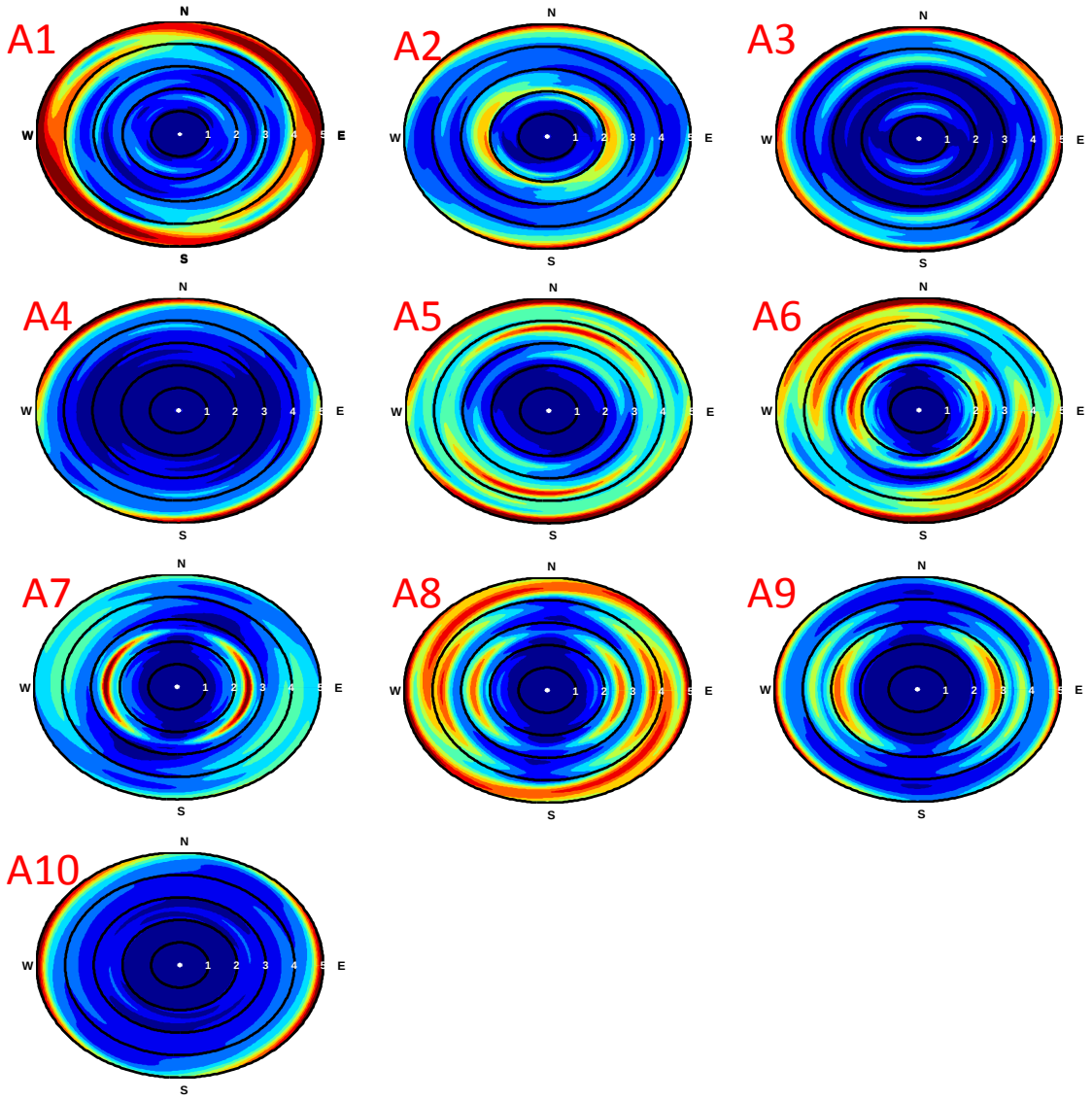

Figure 8.64: Horizontal polarity plots for the HVSR method line A using the median response of the event catalog for Phase II (52 events).

amplification of up to 18 was measured on Station B2 over a frequency range from 1.0-2.0 Hz, which corresponded well with the estimated N-S topographic frequencies of the feature (~1-2 Hz) under Station B2. Amplifications were also measured on a majority of stations for frequencies greater than 2 Hz, but similar to the A line, these were believe to

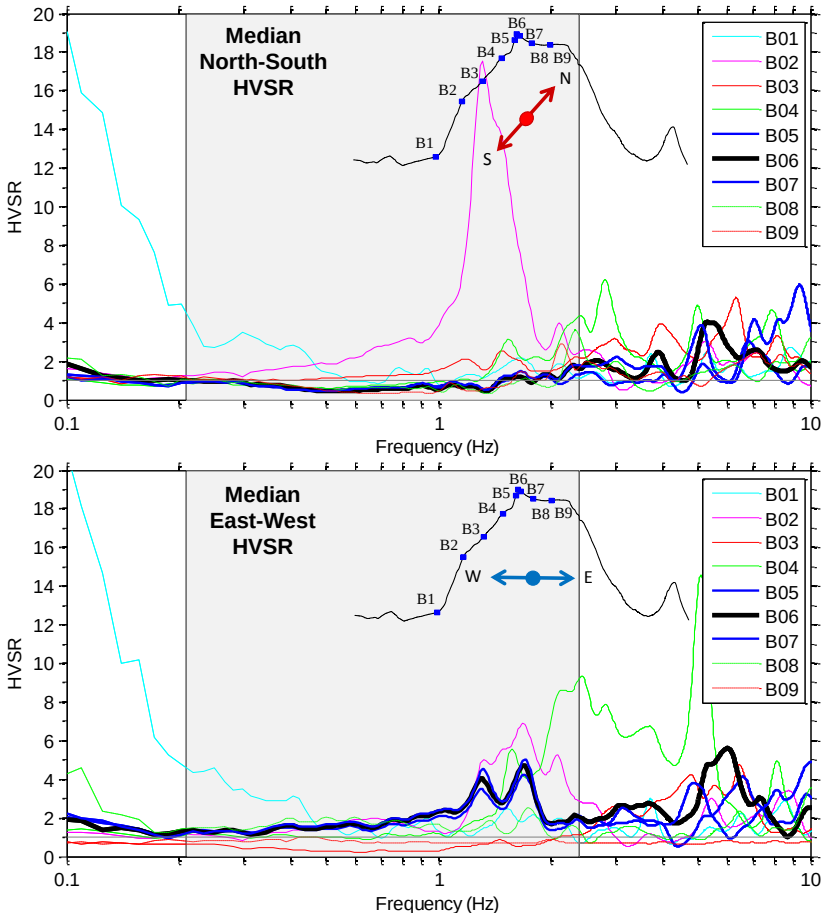

Figure 8.65: Horizontal to Vertical Spectral Ratio (HVSR) for the median of the Phase II event catalog (52 events) line B for the vertical, North-South, and East-West components of motion. The estimated topographic frequency range based on cross-section geometry and average shear wave velocity is shaded.

be caused by soil site effects due to the frequency range and lack of amplification pattern.

For the E-W component, an amplification of up to 4.4 was measured on the crest station B6 in a frequency range from 0.2-2 Hz, which matches well with the estimated topographic frequency range. For Stations B5 and B7, nearly the same amplification pattern was measured with no reduction in spectral ratios from the crest. However, Stations B4 and B8 have an approximately 50% reduction in spectral ratio compared the crest station, B6. This provides good evidence these amplifications were driven by

topography. Station B2 also had a strong amplification peak from 1-3 Hz, which was very similar to what was recorded using the SSR and MRM methods for the B line.

Horizontal polarity plots depicting the median response for all 52 events recorded by Stations B1-B9, based on the HVSR method applied over the frequency range of 0.1 to 5 Hz, are provided in Figure 8.66. Based on the results presented in Figure 8.65, topographic effects are expected at frequencies less than 2 Hz. Stations B4-B7 all had a strong E-W polarity matching the topography in those locations. Station B2, B8-B9 all had a strong N-S polarity, which matched the topography for B2, but Station B8 and B9 were on relatively flat topography. Other stations in the array did not have a strong polarity in any direction.

Overall, an amplification peak was measured on the crest station of line B in the E-W direction from 0.2-2.0 Hz, with a maximum amplification of 4.4. A good pattern of top-down amplification pattern was measured for other stations in the array. Therefore, the E-W amplifications were likely driven by topographic effects. An amplification peak on Station B2 was also measured from approximately 1-2 Hz in both
the N-S and E-W direction. The N-S direction had a large amplification of 18 compared to 6.5 for the E-W direction.

A comparison of the log normal medians for each station in line V using the HVSR method is shown in Figure 8.67. For the North-South component, amplifications were measured in the topographic frequency range of 2.5 and 1.5 for the crest stations B3 and A4, respectively. In the same frequency range, Stations V1 and V2 had a spectral ratio of 0.8-1.0 indicating de-amplification. However, the de-amplifications still formed a good pattern of top-down amplification. Amplifications were also measured on all the stations at frequencies above 2-3 Hz, but these are likely caused by soil site effects

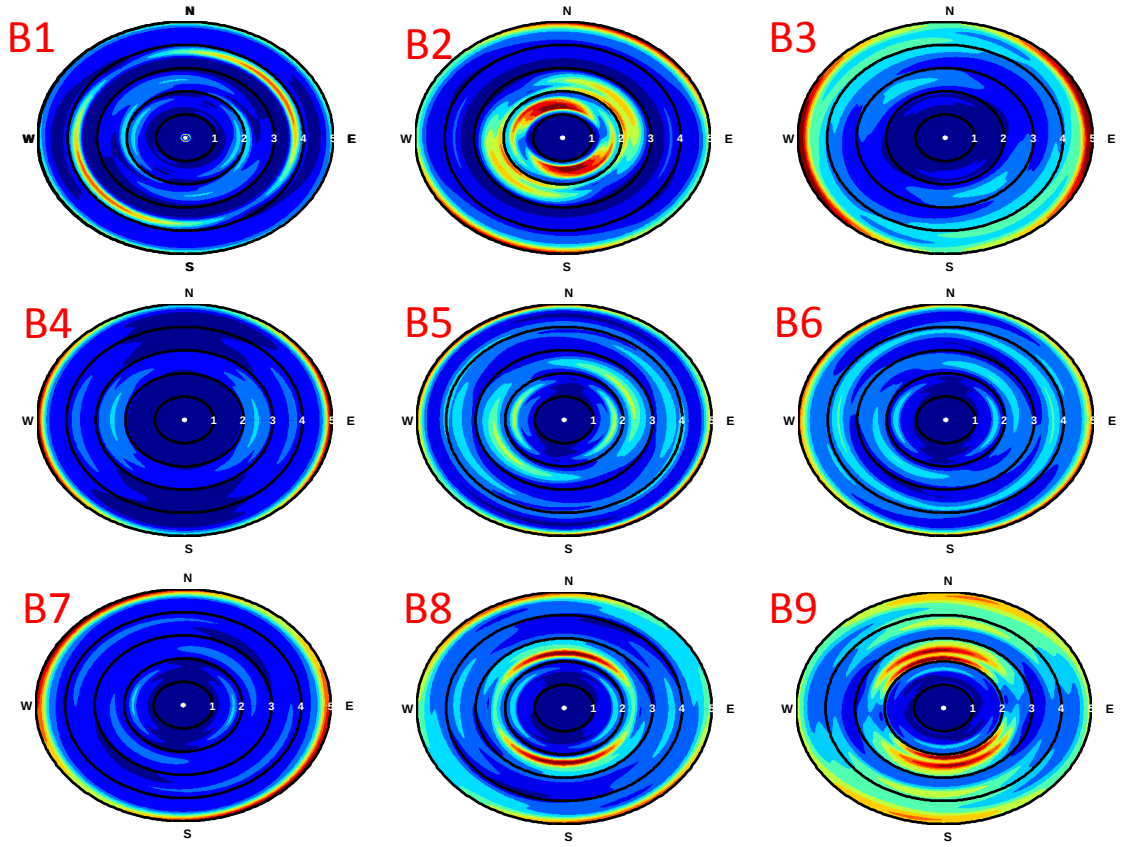

Figure 8.66: Horizontal polarity plots for the HVSR method line B using the median response of the event catalog for Phase II (52 events).

due to the frequency range and lack of amplification pattern. For the E-W component, no amplifications were measured in the topographic frequency range, but similar to the N-S direction, amplifications were measured on all stations at frequencies above 2-3 Hz.

Horizontal polarity plots depicting the median response for all 52 events recorded by Stations A4, V1-V3, and B3, based on the HVSR method applied over the frequency range of 0.1 to 5 Hz, are provided in Figure 8.68. Based on the results presented in Figure 8.67, topographic effects are expected at frequencies less than 2 Hz. In the 2-5 Hz range,

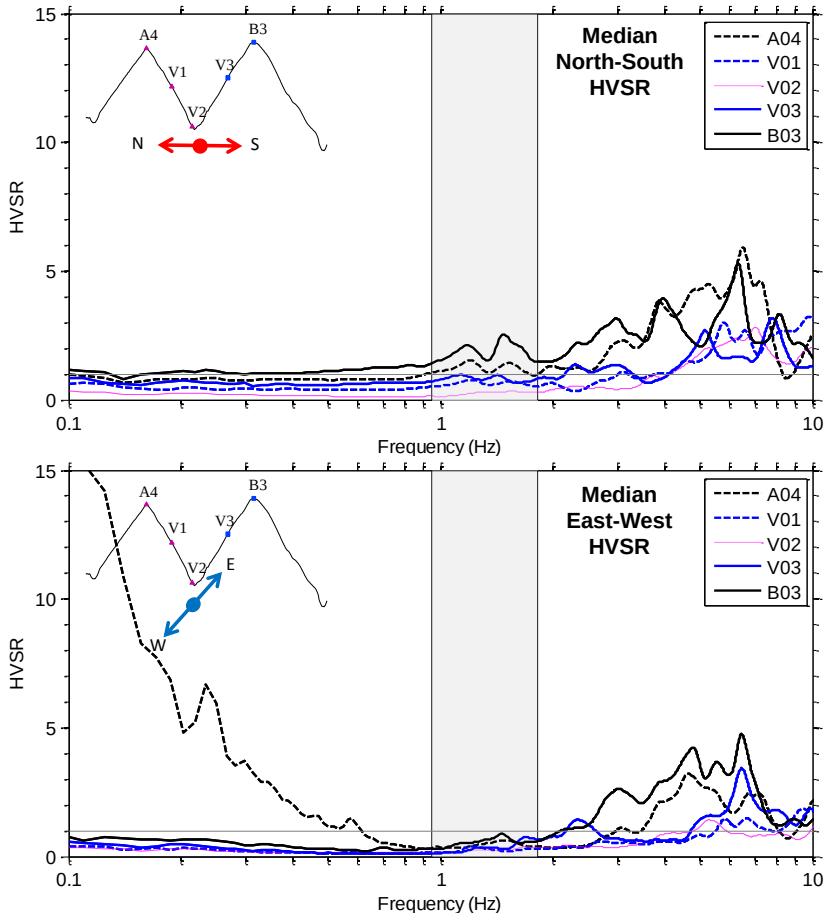

Figure 8.67: Horizontal to Vertical Spectral Ratio (HVSR) for the median of the Phase II event catalog (52 events) line V for the vertical, North-South, and East-West components of motion. The estimated topographic frequency range based on cross-section geometry and average shear wave velocity is shaded.

the amplifications dominate the polarity plots and make a determination of polarity in the topographic frequency range impossible.

Overall, slight amplification peaks were measured in the N-S direction for the two crest stations of 2.5 and 1.5 in the topographic frequency range from 0.95-1.83 Hz. Amplification at frequencies higher than 2-3 Hz in both directions were measured, but presumed to be driven by soil site effects.

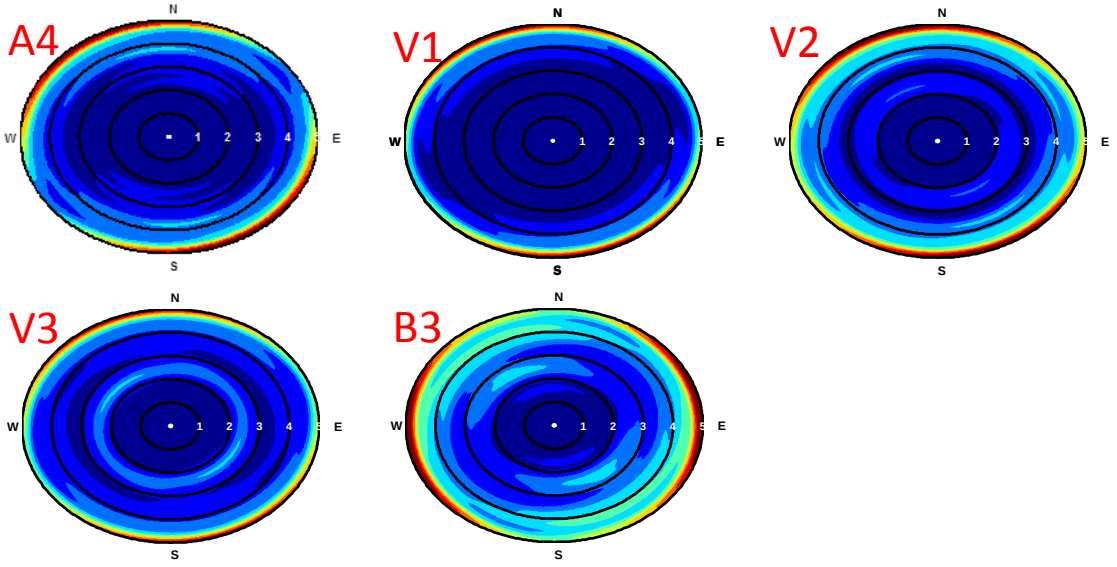

Figure 8.68: Horizontal polarity plots for the HVSR method line V using the median response of the event catalog for Phase II (52 events).

8.5.4 Method Comparison

All 52 events recorded in Phase II (2011) of the topographic effects study were analyzed using three separate methods to assess the effects of topography on the seismic response of the mountain. The log normal medians of the 52 events for each station were then compared, to assess whether amplifications measured in the frequency domain were caused by topographic effects. To determine how well each method performed at identifying topographic frequencies, and at estimating the topographic amplification, the spectral ratios of each of the crest stations (A7, B6, and B3) were compared using all three analysis methods. In Table 8.5, a summary of the topographic amplification ranges measured using each analysis method, along with the maximum amplification observed at the crest station A7 for line A in that same frequency range are provided. In Figure 8.69, the spectral ratios for all three methods are compared for Station A7. Comparing the vertical components over the estimated topographic frequency range (0.24-2.54 Hz), the

SSR method had a slight amplification from 0.3-1.0 Hz with an amplification of up to 2.1, while the MRM had no amplification on the vertical component.

For the North-South component, a slight amplification from 0.4-0.8 Hz was calculated using the SSR method, with a maximum amplification of up to 2, while the other methods indicated no amplification in the topographic frequency range. Given the lack of N-S topography under Station A7, no amplifications are expected in the N-S direction. At frequencies greater than the estimated topographic frequency range (>2.54 Hz), amplifications were calculated using the HVSR and MRM methods, but the amplifications were likely caused by soil site effects due to the frequency range.

For the East-West component, a flat amplification of 1.5 for frequencies less than 1 Hz were calculated using the HVSR and MRM methods. On the other hand, an amplification peak from 0.3-1.0 Hz with a maximum amplification of 3.25 was calculated using the SSR method. For frequencies greater than 1 Hz, a strong amplification peak centered at approximately 2.5 Hz was calculated using the MRM and HVSR methods, and each method indicated amplifications over approximately the same frequency range. However, the methods had significant different amplification factors of 12 for the HVSR method, and just 3.25 for the MRM method. Since the spectral ratios calculated using the HVSR method had been shown by many authors to not correctly represent the possible amplification at a site, the MRM results were likely the most accurate. The SSR method did not match the frequency amplification pattern of the HVSR and MRM methods, and only had two small amplification peaks just above the estimated topographic frequency range.

Overall, the methods did not calculate strong amplification peaks on either the V or N-S components, but each method did calculate amplifications in the E-W direction. The amplification frequency ranges for the HVSR and MRM methods matched well for

Table 8.5: Summary of the topographic amplification frequency range for the median analysis of the A line for all three methods. The maximum amplification was measured on the crest station within the same frequency range.

	Amplification Range (Hz)			Max Amplification		
Method	**V**	**N-S**	**E-W**	**V**	**N-S**	**E-W**
SSR	0.3-1.0	0.3-1.0	0.3-1.0	1.5	2.1	3.25
MRM	NA	NA	0.1-5.0	NA	NA	3.25
HVSR	NA	NA	1.0-5.0	NA	NA	12

the E-W component, but varied significantly for the calculated amplification factors with over a 100% difference between the methods. The SSR method calculated a much narrower amplification frequency range compared to the MRM and HVSR methods. For the A line, the MRM method seemed to produce the best amplification factors and amplification frequency range. The HVSR method indicated a similar amplification range to the MRM method, but likely overestimated the amplification factor by over 250%. The SSR method resulted in some amplification, but they did not match well with the other estimation methods.

As with the analysis of event 200.19.5, the log normal median of all 52 events using the SSR method for Station A7 is plotted along with the log normal median using the MRM method for Stations A7 and A1 (see Figure 8.70). As was shown for event 200.19.5, the SSR for Station A7 was the result of the combination of the MRM of Station A7 divided by the MRM of Station A1. It can be seen on all components that the amplification or de-amplification of Station A1 was driving the calculated topographic amplification factors for the SSR method, and were likely leading to false amplification factors for other stations when using the SSR method.

In Table 8.6, a summary of the topographic amplification ranges measured using each analysis method, along with the maximum amplification observed at the crest station, B6, for line B in that same frequency range are provided. In Figure 8.71, the

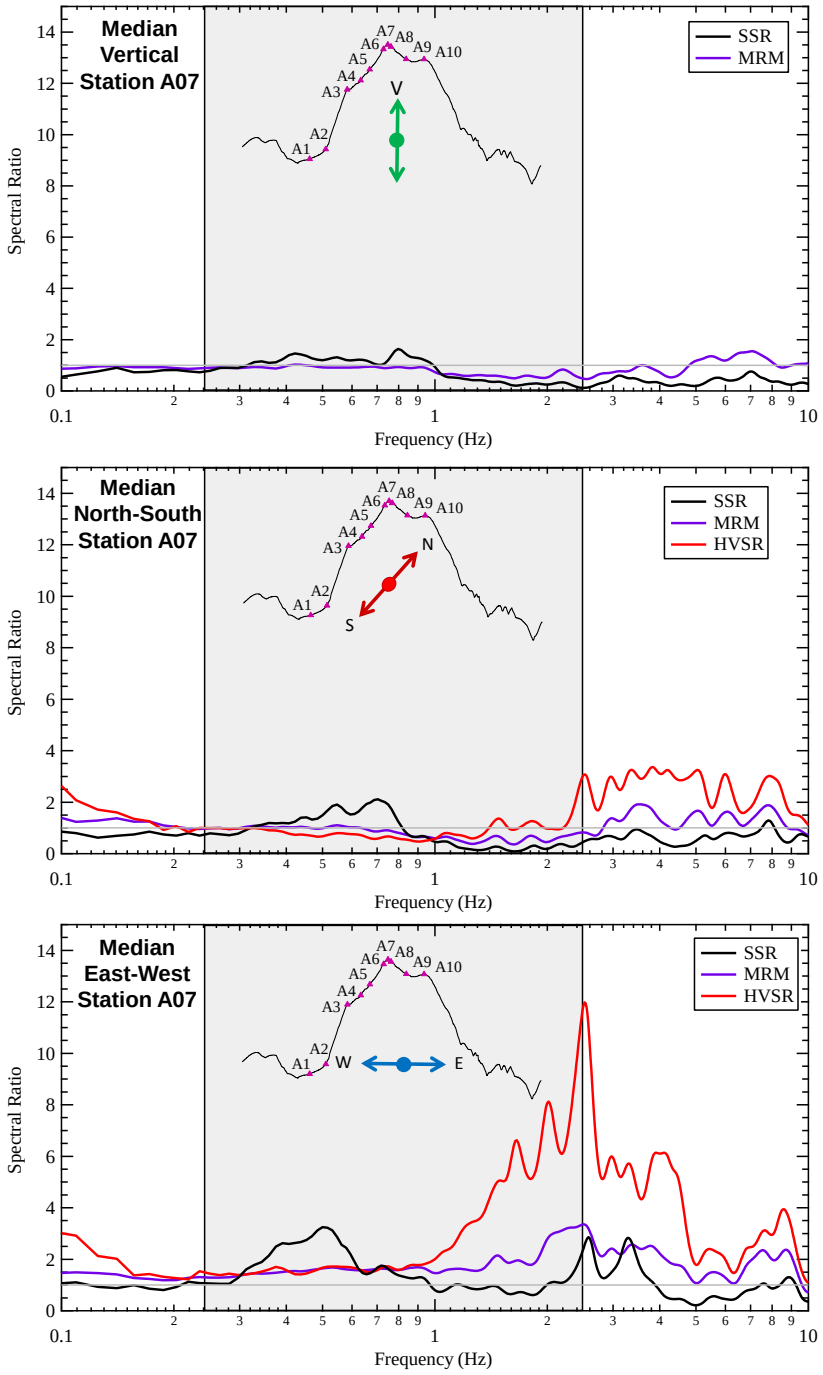

Figure 8.69: Comparison of SSR, MRM, and HVSR results for the median response of all 52 events recorded during Phase II for Station A7 vertical, North-South, and East-West components. The estimated topographic frequency range based on cross-section geometry and average shear wave velocity is shaded.

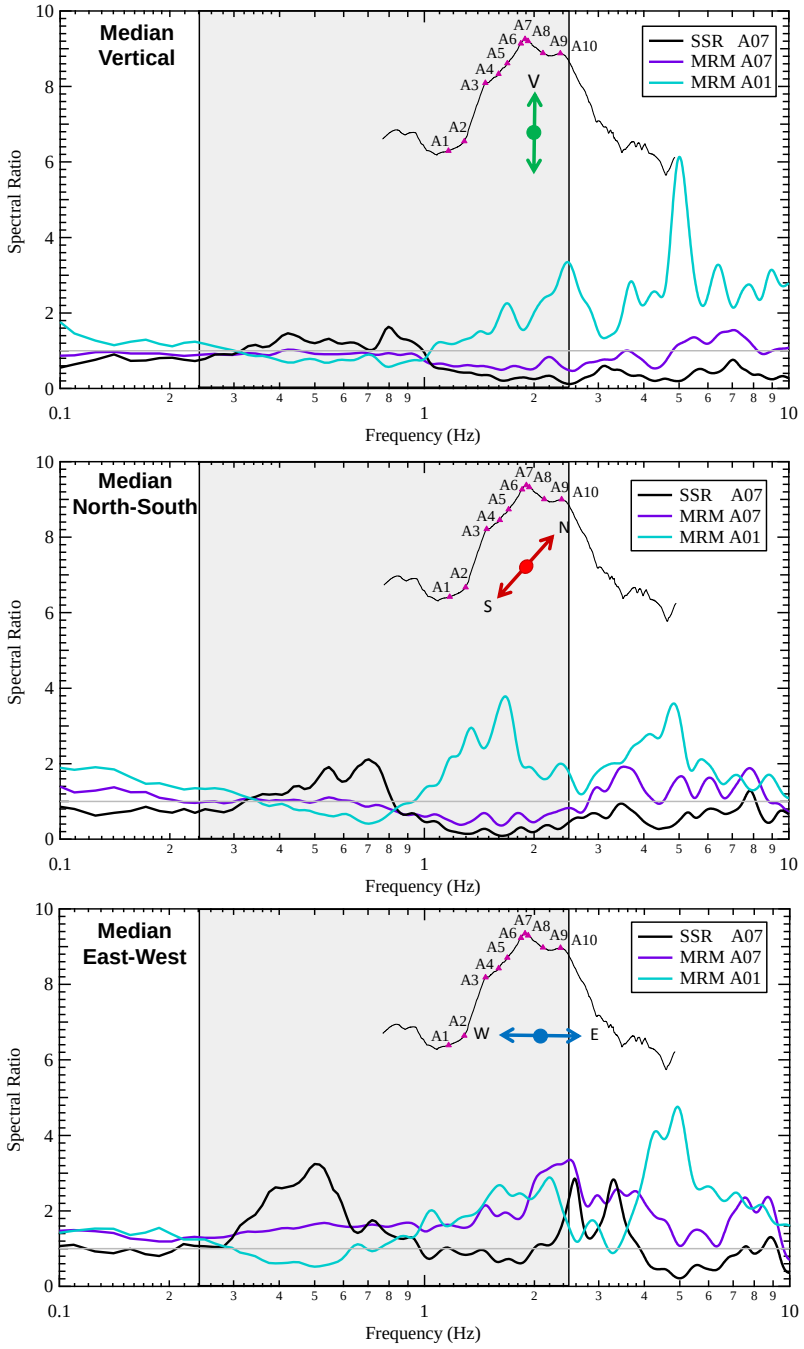

Figure 8.70: Comparison of SSR Station A7 with MRM from Station A7 and A1 results for median response of all 52 events recorded during Phase II for the vertical, North-South, and East-West components. The estimated topographic frequency range based on cross-section geometry and average shear wave velocity is shaded.

Table 8.6: Summary of the topographic amplification frequency range for the median analysis of the B line for all three methods. The maximum amplification was measured on the crest station within the same frequency range.

	Amplification Range (Hz)			Max Amplification		
Method	**V**	**N-S**	**E-W**	**V**	**N-S**	**E-W**
SSR	0.3-1.0	NA	0.4-1.8	1.5	NA	2.9
MRM	NA	NA	0.2-2.0	NA	NA	2.6
HVSR	NA	NA	0.2-2.0	NA	NA	4.4

spectral ratios for all three methods are compared for Station B6. Comparing the vertical components over the estimated topographic frequency range (0.21-2.39 Hz), an amplification peak from 0.3-1.0 Hz with a maximum amplification of 2.3 was calculated using the SSR method. No amplification was calculated in the vertical direction for the MRM method.

For the North-South component, none of the three methods indicated an amplification in the estimated topographic frequency range (0.21-2.39 Hz). However, all three methods indicated slight amplifications between 2.5-3 Hz, but these amplifications were likely not caused by topographic effects due to a lack to top-down amplification pattern observed in the previous sections. For the East-West component, amplifications were measured using all three methods from 0.2/0.4-1.8/2.0 Hz. The methods had similar amplifications usually between 2.5 and 3.0. However, the HVSR method had a larger amplification between 1-2 Hz. The HVSR method also indicated an amplification at approximately 6 Hz that was also calculated using the other two methods.

Overall, very similar results were calculated using the three methods for Station B6, with little to no amplification on the V or N-S components. The SSR method did calculate an amplification peak on the V component that was not calculated using the MRM, but it had an amplification less than 1.5. Amplifications were measured on the E-W component by all three methods, in the same frequency range extending from 0.2/0.4-

1.8/2.0 Hz, which is directly in the estimated topographic frequency range. The methods also had similar amplification factors of 2.6-2.9 with the exception of the HVSR method with an amplification of 4.4. For the B line, each of the method performed well giving similar amplification ranges and values.

As with the analysis of event 200.19.5, the log normal median of all 52 events using the SSR method for Station B6 is plotted along with the log normal median of all 52 events using the MRM method for Stations B6 and B1 (see Figure 8.72). As was shown for event 200.19.5 and the median of Station A7, the SSR for Station B6 matches well with the MRM for Station B6 when the MRM for Station B1 is close to 1.0. Problems with a single reference station can lead to errors in the amplification factors determined using the SSR method and the MRM method is believe to provide the most precise and accurate amplification factors for Phase II.

In Table 8.7, a summary of the topographic amplification ranges measured using each analysis method, along with the maximum amplification observed at the crest station B3 for line V in that same frequency range are provided. In Figure 8.73, the spectral ratios for all three methods are compared for Station B3. Comparing the vertical components over the estimated topographic frequency range (0.95-1.83 Hz), a slight amplification was measured using the MRM and to less of an extent the SSR method, but as stated in the previous section this may be the result of vertically propagating P-wave and not topographic effects.

For the North-South component, amplifications were calculated using the MRM and SSR methods from a frequency of 0.25-5.0 Hz. However, the SSR method had a spectral ratio of 10 times greater than the spectral ratio of the MRM method. The low frequency amplifications calculated on the SSR and MRM methods were not calculated using the HVSR method. The HVSR method only calculated a slight amplification

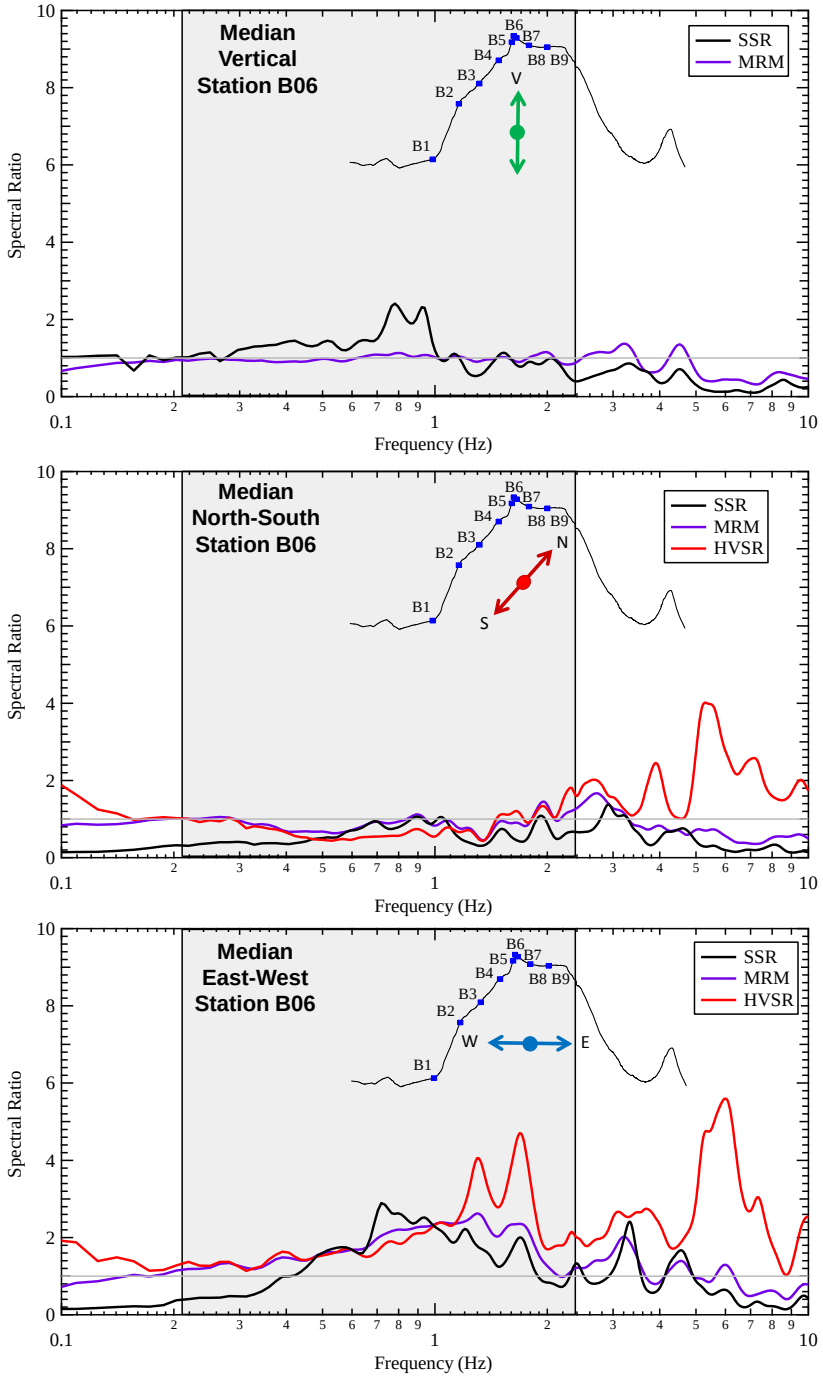

Figure 8.71: Comparison of SSR, MRM, and HVSR results for the median response of all 52 events recorded during Phase II for Station B6 vertical, North-South, and East-West components. The estimated topographic frequency range based on cross-section geometry and average shear wave velocity is shaded.

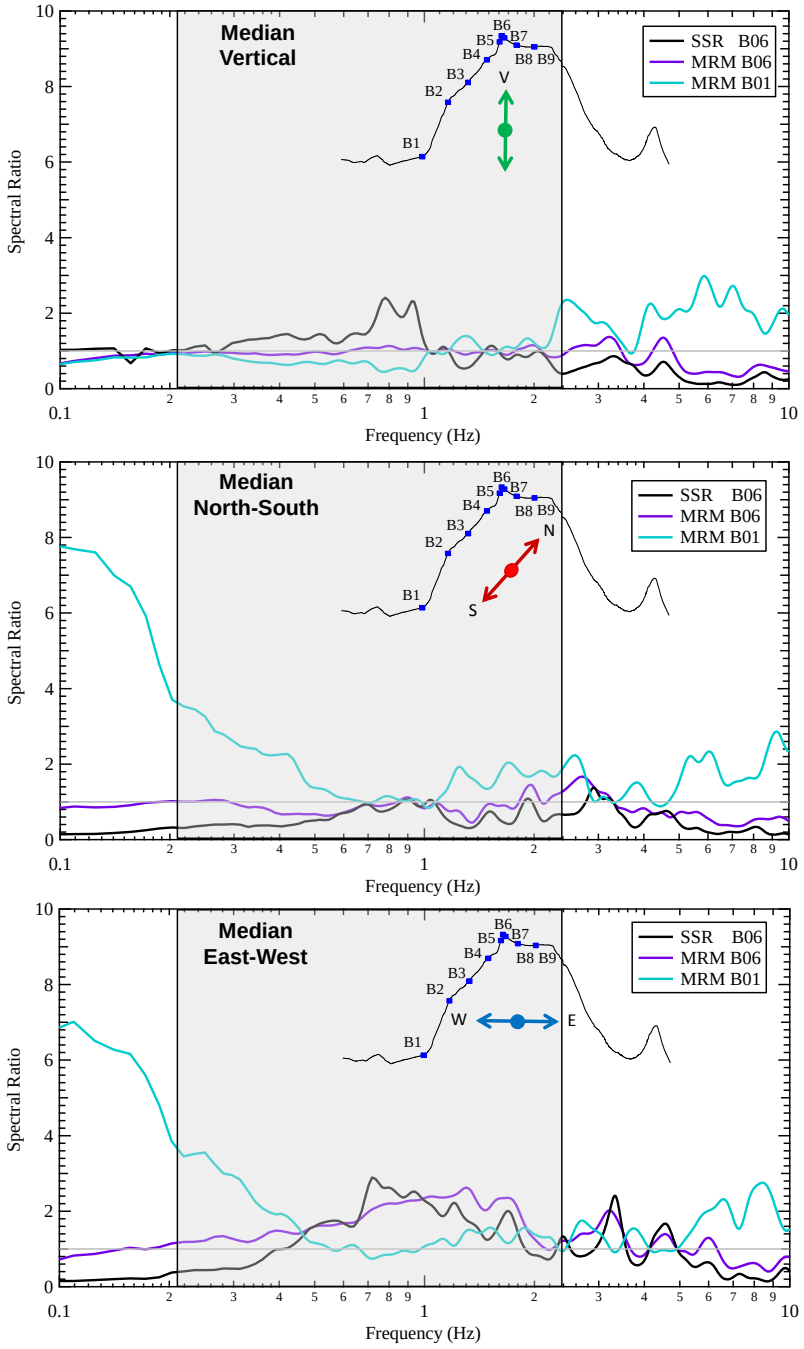

Figure 8.72: Comparison of SSR Station B6 with MRM from Station B6 and B1 results for median response of all 52 events recorded during Phase II for the vertical, North-South, and East-West components. The estimated topographic frequency range based on cross-section geometry and average shear wave velocity is shaded.

Table 8.7: Summary of the topographic amplification frequency range for the median analysis of the V line for all three methods. The maximum amplification was measured on the crest station within the same frequency range.

	Amplification Range (Hz)			Max Amplification		
Method	**V**	**N-S**	**E-W**	**V**	**N-S**	**E-W**
SSR	NA	0.1-10	1.0-1.8	NA	16.75	5.1
MRM	NA	0.3-1.9	NA	NA	3	NA
HVSR	NA	0.9-1.8	NA	NA	2.5	NA

directly in the estimated topographic frequency range of 2.5. Amplification were measured using the HVSR method for frequencies greater than 2.0 Hz, but those were not believed to be driven by topographic effects. For the E-W component, amplifications were measured using all three methods at frequencies greater than 2.0 Hz, but like the N-S direction those amplification are believe to be driven by soil site effects. The SSR method was the only method that identified an amplification peak at frequencies less than 2 Hz, and its amplification range extended to 0.1 Hz. None of the other methods had amplifications in this range. No topography existed in the E-W direction under Station B3, so the SSR method was likely calculation a false amplification peak in the E-W direction.

Overall, the MRM and HVSR methods matched fairly well for all the components. Each identifying amplification peaks in the N-S direction, but not indication amplification in any other directions. However, very large amplifications in both the N-S and E-W directions were calculated using the SSR method, which are believed to highly overestimate the amplification factor for Station B3. The overestimation is likely caused by de-amplification of the SSR reference Station, V2, in the valley of the features.

As with the analysis of event 200.19.5, the log normal median of all 52 events using the SSR method for Station B3 is plotted along with the log normal median of all 52 events using the MRM method for Stations B3 and V2 (see Figure 8.74). As indicated

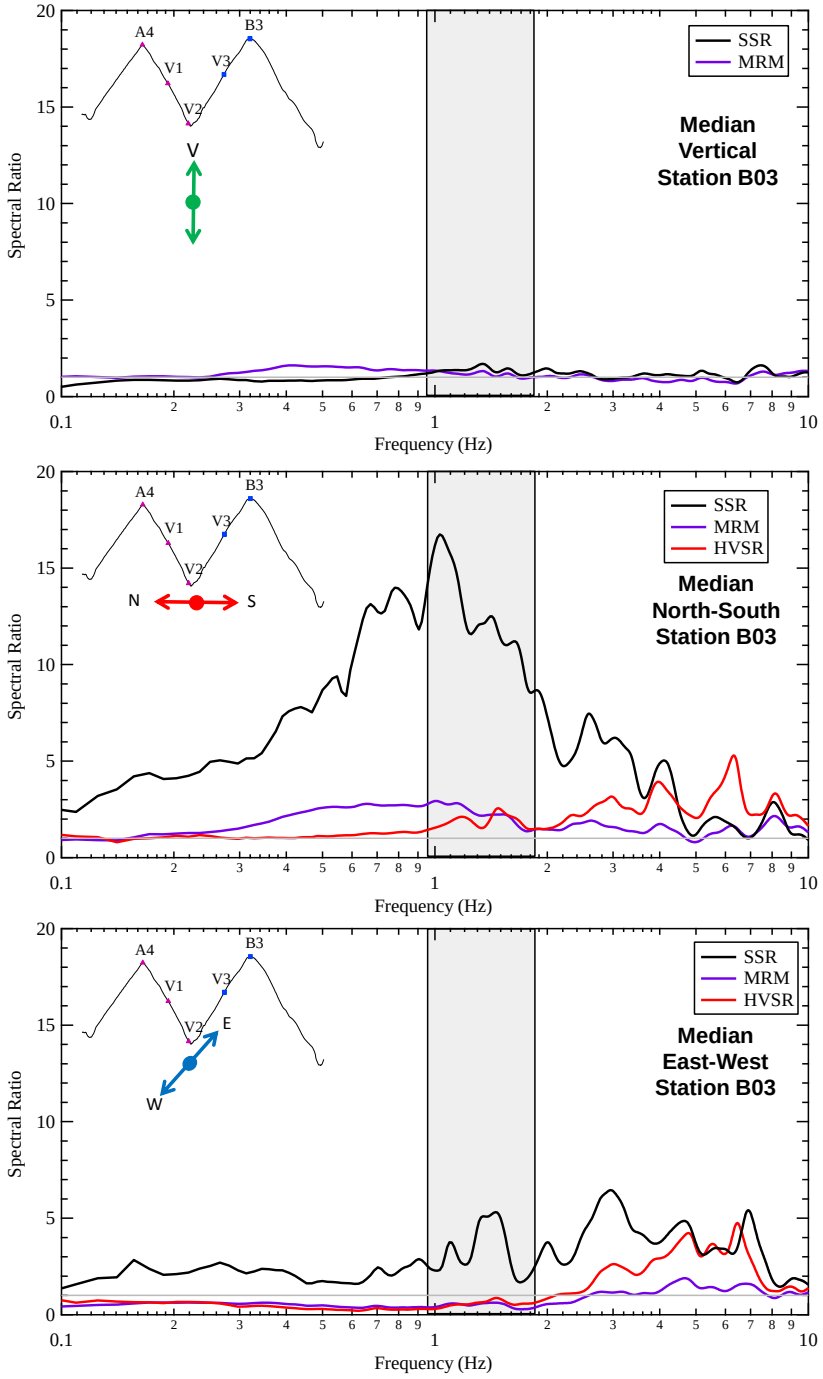

Figure 8.73: Comparison of SSR, MRM, and HVSR results for the median response of all 52 events recorded during Phase II for Station B3 vertical, North-South, and East-West components. The estimated topographic frequency range based on cross-section geometry and average shear wave velocity is shaded.

in the previous paragraph, the spectral ratio for Station V2 is significantly lower than 1.0, which when used as the reference station for the SSR method results in a large overestimation of the topographic amplification for Station B3.

After comparing the median response of the three different lines of stations (A, B, and V) using the three analysis methods (SSR, MRM, HVSR), it was clear that topographic effects were measured by the array of stations in Phase II (2011), based on the spectral amplifications, pattern of amplifications, and the frequency match between the estimated and measured topographic amplification frequencies. For the SSR method, amplifications were measured inside the estimated topographic frequency range for the direction in-line with the topographic cross sections (i.e., E-W for line A, E-W for line B, and N-S for line V) for all three lines of stations. For lines A and B, the calculated amplifications were fairly consistent with numerical results found in the literature (refer to Chapter 2), with maximum amplification values of 3.25 and 2.9, respectively. However, the maximum calculated amplification for the V line was 16.75, far exceeding the values of the A and B lines. Each line had a good pattern of top-down amplification with the maximum at the peak station and de-amplification down the slope and away from the peak. Amplifications were also measured perpendicular to the main topographic cross section for the crest station on the A and V lines, but not on the B line. However, much larger amplifications were measured at stations on the A and B lines that were on topography that varied substantially not only in the E-W direction, but also in the N-S direction (i.e., Stations A3-A5 and B2-B4). These amplifications ranged from 6.5 to 1.5, and were greater than amplification measured at the crest station. The observed amplification frequency range only matched the estimated frequency range for Stations A3 and B2. For other cross-line stations, along with stations in the V line, the estimated

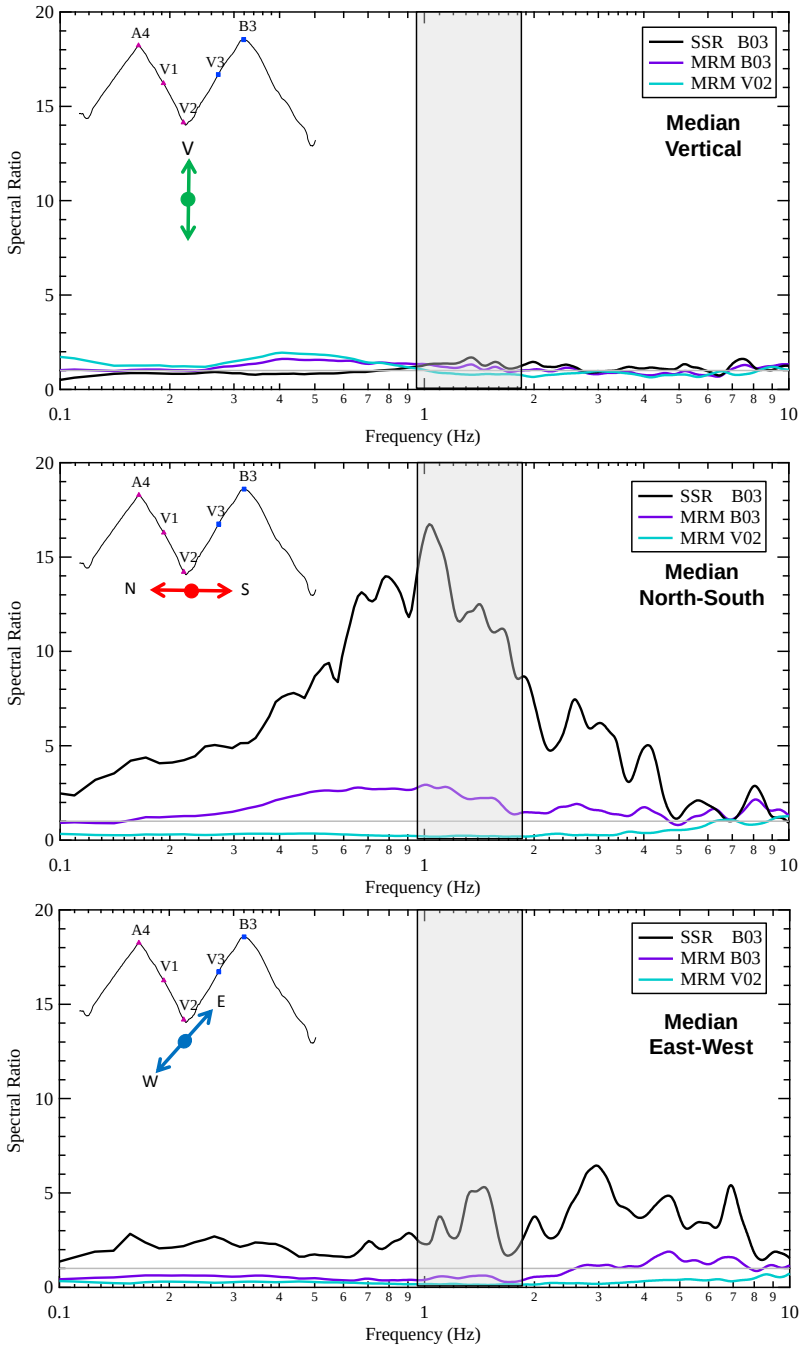

Figure 8.74: Comparison of SSR Station B3 with MRM from Station B3 and V2 results for median response of all 52 events recorded during Phase II for the vertical, North-South, and East-West components. The estimated topographic frequency range based on cross-section geometry and average shear wave velocity is shaded.

topographic amplification range only covered the higher frequency part of the observed amplification range. Meaning, the observed topographic frequency range extended to lower frequencies than the simplified analytical methods predicted. For the vertical component, amplifications were measured at the crest stations on lines A and B over a similar frequency range as amplifications on the horizontal components. Stations directly over the hypocenter on lines A and B also have amplification on the vertical component. Due to the location of the reference station, vertical amplifications were not measured on the V-line, because the reference station, along with all the measurement stations, were equally affected by the vertically propagating P-waves (all the V-line stations were directly above the longwall). Therefore, no relative vertical amplifications were estimated for the V-line stations using the SSR method.

Similar to the SSR method, amplifications were measured for directions in-line with the topographic cross sections for the MRM method. The amplification factors for the in-line crest stations varied from 2.6 to 3.25 with good patterns of top-down amplification. Similar to the SSR method, the observed amplification frequency range matched well with the estimated topographic frequency range. However like the SSR method, the observed topographic frequency range extends to lower frequencies than the predicted range for the V line of stations. For the components cross-line with the topographic cross section, no amplifications were observed on the crest stations. However, amplifications were measured for stations with strong topographic relief in the opposing direction of the main topographic cross sections (i.e., A3-A5 and B2-B4). Stations A3 and B2 had the highest amplification (up to 10), possibly caused by the intersection of a Westward-trending cliff face with a steep N-S trending topographic feature. Stations A4-A5 and B3-B4 had more reasonable amplification factors of 1.5-3.0. For the vertical component, only stations directly above the event hypocenters including

A3-A4, B3-B4, and V1-V3 measured amplifications using the MRM method, which as stated before may be related to vertically propagating P-waves.

The median results for the HVSR method had similar amplifications frequency ranges as the MRM method, and in some cases the SSR method, for components in-line with the main topographic cross sections. However, the amplification factors for the HVSR method were generally higher than the MRM method. The top-down amplification pattern for the HVSR method cannot be seen down the slope as far as observed when using the SSR and MRM methods, often with amplifications only measured for one station on either side of the slope.

8.6 SUMMARY AND DISCUSSION

In Phase II (2011), 52 seismic events were recorded by the topographic array in Central-Eastern Utah. The recorded events varied in frequency and time according to work-shifts and mining schedule at Deer Creek Coal Mine. The 52 events were located using the Hypoellipse program, and the majority of events were determined to be located directly above the longwall mining operation. An average hypocenter location was calculated based on the individual locations of select events. This average hypocenter was used to correct for geometric attenuation of the seismic ground motions between near- and far-stations. To assess the effects of topography on the ground motions at each station, a single event (200.19.5) was processed first in the time domain. The time domain records for each station, along with the peak ground velocity (PGV) for each station, were presented. No correlation between the topography shape and the largest or smallest PGV could be established for any of the stations in Phase II. Next, the time records for each event were transformed to the frequency domain using the DFT. The Fourier Amplitude Spectra (FAS) for each station were then compared. The FAS

indicated that the main energy band for event 200.19.5 was between 1 Hz and 20 Hz, with some stations having slightly higher or lower cutoff frequencies, but all ground motion amplitudes were below the level that could be felt by humans.

To analyze the recorded events for topographic effects, three different methods were used: the Standard Spectral Ratio (SSR), the Median Reference Method (MRM), and the Horizontal to Vertical Spectral Ratio (HVSR). These methods were used to compute the spectral ratios for three separate cross sections or lines of stations: Lines-A, -B, and -V. From processing event 200.19.5, topographic amplifications were measured at stations whose horizontal components were in-line with steep topographic features and near the crest of those same topographic features, for all three analysis methods. The stations that measured topographic amplifications included not only stations at the crest of a defined cross section (i.e., Stations A7, B6, A4, B3 for cross sections A, B, and V), but also any stations off the crest of the cross sections (i.e., Stations A5-A6, A8-A9, B4-B5, B7-B8, V1, and V3) or on the crest of steep topographic features not defined as major cross sections (i.e., Stations A3-A5 and B2-B4).

For the station components in-line with steep topographic features and near the crest of features (i.e., the component is oriented in the same direction as steep topographic relief and near the crest of a feature), the three analysis methods resulted in similar amplification frequency ranges, often overlapping for at least part of the frequency spectrum. These amplification frequencies often corresponded well with estimated topographic frequencies calculated using the height and width methods by Ashford and Sitar (1997) and Paolucci (2002). However, for some of the stations, in particular for the V-line stations and E-W components of Stations A3 and B2, the estimation methods did not properly predict the amplified frequency ranges and no changes (within reason) to the analytical equations input parameters (i.e., feature height,

width or average Vs) could adjust the estimated topographic frequencies to match the observed topographic frequencies. The cause of this miss-prediction is unknown at this time, but may be caused by 3D effects not accounted for in the simplified 2D analytical methods.

Although the amplification frequencies were similar in most cases for horizontal station components in-line with steep topographic relief, the calculated amplification factors varied significantly between the methods. Maximum amplification factors of 5-20 were measured using the SSR and HVSR methods, with some values exceeding 50. Amplification factors greater than 5.0 were never calculated for the MRM, with typical values in the 2-3 range. This major difference between the HVSR, SSR and MRM methods can be explained with two factors: (1) the spectral ratios calculated by the HVSR method are not equal to the actual amplification at a site, because the method is dividing the horizontal components by the vertical component, and a true reference is not being used, and (2) the SSR method commonly employed herein has been shown in this, and earlier, chapters to be influenced by using a de-amplification station at the base of a feature and an amplification station at the crest of a feature, which results in an abnormally high amplification factor. Therefore, the amplification factors determined using the MRM method, which uses the median response of the entire feature as a reference, are believed to be the most accurate and closest to the flat ground-to-crest amplification factor, which is typically sought for topographic effects experiments.

For horizontal components oriented cross-line (perpendicular) to a steep topographic feature (i.e., no steep topographic relief oriented in-line with the component), no topographic amplifications were calculated using the MRM (which is most plausible given that no topography likely equals no topographic amplification). However on some stations, amplifications for these components were calculated using the HVSR method

(typically in the higher estimated topographic frequency range) that were not calculated using the other two methods. This potential for false amplification was also noticed by Massa et al. (2010). The SSR method also indicated amplifications in the cross-line component, but unlike the HVSR method (where amplifications in the cross-line are not always present) the SSR method almost always had matching (though lower spectral ratio) amplification in the cross line component for any amplification on an in-line component. This leads to the assumption that amplification takes place in both directions regardless of the direction of topographic relief. However, the MRM method clearly indicated no amplifications for components not in-line with a topographic feature.

As with the SSR method for the horizontal cross-line component, large amplifications were often calculated in the vertical direction using the SSR method, which were often not calculated using the MRM method. As shown in the previous sections, amplification on the measurement station for the SSR method were just as influence by de-amplification on the reference station as amplification on the measurement station. Therefore, the amplifications calculated by the SSR method are believed to be incorrect. However, vertical amplifications observed using both the SSR and MRM methods are believed to be correct for stations directly over the hypocenters of the events (i.e., A3-A4, B2-B3, and V1-V3). These amplification are typically lower frequency (<1 Hz) and have maximum amplifications of 1-2. The vertical amplifications are believed to be caused by vertically propagating P-waves arriving directly in-line with the vertical component, causing a larger than normal ground motion.

The spectral response of all 52 recorded events from Phase II were then compared for the three lines (A, B, and C) and methods for the crest station of each cross section (A7, B6, and B3), and a log normal median and +/- 1 sigma response was computed for the 52 events. From the analysis, the SSR and HVSR methods had the largest variation in

spectral ratio from event-to-event, along with the largest standard deviation. The calculated COVs of the SSR method often varied between 0.5-1.0 compared to 0.30-0.85 for the HVSR method. The MRM method had the lowest COVs of between 0.20-0.45. In comparison, the spectral ratios for individual events using the SSR and HVSR methods could vary by more than an order of magnitude from the median response. For these recorded events and station setup, the MRM method provided the most stable reference station and spectral ratio values for Phase II.

After processing all 52 events, the log normal medians were compared using the three methods for the three topographic cross sections. Similar to the processing of event 200.19.5, the components of stations in-line with strong topographic features measured amplification using all three analysis methods. Although each method did measure topographic effects within the estimated topographic frequency range, the measured amplification ranges and maximum amplifications were often unique for each method. The SSR method often had different amplification frequencies than the MRM and HVSR methods, and some amplification peaks calculated using the SSR method were not calculated using the other two methods. This was likely the result of problems with the single reference stations used to divide each measurement station. Beyond the differences in the amplifications frequency ranges for each station, the amplification factors for each method were significantly different in some cases. In some cases, amplification factors greater than 12 were calculated using the SSR and HVSR methods for the crest stations (A7, B6, and B3). The MRM calculations, on the other hand, resulted in reasonable amplification factors for each of the in-line components (relative to strong topographic features) of between 2.5-3.25, within the estimated topographic frequency range. The only significant outliers were Stations A3 and B2, which had amplifications up to 10 in the N-S direction. This large amplification was likely caused by the interaction of the

west-facing cliff slope and the large N-S trending topographic feature under the stations, which resulted in a superposition of amplifications because of 3D effects. The measured frequency amplifications matched well with the predicted topographic frequencies from Ashford and Sitar (1997) and Paolucci (2002) for many of the stations and cross sections. However similar to event 200.19.5, measured amplification frequencies on stations in the V line and the East-West components of Stations A3 and B2 did not match well with estimated topographic frequencies. For the V line, the estimation methods only matched the measured amplifications in the higher-frequency range (i.e., 0.95-1.83 Hz) and did not predict a large portion of the amplified frequency range at lower frequencies (i.e., less than 1 Hz). For the E-W components of Stations A3 and B2, the measured amplification frequencies were higher than the predicted amplification frequencies. This may be the result of 3D effects, but the cause is currently unknown.

Good patterns of top-down amplification were observed for the median response of each method, the MRM and SSR methods resulted in the best amplification patterns. These two methods typically had patterns that included more than one station on each side of the crest. These stations off the crest would have lower and lower spectral ratios as the stations got farther and farther from the crest. However, the top-down amplification pattern observed using the HVSR method typically only included one station on either side of the crest, and at higher frequencies that pattern fell apart for some cross sections, indicating that topographic amplifications may not be the only cause of amplification at frequencies higher than the estimated topographic amplification frequency range.

For station components not in-line with strong topographic features, the MRM and HVSR methods did not predict topographic amplification of any significant note. However, the SSR method predicted a slight amplification for the crest stations in the A

line in the N-S direction and the V line in the E-W direction. There is little to no N-S topographic relief near Station A7 or E-W topographic relief near Station B3, and no cross-line amplifications were calculated for other cross sections, so the cause of this amplification is unknown. These false amplification peaks were just another example of the instability of the SSR method for measuring topographic effects.

For the vertical component of motion, the SSR method predicted amplifications on many of the stations in the A and B lines at discrete frequencies that did not match well with estimated topographic frequencies. Some of these vertical amplifications were likely false amplifications caused by errors in the reference stations. However, the MRM also calculated vertical amplification for stations (A3-A5, B3-B4, and V1-V3). These stations were located directly over the event hypocenters and the median vertical spectral ratios for the MRM method were likely caused by vertically propagating P-waves in-line with the vertical component, explaining why the amplifications were not seen on other stations.

Through the polarity analysis, the topographic amplifications on each cross section seem to be polarized in-line with the strongest topographic relief under the station, when the feature is excited by nearly vertically propagating seismic waves (as opposed to seismic waves traveling from a distinct direction).

After comparing the median response of the three different lines of Stations (A, B, and V) using the three analysis methods (SSR, MRM, HVSR), it is clear that topographic effects were measured by the array of stations in Phase II, and amplification on the order of 2.5-3.25 times were calculated, with some amplifications exceeding 10. These amplifications are clearly linked to topographic features, and the spatial and stiffness characteristics of the feature can be used to approximately predict the frequency range of amplification for most cross sections.

Chapter 9: Summary, Conclusions, Recommendations, and Future Work

9.1 SUMMARY

This dissertation details work by researchers at the University of Arkansas at Fayetteville (UA) and the University of Texas at Austin (UT) aimed at recording ground motions on full-scale topographic features. The experiment used the frequent and predictable seismicity produced by underground longwall coal mining in the Wasatch Plateau – Book Cliffs coal mining region of Central-Eastern Utah. The area is home to significant topographic relief due to a series of North-South trending Grabens, formed by relatively young uplift and East-West extension. To record ground motions on this topography, locally dense arrays of seismometers were deployed over various topographic features. The arrays were then used to passively monitor seismic energy produced by mining-induced implosions and/or stress redistribution in the subsurface caused by coal extraction deep below the surface.

The research consisted of two separate studies. The first phase (Phase I) of the study (detailed in Chapter 3) was intended as a pilot study with limited extent to insure that topographic effects could be accurately recorded on full-scale features using the weak motion seismicity produced by underground longwall coal mining. To accomplish this, a 3D surface array of 3-component, 1-Hz geophones was deployed over a steep mountain peak in the Manti-La Sal National Forest in Central-Eastern Utah. The surface array of 12 stations extended in an East-West orientation 750 m horizontally and 110 m vertically, while extending horizontally 550 m in a North-South orientation. The sensors were attached via cables to a single data acquisition system, and set to record continuously. Passive seismic activity was recorded for 7 consecutive days, wherein 52 distinct, small-magnitude ($M_L < 1.6$) seismic events were detected. In addition, surface

wave testing was conducted near the topographic array to determine small-strain shear stiffness profiles of the mountain (detailed in Chapter 5).

The second phase (Phase II) of the study (detailed in Chapter 4) is the main study, in which the number and quality of the sensors were increased along with the overall size of the sensor array. A total of 27 broadband and short period seismometers were deployed in a 3D "H" pattern and circular array over a 25 km^2 area. Each sensor was attached to an individual datalogger and synchronized via GPS timing. Ground motions were recorded for approximately 10 days, wherein a significant number of distinct, small-magnitude ($M_L < 1.6$) seismic events were detected. Of which, 52 of the largest events were selected for further analysis.

9.2 CONCLUSIONS

The data from each phase of the experiment were analyzed for topographic effects in the time domain using the Peak Ground Velocity (PGV), and in the frequency domain using the Standard Spectral Ratio (SSR) method, the Median Reference Method (MRM), and the Horizontal-to-Vertical Spectral Ratio (HVSR) method. The polarity of the horizontal components was also visualized using a directional analysis. The results were used to evaluate the resonant frequencies and amplification factors for the instrumented topography. These methods were compared to assess their ability to accurately estimate the amplification factors for the topographic features, and to accurately determine the topographic frequencies of interest. These values, determined from the field study, were compared to analytically-estimated topographic frequencies to assess the ability of each theoretical method to properly estimate the resonant frequency for real topography, based on the mechanical and geometrical properties of the topography.

9.2.1 Time Domain Results

The time records from all 104 events recorded in Phases I and II were analyzed in the time domain by comparing the measured peak ground velocity (PGV) for each station as a function of the stations topographic location. No correlations could be drawn between the topographic locations of the stations in the array (i.e., crest/ridge verses valley stations) and the measured PGV values. Moreover, the PGV values of all 104 events recorded during both Phase I and II indicated no bias toward higher PGV values at the crest of topographic features and lower PGV values at the base of topographic features, as one might expect from topographic effects. Therefore, it is clear for this dataset, that the time domain method was not able to identify the topographic amplifications present in the data recorded during Phases I and II.

9.2.2 Standard Spectral Ratio (SSR) Results

For Phases I and II of the topographic study, amplifications at each station were calculated using the SSR method. In many cases, good patterns of top-down amplification were observed for each of the topographic cross sections, with a segmental reduction in spectral ratio moving down-slope and away from the crest. Furthermore, the frequency range of observed topographic amplification matched well with the estimated topographic frequency range calculated from simple analytical equations using the geometry and stiffness of the feature. The maximum recorded amplification factors on horizontal components at the crest stations were on the order of 2.5-3.25 times the reference station for the median response of all 52 events in both Phase I and Phase II. However, amplification factors up to 16.75 were calculated on the V-line of stations for the median response of all 52 events in Phase II. Moreover, crest amplification factors from 5 to 20 were frequently measured for single events, with values greater than 50 measured in unique cases. In addition, the amplification factors from a single event, in

general, had a narrower amplification frequency range than the median response. These differences between the single events and the median were highlighted when the SSRs for all 52 events were compared in both Phase I and II. The computed spectral ratios from the SSR method varied significantly from event to event, with COVs between 0.5-1.0 at the measured topographic amplification frequencies. This resulted in the SSR method predicting topographic amplifications at frequencies other than those identified using the MRM and HVSR methods. This instability, and relative errors/discontinuity in the calculated spectral ratios, in terms of both amplitude and frequency range, were likely caused by the single reference station used in the analyses. For the instrumented cross sections, the reference stations for the SSR method were always chosen so that they were off major topographic features as much as possible, but remained on similar geologic layering. For this study and many others before it, this meant placing the reference station at the base of the instrumented topographic feature. It was shown that placing a reference station at the base of a feature leads to dividing stations at the crest (which theoretically would have a higher than free-field ground motion) by a station at the base (which theoretically would have a lower than free-field ground motion). This can result in significantly higher amplification factors for the crest when compared to amplification factors calculated using a truly free-field reference station unaffected by topographic effects (either amplification or de-amplification). This observation starts to explain the quantitative bias between previous numerical and experimental work conducted on topographic effects discussed in Chapter 2, wherein field studies based on the SSR method have often measured much higher topographic amplification factors than those predicted by numerical modeling. In addition, the spectral stability problems of a single reference station make it difficult to accurately assess the amplification at a site without a large number of recorded seismic events. Therefore, the median of a large number of

events has to be calculated in order to determine an accurate amplification factor and amplification frequency range for a given feature. However, even with a large number of events (52 in Phase II), errors in the estimated amplification factors and frequency ranges from the SSR method occurred for the V-line stations in particular.

The polarity of recorded ground motions was shown to be affected by both the orientation of steep topography, and the direction of wave propagation into the slope. For Phase I, the longwall mining operations (the seismic energy source) were located 2.0 km NE of the topographic array. When the seismic waves traveled from the longwall and impacted the topographic feature, stations on the back side of the slope (farthest from the source) recorded higher ground motions at frequencies greater than the estimated topographic effects frequency range. These amplifications also resulted in higher PGV values on the back-side of the slope (i.e., the slope opposed to the direction of wave propagation). These amplifications are referred to as path effects, and are believed to be caused by the inclined waves impacting the western slope of the feature at an angle nearly perpendicular to the slope angle of the feature instrumented in Phase I. In addition to the higher-frequency path effects on the slope opposing wave propagation, the polarity of the horizontal components for crest stations (Stations 4, 5, and 6) indicated that the strongest shaking within the topographic frequency range (relatively lower frequencies) was polarized in-line with the direction of wave propagation. This resulted in measured amplifications in both the N-S and E-W directions for the crest stations, and not just in the direction of the steepest topographic feature.

For Phase II, the longwall was located almost directly underneath the same topographic feature instrumented in Phase I (i.e., the Phase II B-line). During Phase II, when more-vertically propagating waves were impinged upon the slope, topographic amplifications were only measured in the E-W direction for the crest stations of line B

(i.e. the direction in-line with the steepest topography), and no path effects were measured by stations on the slope. Meaning, the polarity of the amplifications was controlled by the shape of the topographic features in Phase II (i.e., amplifications in-line with the direction of steep topography), and not by the direction of wave propagation. Moreover, other stations deployed at the crests of features in Phase II had similar behavior, with amplifications polarized in-line with the steepest topography. However, some of the crest stations processed using the SSR method indicated amplifications in the direction of weak, or no topographic relief, which is contrary to the results of the MRM method, and believed to be an error with the SSR results. This error is believed to be caused by de-amplifications of the single reference station at the base of the feature, which in turn results in apparent amplifications on the measurement stations. In addition to horizontal amplifications, vertical amplifications were also measured for stations directly above the longwall during Phase II only. These amplifications are not believed to be caused by topography, but by vertically propagating P-waves arriving directly in-line with the vertical component of the station, causing a higher than normal vertical ground motion. Due to the location of the reference station, vertical amplifications were not measured on the Phase II V-line, because the reference station, along with all the measurement stations, were equally affected by the vertically propagating P-waves (all the V-line stations were directly above the longwall). Therefore, no relative vertical amplifications were estimated for the V-line stations using the SSR method.

9.2.3 Median Reference Method (MRM) Results

For Phases I and II of the topographic study, the topographic amplifications calculated using the MRM matched well with the estimated topographic frequency range obtained from simple analytical equations for most of the topographic features. In

addition, good patterns of top-down amplification were observed for each of the instrumented cross sections with an incremental reduction in spectral ratio down-slope and away from the crest. For the recorded topographic amplifications, the maximum amplification factors on the horizontal components of the crest stations were on the order of 1.8 to 3.25 the median reference "station" for the median response of all 52 events. Looking at the variability of the MRM method, the computed spectral ratios from the MRM had significantly less variation from event to event than the SSR method. In fact, the COVs for Phase I varied between only 0.13-0.19, while the Phase II COVs were slightly higher, and varied between 0.20 and 0.45. The MRM method also provided a very stable approximation of the spectral ratio. Meaning, each individual event resulted in a similar spectral response in terms of the amplification frequency range and the amplification factor. This allowed a more robust estimation of the median response using a smaller number of events than the SSR method.

As with the SSR method, the polarity of the recorded ground motions from the MRM was shown to be affected by both the orientation of steep topography and the direction of wave propagation into the slope. Similar to the SSR method for Phase I, the stations on the western slope of the feature, furthest from the longwall, had MRM amplifications at frequencies higher than the measured frequency range of topographic effects. These amplifications are, again, believed to be caused by path effects from the inclined waves traveling from the source, and striking the slope opposing the direction of propagation at an angle nearly perpendicular to the slope. This interaction is believed to have caused relatively higher frequency amplifications on the backside of the slope. In addition to the higher frequency path effects for Phase I, the MRM horizontal polarity plots indicate the strongest polarity for the crest stations, in the lower frequency range of topographic amplification, were measured approximately in-line with the direction of the

underground longwall (the seismic source), which was in the NE direction (a similar result was determined using the SSR method). This NE-SW polarity resulted in amplifications on both the N-S and E-W components for the crest stations. However, for Phase II, when the longwall was located almost directly under the same feature, the MRM calculations resulted in crest amplifications in only the E-W direction (in-line with the steepest E-W topographic feature). Moreover in Phase II, amplifications were only calculated in-line with steep topographic features, either in the N-S or E-W directions, but never in a direction where the topography was very shallow or none existent. Therefore, the direction of incoming waves and the orientation of steep topography play an important role in the polarity of strong shaking from topographic effects, which is important for seismic design calculations.

In addition to amplifications on the horizontal components, vertical amplifications during Phase II calculated using the MRM were only observed for stations directly above the longwall. These amplifications are not believed to be caused by topography, but by vertically propagating P-waves arriving directly in-line with the vertical component, causing a higher than normal vertical ground motion. This was also noted in regards to the SSR method discussed above.

Overall, the MRM is believed to provide the most stable spectral estimates in terms of the topographic amplification frequency range and the topographic amplification factors.

9.2.4 Horizontal to Vertical Spectral Ratio (HVSR) Results

For Phases I and II of the topographic study, the topographic amplifications calculated using the HVSR method matched well with the estimated topographic frequency range obtained from simple analytical equations for most of the topographic

features. In some cases (the A line in particular), amplifications at higher frequencies were calculated from the HVSR method than the frequency range estimated using Ashford and Sitar (1997) and Paolucci (2002), or calculated using the MRM method. The HVSR method did indicate some patterns of top-down amplification, but the patterns were often far more erratic and unclear than those obtained from the SSR and MRM methods. The amplification patterns typically only included one station on either side on the crest, and often the pattern did not hold together for the entire amplification frequency range recorded by the crest station, possibly indicating an influence from amplifications other than topographic effects at relatively higher frequencies. Maximum amplification factors on the horizontal components of the crest stations were on the order of 2.5 to 12 for the median response. The majority of the amplification factors determined using the HVSR method were significantly higher than those calculated using the MRM method. As explained in Chapters 7 and 8, the amplification factors determined using HVSR cannot be directly related to the possible topographic amplification at a site (i.e., the recorded H/V spectral ratios at a station cannot be taken directly as the amplification factors for the station), but might potentially be used to obtain the topographic frequency range.

Similar to the SSR method, the computed spectral ratios from the HVSR method had significant variations from event to event. The COVs for Phase I varied between 0.40 and 0.90, while for Phase II the COVs typically varied between 0.30-0.85. The spectral ratios from individual events also varied significantly, with individual events often predicting different amplification ranges and amplification factors. In addition, the measured amplification frequency range for a single event was narrower than the amplification range for the median response, indicating a significant uncertainty in the

calculated amplification frequency range for topographic effects when using the HVSR method.

As with the SSR and MRM methods, the polarity of the recorded ground motions was shown to be affected by both the orientation of steep topography and the direction of wave propagation into the slope. However, the polarity of the ground motions in Phase I was different for the HVSR method than the MRM and SSR methods. For Phase I, HVSR topographic amplifications were measured in both the N-S and E-W directions; however, the polarity plots indicated a NW-SE polarity to the ground motions, which was perpendicular to the direction of wave propagation from the longwall to the topographic array (and opposite of the polarity determined using the SSR and MRM methods). It is not known why the HVSR method indicated an opposite polarity to the other methods. For Phase II, when the longwall was almost directly under the B-line feature, the HVSR calculations resulted in amplifications in only the E-W direction (in-line with the steep E-W topographic feature). This E-W polarity was similar to the polarity determined using the SSR and MRM methods.

9.2.5 Analytical Frequency Estimates

The analytical methods developed by Ashford and Sitar (1997) and Paolucci (2002) were used to estimate the expected frequency range of topographic amplification for each of the cross sections instrumented in Phase I and Phase II. Many of the larger features were broken up into several smaller features according to major breaks/changes in the slope and natural discontinuities in the topography. These smaller features produced higher frequency amplifications than the larger features alone, and were needed to properly predict the relatively higher frequency amplifications measured on some of the features. For the features instrumented in this study, Ashford and Sitar's (1997)

height-based calculations predicted the highest frequency range for a given feature (large or small), and Paolucci's (2002) width-based calculation predicted the lowest frequency range for a given feature (i.e., for the slope angles in this experiment the height based equations always resulted in higher frequencies than the width based equations; refer to Chapter 6 for more information). When the two methods were combined together, and used on the larger and the smaller sub-cross sections of a feature, the two methods did a good job of accurately bracketing the measured topographic amplification frequencies for the majority of cases. However, in some cases, such as for the V-line and the E-W component of Station B2, the estimated topographic frequency range did not cover the entire measured topographic frequency range. These errors in accurately estimating the topographic frequency range were observed at both higher and lower frequencies than estimated using the analytical methods (i.e., the analytical methods both over predicted and under predicted the measured topographic amplification frequencies in a few cases). To determine if the input parameters (i.e., the height, width, or average Vs) were the cause for the error, the parameters were adjusted to account for any errors in determining the size of the topography or the average Vs. It was determined that no changes (within reason) to the input parameters (height, width, and Vs) could shift the estimated topographic frequency range using Ashford and Sitar (1997) and Paolucci (2002) equations to match the observed topographic frequencies. This error in predicted versus measured frequency range is likely the result of using simple 2D analytical equations to predict amplification on true 3D topographic features.

9.3 RECOMMENDATIONS

Recommendations regarding various aspects of measuring topographic effects in the field, and accurately predicting topographic effects on features beyond the ones instrumented in this study, are presented below.

9.3.1 Sensors and Recording Stations

The recording stations and equipment used in Phase I and Phase II were vastly different, but both worked well for the features instrumented in each phase (i.e., a smaller feature in Phase I and larger features in Phase II). However, the long period sensors used in Phase II were required to measure the low frequency topographic amplifications generated by the larger topographic features. The geophones used in Phase I would not have worked well for the large features instrumented in Phase II, because the output (measurement sensitivity) drops off significantly below the natural frequency of the instrument (i.e., 1 Hz). This output drop makes it difficult to accurately apply frequency-dependent calibration factors to geophones well-below their natural frequency, and therefore geophones are not appropriate for topographic studies where large, low frequency features will be instrumented. The dataloggers used in Phase I and Phase II were vastly different also, with Phase I using a single dynamic signal analyzer cabled to the sensors, and Phase II using individual dataloggers for each sensor. The individual dataloggers in Phase II were simpler to layout and setup for the experiment. Difficulties in running wires from each station to a single digitizer in Phase II would have made the experiment nearly impossible. In addition, the GPS timing provided by the Phase II dataloggers was incredibly helpful in syncing the events recorded during Phase II with earthquakes identified by the UUSS. Even though all of the stations in Phase II used individual dataloggers, several different brands and types of sensors and dataloggers were used in Phase II, which made the deployment and data analysis more difficult. Each

combination of sensor and datalogger resulted in a different setup procedure and a different data reduction plan, which was more difficult to keep organized. Moreover, the different manufacturer-supplied calibration factors for each sensor and datalogger combination simply had to be trusted to be correct, because no specific calibration was performed on the sensors and dataloggers during Phase II. Therefore, it would be preferred to keep all stations the same, thereby keeping the calibration factors and procedures the same for all stations.

9.3.2 Station and Mine Locations

In Phase I (2010), the longwall was located approximately 2 km away from the center of the topographic array, which had a maximum horizontal extent of 750 meters. This source-to-array distance precluded the need to correct for geometric attenuation, and kept one more aspect of data processing uncertainty out of the Phase I data. However, in Phase II (2011), the longwall was directly under the topographic arrays (hypocenter distances between 0.19 and 1.52 km were determined for the nearest and farthest stations in the topographic array), which made correcting for geometric attenuation necessary. For future topographic effects studies, it would be better to have the seismic source further from the topographic array, so that correcting for geometric attenuation would not be necessary. However, for topographic effects studies using mine seismicity, it may be necessary to have the source relatively close to the topographic array to insure adequate energy makes it to the array (due to the small magnitude of the events). For the experiments conducted in this study, important information on the polarity of the ground motions was obtained both when the source was located some distance away from the topographic array (as in Phase I), and when the source was located directly under the topographic array (as in Phase II).

The stations during Phases I and II were deployed not only at the crests of features, but also along the slopes of the features. The response of these additional stations help significantly in identifying the correct topographic amplification frequencies by providing a consistent pattern of top-down amplification, where the crest station had the highest amplification followed by lower and lower amplifications for stations off the crest. When this pattern was not available, such as for Stations 11 and 12 during Phase I, it made it impossible to determine if the recorded amplifications were the result of topographic effects or other effects. Therefore, it is advised to include several stations off the crest of the feature and down the slope. The array of stations off the crest should start within 50-100 m from the crest of slope, but can be more spread out as one moves off the slope. Placement of stations along the slope is also necessary to obtain accurate results using the MRM method because an equal number of sensors should be placed at the crest, along the slope, and at the base of the feature to obtain a reference as close as possible to a free-field reference (Maufory et al. 2012).

9.3.3 Feature Characterization

For this study, many different topographic features were instrumented, and the topographic amplification frequencies for each feature were estimated using the analytical methods from Ashford and Sitar (1997) and Paolucci (2002). These analytical methods use the characteristic height, width, and average Vs of each feature to estimate the topographic amplification frequencies for that feature. In addition, the Vs profile was used to estimate the 1-D soil site effects frequencies. These frequencies were critical to the study by helping determine which measured amplifications were caused by topographic effects and which were caused by soil site effects. To define the topographic features, this study had the benefit of a 1-m post spacing, airborne LiDAR DEM of the

site to define the characteristic height and width of the features, and also to simply identify possible topographic cross sections. For experimental topographic amplification studies and for sites where the effect of topography needs to be determined, it is critical to properly define the height and width of the features. The height and width play a strong role in estimating the topographic frequencies using the analytical method, and significant effort should be expended in order to proper define each topographic cross section.

In addition to defining the height and width of the feature, the shear stiffness profile of the feature also must be measured to proper estimate the topographic frequencies (and the soil site effects frequencies too). In this study, only one shear wave velocity profile with a maximum depth of 67 m was available at a location off the topographic feature. This single profile provided a means to estimate the topographic and soil site effects frequencies. However, the surficial geologic units under each station changed as one moved from the crest to the base of the features. It would have been preferred to have shear wave velocity profiles under multiple stations along the crest, in order to more accurately estimate the stiffness of the feature. The accurate estimation of the soil site effects and topographic frequencies is important to prevent confusing soil site effects with topographic effects, and to accurately estimate the topographic amplification frequencies for a feature.

9.3.4 Topographic Effects Analysis Methods

The ground motions recorded during Phase I and II were analyzed in the time domain, using the PGV values for each station, and analyzed in the frequency domain using the Standard Spectral Ratio (SSR), the Median Reference Method (MRM), and the Horizontal to Vertical Spectral Ratio (HVSR) Methods. The time domain analysis using

the PGV values provided no evidence of topographic effects, which indicates that the time domain methods may not be appropriate for studying topographic effects. For the frequency domain analyses, the MRM proved to be the best analysis method in terms of both the consistency of the measured amplification frequency range and the measured amplification factors. With an array of stations disturbed at the crest, along the slope, and at the base of the feature, the MRM method results in the most accurate amplification factors relative to a free-field reference station, which can be extremely hard to define for field studies. In addition, the MRM has the most stable reference "station" response, calculated from the median of all stations in the array, and results in the most repeatable spectral response from event to event. Therefore, the MRM should be used in topographic studies when possible (i.e., if enough stations are available and disturbed appropriately).

In the event the MRM method cannot be used, either due to a limited number of stations available or the positioning of the stations along the feature, the HVSR method (calculated from seismic events, not noise) may be used to estimate the topographic amplification frequencies for a feature. However, users should to be aware that the amplifications determined using the HVSR method do not directly correlate to the topographic amplification at a site, and should only be used to identify the potential topographic amplification frequencies at a site. As was shown in Chapter 7 and 8, the amplification factors, determined using the HVSR method, were much higher than those determined using the MRM method. Moreover, the maximum spectral ratio calculated using the HVSR method may not be the most important topographic amplification frequency. The maximum amplification frequencies calculated using the HVSR often did not match the maximum amplification frequencies calculated using the MRM. Therefore, the highest amplification frequency for the HVSR may not be the most important

topographic amplification frequency. However, the HVSR method often resulted in a similar measured topographic amplification frequency range as the MRM method. Therefore, when using the HVSR method, topographic amplification frequency ranges may be identified correctly. However, any amplifications identified as topographic effects, using a top-down pattern of amplification, should be considered as the possible maximum topographic amplification frequency for the station (i.e., because the maximum amplification frequency for the HVSR method was often greater than the maximum amplification frequency for the MRM). Therefore, the spectral ratio at a particular frequency should only be used to differentiate amplification from de-amplification, and not to identify the actual amplification factor at a particular frequency.

If the SSR method is used to analyze ground motions for topographic effects, the reference station should to be located away from the base of the feature, but on the same geologic unit. Placing the station in this way is very difficult to do in the vicinity of real topographic features, and is a serious problem for this study. The poor placement of the reference station in the SSR method leads to overestimating the topographic amplification factors due to de-amplification at the base (where the reference station is typically located) and amplification at the crest. Even if the single reference station is located in an appropriate location (which is typically impossible for field studies), the instability (i.e., the high standard deviations for the events) using a single reference station can lead to poor results (i.e., inaccurate amplification factors and errors in the measured topographic amplification frequency range), especially if a large number of events are not included in the median analysis.

9.3.5 Topographic Amplification Factors and Amplification Frequencies

Amplification factors determined using the MRM are believed to be the closest to amplification factors relative to the free-field as can be achieved in most field studies. Maximum amplification factors for a cross section were measured at the crest of the cross section, and varied between 2.6 and 3.25. However, amplifications were also measured on the slope leading up to the crest of the feature, although these amplifications were generally less than those measured as the crest. The amplifications for stations along the slope (down from the crest) varied from being equal to the crest a short way down the slope, to zero amplification for stations near the middle of the slope, and ultimately, to de-amplification at the base of the feature. Although most amplifications were in the 2 to 3 range, much larger amplifications (up to 10) were measured on highly irregular 3D features (i.e., when the westward-facing 28 degree slope intersected the N-S steep topographic feature at Stations A3 and B2 in Phase II).

The maximum amplification recorded at the crests of features did not seem to be strongly affected by the overall size (large or small cross sections) of the topographic feature A and B are nearly the same size and shape (refer to Chapter 6; Figures 6.6 and 6.7). However, the maximum amplification factors for features A and B were 3.25 and 2.6, respectively. In fact, a larger topographic amplification factor was determined for feature A by all three frequency domain analysis methods, meaning the feature A likely produced a higher overall amplification than feature B. In addition, the much smaller V line feature (1/3 the size of the larger A and B features) produced a maximum amplification of 3.0, even though its size is much smaller than the other features. Therefore, relatively small features such as the V line feature can produce amplifications approximately equal to or greater than larger features (i.e., features A and B). Whether the feature is a large feature or a small feature does not seem to control the amplification

factor produced by the feature, although the size of the feature (height and width) does seem to control the frequency range of the amplifications. Even though the overall size of the feature does not control the level of amplification, the slope or height to width ratio may control the amplification level. In this study, only slopes with slope angles greater than approximately 15 degrees generated measurable topographic amplifications. However, the overall measured amplification factors could not be correlated to the slope angles of different features (i.e. steeper slopes did not systematically produce higher amplifications than shallower slopes), but the slope, that generated topographic amplification, in this study were generally between 15 and 30 degrees, providing little variety to test this correlation. For most simple topographic features, an amplification of 2-3 should provide an accurate estimate for the possible topographic amplifications; however, in special circumstances much higher amplification factors may be necessary for complex 3-D topographic features.

The topographic amplification frequencies for a feature have been shown to be related to the size and stiffness of the feature (similar to that determined by other authors). In particular, the analytical height- and width-based topographic frequency estimation methods of Ashford and Sitar (1997) and Paolucci (2002), when combined, provide a good estimate of the topographic frequency range for a feature. In general, as the feature size (height and width) increased the topographic amplification frequency range decreased. However, it was determined that to properly estimated the amplification frequency range for larger features, the features should be broken up into smaller features along natural breaks in the slope, this insures that all potential topographic amplification frequencies are covered. When comparing the topographic amplification frequencies estimated using each analytical method, neither performed better in estimating the topographic amplification frequencies. The best results were obtained when the

estimated frequencies from both methods were combined to form a range of potential topographic amplification frequencies. Though for some cross sections and features (particularly the V-line), the estimation methods were not able to properly predict the correct topographic frequency band. Therefore, the 2D analytical methods are not foolproof at predicting the correct topographic amplification frequencies for 3D features.

9.3.6 Polarity of Topographic Effects

The polarity of amplification in Phase I was shown to be influenced by the direction of wave propagation into the slope in two ways: (1) Stations on the back side of the feature, opposing the direction of wave propagation from the source, recorded higher ground motions than stations located on the crest at frequencies greater than the measured topographic amplification range, and (2) the topographic amplifications recorded on the horizontal components at the crest were polarized in the direction of wave propagation, and not in the direction of steepest topography. The higher amplifications on the back side of the feature (referred to as path effects) are not believed to be related to the resonant frequency of the topography, but related to the azimuth and zenith angles of the incoming waves relative to the angle of the slope opposing the direction of wave propagation. These path effects cause an amplification at frequencies higher than the topographic amplification frequencies, resulting in higher ground motions for the stations opposing the direction of wave propagation. Therefore, for structures built on slopes, or for slope stability issues, the possibility of amplifications due to path effects should be investigated, but further information on the level of amplification cannot be provided using data from the current study.

Beyond path effects, the polarity of topographic amplification can also be influenced by the direction of wave propagation. For Phase I, topographic amplifications

were measured in both the N-S and E-W directions at the crest (virtually the same directions as the major topography orientation). However, the major polarity of amplifications was focused in NE-SW direction for the MRM method, which was directly in-line with the direction of wave propagation from the source area located 2 km NE of the topographic array. However for Phase II, when the source was located directly under the topographic array, the same crest station only recorded topographic amplifications in the E-W direction (in-line with the steep E-W topographic feature). Therefore, the direction of wave propagation can influence the direction of amplification recorded on 3D topographic features. Moreover for Phase II, all the topographic amplifications recorded in either the N-S or E-W directions were related to a steep topographic feature orientated in the same direction. In addition, N-S or E-W components not orientated in the direction of a steep topographic feature (i.e., no strong topographic relief in the same direction as the component orientation) measured an amplification of less than or equal to 1.0. Therefore, the topographic amplification polarity was controlled exclusively by the orientation of the topographic feature when the source was directly under the stations and the waves were propagating nearly vertically as they interacted with the slope.

9.4 FUTURE WORK

The use of frequent and predictable coal mine-induced seismicity has been shown to be viable for studying topographic effects in the linear strain range. The study discussed herein was successful at measuring topographic amplifications not only at the crests of features, but also along the slopes of features. Topographic effects have been shown to be a frequency band-limited phenomenon that causes amplifications typically between 2 to 3 times an “equivalent free-field” ground motion, but amplifications up to

10 are possible in unique causes. The polarity and strength of shaking has also been shown to be influenced by the direction and angle of wave propagation.

Given the research conducted in this study, further studies need to be conducted on the how seismic waves interact with 3D topographic features, similar to the topography under Stations A3 and B2, where a westward-facing E-W slope meets a steep N-S topographic feature. These 3D features produced very large (up to 10 using the MRM) amplifications in Phase II, which were not fully explained by the current study. Features that have 3D geometries should be further studied by placing stations along each of the slope faces of the feature to gain insight into how the 3D topography effects the amplification. The influence of wave propagation direction and polarity also need to be further investigated to understand the amplification factors and amplification frequency range of path effects. The influence of wave propagation direction needs to be further investigated to understand how it influences the polarity of topographic effects for 3D features.

Although this dissertations deals exclusively with processing seismic events produced by underground longwall coal mining, this type of seismic activity is not available everywhere (i.e., seismic activity does not occur on a daily basis everywhere in the world). Therefore, the use of background noise to estimate topographic effects needs to be explored. The dataset recorded for this study has significant amounts of data that include only background noise, and should be processed using the SSR, MRM, and HVSR methods to determine if topographic amplification can be identified using background noise and if similar spectral ratios to the one presented in this study can be calculated. The ability to determine topographic amplifications based on background noise would allow topography to be characterized for topographic effects in much the same way that soft soils are characterized for site effects.

To help fully understand the ground motions recorded in this topographic amplification field study, numerical modeling of the features instrumented in Phases I and II needs to be conducted to look at the 3D effects of the mountain. This significant dataset can be used to calibrate numerical models using two different source areas and multiple stations locations. To increase the usefulness of the numerical models, additional shear wave velocity profiles need to be collected on the mountain. With the low noise and high stiffness of the mountain area, shallow Spectral Analysis of Surface Waves (SASW) or Multichannel Analysis of Surface Waves (MASW) testing could be conducted at each of the station locations, and a depth of 15-20 m could be easily achieved under each station with a sledgehammer source. This would be very valuable in determining how topographic and soil site effects are interacting. In addition to the stiffness characteristics, further investigation need to be conducted into the source characteristics of the coal mining-induced seismicity, so that the source can be properly modeled.

Overall, all the results from the different part of this NEES-CR project, along with other projects, needs to be complied together to create a topographic effects provision for the United States building codes. Topographic effects have been shown in this study and many others to cause a frequency band limited amplification, which in many cases can lead to significantly higher ground motions for structures built on topographic features. In the design codes, the design response spectra should be modified by an amplification factor according to the location of the structure on the topographic feature (i.e., at the crest, along the slope, or at the base) and in the frequency range estimated using analytical methods.

This work was supported primarily by the George E. Brown, Jr. Network for Earthquake Engineering Simulation (NEES) of the National Science Foundation under Cooperative Agreement CMS-0126366 with CUREE (for the Consortium Development

project) and under other Cooperative Agreements for the work described herein for the separately funded NEES Equipment Site or System Integration projects. Part of the instruments used in the field program were provided by the PASSCAL facility of the Incorporated Research Institutions for Seismology (IRIS) through the PASSCAL Instrument Center at New Mexico Tech. Data collected during this experiment will be available through the IRIS Data Management Center. The facilities of the IRIS Consortium are supported by the National Science Foundation under Cooperative Agreement EAR-0552316 and by the Department of Energy National Nuclear Security Administration.

References

Aki, K. and K. Lamer (1970). Surface motion of a layered medium having an irregular interface due to incident plane SH waves, J. Geophys. Res. 75, 933-954.

Allen T.I., Dhu, T., Cummins, P.R., Schneider, J.F. (2006). Empirical Attenuation of Ground-Motion Spectral Amplitudes in Southwestern Western Australia, Bulletin of the Seismological Society of America, 96, (2): 572-585.

Ambraseys, N.N., 1960. On the shear response of a two-dimensional truncated wedge subjected to an arbitrary disturbance. Bulletin of the Seismological Society of America, 50, (1): 45-56.

Arabasz, W. J. Nava, S. J. McCarter, M. K. Pankow, K. L. Pechmann, J. C. Ake, J. McGarr, A. (2005). Coal-mining seismicity and ground-shaking hazard: A case study in the Trail Mountain area, Emery County, Utah. Bulletin of the Seismological Society of America, 95: 18-30.

Arabasz, W. J., S. J. Nava, M. K. McCarter, and K. L. Pankow (2002a). Ground-motion recording and analysis of mining-induced seismicity in the Trail Mountain Area, Emery County, Utah, Technical Report, University of Utah Seismograph Stations, Salt Lake City, Utah, 162 pp. Accessible online at www/seis.utah.edu/Reports/sitla2002a.

Arabasz, W. J., and J. C. Pechmann (2001). Seismic characterization of coal-mining seismicity in Utah for CTBT monitoring, Technical Report UCRL-CR-143772, Lawrence Livermore National Laboratory, Livermore, California, LLNL Research Agreement No. B344836, 120 pp. Accessible online at www/seis.utah.edu/Reports/llnl2001.

Arabasz, W. J., S. J. Nava, and W. T. Phelps (1997). Mining seismicity in the Wasatch Plateau and Book Cliffs coal mining districts, Utah, USA, in Rockbursts and Seismicity in Mines, S. J. Gibowicz and S. Lasocki (Editors), A. A. Balkema, Rotterdam, 111–116.

Arabasz, W. J. and Julander, D.R. (1984). Geometry of seismically active faults and crustal deformation within the Basin and Range-Colorado Plateau transition in Utah, Geo. Soc. Am. Special Paper 208, 43-74.

Assimaki, D., Gazetas, G., and Kausel, E. (2005). Effects of local soil conditions on the topographic aggravation of seismic motion: Parametric investigation and recorded

field evidence from the 1999 Athens Earthquake, Bulletin of the Seismological Society of America, 95, (3): 1059-1089.

Assimaki, D., Kausel, E., and Gazetas, G. (2005a). Soil-dependent topographic effects: A case study from the 1999, Athens Earthquake, Earthquake Spectra, 21, (4): 929-966.

Assimaki, D., Kausel, E., and Gazetas, G. (2005b). "Wave propagation and soil-structure interaction on a cliff crest during the 1999 Athens Earthquake," Soil Dynamics and Earthquake Engineering, 25, (7-10): 513-527.

Assimaki, D. and Kausel, E. (2007). Modified topographic amplification factors for a single-faced slope due to kinematic soil-structure interaction, Journal of Geotechnical and Geoenvironmental Engineering, ASCE, 133, (11): 1414-1431.

Ashford, S.A., Sitar, N., Lysmer, J. and Deng, N., 1997. Topographic effects on the seismic response of steep slopes. Bulletin of the Seismological Society of America, 87, (3): 701-709.

Ashford, S.A., Sitar, N., 1997. Analysis of topographic amplification of inclined shear waves in a steep coastal bluff. Bulletin of the Seismological Society of America 87 (3): 692–700.

Athanasopoulos G.A. and Zervas C.S. (1993). Effects of Ridge-like Surface Topography on Seismic. Site Response. Soil Dynamics and Earthquake Engineering VI. Vol. 3 pg 16.

Bard P.Y. (1999). Microtremor measurements: a tool for site effect estimation?. The Effects of Surface Geology on Seismic Motion, eds. K. Irikura, K. Kudo, H. Okada and T. Sasatani (Balkema, Rotterdam), 1251-1279.

Bard P. Y. (1982), Diffracted waves and displacement field over two-dimensional elevated topographies. Geophys. J. Int., 71, 731-760.

Barlow, N. (1933). Charles Darwin's Diary of the Voyage of H.M.S. Beagle, Nora Barlow (Editor), Cambridge U Press, New York.

Boore, D. M. and J. J. Bommer (2005). Processing of strong-motion accelerograms: Needs, options and consequences, Soil Dynamics and Earthquake Engineering 25: 93-115

Boore, D.M. (1972). "A note on the effect of simple topography on seismic SH waves," Bulletin of the Seismological Society of America, 62, (1): 275-284.

Bouchon M. and Barker J.S. (1996), Seismic response of a hill: the example of Tarzana, California, Bull. Seism. Soc. Am., 86, (1a): 66-72.

Bouchon, M., (1973). Effect of topography on surface motion., Bull. Seism. Soc. Am., 63, 615–632.

Borcherdt R.D. (1970), Effects of local geology on ground motion near San Francisco Bay. Bull. Seism. Soc. Am., 60, 29-61.

Bouckovalas, G.D. and Kouretzis, G., (2001). Review of Soil and Topography Effects in the September 7, 1999 Athens (Greece) Earthquake, Proceedings: Fourth International Conference on Recent Advances in Geotechnical Earthquake Engineering and Soil Dynamics and Symposium in Honor of Professor W.D. Liam Finn, San Diego, California.

Bradley, A. B., and M. Cubrinovski (2011). Near-source strong ground motions observed in the 22 February 2011 Christchurch earthquake. Seismological Research Letters 82, 853–865.

Buech, T., Davies, T., and Pettinga, J. (2010). The Little Red Hill Seismic Experimental Study: Topographic Effects on Ground Motion at a Bedrock-Dominate Mountain Edifice, Bulletin of the Seismological Society of America, 100, (5A): 2219-2229.

Buech, F. (2008). Seismic response of Little Red Hill—Towards an understanding of topographic effects and rock slope failure, Ph.D. Thesis, University of Canterbury, Christchurch, New Zealand, 138 pp.

Carver, D. and Hartzell, S.H., (1996). Earthquake site response in Santa Cruz, California. Bulletinof the Seismological Society of America, 86 (1A): 55-65.

Caserta A., F. Bellucci, G. Cultrera, S. Donati, F. Marra, G. Mele, B. Palombo and A. Rovelli (2000). Study of site effects in the area of Nocera Umbra (Central Italy) during the 1997 Umbria-Marche seismic sequence, Journal of Seismology, 4, 555-565.

Celebi, M. (1987). Topographical and geological amplifications determined from strong motion and aftershock records of the 3 March 1985 Chile earthquake, Bull. Seismol. Soc. Am. 77, (4): 1147–1167.

Chávez-García F., Miguel Rodríguez, Edward H. Field, and Denis Hatzfeld (1997). Topographic site effects. A comparison of two non-reference methods, Bull. Seism. Soc. Am., 87, 1667-1673.

Chavez-Garcia F., Sanchez L.R. and Hatzfeld D. (1996), Topographic site effects and HVSR. A comparison between observation and theory, Bull. Seism. Soc. Am., 86, (5): 1559-1573.

Dakoulas, P. and Gazetas, G., (1985). A class of inhomogeneous shear models for seismic response of dams and embankments. Soil Dynamics and Earthquake Engineering, 4, (4): 166-182.

Davis, L. L., and R. West (1973). Observed effects of topography on ground motion, Bull. Seism. Soc. Am. 63, 283–298.

Gao, S., Liu, H., Davis, P.M. and Knopoff, L., (1996). Localized amplification of seismic waves and correlation with damage due to the Northridge earthquake: Evidence for focusing in Santa Monica. Bulletin of the Seismological Society of America, 86, (1B): 209-230.

Geli, L., Bard, P., and Jullien B. (1988). The effect of topography on earthquake ground motion: a review and new results, Bull. Seism. Soc. Am., 78, 42-63.

Griffiths D. W. and Bollinger G. A. (1979). The effect of Appalachian Mountain topography on seismic waves, Bull. Seism. Soc. Am., 69, 1081-1105.

Haeussler, P.J., Schwartz, D.P., Dawson, T.E., Stenner, H.D., Lienkaemper, J.J., Sherrod, B., Cinti, F.R., Montone, P., Craw, P., Crone, A.J., and Personius, S.F., (2004), Surface rupture and slip distribution of the Denali and Totschunda faults in the 3 November 2002 M7.9 earthquake, Alaska: Bulletin of the Seismological Society of America, 94, (6B): S23-S52.

Hartzell, S. H., D. L. Carver, and K. W. King (1994). Initial investigation of site and topographic effects at Robinwood Ridge, California, Bull. Seismol. Soc. Am. 84 (5): 1336–1349.

Hough, S. E., Yong, A., Altidor, J. R., Anglade, D., Given, D., and Mildor, B. S.-L., (2011). Site characterization and site response in Port-au-Prince, Haiti, Earthquake Spectra, 3 (S1): S137-S155.

Hough, S. E., Altidor, J. R., Anglade, D., Given, D., Janvier, M. G., Maharrey, J. Z., Merremonte, M., Mildor, B. S.-L., and Prepetit, C., (2010). Localized damage caused by topographic amplification during the M7.0 Haiti earthquake, Nature Geoscience 3, 778–782.

Joh, S. H., (1996). Advances in interpretation and analysis techniques for spectral-analysis-of-surface-waves (SASW) measurements. Ph.D. Dissertation, Dept. of Civil,

Architectural, and Environmental Engineering, University of Texas, Austin, TX, 240 p.

Kawase H. and K. Aki (1990). Topography effect at the critical SV-wave incidence: possible explanation of damage pattern by the Whittier Narrows, California, earthquake of 1 October 1987, Bull. Seism. Soc. Am., 80, 1-22.

Khazai, B. and Sitar, N., (2003). Evaluation of factors controlling earthquake-induced landslides caused by Chi-Chi earthquake and comparison with the Northridge and Loma Prieta events. Engineering Geology, 71, 79-95.

Kosloff D., Kessler D., Filho Q.A., Tessmer E., Behle A. And Strahilevits R. (1990). Solution of the equation of dynamic elasticity by a Chebychev spectral method, Geophysics, 55, (6), 734-748.

LeBrun, B., Hatzfeld, D., Bard, P.Y. and Bouchon, M., (1999). Experimental study of the ground motion on a large scale topographic hill in Ktiherion (Greece). Journal of Seismology, 3, 1-15.

Lee, S.-J., Chan, Y.-C., Komatitsch, D., Huang, B.-S., Tromp, J., (2009a). Effects of realistic surface topography on seismic ground motion in the Yangminshan region of Taiwan based upon the spectral-element method and Lidar DTM. Bulletin of the Seismological Society of America, 99 (2A): 681–693.

Lee, S.-J., Komatitsch, D., Huang, B.-S., Tromp, J., (2009b). Effects of topography on seismic-wave propagation: an example from northern Taiwan. Bulletin of the Seismological Society of America, 99 (1): 314–325.

Lermo J. and Chavez-Garcia F.J. (1993). Site effect evaluation using spectral ratio with only one station, Bull. Seism. Soc. Am., 83, 1574-1594.

Lovati, S., Bakavoli, M., Massa, M., Ferretti, G., Pacor, F., Paolucci, R., Haghshenas, E., and Kamalian, M. (2011). Estimation of Topographical Effects at Narni Ridge (Central Italy): Comparison between Experimental Results and Numerical Modelling, Bull. Earthquake Eng. 9, (6): 1987-2005.

Lovati, S. (2011). Ground Motion Amplification Induced by Topographic Irregularities: Results, Open Issues, and Future Developments, Ph.D. Dissertation , Graduate School in Mechanics of Fluids and Solids, University studies in Genova, Via Balbi, Genova, pp. 184.

Marzorati S., Ladina C., Falcucci E., Gori S., Ameri G., and Galadini F. (2011). Site effects “on the rock”: the case of Castelvecchio Subequo (L’Aquila, Cnntral Italy), submitted to Bull. EarthquakeEngineering.

Massa, M., Lovati, S., Marzorati, S. and Augliera, P. (2011). Seismic Ground Motion Amplifications Estimated by Means of Spectral Ratio Techniques: Examples for Different Geological and Morphological Settings, Earth and Enviromental Sciences Imran Ahmad Dar and Mithas Ahmad Dar (Ed.), ISBN: 978-953-307-468-9, InTech, Available from: http://www.intechopen.com /articles/show/title/seismic-ground-motion-amplifications-estimated-by-means-of-spectral-ratio-techniques-examples-for-di

Massa, M.; Lovati, S., D'Alema, E., Ferretti, G. & Bakavoli, M. (2010). An experimental approach for estimating seismic amplification effects at the top of a ridge, and the implication for ground-motion predictions: the case of Narni (central Italy), Bull. Seism. Soc. Am., 100, (6): 3020-3034.

Maufroy, E., Cruz-Atienza, V.M., Gaffet, S. (2012). A Robust Method for Assessing 3-D Topographic Site Effects: A Case Study at the LSBB Underground Laboratory, France, Earthquake Spectra, 28, (3): 1097-1115.

Nakamura Y. (1989). A method for dynamic characteristics estimations of subsurface using microtremors on the ground surface, Quarterly Rept. RTRI Japan 30, 25-33.

Paolucci, R., (2002). Amplification of earthquake ground motion by steep topographic irregularities, Earthq. Eng. and Struct. Dyn., 31, 1831–1853.

Paolucci, R., Faccioli, E. and Maggio, F., (1999). 3D Response analysis of an instrumented hill at Matsuzaki, Japan, by a spectral method. Journal of Seismology, 3, 191-209.

Pechmann, J. C., W. J. Arabasz, K. L. Pankow, R. Burlacu, and M. K. McCarter (2008). Seismological report on the 6 August 2007 Crandall Canyon Mine collapse in Utah. Seismological Research Letters 79, 620–636.

Pedersen H., Le Brun B., Hatzfeld D., Campillo M. and Bard P.Y. (1994). Ground-motion amplitude across ridges, Bull. Seism. Soc. Am., 84, 1786-1800.

Pischiutta M., Cultrera G., Caserta A., Luzi L. and Rovelli A. (2010). Topographic effects on the hill of Nocera Umbra, central Italy, Geophysical Journal International, 182, (2): 977–987.

Plafker, G., Ericksen, G.E. and Fernandez Concha, J., 1971. Geological aspects of the May 31, 1970, Peru earthquake. Bulletin of the Seismological Society of America, 61, (3): 543-578.

Ponti, D. J., and R. E. Wells (1991). Off-fault ground ruptures in the Santa Cruz Mountains, California: Ridge-top spreading versus tectonic extension during the 1989 Loma Prieta earthquake, Bull. Seismol. Soc. Am. 81, (5): 1480–1510.

Poppeliers, C., and Pavlis, G. L. (2002). The seismic response of a steep slope: high-resolution observations with a dense, three-component seismic array, Bull. Seism. Soc. Am. 92, 3102–3115.

Rathje, E. M., Bachhuber, J., Dulberg, R., Cox, B. R., Kottke, A., Wood, C., Green, R., Olson, S., Wells, D., Rix, G., (2011). Damage Patterns in Port-au-Prince during the 2010 Haiti earthquake, Earthquake Spectra, 27, (S1): S117-S136.

Sanchez-Sesma, F., Rodriquez, M., Iturraran-Viveros, U, Luzon, F. Campillo, M, Margerin, L, Garcia-Jerez, A., Suarez, M., Santoyo, M. and Rodriquez-Castellanos, A. (2011). A theory for microtremor H/V spectral ratio: application for a layered medium. Geophys. J. Int. 186, 221-225.

Sanchez-Sesma, F. J., (1985). Diffraction of elastic SH waves by wedges, Bull. Seism. Soc. Am. 75, 1435–1446.

Sepúlveda, S.A., Murphy, W., Jibson, R.W. and Petley, D.N., (2005a). Seismically induced rock slope failures resulting from topographic amplification of strong ground motions: The case of Pacoima Canyon, California. Engineering Geology, 80, 336-348.

Sills L. (1978). Scattering of horizontally polarised shear waves by surface irregularities, Geophys. J. R. Astr. Soc. 54, 319-348.

Smith W. D. (1975). The application of finite element analysis to body wave propagation problems, Geophys. J. 42,747-768.

Spudich P., Hellweg M., and Lee W.H.K. (1996). Directional topographic site response at Tarzana observed in aftershocks of the 1994 Northridge, California, earthquake: implications for mainshock motions, Bull. Seism. Soc. Am., 86, 193-208.

Steidl J.H., Tumarkin A.G., Archuleta R.J. (1996). What is a reference site ?, Bulletin of the Seismological Society of America, 86, 1733-1748.

Stewart, J.P. and Sholtis, S.E. (2005). Case study of strong ground motion variations across cut slope, Soil Dynamics and Earthquake Engineering, 25 (7-10), 539-545.

Wald, D.J., Quitoriano, V., Heaton, T.H., and Kanamori, H., (1999). Relationship between Peak Ground Acceleration, Peak Ground Velocity, and Modified Mercalli Intensity in California: Earthquake Spectra, 15, (3): 557-564.

Williams, D.J. and W.J. Arabasz, (1989). Mining-related and tectonic seismicity in the East Mountain area, Wasatch Plateau, U.S.A., PAGEOPH 129, 345-368.

Wilson, D. C., and Pavlis, G. L. (2000). Near-surface site effects in crystalline bedrock: a comprehensive analysis of spectral amplitudes determined from a dense, three-component seismic array, Earth Interactions 4, 1–31.

Wong, I. G. (1993). Tectonic stresses in mine seismicity: are they significant?, in Rockbursts and Seismicity in Mines 93, R. P. Young (Editor), A. A. Balkema, Rotterdam, 273–278.

Wong, H.L. and Jennings, P.C., (1975). Effects of topography on strong ground motion. Bulletin of the Seismological Society of America, 65, (5): 1239-1257.

Yoon S. and Rix G.J. (2009). "Near-field effects on array-based surface wave methods with active sources," *Journal of Geotech. And Geoenvir. Engrg.*, 135, (3): 399-406.

Zahradnik, J. and L. Urban (1984). Effect of a simple mountain range on underground seismic motion, Geophys. J. R. Astr. Soc. 79, 167-183.

Zaslavsky Y. and Shapira A. (2000). Experimental study of topographic amplification using the Israel Seismic Network. Journal of Earthquake Engineering, 4, 43-65.

Zywicki, D.J. (1999). Advanced signal processing methods applied to engineering analysis of seismic surface waves. *Ph.D. Dissertation*, School of Civil and Environmental Engineering, Georgia Institute of Technology, Atlanta, GA, 357 p.

Vita

Clinton Miller Wood was born in Fayetteville, Arkansas in 1984. He is one of three sons born to Jim and Karen Wood. Clinton was raised in Elkins, Arkansas and graduated valedictorian of Elkins High School in 2003. He received his B.S.C.E degree in May 2007 from The University of Arkansas in Fayetteville, Arkansas. He received his M.S.C.E degree in May 2009 from The University of Arkansas. He started his Ph.D. in Civil Engineering at The University of Arkansas in May of 2009, and transferred to The University of Texas at Austin in August of 2012 to complete his degree.

Permanent email: clinton.m.wood@gmail.com

This dissertation was typed by Clinton Miller Wood